

論文 / 著書情報
Article / Book Information

題目(和文)	
Title(English)	Seismic Performance and Design Procedure for Controlled Spine Frame Structures
著者(和文)	陳星辰
Author(English)	Xingchen Chen
出典(和文)	学位:博士(工学), 学位授与機関:東京工業大学, 報告番号:甲第10647号, 授与年月日:2017年9月20日, 学位の種別:課程博士, 審査員:竹内 徹,坂田 弘安,五十嵐 規矩夫,堀田 久人,田村 修次
Citation(English)	Degree:Doctor (Engineering), Conferring organization: Tokyo Institute of Technology, Report number:甲第10647号, Conferred date:2017/9/20, Degree Type:Course doctor, Examiner:,,,,,
学位種別(和文)	博士論文
Type(English)	Doctoral Thesis

Seismic Performance and Design Procedure for Controlled Spine Frame Structures

Doctoral Dissertation, 2017

Xingchen Chen

Supervisor: Prof. Toru Takeuchi

Department of Architecture and Building Engineering
Tokyo Institute of Technology

ACKNOWLEDGEMENTS

This thesis is a summary of five years fulfilling study since I came to Takeuchi Lab. Over the past five years I have received great support and encouragement from a group of wonderful individuals. Without their support, this research would not have been possible. Besides, this is my first experience of studying abroad. They have offered me the warmth of a big family and bring enormous happiness in my life in Japan. The experience was much more than I could have expected and allowed me to further develop my academic skills as well as personality.

In the first place, I would like to express profound gratitude to my supervisor, Prof. Toru Takeuchi. No matter how busy Takeuchi-Sensei is, he has been always available to guide me in my research. He is extremely kind and has taught me much essential knowledge on earthquake engineering as well as research method. He has also provided me many precious opportunities to present myself and expand my horizons. His invaluable and patient support, encouragement, meticulous care enabled me to complete my doctoral study and to start my academic career. I am very fortunate to be Takeuchi-Sensei's student. I deeply esteem his creativity, passion, persistence, and thoughtful as a researcher, engineer and educator. He is a paradigm for me to study. My special thanks go to our assistant professor, Dr. Ryota Matsui for his crucial contribution to my research as well as his caring and effort to help me with my daily life and career development.

Many thanks go to Mr. Bin Huang, Mr. Ben Sitler, Mr. Kazuhiro Fujishita, and Mr. Paochun Lin. Discussion with them always inspired me to come out with fresh ideas and their deep affection in research also encouraged me to persist with my study during the hard time. I would like to express my appreciation to all my great fellow students, particularly to Miss Yuka Yamaura, my tutor when I firstly came, Miss Akiko Kobayashi, Mr. Michiho Yoshida, Miss Saki Mihara, Mr. Shunji Urui, Mr. Daisuke Shiiki, Mr. Yuki Terazawa, and all the other students from Takeuchi Lab. Thank them for offering all the support, advice, and precious friendships to me. All the funny or tough stuffs we have done together will hold a special place in my life's memory bank. Thanks for everything they have done for me. Thanks for being by my side and always generating energy and happiness in our daily lives. Their hard-working also inspire me to endeavor to do better in my study. Wish all of them will have brilliant future.

Moreover, I would like to express my deep appreciation to the examiners of my thesis, Prof. Toru Takeuchi, Prof. Hiroyasu Sakada, Prof. Kikuo Ikarashi, Prof. Hisato Hotta, and Prof. Shuji Tamura for taking time out of their busy schedule to read my thesis and give positive feedback.

Last but not least, I would like to express my deepest appreciation to my father, mother, grandmother and all my lovely families. Thanks for their support, understanding, and absolute trust and love for me to explore my life.

ABSTRACT

This study proposes an innovative controlled spine frame system to prevent damage concentration and ensure continuous usability of buildings after large earthquakes. The proposed spine frame system consists of stiff spine frames, replaceable energy-dissipating members (i.e., dampers), and envelope moment-resisting frames. The spine frames prevent deformation concentration in specific stories. The envelope moment frames are designed to remain elastic and ensure sufficient self-centering capacity. Input seismic energy is absorbed by dampers, which feature significant energy dissipating capacity, and if required can be easily replaced following a large earthquake.

Superior seismic performance of the proposed system in deformation distribution, energy dissipation, self-centering capacity, robustness against severe earthquakes and irregular stiffness, are validated and compared with the conventional shear damper (SD) and post-tension strands equipped uplifting rocking systems (LU) by dynamic analysis with various ground motion intensities. Effect of key structural characteristics on seismic performance of the controlled spine frame system with various heights has been investigated by extensive parametric study. A simplified dual multi-degree-of-freedom (DMD) model with a nonlinear dynamic analysis program is developed for the proposed system, which greatly improves the computing efficiency of the parametric analysis. Range of application of the proposed system and optimal range of key structural parameters are established based on the parametric study.

Segmented spine frame (Sgt) is proposed for an easier application of spine frames in high-rise buildings by avoiding immense demand on energy-dissipating amount of dampers or strength of spine frames. Optimal number of segments, location of each segment, and ‘upper damper’-to-‘bottom damper’ stiffness ratio have been investigated by parametric study.

A simple seismic evaluation and design procedure based on equivalent linearization technique and response spectrum analysis is developed for the proposed spine frame system, based on the further simplified single-degree-of-freedom (SDOF) models. Two sets of processes are developed respectively for structures whose seismic response is first-mode dominant, and structures whose higher-modes effect cannot be ignored. Seismic response of both continuous spine frames (Cnt) and Sgt models are well estimated with appropriate conservatism by utilizing the proposed evaluation method. Distinct limitation for applying the design procedure is established in terms of structural vibration characteristics. Boundary of key structural index is determined based on a desired accuracy of the evaluated results.

Contents

1. Introduction

- 1.1 Background and motivation 1-1
- 1.2 Previous study on various spine frame structures 1-5
- 1.3 Objective and outlines of the dissertation 1-15

2. Concepts and Seismic Performance of Controlled Spine Frames Applied in Low-rise Buildings

2.1 Introduction

- 2.1.1 Conventional frame with shear dampers as BRBs (SD system) 2-1
- 2.1.2 Controlled uplifting rocking frame system (LU system) 2-4
- 2.1.3 Non-uplifting spine frame system (NL system) 2-7
- 2.1.4 Prototype building 2-11
- 2.1.5 Design of the SD, LU, and NL models 2-13

2.2 Seismic performance of regular models

- 2.2.1 Static performances 2-18
- 2.2.2 Seismic responses under Level 2 earthquake 2-18
- 2.2.3 Incremental dynamic analyses 2-27

2.3 Seismic performance of single story structural irregular models

- 2.3.1 Design of single-story structural irregular models 2-29
- 2.3.2 Seismic responses against level 2 earthquake 2-33
- 2.3.3 Incremental dynamic analyses 2-39

2.4 Conclusions 2-47

3. Simplified Dual Multi-Degree-of-Freedom Model of Controlled Spine Frame Structures

3.1 Introduction 3-1

3.2 Design of the benchmark building structures

- 3.2.1 Design of the 5-story building structure 3-2
- 3.2.2 Design of the 10-story building structure 3-6
- 3.2.3 Design of the 20-story buildings structure 3-11

3.3 Dual multi-degree-of-freedom (DMD) model

- 3.3.1 Basic concepts and assumptions of DMD model 3-15

3.3.2	Simplification of the moment frames	3-16
3.3.3	Simplification of the spine frames	3-19
3.4	Programming for nonlinear analysis of DMD model	
3.4.1	Construction of stiffness matrix by static condensation	3-26
3.4.2	Nonlinear time-history analysis algorithm	3-27
3.4.3	Verification of the nonlinear analysis program	3-33
3.5	Verification and limitation of DMD model	3-37
3.6	Conclusions	3-39
4.	Evaluation Method and Design Procedure of Controlled Spine Frames Applied in Low-rise Buildings	
4.1	Introduction	4-1
4.2	Equivalent single-degree-of-freedom (SDOF) model	
4.2.1	Simplification of main frame	4-1
4.2.2	Simplification of damper	4-3
4.2.3	Evaluation of equivalent damping ratio and natural period	4-4
4.2.4	Evaluation of peak deformation and force response	4-9
4.3	Simple design procedure utilizing SDOF model	
4.3.1	Design procedure	4-13
4.3.2	Preliminary verification of design method	4-14
4.4	Parametric study of controlled spine frame structures	
4.4.1	Control parameters	4-14
4.4.2	Effect of yielding drift of dampers	4-20
4.4.3	Effect of damper-to-moment frame stiffness ratio	4-23
4.4.4	Effect of spine-to-moment frame stiffness ratio	4-27
4.4.5	Optimal structural parameters and applicable scope of design procedure	4-31
4.5	Conclusions	4-33
5.	Seismic Performance of Controlled Spine Frames Applied in High-rise Buildings	
5.1	Introduction	5-1
5.2	Benchmark building structures	
5.2.1	Design of the 30-story building structure	5-1
5.2.2	Variable spine frame configurations	5-5
5.2.3	Control parameters	5-7

5.3 Parametric study of continuous spine frame (Cnt) models

5.3.1 Effect of spine-to-moment frame stiffness ratio 5-8

5.3.2 Effect of damper-to-moment frame stiffness ratio 5-11

5.4 Parametric study of partial spine frame (Prt) models

5.4.1 Concept of Prt model 5-14

5.4.2 Vibration characteristics of Prt models 5-15

5.4.3 Seismic performance of Prt models 5-17

5.5 Parametric study of two-segment spine frame (Sgt2) models

5.5.1 Concept of Sgt model 5-18

5.5.2 Vibration characteristics of 20-story Sgt2 models 5-18

5.5.3 Optimal location of segment story of 20-story Sgt2 models 5-20

5.5.4 Optimal damper amount of 20-story Sgt2 models 5-22

5.5.5 Vibration characteristics of 30-story Sgt2 models 5-25

5.5.6 Optimal location of segment story of 30-story Sgt2 models 5-27

5.5.7 Optimal damper amount of 30-story Sgt2 models 5-28

5.6 Parametric study of three-segment spine frame (Sgt3) models

5.6.1 Vibration characteristics of Sgt3 models 5-31

5.6.2 Optimal locations of segment stories 5-33

5.6.3 Optimal damper amount of Sgt3 models 5-36

5.7 Conclusions 5-40

6. Evaluation Method and Design Procedure of Controlled Spine Frames Applied in High-rise Buildings

6.1 Introduction 6-1

6.2 Basic concepts of modal pushover analysis

6.2.1 Linearly elastic systems 6-2

6.2.2 Inelastic systems 6-4

6.2.3 Modal combination rules 6-6

6.3 Seismic evaluation methods

6.3.1 Modal pushover analysis (MPA) 6-7

6.3.2 Response spectrum analysis (RSA) 6-7

6.4 Seismic evaluation of Cnt models

6.4.1 Evaluation of Cnt models by MPA method 6-9

6.4.2 Evaluation of Cnt models by RSA method 6-30

6.5 Seismic evaluation of Sgt models

6.5.1 Evaluation of Sgt models by MPA method 6-48

6.5.2 Evaluation of Sgt models by RSA method 6-60

6.6 Design procedure for high-rise controlled spine frame structures 6-75

6.7 Conclusions 6-79

7. Conclusions 7-1

Appendix

A Detailed Information of Prototype Building A-1

B OpenSees Model Scripts of Spine Frame Structure B-1

C Programming scripts for nonlinear analysis of DMD Model C-1

Notations

Abbreviations

PGV:	peak ground motion velocity
PGA:	peak ground acceleration
SD:	conventional frame with shear dampers as BRBs
LU:	uplifting rocking frame
NL:	non-uplifting spine frame
SMRF:	steel moment-resisting frame
BRC:	buckling-restrained column member
BRB:	Buckling-restrained brace
BRBF:	buckling-restrained braced frame
RF:	rocking frame
CPE:	cumulative plastic strain energy
DCF:	story drift concentration factor (maximum SDR : RDR ratio)
DM:	damage measure
IDA:	incremental dynamic analysis
IM:	intensity measure
PT:	post-tensioned
RDR:	roof drift ratio
ReSDR:	residual story drift ratio
SDR:	story drift ratio
SF:	spine frame
MDOF:	multi-degree-of-freedom
DMD:	dual multi-DOF
MBM:	member-by-member
Cnt:	continuous spine frame

Prt:	partial spine frame
Sgt2:	two-segment spine frame
Sgt3:	three-segment spine frame
Kdf:	damper-to-moment frame stiffness ratio
Ksf:	spine-to-moment frame stiffness ratio
MPA:	modal pushover analysis
RSA:	response spectrum analysis
THA:	time-history analysis
SRSS:	square-root-of-sum-of-squares
CQC:	complete quadratic combination
ABSSUM:	absolute sum
MF:	moment frame
SF:	spine frame
BRC i :	i -th BRC hinge

Subscripts

f :	moment-resisting frame; main frame excluding damper
d :	damper
s :	spine frame
t :	total
i :	floor number; story number; DOF; time step
y :	yielding
eq :	equivalent
b :	beam
c :	column
u :	translational DOF
r :	rotational DOF

t : time variable

Front subscript

n : mode number

r : mode number

Superscripts

j : iteration loop number

T : column top

B : column bottom

Roman Symbols

A_{PT} : sectional area of PT strands

$A_c^{BRC(BRB)}$: sectional area of plastic region of BRC (BRB)

$A_e^{BRC(BRB)}$: sectional area of plastic region of BRC (BRB)

A_i : distribution factor of seismic load along the structure height

${}_nA(t)$: pseudo-acceleration of n th-mode SDOF system

b_{rf} : width of rocking frame (spine frame)

\mathbf{c} : damping matrix

C_0 : standard shear coefficient

D_{h0} : intrinsic damping reduction factor

D_{si} : structure characteristic coefficient

${}_nD(t)$: deformation of n th-mode SDOF system

${}_nD$: peak value of ${}_nD(t)$; deformation spectrum ordinate due to ${}_nT$ and ${}_nh$

${}_nD_y$: yielding deformation of n th-mode SDOF system

E_{BRC} : Young's modulus of BRC material

E_{PT} : Young' modulus of PT strands material

E_{ea} : equivalent elastic strain energy of damper

E_{ef} : equivalent elastic strain energy of main frame

E_{eq}^{BRC} : “equivalent Young’s modulus” of BRC
 E_{pa} : hysteretic energy of damper
 E_{pf} : hysteretic energy of main frame
 $(EI)_{eq}$: equivalent sectional bending stiffness of spine frame
 $(EI/h)_{cij}$: sum of line stiffness of all columns at j -th connection in i -th story of moment frame
 $(EI/l)_{bij}$: sum of line stiffness of all beams at j -th connection in i -th story of moment frame
 F_{LS} : pre-stress loss of PT strands
 F_{PT} : axial force of PT strands when BRCs yield in LU model
 F_e : stiffness factor
 F_{es} : shape factor
 F_s : eccentricity factor
 F_y^{BRC} : axial yielding force of BRC
 ${}_n\mathbf{f}$: peak value of equivalent static force vector, mode n
 G_{rf} : dead load of rocking frame
 $(GA)_{eq}$: equivalent sectional shear stiffness of spine frame
 H : height of entire structure
 H_{Nb} : height of segment story
 H_{eq} : equivalent height
 H_i : height from ground level to i -th floor
 ${}_iH_d$: location of equivalent damping force, mode i
 h_0 : intrinsic damping ratio
 h_{eq} : damping ratio averaged over $\mu=1\sim\mu_t$
 h_{eq}' : equivalent damping ratio corresponding to θ_t
 h_i : height of i -th story
 h_r : damping ratio of design spectrum
 ${}_nh$: damping ratio for n -th mode
 I_{bij} : second moment of sectional area of j -th beam in i -th story

I_{cij} :	second moment of sectional area of j -th column in i -th story
K_{feq} :	equivalent stiffness of main frame
K_a :	stiffness of additional damper system
K_{bi} :	rotational stiffness of representing beam spring at i -th story of moment frame
K_c :	stiffness of spine frame when deform with moment frame
\mathbf{K}_{ci} :	stiffness matrix of representing column at i -th story of moment frame
\mathbf{K}_{cij} :	stiffness matrix of j -th column in i -th story of moment frame
K_{d1} :	rotational stiffness of BRC1
K_{d2} :	rotational stiffness of BRC2
K_d :	stiffness of damper
K_d :	initial stiffness of damper
K_{deg} :	equivalent stiffness of damper
K_{eq} :	equivalent stiffness
K_{f+a} :	stiffness of entire structure
K_f :	stiffness of main frame; or simplified stiffness of moment frame
K_f :	initial stiffness of moment-resisting frame
K_{fh} :	hardening stiffness of main frame
K_s :	simplified stiffness of spine frame
K_{sb} :	equivalent bending stiffness of spine frame
\mathbf{K}_{si} :	stiffness matrix of spine frame at i -th story
K_{ss} :	equivalent shear stiffness of spine frame
${}_nK$:	generalized stiffness for n -th mode
\mathbf{k} :	stiffness matrix
k_{bi} :	lateral stiffness of beams in i -th story of moment frame
k_{ci} :	lateral stiffness of columns in i -th story of moment frame
k_{fi} :	lateral stiffness of i -th story of moment frame
${}^r k_i^{j+1}$:	rotational stiffness of BRC hinge

$\mathbf{1}$:	distribution vector of earthquake effect, $\mathbf{1}^T = [1, 1, 1, \dots, 1]$ herein
l_{BRC} :	length of BRC
l_{PT} :	length of PT strands
$l_c^{\text{BRC (BRB)}}$:	length of plastic region of BRC (BRB)
$l_e^{\text{BRC (BRB)}}$:	length of elastic region of BRC (BRB)
l_{ij} :	length of j -th beam in i -th story
${}_1M_2$:	bending moment of BRC2, mode 1
M_{Lij} :	left end moments at j -th beam in i -th story of moment frame
M_{OT} :	overturning moment
M_{OT_LU} :	initial yielding overturning moment of LU model
M_{OT_NL} :	initial yielding overturning moment of NL model
M_{OT_SD} :	initial yielding overturning moment of SD model
M_{Rij} :	right end moments at j -th beam in i -th story of moment frame
M_{cij} :	bending moment of j -th column in i -th story of moment frame
M_{dy1} :	yielding bending moment of BRC1
M_{eq} :	equivalent weight
M_m :	bending moment of moment frame
M_s :	bending moment of spine frame
M_{si} :	bending moment of i -th story of spine frame
M_t :	bending moment of entire structure
${}_nM$:	generalized mass for n -th mode
${}_nM_{eq}$:	effective modal mass of n th-mode SDOF system
\mathbf{m} :	mass matrix
m_i :	mass of i -th floor
N :	number of DOFs
N :	total number of stories
\mathbf{p} :	external force vector

p :	hardening stiffness ratio of main frame
$\mathbf{p}_{\text{eff}}(\mathbf{t})$:	effective earthquake force vector
${}_n\mathbf{p}_{\text{eff}}(\mathbf{t})$:	$\mathbf{p}_{\text{eff}}(\mathbf{t})$ due to mode n
$Q^{(0)}$:	maximum base shear of elastic main frame with damping ratio $h_0=0.02$
Q_{dy} :	yielding shear force of damper in NL model
Q_u :	shear force bearing capacity (corresponding to 2% story drift ratio)
Q_{uni} :	necessary shear force bearing capacity of i -th story
Q_{yi}^{BRB} :	yielding shear force of BRBs at i -th story in SD model
${}^r q_i^{(j+1)}$:	restoring moment of BRC hinge
q :	damper-to-main frame stiffness ratio
${}_r q(\mathbf{t})$:	r -th modal coordinate
R_a :	acceleration reduction factor
R_d :	displacement reduction factor
$\Delta R_i^{(j)}$:	mass-normalized residual force increment
R_{kfi} :	lateral stiffness reduction ratio of i -th story of moment frame
R_t :	seismic response reducing factor
$r(\mathbf{t})$:	any response quantity
r :	stiffness ratio of main frame and entire structure
r_p :	peak value of combined response
${}_n r(\mathbf{t})$:	$r(\mathbf{t})$ due to mode n
${}_n r$:	peak value of ${}_n r(\mathbf{t})$
${}_n r_p$:	peak value of n th modal response
S_A :	pseudo-acceleration spectrum ordinate, $S_A(T, h)$
S_D :	deformation spectrum ordinate, $S_D(T, h)$
S_V :	pseudo-velocity spectrum ordinate, $S_V(T, h)$
$S_{a,\max}$:	maximum pseudo-acceleration spectrum ordinate
$\overline{S_{pv}}$:	pseudo-velocity spectrum averaged over $T=T_{f+a} \sim T_{eq}$

${}_n\mathbf{s}^*$:	spatial distribution of effective earthquake force for entire structure, mode n
${}_n\mathbf{s}_f^*$:	spatial distribution of effective earthquake force for main frame, mode n
T :	fundamental period
T_c :	ground-type period
T_{eq} :	equivalent period
T_{f+a} :	fundamental period of entire structure
T_f :	fundamental period of main frame
T_i :	critical period
${}_nT_0$:	elastic period of entire structure, mode n
${}_nT_f$:	elastic period of main frame, mode n
$\ddot{\mathbf{u}}$:	acceleration vector
$\dot{\mathbf{u}}$:	velocity vector
\mathbf{u} :	displacement vector
${}^r u_i^{(j+1)}$:	angular displacement of BRC hinge
${}^r \dot{u}_i^{(j+1)}$:	angular velocity of BRC hinge
\ddot{u}_g :	ground motion acceleration
${}_n u_i$:	i -th floor displacement, mode n
u_{dy} :	yielding deformation of damper
u_i :	lateral displacement at i -th floor of moment frame
u_i' :	later displacement of spine frame due to flexural deformation at i -th floor
u_i'' :	later displacement of spine frame due to shear deformation at i -th floor
u_m :	maximum deformation of entire structure
u_r :	static residual deformation
V_{cij} :	lateral force of j -th column in i -th story of moment frame
V_m :	shear force of moment frame
V_s :	shear force of spine frame
V_{si} :	lateral force of i -th story of spine frame

V_t :	shear force of entire structure
${}_nV_b$:	base shear due to n -th mode
W :	weight of entire structure
w_j :	weight of j -th story
Z :	seismic zones coefficient

Greek Symbols

α_i :	weight ratio (i -th to top stories weight / total weight)
γ :	modification factor for force of moment frame, RSA method
γ_{ij} :	bending stiffness ratio of beams and columns at j -th connection in i -th story
δ_i :	lateral displacement of i -th floor in pushover analysis
θ_{Lij} :	left end rotation at j -th beam in i -th story of moment frame
θ_{Rij} :	right end rotation at j -th beam in i -th story of moment frame
θ_{dy}, θ_y :	yielding drift of damper
θ_{fy} :	yielding drift of frame
θ_i :	node rotation at i -th floor of moment frame
θ_{ij} :	rotation angle of j -th beam-to-column connection in i -th story
θ_i^s :	node rotation at i -th floor of spine frame
θ_t :	target drift
θ_y^{LU} :	yielding uplift ratio
$\theta_t^{(0)}$:	maximum drift of elastic main frame with damping ratio $h_0=0.02$
${}_1\theta_1$:	rotation of BRC1, mode 1
${}_1\theta_2$:	rotation of BRC2, mode 1
σ_0 :	initial tensile stress of PT strands
σ_y :	yielding tensile stress of PT strands
${}_n\Phi$:	n -th natural vibration mode of entire structure
${}_n\Phi_f$:	n -th natural vibration mode of main frame

- ${}_n\varphi_i$: i -th element of ${}_n\boldsymbol{\varphi}$
- ρ_{in} : correlation coefficient for i th and n th modes
- ${}_n\beta$: modal participation factor
- ${}_n\Delta_i(t)$: story drift of i -th story in mode n
- μ : ductility ratio
- μ_d : ductility ratio of damper
- μ_f : ductility ratio of main frame
- μ_i : ratio of damper-to main frame ductility ratio

CHAPTER 1

Introduction

- 1.1 Background and motivation 1-1
- 1.2 Review of previous investigations 1-5
- 1.3 Objective and outlines of the dissertation 1-15

Chapter 1 – Introduction

1.1 Background and motivation

Performance-based seismic design of building structures has been under development since the early 1970s in the United States, with the realization that buildings with higher importance level should have higher performance, while enhancing strength alone may neither improve safety nor reduce damage. Performance-based seismic design is the methodology of designing building structures to achieve particular desired performance under earthquake shaking. Over the years, the importance of strength distribution through a building, the inelastic structural response to major earthquakes, as well as requirements for both structural and non-structural components construction quality assurance have been added in the consideration of performance-based building design.

Figure 1.1 shows the basic performance-based design process. Firstly, the quantitative performance objectives are selected. Then preliminary design is carried out and assessed to judge whether the design satisfies the required performance level.

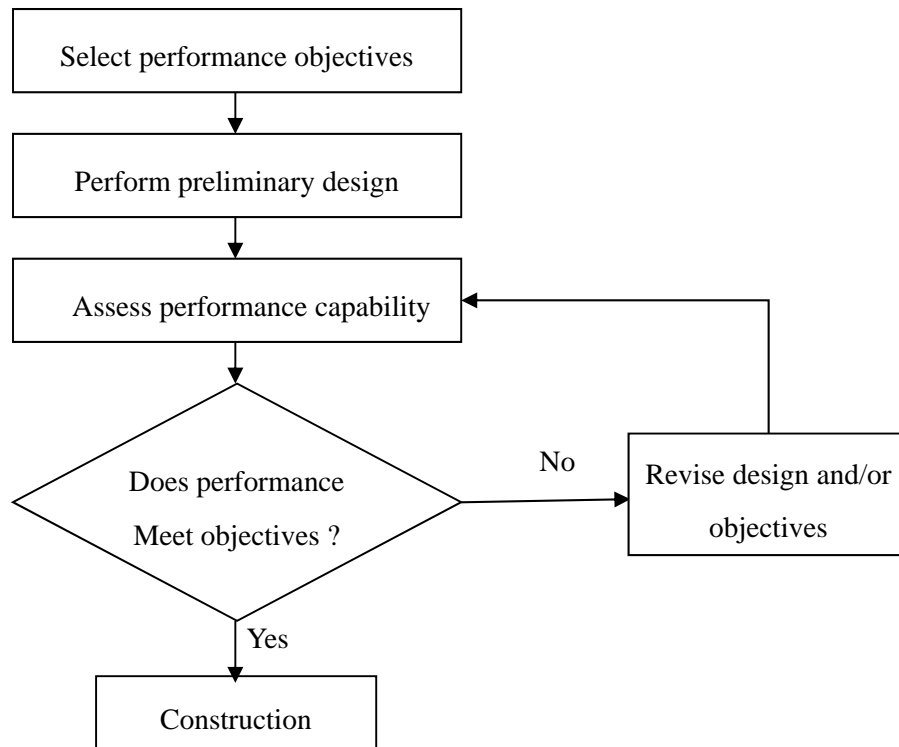


Figure 1.1 Flowchart of the performance-based design process ^[1.1]

Performance objectives are desired performance coupling of expected performance level with expected levels of seismic ground motions. The present-generation performance-based design

identifies performance levels for both structural and non-structural components as the following discrete four levels ^[1.2]:

Fully functional: backup utility services maintain functions; very little damage

Operational / Immediate occupancy: the building remains safe to occupy; any repairs are minor

Life safe: structure remains stable and has significant reserve capacity; hazardous nonstructural damage is controlled

Near collapse / Collapse prevention: the building remains standing, but only barely; any other damage or loss is acceptable

These performance levels are evaluated at a specified ground motion level, as shown in Fig 1.2.

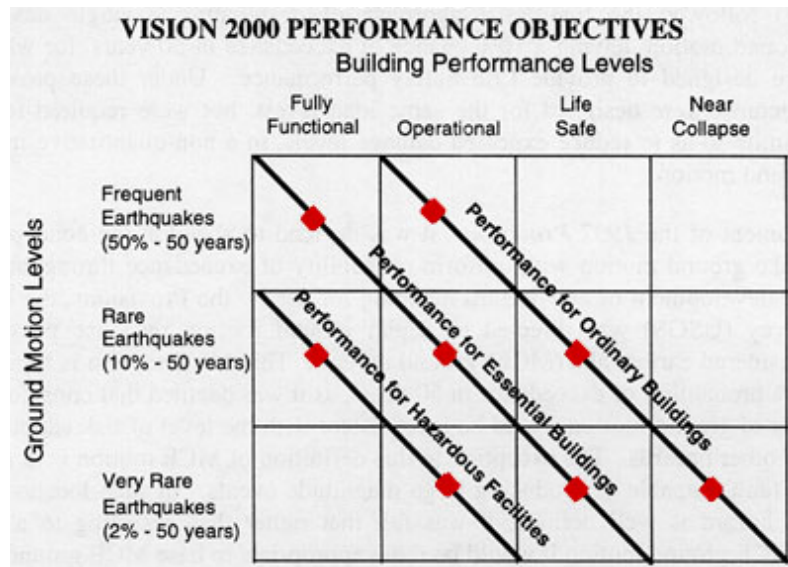


Fig. 1.2 Relationship between ground motion design level and performance level ^[1.2]

The discrete performance levels have been updated to new performance measures that better relate to the decision-making needs of stakeholders in the next-generation performance based seismic design ^[1.3]. It is suggested to evaluate the earthquake consequences of building structures from the view of casualties (deaths and serious injuries), direct economic loss (repair and replacement costs), indirect economic and social losses (red tags, repair and re-occupancy time), and energy and carbon consequences of poor performance.

Lessons learned from the past earthquakes tell us that, different structural systems, all designed to the same criteria, have far different likely seismic performance and earthquake losses. Besides, it is seldom as economic as expected to repair a ductile building which was designed following the performance design, particularly when damage concentration in limited

levels occurred, which has been observed several times in the past major earthquake events. Fig 1.3 shows some mid-level collapse cases in the Great Hanshi earthquake in 1995. As a result, extensive attentions have been raised in improving structural integrity and preventing damage concentration in specific levels. Moreover, developing design method for low damage building structures, which meet the performance objectives as essential buildings or hazardous facilities in Figure 1.2 has been receiving increasing attention in recent years.



Fig 1.3 Mid-level collapse observed in Great Hanshin earthquake 1995

In Japan, a future great earthquake ($M_w 7.0$) under the Tokyo area^[1.4] and a greater earthquake ($M_w 8.0-9.0$) involving rupture along the Nankai megathrust^[1.5] has been proposed as a major risk. Moreover, the $M_w 9.0$ 2011 Tohoku earthquake also raised the alarm of a future super huge earthquake ($M_w > 9.0$) in Nankai megathrust area when its fault segments rupture in combination. Such earthquakes exceed the currently maximum considered earthquake level in design and may bring devastating damage to Japan society. The affected population is expected to be around 59,000,000, which is more than 7.0 times of the 2011 Tohoku earthquake. Therefore, it's highly

required to ensure sufficient safety of building structures against earthquakes even beyond the design level. Furthermore, continuous usability must be provided for the buildings serving as bases of emergency measures activities or safety shelters, such as government office buildings, schools, medical facilities, public halls, stations, etc. In such buildings, damage should be mitigated in main structural members or limited to replaceable energy-dissipating members, so as to reduce the repairing cost and downtime. For example, the base isolation for buildings is one application of the low damage structure.

Performance objectives for low damage seismic design of buildings can be considered in the following aspects: damage mitigation effectiveness, damage concentration prevention effectiveness, self-centering ability, reparability, robustness, non-structural components damage, and so on.

Those performances can be evaluated by several engineering demand parameters. The damage mitigation and damage concentration prevention effectiveness can be evaluated by the maximum story drift ratio (SDR), the drift concentration factor, the energy dissipated by the main structure and the replaceable energy-dissipating members.

Self-centering capacity of a building means that the building can return close to its initial position with small residual deformations after earthquakes below specific levels. The residual deformation of structures can be controlled to small level by designing the post-yield stiffness to be higher than 5%-10% of the initial stiffness of the structure, or introducing elastic post-tensioned structural members or secondary seismic resisting systems to provide additional post yield stiffness.

The reparability of building structure after major earthquake can be more economic if there are energy-dissipating members that help to prevent damage from generating in the main structures and can be replaced easily, such as moment-resisting frame system with buckling restrained braces as dampers.

Some non-structural components can interact with the seismic response of structural components during the ground shaking. Moreover, Damage of nonstructural elements threatens life safety and damage may be disruptive and expensive. The non-structural components are typically classified as fragility group and sliding or overturning group. These fragility groups use either peak floor acceleration or peak story drift as the demand parameter used to determine damage. Sliding and overturning of unanchored components is determined using peak floor velocity as the predictive demand. The content in the building such as computers, printers which have large inertia may also cause life loss because of large floor acceleration.

High seismically redundancy and robustness are necessary for building structures, in order to reduce the risk of structural failure subjected to earthquake shaking beyond the design level, as well as reduce the risk of damage concentration when the strength and stiffness in the structural

configuration discontinue.

1.2 Review of related previous investigations

Since the buckling restrained braces were proposed in 1990^[1.6], the buckling restrained braced frames (BRBF) have become increasingly popular especially in Japan and US because of their high seismic performance — limiting damage, maintaining function, and providing easy repair. Well-balanced buckling-restrained braces (BRCs) are required for ensuring the high seismic performance of BRBFs. This means the yielding forces of BRBs in each story are proportional to the story stiffness thus the BRBs yield at the same time in a first-mode response pattern. However, after the yield of the main frame under large seismic intensity, the low post-yield tangent stiffness of the braces may concentrate damage and residual drift in limited levels, even though brace capacities are relatively well balanced over the height of the structure^[1.7].

Various investigations have been carried out to enhance the story-by-story integrity of ductile frames so as to avoid a weak story mechanism, e.g., the development of “strong column-weak beam” concept, or dual systems utilizing structural components that possess vertically continuous stiffness. Akiyama and Takahashi (1984) investigated the effect of a “spreader column” on mitigating damage concentration of moment-resisting frames.^[1.8] They quantitatively defined the relation between the stiffness K_{eq} of the spreader column and the damage concentration degree based on time history analysis of a basic model, as shown in Fig 1.4. 5-, 10-, and 20-story models were analyzed in their study, but natural periods of all the basic models were designed as 1.0 s. The spreader column is connected to the beam-column frame by pin-end beams and connected to the foundation by a pin joint. The spreader column is elastic while plastic hinges generate at the beam-ends or column-ends. Damage distribution ratio of a specific story, i.e., the ratio of the dissipated energy of that story and energy of the whole structure, is directly described by stiffness and yielding strength distribution throughout the height of the structure. Effect of story yielding strength is greatly emphasized by utilizing an exponential function compared to story stiffness, and the exponent n of the yielding strength is defined as the damage concentration index. The index n increases with the yielding strength decreasing, indicating severe damage concentration in that story. Akiyama and Takahashi proposed a unified relation between the damage concentration index n and the stiffness ratio between the spreader column and the moment frame K_{eq}/K_R , for frames generating either column yield or beam yield mechanisms. They also investigated the effect of K_{eq}/K_R on strength demands in the spreader column, as well as the interaction force between the spreader column and the moment frame, as shown in Fig 1.5, and proposed corresponding evaluation equations. Later they expanded the research subject to a more general model by allowing plasticity in the spreader column and connecting the spreader column rigidly to the foundation and moment

frame. ^[1.9] Their pioneering research validated the effectiveness of a spreader column in achieving uniform damage distribution in frames. However, the effect of vertically irregular stiffness of frames is not the main concern in their study, which in contrast, might be an essential factor for the subject in this study, the low-damage structures. The seismic waves utilized in validation were very limited and the basic models only represented first-mode response dominant structures.

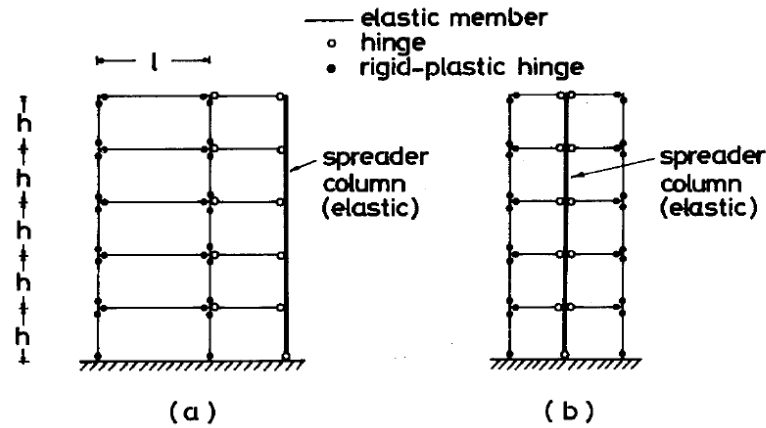


Fig. 1.4 Fundamental model of frame-spreader column structure investigated by Akiyama and Takahashi ^[1.8]

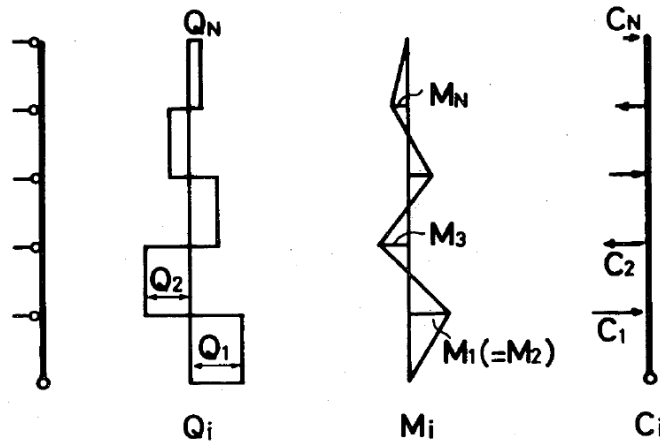


Fig. 1.5 Forces on the spreader column ^[1.8]

Tanimura and Ishida proposed a “Shinbashira – Frame” system based on researches about multi-story Japanese wooden pagoda structures. ^[1.10] The “Shinbashira” is pin connected to the foundation and to the top of the envelope frame. Other stories of the frame can deform freely till colliding with the “Shinbashira”, as shown in Fig 1.6. They noticed two beneficial effects in this system: (1) TMD effect due to whipping phenomenon of upper stories could control the vibration of lower part of the frame, and (2) energy bypass effect of a “Shinbashira” could

prevent deformation concentration of specific stories. Those effects were verified by numerical analysis executed on a 2DOF model with sinusoidal ground motions.

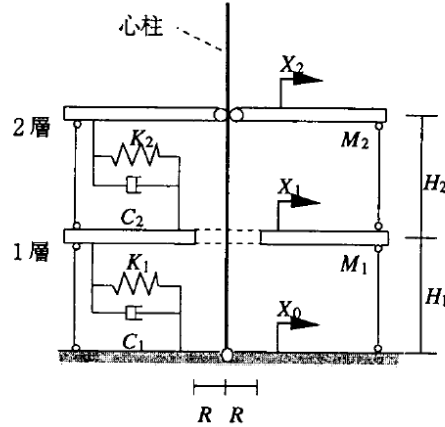
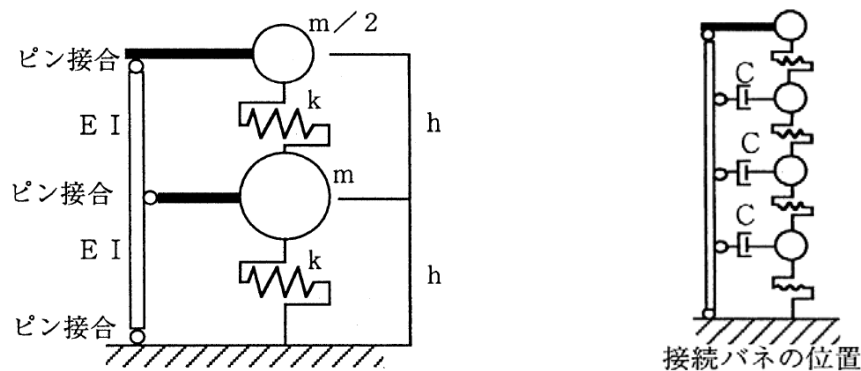


Fig 1.6 Concept of “Shinbashira – Frame” system by Tanimura and Ishida ^[1.10]

Tezuka et al. ^[1.11] were also inspired by the traditional pagoda structures and proposed a “structural seismic damage control system” (Fig 1.7a). A concentrically braced frame possessing much larger stiffness than the moment frame acts as the spine to distribute seismic damage. A 4-story model with weak story was utilized to verify the damage distribution effect of the braced frame by dynamic analysis with observed earthquake ground motions. They might be the earliest researchers who attempted to add additional dampers in such system to reduce the total input energy in moment frames. However, the viscous dampers were equipped horizontally between the braced frame and the moment frame (Fig 1.7b) because they expected the similar energy dissipation mechanism as collision between the two components in Japanese pagoda structures. They found out that the relative horizontal velocity between the two components was too small for the dampers to work effectively.



(a) “Structural seismic damage control system” (b) Locations of viscous dampers

Fig 1.7 “Structural seismic damage control system” by Tezuka et al ^[1.11]

MacRae et al. noticed the similar effect of seismic or gravity columns in steel concentrically braced frames. ^[1.12] Closed form relationships between drift concentration, column stiffness, and strength has been developed for idealized two story structures with uniform strength over their height subjected to pushover analysis, as shown in Fig 1.8. The empirical relationships between drift concentration, column stiffness, and strength have also been developed for multistory structures with variable strength over height subject to pushover analysis and dynamic inelastic time-history analysis. Fig 1.9 shows the static behavior of each structural component subject to the inverse triangular pushover load distribution in their study.

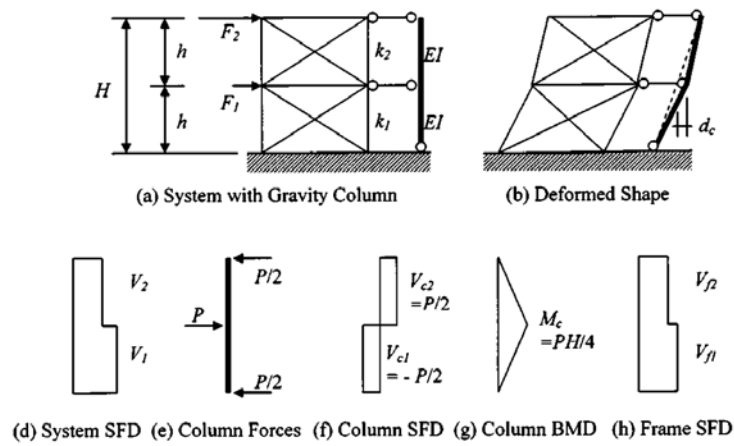


Fig. 1.8 Idealization of two-story frame with gravity column deformation and forces by G. A. MacRae et al. ^[1.12]

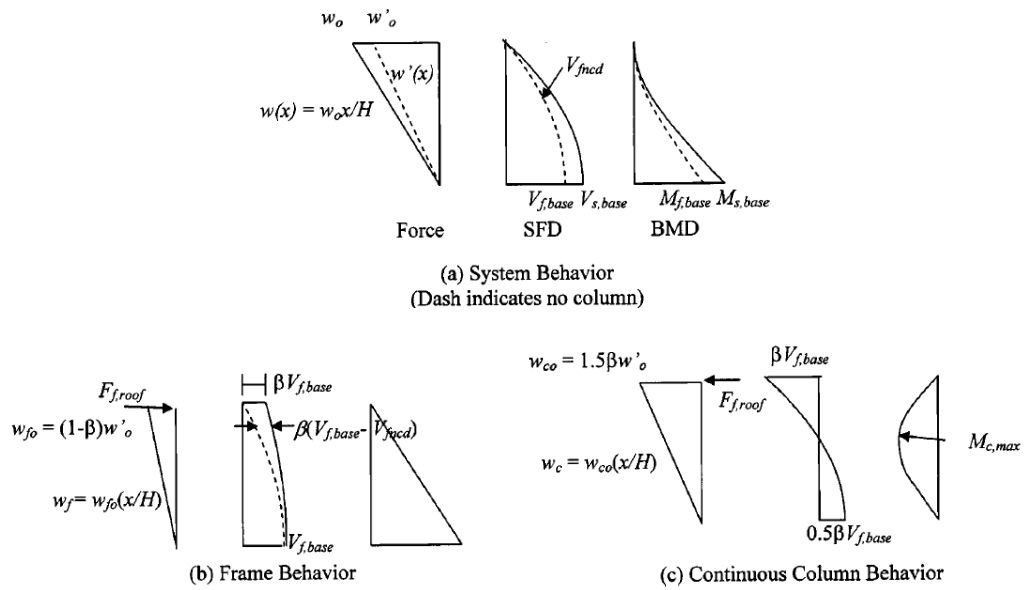


Fig. 1.9 System, frame, and strong column behavior due to pushover analysis at large displacements ^[1.12]

Walls, usually with much larger and especially deeper cross-sections, are much more effective than individual columns for providing flexural stiffness to control story drift. As pointed out by Paulay and Priestley ^[1.13], development of a weak story mechanism can readily be avoided as a result of the considerable stiffness of walls. In examining the effect of foundation flexibility on the seismic performance of a shear wall-frame dual system, they demonstrated the drift control effect and force distribution characteristics of dual systems with pinned base walls. The results of their nonlinear dynamic analysis indicate that loss of wall base restraint would not significantly impair the seismic performance of wall-frame systems.

Alavi and Krawinkler proposed using walls to improve the seismic performance of frame structures subjected to near-fault ground motions. ^[1.14] Twenty-story generic frame models were built and dynamic nonlinear analysis was performed with an equivalent pulse motion as a representation of near-fault ground motions. The performance of hinged walls was compared with conventional fixed-base shear walls. It was found that the strengthening of frame structures with hinged walls is effective in reducing the maximum story drift demands and producing a more uniform distribution of story drifts over the height of the structure. Moreover, the shear and moment demands for a hinged wall are much lower than those for a fixed-base wall.

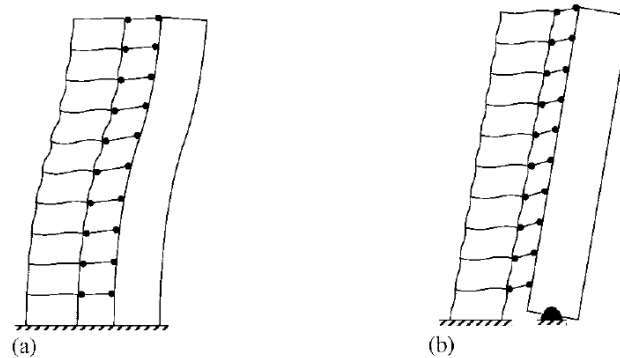


Fig. 1.10 Typical elastic deflected shape of dual systems by Alavi and Krawinkler's ^[1.14]

In the last decade, the spine-frame system with additional dampers gets more noticeable in both retrofitting and new building design. Wada et al. ^[1.15] employed a pivoting spine concept in the seismic retrofitting of a concrete building in Japan (Fig 1.11-12) and Mar et al. ^[1.16] employed a similar spine concept in the seismic retrofitting of a steel building in the USA (Fig 1.13-14). A concrete wall acts as the rocking core of the building to redistribute lateral forces and displacements without adding significant strength. BRBs are equipped between the wall and the frame. By nonlinear time-history analysis, the retrofitted building showed an effective performance of eliminating weak-story failure. Gunay et al. ^[1.17] investigated the seismic performance of non-ductile reinforced concrete frame which was retrofitted with rocking infill walls and proved its efficacy of reducing soft story failure risks.

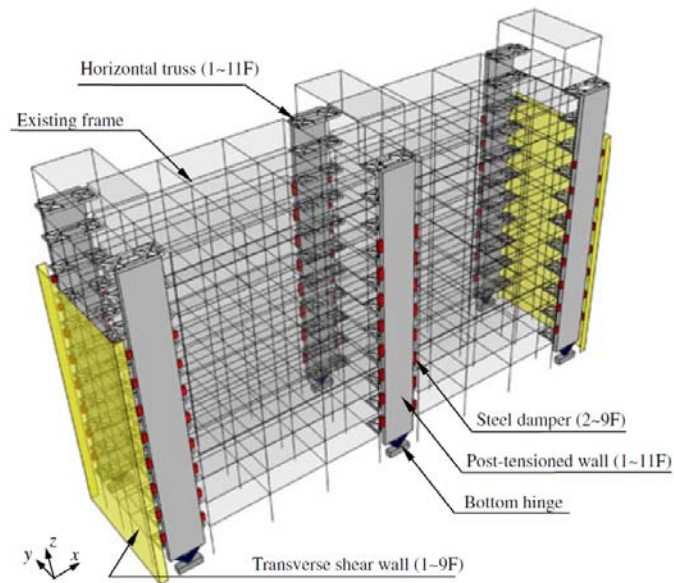


Fig. 1.11 Retrofit plan of G3 building by post-tensioned wall with shear dampers ^[1.15]

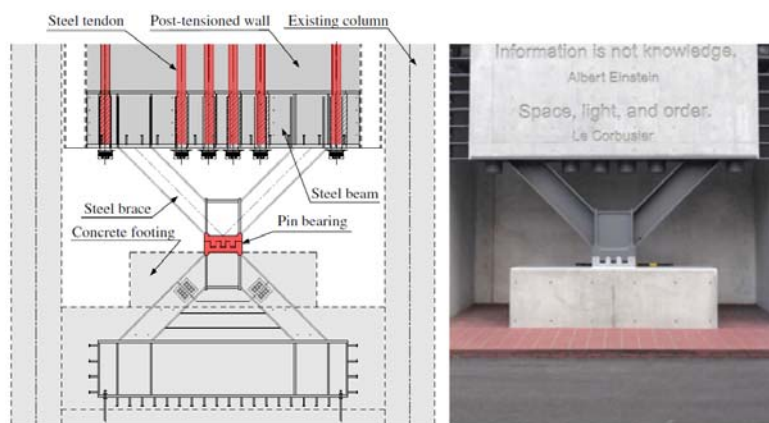
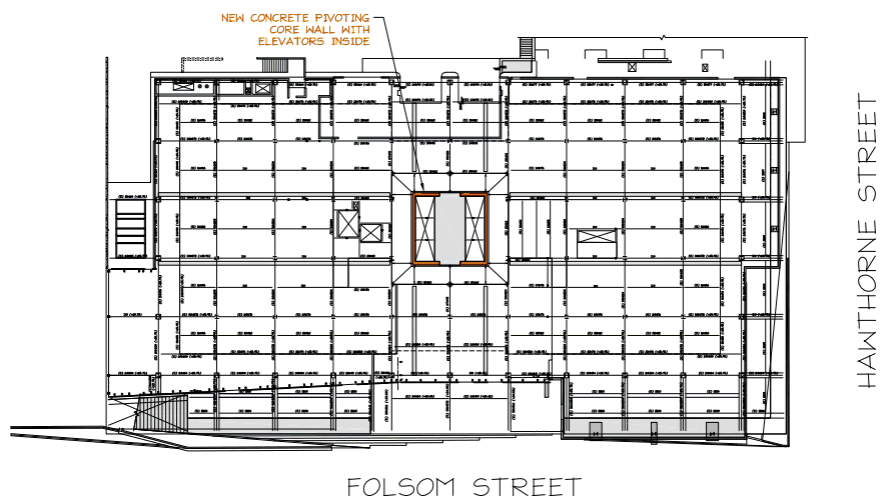


Fig. 1.12 Details at the bottom of the rocking wall in G3 building ^[1.15]



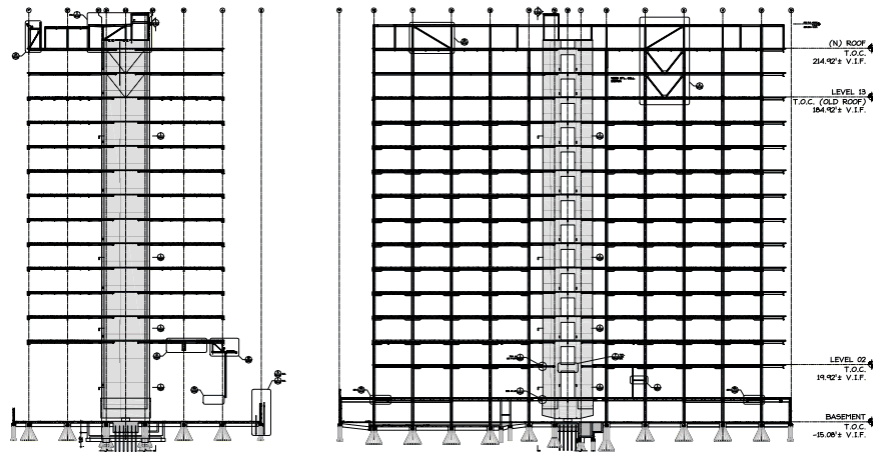


Fig. 1.13 First floor plan and elevations of 680 Folsom Street with new pivoting core wall as a seismic retrofit. ^[1.16]

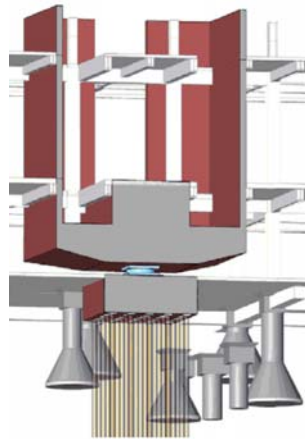


Fig. 1.14 Friction pendulum bearing supporting the core wall ^[1.16]

Lai and Mahin ^[1.18] developed a “strongback” system (Fig 1.15), a modification of the conventional braced frame that utilizes a vertical steel truss to delay or prevent weak-story behavior. A single BRB deforming with the strongback was utilized as the primary energy-dissipating device. A cyclic test was conducted on a nearly full-scale two-story strongback retrofit design. Test results showed that the strongback specimen was effective in impeding the formation concentration and in mobilizing the reserve strength of other structural components.

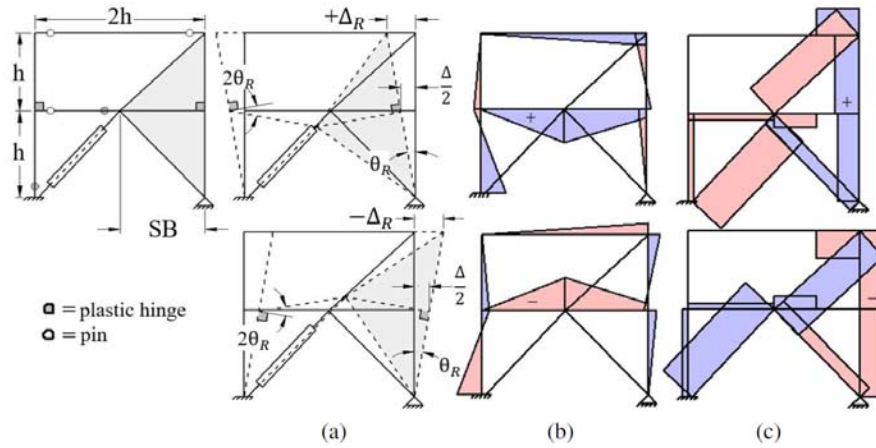


Fig 1.15 Strongback system: (a) kinematic, (b) moment, (c) axial force diagrams ^[1.18]

Besides damped structural systems which utilizing energy-dissipating members to reduce earthquake input energy, self-centering seismic resilient structural systems possessing the ability of limiting residual drifts to negligible magnitude has gathered more and more attention in these years. There are roughly three types of self-centering systems. (1). Moment resisting frames with post-tensioned (PT) beam-to-column connections and flexible floor system which allows gap opening between beam-to-column connections. ^[1.19] (2). Braced frames with self-centering braces or BRBs which can return to their initial length with the effect of super-elastic pre-tensioned elements after loading. ^[1.20&21] (3). Rocking systems which can self-center relying on self-weight, restoring force of envelop frames, or PT elements. ^[1.22 ~ 30]

Structures which can be excited into rocking motion may suffer less damage than stable appearing structures when subjected to same ground motions. This behavior was observed by Housner as early as 1963^[1.31]. New rocking systems with energy-dissipating members have been developed recently. Wada et al. ^[1.22] used the similar concept at the connections of columns in the middle story of a slender tall frame (Fig 1.16). Midorigawa et al. ^[1.23&24] conducted shaking table test of a half-scale three story rocking frame which installed yielding plates at the bottom of columns to dissipate energy (Fig 1.17). Tremblay et al. ^[1.25] proposed a braced steel frame with viscous dampers vertically equipped between the column bases and the foundations (Fig 1.18). Eatherton et al. ^[1.26 ~ 30] studied an uplifting rocking frame system with PT strands which provide self-centering resistance (Fig 1.19). Steel butterfly-shaped fuses and BRB were employed as replaceable energy dissipation members.

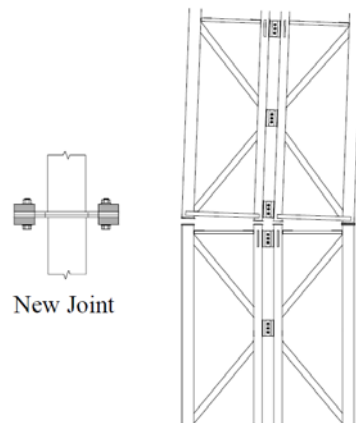


Fig 1.16 A chord joint allowing plastic deformation under tension by Wada et al. [1.22]

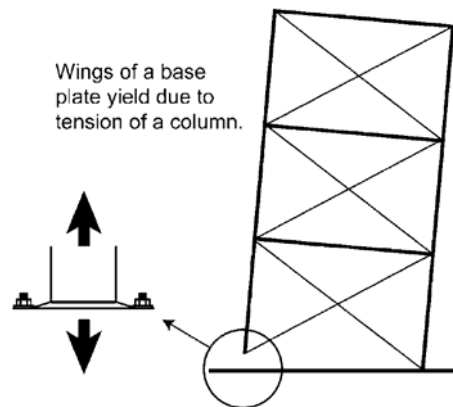


Fig 1.17 A rocking system with yielding base plates by Midorigawa et al. [1.23, 24]

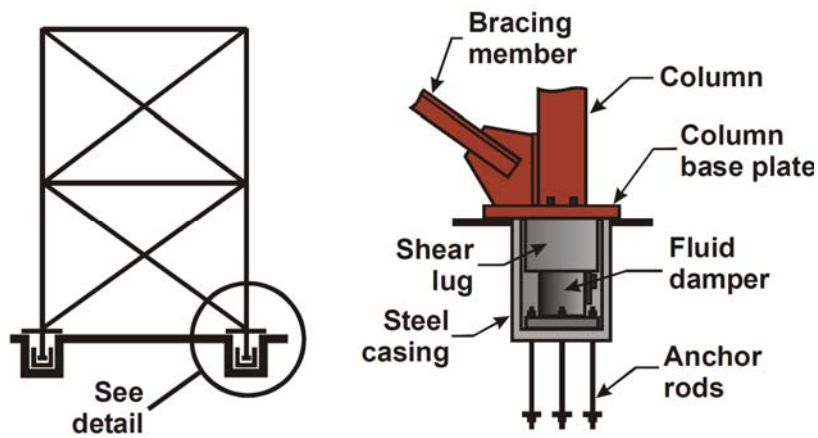


Fig 1.18 A viscously damped controlled seismic rocking braced steel frame system proposed by Tremblay et al. [1.25]

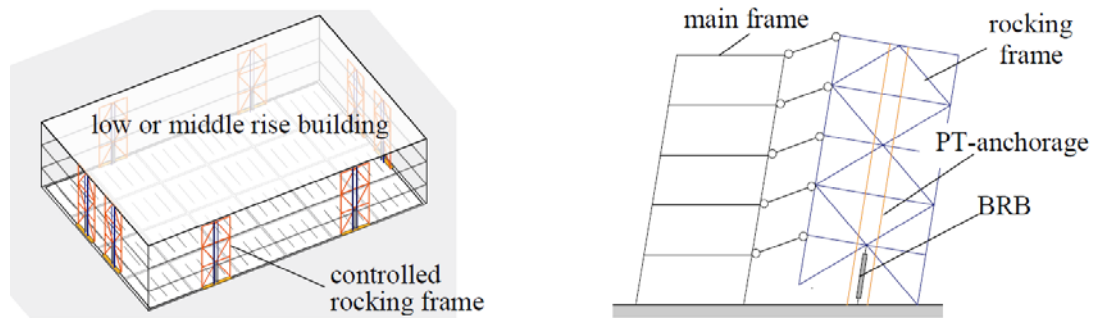


Fig 1.19 An uplifting controlled rocking system proposed by Eatherton et al. ^[1.26–30]

Most researchers scheme energy-dissipating devices at the bottom of the wall, which takes advantage of the efficient vertical deformation, and doesn't interfere architectural space. Similar ideas have appeared in other researches. Ikenaga et al. ^[1.32] have developed a column base consists of PT bars and steel plate dampers. Takamatsu et al. ^[1.33] proposed a column base with anchor bolts which can yield and absorb energy when elongated (Fig 1.20). Takeuchi et al. ^[1.34] used buckling-restraint columns (BRC) at the base of truss frames to concentrate major damage into BRCs and prevent collapses caused by buckling of members in the main structure (Fig 1.21). This method also alleviates the strength demand of foundation structures.

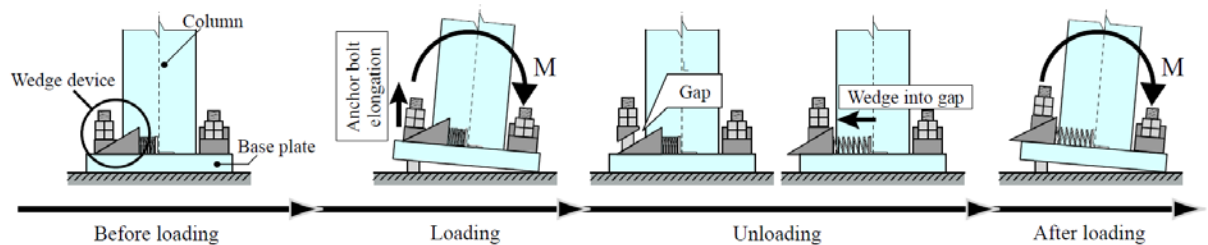


Figure 1.20 A non-slip-type column base with wedge devices by Takamatsu et al. ^[1.33]

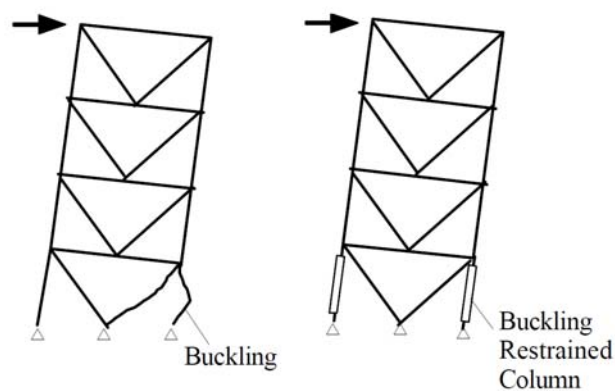


Figure 1.21 Damage tolerant design for truss frames proposed by Takeuchi et al. ^[1.34]

As mentioned above, effective and economical structural systems eliminating damage concentration and residual drift after large earthquakes are needed and have been frequently investigated; however, applications to actual buildings are not yet popular. This is mainly because several obstacles must be overcome, such as the need for large, self-centering PT strands and special treatment at uplift column bases. To eliminate these difficulties, this study investigates a controlled spine frame system without PT strands, whose self-centering capacity is achieved by envelope elastic moment-resisting frames.

1.3 Objective of the dissertation

The dissertation presents the concept of an innovative controlled spine frame system, which has been applied to an actual building being constructed in Japan. (Figure 1.22), and a simple yet very applicable design method is proposed for the system with clear limitations and recommendations for the key structural parameters. This spine frame system consists of (1) a stiff braced steel frame (i.e., spine frame), (2) replaceable energy-dissipating members (buckling restrained columns, BRC), and (3) envelope moment-resisting frames. The spine frame enforces a near-linear deformed shape and prevents deformation concentration in specific stories. The envelope moment frames are designed to remain elastic and reduce residual drifts, providing the self-centering force without resorting to post-tensioning. The input seismic energy is absorbed by BRCs, which feature significant cumulative deformation capacity, and if required can easily be replaced following a large earthquake. This combination of structural elements effectively eliminates repair cost and downtime of buildings suffering major earthquakes.

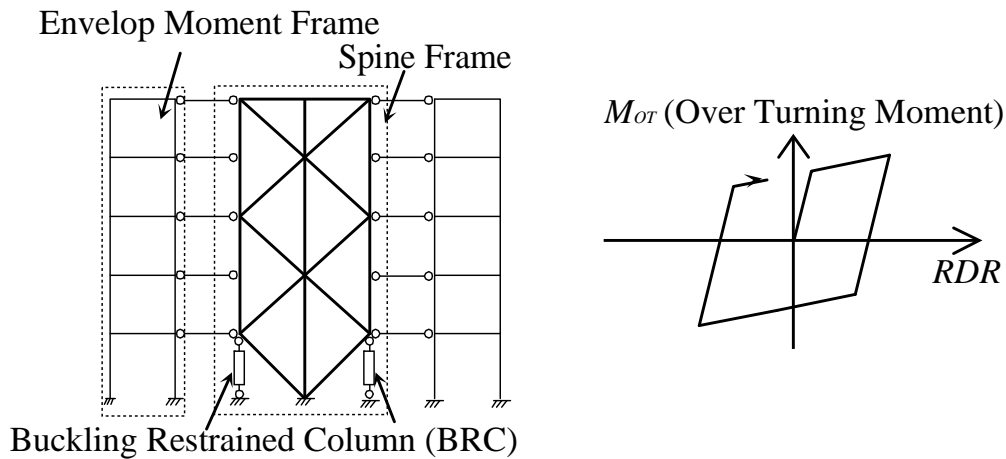


Fig. 1.22 Concept and hysteretic curve of the proposed non-uplifting spine frames

The proposed spine frame system is promising in the improvement of seismic resistance, in reduction of first and repair costs, protection of architectural skin, and reduction of damage and

loss of use. Simple design and construction method makes it easy to apply in actual application. The main objectives of this study are summarized below.

- 1) Verify the low-damage seismic performance as well as easy construction and maintenance of the proposed controlled spine frame structural system.
- 2) Develop a generalized model for the controlled spine frame system with a clear correspondence to the original member-by-member model.
- 3) Expound the relation between seismic performance of the controlled spine frame structures and the key structural characteristics. Verify the application limit of the proposed system
- 4) Propose a simple seismic evaluation and design method for the controlled spine frame system with clear limitations and recommendations.

Reference

- [1.1] BSSC (1997b). "NEHRP Recommended Provisions for Seismic Regulation of New Buildings and Other Structures, FEMA-222." publication pending
- [1.2] SEAOC (1995). "Vision 2000 - A Framework for Performance Based Earthquake Engineering." Vol. 1, January, 1995.
- [1.3] FEMA P-58-1, Seismic performance assessment of buildings, Vol. 1 – Methodology, September 2012
- [1.4] 内閣府：首都直下地震対策検討ワーキンググループ最終報告, 2013.12
- [1.5] 内閣府：南海トラフ巨大地震対策について最終報告, 2013.5
- [1.6] Fujimoto M., Wada A., Saeki E., Takeuchi T., Watanabe A. Developemnt of unbonded brace. *Quarterly Column*. No. 115. Pp. 91-96. 1990
- [1.7] Uriz P., Mahin S. A. Toward earthquake-resistant design of concentrically braced steel-frame structures. PEER-2008/08, Pacific Earthquake Engineering Research Center (PEER), University of California, Berkeley, 2008.
- [1.8] H. Akiyama, M. Takahashi: Ds-value for damage-dispersing type multi-story frames. *Journal of Structural and Construction Engineering* Transaction of AIJ. Vol. 341: 54-61, 1984, (in Japanese)
- [1.9] H. Akiyama, M. Takahashi: Generalization of damage-dispersing type multi-story frames. *Journal of Structural and Construction Engineering* Transaction of AIJ. Vol.365: 20-27, 1986, (in Japanese)
- [1.10] A. Tanimura, S. Ishida: Nonlinear dynamic behavior of a Shinbashira-Frame system. *Journal of Structural Engineering*, AIJ, 1996, Vol42.B:635-642. (in Japanese)
- [1.11] T. Tezuka, H. Kamibara, S. Hirashima: Structural seismic damage control system. 鋼構造論文集, 1998, Vol.5(20).
- [1.12] MacRae G. A., Kimura Y, Roeder C. Effect of column stiffness on braced frame seismic behavior. *Journal of Structural Engineering*, ASCE 2004; 130(3):381-391.
- [1.13] Paulay T., Priestley M.J.N. Seismic design of reinforced concrete and masonry buildings. John

Wiley & Sons, Inc: New York. 1992:500-516.

- [1.14] B. Alavi and H. Krawinkler: Strengthening of moment-resisting frame structures against near-fault ground motion effects. *Earthquake Engineering and Structural Dynamics*. 2004, 33:707-722 (DOI: 10.1002/eqe.370)
- [1.15] Qu Z., Wada A., Motoyui S., Sakata H., Kishiki S. Pin-supported walls for enhancing the seismic performance of building structures. *Earthquake Engineering and Structural Dynamics* 2012; **41**: 2075-2091. DOI: 10.1002/eqe.2175
- [1.16] Janhunen B., Tipping S., Wolfe J., Mar T. Seismic retrofit of a 1960s steel moment-frame highrise using a pivoting spine. *Proceedings of the Structural Engineers Association of California 82nd Annual Convention*, San Diego, USA, 2013.
- [1.17] Günay S., Korolyk M., Mar D., Mosalam K., Rodgers J. Infill walls as a spine to enhance the seismic performance of non-ductile reinforced concrete frames. *Improving the Seismic Performance of Existing Buildings and Other Structures* 2009: 1093-1104. DOI: 10.1061/41084(364)100
- [1.18] J. Lai and S. Mahin: Strongback system: A way to reduce damage concentration in steel-braced frames, *J. Struct. Engen. ASCE*, 141.9(2014)
- [1.19] Garlock M. M., Sause R., Ricles J. M. Behavior and design of posttensioned steel frame systems. *Journal of Structural Engineering* 2007; **133**(3): 389-399. DOI: 10.1061/(ASCE) 0733-9445 (2007)133:3(389)
- [1.20] Miller D. J., Fahnestock L. A., Eatherton M. R. Development and experimental validation of a nickel-titanium shape memory alloy self-centering buckling-restrained brace. *Engineering Structures* 2012; **40**: 288-298. DOI: 10.1016/j.engstruct.2012.02.037
- [1.21] Christopoulos C., Tremblay R., Kim H.-J., Lacerte M. Self-centering energy dissipative bracing system for the seismic resistance of structures: development and validation. *Journal of Structural Engineering* 2008; **134**, SPECIAL ISSUE: Design and Analysis of Structures with Seismic Damping Systems, 96-107. DOI: 10.1061/(ASCE)0733-9445(2008)134:1(96)
- [1.22] Wada A., Yamada S., Fukuta O., Tanigawa M. Passive controlled slender structures having special devices at column connections. *Seventh International Seminar on Seismic Isolation, Passive Energy Dissipation and Active Control of Vibrations of Structures*, Assisi, Italy, 2001.
- [1.23] Midorigawa M., Azuhata T., Ishihara T., Matsuba Y., Matsushima Y., Wada A. Earthquake response reduction of buildings by rocking structural system. *Smart Structures and Materials 2002: Smart Systems for Bridges, Structures, and Highways; Proceedings of SPIE*, 2002; **4696**: 265-272.
- [1.24] Midorikawa M., Azuhata T., Ishihara T., Wada A. Shaking table tests on seismic response of steel braced frames with column uplift. *Earthquake Engineering and Structural Dynamics* 2006; **35**: 1767-1785. DOI: 10.1002/eqe.603
- [1.25] Tremblay R., Poirier L. P., Bouaanani N., Leclerc M., Rene V., Fronteddu L., Rivest S. Innovative viscously damped rocking braced steel frames. *Proceedings of the 14th World Conference on*

- Earthquake Engineering*, Beijing, China, 2008; Paper No. 05-01-0527.
- [1.26] Takeuchi T., Midorikawa M., Kasai K., Deierlein G., Ma X., Hajjar J. F., Hikino T. Shaking table test of controlled rocking frames using multipurpose test bed. *The Sixth European Conference on Steel and Composite Structures*, Budapest, Hungary, 2011.
- [1.27] Eatherton M., Hajjar J., Ma X., Krawinkler H., Deierlein G. Seismic design and behavior of steel frames with controlled rocking—part I: concepts and quasi-static subassembly testing. *The 2010 NASCC & Structures Congress*, Orlando, USA: 1523-1533. DOI: 10.1061/41130(369)138
- [1.28] Eatherton M. R., Hajjar J. F. Residual drifts of self-centering systems including effects of ambient building resistance. *Earthquake Spectra* 2011; **27**(3): 19-774. DOI: 10.1193/1.3605318
- [1.29] Ma X., Eatherton M., Hajjar J., Krawinkler H., Deierlein G. (2010) Seismic design and behavior of steel frames with controlled rocking—part II: large scale shake table testing and system collapse analysis. *The 2010 NASCC & Structures Congress*, Orlando, USA: 1534-1543. DOI: 10.1061/41130(369)139
- [1.30] Deierlein G., Ma X., Eatherton M., Hajjar J., Krawinkler H., Takeuchi T., Kasai K., Midorikawa M. Earthquake resilient steel braced frames with controlled rocking and energy dissipating fuses. *The Sixth European Conference on Steel and Composite Structures*, Budapest, Hungary, 2011.
- [1.31] Housner G. W. The behavior of inverted pendulum structures during earthquakes. *Bulletin of the Seismological Society of America* 1963; **53**(2): 403-417.
- [1.32] Ikenaga M., Nagae T., Nakashima M., Suita K. Development of column bases having self-centering and damping capability. *Proceedings of the Fifth International Conference on Behaviour of Steel Structures in Seismic Areas, STESSA*, Yokohama, Japan, 2006: 703-708.
- [1.33] Takamatsu T., Tamai H., Yamanishi T., Matsuo A. Rehabilitation of steel structure by means of wedge device. *Proceedings of the 14th World Conference on Earthquake Engineering*, Beijing, China, 2008.
- [1.34] Takeuchi T., Suzuki K. Performance-based design for truss-frame structures using energy dissipation devices. *Proceedings of the Fourth International Conference on Behaviour of Steel Structures in Seismic Areas, STESSA*, Naples, Italy, 2003: 55-62.

CHAPTER 2

Concepts and Seismic Performance of Controlled Spine Frames Applied in Low-rise Buildings

2.1 Introduction

- 2.1.1 Conventional frame with shear dampers as BRBs (SD system) 2-1
- 2.1.2 Controlled uplifting rocking frame system (LU system) 2-4
- 2.1.3 Non-uplifting spine frame system (NL system) 2-7
- 2.1.4 Prototype building 2-11
- 2.1.5 Design of the SD, LU, and NL models 2-13

2.2. Seismic performance of regular models

- 2.2.1 Static performances 2-18
- 2.2.2 Seismic responses under Level 2 earthquake 2-18
- 2.2.3 Incremental dynamic analyses 2-27

2.3 Seismic performance of single story structural irregular models

- 2.3.1 Design of single-story structural irregular models 2-29
- 2.3.2 Seismic responses against level 2 earthquake 2-33
- 2.3.3 Incremental dynamic analyses 2-39

2.4 Conclusion 2-47

Chapter 2 – Concepts and Seismic Performance of the Controlled Spine Frames Applied in Low-rise Buildings

2.1 Introduction

2.1.1 Conventional frame with shear dampers as BRBs (SD system)

Reducing the loss from earthquakes and improving safety of buildings with economical technologies is one of the key challenges in earthquake engineering. Recently more and more steel moment-resisting frames with shear dampers as BRBs (SD system) have been applied in steel buildings constructions in high seismic regions, particularly in Japan and the U.S.^[2.1-5] Fig. 2.1 shows a typical new construction application of the SD system. This system has been verified as a promising seismic resisting structural system by its behavior during major earthquake events.

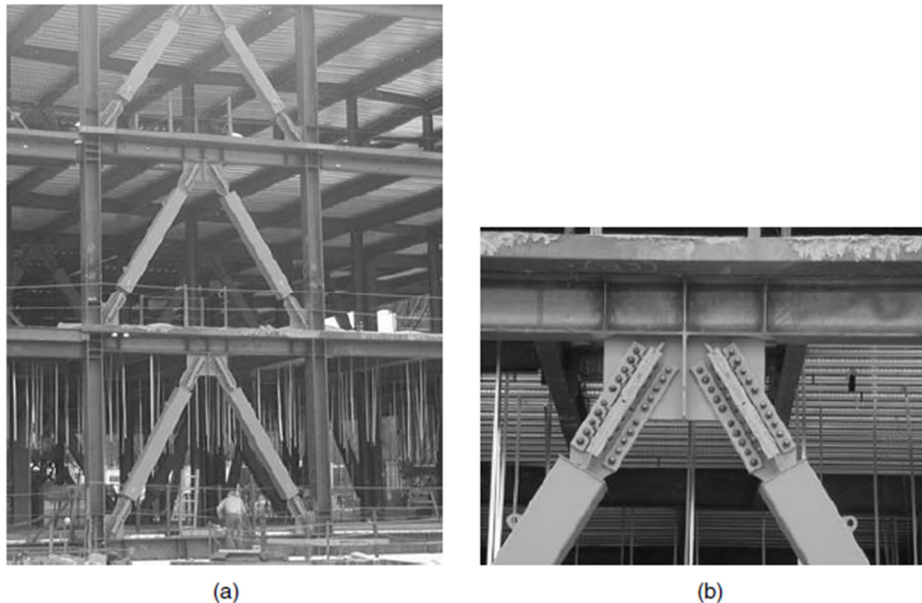


Fig. 2.1 Buckling-restrained brace frames for new construction. (a) Elevation; (b) connection details (courtesy of SIE, Inc.)^[2.3]

Various types of BRBs have been developed but their concepts are similar. Fig. 2.2 shows the major components of a type of BRB. The BRB consists of two main components: 1) a ductile steel core with predictable yield behavior by small variations; 2) buckling-restraining mechanism which typically means mortar with steel casing.

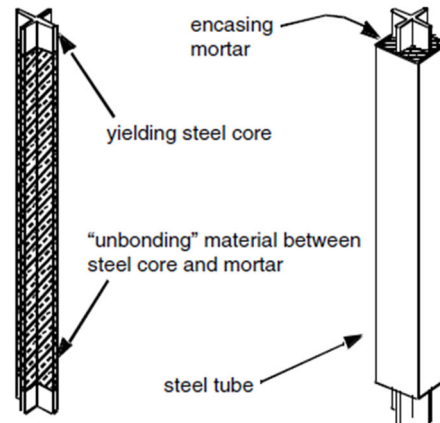


Fig. 2.2 Components of a type of buckling-restrained brace^[2,3]

BRBs can yield without buckling in both tension and compression. Fig. 2.3 expresses the hysteretic behavior of BRBs compared with conventional braces. This behavior eliminates the undesirable buckling of the moment frames braced by conventional braces. It offers flexible design of BRBFs and easy modeling because of the predictable yield behavior with small variations. Moreover, larger energy dissipation is provided and more stable seismic behavior is ensured under high-level earthquake. Under some certain designs of BRBFs, the main moment-resisting frame stays mostly elastic while only the BRBs dissipate energy. After a severe earthquake event, such structural system is expected to be repaired by only replacing the deformed dampers. Fig. 2.4 shows one of the configurations of this system, which is also the configuration used in this study.

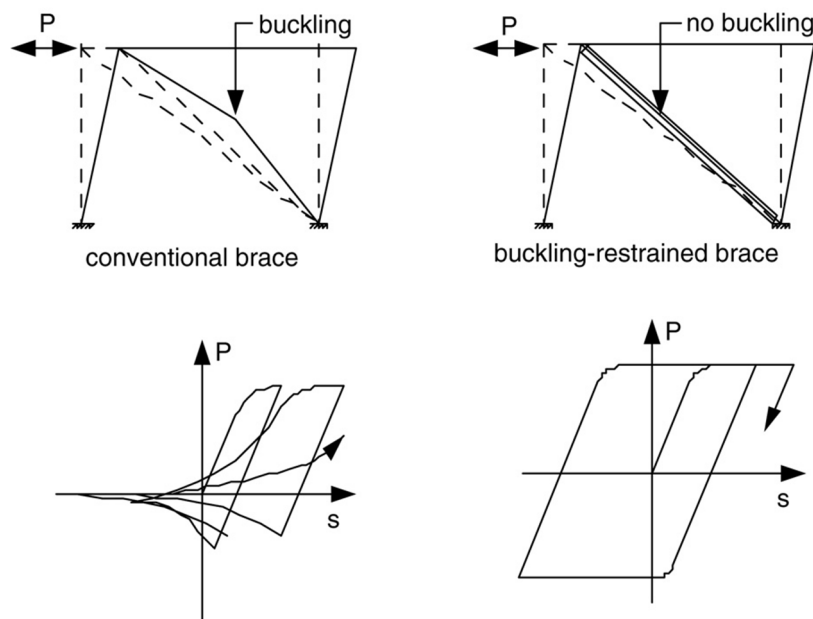


Fig. 2.3 hysteretic behavior of conventional braces and BRBs^[2,3]

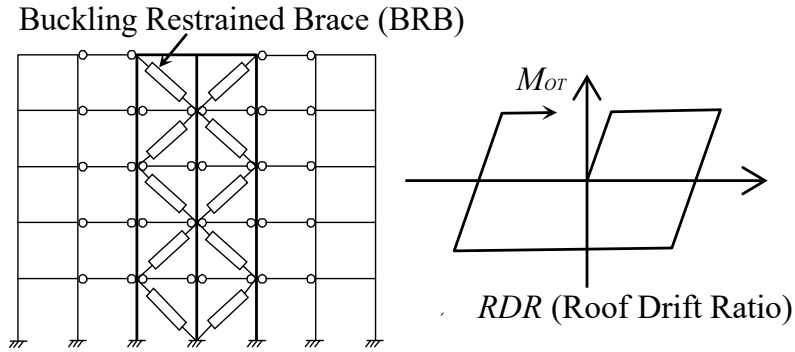


Fig. 2.4 One configuration of SD system with BRBs

Concentrating damage in BRBs is regarded as an effective application of the SD system. The seismic behavior of SD system highly depends on the participant ratio of BRB (β : the horizontal load sharing ratio of BRBs). Fig. 2.5 shows the differences of load-deflection backbone curves of the SD system with different β . With the increase of β , the horizontal stiffness contributed by moment frame decreases, which tend to cause unstable responses and drift concentration in a specific story, as shown in Fig. 2.6. Moreover, the moment frame also yields soon after the BRBs yield, and large residual deformations may remain after earthquakes. On the contrary, if β is small, damage concentration in a specific story might be avoided. However, high-performance BRBs with high ductility will be required to meet the required energy dissipating capacity.

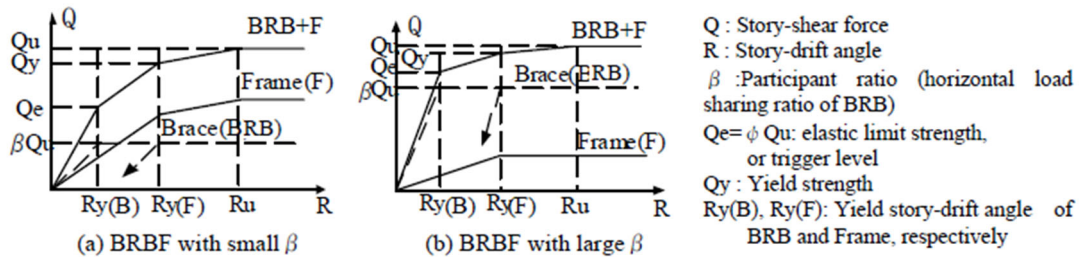


Fig. 2.5 Influence of the participant ratio of BRB on the load-deflection backbone curves of the SD system [2.6]

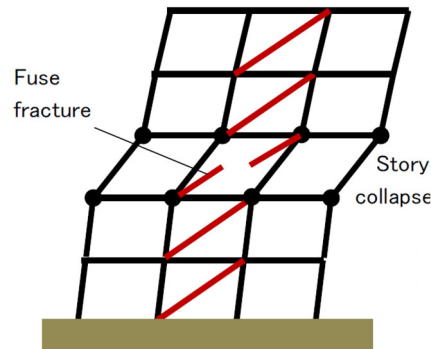


Fig. 2.6 Drift concentration in a specific story causing story collapse in the SD system

2.1.2 Controlled uplifting rocking frame system (LU system)

Based on the previous investigations on concentrically braced steel frame structures, it has been found that permitting foundations to uplift is an effective way to reduce damage to braces. However for low-rise or middle-rise buildings, the gravity load of the braced frame is not enough to overcome the residual force of structural members and provide self-centering, which may cause large residual story drift to remain after the earthquake shaking. One type of uplifting braced frame with post-tensioning and energy dissipating members has been developed in prior studies conducted by Deierlein's et al^[2.7, 2.8]. In this controlled uplifting rocking system, the PT strands connected the braced frame from roof to the foundation and provide self-centering force after earthquake shaking. Multiple applications of LU system by adopting alternative materials, structural configurations, and energy dissipating members have been proposed by prior researchers. Fig. 2.7 shows one scheme of LU system which is studied herein.

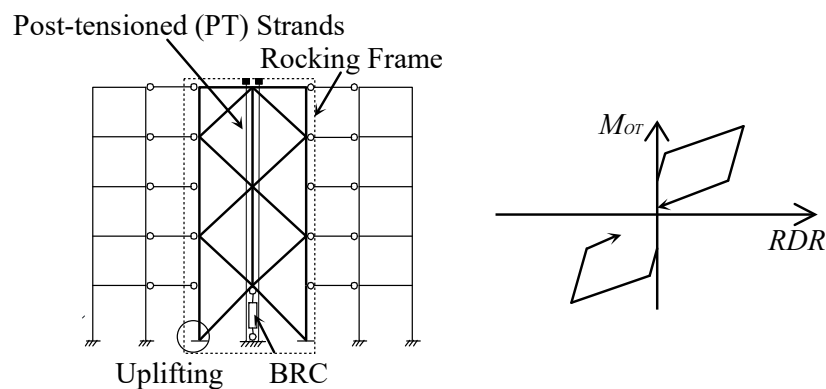


Fig. 2.7 One configuration of a controlled uplifting rocking frame system

The main components of this system are a braced steel frame which is designed to rock on its foundation, the high-strength vertical steel strands that post-tension the braced frame to the ground and provide overturning resistance, and the replaceable energy dissipating fuses. The

braced steel frame and PT strands are designed to remain essentially elastic even during strong ground shaking, while the fuses yield at relative small displacement and dissipate energy. Both the PT strands and energy dissipating fuses provide the overturning resisting force. During the uplift at large lateral displacement, the PT strands are always in tension and tend to pull the frame back towards its foundation, while the force of fuses may against the rocking motion of the braced frame after the fuses experience plastic deformation. The instantaneous input earthquake energy is converted into potential energy due to rocking behavior. Besides, the vibration period of LU system changes after uplifting so the resonance with ground motion is avoided. Moreover, the spine effect of the stiff braced frame can prevent damage concentration in weak or soft story.

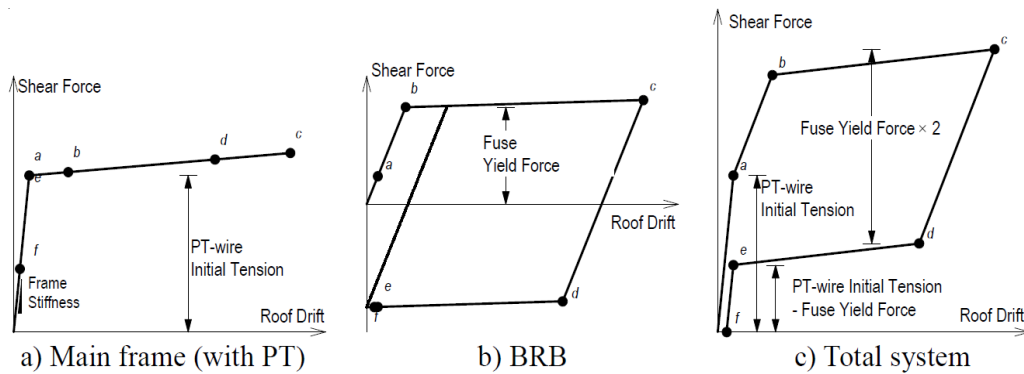


Fig. 2.8 load-deflection backbone curves of the LU system;(a) the envelop frame with the PT strands;(b) the energy dissipating fuses; (c) the total system^[2,7]

The load-deflection backbone curves of the braced frame with PT strands and fuses are shown in Fig. 2.8. The vertical axis is overturning moment which can be calculated from the axial force of PT strands and fuses. The horizontal axis is uplift distance. The stiffness of the braced frame with PT strands changes when it starts to rock. The deformation of fuses is always in tension region. The flag-shaped backbone curve of the LU system can be derived by combining that of the braced frame with PT strands and that of fuses. From the curves we can see that in order to eliminate the residual deformation, the yielding strength should be designed lower than the initial tension force of the PT strands.

Each point on the backbone curves represents a typical state of the LU system; following is the explanation of each state.

- a:** base of the braced frame lifts
- b:** fuses yield during the braced frame uplifting
- c:** rocking direction reversal
- d:** force in fuses reduces to zero
- e:** fuses yield during the braced frame landing

f: residual deformation reduces close to zero, starting next uplift

The critical states that are listed above are expected to exhibit in serviceability condition. For the life safety condition, there are two essential limit states for the UL system, the one is yielding of the PT strands and the other is the overturning of the braced frame or buckling of the braced frame.

The uplift ratio θ_y of the frame when PT strands yield depends on the pre-stress stress f_0^{PT} and the yield stress f_y^{PT} of the PT strands, as expressed by equation (2.1) and (2.2).

$$f_0^{PT} + E_{PT}\epsilon_{PT} = f_y^{PT} \quad (2.1)$$

$$\theta_y = \frac{2H}{L}\epsilon_{PT} = \frac{2H}{L} \cdot \frac{f_y^{PT} - f_0^{PT}}{E_{PT}} \quad (2.2)$$

Where, E_{PT} is the Young's modulus of PT strands.

ϵ_{PT} is the deformation ratio of PT strands after introduce pre-stress force.

L is the width of the rocking frame, which is twice of the distance between PT strands to the uplift base.

H is the height of the rocking frame, which is same with the length of the PT strands.

The critical displacement when the braced frame becomes unstable is expressed by a tipping angle, α , where the mass center of the braced frame is located directly through the leading edge, as shown in Fig. 2.9.

Housner^[2,9] proposed that the fragility function for overturning of rocking objects was related with the peak ground velocity, as expressed by equation (2.3)

$$PGV = 2gR\sqrt{(1 - \cos\alpha)} \quad (2.3)$$

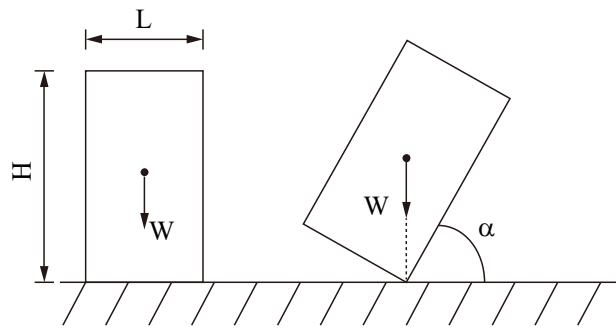


Fig. 2.9 Overturning of rocking objects

Where, PGV is the peak ground motion velocity where overturning occurs;

$$R = \sqrt{\left(\frac{H}{2}\right)^2 + \left(\frac{L}{2}\right)^2}.$$

The collapse of the LU system may also be associated with overloading of the single column and brace that carried the lateral and vertical loads during the uplift at large lateral displacement.

Special attentions are needed for designing the details of the rocking frame column bases, the anchorage of the PT strands, the floor system to ensure the rocking frame and the envelop frame working together, and the connections between the rocking frame and envelop frame. Apart from those points, the braced frame and the moment frame employs fairly standard design and fabrication practices.

2.1.3 Non-uplifting spine frame system (NL system)

There are multiple methods to implement non-uplifting spine frame systems using alternative materials, configurations, and energy-dissipating members. Fig. 2.10 shows one of the structural schemes investigated in this study. The proposed system comprises steel braced frames and replaceable energy-dissipating fuses (BRCs) without PT strands.

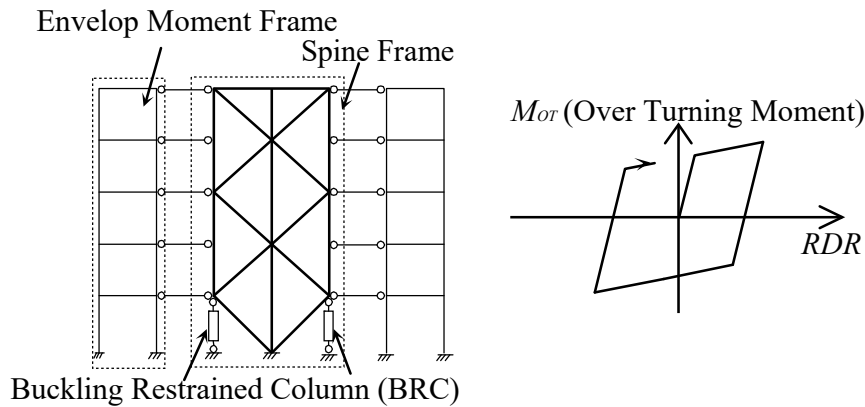


Fig. 2.10 One configuration of a non-uplifting spine frame system

Unlike in the LU system, the columns in the spine frame are replaced by BRCs and are fixed to the foundation, which solves the problems aroused by uplifting motion, such as special construction treatment for uplifting column base details, impact force to the foundation and accompanying noise. Fig. 2.11 shows the rocking mechanism of the proposed NL frame. The BRCs yield when deformation is small and dissipate earthquake energy. Meanwhile the spine frame starts swing. The rocking frames remain elastic while the energy is dissipated by the plastic deformation of replaceable fuses.

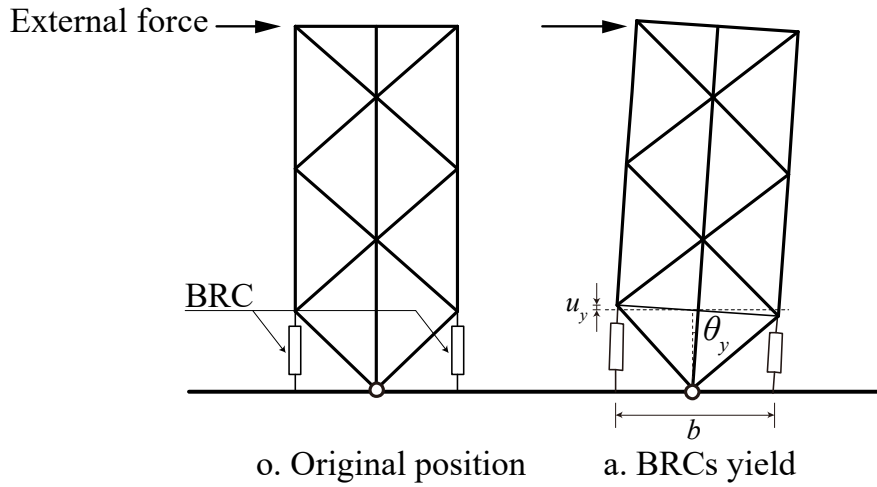


Fig. 2.11 The rocking mechanism of the proposed NL frame

The backbone curve of a single NL spine frame with BRC is shown in Fig. 2.12. The critical states of the NL system are:

- a:** BRCs yield during the braced frame uplifting, the frame starts swing
- b:** rocking direction reversal
- c:** force in BRCs reduces to zero
- d:** BRCs yield during the braced frame landing
- e:** roof drift ratio reaches the maximum value in the reversal direction, the frame starts next swing

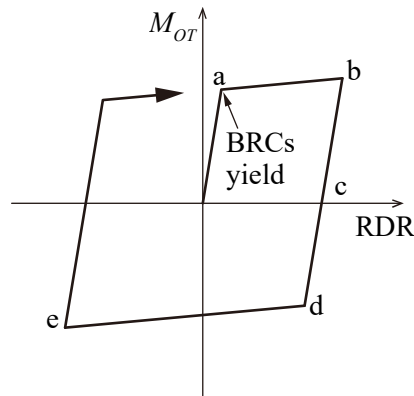


Fig. 2.12 load-deflection backbone curves of the NL frame

Residual deformation has a significant effect on the total loss caused by earthquake events.^[2.10-2.12] In the LU system, PT strands are employed to achieve self-centering and mitigate residual deformation of the rocking frame. For the structural scheme of spine frame under

investigation, the pre-stressed tensile force of PT strands should be larger than the yielding force of BRCs, thus the elastic force from PT strands can resist with the reaction force of the BRCs and pull the frame back to its original position. However, in actual project, the strength requirement of BRC is high and the pre-stress force of PT strands often reaches several thousand kN. PT strands are expensive and the anchor, shear force transfer details are complicate for construction.

In the NL system, PT strands are removed and the self-centering functions are achieved by the elastic restoring force from envelope elastic-moment frames. Although residual deformation of structures greatly depends on phase of ground motions, researches have also found that the post-yielding stiffness of structure itself significantly affects the residual deformation. [2.11] The envelope moment-resisting frame designed following Japanese seismic code exhibits high stiffness and strength. Even if the envelop frame includes weak or soft stories, the spine frame forces each story work together and enough restoring force can be provided. In Fig. 2.13, the force-deflection backbone curves of the proposed NL system with different envelope frames are compared.

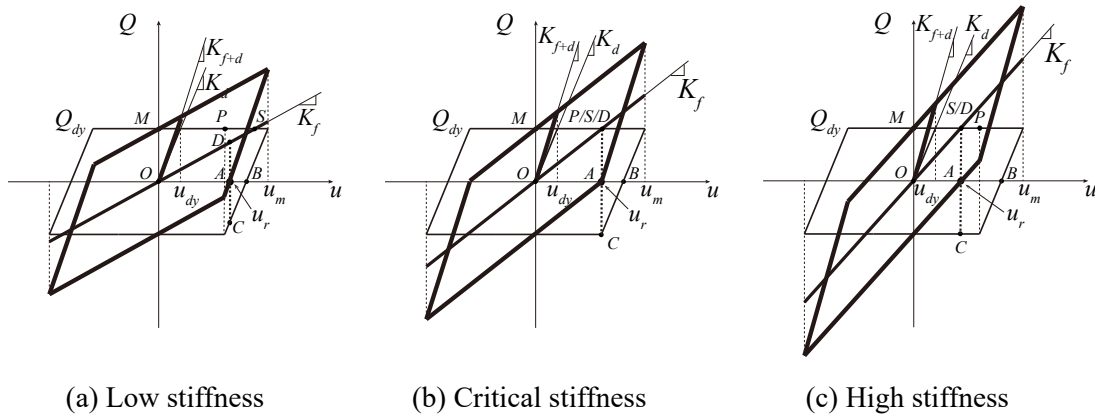


Fig. 2.13 Backbone curves of NL systems with different envelop frame stiffness

From Fig. 2.13 we can see that if the stiffness of the moment-resisting frame is enough strong, the residual deformation can be reduced significantly.

Simplify the hysteretic curve of the spine frame with energy-dissipating members as bilinear, assume isotropic hardening, and assume the stiffness of the moment-resisting frame is α times of the initial stiffness of the spine frame:

$$K_f = \alpha K_d \quad (2.4)$$

$$Q_{dy} = K_d u_y, \quad Q_y = (\alpha + 1) Q_{dy}, \quad Q_m = \alpha K_d u_m + Q_y \quad (2.5) \quad (2.6) \quad (2.7)$$

Where,

K_d : initial stiffness of the additional damper system

K_f : stiffness of the moment-resisting frame

u_{dy} : yielding deformation of the damper system

Q_{dy} : yielding force of the damper system

Q_y : force of the entire structure when dampers yield

u_m : maximum deformation of the entire structure

Q_m : maximum force of the entire structure

The static residual deformation of the NL system u_r can be calculated by the following equations (there are two cases according to whether the fuses yield before the total force reduces to zero):

Case 1 (the dampers yield after the total force reduces to zero):

$$|MS| \geq |MP|, \text{ e.i. } \frac{K_f}{K_d} \leq \frac{1}{\mu - 2} (\mu > 2), \text{ or any } \frac{K_f}{K_d} \text{ when } 1 \leq \mu \leq 2$$

$$|AD| = |AC|: u_r \cdot K_f = (u_m - u_{dy} - u_r) K_d \quad (2.8)$$

$$u_r = \frac{(1 - 1/\mu) u_m}{K_f / K_d + 1} \quad (2.9)$$

$$\text{When } \frac{K_f}{K_d} \leq \frac{1}{\mu - 2} (\mu > 2): u_r \geq \left(1 - \frac{2}{\mu}\right) u_m$$

$$\text{When } 1 \leq \mu \leq 2: u_r \leq \frac{1}{2} u_m$$

Case 2 (the dampers yield before the total force reduces to zero):

$$|MS| < |MP|, \text{ e.i. } \frac{K_f}{K_d} > \frac{1}{\mu - 2} (\mu > 2)$$

$$|AD| = |AC| = Q_{dy}: u_r \cdot K_f = Q_{dy} \quad (2.10)$$

$$u_r = \frac{u_m}{\mu K_f / K_d} \quad (2.11)$$

$$u_r < \left(1 - \frac{2}{\mu}\right) u_m \quad (2.12)$$

μ is the ductility ratio:

$$\mu = \frac{u_m}{u_{dy}} \quad (2.13)$$

From Eqs. (2.9), (2.11) we can see that, the static residual deformation is related with the maximum deformation, ductility ratio, and frame-damper stiffness ratio. The residual deformation increases with maximum deformation increases; while the residual deformation decreases when the ductility ratios or the frame-damper stiffness ratio increases.

For instance, if K_f/K_d is designed as 1.0, which can be easily realized in low-rise spine frame structures, and the ductility ratio is larger than 5.0, then the residual deformation will be less than 20% of the maximum deformation.

For the structure in this study, whose moment frame is designed following the current Japanese seismic design code, the stiffness of the first story is approximately 1.1 times of that of the spine frame. The residual deformation can be controlled within small value.

As can be seen from the hysteretic curves, compared with the LU system, the NL frame has smaller hardening stiffness and larger energy-dissipating capacity. The fundamental period of the total structure will not be decrease as much as the LU system. Moreover, the NL system tends to have larger system damping ratio compared with the LU rocking frame, which can decrease the velocity and acceleration response.

2.1.4 Prototype building

The prototype building is a research institute called MCES in Tokyo Institute of Technology Suzukakedai campus, Tokyo, Japan. The building structure was designed by Takeuchi-lab. A NL frame is employed in the X-Dir. while the SD system is employed in the Y-Dir. Fig. 2.14, 2.15 and 2.16 illustrate the perspective view, plan and structural system of the building, respectively. Although the structure was designed with a rocking frame in the X-direction and shear BRBs in the Y-direction, the BRBs in the Y-direction are not modeled in the comparison of the three structural systems.

The story height of the building is typically 4 m at regular stories; the first story is 4.2 m high. The plan dimensions are 27 m \times 27 m: 4.5 m \times 4.5 m bays for the external frames and 9.0 m \times 9.0 m bays for the internal frames. The braced bay is located in the middle of the building. Detailed information about members' size and materials are listed in Appendix A. Table 2.1 gives the gravity load and mass distribution.



Fig. 2.14 MCES Building

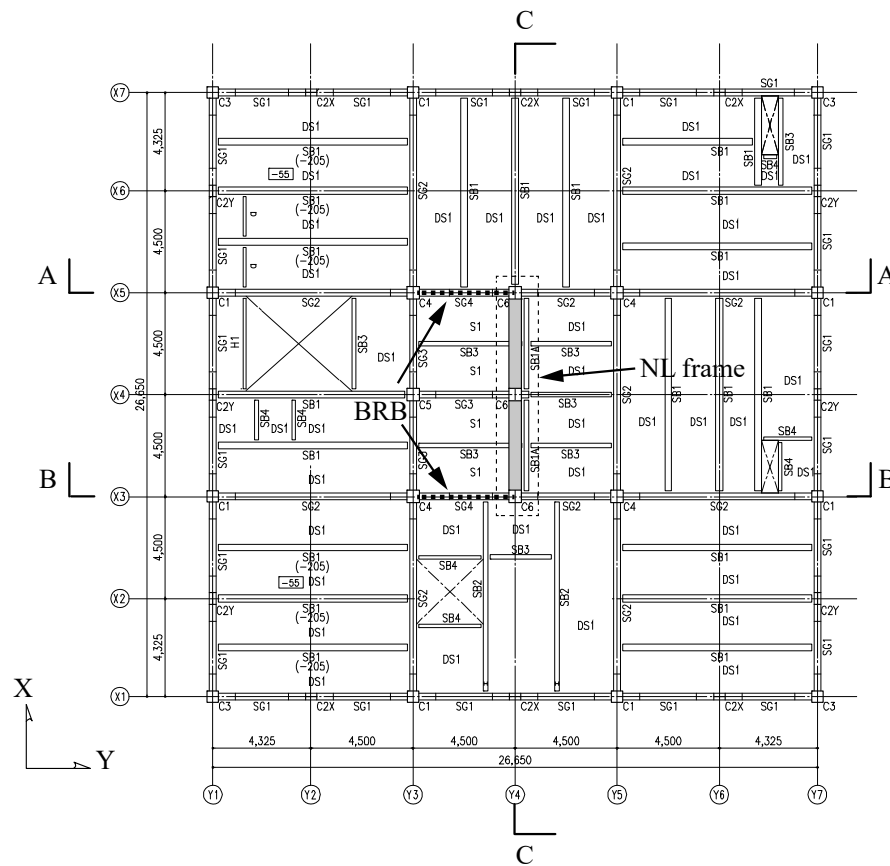


Fig. 2.15 Structural Plan of MCES Building

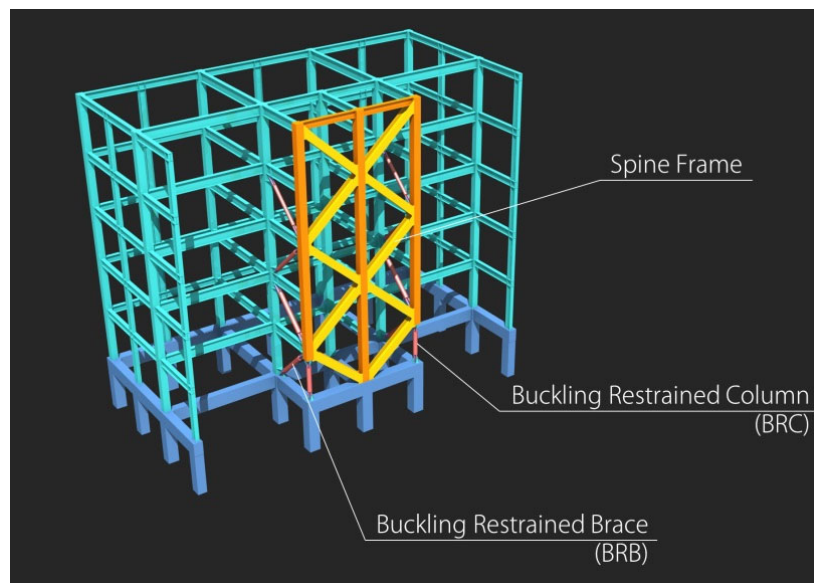


Fig. 2.16 Structural system of MCES Building

Table 2.1 Gravity load and mass distribution

	Gravity load (kN/m ²)	Mass (kN/m ²)
Roof	11.3	10.6
Second–fifth floor	7.65	6.65
Total	30500 kN	27000 kN

2.1.5 Design of the SD, LU, and NL models

The envelope steel moment-resisting frame in the MCEs building was designed according to the seismic design code of Japan^[2,13]. All of the structural components were elastic against the shear force in Lv. 1 design. In Lv. 2 design, the maximum story drift ratio is 0.43%, less than 1.0%. Besides, the ratio of the shear force capacity and necessary story shear force is 2.342 with high safety. Fig. 2.17 shows the story shear force and story drift ratio curves of each story of the envelop SMRF obtained from pushover analysis. The response at Lv. 1, Lv. 2, and Q_u are illustrated in the same Figure.

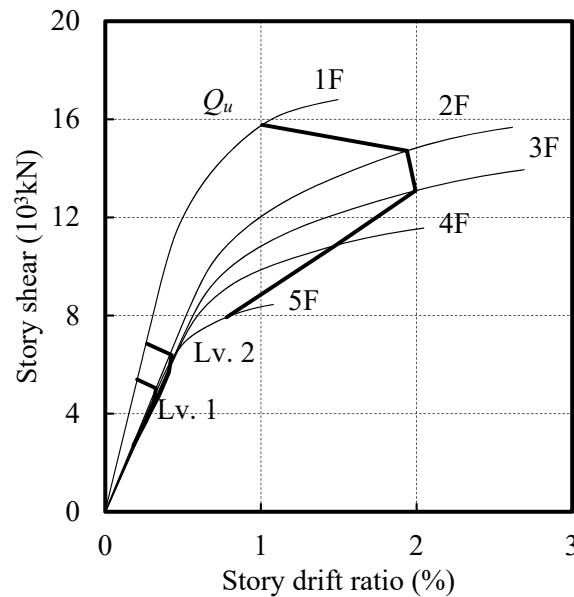


Fig. 2.17 Story shear force and drift ratio curves of each story of the envelope SMRF (Q_u represents the shear force bearing capacity of each story, which is the story shear force when the maximum story drift ratio reaches 2%.)

Design of the SD model:

The story drift ratio of each story is expected to be uniform when the main frame reaches the maximum deformation against Lv.2 earthquake ground motions. Thus deformation concentration can be prevented from occurring in the BRBs or the envelop SMRF in specific

stories. When the main frame reaches the maximum shear force under seismic loading, the summary of shear force of the main frame and the shear force of the BRBs were designed to comply with the A_i distribution. The story drift corresponding to BRB yielding was set as 6 mm (story drift ratio = 1/800). Based on the applications data of BRBs, the ratio of the length of plastic region and the total length of the brace is 1/3 ($l_c^{BRB}/(l_c^{BRB}+l_e^{BRB})=1/3$); the ratio of the area of the plastic core and the area of the elastic region is 1/2 ($A_c^{BRB}/A_e^{BRB}=1/2$). The detail parameters of BRBs in each story are listed in Table 2.2. The horizontal load sharing ratio of BRBs is 0.31 in each story. The story shear force and story drift ratio curves of the total frame compared with the shear force contribution of BRBs are shown in Fig. 2.18.

Table 2.2 Parameters of BRBs in each story in the SD model

Story	Sectional area (mm ²)	Stiffness (kN/mm)	Number	Yielding shear force $Q_{y,i}^{BRB}$ (kN)	Shear force bearing capacity Q_u (kN)	Horizonral load allocation ratio	Yielding drift ratio (%)
5	4318	196	2	1452	9432	0.31	0.17
4	5894	269	2	1982	12903	0.31	0.22
3	7092	323	2	2386	15556	0.31	0.24
2	7956	364	2	2676	17489	0.31	0.25
1	8697	396	2	2861	18746	0.31	0.16

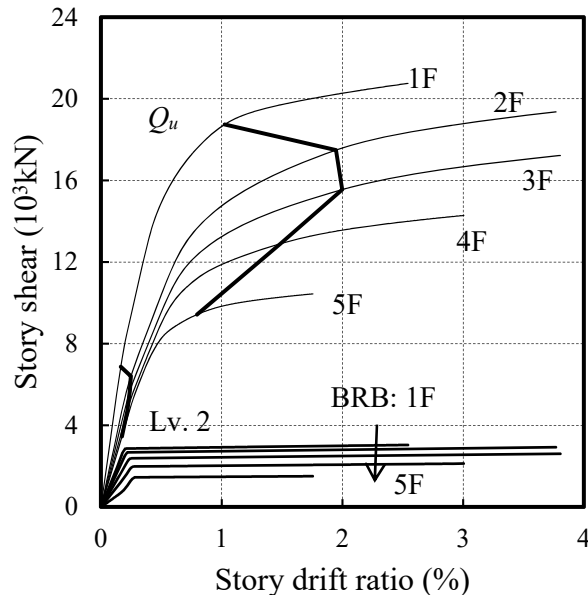


Fig. 2.18 Story shear force and story drift ratio curves of the SD model compared with the shear force contribution of BRBs

Design of the LU model:

The LU model with BRCs and PT strands was designed by replacing BRBF in the SD model with an enough stiff rocking frame, which remains mostly elastic in the second limit state. The cross-sectional size is H-550×550×19×25 and material is SN490B for the braces. The yielding force of the BRC and the pre-stress force of the PT strands were selected by determining an initial yielding overturning resistance of the rocking frame that was equal to the yielding overturning moment of the SD model.

The overturning moment of the SD model was calculated by equation (2.14).

$$M_{OT_SD} = Q_{y_5}^{BRB} H + \sum_{i=1}^4 (Q_{y_i}^{BRB} - Q_{y_i}^{BRB}) H_i \quad (2.14)$$

$$M_{OT_SD} = 1452 \times 20.2 + (1982 - 1452) \times 16.2 + (2386 - 1982) \times 12.2$$

$$+ (2676 - 2386) \times 8.2 + (2861 - 2676) \times 4.2$$

$$= 46000 \text{ (kNm)}$$

Equation (2.15) expresses the initial yielding overturning moment of the LU rocking frame.

$$M_{OT_LU} = (G_{rf} + F_{PT} + F_y^{BRC}) \cdot \frac{b_{rf}}{2} \quad (2.15)$$

where

M_{OT_LU} is the initial yielding overturning moment of the LU rocking frame;

G_{rf} is the dead load of the rocking frame;

$$G_{rf} = (11.3 + 7.65 \times 4) \times 27 = 3394 \text{ kN}$$

F_y^{BRC} is the axial yielding force of the BRC;

$$F_y^{BRC} = 13900 \times 325 \times 1.1 = 4969.25 \text{ kN}$$

b_{rf} is the width of the rocking frame; $b_{rf} = 9 \text{ m}$

F_{PT} is the axial force of the PT strands when the BRC yields;

$$F_{PT} = 46000 / 4.5 - 4969.25 - 3394 = 1859 \text{ kN}$$

The pre-stressing loss caused by the deformation of BRC can be calculated by Equation (2.16)

$$F_{LS} = \frac{E_{PT}}{E_{eq}} \frac{l_{BRC}}{l_{PT}} F_y^{BRC} \quad (2.16)$$

$$F_{LS} = \frac{205000}{236477} \times \frac{4.2}{20.2} \times 325 \times 1.1 = 64.44 \text{ kN}$$

E_{eq}^{BRC} is the equivalent stiffness of the BRC. It is calculated by the following Equation (2.17):

$$E_{eq}^{BRC} = \frac{E_{BRC}}{\frac{l_c^{BRC}}{l_{BRC}} + \frac{l_e^{BRC}}{l_{BRC}} \frac{A_c^{BRC}}{A_e^{BRC}}} \quad (2.17)$$

$$E_{eq}^{BRC} = \frac{205000}{\frac{1291}{4200} + \frac{2909}{4200} \times \frac{13888}{17192}} = 236477 \text{ MPa}$$

The pre-stressing loss caused by the gravity load is 11% of the initial tension force. So the total area of the PT strands can be expressed by Equation (2.18)

$$A_{PT} = \frac{F_{PT}}{(1 - 11\%) \sigma_0 + F_{LS}} \quad (2.18)$$

The initial tensile stress σ_0 of the PT strands was decided by the yield uplift ratio θ_y^{LU} , which was set to be 3.08%. From equations (2.1) and (2.2) we can obtain the expression for σ_0 :

$$\sigma_0 = \sigma_y - \frac{b_{rf}}{2l_{PT}} E_{PT} \theta_y^{LU} \quad (2.19)$$

Where, $\sigma_y = 1586.5 \text{ N/mm}^2$, $E_{PT} = 205000$. So, $\sigma_0 = 179.5 \text{ N/mm}^2$.

From equation (2.16) we can get the total area of the PT strands is 8300 mm^2 . The initial tension force was 1390 kN, which is 11.3% of the yielding force of the PT strands. Fig. 2.19 shows the story shear force and story drift ratio curves of the LU model compared with the shear force contribution of the rocking frame (RF).

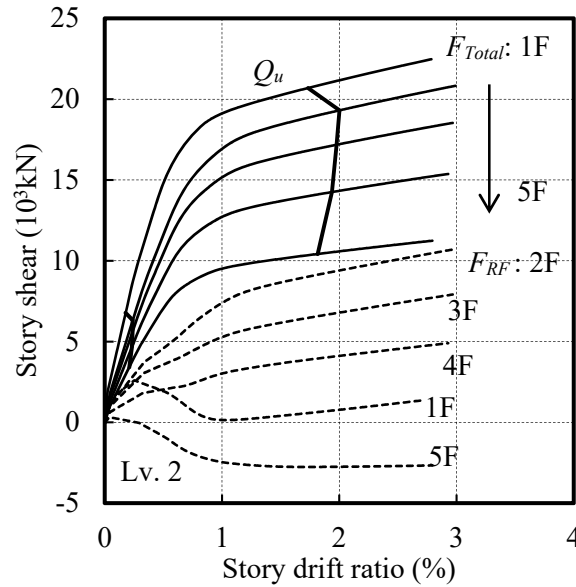


Fig. 2.19 Story shear force and story drift ratio curves of the LU model compared with the shear force contribution of the rocking frame (RF)

Design of the NL model:

The proposed NL model employs the same rocking spine frame as that in the LU model, and energy-dissipation fuses (BRCs) are distributed at the bases of side columns of the spine frame. The braces and central column are rigidly connected to the foundation, and plastic hinges

activate at large rocking drift. The BRCs are located along the lines of the side columns to maximize their energy-dissipation performance. The yielding force of the BRCs was selected by determining an initial yielding overturning resistance of the spine frame that was equal to that of the LU model. Equation (2.20) expresses the initial yielding overturning moment of the spine frame of the NL model.

$$M_{OT_NL} = F_y^{BRC} b_{rf} \quad (2.20)$$

where, M_{OT_NL} is the overturning moment of the spine frame; F_y^{BRC} is the yielding axial force of the BRC on one side; and b_{rf} is the width of the spine frame. The cross-sectional area and the yielding force of the BRCs were 13900 mm² and 4969.25 kN, respectively. Fig. 2.20 shows the story shear force and story drift ratio curves of the NL model compared with the shear force contribution of the spine frame (SF).

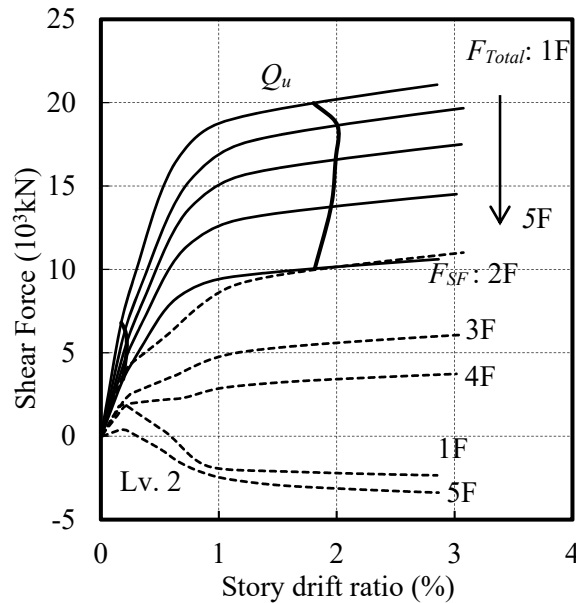


Fig. 2.20 Story shear force and story drift ratio curves of the NL model compared with the shear force contribution of the spine frame (SF)

Detailed three-dimensional numerical modeling of the SD, LU, and NL systems were conducted using the Open System for Earthquake Engineering Simulation (OpenSEES) software^[2,14], which has advanced capabilities for modeling and analyzing the nonlinear response of systems using a wide range of material models, elements, and solution algorithms. Centerline dimension models, which ignore the effects of panel zones and gusset plates, were employed for all models. A rigid floor was assumed, to ensure that the braced frame worked together with the envelope moment-resisting frame. Rayleigh damping that including mass matrix and tangent stiffness matrix proportional components were adopted. 0.02 critical damping ratio matching at the first and second modes was implemented in the numerical model.

2.2 Seismic performance of regular models

2.2.1 Static performances

Pushover analyses were carried out under the external lateral force on each floor proportional to the equivalent elastic lateral force obtained by the first vibration mode response (A_1 distribution) for each model. The overturning moment and roof drift ratio (RDR) curves of the braced frames and the base shear and roof drift ratio curves of the total structures are shown in Fig. 2.21. The yielding overturning moments of the three models were calibrated at approximately 46000 kNm. The LU rocking frame featured a larger hardening ratio than the other two models because the PT strands remained elastic during loading, but the difference was smaller in the responses of the entire structures.

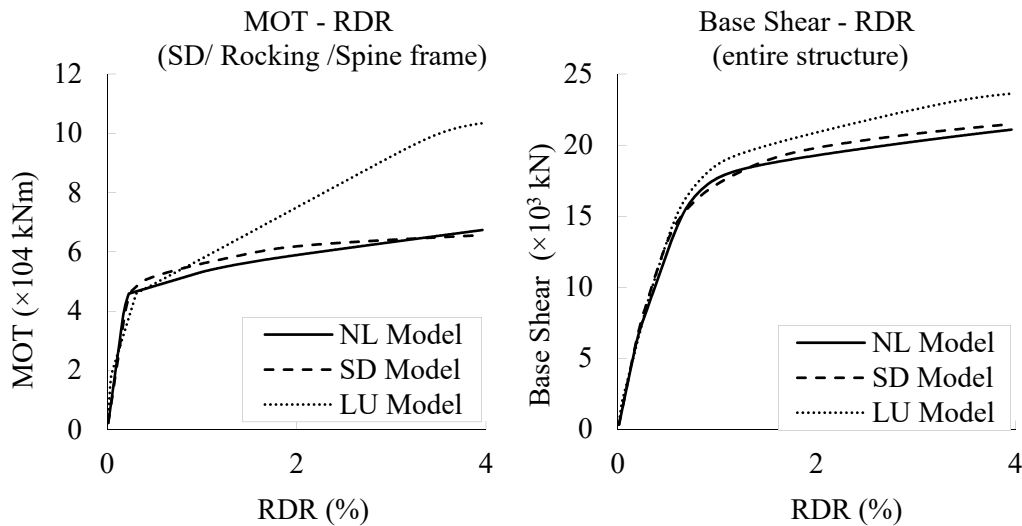


Fig. 2.21 Pushover results of the three models

2.2.2 Seismic responses under Level 2 earthquake

The number of ground motion pairs depends on how well the spectral shape of the scaled ground motions fits that of the target spectrum. If the spectral shape of the scaled ground motions matches well with that of the target spectrum, fewer motions can ensure a good evaluation of structures. The ground motions used herein included one artificial wave (BCJ-L2) and four observed waves: El Centro NS (1940), JMA Kobe NS (1995), TAFT EW (1925), and Hachinohe NS (1968). The duration and time interval of BCJ-L2 was 120 sec, 0.01 sec. The duration and time interval of the four observed waves was 30 sec, 0.02 sec for each wave.

In order to eliminate the variety among the response spectra of different ground motions and produce unbiased evaluation of the three models, the response acceleration spectra of the four recorded ground motions were scaled to match the target spectrum. In this study the target spectrum is the design spectra averaged for the life-safety limit state (BRI-L2, 10% probability of exceedance in a 50-year period) in Japan.

Acceleration spectrum:

$$S_A(T) = \begin{cases} 350D_{h_0} & (T < 0.05) \\ 350D_{h_0}(T/0.05)^{\{1+\log(S/7)/2\log 2\}} & (0.05 \leq T < 0.2) \\ 100D_{h_0} & (0.2 \leq T < \pi/5) \\ 100D_{h_0}/(T/2\pi) & (\pi/5 \leq T) \end{cases} \quad (2.21)$$

Velocity spectrum:

$$S_V = S_A(T/2\pi) \quad (2.22)$$

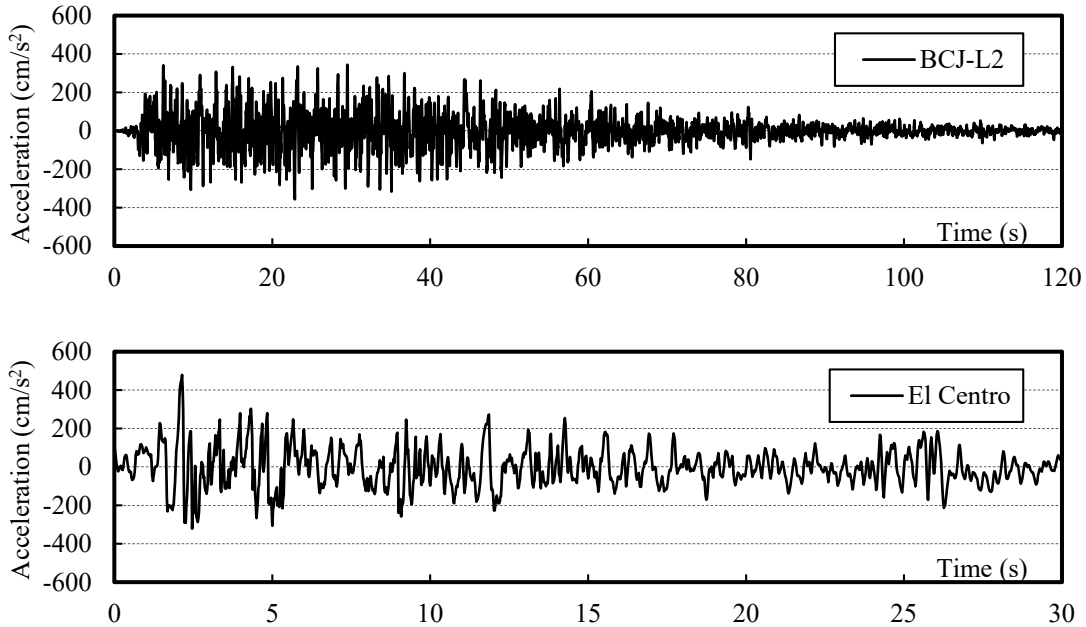
Displacement spectrum:

$$S_D = S_A(T/2\pi)^2 \quad (2.23)$$

$$D_{h_0} = \sqrt{\frac{(1+\alpha h_r)}{(1+\alpha h_0)}} (\alpha = 75) \quad (2.24)$$

Where, T is the fundamental period (sec), $h_r=0.05$, h_0 is the damping ratio of the modeled structure. The four observed ground motion waves were calibrated to follow the response spectra expressed by Equation (2.21) considering their phase characteristics. ^[2.15]

The time history curves of the 5 waves are shown in Fig. 2.22 and their acceleration spectra are shown in Fig. 2.23. The elastic natural periods of the third and sixth modes of each model are shown in Table 2.3. The periods of these two modes were similar in each model.



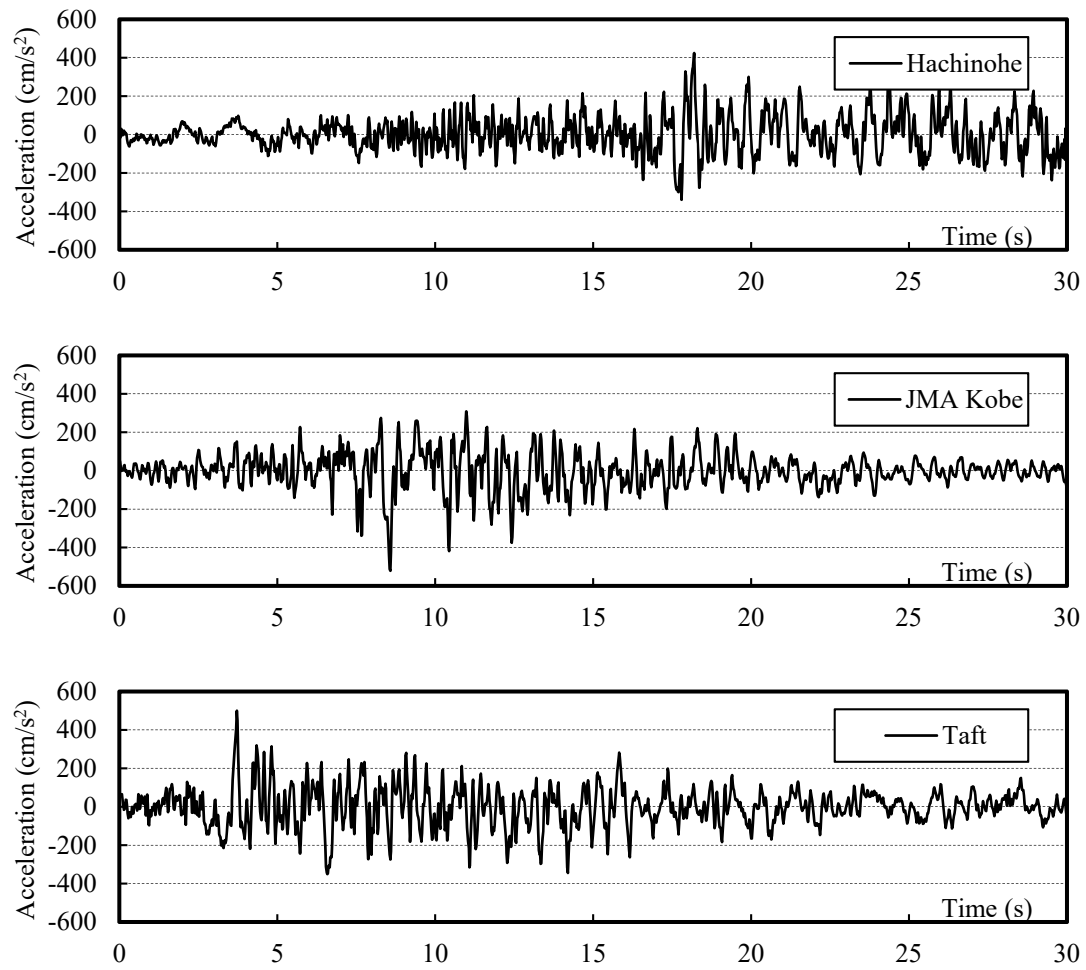


Fig. 2.22 Acceleration time history curves of the 5 ground motions

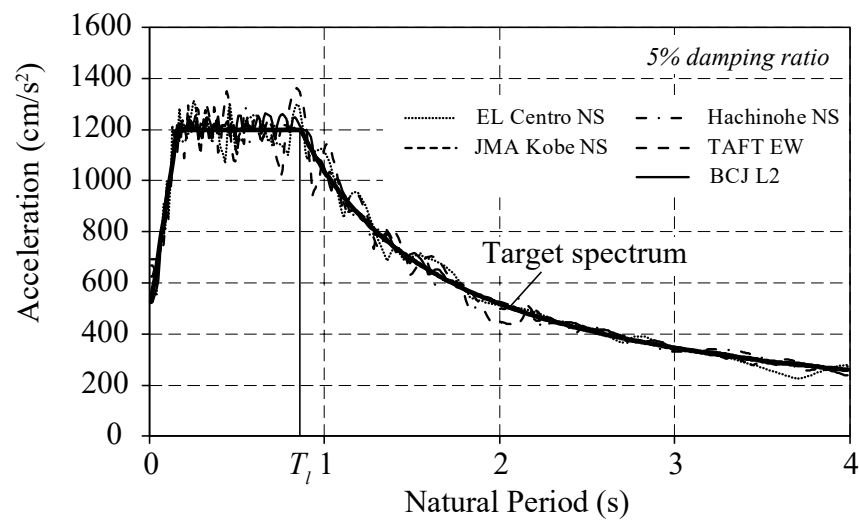


Fig. 2.23 acceleration spectra of the 5 input ground motion waves

Table 2.3. Elastic natural periods (unit: s)

Mode	Third	Sixth
NL model	0.630	0.152
LU model	0.516	0.149
SD model	0.646	0.198

Nonlinear response history analysis was used to evaluate performance of the three models at Lv2 ground shaking intensity. Key response parameters are maximum story drift ratio, residual story drift ratio, floor velocities, floor accelerations, and cumulative plastic energy in each story. Statistics analysis has been widely used to obtain median values and dispersions of the structural response, in order to assess the peak values and dispersion in structural response. However, as there are only 5 ground motions used in this study, only peak values in response were investigated and discussed.

Fig. 2.24 shows the overturning moment and roof drift ratio loops of the three models, determined from time-history analysis with Hachinohe NS ground motion input. The self-centering flag-shaped behavior of the LU model was confirmed in the response during numerical simulation.

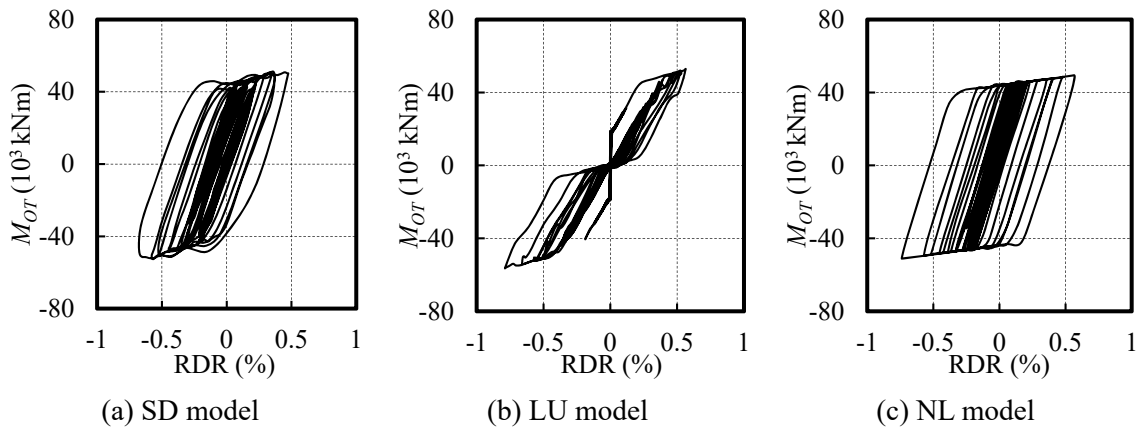


Fig. 2.24 Overturning moment and roof drift ratio hysteresis loops (Hachinohe NS)

The maximum shear force and story drift ratio response in each story of the three models under five ground motions that were scaled to match the Lv2 earthquake intensity was shown in Fig. 2.25. Fig. 2.25 (a), (c) and (e) show the shear force response of the SD, LU and NL model respectively. Fig. 2.25 (b), (d), and (f) show the story drift ratio response of the SD, LU and NL model respectively. The maximum shear force and maximum story drift ratio of each model against every ground motion were approximate with or less than the yielding value in their pushover curves, which indicates that the three models were mainly elastic under Lv.2 level

earthquake input. Both of the shear force and story drift ratio results against Hachinohe input were mostly the largest value while the results against JMA Kobe input were mostly the smallest in each story of the three models. The results from the artificial wave BCJ-L2 in the LU model were close to the middle values of the results from the four observed waves, while the results from BCJ-L2 in the SD and NL models were smaller than the middle values.

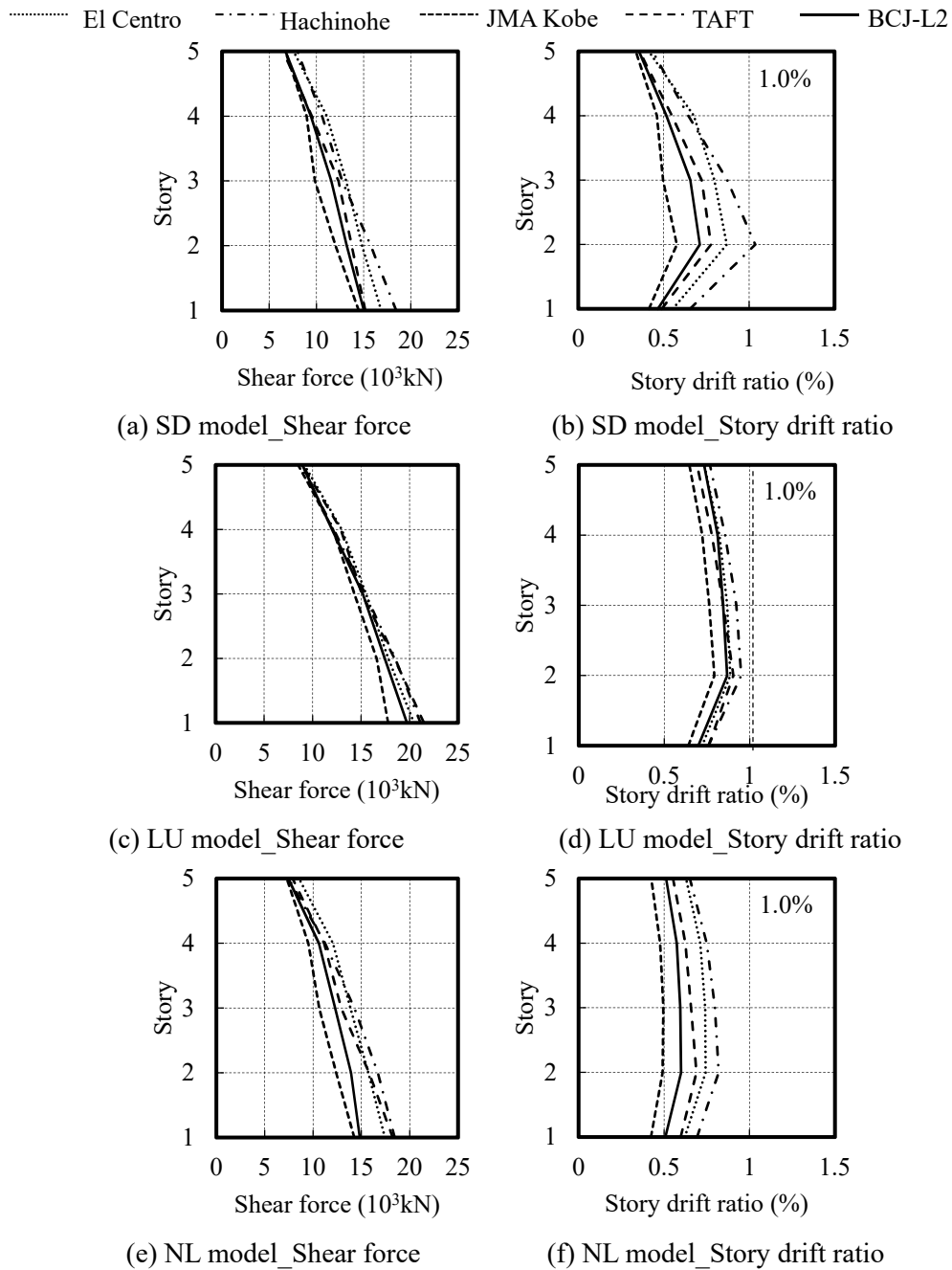


Fig. 2.25 Story shear and SDR of each model under Lv2 earthquake input

The SD model exhibited the smallest shear force almost in every story among the three models. On the contrast, the LU model exhibited the largest shear force in every story among the three models. The shear force of the NL model was between that of the SD model and the LU model, and tended to be closer with the shear force of the SD model in lower stories. The shear force sequence was identical with the fundamental period sequence of the three models, indicating that the first modes of the models dominated the dynamic response.

The SD model exhibited the smallest story drift ratio in the first, forth and fifth stories but the largest story drift ratio in the second story among the three models. The LU and NL model also possessed the largest story drift ratio in the second story but with the difference between other stories was relatively smaller than the SD model. Moreover, the maximum story drift ratio of the NL model was the smallest among the three models.

The SD model had a strong tendency to concentrate deformation in the second story. In contrast, the LU and NL models distributed a more uniform SDR owing to their spine mechanisms. To better understand the effectiveness of spine frames in reducing deformation concentration, the ratio of maximum SDR to RDR is used to express the story drift concentration factor (DCF). As shown in Fig. 2.26, under all five ground motions, the proposed NL model exhibited the smallest DCF, the DCF of the LU model was higher, and the SD model displayed the highest DCF. Among all three models, the NL model exhibited the smallest peak story drift and the smallest DCF.

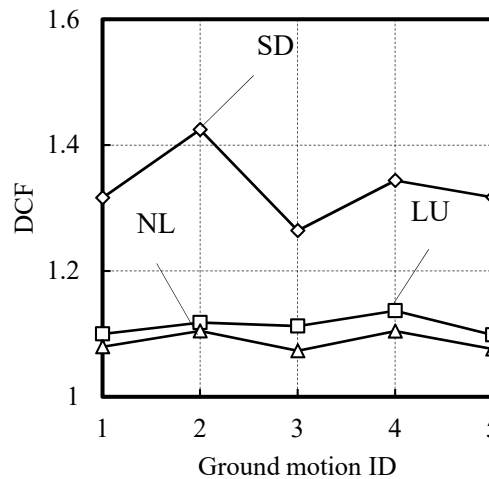


Fig. 2.26 Drift concentration factors of SD, LU, and NL models
(Ground motion IDs: 1. El Centro; 2. Hachinohe; 3. JMA Kobe; 4. TAFT; 5. BCJ-L2;
these are the same in the following figures)

Residual drift predicted by nonlinear analysis is highly sensitive to component modeling assumptions related to post-yield hardening/softening slope and unloading response. Accurate statistical simulation of residual drift requires the use of advanced component models, careful attention to cyclic hysteretic response, and a large number of ground motion pairs. Although the number of ground motion pairs is relatively small in this study, the accuracy of residual drift simulation is enough for comparing the self-centering capacity of the SD, LU, and NL models.

Fig. 2.27 shows the residual story drift ratio (ReSDR) of each story in all three models. All the story drift ratio values were less than 0.12%, and less than 0.05% in the LU and NL models. As shown in Fig. 2.25, the base shear forces were close to the yielding strength obtained from the pushover analysis, which means that the main frames were almost elastic. The maximum shear force of the LU model tended to be greater than that of the SD model; however, the residual story drift ratio of the LU model was smaller than or similar to that of the SD model. Unlike the case of the LU model, the maximum shear force of the NL spine system was identical to that of the SD model, whereas the residual story drift ratio of the NL model was smaller than that of the SD model in all cases. This suggests that the elastic reaction forces from the envelope frame of the NL spine system were sufficiently large to overcome the residual axial force of the BRCs. The proposed NL spine system possesses excellent resilience capacity when the envelope SMRF is elastic or yields slightly.

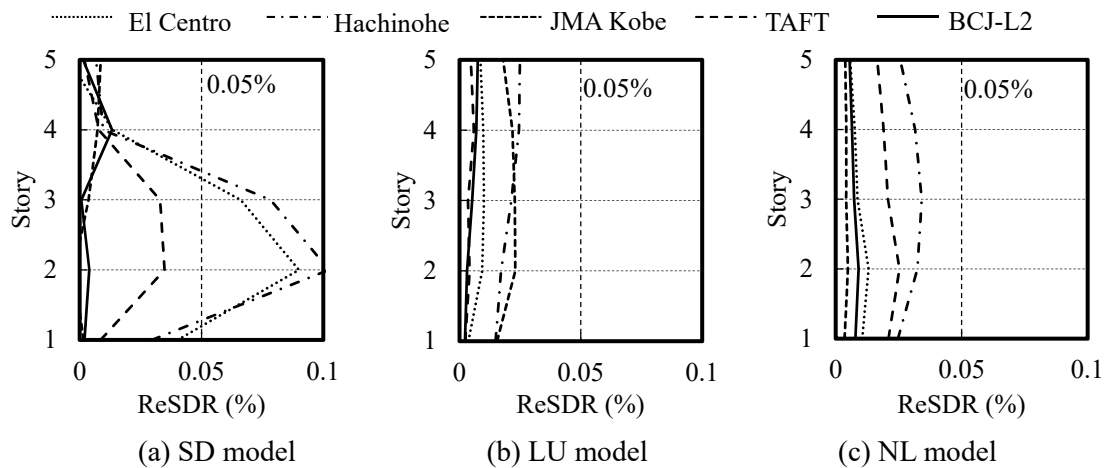
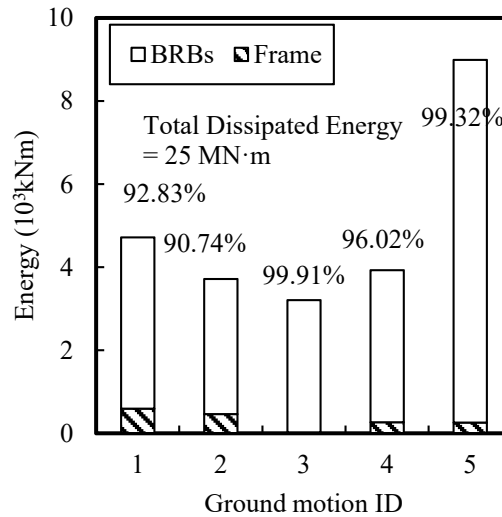


Fig. 2.27 Residual story drift ratio of SD, LU, and NL models

The input energy is dissipated by the system damping mechanism and the cumulative plastic deformation of the fuses and the main frame. In this study, the analysis time was long enough to obtain stable residual story drift ratio, so the kinetic energy and elastic strain energy were negligible at the end of the analysis compared with the damping and cumulative plastic strain energy (CPE). The cumulative plastic strain energy of the five ground motion inputs for the SD,

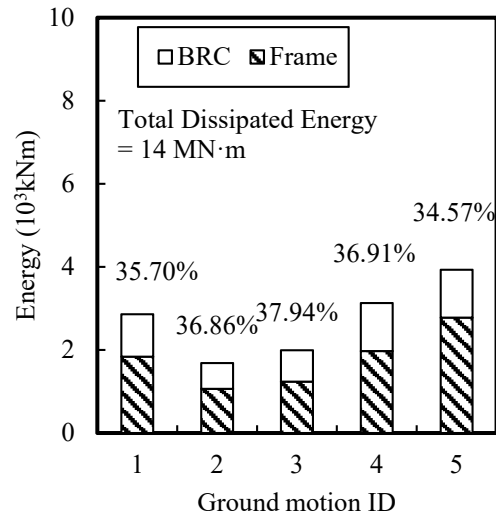
LU, and NL models were 25 MNm, 14 MNm, and 25 MNm, respectively; the damping energy values were 14 MNm, 24 MNm, and 15 MNm, respectively; and the total input energy values were 39 MNm, 38 MNm, and 40 MNm, respectively. The input energy values of the three models were close to each other. Conversely, the damping energy of the LU model was larger than that of the SD and NL models. A larger velocity response was observed in the LU model than in the SD and NL models. This indicates that the flag-shaped hysteretic response of the LU model had a lower capacity for energy dissipation. As a result, the amount of input energy that was converted into kinetic energy and absorbed by the damping mechanism in the LU model was larger than that in the SD and NL models.

In Fig. 2.28, the non-hatched areas in the bar chart represent the cumulative plastic strain energy of the BRBs or BRCs, and the hatched areas represent the envelope frames. The numbers above each bar denote the percentage of plastic strain energy of the BRBs or BRCs in the total plastic strain energy of the structures. In the proposed NL spine system, the earthquake input energy was greatly dissipated by the two BRCs at the bottom of the spine frame. The percentages of plastic strain energy of the BRCs in the total plastic strain energy of the structure ranged from 90.74% to 99.91%. Similar to the NL spine system, the BRBs in the SD system dissipated more than 85% of the total plastic strain energy. For the LU rocking system, the main frame dissipated up to 60% of the total plastic strain energy, which was greater than the energy dissipated by the BRC.

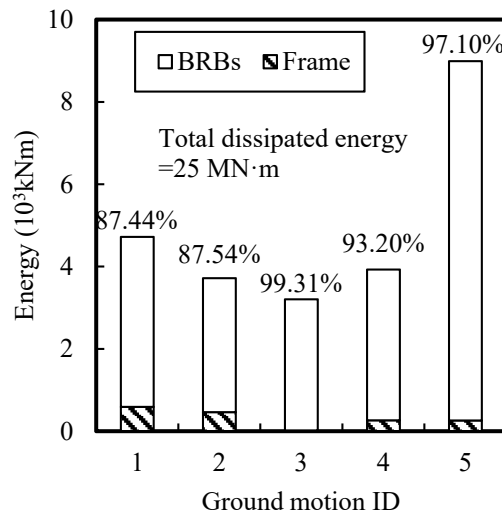


(a) SD model

Fig. 2.28 (a) Cumulative earthquake energy dissipation ratios of dampers
(Ground motion IDs: 1. El Centro; 2. Hachinohe; 3. JMA Kobe; 4. TAFT; 5. BCJ-L2)



(b) LU model



(c) NL model

Fig. 2.28 (b-c) Cumulative earthquake energy dissipation ratios of dampers
(Ground motion IDs: 1. El Centro; 2. Hachinohe; 3. JMA Kobe; 4. TAFT; 5. BCJ-L2)

Because the duration of the BCJ-L2 ground motion was longer than that of the four observed ground motions, the cumulative plastic strain energy of the main frame was compared among only the four observed waves. The proposed NL model had the best distribution of energy dissipation and the lowest plastic strain energy of the envelope frame, as illustrated in Fig. 2.29. This model dissipated energy through the beams from the first floor to the fourth floor; however, all the members in the spine frame and columns remained elastic. The largest amount of cumulative plastic strain energy in one story of the envelope frame in the NL model was 125.12

kNm. The envelope frame in the SD model dissipated the most energy in the second and third floors, as shown in Fig. 2.29 (a), which indicates that damage was concentrated at those locations. The largest amount of plastic strain energy in one story of the SD model was 246.46 kNm. The main frame in the LU model dissipated the largest amount of energy compared with the other two systems. The peak value of plastic strain energy in one story of the LU model was 677.90 kNm. The main frame of the proposed NL model suffered the least damage among all three models.

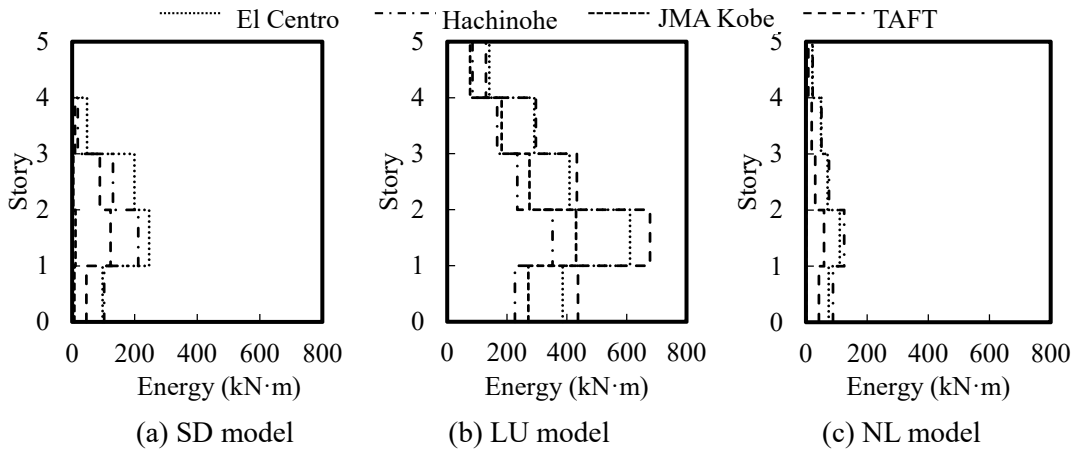


Fig. 2.29 Cumulative earthquake energy dissipated by the envelop frame

2.2.3 Incremental dynamic analysis

The LU rocking frame is expected to avoid damage concentration and eliminate permanent story drifts of the structures. However, its robustness remains unclear under unexpectedly strong earthquakes, which may lead to yielding of the PT strands. Incremental dynamic analysis (IDA)^[2,16] was conducted to compare the seismic safety of the three structural systems, focusing particularly on the ultimate state of the LU rocking system after yielding of the PT strands and the performance of the NL spine system subjected to the same earthquake level.

The intensity measure (IM) was the peak ground acceleration (PGA). The damage measure (DM) was the maximum story drift ratio and residual story drift ratio. The selected ground motions were scaled up until the maximum story drift ratio reached 10% or until the PGA reached 60 m/s^2 . The maximum story drift ratio IDA curves of the three models are compared in Fig. 2.30.

Generally, for the SD model, the softening of the IDA curves was more significant than that of the NL and LU models, although the strength deterioration was not considered in the models. Yielding of the PT strands occurred when the maximum story drift ratio was approximately 5%. Only under the Hachinohe ground motion input, after the PT strands yielded, the maximum story drift ratio in the LU frame grew significantly faster than the NL frame with increased

earthquake input intensity. Under other earthquake inputs, the differences were not significant between the IDA curves of the LU and NL models immediately after the PT strands yielded; generally, the maximum story drift ratio of the SD model exceeded those of the NL and LU models with the same ground motion intensities.

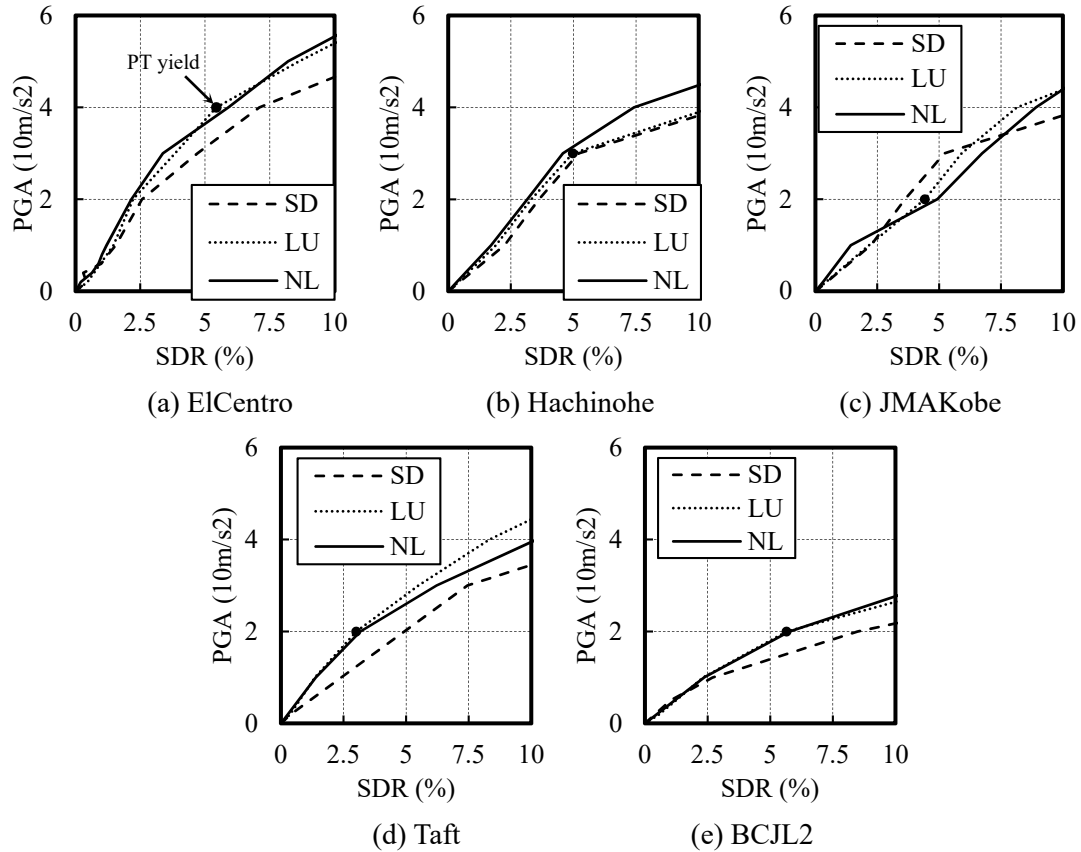


Fig. 2.30 IDA curves of maximum story drift ratio

The residual story drift ratio IDA curves of the three models are compared in Fig. 2.31. When the PGA is less than 5m/s^2 , the residual story drift ratios were almost 0.0% in the three models. After the PGA exceeded 5m/s^2 , the residual story drift ratio in the SD frame grew significantly faster than the NL and LU frame with increased earthquake input intensity, except in the analysis case with JMA Kobe ground motion input. The residual story drift ratio response of three models against BCJ-L2 ground motion were significantly larger than the response of other four observed ground motions, mainly due to the longer duration of BCJ-L2 input. The maximum story drift ratio response of BCJ-L2 input also showed similar results. Among the response of four observed waves, the JMA Kobe resulted in the smallest residual story drift ratio, which kept less than 3% even when the PGA increased to 40m/s^2 , which might be because there is only one main pulse in the JMA Kobe ground motion. Fig. 2.30 illustrated that the PT element

in the LU model yielded when $\text{PGA}=40\text{m/s}^2$, 30 m/s^2 , 20 m/s^2 , 20 m/s^2 in the analysis under El Centro, Hachinohe, JMA Kobe, Taft input, respectively. However, yielding of the PT element didn't have much influence on the residual story drift ratio, which also indicated that the envelope moment-resisting frame was stiff enough and well balanced to ensure the robustness even after the PT element yielded.

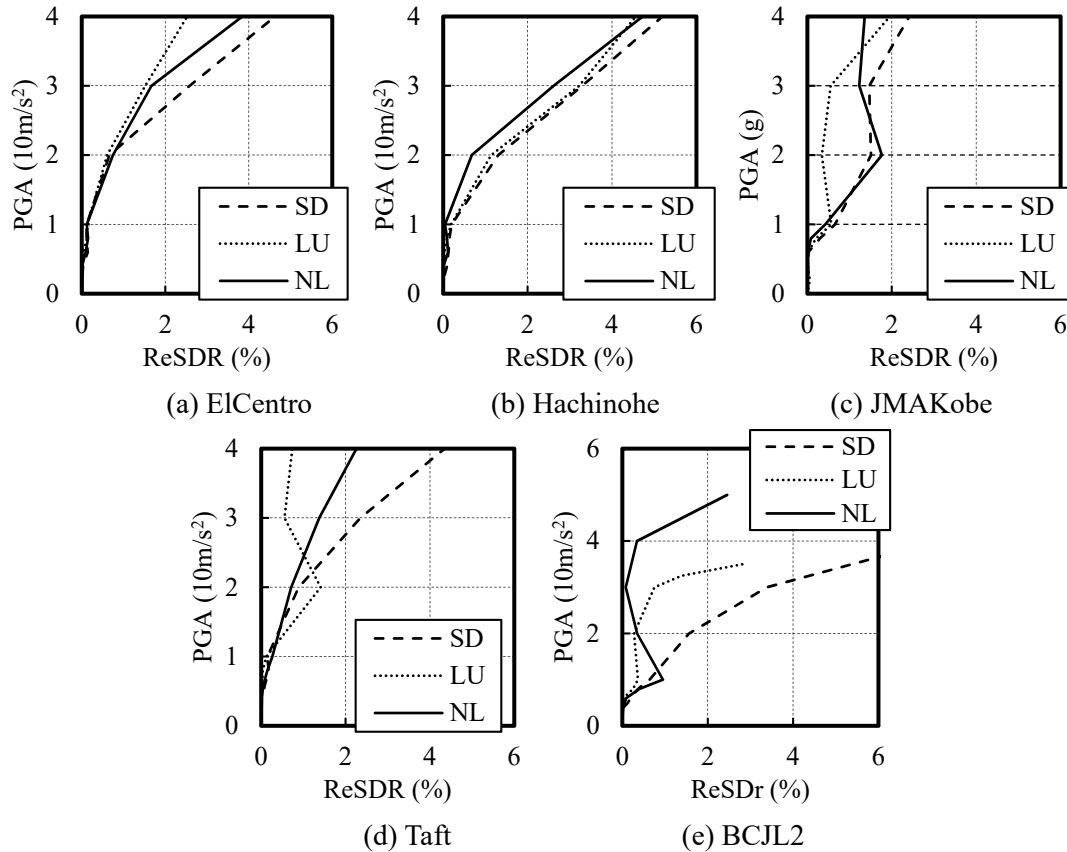


Fig. 2.31 IDA curves of residual story drift ratio

2.3 Seismic performance of single-story structural irregular models

2.3.1 Design of single-story structural irregular models

Building structures with vertically unbalanced strength distributions are commonly seen in modern urban areas, primarily because of architectural constraints. According to previous studies, the strength, stiffness, and mass irregularity significantly degrade the seismic behavior of these structures [2.17-2.21]. Special attention is necessary in the design of such irregular buildings. The proposed NL spine frame system is expected to distribute damage throughout the structure under a certain level, even for irregular building configurations. To evaluate the structural response of the three systems with vertical irregularities, the models in previous sections were modified by degrading both the stiffness and strength of all columns in a certain

story of the moment-resisting frame.

Five groups of different vertical structural irregular models were created corresponding to different weakened stories by reducing the section area or material strength of columns. The column numbers are shown in Fig. 2.32 and the details of the weakened columns are summarized in Table 2.4.

Table 2.4 Sections & material strength decreasing of columns in each model
(unit: mm, MPa)

First story weakened model					
SC1	BOX-500×500×22	357.5	Weaken to	BOX-320×320×22	258.5
SC3	BOX-500×500×19	357.5		BOX-320×320×19	258.5
SC4	BOX-550×550×22	357.5		BOX-320×320×22	258.5
SC5	BOX-550×550×22	357.5		BOX-320×320×22	258.5
Second story weakened model					
SC1	BOX-500×500×19	357.5	Weaken to	BOX-320×320×19	258.5
SC3	BOX-500×500×19	357.5		BOX-320×320×19	258.5
SC4	BOX-550×550×22	357.5		BOX-320×320×19	258.5
SC5	BOX-550×550×22	357.5		BOX-320×320×19	258.5
Third story weakened model					
SC1	BOX-500×500×19	258.5	Weaken to	BOX-300×300×19	258.5
SC3	BOX-500×500×19	258.5		BOX-300×300×19	258.5
SC4	BOX-550×550×22	258.5		BOX-320×320×22	258.5
SC5	BOX-550×550×19	258.5		BOX-320×320×19	258.5
Fourth story weakened model					
SC1	BOX-500×500×19	258.5	Weaken to	BOX-300×300×19	258.5
SC3	BOX-500×500×19	258.5		BOX-300×300×19	258.5
SC4	BOX-550×550×19	258.5		BOX-320×320×19	258.5
SC5	BOX-550×550×19	258.5		BOX-320×320×19	258.5
Fifth story weakened model					
SC1	BOX-500×500×16	258.5	Weaken to	BOX-300×300×16	258.5
SC3	BOX-500×500×16	258.5		BOX-300×300×16	258.5
SC4	BOX-550×550×19	258.5		BOX-320×320×19	258.5
SC5	BOX-550×550×19	258.5		BOX-320×320×19	258.5

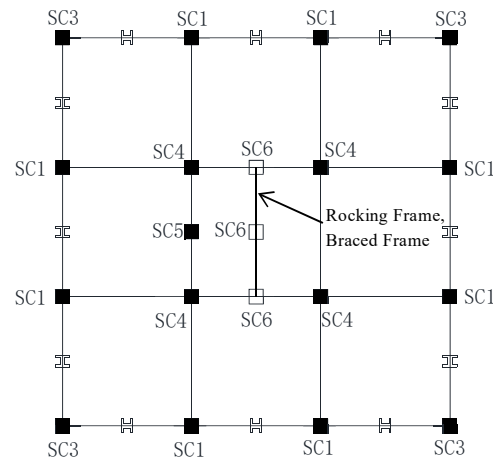


Fig. 2.32 Columns positions in structural plan

Static pushover analysis with equivalent horizontal force following A_i distribution of each irregular model was carried out. Fig. 2.33 shows the story shear force and story drift ratio relationship of each model.

For all the SD, LU, and NL models, the degradation of the first-story columns caused obvious degradation in the strength of every story, particularly for the first story of the SD model.

The degradation of the columns in the second story significantly decreased the stiffness and strength of the second story in the SD model, and the second story degradation also led to slight strength degradation in the third, fourth, and fifth stories in the SD model. On the contrast, weakening of the columns in the second story had a negligible influence on the stiffness and strength of every story in the LU and NL models. Only slight stiffness decreasing of the second story in the LU model, as well as slight stiffness and strength decreasing of the first and second story in the NL model, can be observed from the pushover results.

Significant story stiffness and strength decreasing can be observed from the pushover results of the SD models with degraded columns in either the third story or the fourth story. Relatively small strength decreasing can also be observed in the other stories of the SD models. While for the LU and NL models, degradation of columns in the third or fourth story had negligible influence on the stiffness and strength of every story, except slightly stiffness decreasing of the weakened stories.

Degradation of columns in the fifth story caused similar strength degradation in each story of all the three models and stiffness degradation in each story of the LU and NL models.

In conclusion, degradation of columns in the first story significantly decreased the horizontal force resistance capacity of each story if the NL and LU models. Degradation of columns in the top story also cause slight story degradation in the lower stories, but the degradation of columns in the middle stories has negligible influence on the horizontal force resistance capacity of each

story in the LU and NL models due to the rigid body mechanism. For the SD model, degradation of columns in each story led to overall horizontal force resistance capacity decreasing, particularly in the weakened story.

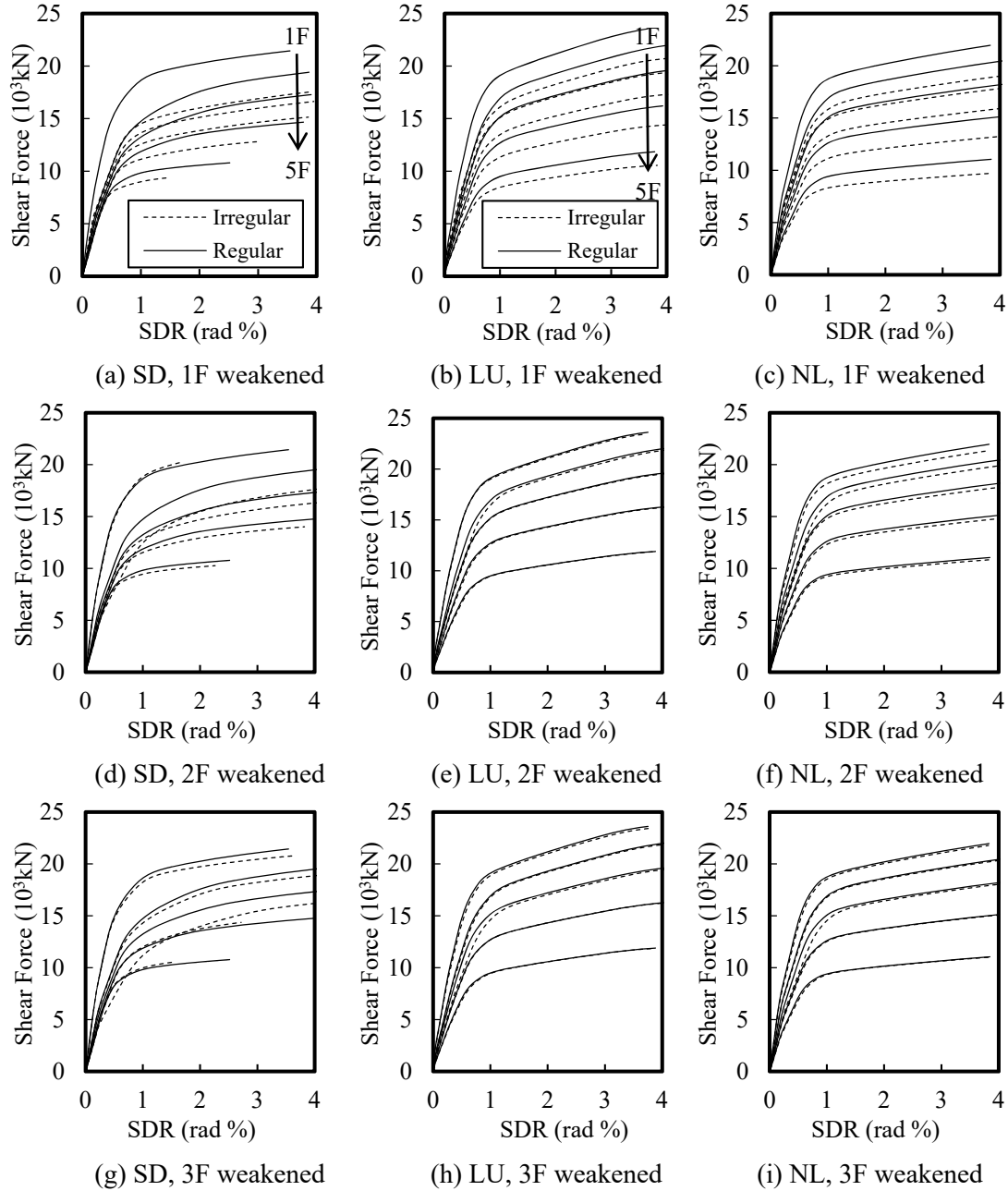


Fig. 2.33 (a-i) Shear force – story drift ratio relationship of 1-3F weakened models

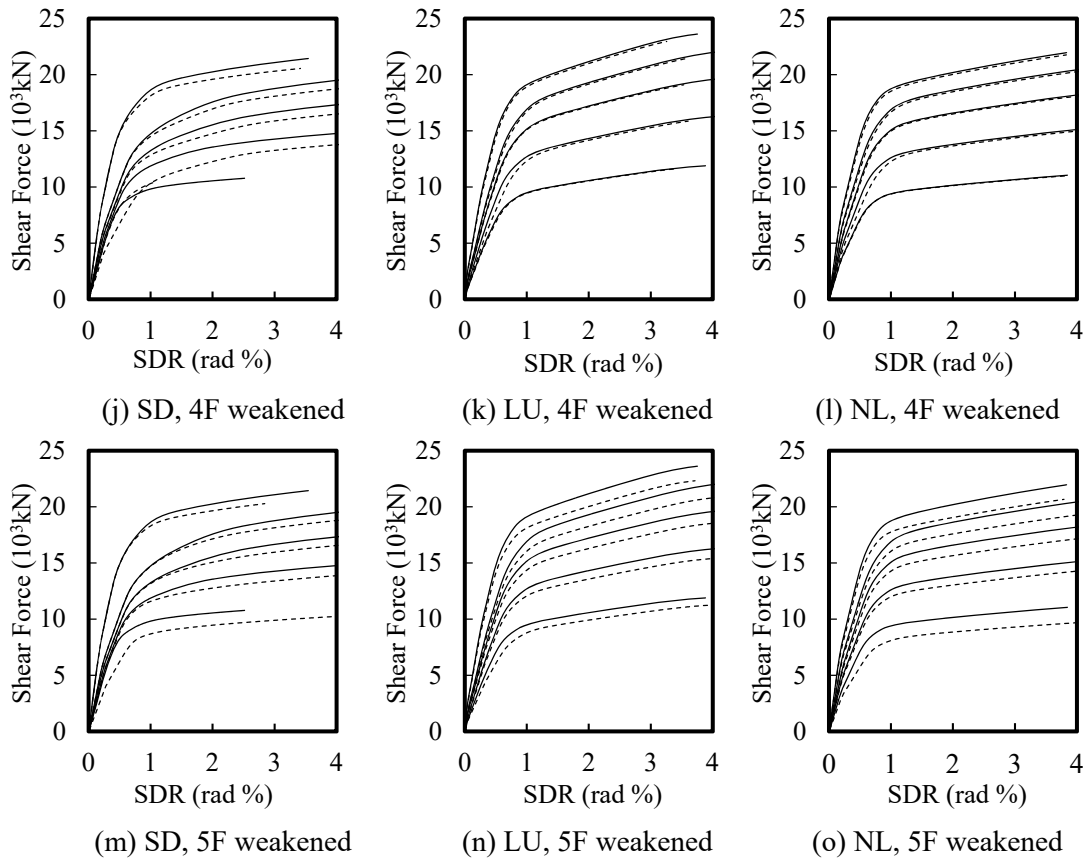


Fig. 2.33 (j-o) Shear force – story drift ratio relationship of 4-5F weakened models

2.3.2 Seismic responses against level 2 earthquake

Time history analysis with same earthquake ground motion series used for the regular models was carried out for the irregular models as well. The maximum story drift ratio (SDR), residual story drift ratio (ReSDR), and maximum story shear force of the 1st-story and 2nd-story irregular models were summarized in Fig. 2.34.

The maximum shear force and maximum story drift ratio of each irregular model of the LU and NL models against every ground motion were approximate with or less than the yielding value in their pushover curves, which indicates that the two groups of models were still mainly elastic under Lv.2 level earthquake input even with structural irregularities. However, for the irregular SD models, the maximum story drift ratio exceeded 1.0%, particularly in the first-story and second-story irregular models, which indicates that plasticity had developed in those models when the structure was against Lv. 2 level ground motion. Similar to the results of regular models, both of the shear force and story drift ratio results against Hachinohe input were mostly the largest value while the results against JMA Kobe input were mostly the smallest value in each story of the three models.

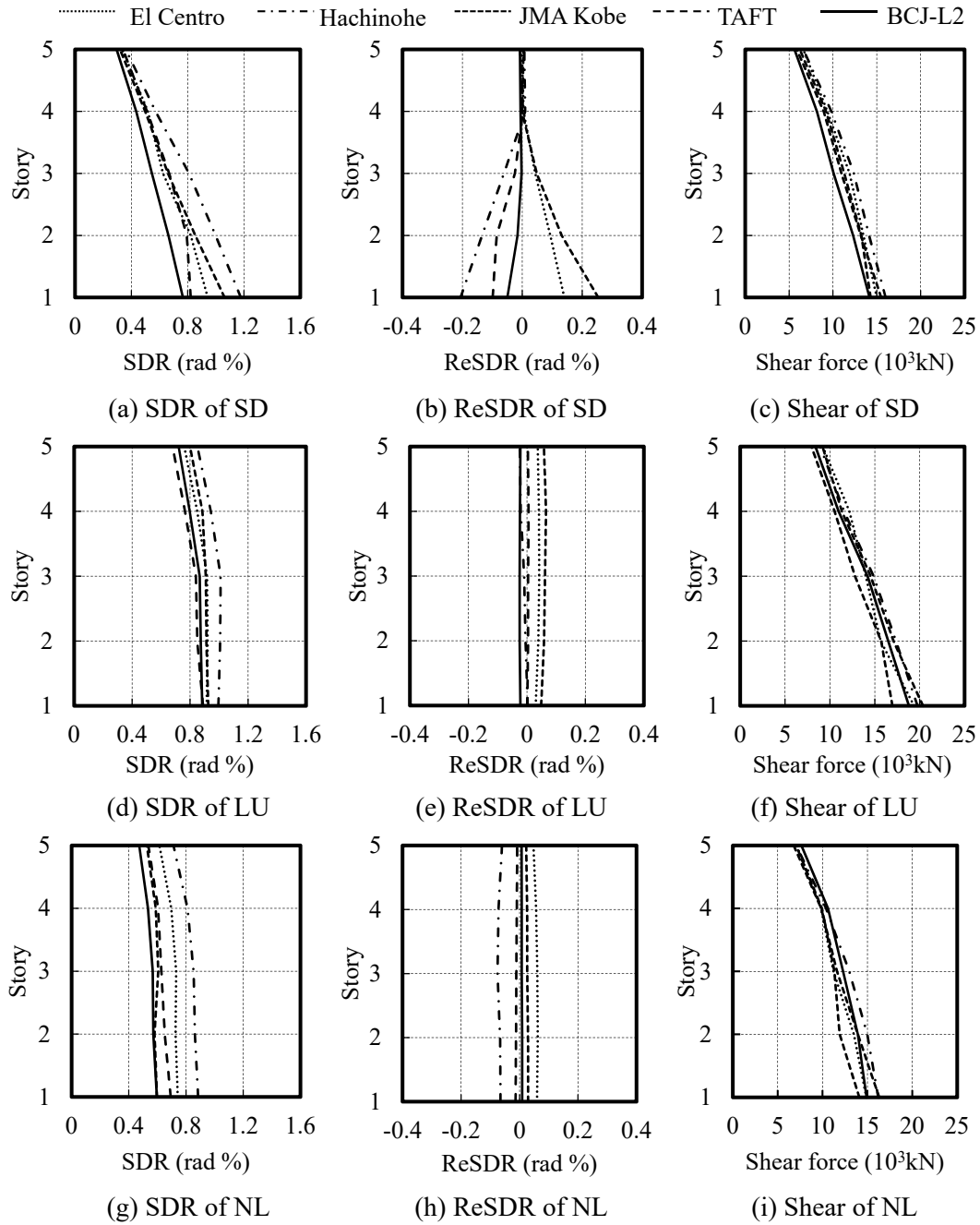


Fig. 2.34.1 Seismic responses of the 1st story irregular models

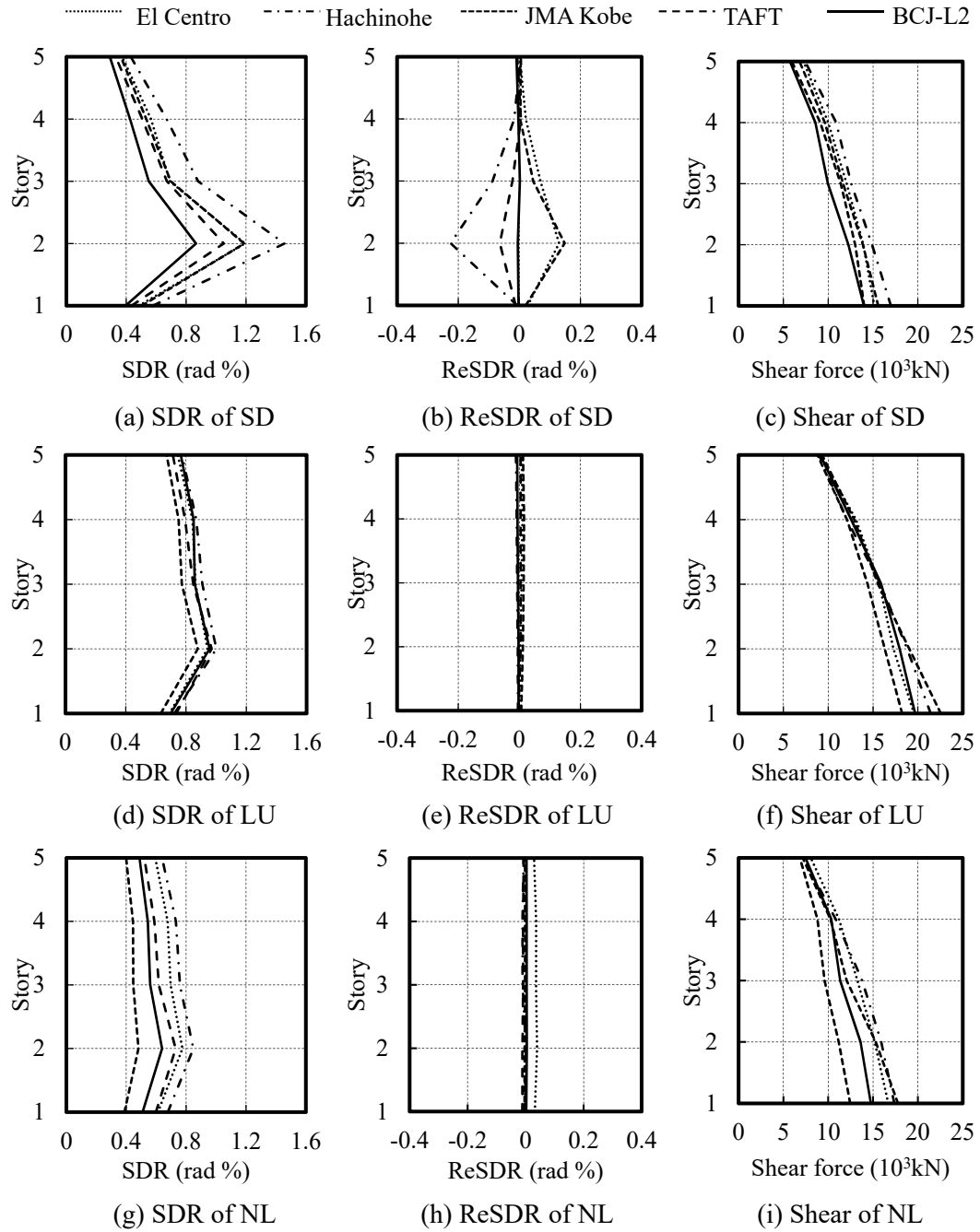


Fig. 2.34.2 Seismic responses of the 2nd story irregular models

Among the first-story irregular models, the maximum story drift ratio of the SD model was approximately 1.2%, and that of the LU and NL models were approximately 1%. Among the second-story and third-story irregular models, the maximum story drift ratio of the SD model was approximately 1.5%, that of the LU model was again approximately 1%, and that of the proposed NL model was the smallest among the three models. Among the fourth-story and fifth-story irregular models, the maximum story drift ratios of the SD and LU models were approximately 1%, and that of the proposed NL model was again the smallest among the three models.

It is clear that even for the irregular models; serious deformation concentration occurred in the SD models, particularly in the first and second irregular models. On the contrary, the LU and NL models controlled a more uniform story drift distribution over the height of the building than the SD model did. Moreover, the uniform distribution ability of the LU and NL models were close with each other. The drift concentration factors of the first-story and second-story irregular models are shown in Fig. 2.35.

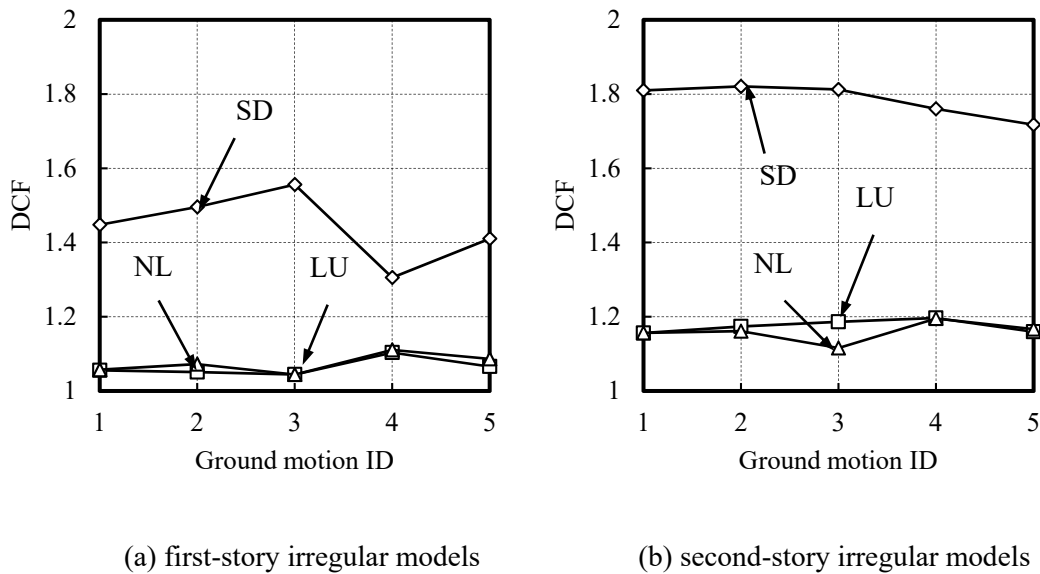


Fig. 2.35 Drift concentration factors of the first-story and second-story irregular models

Among the first-story irregular models, the maximum residual story drift ratio of the SD model was approximately 0.25%; conversely, the maximum residual story drift ratios of the LU and NL models were approximately 0.05%. For the second-story irregular models, the maximum residual story drift ratio of the SD model was also approximately 0.25%, and those of the LU and NL models were even smaller than those of the first-story irregular models. For the other story irregular models, the maximum residual story drift ratios of the SD model were

smaller than 0.2% but larger than 0.1%, while that of the LU and NL models were similar with the residual story drift ratios of their regular models. Even for the irregular models, the LU and NL models were verified to possess sufficient self-centering capacity.

Same with the regular models, for the irregular models, the input energy was mainly converted into damping energy and cumulative plastic strain energy (CPE). The irregular models were almost identical with the regular models in terms of the total input, damping, and plastic energy amount. Similar with the regular LU model, the damping energy of the irregular LU models was larger than that of the irregular SD and NL models caused by larger velocity response.

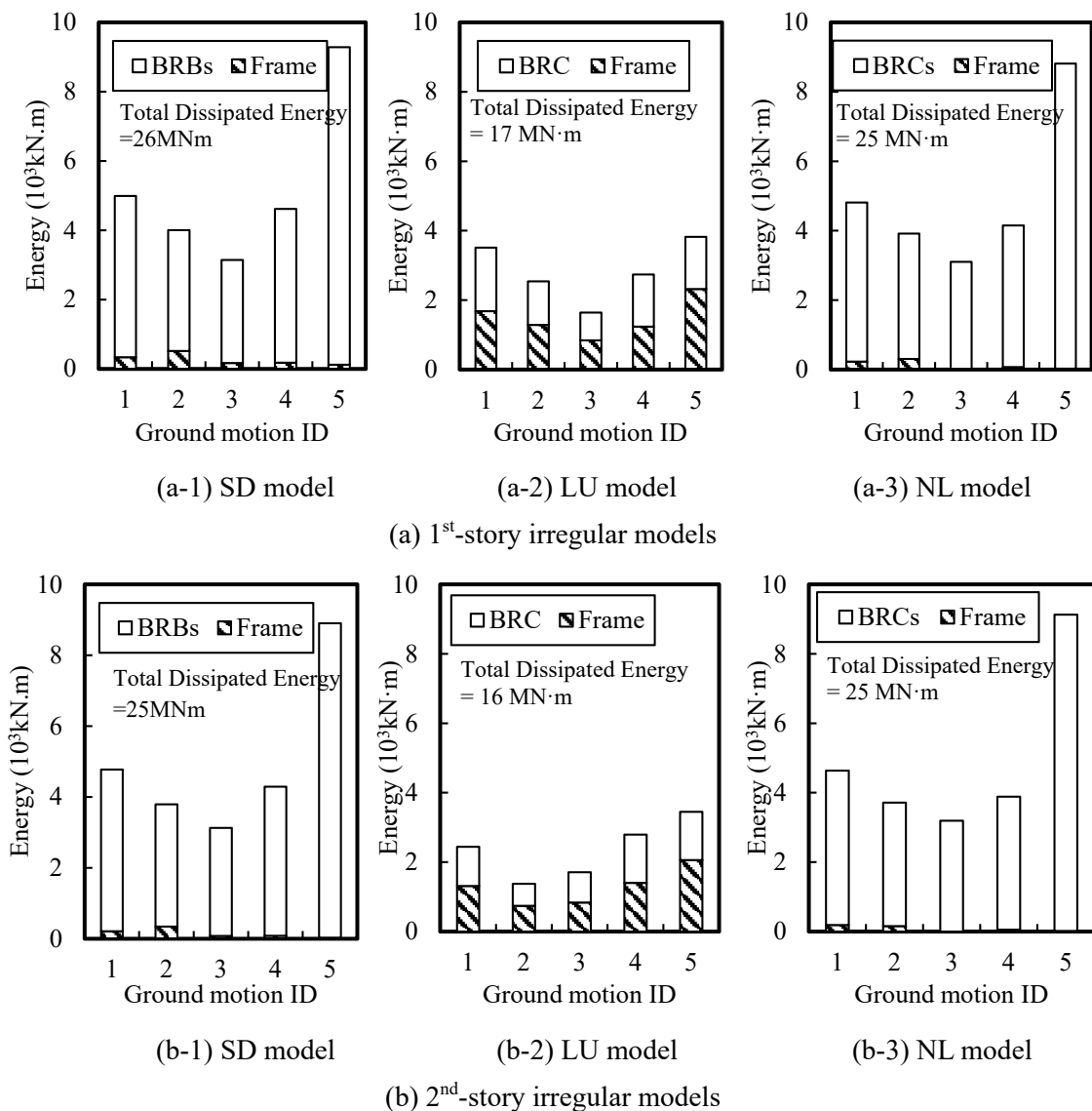


Fig. 2.36 Cumulative earthquake energy dissipation ratios of fuses in the 1st-story and 2nd-story irregular models

(Ground motion IDs: 1. El Centro; 2. Hachinohe; 3. JMA Kobe; 4. TAFT; 5. BCJ-L2)

Fig. 2.36 shows the cumulative earthquake energy dissipation ratios of fuses in the 1st-story irregular models and 2nd-story irregular models. The numbers above each bar denote the percentage of plastic strain energy of the BRBs or BRCs in the total plastic strain energy of the structures. For the proposed NL spine system, even for the irregular models, the earthquake input energy was greatly dissipated by the two BRCs at the bottom of the spine frame. The percentages of plastic strain energy of the BRCs in the total plastic strain energy of the structure ranged from 92.22% to 99.70% in the first-story irregular model and from 95.71% to 99.99% in the second-story irregular model. Similar with the NL models, the BRBs in the SD models dissipated more than 85% of the total plastic strain energy. The percentages of plastic strain energy of the BRBs in the total plastic strain energy of the structure ranged from 87.14% to 98.71% in the first-story irregular model and 90.99% to 99.67% in the second-story irregular model. In the irregular LU models, the percentages decreased from around 90% to around 50%. Although this value is slightly larger than that of the regular LU model, the main frame still dissipated up to 50% of the total plastic strain energy.

The cumulative plastic strain energy of the main frame of the first-story irregular models and the second-story irregular models were compared in Fig. 2.37. The proposed NL model had the best distribution of energy dissipation and the lowest plastic strain energy of the envelope frame, as illustrated in Fig. 2.37(c). The envelope frame in the first-story irregular SD model dissipated the most energy in the first floor, and the envelop frame in the second-story irregular SD model dissipated the most energy in the second floor, as shown in Fig. 2.37(a), which indicates damage concentration in the specific stories. The main frame in the irregular LU model dissipated the largest amount of energy compared with the other two systems. The envelope frame in the first-story irregular LU model dissipated the most energy in the second and third floors, and the envelop frame in the second-story irregular LU model dissipated the most energy in the fourth floor, as shown in Fig. 2.37(b). That's because the weaken stories dissipated less energy than other stories with identical inter-story deformation maintained by the spine effect. The main frame of the proposed NL model suffered the least damage among all three models.

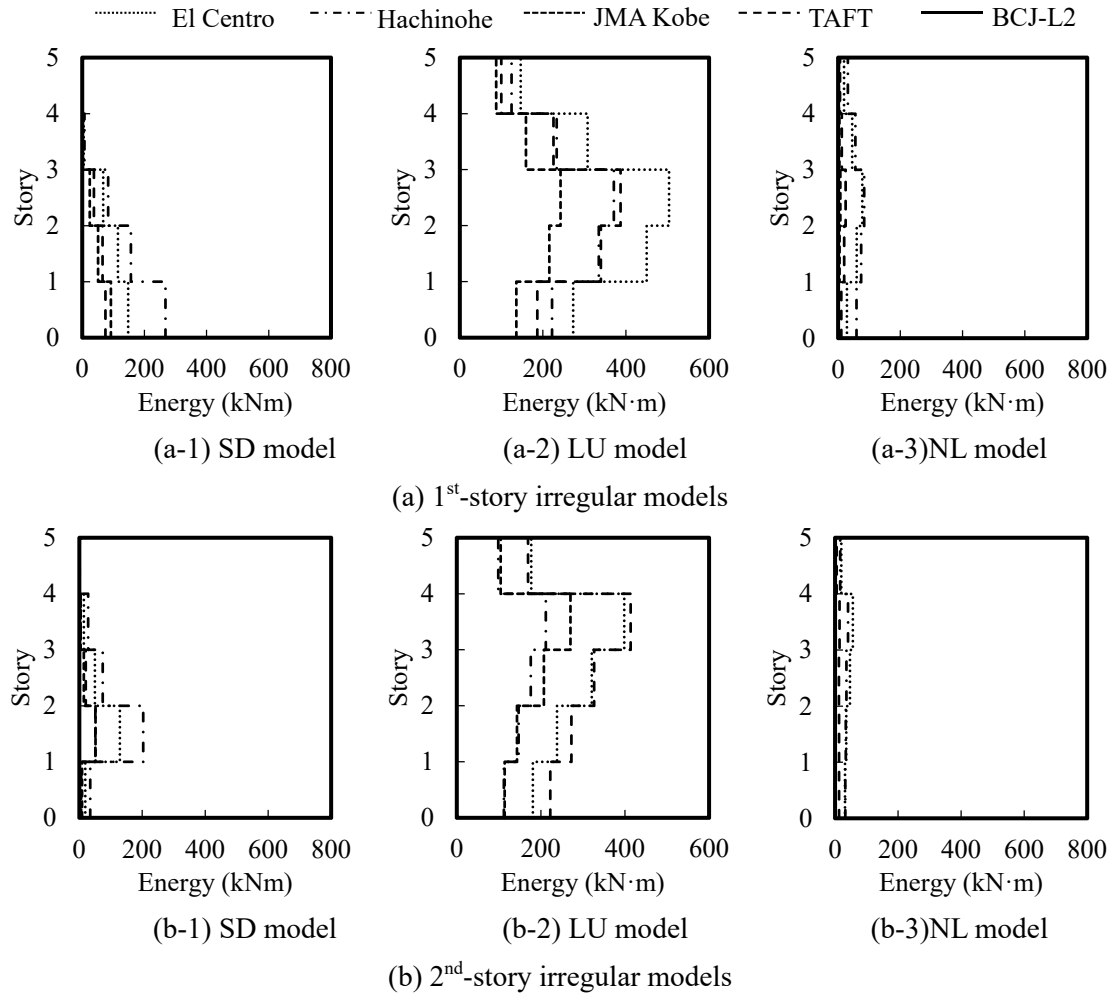
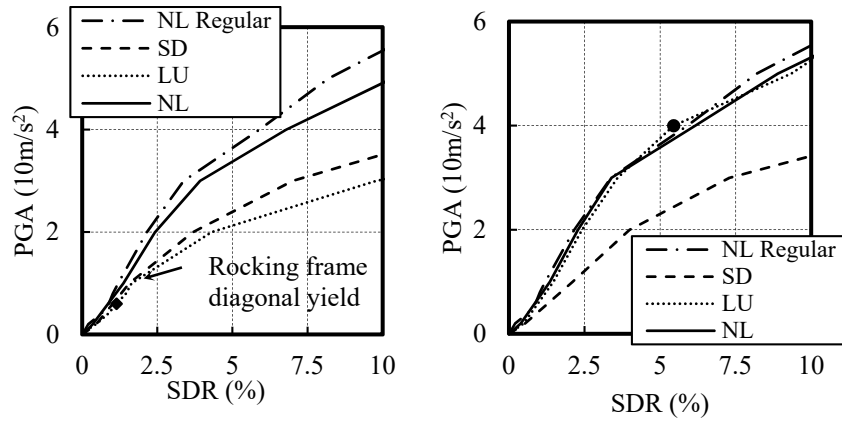


Fig. 2.37 Cumulative earthquake energy dissipated by the envelop frames in the 1st-story and 2nd-story irregular models

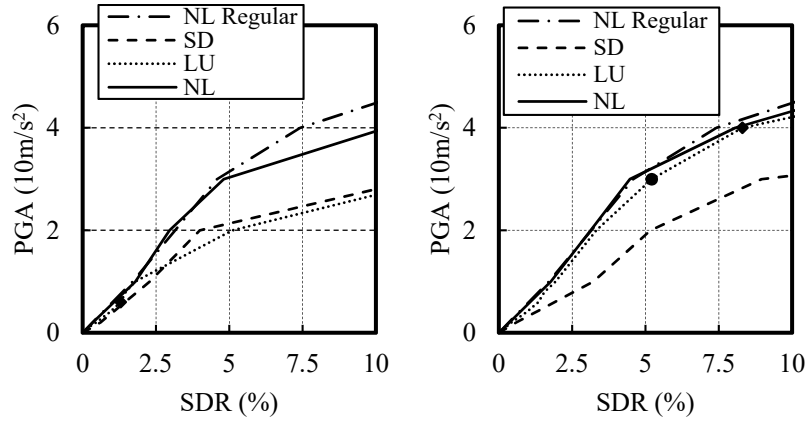
2.3.3 Incremental dynamic analysis

The seismic robustness of the vertical structural irregular models were investigated by carrying out Incremental dynamic analysis (IDA), same intensity measure (peak ground acceleration) and damage measure (maximum story drift ratio and residual story drift ratio) were employed. When using the maximum story drift ratio as the damage measure, the selected ground motions were scaled up until the maximum story drift ratio reached 10% or until the PGA reached 60 m/s^2 . When using the residual story drift ratio, the selected ground motions were scaled up until the residual story drift ratio reached 6% or until the PGA reached 40 m/s^2 , as some analysis with higher PGA stopped at the moment when the maximum story drift ratio occurred. The maximum story drift ratio IDA curves of the irregular models are compared in Fig.

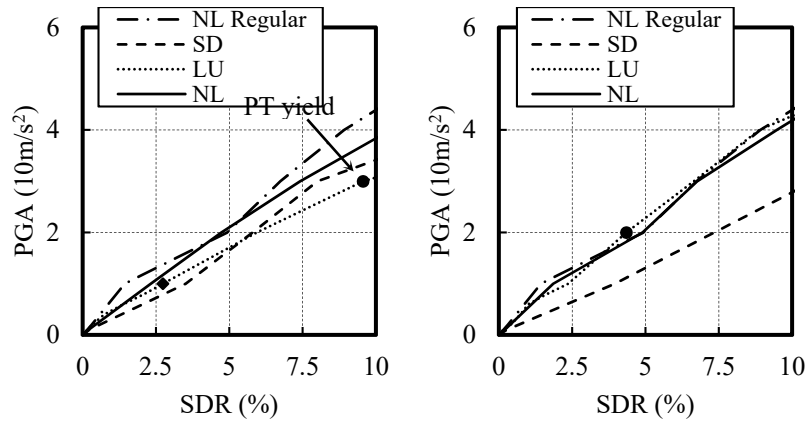
2.38.



(a) El Centro: 1st-story irregular model 2nd-story irregular model



(b) Hachinohe: 1st-story irregular model 2nd-story irregular model



(c) JMA Kobe: 1st-story irregular model 2nd-story irregular model

Fig. 2.38 (a-c) IDA curves of maximum story drift ratio of irregular models

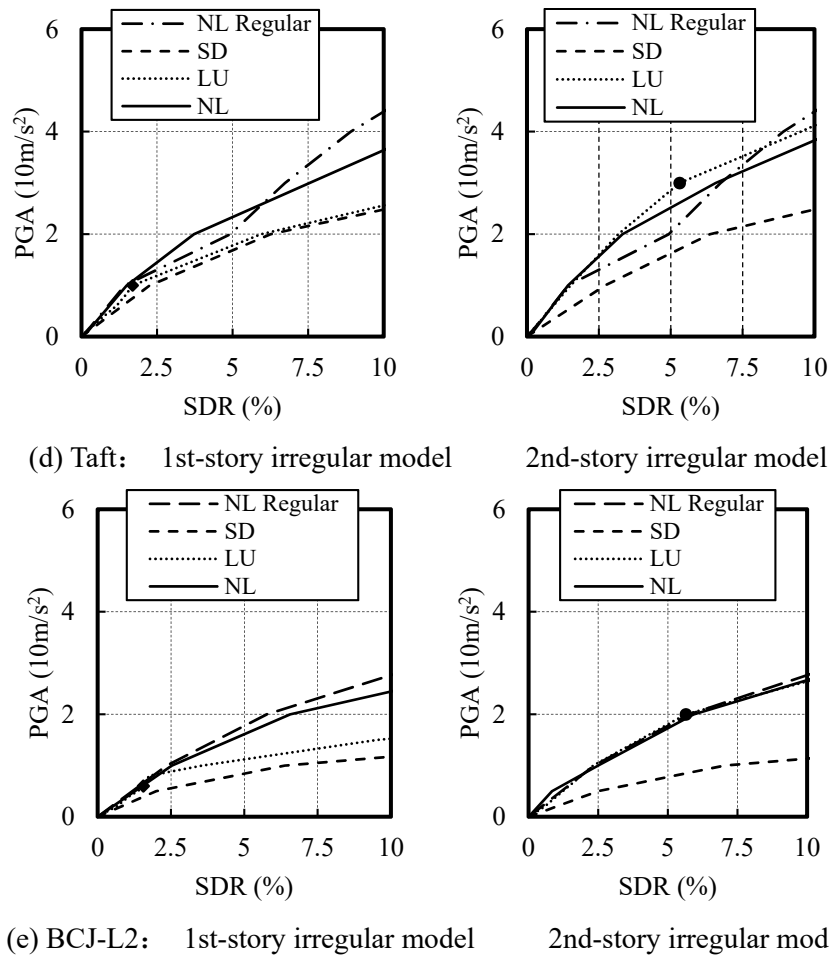


Fig. 2.38 (d-e) IDA curves of maximum story drift ratio of irregular models

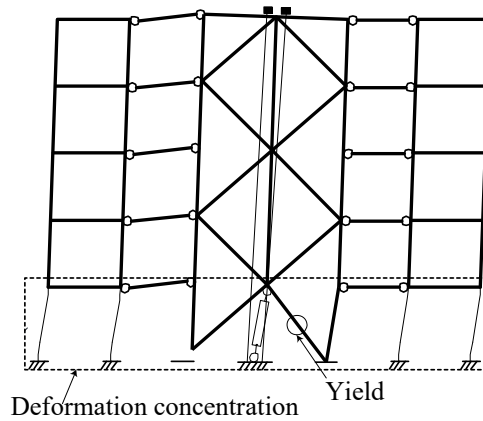


Fig. 2.39 Collapse mechanism of the first story irregular LU model

Among the first-story irregular models, the bottom diagonal member in the rocking frame of the LU model yielded when the PGA of input ground motions was 6–10 m/s². After the diagonals yielded when the PGA was around 10m/s², the maximum story drift ratio of the LU

model increased rapidly as the earthquake input intensity increased, as shown in the left column of Fig. 2.38; this value was much weaker than that in the NL model, but was similar to that of the SD model. This is because the yielded diagonals could not maintain the rocking mechanism, so the upper stories deformed by sliding from the first floor, as shown in Fig. 2.39. This deformation pattern resulted into severe damage concentration in the first story. Fig. 2.40 compared the cumulative plastic strain energy dissipated by the envelop frame in the first-story irregular SD and LU model when the PGA of the input earthquake was 20 m/s^2 . Significant energy concentration occurred at the first-story of the LU model. Fig. 2.41 shows the response of the bottom diagonal in the rocking frame of the first-story irregular LU models when the PGA was 20 m/s^2 . All of the response exceeded elastic limit and reached ultimate limit. Because of this phenomenon, the PT strands did not yield when the maximum story drift ratio was approximately 5%, but yielded when the maximum story drift ratio was larger than 9%. The degradation of the bottom diagonal is another factor that influences the robustness of the LU model. For the first-story irregular NL model, in comparison, the maximum story drift ratio at the same input intensity increased compared with the regular models, but the slope of its IDA curves decreased much more slowly than those of the LU and SD models, which indicates a more stable seismic behavior.

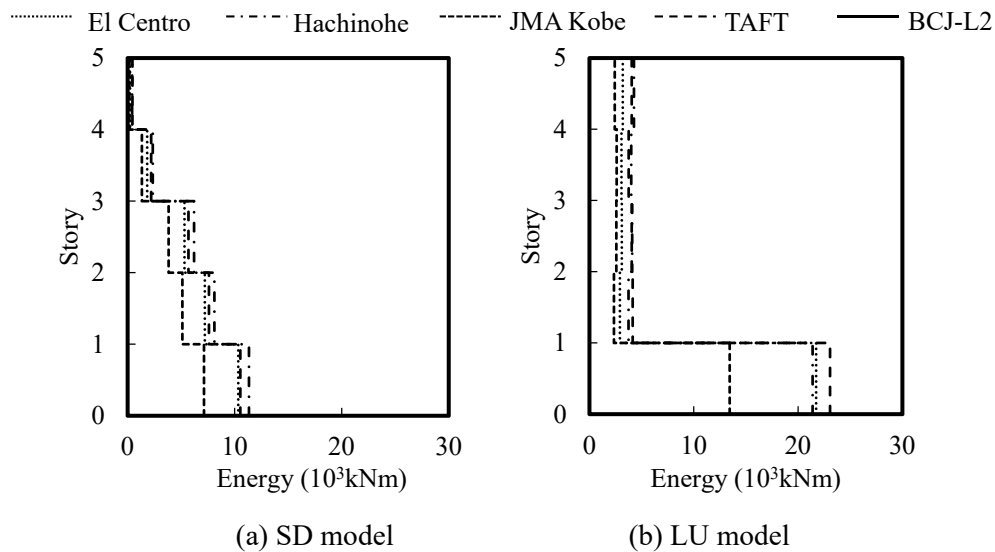


Fig. 2.40 Cumulative plastic strain energy dissipated by the envelop frames in the first-story irregular SD and LU models (PGA=20m/s²)

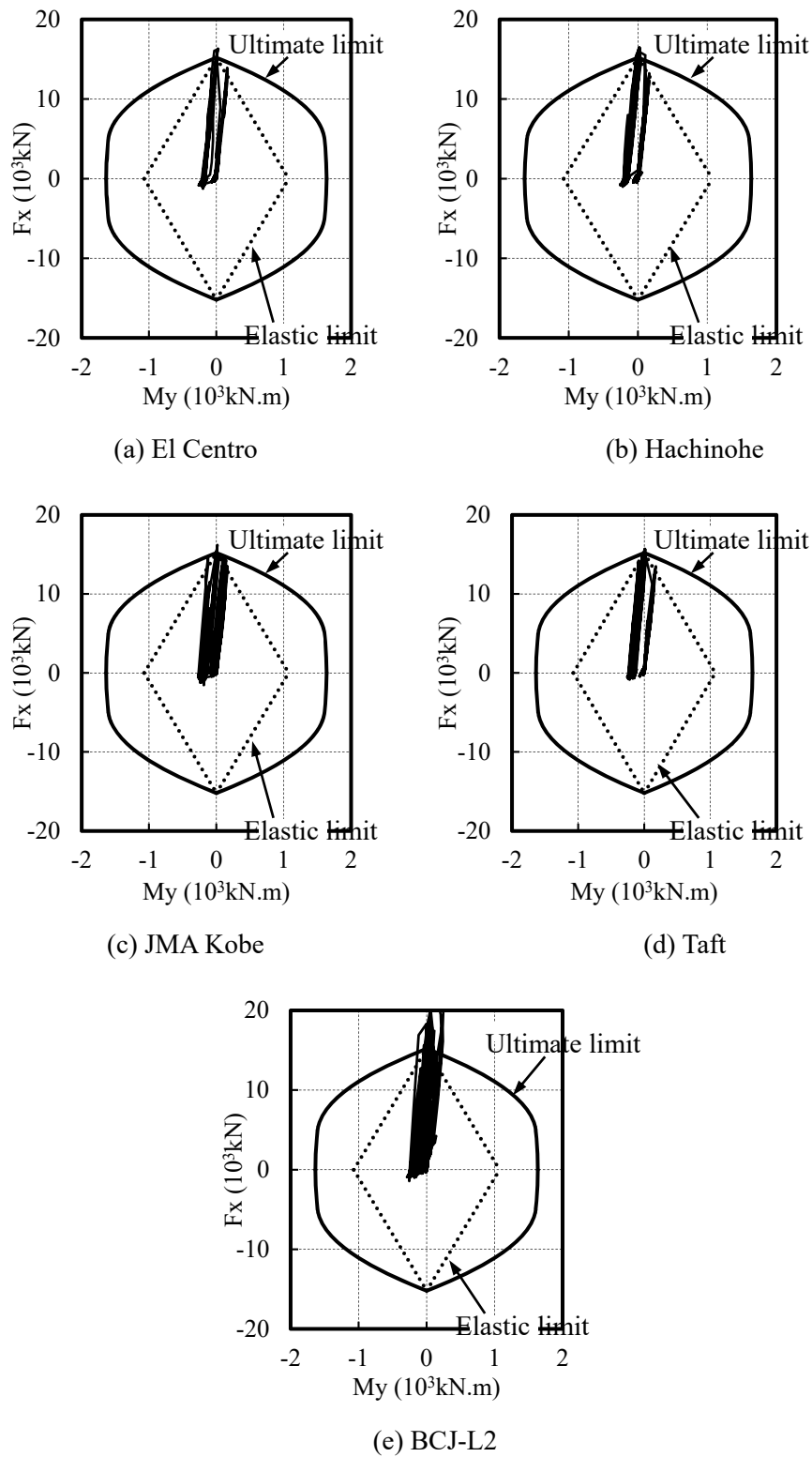


Fig. 2.41 Axial force and bending moment response of the bottom diagonal in the rocking frame of the first-story irregular LU models ($\text{PGA}=20\text{m/s}^2$)

Among the second-story irregular models, the SD model exhibited similar IDA curves to the first-story irregular SD model; whereas the LU and NL models both exhibited similar IDA curves to their regular models. The PT strands yielded when the maximum story drift ratio was approximately 5%, and the bottom braces yielded after the PT strands yielded. Before the yielding of the bottom diagonals, the IDA curves of the LU model were entirely coincident with the curves of the NL model. However, after the bottom diagonals yielded, the slope of the IDA curves in the LU model decreased more than that of the NL model, although this result is not shown here. Thus, the proposed NL spine system showed the best damage distribution performance and self-centering performance among all cases even without PT strands.

The residual story drift ratio IDA curves of the irregular models are compared in Fig. 2.42. The residual story drift ratio response curves showed obvious “waving” with the increase of the input earthquake intensity, which was mainly caused by the phase of input ground motion waves as well as the structural characteristics. In the response of the second-story irregular SD model against Hachinohe ground motion, an obvious residual story drift ratio reduce from $\text{PGA}=30\text{m/s}^2$ to $\text{PGA}=40\text{ m/s}^2$ happened, which indicated the influence of the phase of the ground motion. Detailed story drift ratio responses against those two level input were compared in Fig. 4.43. As a result, the following discussion is based on the general tendency of each IDA curve.

Similar with the regular models, except the first-story irregular SD model, the residual story drift of the irregular models didn’t develop until the PGA exceeded around 5m/s^2 . After the diagonals yielded, generally the residual story drift ratio of the LU model increased much more rapidly as the earthquake input intensity increased than that in the NL model, but was similar to that of the SD model. The influence of maximum story drift ratio on the residual story drift ratio can be observed from the comparison between the LU models and SD models. As shown in the left columns of Fig. 2.38, the maximum story drift ratios of the first-story irregular LU model were larger than those of the first-story irregular SD model with El Centro, Hachinohe, and JMA Kobe input, while the results of the LU model were smaller than those of the SD model with Taft and BCJ-L2 input. Same sequence can be observed in the residual story response: the residual story drift ratios of the first-story irregular LU model were larger than those of the SD model with El Centro, Hachinohe and JMA Kobe input.

Among the second-story irregular models, the SD model exhibited similar residual story drift ratio IDA curves to the first-story irregular SD model; whereas the LU and NL models both exhibited similar residual IDA curves to their regular models. The yielding of the PT elements seemed to have negligible influence on the self-centering capacity of the second-story irregular LU models.

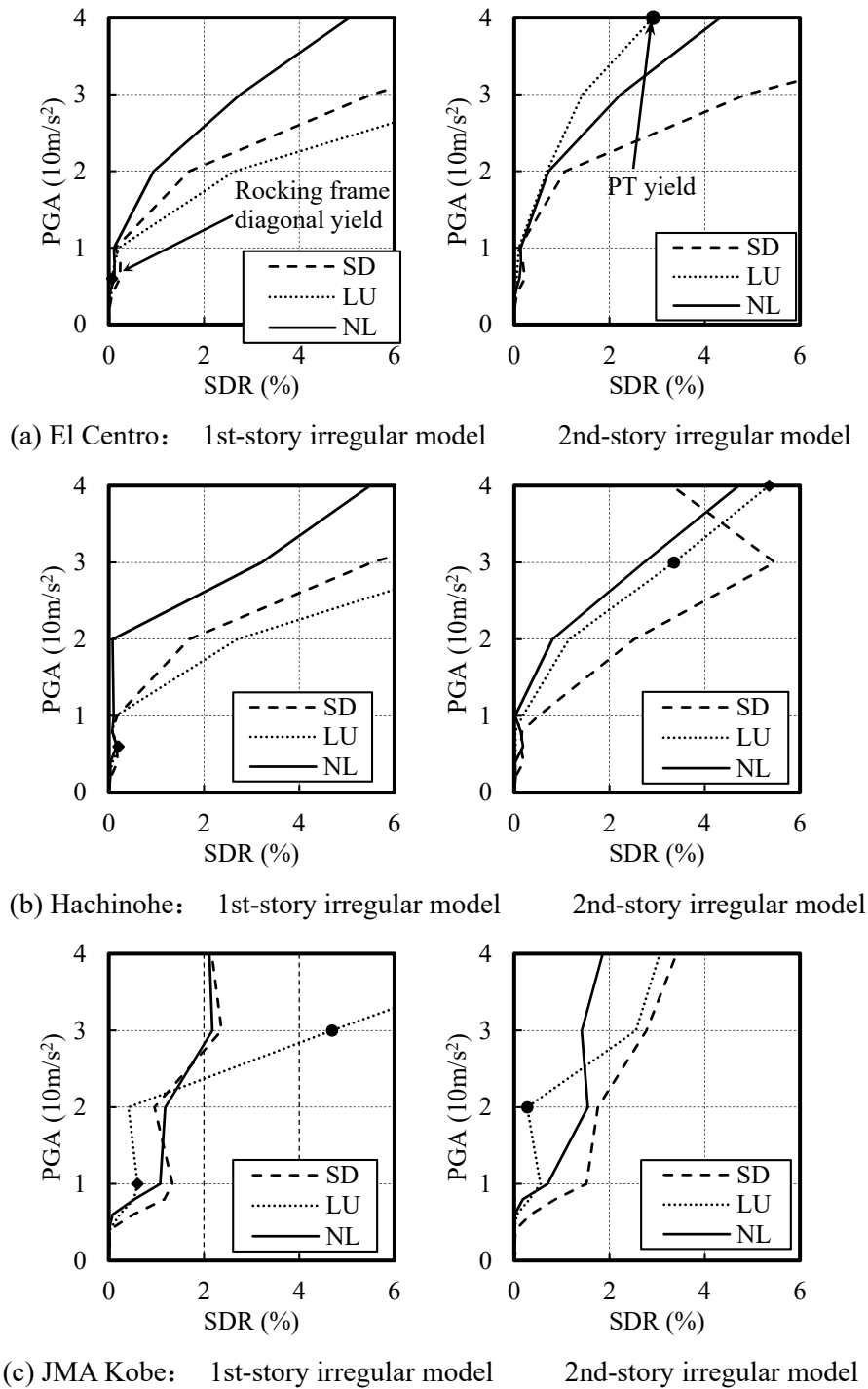


Fig. 2.42 (a-c) IDA curves of residual story drift ratio of the irregular models

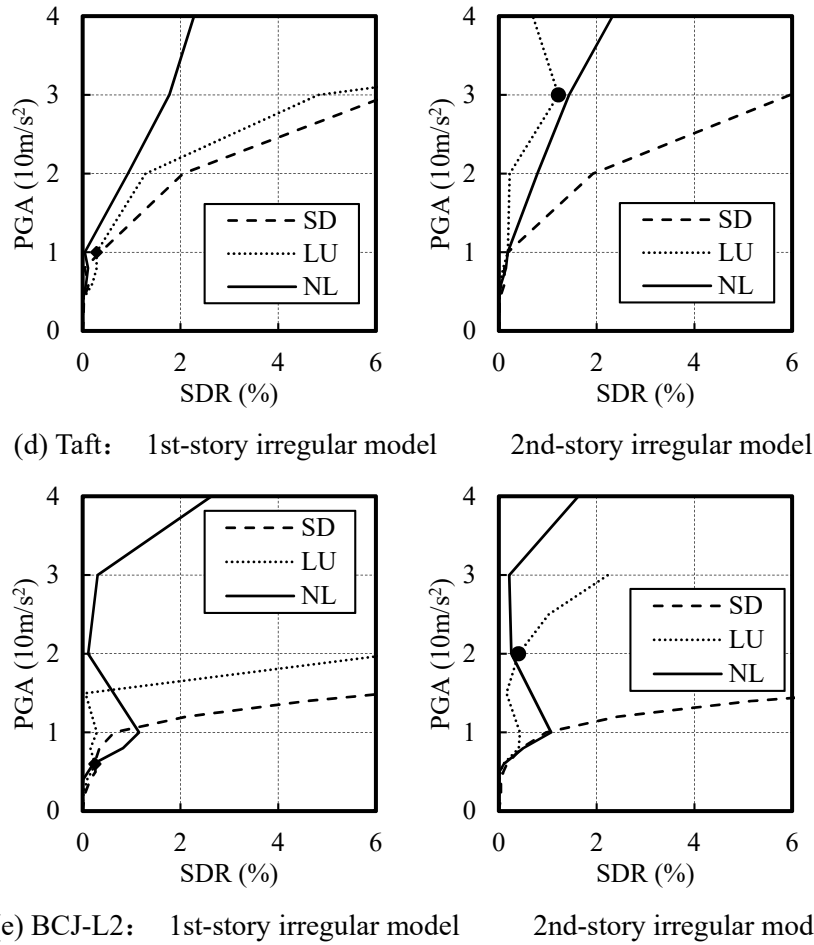


Fig. 2.42 (d-e) IDA curves of residual story drift ratio of the irregular models

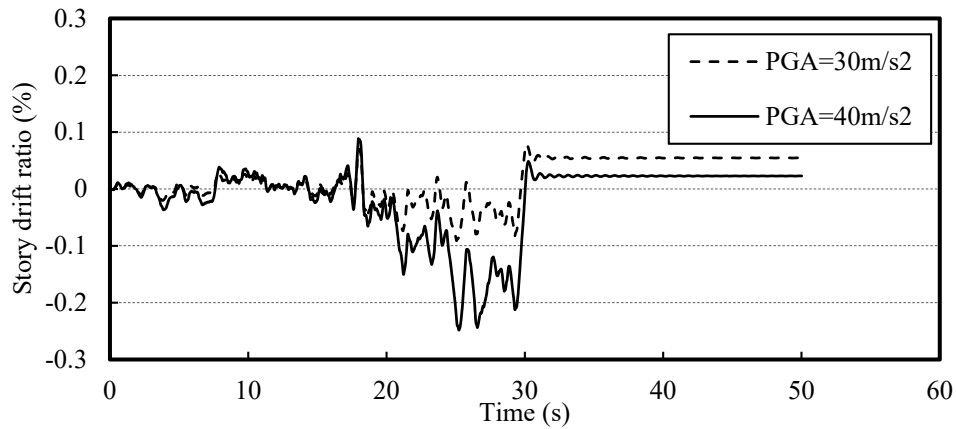


Fig. 2.43 Comparison of SDR response of the second-story irregular SD model against input ground motions with $\text{PGA}=30\text{m/s}^2$ and 40m/s^2

2.4 Conclusion

A NL system without PT strands and with elastic envelope frames was proposed as a new seismic-response control structural system. Its seismic performance was compared with a conventional shear damper (SD) system and a controlled uplifting rocking (LU) system through application to an actual building prototype under construction. The obtained findings are summarized as follows.

(1) The design method of controlling same value of yielding overturning moment of the BRB frame, the uplifting rocking frame, and the non-uplifting spine frame in each model was confirmed to be able to provide adequately comparable models possessing similar seismic resisting capacity.

(2) Due to the rigid body effect of the spine frame, the NL model with balanced vertical strength distributions showed uniform inter-story deformation and damage distribution over the building height when the model was subjected to design-level earthquakes. The LU model showed similar deformation balance behavior. However, the SD model showed a strong tendency to concentrate deformation in specific stories.

(3) Sufficient self-centering capacity of the proposed NL model was shown from the residual deformation that was as small as that of the LU model. It is proved that the elastic restoring force of the moment-resisting frame was large enough to resist the residual force of the plastic members, which were the BRCs in this study.

(4) Moreover, the proposed NL model showed stable seismic performance as earthquake intensity increasing even including the first-story and second-story irregular models. The LU model with regular and second-story irregular structural configuration also showed same stable performance as the NL models, regardless of the yielding of the PT strands. On the contrary, the first-story irregular LU model exhibited significant degradation after its bottom diagonal members in the rocking frame yielded, similar to the degradation of the SD model. Severe damage concentration in the irregular story was observed in the SD models.

(5) Similar amount of total earthquake energy was input into the three models. However, the LU model absorbed much more energy by the inherent damping mechanism and exhibited larger velocity response. The LU model had a lower capacity of absorbing earthquake energy through cumulative plastic deformation because of its flag-shaped hysteretic response. More energy was converted into kinetic energy and inherent damping energy. The LU model resulted in the largest amount of damage in the envelope frames among the three models.

Reference

- [2.1] M. Fujimoto, A. Wada, E. Saeki, T. Takeuchi, A. Watanabe: Development of unbonded brace, *Quarterly Column*, No.115, p91-96, 1990.
- [2.2] R. Sabelli, et al. Investigation of the nonlinear seismic response of special concentric and buckling restrained braced frames and implications for design, Report to EERI, FEMA/EERI Professional Fellowship Report, 2001.
- [2.3] C. M. Uang, M. Nakashima: “Steel buckling-restrained braced frames”, Chapter 16 in *Earthquake Engineering: Recent Advances and Applications*, CRC Press, 2004.
- [2.4] Q. Xie: State of the art of buckling-restrained braces in Asia. *Journal of Constructional Steel Research*. Vol. 61, p727-748, 2005.
- [2.5] P. Uriz, S. A. Mahin: Toward Earthquake-resistant design of concentrically braced steel-frame structures. *Pacific Earthquake Engineering Research Center Report* 2008/8, 2008.
- [2.6] T. Nagao, A. Takahatao, E. Bao: Damage concentration in multi-story buckling restrained braced frame(BRBF)-relations with participant ratio β of BRB. *The Fourteenth World Conference on Earthquake Engineering*, Beijing, China, 2008.
- [2.7] G. Deierlein, H. Krawinkler, X. Ma, T Takeuchi et al: Earthquake resilient steel braced frames with controlled rocking and energy dissipating fuses. *Steel Construction*. Vol 4(3):171-175, 2011.
- [2.8] T. Takeuchi, M. Midorikawa, K. Kasai et al: Shaking table test of controlled rocking frames using multipurpose test bed. *The Sixth European Conference on Steel and Composite Structures*, Budapest, Hungary, 2011.
- [2.9] G. W. Housner: The behavior of inverted pendulum structures during earthquakes. *Bulletin of the Seismological Society of America*. Vol 53(2): 403-417, 1963.
- [2.10] K. Kawashima, G. A. MacRae, J. Hoshikuma, et al: Residual displacement response spectrum. *Journal of Structural Engineering*, Vol. 124, p523-530, 1998.
- [2.11] L. Ye, X. Lu, Q. L et al: Study on the influence of post-yielding stiffness to the seismic response of building structures. *The Fourteenth World Conference on Earthquake Engineering*, Beijing, China, 2008.
- [2.12] C. M. Ramirez and E. Miranda: Significance of residual drifts in building earthquake loss estimation. *Earthquake Engineering and Structural Dynamics*. Vol.41, p1477-1493, 2012.
- [2.13] 耐震構造の設計 (学びやすい構造設計, 「7」) 日本建築学会関東支部編, 2012.10 第4版。
- [2.14] S. Mazzoni, F. McKenna, M. H. Scott, G. L. Fenves: OpenSEES version 2.0 user manual. Pacific Earthquake Engineering Research Center (PEER), University of California, Berkeley, 2009. Available from: <http://opensees.berkeley.edu> (last accessed May 2017).
- [2.15] 大崎順彦：新・地震動のスペクトル解析入門，鹿島出版社，2013.2 第11刷。
- [2.16] D. Vamvatsikos, C. A. Cornell: Incremental dynamic analysis. *Earthquake Engineering and Structural Dynamics* 2002; 31(3): 491-514. DOI: 10.1002/eqe.141

- [2.17] E. V. Valmundsson and J. M. Nau: Seismic response of building frames with vertical structural irregularities”, *Journal of Structural Engineering*, ASCE, Vol. 123(1), p30-41, 1997.
- [2.18] Al-Ali, A.A.K. and H. Krawinkler: Effects of vertical irregularities on seismic behavior of building structures, Report No. 130, The John A. Blume Earthquake Engineering Center, Department of Civil and Environmental Engineering, Stanford University, Stanford, U.S.A, 1998.
- [2.19] S. Das and J. M. Nau: Seismic design aspects of vertically irregular reinforced concrete buildings, *Earthquake Spectra*, Vol. 19(3), p455-477, 2003.
- [2.20] C. Chintanapakdee and A. K. Chopra: Seismic response of vertically irregular frames: response history and modal pushover analyses, *Journal of Structural Engineering*, ASCE, Vol. 130(8), p1177-1185, 2004.
- [2.21] M. Fragiadakis, D. Vamvatsikos, M. Papadrakakis: Evaluation of the influence of vertical irregularities on the seismic performance of a nine-storey steel frame, *Earthquake Engineering and Structural Dynamics*, Vol. 35(12), p1489-1509, 2006.

CHAPTER 3

Simplified Dual Multi-Degree-of-Freedom Model of Controlled Spine Frame Structures

3.1 Introduction 3-1

3.2 Design of the benchmark building structures

3.2.1 Design of the 5-story building structure 3-2

3.2.2 Design of the 10-story building structure 3-6

3.2.3 Design of the 20-story buildings structure 3-11

3.3 Dual multi-degree-of-freedom (DMD) model

3.3.1 Basic concepts and assumptions of DMD model 3-15

3.3.2 Simplification of the moment frames 3-16

3.3.3 Simplification of the spine frames 3-19

3.4 Programming for the nonlinear analysis of the DMD model

3.4.1 Construction of stiffness matrix by static condensation 3-26

3.4.2 Nonlinear time-history analysis algorithm 3-27

3.4.3 Verification of the nonlinear analysis program 3-33

3.5 Verification and limitation of the DMD model 3-37

3.6 Conclusion 3-39

Chapter 3 – Simplified Dual Multi-Degree-of-Freedom Model for the Controlled Spine Frame Structures

3.1 Introduction

Prior studies have documented the excellent performance of the proposed controlled spine frame structures in preventing the concentration of damage in soft stories as well as in providing self-centering. However, the performance of such structural system in taller structures and the effect of main structural parameters on seismic performance remain unclear. Additionally, an easy and reliable seismic design procedure is urgently required to improve the system efficiency and promote the concept in the industry.

In this chapter, a simplified dual multi-degree-of-freedom (DMD) model was constructed to examine the dynamic characteristics of the spine frame structures. The DMD model was expected to exhibit nonlinear behavior similar to the full member-by-member (MBM) structure, particularly in terms of the distribution and maximum amounts of story drift and story shear, and damper behavior.

Based on this model, the optimal design of the controlled spine frame structure has been investigated, and a simple design procedure was proposed based on an equivalent single-degree-of-freedom (SDOF) system in the following chapter. To search for the optimal value of key structural parameters, parametric study with representative design indices was conducted to compare the seismic responses of the DMD and SDOF models. In order to improve the computing efficiency of the parametric study of the DMD models, a nonlinear dynamic analysis program was constructed in this chapter.

3.2 Design of benchmark building structures

Height of the studied building was extended from 5 stories up to 20 stories in the following section. Different from the school building utilized in chapter 2, herein three benchmark buildings possessing a typical office building plan were newly designed, consisting of a 5-story, 10-story, and 20-story buildings. Plan of the original three dimension structures is shown in Fig 3.1 (a). The structure plan was symmetric about the center axes in both directions. The self-weight and vertical load distributions were assumed to be symmetric as well. Rigid floor diaphragm was adopted herein as the often case. Fig 3.1 (b) illustrates the structural elevations of the three frames extracted from half of the original structure in one direction. They composed the plane benchmark models. Detailed dimension of the frames and section No. of the structural members were shown in Fig 3.1 (c).

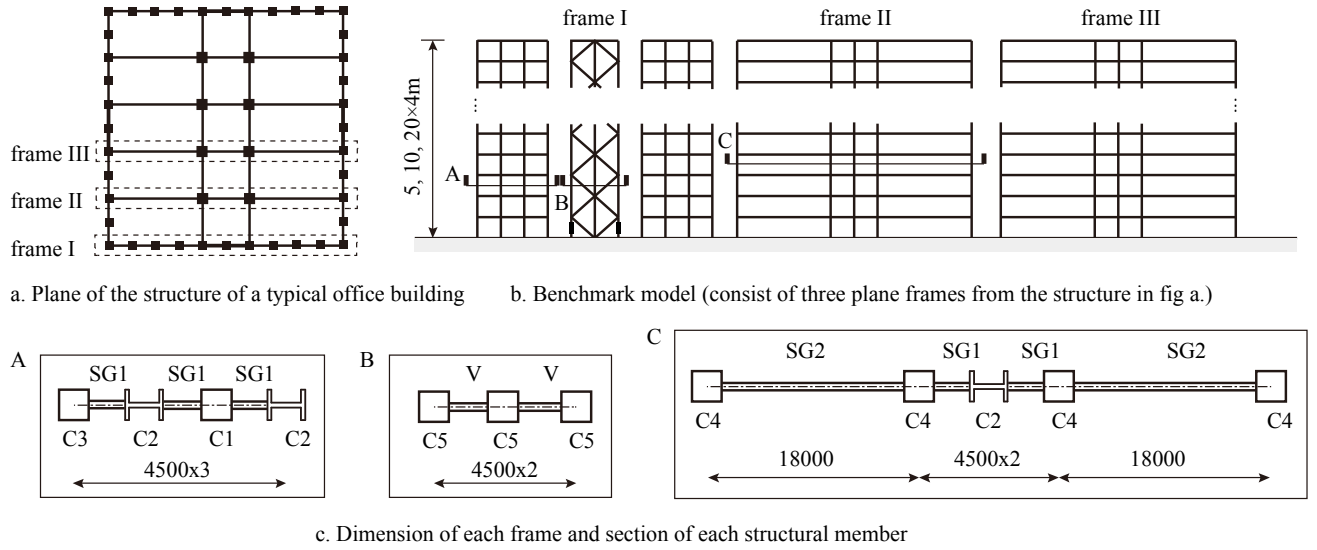


Fig. 3.1 benchmark models of the controlled spine frame structures

3.2.1 Design of the 5-story model

The 5-story model was designed based on root 2, in which only the allowable stress design is required. In the allowable stress design, every structural member should be elastic when the structure is loaded with the equivalent static horizontal load corresponding to level 1 earthquake. The equivalent static load is calculated by Eq. (3.1) - (3.4)

$$Q_i = C_i \cdot \sum_{j=1}^N w_j \quad (3.1)$$

$$C_i = Z \cdot R_i \cdot A_i \cdot C_0 \quad (3.2)$$

$$R_i = 1 - 0.2 \left(\frac{T}{T_c} - 1 \right)^2 \quad (3.3)$$

$$A_i = 1 + \left(\frac{1}{\sqrt{\alpha_i}} - \alpha_i \right) \frac{2T}{1 + 3T}, \quad \alpha_i = \frac{\sum_{j=1}^N w_j}{W} \quad (3.4)$$

Where, w_i is the weight of each story; W is the weight of the entire structure; Z is seismic zoning coefficient, herein $Z=1.0$; C_0 is standard shear force coefficient, $C_0=0.2$ for level 1 earthquake; T is the fundamental period of the structure, which is 0.716 second obtained from eigenvalue analysis; T_c is decided by the ground type. Tokyo belongs to type 2, for which $T_c=0.6$ s.

Table 3.1 lists the story weight and equivalent static load at each story. Table 3.2 summarizes the cross sectional dimension of each structural member. Fig. 3.2 illustrates the lateral stiffness reduction along the height of the structure. Lateral stiffness reduction ratio R_{kfi} is computed by Eqs. (3.5) - (3.6)

$$k_{fi} = \frac{1}{\frac{1}{k_{ci}} + \frac{1}{k_{bi}}} \quad (3.5)$$

$$R_{kfi} = \frac{k_{fi}}{k_{f1}} \quad (3.6)$$

where, k_{fi} denotes the lateral stiffness of the i -th story of the moment frames. k_{ci} denotes the lateral stiffness contributed by columns in the i -th story. k_{bi} denotes the lateral stiffness contributed by beams in the i -th story. They are computed by Eqs. (3.7) & (3.8)

$$k_{ci} = \sum_{j=1}^{n_c} \frac{EI_{cij}}{h_i} \quad (3.7)$$

$$k_{bi} = \sum_{j=1}^{n_b} \frac{EI_{bij}}{l_{ij}} \quad (3.8)$$

where, E denotes the Young's modulus of steel material. I_{cij} denotes the second moment of area of the cross-section of the j -th column in the i -th story. h_i denotes the height of the i -th story. I_{bij} denotes the second moment of area of the cross-section of the j -th beam in the i -th story. l_{ij} denotes the length of the j -th beam in the i -th story. Fig. 3.3 shows the stress state of each structural member in the 5-story model (The yield strength of the material of all the members is assumed to be 325N/mm²). All structural members are elastic under the equivalent lateral load.

Table 3.1 Equivalent static load of level 1 earthquake loaded on the 5-story model

Story	Story weight w_i (kN)	$\sum w_i$ (kN)	α_i	A_i	C_i	Story shear force Q_i (kN)	External lateral force (kN)
5	11404	11404	0.27	1.76	0.35	4014	4014
4	7846	19250	0.45	1.47	0.29	5673	1659
3	7846	27096	0.63	1.28	0.26	6956	1283
2	7846	34942	0.82	1.13	0.23	7910	954
1	7846	42788	1.00	1.00	0.20	8558	647

Table 3.2 Cross sections of structural members in the 5-story model

(1) Cross sections of columns in the moment frames

Story	C1= C3	C2	C4	C5
5	□-500×500×19	H-500×350×25×28	□-600×600×32	□-550×550×25
4	□-500×500×19	H-500×350×25×28	□-600×600×32	□-550×550×25
3	□-500×500×19	H-500×350×25×32	□-600×600×32	□-550×550×25
2	□-500×500×22	H-500×350×25×32	□-600×600×32	□-550×550×25
1	□-500×500×22	H-500×350×25×32	□-600×600×32	□-550×550×25

(2) Cross sections of braces in the spine frames and beams in the moment frames

Story	V	SG1	SG2
5	H-550×600×25×25	H-600×300×12×22	H-1000×300×19×32
4	H-550×600×25×25	H-600×300×12×22	H-1000×300×19×32
3	H-550×600×25×25	H-600×300×12×25	H-1000×300×19×32
2	H-550×600×25×25	H-600×300×12×25	H-1000×300×19×32
1	H-550×600×25×25	H-600×300×12×25	H-1000×300×19×32

(3) Section of BRCs

A (mm ²)	13900
F _y (N/mm ²)	325

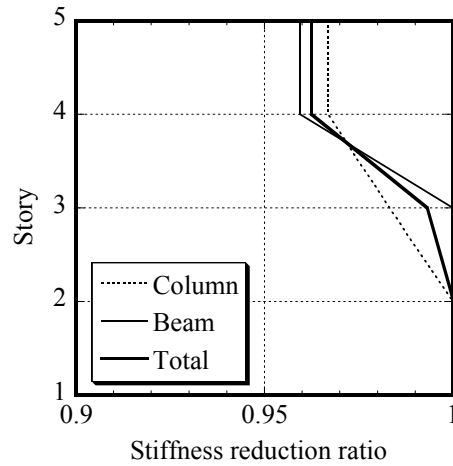
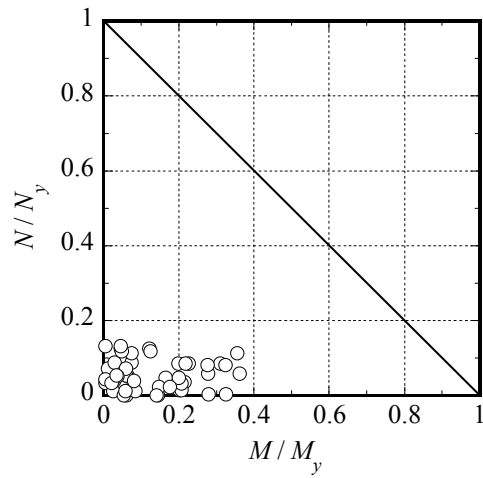


Fig. 3.2 Lateral stiffness reduction ratio along the height of the 5-story model



(a) Braces in spine frames

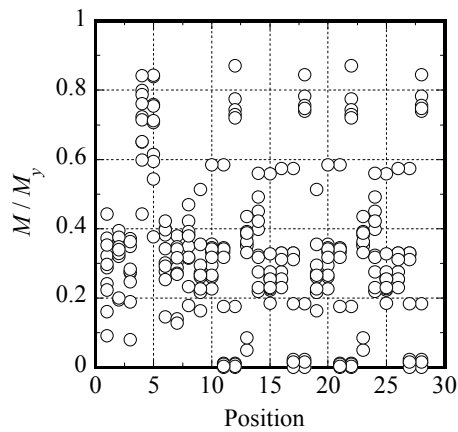
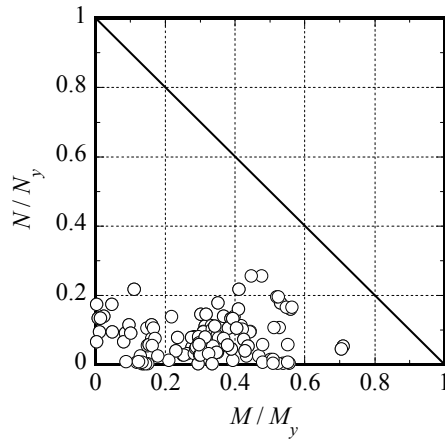


Fig. 3.3 Stress state of the structural members in the 5-story model

3.2.2 Design of the 10-story model

The 10-story model was designed based on root 3, in which both allowable stress design and horizontal load bearing capacity validation are required. Firstly, the allowable stress design is carried out. Table 3.3 summarizes the equivalent static load of level 1 earthquake. Table 3.4 summarizes the cross sectional dimension of each structural member. Fig. 3.4 illustrates the lateral stiffness reduction along the height of the structure. Fig. 3.5 shows the stress state of each structural member in the 10-story model. All structural members are elastic under the equivalent lateral load. Moreover, the maximum story drift ratio is 0.003, smaller than 0.005.

Table 3.3 Equivalent static load of level 1 earthquake for the 10-story model ($T_1=1.36s$)

Story	Story weight w_i (kN)	$\sum w_i$ (kN)	α_i	A_i	C_i	Story shear force Q_i (kN)	External lateral force (kN)
10	11406	11406	0.14	2.37	0.47	5401	5401
9	7922	19328	0.23	1.98	0.40	7663	2262
8	7922	27250	0.33	1.76	0.35	9572	1909
7	7922	35172	0.43	1.59	0.32	11208	1636
6	7922	43094	0.52	1.46	0.29	12607	1399
5	7922	51016	0.62	1.35	0.27	13789	1182
4	7922	58938	0.71	1.25	0.25	14766	977
3	7922	66860	0.81	1.16	0.23	15547	781
2	7922	74782	0.90	1.08	0.22	16137	590
1	7922	82704	1.00	1.00	0.20	16541	404

Table 3.4 Cross sections of structural members in the 10-story model

(1) Cross sections of columns in the moment frames

Story	C1	C2	C3	C4	C5
10	□-600×600×19	H-650×400×16×22	□-600×600×19	□-650×650×28	□-550×550×25
9	□-600×600×19	H-650×400×16×22	□-600×600×19	□-650×650×30	□-550×550×25
8	□-600×600×22	H-650×400×16×22	□-600×600×19	□-650×650×30	□-550×550×25
7	□-600×600×22	H-650×400×16×25	□-600×600×19	□-650×650×30	□-550×550×25
6	□-600×600×22	H-650×400×16×25	□-600×600×22	□-650×650×30	□-550×550×25
5	□-600×600×22	H-650×400×16×25	□-600×600×22	□-650×650×32	□-550×550×25
4	□-600×600×28	H-650×400×16×25	□-600×600×22	□-650×650×32	□-550×550×25
3	□-600×600×28	H-650×400×16×28	□-600×600×22	□-650×650×32	□-550×550×25
2	□-600×600×28	H-650×400×16×28	□-600×600×25	□-650×650×32	□-550×550×25
1	□-600×600×28	H-650×400×16×28	□-600×600×25	□-650×650×32	□-550×550×25

(2) Cross sections of braces in the spine frames and beams in the moment frames

Story	V	SG1	SG2
10	H-550×600×25×25	H-650×300×16×25	H-900×300×19×25
9	H-550×600×25×25	H-650×300×16×25	H-900×300×19×25
8	H-550×600×25×25	H-650×300×16×25	H-900×300×19×25
7	H-550×600×25×25	H-650×300×16×25	H-900×300×19×25
6	H-550×600×25×25	H-650×300×16×28	H-900×300×19×25
5	H-550×600×25×25	H-650×300×16×28	H-900×300×19×25
4	H-550×600×25×25	H-650×300×16×28	H-900×300×19×25
3	H-550×600×25×25	H-650×300×16×32	H-900×300×19×25
2	H-550×600×25×25	H-650×300×16×32	H-900×300×19×25
1	H-550×600×25×25	H-650×300×16×32	H-900×300×19×25

(3) Section of BRCs

A (mm ²)	54400
F _y (N/mm ²)	325

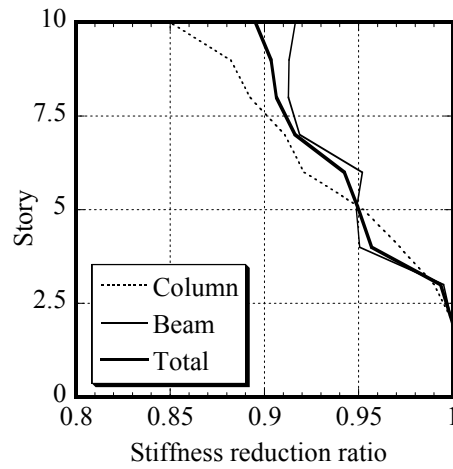
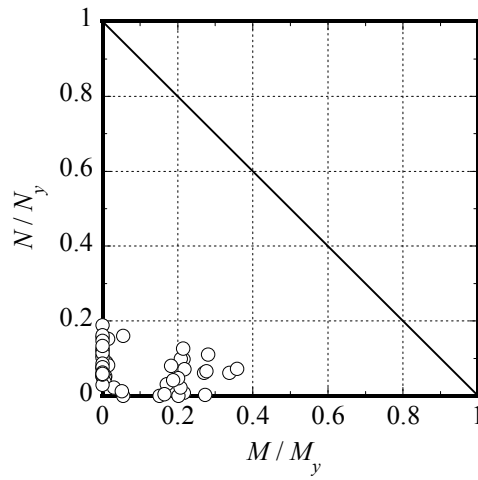
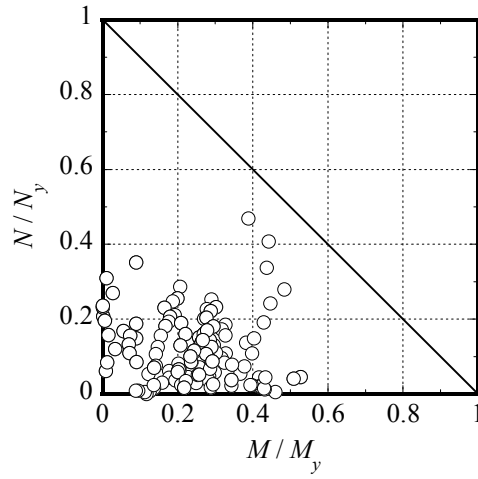


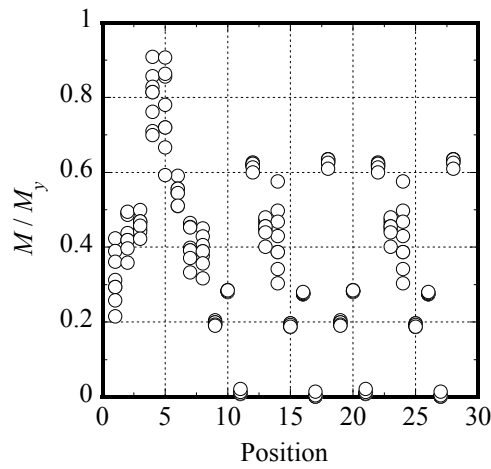
Fig. 3.4 Stiffness reduction ratio along the height of the 10-story model



(a) Braces in spine frames



(b) Columns in moment frames



(c) Beams in moment frames

Fig. 3.5 Stress state for structural members in the 10-story model

Secondly, horizontal load bearing capacity was validated. Eq. (3.9) and Eq. (3.10) give the calculation of necessary horizontal load bearing capacity.

$$Q_{uni} = D_{si} \cdot F_{esi} \cdot Q_{udi} \quad (3.9)$$

$$Q_{udi} = Z \cdot R_t \cdot A_i \cdot C_0 \cdot W_i \quad (3.10)$$

Where, D_{si} is the structure characteristic coefficient, and its value at each story is shown in Table 3.5; F_{esi} is the shape coefficient, and its value at each story is shown in Table 3.6. C_0 is standard shear force coefficient, $C_0=1.0$ for level 2 earthquake. The other variables are same with those in Eq. (3.1) ~ Eq. (3.4)

Pushover analysis has been conducted in order to evaluate the horizontal load bearing capacity of the 10-story model. During the analysis, the lateral load on the model was always proportional to the equivalent static load calculated by Eq. (3.1) ~ Eq. (3.4). Shear force when the maximum story drift ratio reach 1% is defined as the evaluated bearing capacity of the structure, Q_u . Fig. 3.6 shows results obtained from the pushover analysis. The evaluated bearing capacity Q_u was compared with the necessary bearing capacity Q_{un} in Table 3.7. The safety factor was higher than 1.4 in every story, which satisfied the design requirement.

Table 3.5 Structure characteristic coefficient D_s of the 10-story model

story	Columns & beams					Braces				β_u	D_s
	beam	column	γ_A	γ_C	Member group	Brace	γ_A	γ_C	Member group		
10	FA	FA	1.00	0.00	A	BB	0.00	0.00	B	-0.52	0.30
9	FA	FA	1.00	0.00	A	BB	0.00	0.00	B	0.08	0.25
8	FA	FA	1.00	0.00	A	BB	0.00	0.00	B	0.10	0.25
7	FA	FA	1.00	0.00	A	BB	0.00	0.00	B	0.28	0.25
6	FA	FA	1.00	0.00	A	BB	0.00	0.00	B	0.30	0.25
5	FA	FA	1.00	0.00	A	BB	0.00	0.00	B	0.34	0.30
4	FA	FA	1.00	0.00	A	BB	0.00	0.00	B	0.22	0.25
3	FA	FA	1.00	0.00	A	BB	0.00	0.00	B	0.28	0.25
2	FA	FA	1.00	0.00	A	BB	0.00	0.00	B	0.37	0.30
1	FA	FA	1.00	0.00	A	BB	0.00	0.00	B	-0.18	0.25

Table 3.6 Shape coefficient F_{es} of the 10-story model

Story	Story height (mm)	Story drift ratio (rad)	Stiffness Ratio R_e	F_s	Eccentricity ratio R_s	F_e	Shape coefficient F_{es}
10	4000	0.22%	1.25	1.0	0.00	1.0	1.00
9	4000	0.25%	1.10	1.0	0.00	1.0	1.00
8	4000	0.28%	1.00	1.0	0.00	1.0	1.00
7	4000	0.29%	0.95	1.0	0.00	1.0	1.00
6	4000	0.31%	0.90	1.0	0.00	1.0	1.00
5	4000	0.31%	0.90	1.0	0.00	1.0	1.00
4	4000	0.29%	0.96	1.0	0.00	1.0	1.00
3	4000	0.29%	0.94	1.0	0.00	1.0	1.00
2	4000	0.29%	0.95	1.0	0.00	1.0	1.00
1	4000	0.24%	1.18	1.0	0.00	1.0	1.00

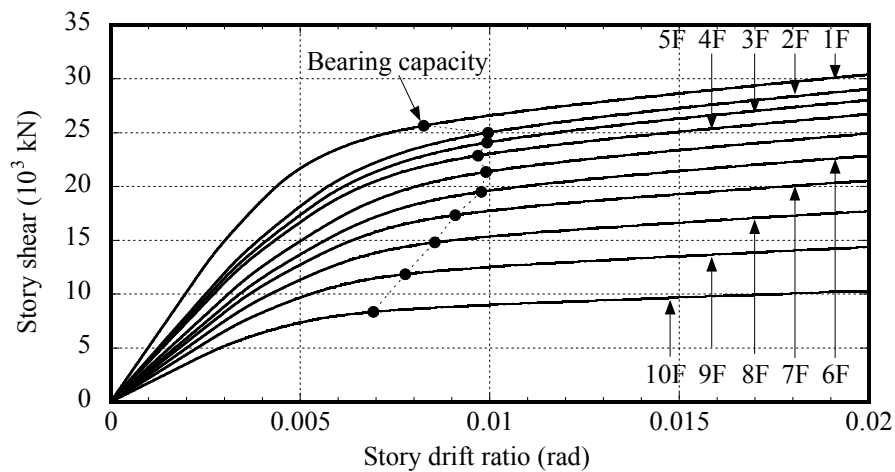


Fig. 3.6. Bearing capacity of the 10-story model (i.e., story shear when the maximum story drift ratio reaches 0.01)

Table 3.7 Comparison of necessary and evaluated horizontal load bearing capacity

Story	Q_{ud} (kN)	F_{es}	D_s	Q_{un} (kN)	Q_u (kN)	Q_u/Q_{un}	Judge
10	19492	1.00	0.3	5848	8346	1.43	OK
9	27666	1.00	0.25	6917	11846	1.71	OK
8	34570	1.00	0.25	8642	14802	1.71	OK
7	40491	1.00	0.25	10123	17338	1.71	OK
6	45558	1.00	0.25	11389	19507	1.71	OK
5	49843	1.00	0.3	14953	21342	1.43	OK
4	53391	1.00	0.25	13348	22861	1.71	OK
3	56231	1.00	0.25	14058	24077	1.71	OK
2	58384	1.00	0.3	17515	24999	1.43	OK
1	59867	1.00	0.25	14967	25634	1.71	OK

3.2.3 Design of the 20-story model

The 20-story model was designed based on time-history analysis. The fundamental period of the 20-story model was 3.299 second. The input ground motions used herein were BCJ-L2 (120s) as well as 4 observed waves (30s for each): El Centro NS (1940), JMA Kobe NS (1995), Hachinohe NS (1968), and Taft EW (1925). The response acceleration spectra of the observed ground motions were scaled to follow the design spectra of the BRI-L2 (Level 2 earthquake) in Japan. Table 3.8 summarizes the cross sectional dimension of each structural member. Fig. 3.7 illustrates the lateral stiffness reduction along the height of the structure. Fig. 3.8 shows the story drift ratio and story shear results obtained from the time-history analysis.

Table 3.8 Cross sections of structural members in the 20-story model

(1) Cross sections of columns in the moment frames

Story	C1	C2	C3	C4	C5
20	□-600×600×19	H-650×400×16×22	□-600×600×19	□-650×650×28	□-550×550×25
19	□-600×600×19	H-650×400×16×22	□-600×600×19	□-650×650×28	□-550×550×25
18	□-600×600×19	H-650×400×16×22	□-600×600×19	□-650×650×30	□-550×550×25
17	□-600×600×19	H-650×400×16×22	□-600×600×19	□-650×650×30	□-550×550×25
16	□-600×600×22	H-650×400×16×22	□-600×600×19	□-650×650×30	□-550×550×25
15	□-600×600×22	H-650×400×16×22	□-600×600×19	□-650×650×30	□-550×550×25
14	□-600×600×22	H-650×400×16×25	□-600×600×19	□-650×650×30	□-550×550×25
13	□-600×600×22	H-650×400×16×25	□-600×600×19	□-650×650×30	□-550×550×25
12	□-600×600×22	H-650×400×16×25	□-600×600×22	□-650×650×30	□-550×550×25
11	□-600×600×22	H-650×400×16×25	□-600×600×22	□-650×650×30	□-550×550×25
10	□-600×600×22	H-650×400×16×25	□-600×600×22	□-650×650×32	□-550×550×25
9	□-600×600×22	H-650×400×16×25	□-600×600×22	□-650×650×32	□-550×550×25
8	□-600×600×28	H-650×400×16×25	□-600×600×22	□-650×650×32	□-550×550×25
7	□-600×600×28	H-650×400×16×25	□-600×600×22	□-650×650×32	□-550×550×25
6	□-600×600×28	H-650×400×16×28	□-600×600×22	□-650×650×32	□-550×550×25
5	□-600×600×28	H-650×400×16×28	□-600×600×22	□-650×650×32	□-550×550×25
4	□-600×600×28	H-650×400×16×28	□-600×600×25	□-650×650×32	□-550×550×25
3	□-600×600×28	H-650×400×16×28	□-600×600×25	□-650×650×32	□-550×550×25
2	□-600×600×28	H-650×400×16×28	□-600×600×25	□-650×650×32	□-550×550×25
1	□-600×600×28	H-650×400×16×28	□-600×600×25	□-650×650×32	□-550×550×25

(2) Cross sections of braces in the spine frames and beams in the moment frames

Story	V	SG1	SG2
20	H-550×600×25×25	H-700×300×16×22	H-900×300×19×25
19	H-550×600×25×25	H-700×300×16×22	H-900×300×19×25
18	H-550×600×25×25	H-700×300×16×22	H-900×300×19×25
17	H-550×600×25×25	H-700×300×16×22	H-900×300×19×25
16	H-550×600×25×25	H-700×300×16×25	H-900×300×19×25
15	H-550×600×25×25	H-700×300×16×25	H-900×300×19×25
14	H-550×600×25×25	H-700×300×16×25	H-900×300×19×25
13	H-550×600×25×25	H-700×300×16×25	H-900×300×19×25
12	H-550×600×25×25	H-700×300×16×28	H-900×300×19×25
11	H-550×600×25×25	H-700×300×16×28	H-900×300×19×25
10	H-550×600×25×25	H-700×300×16×28	H-900×300×19×25
9	H-550×600×25×25	H-700×300×16×30	H-900×300×19×25
8	H-550×600×25×25	H-700×300×16×30	H-900×300×19×25
7	H-550×600×25×25	H-700×300×16×30	H-900×300×19×25
6	H-550×600×25×25	H-700×300×16×32	H-900×300×19×25
5	H-550×600×25×25	H-700×300×16×32	H-900×300×19×25
4	H-550×600×25×25	H-700×300×16×32	H-900×300×19×25
3	H-550×600×25×25	H-700×300×16×32	H-900×300×19×25
2	H-550×600×25×25	H-700×300×16×32	H-900×300×19×25
1	H-550×600×25×25	H-700×300×16×32	H-900×300×19×25

(3) Section of BRCs

A (mm ²)	54400
F _y (N/mm ²)	325

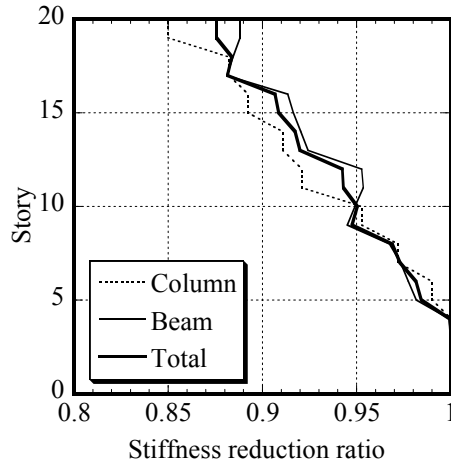


Fig. 3.7 Stiffness reduction ratio along the height of the 20-story model

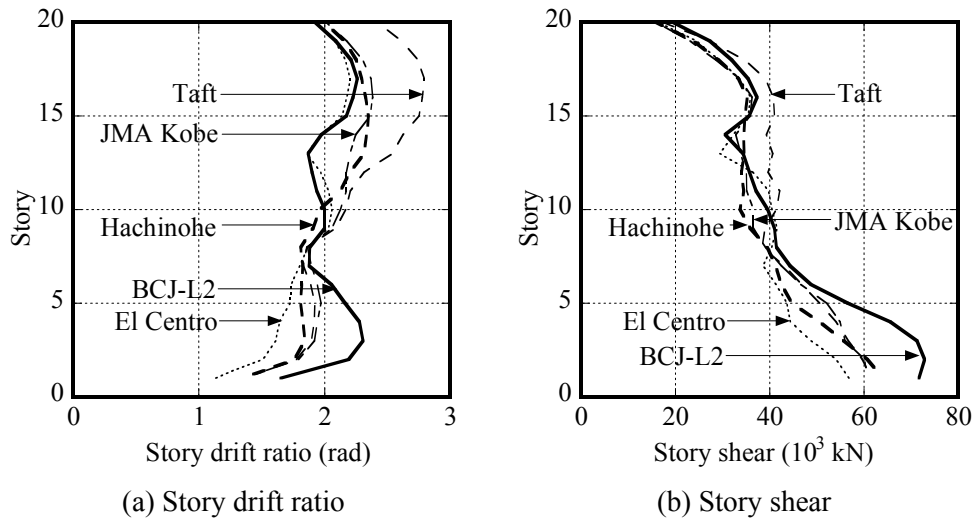


Fig. 3.8 Time-history analysis results of the 20-story model

3.3 Dual multi-degree-of-freedom (DMD) model

A simplified Dual Multi-DOF (DMD) model for the controlled spine frame structures has been developed. This DMD model is expected to exhibit similar nonlinear behaviors of the original structure, particularly in terms of distribution and maximum amounts of story drift and story shear, as well as the behavior of the BRCs. This simplified model has been verified by comparing with the Member-by-Member (MBM) model in OpenSees. By utilizing this simplified DMD model, seismic behavior of the controlled spine frames system will be further studied by parametric studies. Design methods will be proposed based on the results obtained from parametric study.

3.3.1 Concepts and assumptions of the DMD model

The controlled spine frame structure is simplified as two Multi-Degree-of-Freedom (MDOF) models in parallel. Fig. 3.10 shows the DMD model as a simplified model for the corresponding MBM model in Fig. 3.9. In the DMD model, the left system represents moment frames, while the right one represents spine frames. The moment frames constrain lateral deformation of the spine frames. Interaction forces between the two systems are restricted in the lateral direction, i.e., there is no vertical force or bending moment transferred between the two systems. Mass is lumped at the floor levels. BRCs at the bottom of the spine frames are simplified into a plasto-elastic hinge. Details on the simplification of each structural component are explained in the following sections.

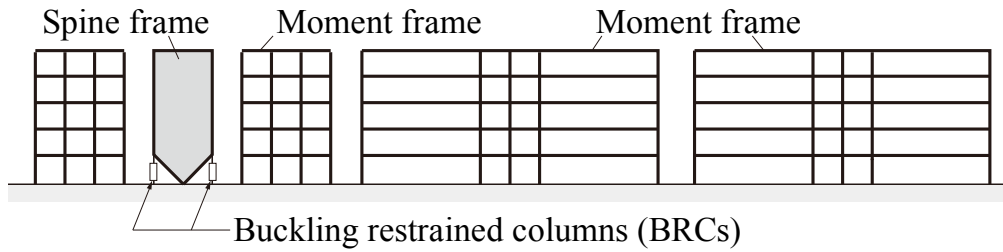


Fig. 3.9 Member-by-member model of the 5-story benchmark building

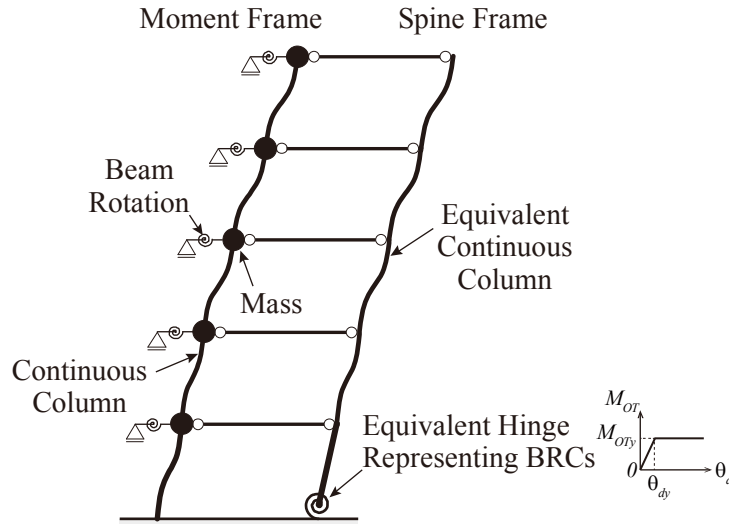


Fig. 3.10 Concept of the DMD model for controlled spine frame structures

3.3.2 Simplification of moment frames

The moment frame was simplified into a generic model based on the method proposed by Ogawa et al. [3.1 - 7]. In the generic model, a “rotational spring” represents all beams at one floor level; a “representative column” represents all columns in one story, as shown in Fig 3.11. Following assumptions are utilized in the simplification:

- All the beam-to-column connections at the same floor level generate identical rotation angle.
- Axial elongation and contraction, as well as shear deformation of beams and columns is neglected, i.e. only bending deformation is considered.
- Panel zone deformation of the beam-to-column connections is neglected.

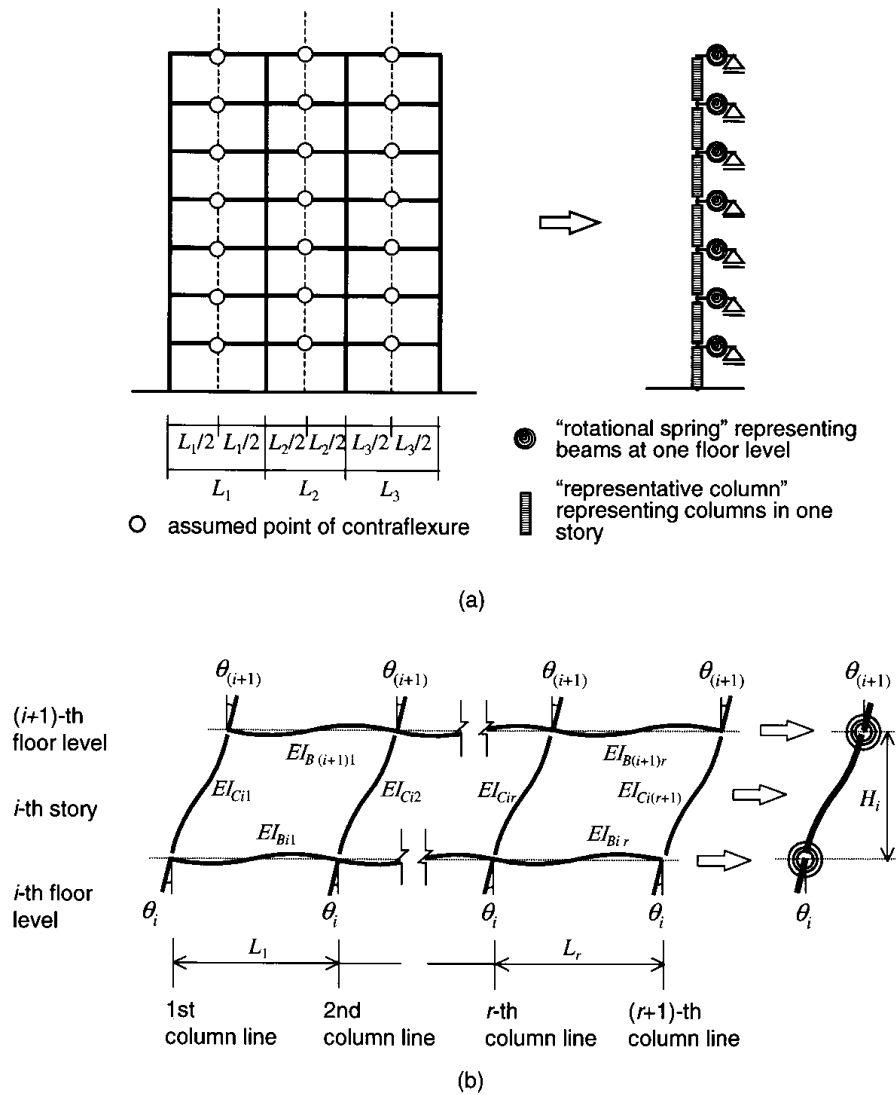


Fig 3.11 Generic frame model: (a) modeling; (b) conversion of beams and columns to rotational spring and representative column. [3.2]

The assumption (a) restricts the point of contra-flexure of all beams to their mid-spans. Nakashima et al. proposed that all beams at each floor level could be condensed into one rotational spring, and all columns in each story could also be condensed into one representative column, as long as each structural member had a uniform cross-section and effects of floor slabs on beam stiffness and strength were neglected. The current study found that the assumption (a) might result in significant inaccuracy for buildings with beams possessing distinctively diverse spans, which was the often case for office buildings. It is mainly because the beams possessing distinctively diverse spans generally exhibit distinctively diverse bending stiffness, and lead to significantly different bending stiffness ratio of beams and columns at different connections at the same floor level. The more different the bending stiffness ratios are, the more unrealistic the assumption (a) goes.

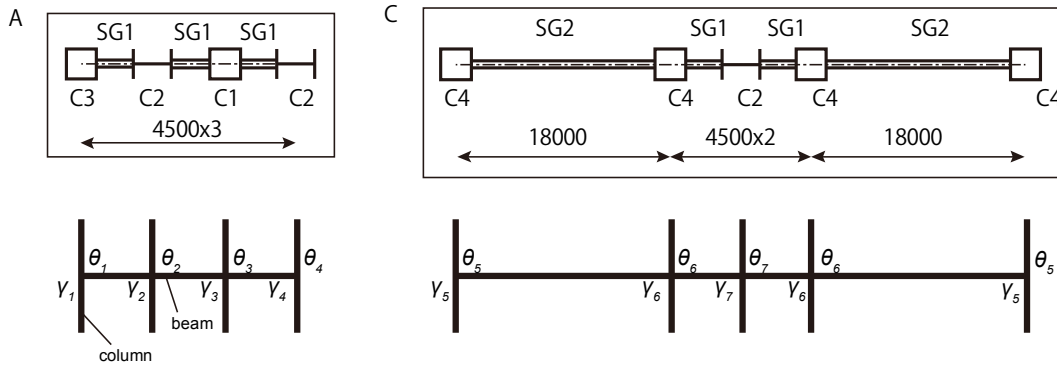


Fig. 3.12 Rotation at each beam-column connection

The current study has observed that rotations at beam-to-column connections were roughly inversely proportional to the corresponding bending stiffness ratio of beams and columns at each floor level. This inversely proportion relation was adopted as the assumption to replace assumption (a).

Calculation of stiffness of beams was modified according to the distribution of bending stiffness ratio of beams and columns at each connection. Fig. 3.12 illustrates the rotation at each beam-column connection at any floor level. The rotation angles during earthquake effect were expressed by Eq. (3.11) and (3.12). In the instance of i -th story, θ_{ij} denotes the rotation angle of the j -th beam-to-column connection. k_i is a constant value. γ_{ij} is the bending stiffness ratio of beams and columns at the j -th connection. $(EI/h)_{cij}$ and $(EI/l)_{bij}$ are the sum of line stiffness of all the columns and beams at the j -th connection.

$$\theta_{ij} = \frac{k_i}{\gamma_{ij}} \quad (3.11)$$

$$\gamma_{ij} = \frac{\sum (EI / l)_{bij}}{\sum (EI / h)_{cij}} \quad (3.12)$$

Eq. (3.13) gives the average rotation angle of all the beam-to-column connections at the same floor level.

$$\bar{\theta}_i = \frac{\frac{1}{\gamma_{i1}} + \frac{1}{\gamma_{i2}} + \frac{1}{\gamma_{i3}} + \frac{1}{\gamma_{i4}} + \frac{2}{\gamma_{i5}} + \frac{2}{\gamma_{i6}} + \frac{1}{\gamma_{i7}}}{9} k_i \quad (3.13)$$

The sum of all beam-end bending moment is computed by Eqs. (3.14) and (3.15).

$$M_{Lij} = \frac{4EI_{ij}}{l_{ij}} \theta_{Lij} + \frac{2EI_{ij}}{l_{ij}} \theta_{Rij}, \quad M_{Rij} = \frac{2EI_{ij}}{l_{ij}} \theta_{Lij} + \frac{4EI_{ij}}{l_{ij}} \theta_{Rij} \quad (3.14)$$

$$\sum M_{bi} = 2 \sum_{j=1}^7 (M_{Lij} + M_{Rij}) = \left[12E \frac{I_1}{L_1} \left(\frac{1}{\gamma_{i1}} + \frac{2}{\gamma_{i2}} + \frac{2}{\gamma_{i3}} + \frac{1}{\gamma_{i4}} + \frac{2}{\gamma_{i6}} + \frac{2}{\gamma_{i7}} \right) + 12E \frac{I_2}{L_2} \left(\frac{2}{\gamma_{i5}} + \frac{2}{\gamma_{i6}} \right) \right] k_i \quad (3.15)$$

where, M_{Lij} and M_{Rij} are the left and right end moments at beam j ; θ_{Lij} and θ_{Rij} are the left and right end rotations at beam j . I_{ij} and l_{ij} is the moment of inertia and length of the j -th beam. I_1 , I_2 are the moments of inertia of beams SG1, SG2, respectively. L_1 , L_2 are the spans of beam SG1, SG2, respectively.

The sum of bending moment divided by the average rotation is the rotational stiffness of the representing rotational spring for beams, as expressed by Eq. (3.16). The constant k is eliminated through the dividing calculation.

$$K_{bi} = \sum M_{bi} / \bar{\theta}_i$$

$$K_{bi} = \frac{12E \frac{I_1}{L_1} \left(\frac{1}{\gamma_{i1}} + \frac{2}{\gamma_{i2}} + \frac{2}{\gamma_{i3}} + \frac{1}{\gamma_{i4}} + \frac{2}{\gamma_{i6}} + \frac{2}{\gamma_{i7}} \right) + 12E \frac{I_2}{L_2} \left(\frac{2}{\gamma_{i5}} + \frac{2}{\gamma_{i6}} \right)}{\frac{\frac{1}{\gamma_{i1}} + \frac{1}{\gamma_{i2}} + \frac{1}{\gamma_{i3}} + \frac{1}{\gamma_{i4}} + \frac{2}{\gamma_{i5}} + \frac{2}{\gamma_{i6}} + \frac{1}{\gamma_{i7}}}{9}} \quad (3.16)$$

Construction of the stiffness matrix of columns was same with the generic model proposed by Nakashima et al. The stiffness matrix of the j -th column at the i -th story in the original frame is expressed in a 4×4 matrix $[K_{cij}]$ as in Eq. (3.17) & (3.18), since only the bending deformation is considered.

$$\begin{Bmatrix} V_{cij}^T \\ M_{cij}^T \\ V_{cij}^B \\ M_{cij}^B \end{Bmatrix} = [K_{cij}] \begin{Bmatrix} u_{i+1} \\ \theta_{i+1} \\ u_i \\ \theta_i \end{Bmatrix} \quad (3.17)$$

$$[K_{cij}] = \begin{Bmatrix} 2\frac{K_{cij}}{h_i^2} & -\frac{K_{cij}}{h_i} & -2\frac{K_{cij}}{h_i^2} & -\frac{K_{cij}}{h_i} \\ -\frac{K_{cij}}{h_i} & \frac{2}{3}K_{cij} & \frac{K_{cij}}{h_i} & \frac{1}{3}K_{cij} \\ -2\frac{K_{cij}}{h_i^2} & \frac{K_{cij}}{h_i} & 2\frac{K_{cij}}{h_i^2} & \frac{K_{cij}}{h_i} \\ -\frac{K_{cij}}{h_i} & \frac{1}{3}K_{cij} & \frac{K_{cij}}{h_i} & \frac{2}{3}K_{cij} \end{Bmatrix} \quad (3.18)$$

where,

$$K_{cij} = 6 \frac{EI_{cij}}{h_i}$$

here, u_i is the lateral deformation at the i -th floor level. θ_i is the node rotation at the i -th floor level. V_{cij} and M_{cij} are the corresponding lateral force and moment. Superscripts T and B denote the top and bottom of the column. h_i is the height of the i -th story. I_{cij} is the moment of inertia and length of the j -th column at the i -th story.

The sums of all stiffness matrix of the single column are the stiffness matrix of the representing column for all the columns at the i -th story.

$$[K_{ci}] = \sum_{j=1}^{n_c} [K_{cij}] \quad (3.19)$$

3.3.3 Simplification of spine frames

The spine frames were simplified into a continuous column considering both bending and shear deformation. As for each structural member—the braces and columns in the spine frames were assumed as pin-connected thus only axial elongation and contraction of them were considered in computing the bending and shear stiffness of the spine frames.

Previous researchers have proposed a procedure to compute the equivalent stiffness matrix of plane truss beams.^[3,8] As shown in Fig 3.13, the spine frame is constrained as a cantilever truss beam and there are three external forces P_1, P_2, P_3 loaded at the free end in three directions and u_1, u_2, u_3 are the corresponding deflections. Their relation is expressed by Eq (3.20) through matrix $[A]$.

$$\begin{Bmatrix} u_1 \\ u_2 \\ u_3 \end{Bmatrix} = \begin{bmatrix} A_{11} & A_{12} & A_{13} \\ A_{21} & A_{22} & A_{23} \\ A_{31} & A_{32} & A_{33} \end{bmatrix} \begin{Bmatrix} P_1 \\ P_2 \\ P_3 \end{Bmatrix} \quad (3.20)$$

Here, A is a symmetric matrix. N , M , and Q are the internal forces (axial force, bending moment, shear force) at the free end section. ε , κ , and γ are the axial strain, curvature, shear strain at the free end section, respectively. Their relation is expressed by the flexibility matrix $[S]$ as in Eq. (3.21)

$$\begin{Bmatrix} \varepsilon \\ \kappa \\ \gamma \end{Bmatrix} = \begin{bmatrix} s_{11} & s_{12} & s_{13} \\ s_{21} & s_{22} & s_{23} \\ s_{31} & s_{32} & s_{33} \end{bmatrix} \begin{Bmatrix} N \\ M \\ Q \end{Bmatrix} \quad (3.21)$$

$[S]$ is also a symmetric matrix. Relation between the external forces and internal forces is:

$$N = P_1, \quad M = P_2 + P_3 \cdot x, \quad Q = P_3 \quad (3.22)$$

The elastic work done by external forces is identical with that done by the internal force, so

$$\begin{aligned} W &= \frac{1}{2} \begin{Bmatrix} P_1 \\ P_2 \\ P_3 \end{Bmatrix}^T \begin{Bmatrix} u_1 \\ u_2 \\ u_3 \end{Bmatrix} = \frac{1}{2} \begin{Bmatrix} P_1 \\ P_2 \\ P_3 \end{Bmatrix}^T \begin{bmatrix} A_{11} & A_{12} & A_{13} \\ A_{21} & A_{22} & A_{23} \\ A_{31} & A_{32} & A_{33} \end{bmatrix} \begin{Bmatrix} P_1 \\ P_2 \\ P_3 \end{Bmatrix} \\ &= \frac{1}{2} \int_0^l \begin{Bmatrix} N \\ M \\ Q \end{Bmatrix}^T \begin{Bmatrix} \varepsilon \\ \kappa \\ \gamma \end{Bmatrix} dx = \frac{1}{2} \int_0^l \begin{Bmatrix} N \\ M \\ Q \end{Bmatrix}^T \begin{bmatrix} s_{11} & s_{12} & s_{13} \\ s_{21} & s_{22} & s_{23} \\ s_{31} & s_{32} & s_{33} \end{bmatrix} \begin{Bmatrix} N \\ M \\ Q \end{Bmatrix} dx \end{aligned} \quad (3.23)$$

Substitute Eq. (3.22) into Eq. (3.23) and compute $\partial M / \partial P_i \partial P_j$ to obtain the expression of A_{ij}

by s_{ij} as shown by Eq. (3.24)

$$\begin{cases} A_{11} = s_{11}l \\ A_{12} = s_{12}l \\ A_{13} = s_{13}l + s_{12}l^2 / 2 \\ A_{22} = s_{22}l \\ A_{23} = s_{23}l + s_{22}l^2 / 2 \\ A_{33} = s_{33}l + s_{23}l^2 + s_{22}l^3 / 3 \end{cases} \quad (3.24)$$

So s_{ij} expressed by A_{ij} is

$$\begin{cases} s_{11} = A_{11} / l \\ s_{12} = A_{12} / l \\ s_{13} = A_{13} / l - A_{12} / 2 \\ s_{22} = A_{22} / l \\ s_{23} = A_{23} / l - A_{22} / 2 \\ s_{33} = A_{33} / l - A_{23} + A_{22} l / 6 \end{cases} \quad (3.25)$$

The reversal matrix of $[S]$ is the stiffness matrix $[K]$.

$$\begin{Bmatrix} N \\ M \\ Q \end{Bmatrix} = \begin{bmatrix} s_{11} & s_{12} & s_{13} \\ s_{21} & s_{22} & s_{23} \\ s_{31} & s_{32} & s_{33} \end{bmatrix}^{-1} \begin{Bmatrix} \varepsilon \\ \kappa \\ \gamma \end{Bmatrix} \quad (3.26)$$

$$[K] = \begin{bmatrix} s_{11} & s_{12} & s_{13} \\ s_{21} & s_{22} & s_{23} \\ s_{31} & s_{32} & s_{33} \end{bmatrix}^{-1} \quad (3.27)$$

The virtual work principle is utilized to compute A_{ij} . As shown in Fig 3.14, A and A_w denotes the sectional areas of columns and braces in the spine frame. Uniform columns and braces are equipped in the spine frames. l is the length of a unit spine frame. b is the width of the spine frame. θ is the angle between columns and braces.

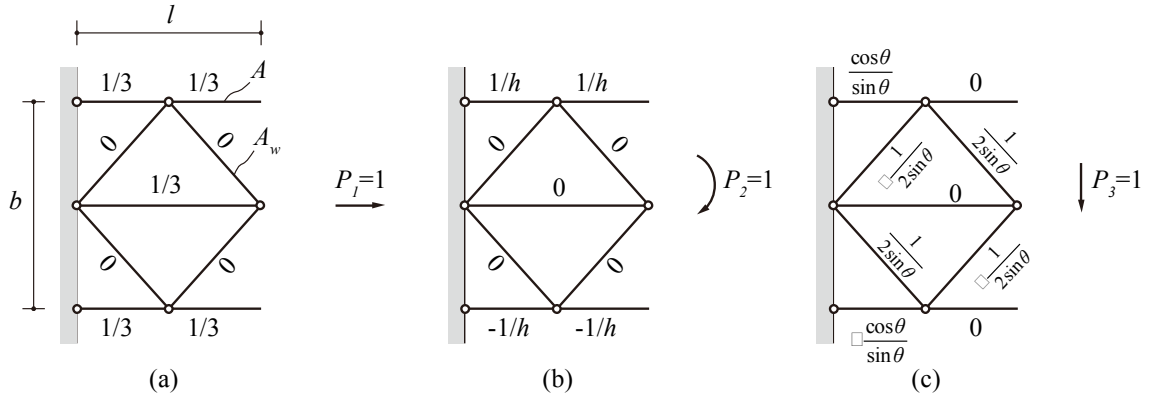


Fig 3.14 Internal forces in one unit of the spine frame corresponding to the unit virtual force: (a) $P_1=1$, (b) $P_2=1$, (c) $P_3=1$

When the external force $P_1=1$, $P_2=0$, $P_3=0$, the axial deflection u_l is computed by assuming a virtual external force same as P_l . Internal forces against the real and virtual external forces are identical, as shown in Fig 3.14 (a). u_l and A_{11} are expressed by Eq. (3.28)

$$A_{11} = \left(\frac{1}{3}\right)^2 \frac{l}{2EA} \cdot 4 + \left(\frac{1}{3}\right)^2 \frac{l}{EA} = \frac{l}{3EA} \quad (3.28)$$

Similarly, A_{21} is computed when the external force is $P_1=1$ and the virtual force is $P_2=1$, (Fig 3.14 a & b)

$$A_{21} = \left(\frac{1}{3}\right) \frac{1}{b} \frac{l}{2EA} \cdot 2 + \left(\frac{1}{3}\right) \left(-\frac{1}{b}\right) \frac{l}{2EA} \cdot 2 = 0 \quad (3.29)$$

A_{22} is computed when the external force is $P_2=1$ and the virtual force is $P_2=1$, (Fig 3.14 b & b)

$$A_{22} = \left(\frac{1}{b}\right)^2 \frac{l}{2EA} \cdot 4 = \frac{2l}{b^2 EA} \quad (3.30)$$

A_{31} is computed when the external force is $P_3=1$ and the virtual force is $P_1=1$, (Fig 3.14 a & c)

$$A_{31} = 0 \quad (3.31)$$

A_{32} is computed when the external force is $P_3=1$ and the virtual force is $P_2=1$, (Fig 3.14 b & c)

$$A_{32} = \left(\frac{1}{b}\right) \frac{\cos \theta}{\sin \theta} \frac{l}{2EA} \cdot 2 = \frac{l^2}{b^2 EA} = \frac{\cos^2 \theta}{\sin^2 \theta EA} \quad (3.32)$$

A_{33} is computed when the external force is $P_3=1$ and the virtual force is $P_3=1$, (Fig 3.14 c & c)

$$\begin{aligned} A_{33} &= \left(\frac{\cos \theta}{\sin \theta}\right)^2 \cdot \frac{l}{2EA} \cdot 2 + \left(\frac{1}{2 \sin \theta}\right)^2 \cdot \frac{l}{2 \cos \theta EA_w} \cdot 4 \\ &= \frac{\cos^2 \theta l}{\sin^2 \theta EA} + \frac{l}{2 \sin^2 \theta \cos \theta EA_w} \end{aligned} \quad (3.33)$$

Substitute Eqs. (3.28) - (3.33) into Eq. (3.25), we could obtain

$$\left\{ \begin{array}{l} s_{11} = \frac{1}{3EA} \\ s_{12} = s_{21} = 0 \\ s_{13} = s_{31} = 0 \\ s_{22} = \frac{2}{b^2 EA} \\ s_{23} = s_{32} = 0 \\ s_{33} = \frac{1 + \frac{2}{3} \frac{A_w}{A} \cos^3 \theta}{2 \sin^2 \theta \cos \theta EA_w} \end{array} \right. \quad (3.34)$$

So the equivalent stiffness matrix of the spine frames is

$$[\mathbf{K}] = \begin{bmatrix} s_{11} & s_{12} & s_{13} \\ s_{21} & s_{22} & s_{23} \\ s_{31} & s_{32} & s_{33} \end{bmatrix}^{-1} = \begin{bmatrix} 3EA & 0 & 0 \\ 0 & \frac{b^2 EA}{2} & 0 \\ 0 & 0 & \frac{2 \sin^2 \theta \cos \theta EA_w}{1 + \frac{2}{3} \frac{A_w}{A} \cos^3 \theta} \end{bmatrix} \quad (3.35)$$

From Eq. (3.35) we could easily obtain the equivalent bending stiffness and shear stiffness of the spine frames.

$$(EI)_{eq} = \frac{b^2 EA}{2} \quad (3.36)$$

$$(GA)_{eq} = \frac{2 \sin^2 \theta \cos \theta EA_w}{1 + \frac{2}{3} \frac{A_w}{A} \cos^3 \theta} \quad (3.37)$$

Then, similar with the representing column for moment frame, the elastic end force versus end deformation relation of the spine frame in the original frame is also expressed in a 4×4 matrix, as shown by Eq. (3.38) - (3.40).

$$\begin{Bmatrix} V_{si}^T \\ M_{si}^T \\ V_{si}^B \\ M_{si}^B \end{Bmatrix} = [\mathbf{K}_{si}] \begin{Bmatrix} u'_{i+1} \\ \theta^S_{i+1} \\ u'_i \\ \theta^S_i \end{Bmatrix} \quad (3.38)$$

with

$$[\mathbf{K}_{si}] = \begin{Bmatrix} 2 \frac{K_{si}}{h_i^2} & -\frac{K_{si}}{h_i} & -2 \frac{K_{si}}{h_i^2} & -\frac{K_{si}}{h_i} \\ -\frac{K_{si}}{h_i} & \frac{2}{3} K_{si} & \frac{K_{si}}{h_i} & \frac{1}{3} K_{si} \\ -2 \frac{K_{si}}{h_i^2} & \frac{K_{si}}{h_i} & 2 \frac{K_{si}}{h_i^2} & \frac{K_{si}}{h_i} \\ -\frac{K_{si}}{h_i} & \frac{1}{3} K_{si} & \frac{K_{si}}{h_i} & \frac{2}{3} K_{si} \end{Bmatrix} \quad (3.39)$$

Here,

$$K_{si} = 6 \frac{(EI)_{eq}}{h_i} \quad (3.40)$$

Where, θ^S denotes the node rotation in the spine frames, which is independent from the moment frames. Please note that u' , u'' are the nodal displacements caused by flexural deformation and shear deformation in a story of spine frames, respectively. Their sum equals to

the lateral displacement of the moment frame, u .

$$u_{i+1} = u'_{i+1} + u''_{i+1}, u_i = u'_i + u''_i \quad (3.41)$$

Stiffness matrix of a beam including both bending and shear deformation is derived in Eqs. (3.42-47) [3.9] Relation between the story shear deformation and story shear is shown as Eq. (3.42):

$$u''_{i+1} - u''_i = \frac{V_{si}^T h_i}{(GA)_{eq}} \quad (3.42)$$

Substitute Eqs. (3.41) into Eq. (3.38) :

$$\begin{Bmatrix} V_{si}^T \\ M_{si}^T \\ V_{si}^B \\ M_{si}^B \end{Bmatrix} = [K_{si}] \begin{Bmatrix} u_{i+1} - u''_{i+1} \\ \theta_{i+1}^S \\ u_i - u''_i \\ \theta_i^S \end{Bmatrix} = [K_{si}] \begin{Bmatrix} u_{i+1} \\ \theta_{i+1}^S \\ u_i \\ \theta_i^S \end{Bmatrix} - [K_{si}] \begin{Bmatrix} u''_{i+1} \\ 0 \\ u''_i \\ 0 \end{Bmatrix} \quad (3.43)$$

By substituting $[K_{si}]$ as expressed by Eq. (3.39) and utilizing the relation between u'' and shear force we could obtain

$$[K_{si}] \begin{Bmatrix} u''_{i+1} \\ 0 \\ u''_i \\ 0 \end{Bmatrix} = \frac{12(EI)_{eq}}{(GA)_{eq} h_i^2} \begin{bmatrix} 1 & 0 & 0 & 0 \\ -\frac{h_i}{2} & 0 & 0 & 0 \\ -1 & 0 & 0 & 0 \\ -\frac{h_i}{2} & 0 & 0 & 0 \end{bmatrix} \begin{Bmatrix} V_{si}^T \\ M_{si}^T \\ V_{si}^B \\ M_{si}^B \end{Bmatrix} \quad (3.44)$$

By substituting Eq. (3.44) into Eq. (3.43), we could extract the direct relation between forces and total deformations.

$$\left[[1] + \frac{12(EI)_{eq}}{(GA)_{eq} h_i^2} \begin{bmatrix} 1 & 0 & 0 & 0 \\ -\frac{h_i}{2} & 0 & 0 & 0 \\ -1 & 0 & 0 & 0 \\ -\frac{h_i}{2} & 0 & 0 & 0 \end{bmatrix} \right] \begin{Bmatrix} V_{si}^T \\ M_{si}^T \\ V_{si}^B \\ M_{si}^B \end{Bmatrix} = [K_{si}] \begin{Bmatrix} u_{i+1} \\ \theta_{i+1}^S \\ u_i \\ \theta_i^S \end{Bmatrix} \quad (3.45)$$

Reversing Eq. (3.45) we could obtain the stiffness matrix considering shear deformation

$$\begin{Bmatrix} V_{si}^T \\ M_{si}^T \\ V_{si}^B \\ M_{si}^B \end{Bmatrix} = \left[[1] + \frac{12(EI)_{eq}}{(GA)_{eq} h_i^2} \begin{bmatrix} 1 & 0 & 0 & 0 \\ -\frac{h_i}{2} & 0 & 0 & 0 \\ -1 & 0 & 0 & 0 \\ -\frac{h_i}{2} & 0 & 0 & 0 \end{bmatrix} \right]^{-1} [K_{si}] \begin{Bmatrix} u_{i+1} \\ \theta_{i+1}^S \\ u_i \\ \theta_i^S \end{Bmatrix} \quad (3.46)$$

By simplifying Eq. (3.46), we could get

$$\begin{Bmatrix} V_{si}^T \\ M_{si}^T \\ V_{si}^B \\ M_{si}^B \end{Bmatrix} = \frac{6(EI)_{eq}}{(1+6\alpha)h_i} \begin{Bmatrix} \frac{2}{h_i^2} & -\frac{1}{h_i} & -\frac{2}{h_i^2} & -\frac{1}{h_i} \\ -\frac{1}{h_i} & \frac{2}{3} + \alpha & \frac{1}{h_i} & \frac{1}{3} - \alpha \\ -\frac{2}{h_i^2} & \frac{1}{h_i} & \frac{2}{h_i^2} & \frac{1}{h_i} \\ -\frac{1}{h_i} & \frac{1}{3} - \alpha & \frac{1}{h_i} & \frac{2}{3} + \alpha \end{Bmatrix} \begin{Bmatrix} u_{i+1} \\ \theta_{i+1}^S \\ u_i \\ \theta_i^S \end{Bmatrix}, \alpha = \frac{2(EI)_{eq}}{h_i^2 (GA)_{eq}} \quad (3.47)$$

From the equations above we can see that at each floor level of the system there are 3 global deformations, lateral displacement u_i , rotation of the moment frame θ_i , and rotation of the spine frame θ_i^S .

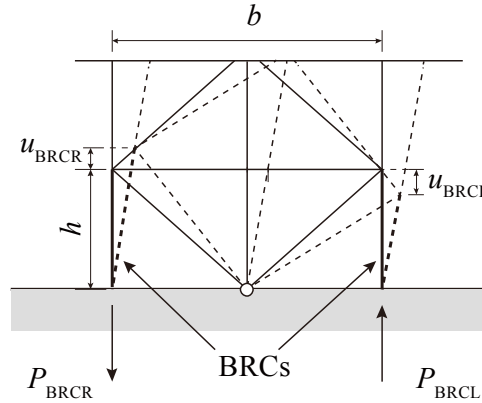


Fig. 3.15 Key parameters of the BRCs

An elasto-plastic hinge was placed at the bottom to represent BRCs. Rotation stiffness of the hinge is $P_{BRCR}b / ((u_{BRCL} + u_{BRCR})/b)$, as shown in Fig. 3.15. Bending stiffness of the spine frame column in the first story is large enough to ensure rotation of the top node of the first story in the spine frames is same with that of the BRCs. Shear stiffness of the spine frame column in the first story is the computed value so the additional shear deformation of the spines at the first floor level could still be taken account.

3.4 Programming for nonlinear analysis of DMD Models

A Time-history analysis program written in FORTRAN has being developed for the DMD model. In the dynamic analysis, all of the translational DOFs and rotational DOFs are included. In the eigenvalue analysis, static condensation is used to eliminate those DOFs to which zero mass is assigned, because the eigenvalue problem solver can only handle positive-definite matrix. Newmark- β method is used for integration and Newton-Raphson algorithm is used for the iteration computing. Except for the state determination, dynamic analysis theory and commutating techniques involved in this program mainly follow ref. [3.10].

3.4.1 Construction of stiffness matrix

The node rotational inertia is ignored since it has less effect on the seismic response of regular structures against horizontal earthquake motions. The equations of motion for a system including damping are written in the partitioned form:

$$\begin{bmatrix} \mathbf{m}_u & \mathbf{0} \\ \mathbf{0} & \mathbf{0} \end{bmatrix} \begin{Bmatrix} \ddot{\mathbf{u}}_u \\ \ddot{\mathbf{u}}_r \end{Bmatrix} + \begin{bmatrix} \mathbf{c}_{uu} & \mathbf{c}_{ur} \\ \mathbf{c}_{ru} & \mathbf{c}_{rr} \end{bmatrix} \begin{Bmatrix} \dot{\mathbf{u}}_u \\ \dot{\mathbf{u}}_r \end{Bmatrix} + \begin{bmatrix} \mathbf{k}_{uu} & \mathbf{k}_{ur} \\ \mathbf{k}_{ru} & \mathbf{k}_{rr} \end{bmatrix} \begin{Bmatrix} \mathbf{u}_u \\ \mathbf{u}_r \end{Bmatrix} = \begin{Bmatrix} \mathbf{p}_u \\ \mathbf{0} \end{Bmatrix} \quad (3.48)$$

where the subscript \mathbf{u} denotes the DOFs with mass (translational DOFs) and the subscript \mathbf{r} denotes the DOFs with zero mass (rotational DOFs). Assuming that no damping forces are associated with the rotational DOFs, then $\mathbf{c}_{ru} = \mathbf{c}_{rr} = \mathbf{0}$. Because the damping matrix is symmetric, \mathbf{c}_{ur} is also $\mathbf{0}$. Eq. (3.48) becomes:

$$\begin{bmatrix} \mathbf{m}_u & \mathbf{0} \\ \mathbf{0} & \mathbf{0} \end{bmatrix} \begin{Bmatrix} \ddot{\mathbf{u}}_u \\ \ddot{\mathbf{u}}_r \end{Bmatrix} + \begin{bmatrix} \mathbf{c}_{uu} & \mathbf{0} \\ \mathbf{0} & \mathbf{0} \end{bmatrix} \begin{Bmatrix} \dot{\mathbf{u}}_u \\ \dot{\mathbf{u}}_r \end{Bmatrix} + \begin{bmatrix} \mathbf{k}_{uu} & \mathbf{k}_{ur} \\ \mathbf{k}_{ru} & \mathbf{k}_{rr} \end{bmatrix} \begin{Bmatrix} \mathbf{u}_u \\ \mathbf{u}_r \end{Bmatrix} = \begin{Bmatrix} \mathbf{p}_u \\ \mathbf{0} \end{Bmatrix} \quad (3.49)$$

Eq. (3.49) is simplified into two equations:

$$\mathbf{m}_u \ddot{\mathbf{u}}_u + \mathbf{c}_{uu} \dot{\mathbf{u}}_u + \mathbf{k}_{uu} \mathbf{u}_u + \mathbf{k}_{ur} \mathbf{u}_r = \mathbf{p}_u \text{ (a), } \mathbf{k}_{ru} \mathbf{u}_u + \mathbf{k}_{rr} \mathbf{u}_r = \mathbf{0} \text{ (b)} \quad (3.50)$$

A static relationship between \mathbf{u}_u and \mathbf{u}_r is obtained from Eq. (3.50b):

$$\mathbf{u}_r = \mathbf{k}_{rr}^{-1} \mathbf{k}_{ru} \mathbf{u}_u \quad (3.51)$$

Substituting Eq. (3.51) in Eq. (3.50a) gives

$$\mathbf{m}_u \ddot{\mathbf{u}}_u + \mathbf{c}_{uu} \dot{\mathbf{u}}_u + \hat{\mathbf{k}}_{uu} \mathbf{u}_u = \mathbf{p}_u \quad (3.52)$$

where $\hat{\mathbf{k}}_{uu}$ is the condensed stiffness matrix given by

$$\hat{\mathbf{k}}_{uu} = \mathbf{k}_{uu} - \mathbf{k}_{ru} \mathbf{k}_{rr}^{-1} \mathbf{k}_{ru} \quad (3.53)$$

The mass, stiffness, and damping matrix in Eq. (3.52) are all positive-definite matrix and are able to be utilized in the eigenvalue analysis. As for the nonlinear time-history analysis, matrix including all the DOFs were utilized instead of the condensed ones, so as to saving the computing time and memory space involved with the iterations. Computing error could also be reduced, which was very helpful for achieving a convergence solution in the nonlinear analysis.

Rayleigh damping was utilized to construct the damping matrix.

$$\mathbf{c} = a_0 \mathbf{m} + a_1 \mathbf{k} \quad (3.54)$$

a_0, a_1 are constants determined by Eqs. (3.55) and (3.56).

$$a_0 = \frac{2 w_n \dot{w}_m w (h_n \dot{w}_m w - h_m \dot{w}_n w)}{(w_m)^2 - (w_n)^2}, \quad a_1 = \frac{2 (\zeta_m \dot{w}_m w - \zeta_n \dot{w}_n w)}{(w_m)^2 - (w_n)^2} \quad (3.55), (3.56)$$

where, w_n and ζ_n are the elastic frequency and damping ratio of the n -th mode response. w_m and ζ_m are the elastic frequency and damping ratio of the m -th mode response.

In an N -story DMD model, the dimensions of \mathbf{u}_t and \mathbf{u}_r are N and $(2N+1)$, because the translational node deflections of spine frames are identical with the moment frames, while the rotational node deflections of spine frames and moment frames are independent. The additional “one” in the rotational DOF corresponds to the rotation of the BRC hinge.

3.4.2 Nonlinear time-history analysis algorithm

3.4.2.1 Numerical integration and iteration method

The Taylor series expansions of displacement and velocity at time $(t+\Delta t)$ are:

$$\mathbf{u}_{t+\Delta t} = \mathbf{u}_t + \Delta t \dot{\mathbf{u}}_t + \frac{(\Delta t)^2}{2} \ddot{\mathbf{u}}_{t1}, \quad \dot{\mathbf{u}}_{t+\Delta t} = \dot{\mathbf{u}}_t + \Delta t \ddot{\mathbf{u}}_{t2} \quad (3.57)$$

Newmark- β method assumes a convex combination for the remainder terms in Eq. (3.57),

$$\ddot{\mathbf{u}}_{t1} = (1-2\beta)\ddot{\mathbf{u}}_t + 2\beta\ddot{\mathbf{u}}_{t+\Delta t}, \quad \ddot{\mathbf{u}}_{t2} = (1-\delta)\ddot{\mathbf{u}}_t + \delta\ddot{\mathbf{u}}_{t+\Delta t} \quad (3.58)$$

Substituting Eq. (3.58) in Eq. (3.57) gives

$$\begin{aligned} \mathbf{u}_{t+\Delta t} &= \mathbf{u}_t + \Delta t \dot{\mathbf{u}}_t + \frac{(\Delta t)^2}{2} ((1-2\beta)\ddot{\mathbf{u}}_t + 2\beta\ddot{\mathbf{u}}_{t+\Delta t}) \\ \dot{\mathbf{u}}_{t+\Delta t} &= \dot{\mathbf{u}}_t + \Delta t ((1-\delta)\ddot{\mathbf{u}}_t + \delta\ddot{\mathbf{u}}_{t+\Delta t}) \end{aligned} \quad (3.59)$$

In this program, $\delta=1/2$, $\beta=1/4$ are employed since they give unconditionally stable solution. Then Eq. (3.59) can be written as

$$\Delta \mathbf{u}_{t+\Delta t} = \Delta t \dot{\mathbf{u}}_t + \frac{(\Delta t)^2}{2} \ddot{\mathbf{u}}_t + \frac{(\Delta t)^2}{4} \Delta \ddot{\mathbf{u}}_t, \quad \Delta \dot{\mathbf{u}}_{t+\Delta t} = \Delta t \ddot{\mathbf{u}}_t + \frac{(\Delta t)^2}{2} \Delta \ddot{\mathbf{u}}_t \quad (3.60)$$

The equation of motion should be satisfied at each time instant.

$$\mathbf{m} \ddot{\mathbf{u}}_t + \mathbf{c}_t \dot{\mathbf{u}}_t + \mathbf{k}_t \mathbf{u}_t = -\ddot{u}_{gt} \mathbf{m} \mathbf{1} \quad (3.61)$$

where, $\mathbf{1}^T = [1, 1, 1, \dots, 1]$

Substituting Eq. (3.60) in Eq. (3.61) gives

$$\bar{\mathbf{k}}_t \Delta \ddot{\mathbf{u}}_t = \bar{\mathbf{p}}_t \quad (3.62)$$

$$\text{Here,} \quad \bar{\mathbf{k}}_t = \mathbf{m} + \mathbf{c}_t \frac{\Delta t}{2} + \mathbf{k}_t \frac{(\Delta t)^2}{4}, \quad \bar{\mathbf{p}}_t = -\ddot{u}_{gt} \mathbf{m} \mathbf{1} - \mathbf{c}_t \Delta t \ddot{\mathbf{u}}_t - \mathbf{k}_t (\Delta t \dot{\mathbf{u}}_t + \frac{(\Delta t)^2}{2} \ddot{\mathbf{u}}_t) \quad (3.63)$$

From Eq. (3.62) and (3.63) we could compute the acceleration increment $\Delta \ddot{\mathbf{u}}_t$ at time t based on the ground motion \ddot{u}_g , displacement \mathbf{u}_t , velocity $\dot{\mathbf{u}}_t$, and acceleration $\ddot{\mathbf{u}}_t$. So the displacement and velocity increments $\Delta \mathbf{u}_t$ and $\Delta \dot{\mathbf{u}}_t$ could be determined by substituting the acceleration increment $\Delta \ddot{\mathbf{u}}_t$ into Eq. (3.60).

Below is the flow chart of solving the equation of motion by utilizing Newmark's numerical integration method with Newton-Raphson iteration for considering material nonlinearity.

Step 1. Initialize the acceleration, velocity, and displacement.

$$\ddot{\mathbf{u}}_0 = -\ddot{u}_{g0} \mathbf{1}$$

$$\dot{\mathbf{u}}_0 = \mathbf{0}$$

$$\mathbf{u}_0 = \mathbf{0}$$

Step 2. Calculations for the i -th time instant ($i=1, 2, 3, \dots$)

Initialize acceleration, velocity, and displacement increments based on the results in last time instant:

$$\Delta \ddot{\mathbf{u}}_i^{(0)} = \mathbf{0}$$

$$\Delta \dot{\mathbf{u}}_i^{(0)} = \Delta t \ddot{\mathbf{u}}_{i-1}$$

$$\Delta \mathbf{u}_i^{(0)} = \Delta t \dot{\mathbf{u}}_{i-1} + \frac{(\Delta t)^2}{2} \ddot{\mathbf{u}}_{i-1}$$

Initialize stiffness matrix and damping matrix based on the matrix in last time instant:

$$\mathbf{c}_i^{(0)} = \mathbf{c}_{i-1}$$

$$\mathbf{k}_i^{(0)} = \mathbf{k}_{i-1}$$

Here the superscript “(0)” denotes the initial step of iteration.

Step 3. Calculations for the j -th iteration ($j=0, 1, 2, 3, \dots$)

3.1 Calculate the mass-normalized residual force increment $\Delta R_i^{(j)}$ by using the newly updated stiffness matrix and damping matrix:

$$\mathbf{m}\Delta\ddot{\mathbf{u}}_i^{(j)} + \mathbf{c}_i^{(j)}\Delta\dot{\mathbf{u}}_i^{(j)} + \mathbf{k}_i^{(j)}\Delta\mathbf{u}_i^{(j)} = \Delta R_i^{(j)}\mathbf{m}\mathbf{1}$$

3.2 Check convergence: if $|-(\ddot{u}_{gi} - \ddot{u}_{g\ i-1}) - \Delta R_i^{(j)}| < \textit{Tolerance}$ and $j \geq 1$, skip the following steps and directly go to step 4; otherwise implement steps 3.3 to 3.7.

3.3 Compute the generalized stiffness matrix based on the j -th iteration's matrix:

$$\bar{\mathbf{k}}_i^{(j)} = \mathbf{m} + \mathbf{c}_i^{(j)} \frac{\Delta t}{2} + \mathbf{k}_i^{(j)} \frac{(\Delta t)^2}{4}$$

3.4 Compute the solution of acceleration for the $(j+1)$ -th iteration:

$$\bar{\mathbf{k}}_i^{(j)}\Delta\ddot{\mathbf{u}}_i^{(j+1)} = -(\ddot{u}_{gi} - \ddot{u}_{g\ i-1}) - \Delta R_i^{(j)}$$

3.5 Compute the solutions of velocity and displacement by using the acceleration obtained from step 3.5.

$$\Delta\dot{\mathbf{u}}_i^{(j+1)} = \Delta\dot{\mathbf{u}}_i^{(j)} + \frac{\Delta t}{2}\Delta\ddot{\mathbf{u}}_i^{(j+1)}$$

$$\Delta\mathbf{u}_i^{(j+1)} = \Delta\mathbf{u}_i^{(j)} + \frac{(\Delta t)^2}{4}\Delta\ddot{\mathbf{u}}_i^{(j+1)}$$

3.6 State determinations

Compute the displacement and velocity for the $(j+1)$ -th iteration:

$$\dot{\mathbf{u}}_i^{(j+1)} = \dot{\mathbf{u}}_{i-1} + \Delta\dot{\mathbf{u}}_i^{(j+1)}$$

$$\mathbf{u}_i^{(j+1)} = \mathbf{u}_{i-1} + \Delta\mathbf{u}_i^{(j+1)}$$

Extract rotational velocity ${}^r\dot{u}_i^{(j+1)}$ and rotational deflection ${}^r u_i^{(j+1)}$ of the BRC hinge

from the displacement and velocity vectors. Determine the restoring moment ${}^r q_i^{(j+1)}$ according to the Return Map Algorithm (explained in section 3.4.2.2).

Update the rotational stiffness ${}^r k_i^{j+1}$ of the BRC hinges according to the restoring

moment and rotational deflection increments.

$${}^r k_i^{j+1} = \left| \frac{{}^r q_i^{(j+1)} - {}^r q_{i-1}}{{}^r u_i^{(j+1)} - {}^r u_{i-1}} \right|$$

3.7 Replace j by $j+1$ and repeat steps 3.1 to 3.6.

Step 4. The convergence solutions obtained from iterations are denoted as $\Delta \ddot{\mathbf{u}}_i$, $\Delta \dot{\mathbf{u}}_i$, $\Delta \mathbf{u}_i$, \mathbf{k}_i , \mathbf{c}_i , ${}^r u_i$, ${}^r \dot{u}_i$, ${}^r q_i$. So the acceleration, velocity, and displacement at the i -th time instant are:

$$\ddot{\mathbf{u}}_i = \ddot{\mathbf{u}}_{i-1} + \Delta \ddot{\mathbf{u}}_i$$

$$\dot{\mathbf{u}}_i = \dot{\mathbf{u}}_{i-1} + \Delta \dot{\mathbf{u}}_i$$

$$\mathbf{u}_i = \mathbf{u}_{i-1} + \Delta \mathbf{u}_i$$

Step 5. Repetition for the $(i+1)$ -th time instant.

Replace i by $i+1$ and implement steps 2 to 4

3.4.2.2 State determination in nonlinear analysis by return mapping algorithm

A robust method—Return mapping algorithm^[3.11, 12] is adopted for the state determination of the BRC hinge. The hysteretic behavior of the BRC hinge is assumed to be bilinear with linear kinematic hardening. Material of the bilinear hinge is represented as a series model of two component, as shown in Fig. 3.16: the first component is a linear elastic spring with Young modulus E , and the second component is a rigid-plastic device with yield strength f_y and kinematic hardening modulus H_k .



Fig. 3.16. A series model representing the bilinear behavior of the BRC hinge

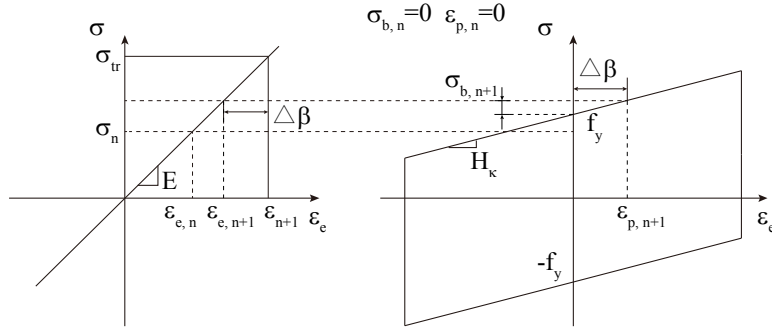


Fig. 3.17. An example of state determination by using the return mapping algorithm

The discrete form of the governing equations of the series model at time instant $t=t_{n+1}$ are expressed by Eqs. (3.64) - (3.68)

Additive strain decomposition:

$$\varepsilon_{n+1} = \varepsilon_{e,n+1} + \varepsilon_{p,n+1} \quad (3.64)$$

$\varepsilon_{e,n+1}$ — strain of the elastic spring

$\varepsilon_{p,n+1}$ — strain of the rigid-plastic device

ε_{n+1} — total strain of the series model

Stress-strain relation:

$$\sigma_{n+1} = E\varepsilon_{e,n+1} = E(\varepsilon_{n+1} - \varepsilon_{p,n+1}) \quad (3.65)$$

σ_{n+1} — stress of the series model

Yield condition:

$$f(\sigma_{n+1}) = |\sigma_{n+1} - \sigma_{b,n+1}| - f_y \leq 0 \quad (3.66)$$

$\sigma_{b,n}$ — back stress of the series model, $\sigma_{b,n+1} = H_\kappa \cdot \varepsilon_{p,n+1}$

Flow rule and kinematic hardening rule:

$$\varepsilon_{p,n+1} = \varepsilon_{p,n} + \Delta\beta \text{sign}(\sigma_{n+1} - \sigma_{b,n+1}) \quad (3.67)$$

$$\sigma_{p,n+1} = \sigma_{p,n} + H_\kappa \Delta\beta \text{sign}(\sigma_{n+1} - \sigma_{b,n+1}) \quad (3.68)$$

$\Delta\beta$ — plastic flow, $\Delta\beta \geq 0$

Consistency conditions:

$$\Delta\beta f(\sigma_{n+1}, \sigma_{b,n+1}) = 0 \quad (3.69)$$

The procedure of the return map algorithm is:

Step 1. For a given ε_{n+1} , determine the trial stress from Eq.(3.70). Increments of plastic strain and back stress are assumed as 0 preliminary.

$$\sigma_{tr,n+1} = E(\varepsilon_{n+1} - \varepsilon_{p,n}) \quad (3.70)$$

Step 2. Check the yield condition.

$$f(\sigma_{tr,n+1}) = |\sigma_{tr,n+1} - \sigma_{b,n}| - f_y \quad (3.71)$$

Step 3.

Case 1. $f(\sigma_{tr,n+1}) = 0$

In this case, the trial stress does not exceed the yield strength, i.e. the step is linear elastic, then there is neither plastic strain nor back stress increments, so that $\Delta\beta = 0$, $\varepsilon_{p,n+1} = \varepsilon_{p,n}$,

$\sigma_{b,n+1} = \sigma_{b,n}$. The corresponding tangent modulus is E.

Case 2. $f(\sigma_{tr,n+1}) > 0$

In this case, the step is involved with plastic flow, so the trial stress needs to be corrected. The plastic flow increment is determined from Eq (3.72)

$$\Delta\beta = \frac{|\sigma_{tr,n+1} - \sigma_{b,n}| - f_y}{E + H_\kappa} \quad (3.72)$$

The plastic strain increment is

$$\Delta\varepsilon_{p,n+1} = \Delta\beta \text{sign}(\sigma_{tr,n+1} - \sigma_{b,n}) \quad (3.73)$$

Update the plastic strain for the current step

$$\varepsilon_{p,n+1} = \varepsilon_{p,n} + \Delta\varepsilon_{p,n+1} \quad (3.74)$$

Correct the trial stress

$$\sigma_{n+1} = \sigma_{tr,n+1} - E\Delta\varepsilon_{p,n+1} \quad (3.75)$$

The corresponding tangent modulus is

$$E_h = \frac{1}{\frac{1}{E} + \frac{1}{H_\kappa}} = \frac{EH_\kappa}{E + H_\kappa} \quad (3.76)$$

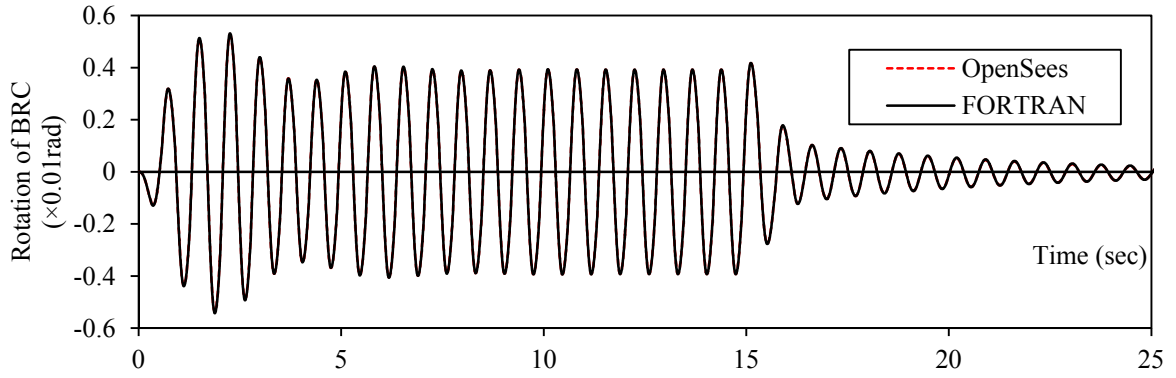
Finally, update the back stress for the $(n+1)$ -th time instant by Eq. (3.77)

$$\sigma_{b,n+1} = \sigma_{b,n} + H_\kappa \Delta \epsilon_{p,n+1} \quad (3.77)$$

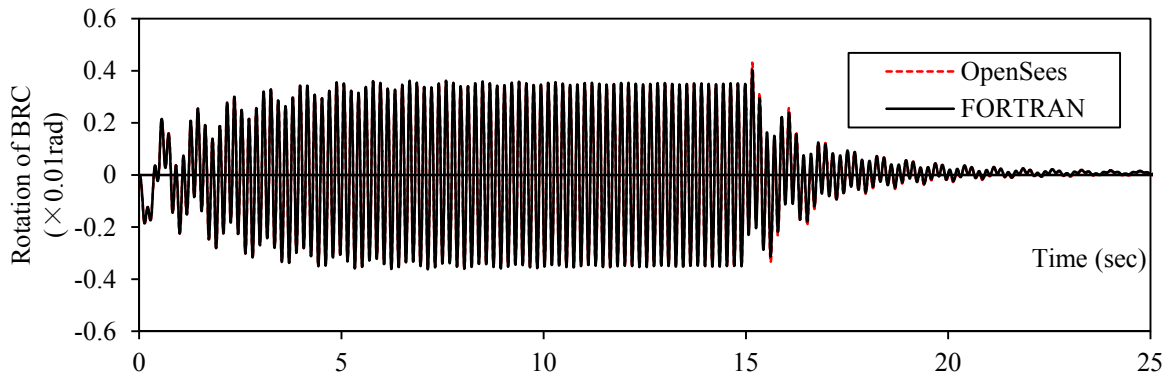
The back stress and the plastic strain need to be stored in memory at each time step. Fig. 3.17 shows an example of Case 2. The complete source code of the nonlinear analysis program is presented in the Appendix C.

3.4.3 Program verification

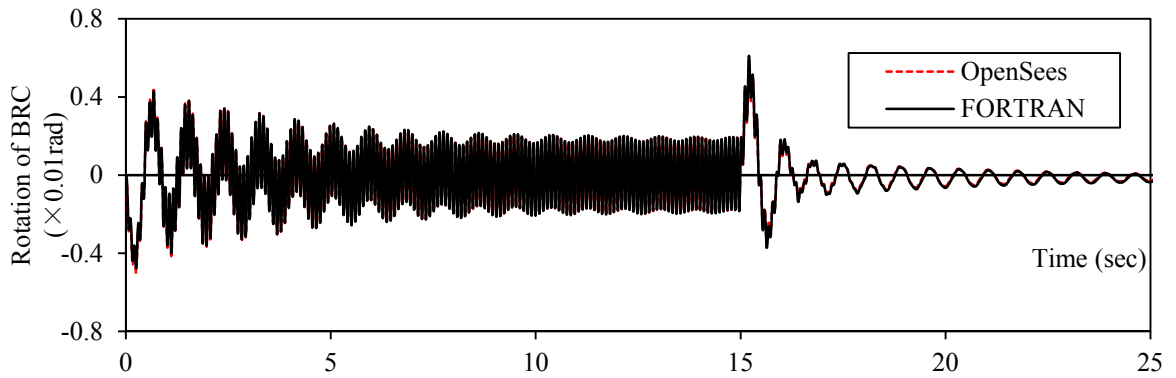
The nonlinear analysis program has been verified by running identical time-history analysis of identical 5-, 10-, and 20-story DMD models created by OpenSees.^[3.13] Input ground motions were sinusoidal excitations with frequencies equaling to the first, second, or third natural frequency of the target model. Ground motion duration was 15 seconds and analysis duration was 50 seconds, including 35 seconds free vibration. Analysis time interval dt was 0.01sec. Comparison of BRC hinge response of the DMD model analyzed by OpenSees and the self-constructed FORTRAN program is shown in Fig. 3.18. Their results almost exactly matched with each other in all cases.



(a) 5-story model, input ground motion accel= $150\sin(w_1t)$ (cm/s^2)



(b) 5-story model, input ground motion accel= $1000\sin(w_2t)$ (cm/s^2)



(c) 5-story model, input ground motion accel= $4000\sin(w_3t)$ (cm/s^2)

Fig. 3.18(a-c) Comparison of the time-history analysis results of the DMD model analyzed by OpenSees and the self-constructed FORTRAN program, 5-story model

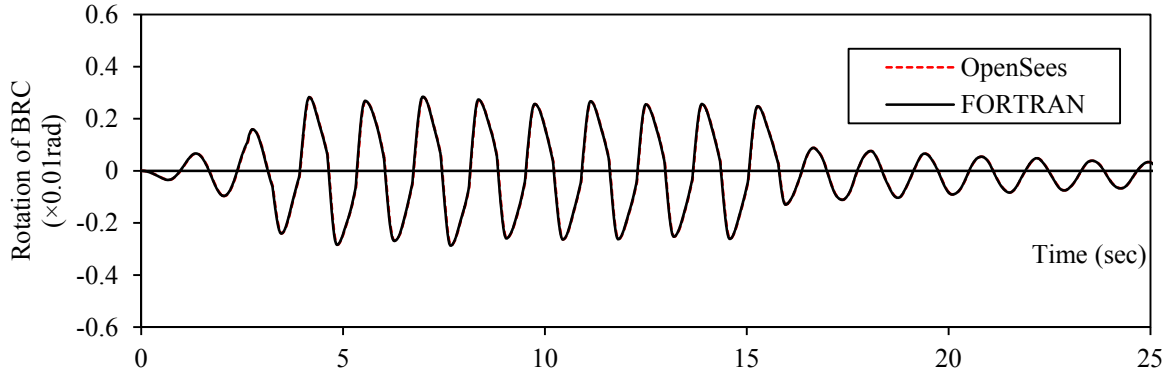
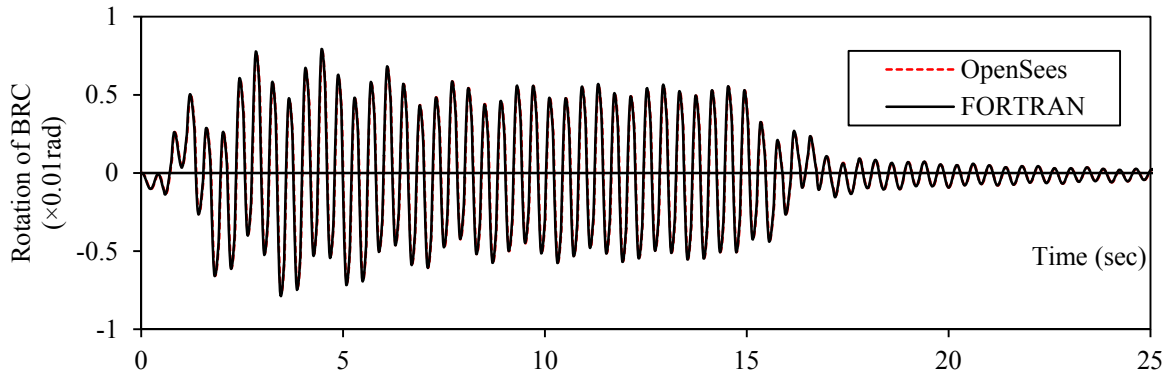
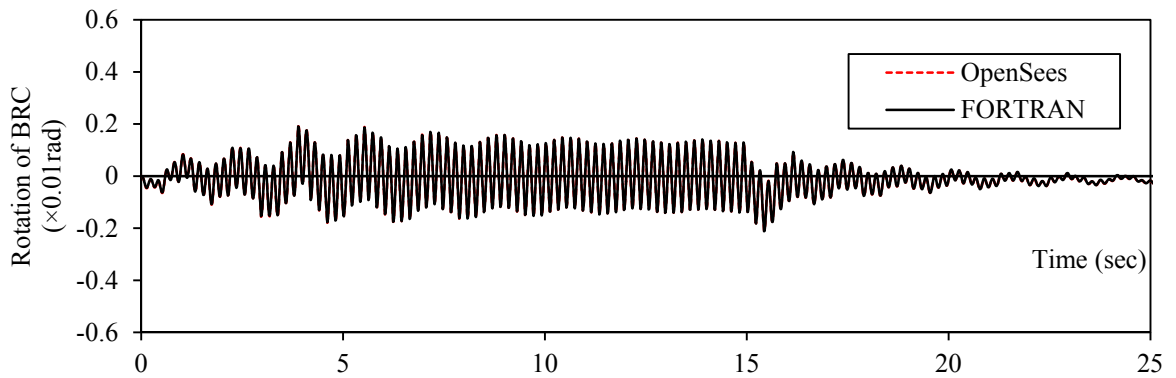
(d) 10-story model, input ground motion accel= $50\sin(w_1t)$ (cm/s^2)(e) 10-story model, input ground motion accel= $550\sin(w_2t)$ (cm/s^2)(f) 10-story model, input ground motion accel= $580\sin(w_3t)$ (cm/s^2)

Fig. 3.18(d-f) Comparison of the time-history analysis results of the DMD model analyzed by OpenSees and the self-constructed FORTRAN program, 10-story model

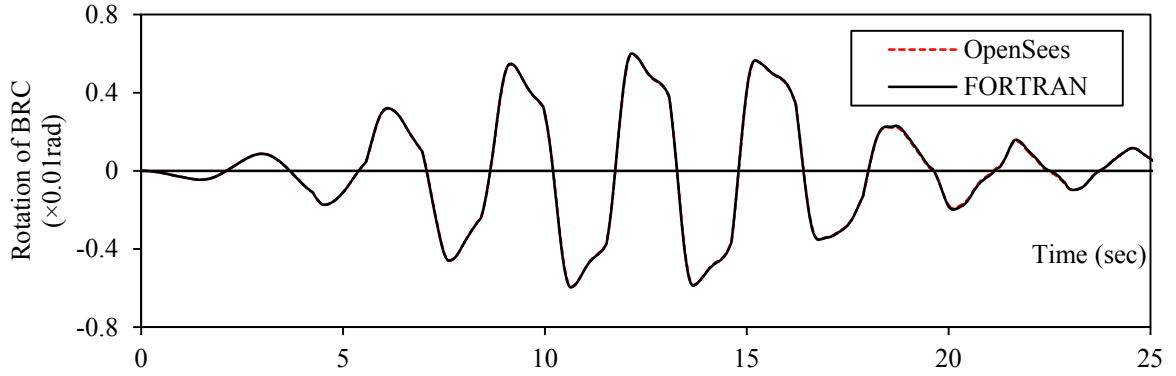
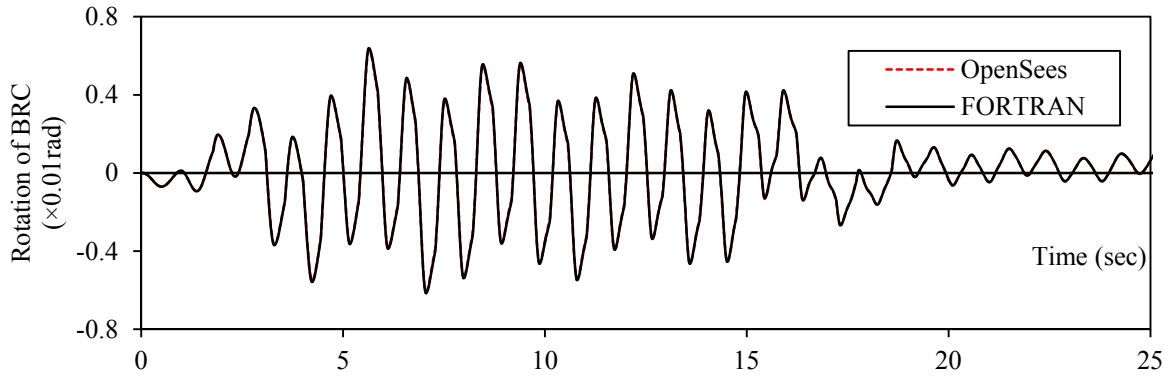
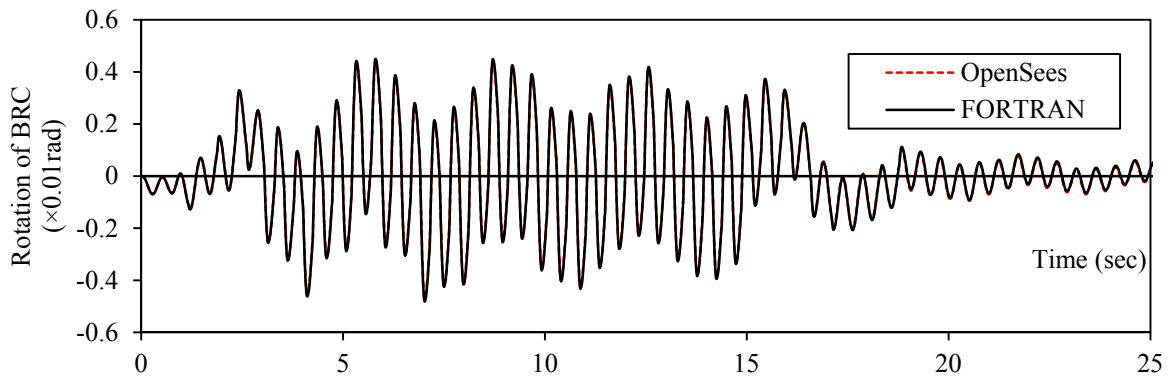
(g) 20-story model, input ground motion accel= $30\sin(w_1t)$ (cm/s²)(h) 20-story model, input ground motion accel= $150\sin(w_2t)$ (cm/s²)(i) 20-story model, input ground motion accel= $300\sin(w_3t)$ (cm/s²)

Fig. 3.18(g-i) Comparison of the time-history analysis results of the DMD model analyzed by OpenSees and the self-constructed FORTRAN program, 20-story model

3.5 Verification and limitation of DMD models

Eigenvalue analysis and time-history analysis was carried out to compare the DMD model with the MBM model of the three benchmark buildings. The input ground motions were BCJ-L2 and 4 observed waves (50s each): El Centro NS (1940), Hachinohe NS (1968), JMA Kobe NS (1995), and TAFT EW (1925). The response acceleration spectra of these recorded ground motions were scaled to follow the design spectra of level 2 earthquake.

Rayleigh damping was assigned for the DMD Model. Basic damping ratio is 0.02. To ensure a relatively identical damping ratio of each mode, factors α_0 and α_1 were calculated by assigning basic damping ratio to the first and third mode of the models.

The elastic natural periods of the first 3 modes of DMD and MBM models are listed in Table 3.9. Error of the first 3 modal periods of DMD models was less than 1%, 5%, and 10% in the 5-story, 10-story, and 20-story models, respectively. Fig. 3.19 compares the maximum seismic response of the DMD and MBM models with BCJ-L2 input. Similar results were obtained from the analysis using the other ground motions. The seismic response of the 5- and 10-story buildings analyzed by DMD models agreed well with the response obtained by MBM models. The obvious difference exhibited for the 20-story building was mainly due to the significant axial deformation of the columns in the moment frames.

Table 3.9 Difference of the first 3 modes periods between MBM and DMD models

Models	Mode	MBM	DMD	Difference
5-story	1	0.716	0.713	-0.4%
	2	0.180	0.180	0.3%
	3	0.096	0.096	-0.3%
10-story	1	1.359	1.379	1.4%
	2	0.387	0.402	4.1%
	3	0.196	0.204	4.1%
20-story	1	3.299	3.017	-8.6%
	2	0.927	0.929	0.2%
	3	0.461	0.481	4.5%

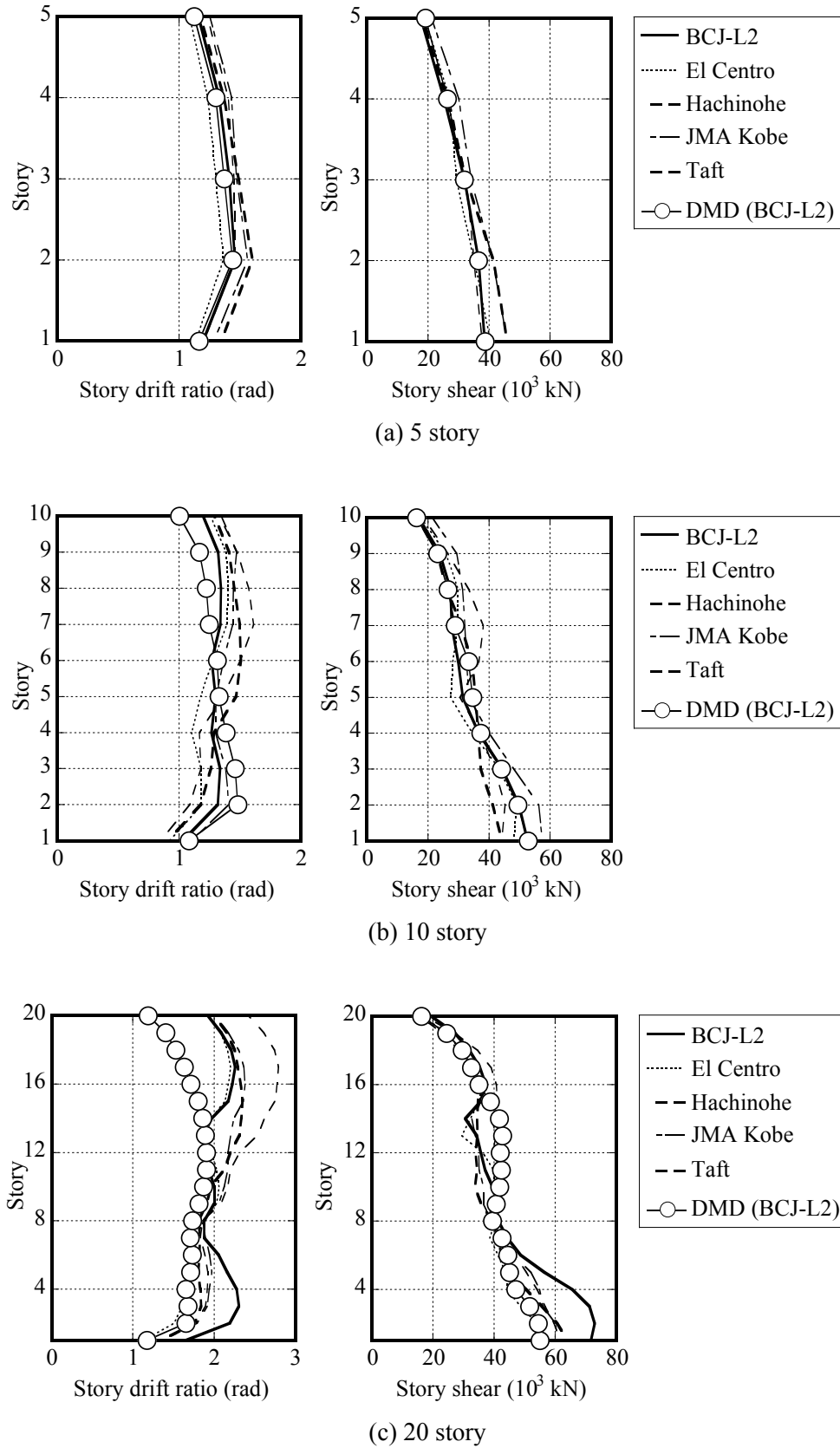


Fig. 3.19 Time-history analysis results of DMD models and MBM models

3.6 Conclusion

A simplified dual multi-degree-of-freedom (DMD) model along with a nonlinear dynamic analysis program is developed to further explore the dynamic characteristics of the proposed spine frame system. The DMD model is capable to represent nonlinear seismic behavior of the member-by-member structure, particularly in terms of the distribution and maximum amounts of floor deformation, story drift, story shear force and behavior of dampers. The dynamic analysis program is confirmed to be robust and possess high precision, high computational efficiency by comparing with OpenSees. This model is used in the extensive parametric study of low-rise buildings in chapter 4.

Reference

- [3.1] K. Ogawa, H. Kamura, K. Inoue: Modeling of moment resisting frame to fishbone-shaped frame for response analysis. *Journal of Structural and Construction Engineering (AIJ)*. No.521, p119–126, 1999. (in Japanese)
小川厚治、加村久哉、井上一郎：剛構造ラーメン骨組の魚骨組地震応答解析モデル，日本建築学会構造系論文集，No.521, p119-126, 1999.
- [3.2] M. Nakashima, K. Ogawa, K. Inoue: Generic frame model for simulation of earthquake responses of steel moment frames. *Earthquake Engineering and Structural Dynamics*. Vol.31(3), p671-692, 2002.
- [3.3] N. Luco, Y. Mori, Y. Funahashi, et al. Evaluation of predictors of non-linear seismic demands using ‘fishbone’ models of SMRF buildings. *Earthquake Engineering and Structural Dynamics*. Vol. 32(14), p2267-2288, 2003.
- [3.4] T. Matsumiya, M. Nakashima, K. Suita, et al. Accuracy of numerical analysis for prediction of inelastic cyclic behavior of full-scale steel moment frame. *Journal of Structural and Construction Engineering (AIJ)* No. 585 p215-221, 2004. (in Japanese)
松宮智央、中島正愛、吹田啓一郎等：実大鋼構造ラーメンの繰り返し載荷挙動に対して弾塑性数値解析がもつ予測精度，日本建築学会構造系論文集，No.585, p215-221, 2004.
- [3.5] G. D. Lignos, C. Putman, H. Krawinkler: Application of Simplified Analysis Procedures For Performance-Based Earthquake Evaluation of Steel Special Moment Frames. *Earthquake Spectra*, Vol. 31(4), p 1949-1968, 2015.
- [3.6] J. S. Kuang and K. Huang: Simplified multi-degree-of-freedom mode for estimation of seismic response of regular wall-frame structures. *The Structural Design of Tall and Special Buildings*. Vol.20, p418-432, 2011.
- [3.7] A. R. Khaloo, H. Khosravi: Modified fish-bone model: A simplified MDOF model for simulation of seismic responses of moment resisting frames. *Soil Dynamics and Earthquake Engineering*. Vol.55, p195-210, 2013.
- [3.8] T. Saka. Doctor Thesis. “Load bearing capability analysis of double-layer truss plates with

continuous shell analogy.” 1988. (in Japanese)

坂 寿二：二層立体トラス平板の耐力の連続体的解析に関する研究， 1988.

[3.9] 有限要素法ハンドブック I 基礎編 p212-213

[3.10] 大崎順彦：建築振動理論，彰国社， 1996.

[3.11] J.C. Simo, R.L. Taylor: A return mapping algorithm for plane stress elastoplasticity. *Numerical Methods in Engineering*. Vol. 22 (3), p649-670, 1986.

[3.12] J. Huang and D. V. Griffiths: Observations on return mapping algorithms for piecewise linear yield criteria. *International Journal of Geomechanics*. Vol.8(4), p253-265, 2008.

[3.13] Open system for earthquake engineering simulation (OpenSees) version 2.5.0. Sponsored by Pacific Earthquake Engineering Research Center (PEER), University of California, Berkeley. Available from: <http://opensees.berkeley.edu> (last accessed May 2017).

CHAPTER 4

Evaluation Method and Design Procedure of Controlled Spine Frames Applied in Low-rise Buildings

4.1 Introduction 4-1

4.2 Equivalent single-degree-of-freedom (SDOF) model

4.2.1 Simplification of main frame 4-1

4.2.2 Simplification of damper 4-3

4.2.3 Evaluation of equivalent damping ratio and natural period 4-4

4.2.4 Evaluation of peak deformation and force response 4-9

4.3 Simple design procedure utilizing SDOF model

4.3.1 Design procedure 4-13

4.3.2 Preliminary verification of design method 4-14

4.4 Parametric study of controlled spine frame structures

4.4.1 Control parameters 4-14

4.4.2 Effect of yielding drift of dampers 4-20

4.4.3 Effect of damper-to-moment frame stiffness ratio 4-23

4.4.4 Effect of spine-to-moment frame stiffness ratio 4-27

4.4.5 Optimal structural parameters and applicable scope of design procedure 4-31

4.5 Conclusion 4-33

Chapter 4 – Evaluation Method and Design Procedure for Controlled Spine Frames Applied in Low-rise Buildings

4.1 Introduction

Performance-based design framework and several practical design procedures have been proposed for the self-centering rocking frame systems.^[4.1-4.6] However, application of the rocking system is not popular yet. This study aims to develop a rather simple design procedure for the new controlled spine frame system, and establish clear recommendation on the applicable limit of the controlled spine frame system along with the design method, as well as recommendations on the optimal value of primary structural parameters. Design for post-tensioned structural elements and shear force transfer mechanism are not required herein. As a result it's highly possible to design the controlled spine frame structures by utilizing the existing design framework for regular moment-resisting frames^[4.7].

The DMD model proposed in chapter 3 has been confirmed to be able to produce a good estimate of deformation and force responses for the 5-story and 10-story structures. To develop a practical design method, the structure was further simplified into a single-degree-of-freedom (SDOF) model^[4.8-4.13]. This neglects higher mode effects, but enables the equivalent linearization technique to be applied, a direct and clear method to design the system stiffness ratios and damper yield point and achieve optimal response reduction.^[4.14-4.16] While the benchmark buildings introduced previously featured elastic moment frames, the method introduced in this section is generalized to permit inelastic moment frames.

Based on this model, the optimal design of the controlled spine frame structure was investigated, and a simple design procedure was proposed based on the SDOF model.

A parametric study was conducted to validate the proposed simplified procedure against the DMD model, examine the response trends and influence of the various control parameters, and finally to optimize the stiffness ratios.

4.2 Equivalent single-degree-of-freedom (SDOF) model

4.2.1 Simplification of main frame

The main frame excluding the BRCs was first simplified as a MDOF model, and then equivalent SDOF properties assembled, as illustrated by Fig. 4.1. The equivalent heights H_{eq} and weights M_{eq} of the SDOF model are obtained by Eqs. (4.1)–(4.3):

$$M_{eq} = \frac{(\sum_{i=1}^n m_i \cdot \delta_i)^2}{\sum_{i=1}^n m_i \cdot \delta_i^2} \quad (4.1)$$

$$\delta_{eq} = \frac{\sum_{i=1}^n m_i \cdot \delta_i^2}{\sum_{i=1}^n m_i \cdot \delta_i} \quad (4.2)$$

$$H_{eq} = \frac{\sum_{i=1}^N m_i \delta_i H_i}{\sum_{i=1}^N m_i \delta_i} \quad (4.3)$$

where m_i denotes the mass of the i -th floor, including the self-weight of the columns and walls in the half story above and below. δ_i denotes the lateral displacement of the i -th floor against lateral forces following the first mode response distribution (Ai distribution) of the Japanese building code. H_i denotes the height from the i -th floor to the ground.

An eigenvalue analysis was then conducted to obtain the elastic first mode period T_f and the equivalent elastic frame stiffness was obtained from Eq. (4.4):

$$K_f = M_{eq} \left(\frac{2\pi}{T_f} \right)^2 \quad (4.4)$$

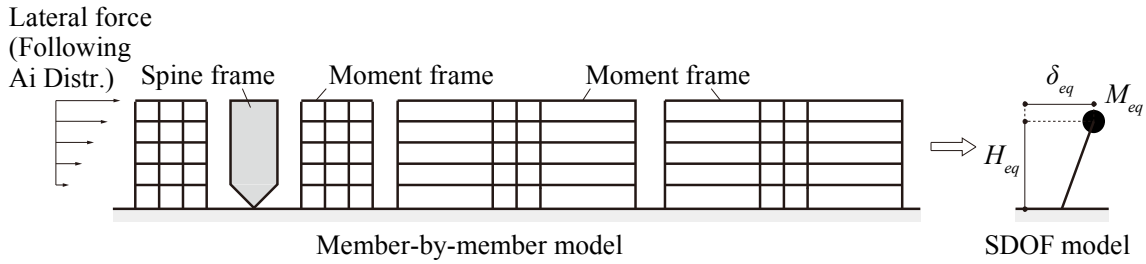


Fig. 4.1 Simplification of the main frame without BRCs

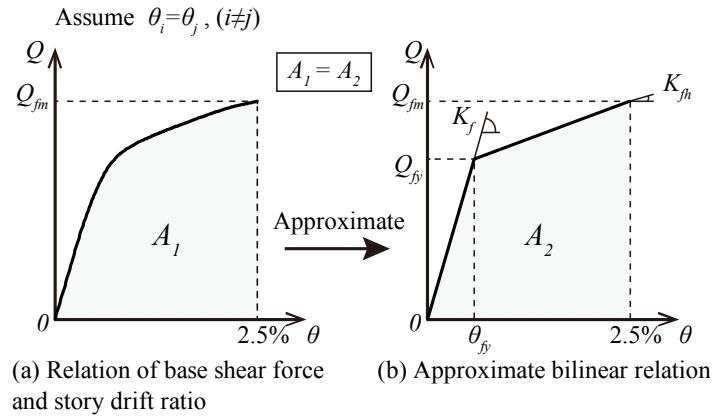


Fig. 4.2 Approximate backbone curve of the main frame

The nonlinear relation between base shear force and the story drift ratio was obtained from a pushover analysis, applying horizontal forces following the Ai distribution. The pushover curve for the main frame was idealized as bilinear, as in Fig 4.2. To ensure the same damping ratio and natural period with the original structure, the idealized bilinear curve was determined by matching both the shear force at 2.5% drift and area under the curve up to 2.5% drift in the original nonlinear pushover curve.

4.2.2 Simplification of damper

Generally, connection elements have a significant influence on the effectiveness of damping devices, reducing the imposed local deformations, and hence achieved damping, for a given level of drift. For controlled spine frame structures, the spine frame flexural stiffness reduces the effective damper stiffness and must be accounted for. To isolate the spine frame stiffness in the member-by-member model, pushover analysis was first conducted with the dampers substituted with rigid elements (Fig 4.3 (a)) and secondly with the dampers removed (Fig 4.3 (b)). Thus, the stiffness of the spine frame K_c could be isolated from the frame K_f by subtracting the results of the first pushover analysis ($K_c + K_f$) from the second (K_f).

Next, the local damper stiffness was calculated from Eq. (4.5) ~ (4.8). The first story yield drift ratio, θ_{dy} , neglecting the brace shear deformation, is given by:

$$\theta_{dy} = 2u_{dy} / b \quad (4.5)$$

The overturning moment at the bottom of the spine frame, denoted by M_{dy} , is as follows:

$$M_{dy} = F_{dy} \cdot b \quad (4.6)$$

The spine frame base shear, denoted by Q_{dy} , assumes that the first-mode response is dominant and is expressed as:

$$Q_{dy} = \frac{M_{dy}}{H_{eq}} \quad (4.7)$$

Finally, the horizontal stiffness of the BRCs, denoted by K_d , is calculated from Eq. (4.8):

$$K_d = \frac{Q_{dy}}{\theta_{dy} H_{eq}} \quad (4.8)$$

where, u_{dy} represents the yield deformation of each BRC, b represents the width of spine frame,

F_{dy} represents the yielding force of BRC, as shown in Fig. 4.4.

Fig. 4.3 (d) shows the full structural system, with the damper stiffness expressed by Eq. (4.9), including the flexural deformation of the spine frame:

$$K_a = \frac{1}{\frac{1}{K_d} + \frac{1}{K_R - K_f}} \quad (4.9)$$

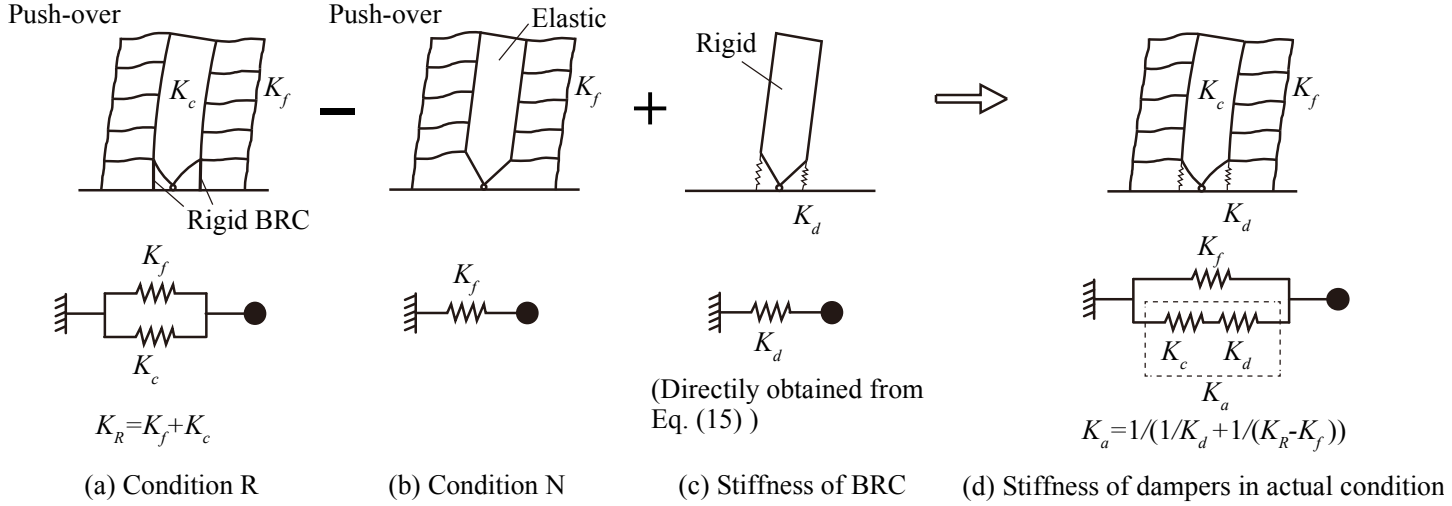


Fig. 4.3 Spring models for each condition
(moment frames are represented by two columns;
such representation is used in the following schemas of spine frame structures)

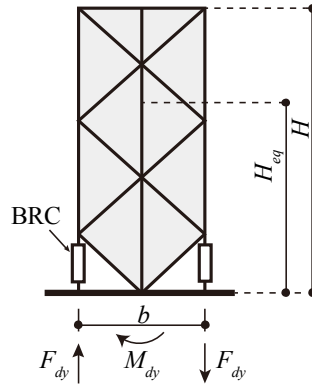


Fig. 4.4 An illustration of the BRCs in a spine frame

4.2.3 Evaluation of equivalent damping ratio and natural period

For a given target drift θ_t , the equivalent damping ratio h_{eq}' can be evaluated from the strain energy and dissipated energy of the main frame and dampers, expressed by Eq. (4.10) and Fig. 4.5.

$$h_{eq}' = h_0 + \frac{E_{pf} + E_{pa}}{4\pi(E_{ef} + E_{ea})}, \quad h_0 = 0.02 \quad (4.10)$$

where E_{pf} and E_{pa} represent the hysteretic energy of the main frame and BRCs, respectively, and E_{ef} and E_{ea} represent the equivalent elastic strain energy. The equivalent damping ratio h_{eq} of the system was calculated using Eq. (4.11), using an integration method originally proposed by

Newmark and Rosenblueth, and described by Kasai et al. ^[4.14]

$$h_{eq} = \frac{1}{\mu_t} \int_0^{\mu_t} h_{eq}'(\mu') d\mu' = h_0 + \frac{1}{\mu_t} \int_1^{\mu_t} \frac{E_{pf} + E_{pa}}{4\pi(E_{ef} + E_{ea})} d\mu' \quad (4.11)$$

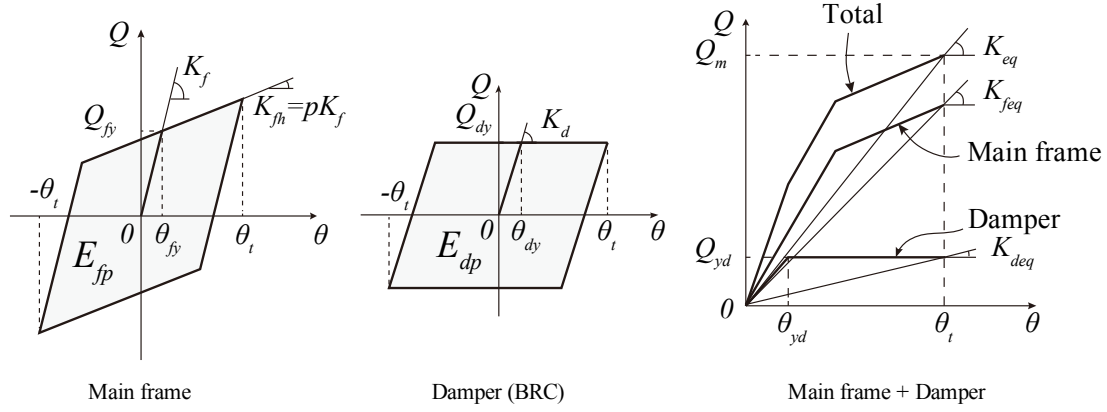


Fig. 4.5 Hysteretic features of main frame and damper

Ductility ratios of the damper μ_d and frame μ_f are expressed using a peak story drift θ_t , as Eqs. (4.12) and (4.13)

$$\mu_d = \frac{\theta_t}{\theta_{dy}}, \quad \mu_f = \frac{\theta_t}{\theta_{fy}} \quad (4.12), (4.13)$$

(A) In the case of $\mu_f < 1$, $\mu_d > 1$

When the story drift is θ , the area of the hysteresis loop is calculated as follows,

$$E_{pd} = 4K_d(\theta_{dy})(\theta - \theta_{dy}), \quad E_{pf} = 0 \quad (4.14)$$

The potential energy $(E_{ef} + E_{ed})$ is calculated as follows,

$$E_{ed} = \frac{1}{2} K_d \theta_{dy} \theta, \quad E_{ef} = \frac{1}{2} K_f \theta^2 \quad (4.15)$$

The equivalent damping ratio is represented as

$$\begin{aligned} h_{eq} &= h_0 + \frac{1}{\mu_d} \int_1^{\mu_d} \frac{E_{pd} + E_{pf}}{4\pi(E_{ed} + E_{ef})} d\mu'_d \\ &= h_0 + \frac{2}{\mu_d \pi} \int_1^{\mu_d} \frac{(1-r)(\mu'_d - 1)}{\mu'_d (1-r + r\mu'_d)} d\mu'_d \end{aligned} \quad (4.16)$$

Where the coefficient r represents:

$$r = \frac{K_f}{K_d + K_f} \quad (4.17)$$

Thus,

$$h_{eq} = h_0 + \frac{2}{\mu_d \pi r} \ln \frac{(1-r+r\mu_d)}{(\mu_d)^r} \quad (4.18)$$

Here from Eq (4.16)

$$\begin{aligned} h'_{eq}(\mu'_d) &= h_0 + \frac{E_{pd} + E_{pf}}{4\pi(E_{ed} + E_{ef})} \\ &= h_0 + \frac{2(1-r)(\mu'_d - 1)}{\pi \mu'_d (1-r+r\mu'_d)} \end{aligned} \quad (4.19)$$

(B) In the case of $\mu_f > 1$

When the story drift is θ , the area of the hysteresis loop of the damper is calculated by Eq. (4.20)

$$E_{pd} = 4K_d \theta_{dy} (\theta - \theta_{dy}) \quad (4.20)$$

Similarly, that of the frame is calculated by Eq. (4.21)

$$E_{pf} = 4K_f \theta_{fy} (\theta - \theta_{fy}) (1-p) \quad (4.21)$$

where, p is the hardening stiffness ratio of the main frame.

Also the potential energy is calculated by Eqs. (4.22) and (4.23)

$$E_{ed} = \frac{1}{2} K_d \theta_{dy} \theta \quad (4.22)$$

$$E_{ef} = \frac{1}{2} K_f \theta_{fy} \theta (1-p + p\mu_f) \quad (4.23)$$

Here, when the ductility ratio $\mu_f > 1$, a function $h'_{eq}(\mu'_f)$ is determined as Eq. (4.24) using Eqs. (4.20)-(4.23)

$$\begin{aligned} h'_{eq}(\mu'_f) &= \frac{E_{pd} + E_{pf}}{4\pi(E_{ed} + E_{ef})} \\ &= \frac{2(\mu'_f)^2 (\mu'_f - 1)(1-p) + q(\mu'_f \mu'_f - 1)}{\pi (\mu'_f)^2 (1-p + p\mu'_f) \mu'_f + q\mu'_f \mu'_f} \end{aligned} \quad (4.24)$$

When $\mu_f < 1$, $p = 0$

$$h_{eq}''(\mu_f') = \frac{2}{\pi} \frac{q(\mu_l \mu_f' - 1)}{(\mu_l \mu_f')^2 + q \mu_l \mu_f'} \quad (4.25)$$

where,

$$\mu_l = \frac{\mu_d}{\mu_f} = \frac{\theta_{fy}}{\theta_{dy}} \quad (4.26)$$

$$q = \frac{K_d}{K_f} \quad (4.27)$$

The equivalent damping ratio h_{eq} is determined using Eqs. (4.19) and (4.24)

$$h_{eq}'(\mu_f') = h_0 + \frac{1}{\mu_f} \int_{\mu_l}^1 h_{eq}''(\mu_f') d\mu_f' + \frac{1}{\mu_f} \int_1^{\mu_f} h_{eq}'(\mu_f') d\mu_f' \quad (4.28)$$

Set $\mu_f' = \frac{\mu_d'}{\mu_l}$, so $d\mu_f' = \frac{1}{\mu_l} d\mu_d'$, $\mu_l \mu_f' = \mu_d'$

$$\begin{aligned} & \frac{1}{\mu_f} \int_{\mu_l}^1 h_{eq}''(\mu_f') d\mu_f' \\ &= \frac{1}{\mu_f} \frac{1}{\mu_l} \int_1^{\mu_l} \frac{2}{\pi} \frac{q(\mu_d' - 1)}{(\mu_d')^2 + q \mu_d'} d\mu_d' \\ &= \frac{1}{\mu_d} \int_1^{\mu_l} \frac{2}{\pi} \frac{q(\mu_d' - 1)}{(\mu_d')^2 + q \mu_d'} d\mu_d' \\ &= \frac{2}{\mu_d \pi r} \ln \frac{(1-r+r\mu_l)}{(\mu_l)^r} \end{aligned} \quad (4.29)$$

The integration of $\int_1^{\mu_f} h_{eq}'(\mu_f') d\mu_f'$ can be calculated as follows.

$$\begin{aligned} & \frac{2}{\pi} \int_1^{\mu_f} \frac{(\mu_l)^2 (\mu_f' - 1)(1-p) + q(\mu_l \mu_f' - 1)}{(\mu_l)^2 (1-p + p\mu_f') \mu_f' + q \mu_l \mu_f'} d\mu_f' \\ &= \frac{2}{\pi} \int_1^{\mu_f} \frac{[\mu_l(1-p) + q] \mu_l \mu_f' - (\mu_l)^2 (1-p) - q}{[p\mu_l \mu_f' + \mu_l(1-p) + q] \mu_l \mu_f'} d\mu_f' \end{aligned} \quad (4.30)$$

$$\begin{aligned} &= \frac{2}{\pi} \int_1^{\mu_f} \left\{ \frac{\mu_l(1-p) + q}{p\mu_l \mu_f' + \mu_l(1-p) + q} - \frac{(\mu_l)^2 (1-p) + q}{[p\mu_l \mu_f' + \mu_l(1-p) + q] \mu_l \mu_f'} \right\} d\mu_f' \\ &= \frac{A}{\mu_f'} + \frac{B}{\mu_l [p\mu_l \mu_f' + \mu_l(1-p) + q]} \end{aligned} \quad (4.31)$$

$$A = \frac{(\mu_l)^2(1-p) + q}{\mu_l[\mu_l(1-p) + q]} \quad (4.32)$$

$$B = -p(\mu_l)^2 A \quad (4.33)$$

Here, constant values P, J and S are determined as follows,

$$P = \mu_l(1-p) + q \quad (4.34)$$

$$S = (\mu_l)^2(1-p) + q \quad (4.35)$$

$$J = \mu_l p \quad (4.36)$$

A and B are summarized as follows

$$A = \frac{S}{\mu_l P} \quad (4.37)$$

$$B = -\mu_l S \frac{J}{\mu_l P} = -\frac{J \cdot S}{P} \quad (4.38)$$

Eq. (4.31) is obtained as Eq. (4.39)

$$\frac{S}{\mu_l P \mu_f'} - \frac{J \cdot S}{\mu_l P (J \mu_f' + P)} \quad (4.39)$$

Thus, Eq. (4.30) is calculated as follows

$$\begin{aligned} & \frac{2}{\pi} \int_1^{\mu_f} \left(\frac{P}{J \mu_f' + P} - \frac{S}{\mu_l P \mu_f'} + \frac{J \cdot S}{\mu_l P (J \mu_f' + P)} \right) d\mu_f' \\ &= \frac{2}{\pi} \int_1^{\mu_f} \left[\left(P + \frac{J \cdot S}{\mu_l P} \right) \frac{1}{J \mu_f' + P} - \frac{S}{\mu_l P} \frac{1}{\mu_f'} \right] d\mu_f' \\ &= \frac{2}{\pi} \left[\left(\frac{P}{J} + \frac{S}{\mu_l P} \right) \ln(J \mu_f' + P) - \frac{S}{\mu_l P} \ln \mu_f' \right] \Big|_1^{\mu_f} \\ &= \frac{2}{\pi} \left[\left(\frac{P}{J} + \frac{S}{\mu_l P} \right) \ln(J \mu_f + P) - \frac{S}{\mu_l P} \ln \mu_f - \left(\frac{P}{J} + \frac{S}{\mu_l P} \right) \ln(J + P) \right] \\ &= \frac{2}{\pi} \ln \frac{\left(\frac{J \mu_f + P}{J + P} \right)^{\left(\frac{P}{J} + \frac{S}{\mu_l P} \right)}}{\mu_f^{\frac{S}{\mu_l P}}} \end{aligned} \quad (4.40)$$

Using Eqs. (4.29) and (4.40), the equivalent damping ratio is calculated by Eq. (4.41)

$$\begin{aligned} h_{eq} &= h_0 + \frac{2}{\pi \mu_d r} \ln \frac{(1-r+r\mu_l)}{(\mu_l)^r} \\ &\quad + \frac{1}{\mu_f} \frac{2}{\pi} \ln \frac{\left(\frac{J \mu_f + P}{J + P} \right)^{\left(\frac{P}{J} + \frac{S}{\mu_l P} \right)}}{\mu_f^{\frac{S}{\mu_l P}}} \end{aligned} \quad (4.41)$$

Formula for computing the equivalent damping ratio has been derived from Eqs. (4.11)-(4.41).

Eq (4.42) summarizes the final form of the equivalent damping ratio equations:

If $\mu_f \leq 1$ and $\mu_d > 1$,

$$h_{eq} = h_0 + \frac{2}{\pi \mu_d r} \ln \frac{(1-r+r\mu_d)}{(\mu_d)^r} \quad (4.42-1)$$

If $\mu_f > 1$, and $\mu_d > 1$,

$$h_{eq} = h_0 + \frac{2}{\pi \mu_d r} \ln \frac{(1-r+r\mu_l)}{(\mu_l)^r} + \frac{1}{\mu_f} \frac{2}{\pi} \ln \frac{\left(\frac{J\mu_f + P}{J+P}\right)^{\left(\frac{P}{J} + \frac{S}{\mu_l P}\right)}}{(\mu_f)^{\frac{S}{\mu_l P}}} \quad (4.42-2)$$

where,

$$p = \frac{K_{fh}}{K_f}, \quad q = \frac{K_d}{K_f}, \quad r = \frac{K_f}{K_f + K_d}$$

$$\mu_f = \frac{\theta_t}{\theta_{fy}}, \quad \mu_d = \frac{\theta_t}{\theta_{dy}}, \quad \mu_l = \frac{\mu_d}{\mu_f}$$

$$P = \mu_l(1-p) + q, \quad S = (\mu_l)^2(1-p) + q, \quad J = \mu_l p$$

The equivalent period T_{eq} can be evaluated by the secant stiffness corresponding to the maximum drift ratio, as expressed from Eq. (4.43) to (4.46).

If $\mu_f \leq 1$ and $\mu_d > 1$,

$$T_{eq} = T_f \sqrt{\frac{1}{1+q/\mu_d}} \quad (4.43)$$

If $\mu_f > 1$,

$$K_{feq} = \frac{1-p+p\mu_f}{\mu_f} K_f, \quad K_{deq} = \frac{1}{\mu_d} K_d \quad (4.44)$$

$$K_{eq} = K_{feq} + K_{deq} \quad (4.45)$$

$$T_{eq} = T_f \sqrt{\frac{K_f}{K_{eq}}} = T_f \sqrt{\frac{\mu_f \mu_l}{q + (1-p+p\mu_f)\mu_l}} \quad (4.46)$$

4.2.4 Evaluation of peak deformation and force response

For the equivalent linearized system corresponding to the maximum deformation, relation between its displacement response spectrum and pseud velocity response spectrum is:

$$S_d(T_{eq}, h_{eq}) = \frac{T_{eq}}{2\pi} S_{pv}(T_{eq}, h_{eq}) \quad (4.47)$$

For the initially elastic main frame excluding dampers, relation between its displacement response spectrum and pseud velocity response spectrum is:

$$S_d(T_f, h_0) = \frac{T_f}{2\pi} S_{pv}(T_f, h_0) \quad (4.48)$$

The response reduction effect due to damping is

$$S_{pv}(T_{eq}, h_{eq}) = D_h \overline{S_{pv}}(T_{eq}, h_0) \quad (4.49)$$

$$D_h = \sqrt{\frac{1 + \alpha h_0}{1 + \alpha h_{eq}}} \quad (4.50)$$

where α is an empirical value, set as $\alpha = 25$.

Therefore, the displacement response reduction factor is expressed by Eq. (4.51)

$$R_d = \frac{T_{eq}}{T_f} D_h \frac{\overline{S_{pv}}(T_{eq}, h_0)}{S_{pv}(T_f, h_0)} \quad (4.51)$$

The period shift effect on velocity response was considered by utilizing the approach proposed by Kasai et al. ^[*] and is given by Eq. (4.52). Notice that the shifting range of the period is from the initial elastic period to the equivalent period of the system, i.e. from T_{f+a} to T_{eq}

$$\overline{S_{pv}}(T_{eq}, h_0) = \frac{1}{T_{eq} - T_{f+a}} \int_{T_{f+a}}^{T_{eq}} S_{pv}(T, h_0) dT \quad (4.52)$$

$$\text{where, } T_{f+a} = T_f \sqrt{\frac{K_f}{K_f + K_a}}$$

Relation between pseud velocity response spectrum and pseud acceleration response spectrum is

$$S_{pv}(T, h_0) = \begin{cases} \frac{S_{a,\max}}{2\pi} T & (T \leq T_l) \\ \frac{S_{a,\max}}{2\pi} T_l & (T > T_l) \end{cases} \quad (4.53)$$

where, $T_l = 0.864 \text{ sec}$

Therefore, Eq. (4.52) needs to be solved according to three different conditions.

$$(A) \quad T_{eq} \geq T_{f+a} \geq T_l$$

$$\begin{aligned}
 \overline{S_{pv}}(T_{eq}, h_0) &= \frac{1}{T_{eq} - T_{f+a}} \int_{T_{f+a}}^{T_{eq}} S_{pv}(T, h_0) dT \\
 &= \frac{1}{T_{eq} - T_{f+a}} \left(\int_{T_{f+a}}^{T_{eq}} \frac{S_{a, \max}}{2\pi} T_l dT \right) \\
 &= \frac{S_{a, \max} T_l}{2\pi}
 \end{aligned} \tag{4.54}$$

(B) $T_{eq} \geq T_l \geq T_{f+a}$

$$\begin{aligned}
 \overline{S_{pv}}(T_{eq}, h_0) &= \frac{1}{T_{eq} - T_{f+a}} \int_{T_{f+a}}^{T_{eq}} S_{pv}(T, h_0) dT \\
 &= \frac{1}{T_{eq} - T_{f+a}} \left(\int_{T_{f+a}}^{T_l} S_{pv}(T, h_0) dT + \int_{T_l}^{T_{eq}} S_{pv}(T, h_0) dT \right) \\
 &= \frac{1}{T_{eq} - T_{f+a}} \left(\int_{T_{f+a}}^{T_l} \frac{S_{a, \max}}{2\pi} T dT + \int_{T_l}^{T_{eq}} \frac{S_{a, \max}}{2\pi} T_l dT \right) \\
 &= \frac{S_{a, \max}}{4\pi(T_{eq} - T_{f+a})} \left[T_l(2T_{eq} - T_l) - T_{f+a}^2 \right]
 \end{aligned} \tag{4.55}$$

(C) $T_l \geq T_{eq} \geq T_{f+a}$

$$\begin{aligned}
 \overline{S_{pv}}(T_{eq}, h_0) &= \frac{1}{T_{eq} - T_{f+a}} \int_{T_{f+a}}^{T_{eq}} S_{pv}(T, h_0) dT \\
 &= \frac{1}{T_{eq} - T_{f+a}} \left(\int_{T_{f+a}}^{T_{eq}} \frac{S_{a, \max}}{2\pi} T dT \right) \\
 &= \frac{S_{a, \max}}{4\pi} (T_{eq} + T_{f+a})
 \end{aligned} \tag{4.56}$$

Pseud velocity response spectrum of the main frame excluding dampers consists of two segments as well:

$$S_{pv}(T_f, h_0) = \begin{cases} \frac{S_{a, \max}}{2\pi} T_f & (T_f \leq T_l) \\ \frac{S_{a, \max}}{2\pi} T_l & (T_f > T_l) \end{cases} \tag{4.57}$$

Substitute Eqs. (4.54) – (4.57) into Eq. (4.51), displacement reduction factor could be computed by

$$R_d = \begin{cases} \frac{T_{eq}}{T_f} D_h & T_{eq} \geq T_{f+d} \geq T_l \\ \frac{T_{eq}}{T_f} D_h \frac{T_l(2T_{eq} - T_l) - (T_{f+d})^2}{2(T_{eq} - T_{f+d}) \min(T_l, T_f)} & T_{eq} \geq T_l \geq T_{f+d} \\ \frac{T_{eq}}{T_f} D_h \frac{T_{eq} + T_{f+d}}{2 \min(T_l, T_f)} & T_l \geq T_{eq} \geq T_{f+d} \end{cases} \quad (4.58)$$

Drift is then obtained from Eq. (4.59), with the updated ductility ratio used to recalculate h_{eq} using Eq. (4.42), iterating until convergence is achieved.

$$\theta = R_d \theta_t^{(0)} \quad (4.59)$$

The resultant force is given by Eqs. (4.60) ~ (4.61), evaluated by equating the displacement and acceleration reduction response factors:

$$R_a = R_d \left(\frac{T_f}{T_{eq}} \right)^2 \quad (4.60)$$

$$Q = R_a Q^{(0)} \quad (4.61)$$

From section 4.2.3 ~ 4.2.4, the displacement reduction factor, denoted by R_d , was determined from the target story drift ratio, denoted by θ_t , the stiffness ratio of dampers and main frame, denoted by q , and the ductility factor of the dampers, denoted by μ_a . Fig 4.6 shows the relation between R_a and R_d for the five-story benchmark building. These curves are referred to as performance curves and as they are normalized, can be prepared as a generic design aid.

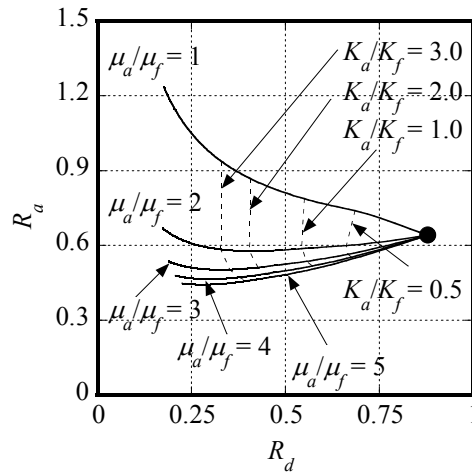


Fig. 4.6 Performance curve of the five-story building (target drift=1.26%)

4.3 Simple design procedure utilizing SDOF model

4.3.1 Design procedure

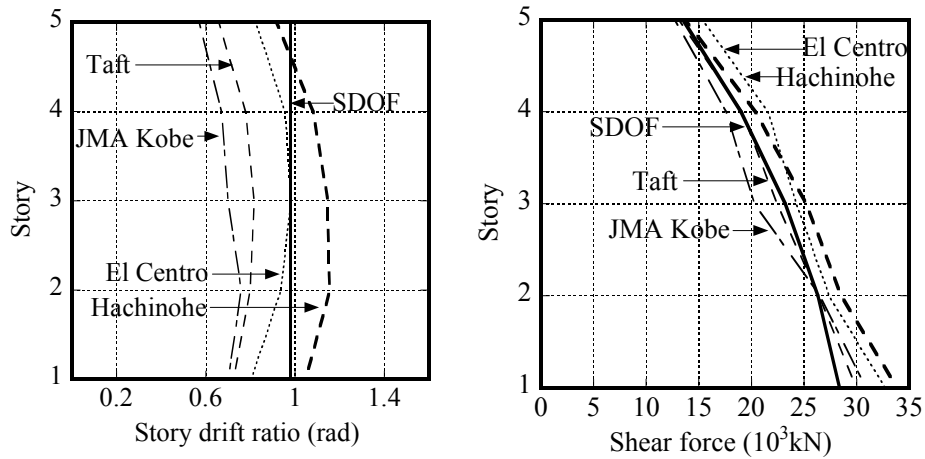
Following from the response reduction equations detailed above, a simple design procedure for the controlled spine frame using the SDOF model is proposed:

Step 1. Design the main frame for the target drift level without dampers

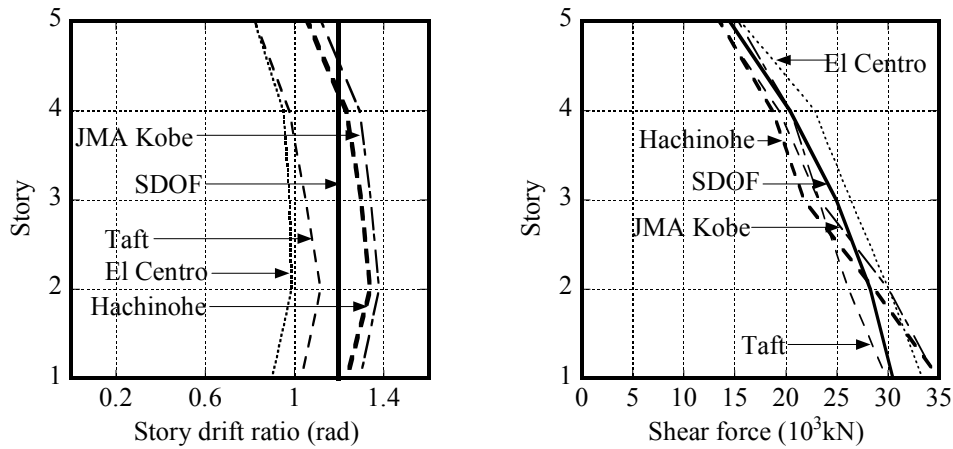
Step 2. Evaluate the elastic displacement and force response of the main frame, and hence the required displacement and force reduction factors required to achieve the performance targets.

Step 3. Select the ductility μ_d/μ_f and stiffness ratio K_d/K_f from the performance curve that satisfy the target drift ratio and acceleration response.

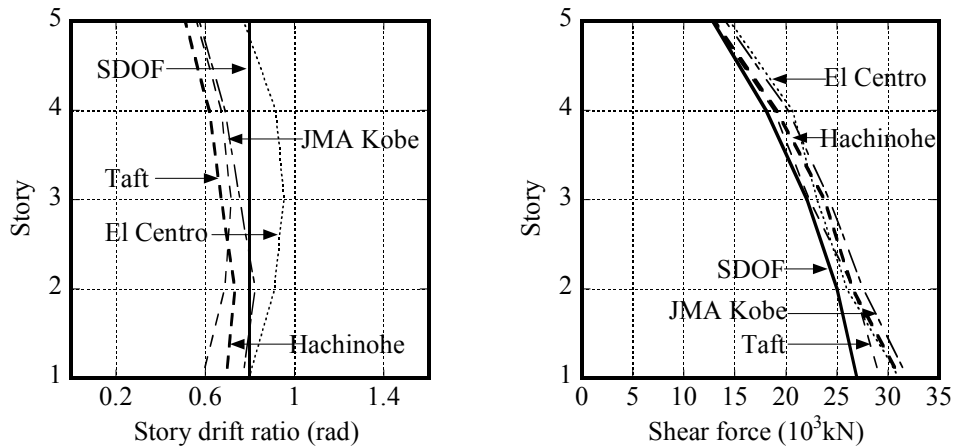
Step 4. Design the dampers for the selected ductility and stiffness, and confirm the final overall response using the equivalent linearization technique. Validate results with time-history analysis as required.



(a). Target story drift ratio = 1.0%



(b). Target story drift ratio = 1.2%



(c). Target story drift ratio = 0.8%

Fig. 4.7 Comparison of time-history analysis results of the 5-story model with its design targets.

4.3.2 Preliminary verification of design method

The 5-story benchmark model is used for preliminary verification of the design method. Fig. 4.7 provides the peak story drift ratio and shear force results from time-history analysis of the building designed with target drift ratio as 1%, 1.2%, and 0.8%. All of them are in good agreement with the design targets.

4.4 Parametric study of controlled spine frame structures

The 5-, 10- and 20-story benchmark models from chapter 3 were evaluated using the simplified design procedure based on the SDOF model, with a comparison to the DMD model introduced in chapter 3. Good agreement was achieved for the shorter structures, but the error became notable for the taller 20 story model. This was mainly due to the effect of higher-modes force responses and the overall flexural deformation. The following section discusses the optimal design parameters of the controlled spine frame structures and the applicable range of the simplified design procedure.

4.4.1 Control parameters

A parametric study was conducted to investigate the structural characteristics of the controlled spine frame, varying the stiffness of the spine frame, moment frame, and BRCs, as well as the BRC yielding drift.

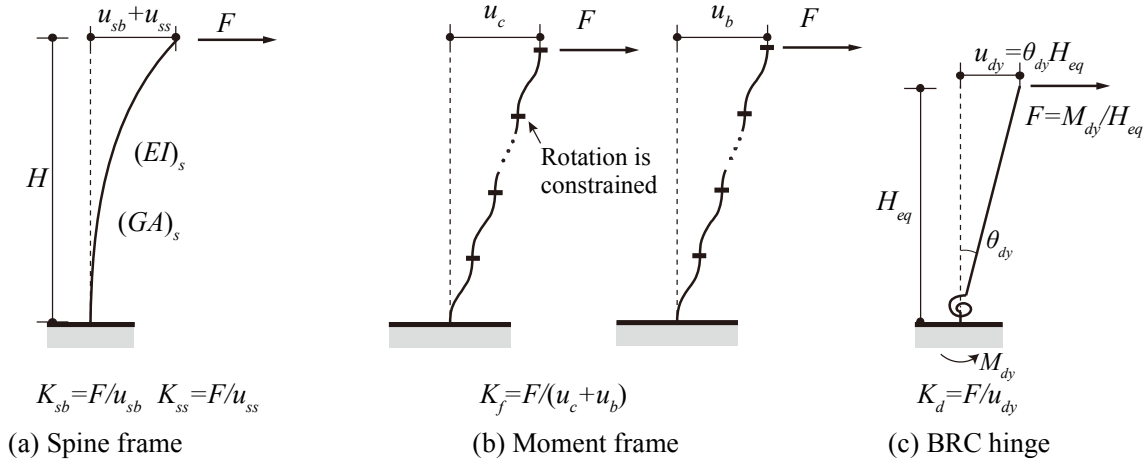


Fig. 4.8. Definition of representative stiffness for each component

In order to simplify the parametric study, the equivalent stiffness parameters for spine frames and moment frames are given by Eqs. (4.62) – (4.63), rather than the accurate stiffness developed for the DMD model or the stiffness for the SDOF model computed from a suit of eigenvalue analysis. The lateral stiffness of the spine frame is defined in Eq. (4.63) as a function of the bending and shear stiffness:

$$K_{sb} = \frac{3(EI)_s}{H^3}, \quad K_{ss} = \frac{(GA)_s}{H}, \quad K_s = \frac{1}{\frac{1}{K_{ss}} + \frac{1}{K_{sb}}} \quad (4.62)$$

where, $(EI)_s$ is the equivalent sectional bending stiffness of the spine frame. $(GA)_s$ is the equivalent sectional shear stiffness of the spine frame. H is the total height of the structure, which is identical to the height of the spine frame. K_{sb} , K_{ss} are the equivalent bending stiffness and shear stiffness of the spine frame, respectively.

Note that K_s is different from K_c in Fig. 4.3 due to different constraint conditions. As shown in Fig 4.8(a), here the spine frame was simply assumed as a cantilever beam. It is suggested to use K_s in the primary design and K_c in the final detailed design for the spine frame.

The lateral stiffness of the moment frame is given by:

$$K_f = \frac{12}{h^2 \sum_{n=1}^N \left(\frac{1}{(EI/h)_{cn}} + \frac{1}{(EI/l)_{bn}} \right)} \quad (4.63)$$

where, h represents the story height, $(EI/h)_{cn}$ and $(EI/l)_{bn}$ are the sums of line stiffness of all the columns and beams at the n -th story. N is the total number of the stories.

Also note that K_f slightly differs from K_f in Fig. 4.3 because the simplified constraint conditions. As shown in Fig 4.8(b), lateral stiffness of columns and beams in the original

structure were presented by two representative columns by assuming the rotation angles of all the beam-column connections at one story were identical. Additionally, the degree of freedom of rotation was constrained at both ends of those representative columns, which was similar with the procedure of constructing stiffness matrix for the moment frames in the DMD model. Lateral deformation obtained only from the representative column for the columns in the original structure was obviously smaller than the actual deformation, because beams were not rigid in the original structure. The additional lateral deformation caused by beams could be considered by the representative column for the beams. Moreover, lateral deformation of all the stories was assumed to be identical as well. The last assumption could be close to the actual condition when the spine frame was stiff enough.

The lateral stiffness of BRC hinge is K_d calculated from Eq. (4.8) with H_{eq}/H as 0.73, utilizing the same simplification concept as used for the SDOF model.

The stiffness of each component of the three benchmark structures is listed in Table 4.1, referring to Fig. 4.8. Table 4.1 (a) lists the intermediate stiffnesses for calculating the representative stiffness of each component in Table 4.1 (b) by Eqs. (4.62-63). Stiffnesses in Table 4.1 (c) were calculated by pushover or eigenvalue analysis along with Eqs (4.5-9).

The stiffness of spine frames K_s in Table b was much smaller than the K_c in Table a, because the cantilever assumption was out of reality when the spine frames deformed consistently with the moment frames. Ratios between the two spine frames stiffness was around 3.0 for all the three models, so it was still suitable to utilizing K_s as an index of spine frames stiffness in the parametric study.

The stiffness of moment frames K_f in Table b was approximately 20% smaller than the K_f in Table c in the 5- and 10-story models, and 40% smaller in the 20-story models. It was mainly because the K_f in Table b is pure lateral stiffness contributed by the beams and columns in the moment frames, while the K_f in Table c included additional stiffness generated by the spine frame. Difference between the two moment frames stiffness was related with the stiffness ratio between spine frames and moment frames, as well as the structure height. The spine-to-moment frame stiffness ratio computed from Table b was approximately 50% of the results computed from Table c.

The stiffness of dampers in Table b and c were calculated by the same method and only the equivalent height was slightly different. So the two dampers stiffnesses were essentially identical. The damper-to-moment frame stiffness ratio computed from Table b was approximately 1.4 times of the results obtained from Table c.

The response of a controlled spine frame was characterized by the yield rotation of the BRC hinge, denoted by θ_y , the normalized damper-to-moment frame stiffness ratio, denoted by K_d / K_f , and spine-to-moment frame stiffness ratio, denoted by K_s / K_f . These are summarized in Table

4.1 (d).

The range investigated in this study was selected to represent realistic code-compliant and buildable structures. Namely, θ_y varied between 0.05%, 0.1% and 0.2%, K_d / K_f ranged from 0.5 to 4.0, and K_s / K_f ranged from 0.05 to 2.0. The specific values selected for the three structures are listed in Table 4.2 – 4.4.

Table 4.1. Various stiffnesses of the controlled spine frame structure

(a) Original stiffness of each component calculated from member sectional size

Story	H (mm)	$(EI)_s$ (kNmm ²)	$(GA)_s$ (kN)	$(EI/h)_{cl}$ (kNmm)	$(EI/l)_{bl}$ (kNmm)
5	2×10^4	4.09×10^{14}	5.55×10^6	2.36×10^{10}	1.59×10^{10}
10	4×10^4	4.09×10^{14}	5.55×10^6	3.50×10^{10}	1.51×10^{10}
20	8×10^4	4.09×10^{14}	5.55×10^6	2.03×10^{11}	1.62×10^{10}

(b). Representative stiffness of each component for the DMD model obtained from calculations for each story level ($H_{eq} / H = 0.73$)

Story	K_{sb} (kN/mm)	K_{ss} (kN/mm)	K_s (kN/mm)	K_f (kN/mm)	K_d (kN/mm)
5	153.4	277.5	98.8	140.7	174.0
10	19.2	138.7	16.8	75.1	170.3
20	2.4	69.4	2.3	39.0	42.6

(c) Stiffness of each component obtained from a pushover analysis with lateral forces following the first-mode distribution

Story	K_f (kN/mm)	H_{eq} / H (mm)	K_d (kN/mm)	K_a (kN/mm)	K_c (kN/mm)
5	181.6	0.76	160.5	94.8	261.6
10	95.5	0.72	175.1	39.2	52.9
20	61.2	0.70	46.3	4.7	6.5

(d). Normalized stiffness obtained from the representative stiffness

Story	K_d / K_f	K_s / K_f	θ_y
5	1.24	0.702	0.11%
10	2.27	0.224	0.11%
20	1.09	0.059	0.11%

Table 4.2 Value of each parameter for various cases of the 5-story structure

Case	K_f (kN/mm)	K_d (kN/mm)	K_d/K_f	A_c (mm ²)	L_p (mm)
S5Kdf0.50y05		70.4	0.5	2565	
S5Kdf10y05	140.7	140.7	1	5129	1825
S5Kdf20y05		281.4	2	10258	
S5Kdf40y05		562.8	4	20518	

Case	K_s (kN/mm)	K_s/K_f
S5Kdf1Ksf0.050y05	7.04	0.05
S5Kdf1Ksf0.10y05	14.1	0.1
S5Kdf1Ksf0.20y05	28.1	0.2
S5Kdf1Ksf0.30y05	42.2	0.3
S5Kdf1Ksf0.40y05	56.3	0.4
S5Kdf1Ksf0.50y05	70.4	0.5
S5Kdf1Ksf1.00y05	140.7	1.0
S5Kdf1Ksf1.50y05	211.1	1.5
S5Kdf1Ksf2.00y05	281.4	2.0

Case	K_f (kN/mm)	K_d (kN/mm)	K_d/K_f	A_c (mm ²)	L_p (mm)
S5Kdf0.50y1		70.4	0.5	5129	
S5Kdf10y1	140.7	140.7	1	10258	3650
S5Kdf20y1		281.4	2	20518	
S5Kdf40y1		562.8	4	41032	

Case	K_s (kN/mm)	K_s/K_f
S5Kdf1Ksf0050y1	7.04	0.05
S5Kdf1Ksf010y1	14.1	0.1
S5Kdf1Ksf020y1	28.1	0.2
S5Kdf1Ksf030y1	42.2	0.3
S5Kdf1Ksf040y1	56.3	0.4
S5Kdf1Ksf050y1	70.4	0.5
S5Kdf1Ksf10y1	140.7	1.0
S5Kdf1Ksf150y1	211.1	1.5
S5Kdf1Ksf20y1	281.4	2.0

Case	K_f (kN/mm)	K_d (kN/mm)	K_d/K_f	A_c (mm ²)	L_p (mm)
S5Kdf0.50y2		70.4	0.5	10258	
S5Kdf10y2	140.7	140.7	1	20518	7300
S5Kdf20y2		281.4	2	41036	
S5Kdf40y2		562.8	4	82072	

Case	K_s (kN/mm)	K_s/K_f
S5Kdf1Ksf0.050y2	7.04	0.05
S5Kdf1Ksf0.10y2	14.1	0.1
S5Kdf1Ksf0.20y2	28.1	0.2
S5Kdf1Ksf0.30y2	42.2	0.3
S5Kdf1Ksf0.40y2	56.3	0.4
S5Kdf1Ksf0.50y2	70.4	0.5
S5Kdf1Ksf1.00y2	140.7	1.0
S5Kdf1Ksf1.50y2	211.1	1.5
S5Kdf1Ksf2.00y2	281.4	2.0

Table 4.3 Value of each parameter for various cases of the 10-story structure

Case	K_f (kN/mm)	K_d (kN/mm)	K_d/K_f	A_c (mm ²)	L_p (mm)
S10Kdf0.50y05		37.6	0.5	5484	
S10Kdf10y05	75.1	75.1	1	10968	1825
S10Kdf20y05		150.2	2	21935	
S10Kdf40y05		300.4	4	43870	

Case	K_s (kN/mm)	K_s/K_f
S5Kdf1Ksf0.050y05	3.8	0.05
S5Kdf1Ksf0.10y05	7.5	0.1
S5Kdf1Ksf0.20y05	15.0	0.2
S5Kdf1Ksf0.30y05	22.5	0.3
S5Kdf1Ksf0.40y05	30.0	0.4
S5Kdf1Ksf0.50y05	37.6	0.5
S5Kdf1Ksf1.00y05	75.1	1.0
S5Kdf1Ksf1.50y05	112.7	1.5
S5Kdf1Ksf2.00y05	150.2	2.0

Case	K_f (kN/mm)	K_d (kN/mm)	K_d/K_f	A_c (mm ²)	L_p (mm)
S10Kdf0.50y1		37.6	0.5	10968	
S10Kdf10y1	75.1	75.1	1	21935	3650
S10Kdf20y1		150.2	2	43870	
S10Kdf40y1		300.4	4	87740	

Case	K_s (kN/mm)	K_s/K_f
S5Kdf1Ksf0.050y1	3.8	0.05
S5Kdf1Ksf0.10y1	7.5	0.1
S5Kdf1Ksf0.20y1	15.0	0.2
S5Kdf1Ksf0.30y1	22.5	0.3
S5Kdf1Ksf0.40y1	30.0	0.4
S5Kdf1Ksf0.50y1	37.6	0.5
S5Kdf1Ksf1.00y1	75.1	1.0
S5Kdf1Ksf1.50y1	112.7	1.5
S5Kdf1Ksf2.00y1	150.2	2.0

Case	K_f (kN/mm)	K_d (kN/mm)	K_d/K_f	A_c (mm ²)	L_p (mm)
S10Kdf0.50y2		37.6	0.5	21935	
S10Kdf10y2	75.1	75.1	1	43870	7300
S10Kdf20y2		150.2	2	87740	
S10Kdf40y2		300.4	4	175480	

Case	K_s (kN/mm)	K_s/K_f
S5Kdf1Ksf0.050y2	3.8	0.05
S5Kdf1Ksf0.10y2	7.5	0.1
S5Kdf1Ksf0.20y2	15.0	0.2
S5Kdf1Ksf0.30y2	22.5	0.3
S5Kdf1Ksf0.40y2	30.0	0.4
S5Kdf1Ksf0.50y2	37.6	0.5
S5Kdf1Ksf1.00y2	75.1	1.0
S5Kdf1Ksf1.50y2	112.7	1.5
S5Kdf1Ksf2.00y2	150.2	2.0

Table 4.4 Value of each parameter for various cases of the 20-story structure

Case	K_f (kN/mm)	K_d (kN/mm)	K_d/K_f	A_c (mm ²)	L_p (mm)
S20Kdf0.50y05		19.5	0.5	11334	
S20Kdf10y05	39.0	39.0	1	22667	1825
S20Kdf20y05		78.0	2	45333	
S20Kdf40y05		156.0	4	90666	

Case	K_s (kN/mm)	K_s/K_f
S5Kdf1Ksf0.050y1	1.95	0.05
S5Kdf1Ksf0.10y1	3.9	0.1
S5Kdf1Ksf0.20y1	7.8	0.2
S5Kdf1Ksf0.30y1	11.7	0.3
S5Kdf1Ksf0.40y1	15.6	0.4
S5Kdf1Ksf0.50y1	19.5	0.5
S5Kdf1Ksf1.00y1	39.0	1.0
S5Kdf1Ksf1.50y1	58.5	1.5
S5Kdf1Ksf2.00y1	78.0	2.0

Case	K_f (kN/mm)	K_d (kN/mm)	K_d/K_f	A_c (mm ²)	L_p (mm)
S20Kdf0.50y1		19.5	0.5	22667	
S20Kdf10y1	39.0	39.0	1	45333	3650
S20Kdf20y1		78.0	2	90666	
S20Kdf40y1		156.0	4	181332	

Case	K_s (kN/mm)	K_s/K_f
S5Kdf1Ksf0.050y1	1.95	0.05
S5Kdf1Ksf0.10y1	3.9	0.1
S5Kdf1Ksf0.20y1	7.8	0.2
S5Kdf1Ksf0.30y1	11.7	0.3
S5Kdf1Ksf0.40y1	15.6	0.4
S5Kdf1Ksf0.50y1	19.5	0.5
S5Kdf1Ksf1.00y1	39.0	1.0
S5Kdf1Ksf1.50y1	58.5	1.5
S5Kdf1Ksf2.00y1	78.0	2.0

Case	K_f (kN/mm)	K_d (kN/mm)	K_d/K_f	A_c (mm ²)	L_p (mm)
S20Kdf0.50y2		19.5	0.5	45333	
S20Kdf10y2	39.0	39.0	1	90666	7300
S20Kdf20y2		78.0	2	181332	
S20Kdf40y2		156.0	4	362664	

Case	K_s (kN/mm)	K_s/K_f
S5Kdf1Ksf0.050y1	1.95	0.05
S5Kdf1Ksf0.10y1	3.9	0.1
S5Kdf1Ksf0.20y1	7.8	0.2
S5Kdf1Ksf0.30y1	11.7	0.3
S5Kdf1Ksf0.40y1	15.6	0.4
S5Kdf1Ksf0.50y1	19.5	0.5
S5Kdf1Ksf1.00y1	39.0	1.0
S5Kdf1Ksf1.50y1	58.5	1.5
S5Kdf1Ksf2.00y1	78.0	2.0

4.4.2 Effect of yielding drift of dampers

The parametric study is used to validate the proposed simplified procedure against the DMD model, examine the response trends and influence of the various control parameters, and finally to optimize the control parameters.

The ground motions used for time history analysis included the artificial ground motion BCJ-L2 (120s), as well as four recorded ground motions: El Centro NS (1940), JMA Kobe NS (1995), TAFT EW (1925), and Hachinohe NS (1968), each 30 s long. The acceleration response spectra for the four recorded ground motions were spectrally matched to follow the Japanese life-safety design spectrum (BRI-L2), as shown in Fig. 4.9. Rayleigh damping was adopted for the DMD Model, with the damping ratio set as 0.02 for the first and third modes, in order to achieve a near-constant value of damping for all modes with frequencies between these two modes.

The peak story drift ratio (SDR) and shear force of 5- and 10-story structures as a function of θ_y are shown in Figs. 4.10 and 11. Generally, the simplified method slightly overestimated the base shear and maximum story drift ratios. Both the deformation and force responses are not significantly affected by the yielding drift ratio of dampers ranging from 0.05% to 0.2%.

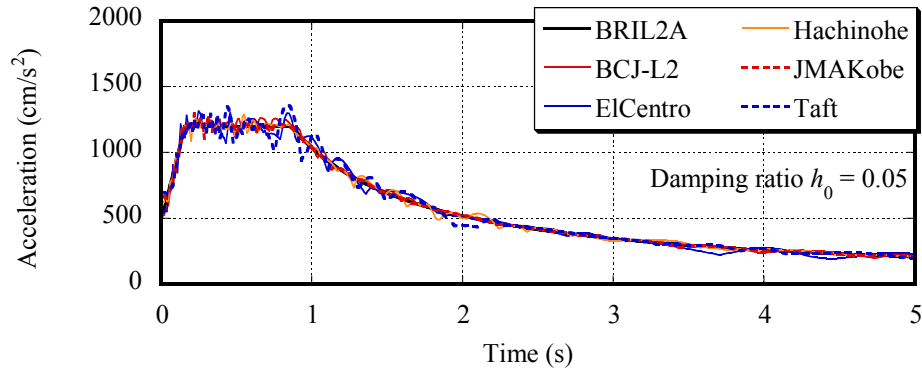
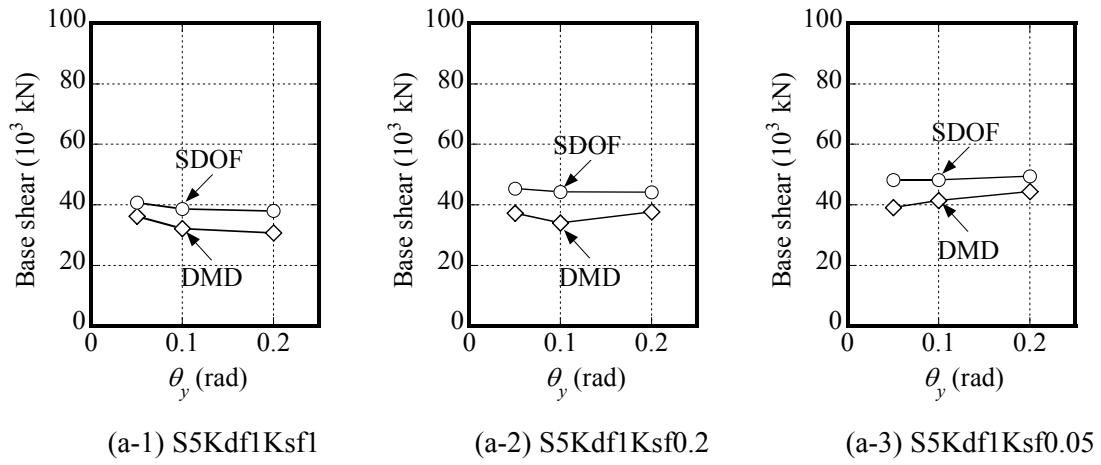
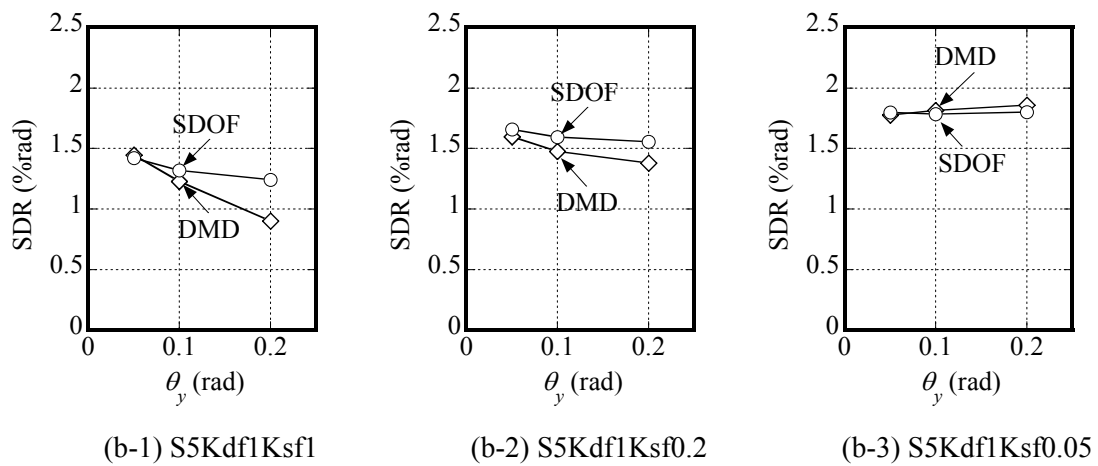


Fig. 4.9 Acceleration spectra of normalized input ground motions



(a) Maximum base shear force



(b) Maximum story drift ratio

 Fig. 4.10 Comparison of the seismic responses between the DMD and SDOF models of the 5-story structures with various θ_y (input: BCJ-L2)

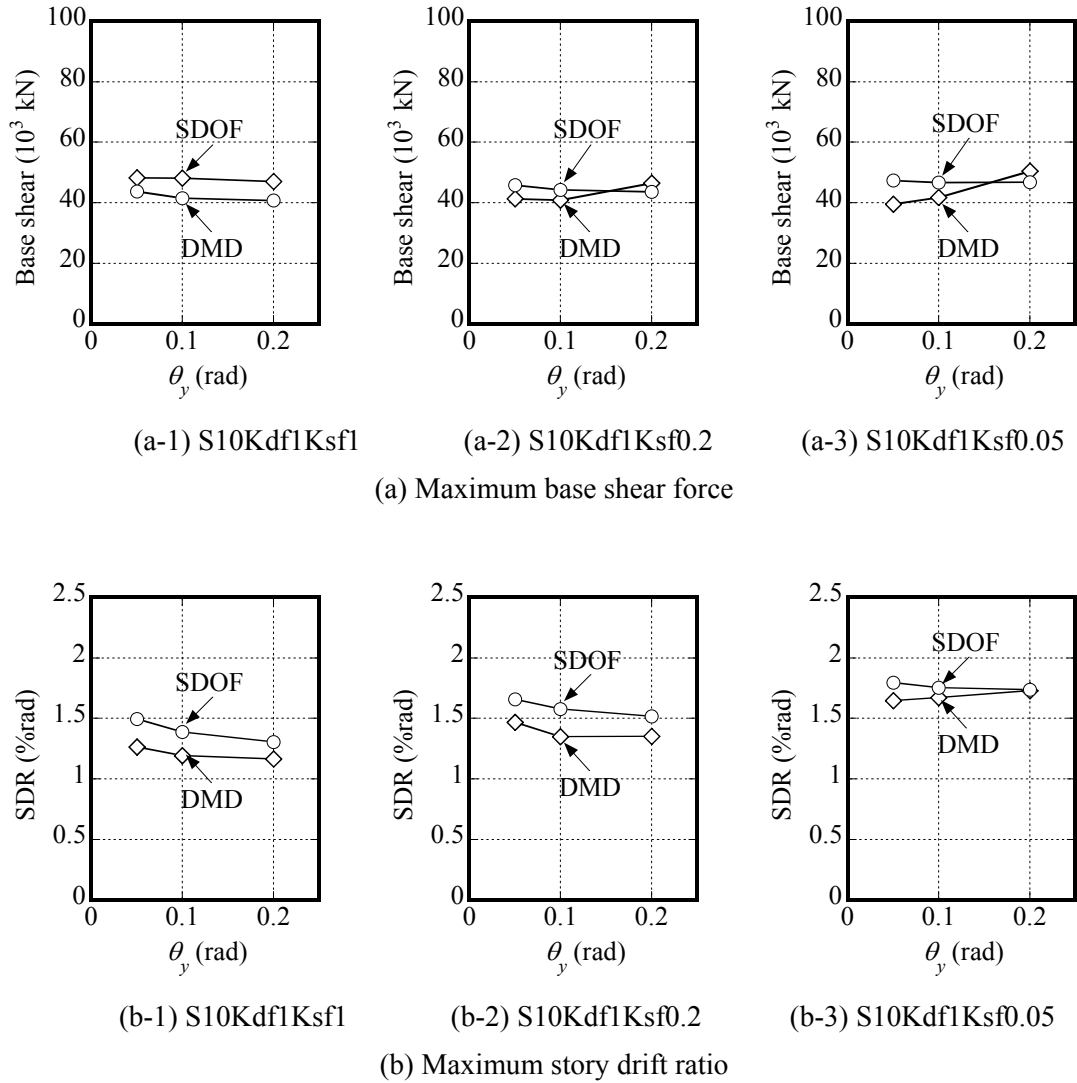


Fig. 4.11 Comparison of the seismic responses between the DMD and SDOF models of the 10-story structures with various θ_y (input: BCJ-L2)

4.4.3 Effect of damper-to-moment frame stiffness ratio

The peak story drift ratio and shear force of the 5-, 10-, 20-story structures as a function of K_d/K_f are shown in Figs. 4.12 - 14. As illustrated in Fig. 4.12 for the 5-story structure, increasing K_d/K_f resulted in decreasing deformations and shear forces of both the SDOF and DMD models when K_s/K_f was larger than 0.05. Generally, the base shear of the DMD and SDOF models was in good agreement. For exceptionally large dampers with K_d/K_f in the range of 2.0–4.0, a significant discrepancy was observed with respect to the deformations between SDOF and DMD methods. This was mainly because the response distribution of the SDOF model followed that of the main frame excluding dampers. Distribution of the responses had significant effect on the maximum response. Therefore, the SDOF model could provide better estimation for the structures in which the dampers yielded to a greater extent, i.e. to a larger ductility ratio. This reason will be explained in detail in chapter 6. Since highly nonlinear response could not be accurately captured in the SDOF model, it is recommended that K_d/K_f should be less than 2.0 when the SDOF method is applied. Additionally, at least a reasonable damper stiffness of $K_d/K_f \geq 0.5$ should be provided to effectively control the seismic response.

Residual story drift ratio of the 5-story DMD model was always smaller than 0.05%, despite of the value of K_d/K_f , as in Fig 4.12 (c), indicating that sufficient self-centering capacity was provided by the envelop moment frames.

A similar trend for K_d/K_f could be observed in the results of the 10-story structures, as shown in Fig. 4.13. Increasing K_d/K_f resulted in decreasing deformations and shear forces of both the SDOF and DMD models when K_s/K_f was larger than 0.05. Base shear of the DMD and SDOF models generally agreed with various K_d/K_f , while the SDR of the two models agreed when K_d/K_f was less than 1.0. Residual SDR of the 10-story DMD model was also always smaller than 0.05%, despite of the value of K_d/K_f , as in Fig 4.13 (c).

Shear force of the DMD model exceeded that of the SDOF model in the 20-story structure, except for the case when $K_d/K_f = 2.0$, as in Fig 4.14 (a). This indicated that the significant higher-mode effects might be mitigated when the damper-to-frame stiffness K_d/K_f increases up to a specific level in taller buildings. Similar with the 5- and 10-story structures, SDR of the SDOF and DMD models agreed when K_d/K_f was less than 1.0, as in Fig 4.14 (b). Residual SDR of the 20-story DMD model was smaller than 0.05%, except for the case when $K_d/K_f = 4.0$ and $K_s/K_f = 0.05$, as in Fig 4.14 (c).

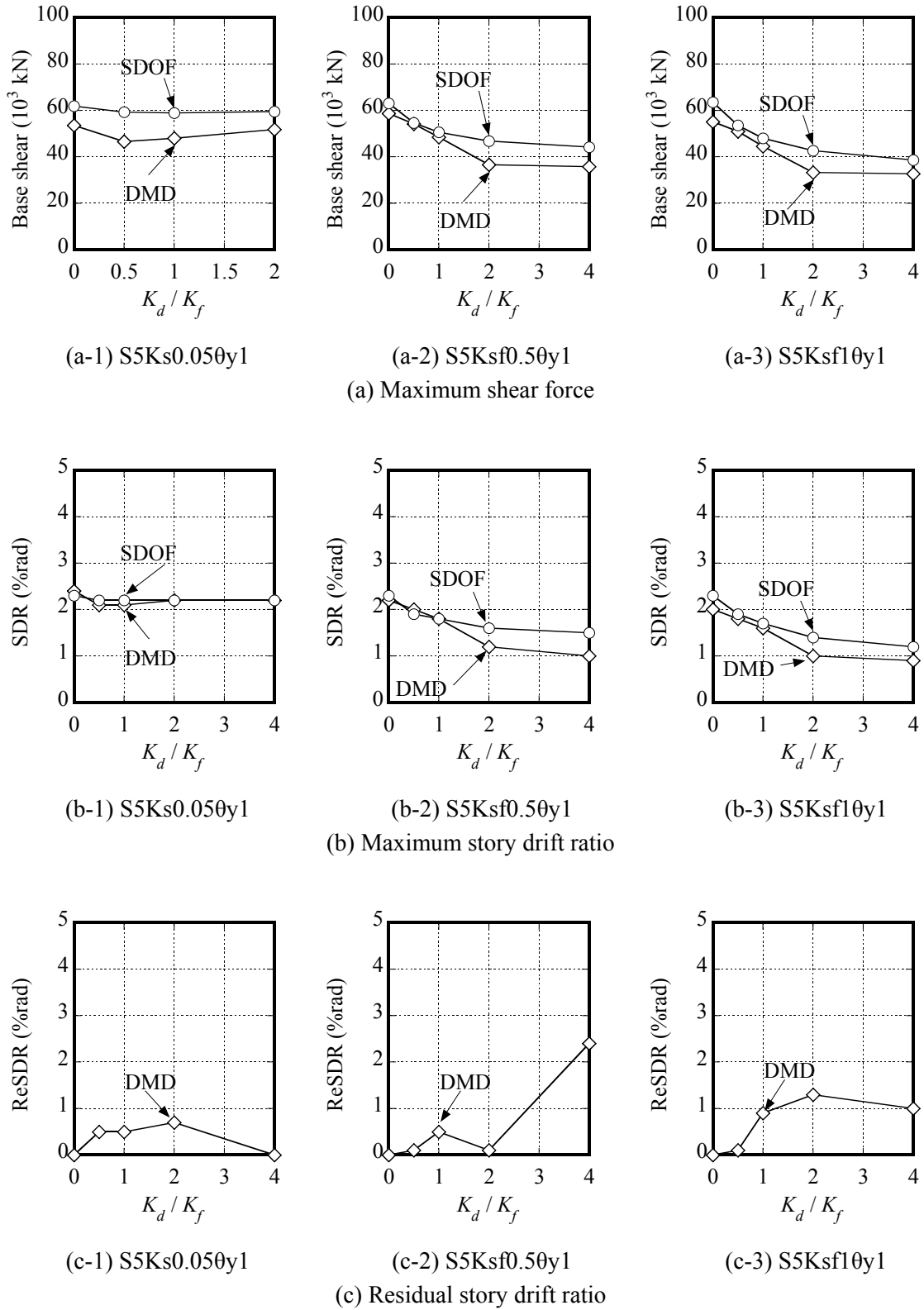


Fig. 4.12. Comparison of the seismic responses between the DMD and SDOF models of the 5-story structures with various K_d/K_f (input: BCJ-L2, $\theta_y=0.1\%$)

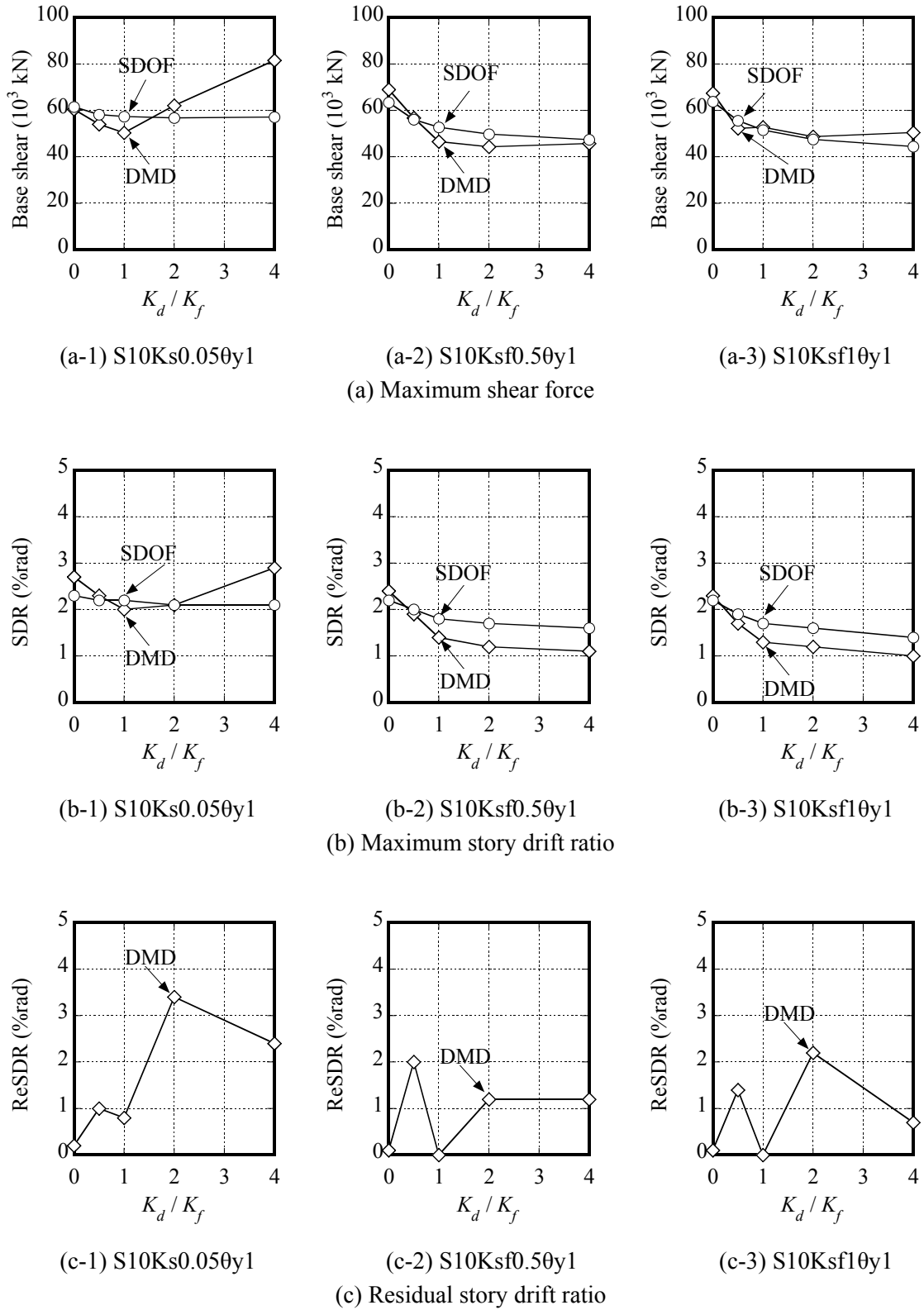


Fig. 4.13. Comparison of the seismic responses between the DMD and SDOF models of the 10-story structures with various K_d/K_f (input: BCJ-L2, $\theta_y=0.1\%$)

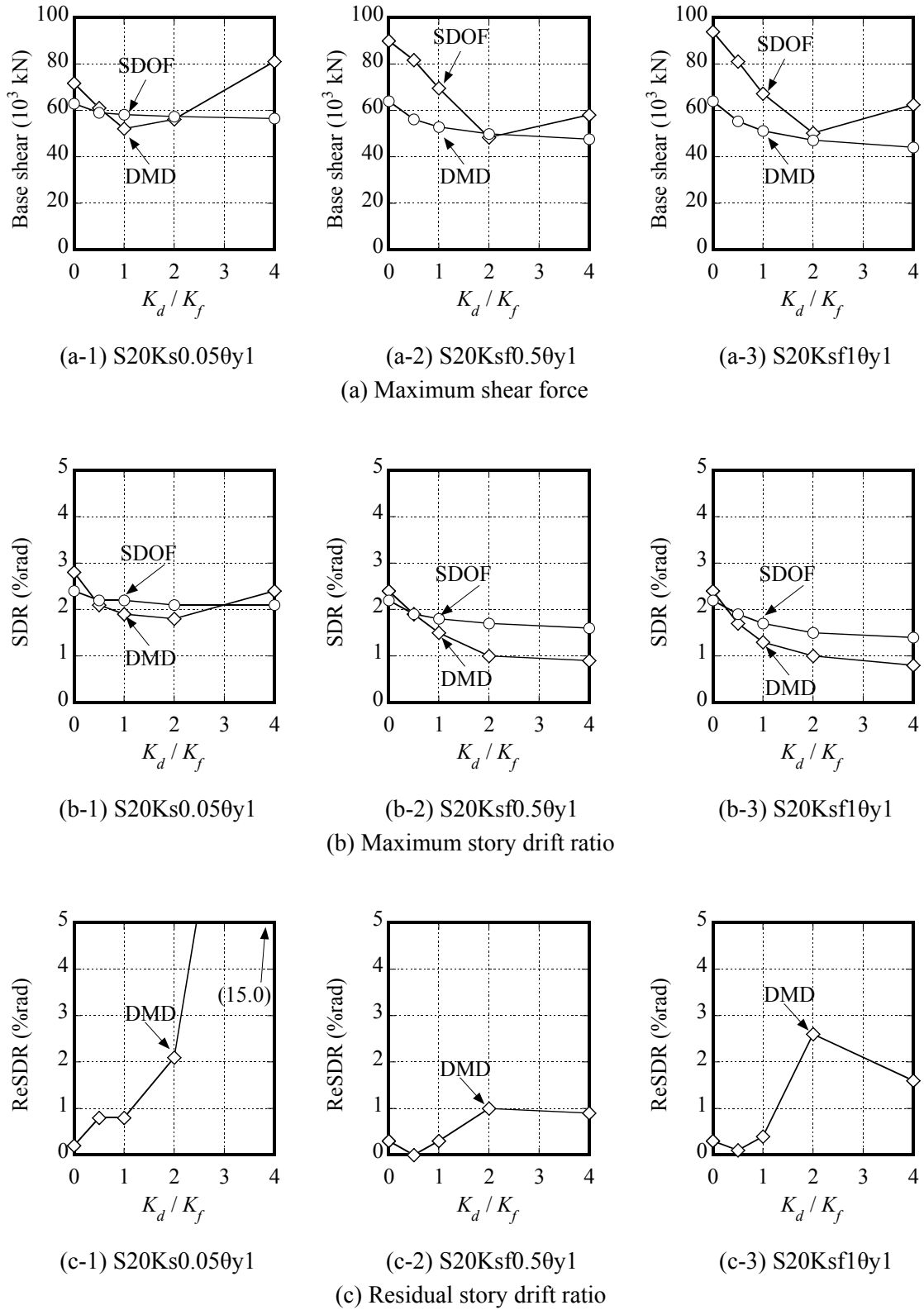


Fig. 4.14. Comparison of the seismic responses between the DMD and SDOF models of the 20-story structures with various K_d/K_f (input: BCJ-L2, $\theta_y=0.1\%$)

4.4.4 Effect of spine-to-moment frame stiffness ratio

The peak story drift ratio and shear force of the 5-, 10-, 20-story structures as a function of K_s/K_f are shown in Figs. 4.15 - 17. As illustrated in Fig. 4.15 for the 5-story structure, increasing K_s/K_f resulted in decreasing deformations and shear forces of both the SDOF and DMD models, but when K_s/K_f was larger than 1.0, the decreasing tendency in base shear was much gentler. This indicated that the spine effect on base shear might be mitigated when the spine-to-frame stiffness K_s/K_f increases up to a specific level.

Generally, the base shear and SDR of the DMD and SDOF models were in good agreement, despite of K_s/K_f as if K_d/K_f was less than 2.0. Residual SDR of the 5-story DMD model was always smaller than 0.05%, despite of K_s/K_f as well, as in Fig 4.15 (c).

As shown in Fig. 4.15(d), concentration of SDR (that is, the maximum SDR divided by the average SDR among all the stories) decreased rapidly when K_s/K_f increased from 0 to 1.0, indicating that higher K_s/K_f was strongly associated with a more uniform SDR distribution.

A similar trend for K_s/K_f could be observed in the results of the 10-story structures, as shown in Fig. 4.16. Increasing K_s/K_f resulted in decreasing deformations and slightly decreasing for shear forces of both the SDOF and DMD models. Residual SDR of the 10-story DMD model was always smaller than 0.05%, despite of K_s/K_f . Concentration of SDR decreased rapidly when K_s/K_f increased from 0 to 0.5.

Increasing K_s/K_f resulted in decreasing deformations of both the SDOF and DMD models for the 20-story structure. Residual SDR was still always smaller than 0.05%, despite of K_s/K_f . Concentration of SDR decreased rapidly when K_s/K_f increased from 0 to 0.5.

However, the shear force obtained by using the DMD model in Fig. 4.17 (a) exhibited significant fluctuations and much larger than the SDOF model. These fluctuations in the shear force of the taller structures were attributed to the higher-mode effect. Therefore, the SDOF model seems not suitable for estimating seismic performance of structures taller than 20 stories.

In conclusion, for the full range of K_s/K_f and 0.0-2.0 of K_d/K_f , the proposed simplified evaluation method was able to predict the seismic performance to within an acceptable margin for both the deformation and force response of the 5-story and 10-story structures, and deformation response of the 20-story structure. However, increasing K_s/K_f did not eliminate the higher-mode effect on shear forces, and so the simplified procedure did not accurately predict the force response of the 20-story structure.

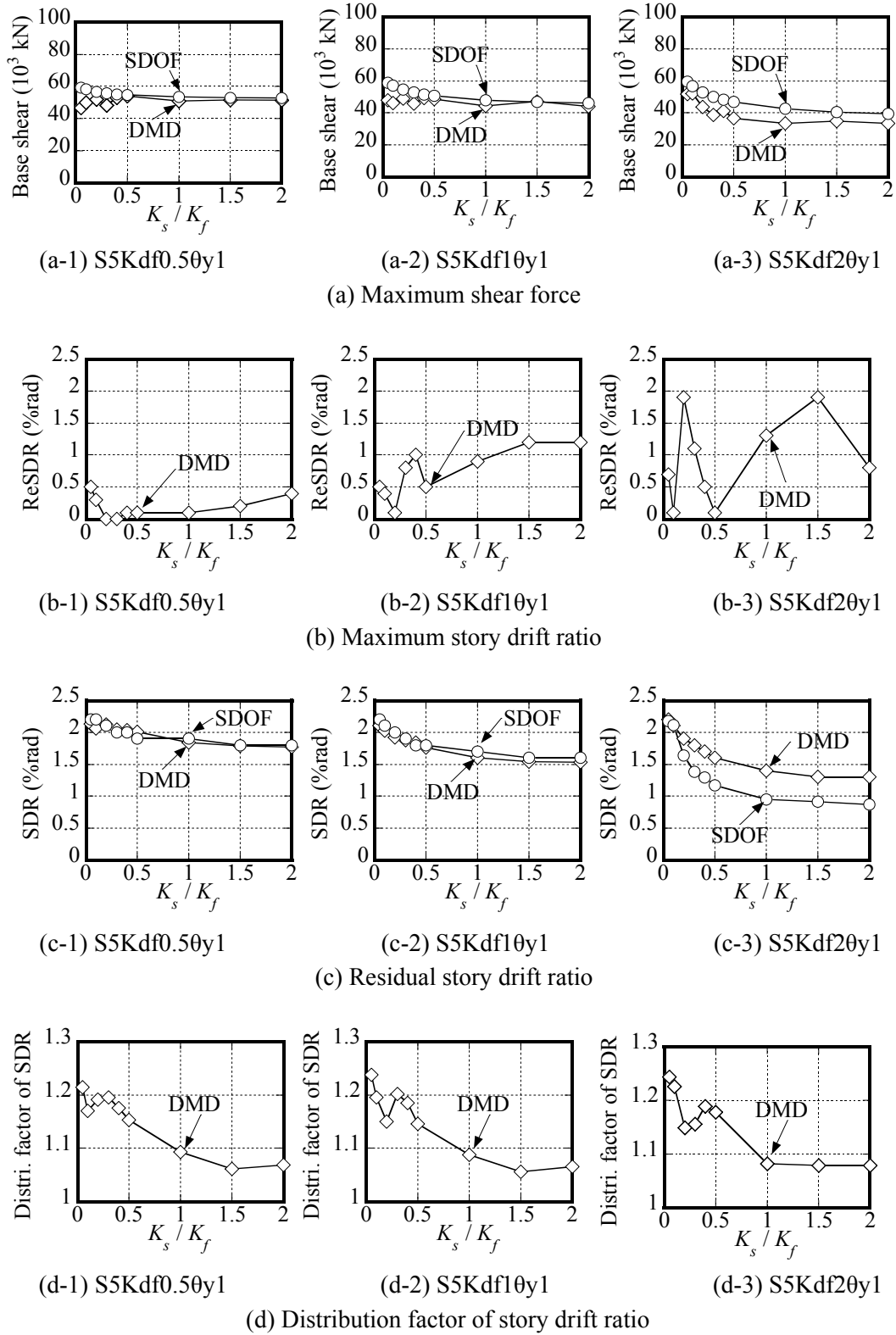


Fig. 4.15. Comparison of the seismic responses between the DMD and SDOF models of the 5-story structures with various K_s/K_f (input: BCJ-L2, $\theta_y=0.1\%$)

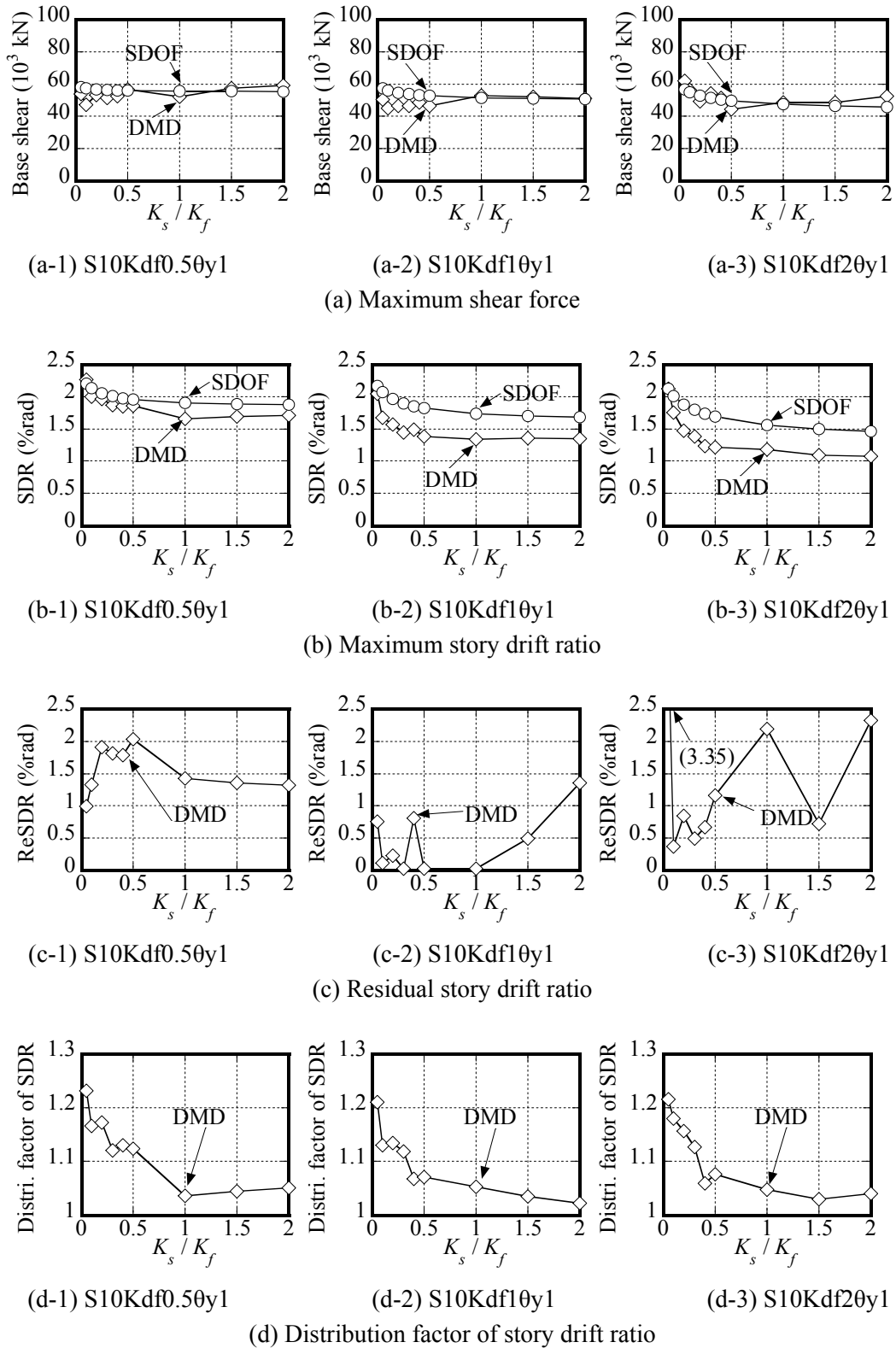


Fig. 4.16. Comparison of the seismic responses between the DMD and SDOF models of the 10-story structures with various K_s/K_f (input: BCJ-L2, $\theta_y=0.1\%$)

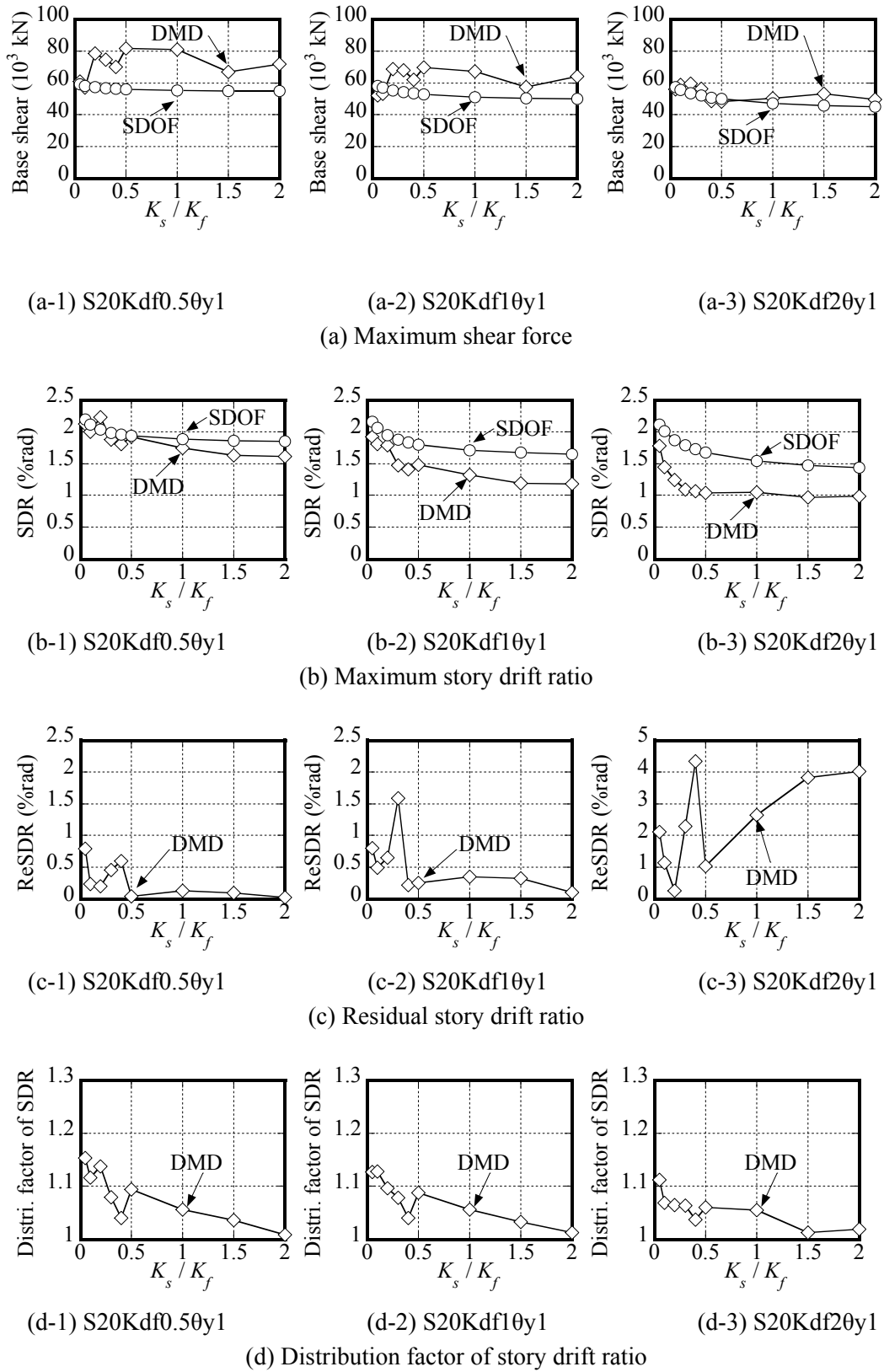


Fig. 4.17. Comparison of the seismic responses between the DMD and SDOF models of the 20-story structures with various K_s/K_f (input: BCJ-L2, $\theta_y=0.1\%$)

4.4.5 Optimal structural parameters and applicable range of design procedure

Figure 4.18 compares the peak shear force and story drift ratio of the DMD models with those of the SDOF models for K_d/K_f of 0.5 ~ 2.0 and K_s/K_f of 0.05 ~ 2.0 in 5-story and 10-story structures. Generally, the proposed design procedure slightly overestimates the base shear and maximum story drift ratios; with the one exception in Fig. 4.18 (a) being that base shear of the 10-story structures was underestimated. General trends are captured, and error is controlled to within approximately 20% for the base shear and 30% for the maximum story drift ratios.

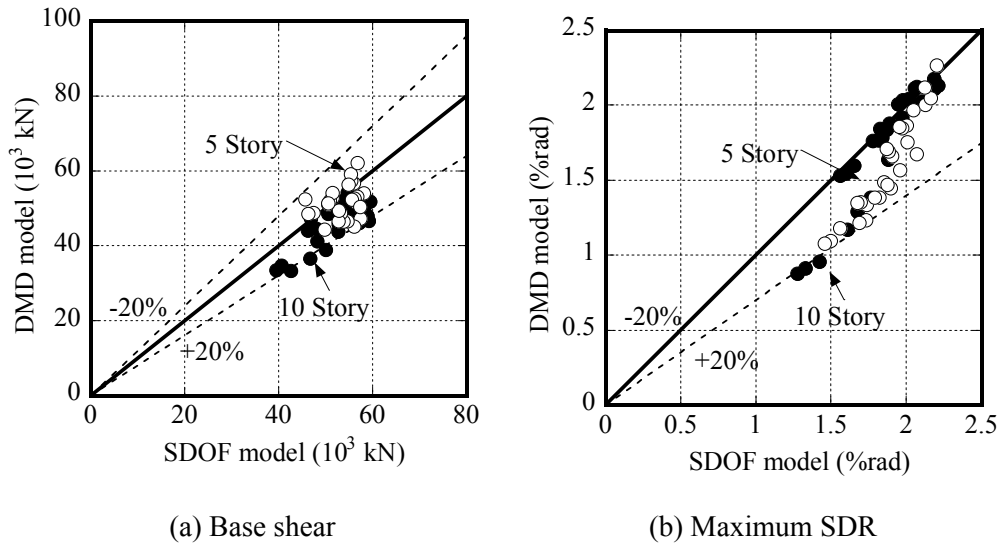


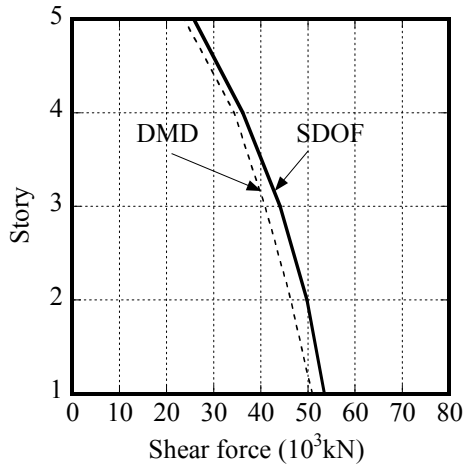
Fig. 4.18 Validation of the proposed design procedure via SDOF models
($0.5 \leq K_d/K_f \leq 2.0$, $0.05 \leq K_s/K_f \leq 2.0$, for 5-story and 10-story structures)

From Fig 4.19 we could see the significant higher-modes effect in the shear force of the 20-story model compared to the other two models. To examine the minimum participation factor of the 1st-mode response in base shear required for utilizing the SDOF model, eigenvalue analysis on the main frame of the 5-, 10-, and 20-story structures was carried out with K_s/K_f varying from 1.0 to 12.0.

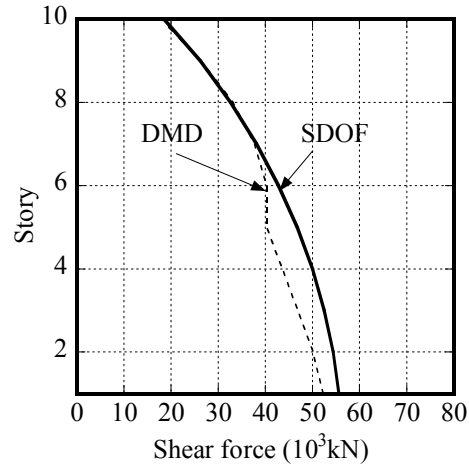
Effect of spine frame stiffness was not so significant on the participation factor of the 1st-mode response in base shear for all the three structures, as shown in Fig 4.20. This participation factor increased from 83% to 89% for the 5-story model, 69% to 76% for the 10-story model, and 54% to 59% for the 20-story model. We could preliminarily conclude that around 70% is the minimum required first-mode participation factor of base shear for utilizing the SDOF model.

70% is almost impossible to be realized in the 20-story structure since even $K_s/K_f=1.0$ requires unrealistic large scale of spine frames in the actual design. The self-centering capacity

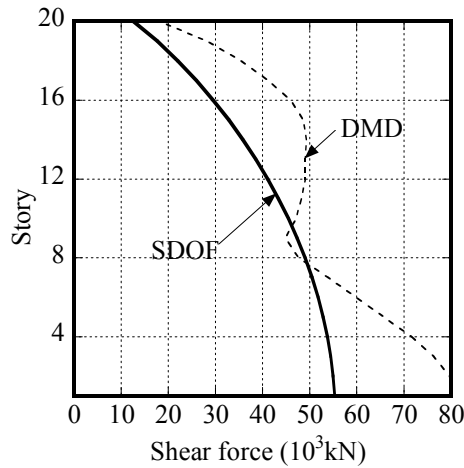
might not be ensured when K_s/K_f was too large as well. Moreover, the overall flexural deformation is more significant in the tall buildings and increases the difference between the SDOF model and the original structure, although such deformation was ignored in the DMD model. Therefore, 10 stories might be the height limitation for utilizing the SDOF model to estimate seismic responses.



(a) S5Kdf0.5Ksf1.00y1



(b) S10Kdf0.5Ksf1.00y1



(c) S20Kdf0.5Ksf1.00y1

Fig 4.19 Shear force distribution of some typical 5-, 10-, and 20-story models
($K_d/K_f=0.5$, $K_s/K_f=1.0$, $\theta_y=1$)

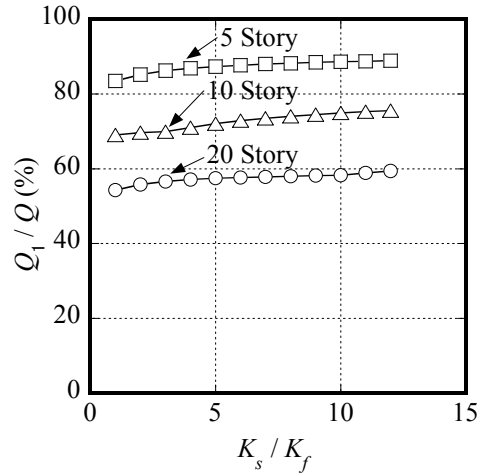


Fig 4.20 Contribution factor of the 1st mode response in base shear of the 5-, 10-, and 20-story models with various K_s/K_f ($K_d/K_f=0.5$, $\theta_y=1$)

4.5 Conclusions

In this chapter, a seismic performance evaluation method and design procedure was proposed for the controlled spine frames. A parametric study was conducted to examine suitable values for key structural parameters and the applicable range of the evaluation method and design procedure. The following conclusions were drawn from this study:

(1) A seismic performance evaluation method based on an equivalent SDOF model has been proposed for the controlled spine frames.

(2) By utilizing the evaluation method, a graphical performance curve has been proposed to efficiently select the damper yield drift and damper-to-frame stiffness ratio K_d/K_f . This is a practical method to quickly arrive at optimal designs that achieve the force and deformation performance targets.

(3) The stiff spine frame has a dramatic effective in achieving a more uniform deformation distribution along the height of a structure. To ensure the effectiveness of the dampers, K_s/K_f should exceed 0.5 for the 5- and 10-story structures, but the spine effect seems less effective when K_s/K_f exceed 1.0.

(4) Increasingly stiff dampers lead to a greater predicting error when utilizing the SDOF model. It is mainly because the response distribution shape is assumed to be identical with that of the main frame excluding dampers. It is recommended that the spine-to-moment frame stiffness ratio K_d/K_f should not exceed 2.0 for the typical cases of $0.5 \leq K_s/K_f \leq 2.0$ for using the SDOF model.

(5) Residual story drift ratios of the 5- and 10-story structures were always less than 0.05% for the typical cases of $0.5 \leq K_s/K_f \leq 2.0$ and $K_d/K_f \leq 2.0$.

(6) The proposed simplified procedure based on the SDOF model is valid for structures in which the first modal contribution factor for shear force exceeds 70%. This corresponds to ordinary spine frame structures with no higher than 10 stories and spine-to-moment frame stiffness ratios K_s/K_f of 0.5 to 2.0. Error could be controlled to within approximately 20% for the base shear and 30% for the maximum story drift ratios.

Reference

- [4.1] M. R. Eatherton, G. G. Deierlein, X. Ma et al: Toward a performance-based design framework for self-centering rocking braced-frame spine system. 15th WCEE, Lisboa 2012.
- [4.2] Stefano Pampanin: PRESSS technology design handbook
- [4.3] Stefano Pampanin: Seismic design guide for post-tensioned timber frames and walls (pres-lam technology), 2012.
- [4.4] L. Wiebe, C. Christopoulos. Performance-based seismic design of controlled rocking steel braced frames. I: Methodological framework and design of base rocking joint. *ASCE Journal of Structural Engineering*. Vol. 141(9), 2015
- [4.5] L. Wiebe, C. Christopoulos: Performance-based seismic design of controlled rocking steel braced frames. II: Design of capacity-protected elements. *ASCE Journal of Structural Engineering*. Vol. 141, Issue 9, 2015
- [4.6] T. C. Steele, L. D. A. Wiebe: Dynamic and equivalent static procedures for capacity design of controlled rocking steel braced frames. *Earthquake Engineering and Structural Dynamics*. Vol. 45, p2349-2369. 2016
- [4.7] 柴田明德：最新 耐震構造解析、最新建築学シリーズ、森北出版、1981.
- [4.8] 塩原等、小谷俊介、青山博之：縮約モデルによる構造物の弾塑性応答解析、構造工学シンポジウム論文集、Vol.28, p101-112, 1982.
- [4.9] 堀則男、河本慎一郎、井上範夫、柴田明德：梁降伏型RC造骨組の縮約1自由度系による耐震設計手法の検討、構造工学論文集、Vol.42B, p33-40, 1996
- [4.10] 小川厚治：魚骨形骨組の等価1自由度系への置換に関する研究、日本建築学会構造系論文集、Vol5(17), p143-150, 2001.
- [4.11] 日本建築学会：地震荷重—地震動の予測と建築物の応答、日本建築学会、1992.
- [4.12] 石山祐二：A i 分歩の誕生とその経緯、日本建築学会大会学術講演梗概集（北陸）、1992.
- [4.13] H. Kuramoto, M. Teshigawara, N. Koshika, H. Isoda: Conversion of multi-story building into equivalent SDOF system and its predictability for earthquake response. *Journal of Structural and Construction Engineering (AIJ)*, No. 546, p79-85, 2001. (in Japanese)

倉本洋、勅使川原正臣、小鹿紀英、五十田博：多層建築物の等価 1 自由度系縮約法と地震応答予測精度，日本建築学会構造系論文集, No. 546, p79-85, 2001.

- [4.14] K. Kasai, H. Ito, A. Watanabe: Peak response prediction rule for a SDOF elasto-plastic system based on equivalent linearization technique. *Journal of Structural and Construction Engineering (AIJ)*, No. 571, p53-62, 2003. (in Japanese)

笠井和彦、伊藤浩資、渡辺厚：等価線形化手法による一質点弾塑性構造の最大応答予測法，日本建築学会構造系論文集，No. 571, p53-62, 2003.

- [4.15] T. Takeuchi, Y. Ichikawa, H. Nakashima, K. Kasai: Response evaluation of passively controlled multistory building with non-uniform damper distribution. *Journal of Structural and Construction Engineering (AIJ)*, No. 583, p115-122, 2004. (in Japanese)

竹内徹、市川康、中島秀雄、笠井和彦：ダンパーが不均等配置された多層パッシブ制振構造の応答予測，日本建築学会構造系論文集 No. 583, p115-122, 2004.

- [4.16] K. Kasai, I. Hiroshi: Passive control design method based on tuning of stiffness, yield strength, and ductility of elasto-plastic damper. *Journal of Structural and Construction Engineering (AIJ)*, No. 595, p45-55, 2005. (in Japanese)

笠井 和彦、伊藤 浩資：弾塑性ダンパーの剛性・降伏力・塑性率の調節による制振構造の応答制御手法，日本建築学会構造系論文集 No. 595, p45-55, 2005.

CHAPTER 5

Seismic Performance of Controlled Spine Frames Applied in High-rise Buildings

5.1 Introduction	5-1
5.2 Benchmark building structures	
5.2.1 Design of the 30-story building structure	5-1
5.2.2 Variable spine frame configurations	5-5
5.2.3 Control parameters	5-7
5.3 Parametric study of continuous spine frame (Cnt) models	
5.3.1 Effect of spine-to-moment frame stiffness ratio	5-8
5.3.2 Effect of damper-to-moment frame stiffness ratio	5-11
5.4 Parametric study of partial spine frame (Prt) models	
5.4.1 Concept of Prt model	5-14
5.4.2 Vibration characteristics of Prt models	5-15
5.4.3 Seismic performance of Prt models	5-17
5.5 Parametric study of two-segment spine frame (Sgt2) models	
5.5.1 Concept of Sgt model	5-18
5.5.2 Vibration characteristics of 20-story Sgt2 models	5-18
5.5.3 Optimal location of segment story of 20-story Sgt2 models	5-20
5.5.4 Optimal damper amount of 20-story Sgt2 models	5-22
5.5.5 Vibration characteristics of 30-story Sgt2 models	5-25
5.5.6 Optimal location of segment story of 30-story Sgt2 models	5-27
5.5.7 Optimal damper amount of 30-story Sgt2 models	5-28
5.6 Parametric study of three-segment spine frame (Sgt3) models	
5.6.1 Vibration characteristics of Sgt3 models	5-31
5.6.2 Optimal locations of segment stories	5-33
5.6.3 Optimal damper amount of Sgt3 models	5-36
5.7 Conclusion	5-40

Chapter 5 – Seismic Performance of Controlled Spine Frames Applied in High-rise Buildings

5.1 Introduction

In previous chapters we have proposed a controlled spine frame system for seismic resistant design in new building applications. Both the spine frame concept and controlled version offers superior performance in preventing damage concentration and reducing residual deformation. A simplified design procedure based on equivalent dual multi-degree-of-freedom (DMD) and single-degree-of-freedom (SDOF) representations has been developed. The design procedure and the two simplified representations are validated with parametric study.

However, seismic performance of the spine frame structure utilized in tall buildings is not clarified, because the previously proposed DMD model significantly underestimated responses of the 20-story structure due to the exclusion of axial forces in columns. In this chapter, the more precise member-by-member (MBM) model is adopted for investigating seismic responses of the 20-story structure. Another 30-story building height of 120m was designed as a supplement for the suit of tall buildings.

To demonstrate the influence on seismic performance from the key structural parameters, i.e. stiffness ratio between spine frames, moment frames, and dampers, parametric study is carried out for both 20- and 30-story structures. Besides, the concept of segmented spine frames are proposed for the tall buildings, considering that the dampers amount at one location could easily exceed the upper limitation in actual applications in the continuous spine frame structures. Additional key structural parameters coming with the segmented spine frames include number of segments, location of dampers i.e. segment story, stiffness ratio between dampers at different segment stories. Seismic performance of the segmented spine frame structures has been investigate and compared with the continuous spine frame structures. Effect of the key structural parameters has been demonstrated based on parameter study utilizing time-history analysis.

5.2 Benchmark building structures

5.2.1 Design of the 30-story building structure

Parametric study based on nonlinear time-history analysis was used to investigate the seismic performance of the controlled spine system with diverse structural properties. The benchmark structures of the 5-, 10-, and 20-story buildings designed in Chapter 3 are utilized in this chapter. Some results of 5- and 10-story buildings are extracted from the previous chapter as comparison for the seismic responses of tall buildings. Additionally, a new 30-story building was designed. Fig 5.1 (a) – (c) shows the structural layout and dimensions. Structural plan remains unchanged, and the structural members of the main frame were designed in elastic ranges as per the base

shear ratio of 0.03 with A_i distributions. Similar with previous chapters, the moment frames were assumed to remain elastic during Level-2 (similar as DBE in U.S. Calif.) earthquake events. Although the spine frames can suppress soft story formation, for this study the lateral stiffness of the moment frames were set approximately proportional to the story shear. The spine frames were also assumed to be elastic during considered earthquake events. Spine frames in 5-story and 10-story buildings were assumed to be pin-supported steel trusses, and that in the 20-story and 30-story buildings were pin-supported reinforced concrete walls, to achieve the required stiffness for the parameter studies described later. RC walls were assumed to be pre-stressed by post-tensioning tendons to prevent cracking, thus the stiffness degradation of the RC wall was not considered.

Design procedure of the main frame is same with those of the 20-story building. Lateral stiffness of the moment frame computed by Eq. (4.63) is 34.9 kN/mm for the 30-story building. To achieve a 0.3 stiffness ratio between the spine frame and the moment frame, thickness of the core wall need to be 1.2m if a rectangle section is utilized, and the width need to be 12m. To achieve a 1.0 stiffness ratio between dampers and the moment frame, although distance between two sides increases to 12m, required sectional area of each BRC is still unrealistically large, 68000mm^2 , and yielding axial force is 22000kN. To reduce wall thickness and capacity requirement for BRCs, H-shape wall is utilized instead of the rectangular wall. Cross-section of the core wall is H-1200×280×70×60. BRCs with sectional area of 34000mm^2 is equipped (yielding axial force 11000kN) at each edge of the H-shape wall.

Table 5.1 lists detailed sectional properties of beams and columns. Stiffness distribution is essentially linear as shown in Fig 5.2. Regular member dimensions in each benchmark model are compared in Table 5.2. Detailed cross section information is given in their corresponding design sections.

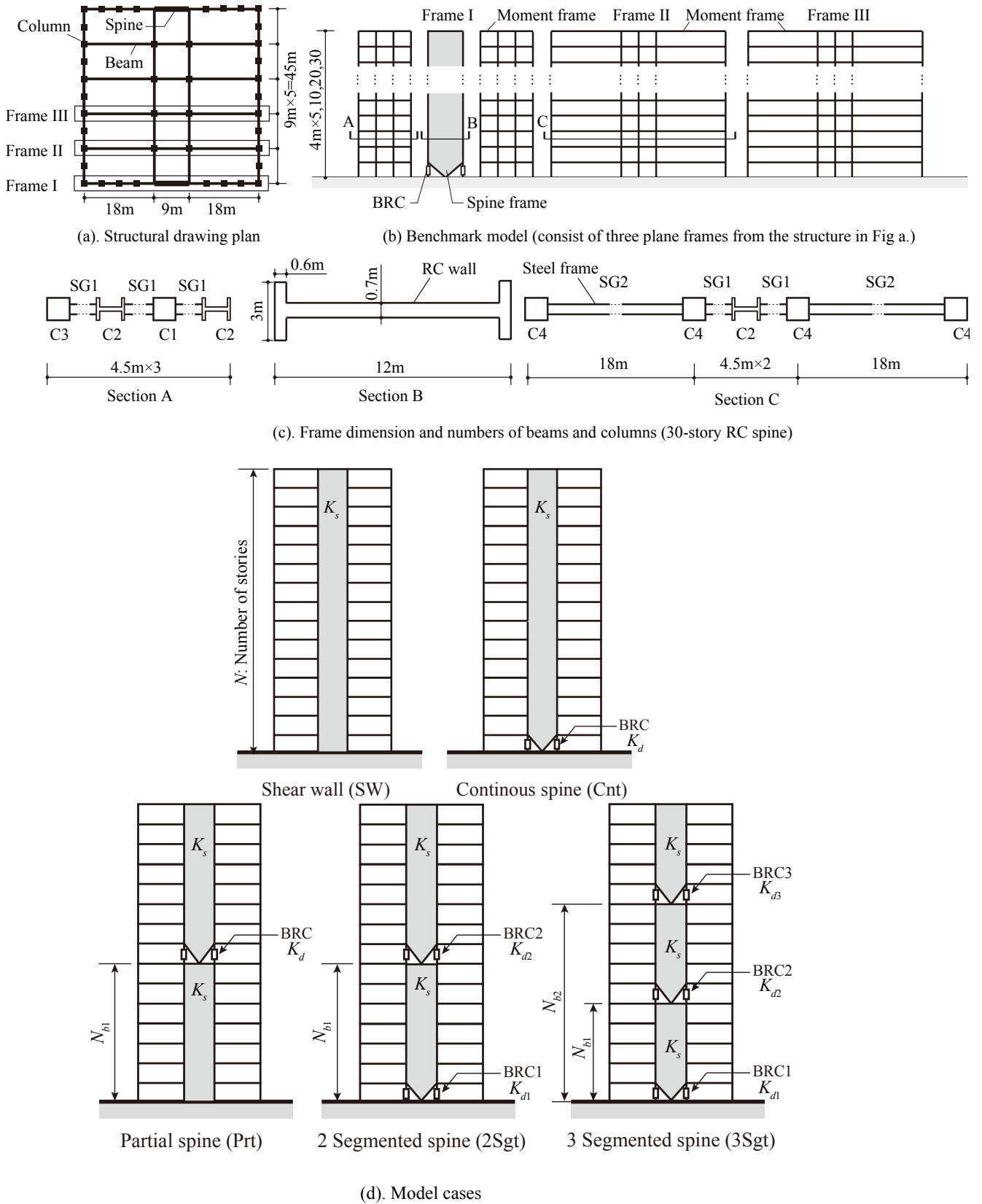


Fig. 5.1 Benchmark models of the controlled spine frame structures

Table 5.1 Sectional sizes of columns and beams in the 30-story building

Story	C1	C2	C3	C4	SG1
30	□-700×700×19	H-750×500×16×22	□-700×700×19	□-750×750×28	H-750×300×16×22
29	□-700×700×19	H-750×500×16×22	□-700×700×19	□-750×750×28	H-750×300×16×22
28	□-700×700×19	H-750×500×16×22	□-700×700×19	□-750×750×28	H-750×300×16×22
27	□-700×700×19	H-750×500×16×22	□-700×700×19	□-750×750×30	H-750×300×16×22
26	□-700×700×19	H-750×500×16×22	□-700×700×19	□-750×750×30	H-750×300×16×22
25	□-700×700×19	H-750×500×16×22	□-700×700×19	□-750×750×30	H-750×300×16×22
24	□-700×700×22	H-750×500×16×22	□-700×700×19	□-750×750×30	H-750×300×16×25
23	□-700×700×22	H-750×500×16×22	□-700×700×19	□-750×750×30	H-750×300×16×25
22	□-700×700×22	H-750×500×16×22	□-700×700×19	□-750×750×30	H-750×300×16×25
21	□-700×700×22	H-750×500×16×25	□-700×700×19	□-750×750×30	H-750×300×16×25
20	□-700×700×22	H-750×500×16×25	□-700×700×19	□-750×750×30	H-750×300×16×25
19	□-700×700×22	H-750×500×16×25	□-700×700×19	□-750×750×30	H-750×300×16×25
18	□-700×700×22	H-750×500×16×25	□-700×700×22	□-750×750×30	H-750×300×16×28
17	□-700×700×22	H-750×500×16×25	□-700×700×22	□-750×750×30	H-750×300×16×28
16	□-700×700×22	H-750×500×16×25	□-700×700×22	□-750×750×30	H-750×300×16×28
15	□-700×700×22	H-750×500×16×25	□-700×700×22	□-750×750×32	H-750×300×16×28
14	□-700×700×22	H-750×500×16×25	□-700×700×22	□-750×750×32	H-750×300×16×28
13	□-700×700×22	H-750×500×16×25	□-700×700×22	□-750×750×32	H-750×300×16×28
12	□-700×700×28	H-750×500×16×25	□-700×700×22	□-750×750×32	H-750×300×16×30
11	□-700×700×28	H-750×500×16×25	□-700×700×22	□-750×750×32	H-750×300×16×30
10	□-700×700×28	H-750×500×16×25	□-700×700×22	□-750×750×32	H-750×300×16×30
9	□-700×700×28	H-750×500×16×28	□-700×700×22	□-750×750×32	H-750×300×16×30
8	□-700×700×28	H-750×500×16×28	□-700×700×22	□-750×750×32	H-750×300×16×30
7	□-700×700×28	H-750×500×16×28	□-700×700×22	□-750×750×32	H-750×300×16×30
6	□-700×700×28	H-750×500×16×28	□-700×700×25	□-750×750×32	H-750×300×16×32
5	□-700×700×28	H-750×500×16×28	□-700×700×25	□-750×750×32	H-750×300×16×32
4	□-700×700×28	H-750×500×16×28	□-700×700×25	□-750×750×32	H-750×300×16×32
3	□-700×700×28	H-750×500×16×28	□-700×700×25	□-750×750×32	H-750×300×16×32
2	□-700×700×28	H-750×500×16×28	□-700×700×25	□-750×750×32	H-750×300×16×32
1	□-700×700×28	H-750×500×16×28	□-700×700×25	□-750×750×32	H-750×300×16×32

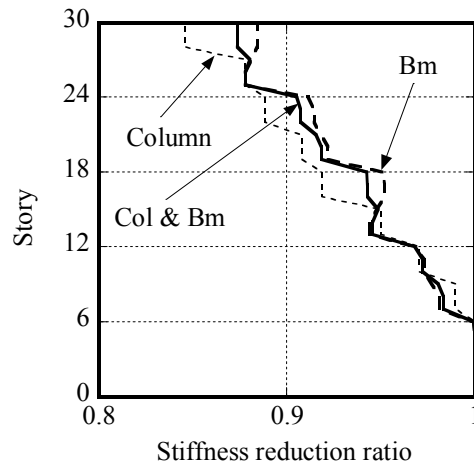


Fig. 5.2 Stiffness reduction ratio of each story of the 30-story building

Table 5.2 (a) Dimensions of beams and columns in the moment frame (unit: mm)

Model	C1	C2	C3	C4	SG1	SG2
5-story	□-500×19 ~22	□-500×350 ×25×28~32	□-500×19 ~22	□-600×32	H-600×300×12 ×22~25	H-1000×300 ×19×32
10-story	□-600×19 ~28	□-650×400 ×16×22~28	□-600×19 ~25	□-650×28 ~32	H-650×300×16 ×25~32	H-900×300 ×19×25
20-story	□-600×19 ~28	□-650×400 ×16×22~28	□-600×19 ~25	□-650×28 ~32	H-700×300×16 ×22~30	H-900×300 ×19×25
30-story	□-700×19 ~28	□-750×500 ×16×22~28	□-700×19 ~25	□-750×28 ~32	H-750×300×16 ×22~32	H-1000×300 ×19×25

Table 5.2 (b) Structural properties of spine frame and BRC hinge, and equivalent stiffness of each component

Models	Spine frame		BRC hinge		Equivalent stiffness		
	EI (kNm ²)	GA (kN)	M_y (kNm)	θ_y (rad)	K_f (kN/m)	K_s (kN/m)	K_d (kN/m)
5-story	2.9×10^8	4.0×10^6	3.0×10^4	0.10%	1.4×10^5	7.0×10^4	1.4×10^5
10-story	9.1×10^8	1.2×10^7	6.4×10^4	0.10%	7.5×10^4	3.8×10^4	7.5×10^4
20-story	2.0×10^9	1.4×10^8	1.3×10^5	0.10%	3.9×10^4	1.2×10^4	3.9×10^4
30-story	6.0×10^9	2.1×10^8	2.6×10^5	0.10%	3.5×10^4	1.0×10^4	3.5×10^4

5.2.2 Variable spine frame configurations

Previous researches on rocking frame system have proposed multiple rocking section and mid-level rocking configurations and verified their advantages in mitigating higher mode effects and reducing force response.^[5.1-7] In this spine frame study, derived from the benchmark

buildings, five different spine configurations were compared in this chapter, as in Fig 5.1 (d). The original benchmark building is named as the continuous single spine (Cnt) model. The corresponding shear wall (SW) model was compared with the Cnt model in the cases of the 5-, 10-, 20-, and 30-story buildings, while the partial spine (Prt), two-segment-spine (Sgt2), and three-segment-spine (Sgt3) models was compared with the Cnt model in the cases of the 20- and 30-story buildings. Concept of the Prt and Sgt structures will be introduced in the later sections.

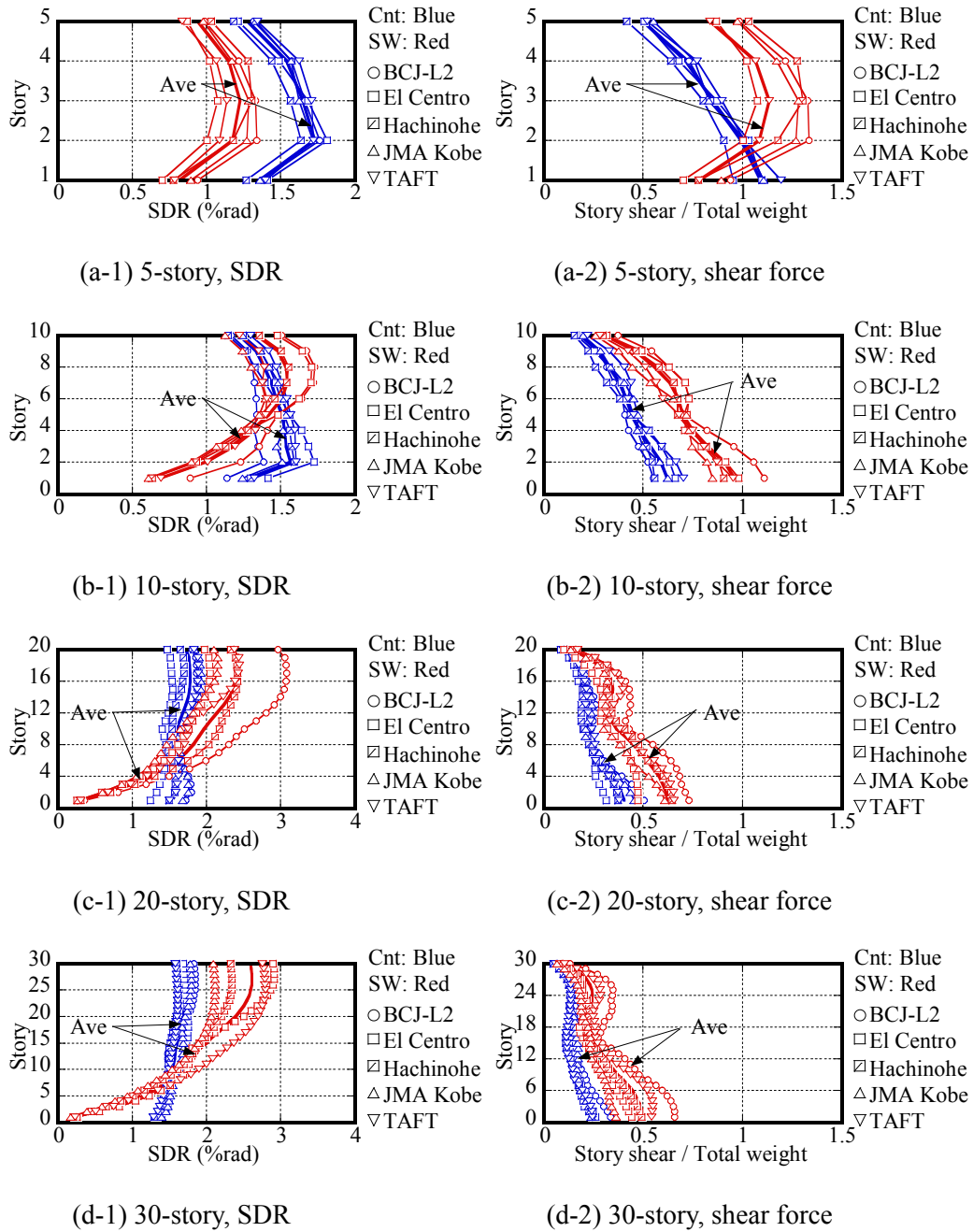


Fig. 5.3 Seismic performance of controlled spine frame models and shear wall models

Member-by-member (MBM) models of the 20- and 30-story benchmark buildings were built in OpenSees. Time-history analysis was carried out to examine their seismic performance. The Level-2 ground motion used herein was the artificial wave BCJ-L2 with duration of 120 s. Time-history analysis results of story drift ratio (SDR) and story shear of the 20- and 30-story buildings along with the 5- and 10-story ones are summarized in Fig 5.3. The natural periods of the first mode are also shown in Fig 5.3.

Maximum SDR of the 5-story and 10-story buildings for Cnt models are less than 1.5% and that of the 20-story and 30-story buildings are less than 2%. The shear force distribution of the 5-story building is almost linear. Higher mode effect is observed in the shear force distribution of the 20-story to 30-story buildings. Except for the SDR results of the 5-story building, both the SDR and shear force response of the controlled continuous spine frame (Cnt) models are smaller than the shear wall (SW) models.

Table 5.3 Value of parameters in different types of models

Sgt3-Ksf0.3-Nb10-20-Kdf1.0-1.0-1.0

①

②

③

④

① Model type

SW: Shear wall Cnt: Continuous spine

Prt: Partial spine model Sgt2: 2 Segmented spines Sgt3: 3 Segmented spines

② Stiffness ratio of the spine and the moment frame

Ksf K_s/K_f

③ Stories of the upper BRCs

(excluded in SW or Cnt model)

Prt / Sgt2: Nb N_{b1}

Sgt3: Nb N_{b1} - N_{b2}

④ Stiffness ratio of the dampers and the moment frame (excluded in SW model)

Cnt / Prt: Kdf K_d/K_f

Sgt2: Kdf K_{d1}/K_f - K_{d2}/K_f

Sgt3: Kdf K_{d1}/K_f - K_{d2}/K_f - K_{d3}/K_f

All	K_s/K_f	0.1	0.3	0.5	0.7	1	2			
Cnt	K_d/K_f	0	0.5	0.8	1	1.3	1.5	2	3	4
Prt	N_{b1}	3~29								
	K_d/K_f	0	0.5	0.8	1	1.3	1.5			
Sgt2	N_{b1}	3~29								
	K_{d1}/K_f	0	0.5	0.8	1	1.3	1.5			
Sgt3	K_{d2}/K_{d1}	0.5	0.8	1						
	N_{b1}	10~20								
Sgt3	N_{b2}	14~28								
	$K_{d1(2,3)}/K_f$	1								

5.2.3 Control parameters

Similar with the previous parametric study, key structural parameters were utilized to compare the seismic performance of each model. Three equivalent stiffness indices proposed in chapter 4 to present the stiffness of the dampers, spine frames, and the moment frames are adopted for the 20- and 30-story buildings herein.

Parametric study conducted in the previous chapter has found that effect of θ_y on the seismic performance of all the buildings was negligible. Therefore in the following discussion, θ_y keeps constant as 0.10%, which is derived from ordinary BRC core steel strength. So the stiffness of BRCs can also measure the strength, or the amount of BRCs. In the benchmark models, $\theta_y=0.1\%$, $K_d/K_f=1.0$, $K_s/K_f=0.5$ in 5- and 10-story buildings while $\theta_y=0.1\%$, $K_d/K_f=1.0$, K_s/K_f

=0.3 in 20- and 30-story buildings. Considering seismic design code and construction requirement, in the parametric study, K_d/K_f ranges from 0.5 to 4.0, and K_s/K_f ranges from 0.1 to 2.0. Table 5.3 summarizes the value of each parameter in different types of models.

5.3 Parametric study of continuous spine frame (Cnt) models

Seismic performance of the continuous spine frame models were compared with the conventional shear wall models. As shown in Fig 5.3, both the SDR and shear force are greatly reduced in the Cnt models against SW models as long as $K_d/K_f=1.0$ and $K_s/K_f=0.3\sim 0.5$ are provided to effectively control the seismic response.

5.3.1 Effect of spine-to-moment frame stiffness ratio

Fig 5.4 demonstrates the effect of the spine-to-moment frame stiffness ratio K_s/K_f on the seismic response of the 5-, 10-, 20-, and 30-story Cnt models, with K_d/K_f held constant at 1.0. As shown in Fig 5.4(a), max SDR decreases as K_s/K_f increases and tends to be constant after K_s/K_f exceeding 1.0. Decreasing in SDR is closely relevant with the uniformity of SDR distribution. Such uniformity can be improved by increasing spine frame stiffness. The improvement is significant when spine frame stiffness increases from a relatively small value, but less effective after the spine frame stiffness exceed some particular value, which is the maximum effective value in terms of reducing SDR. When $K_d/K_f=1.0$, the maximum effective spine frame and moment frame stiffness ratio is 1.0 for 20- and 30-story buildings in this study. Fig 5.5.1 shows effect of K_s/K_f on SDR with different K_d/K_f . When $K_d/K_f \geq 0.5$, the maximum effective K_s/K_f is always approximately 1.0.

From Fig 5.4(b) we can see that, base shear of the 5-story model is relatively independent of K_s/K_f , base shear of the 10-story model increases till K_s/K_f reaches 1.0, while base shear of the 20- and 30-story buildings increases slowly with K_s/K_f increasing. It might be because force responses of higher modes contribute more to the total force response in tall buildings compared to the low buildings, and increasing stiffness of spine frame increases higher-modes base shear. Fig 5.5.2 shows results from other models with different K_d/K_f . We can see that, base shear does not always increase with K_s/K_f . Particularly when K_d/K_f is larger than 2.0, base shear ratio is essentially flat in both 20- and 30-story model after K_s/K_f exceed 1.0. It might be because higher-modes natural period is already in the platform segment of the acceleration response spectrum when $K_s/K_f=1.0$. However, after checking detailed results of natural periods, we found that even when $K_d/K_f=1.0$, second mode natural period of the 20-story Cnt model is as small as 0.47s and 0.36s in case of $K_s/K_f=1.0$ and 2.0, respectively. To figure out the reason of base shear increasing, base shear of moment frames and spine frames of the 20-story Cnt model were separated from the total base shear, as shown in Fig 5.6. We can see that K_s/K_f has little effect on

base shear of moment frames, only base shear of spine frames increases with K_s/K_f increasing. So increasing in the total base shear is mainly caused by the increasing in the spine frames.

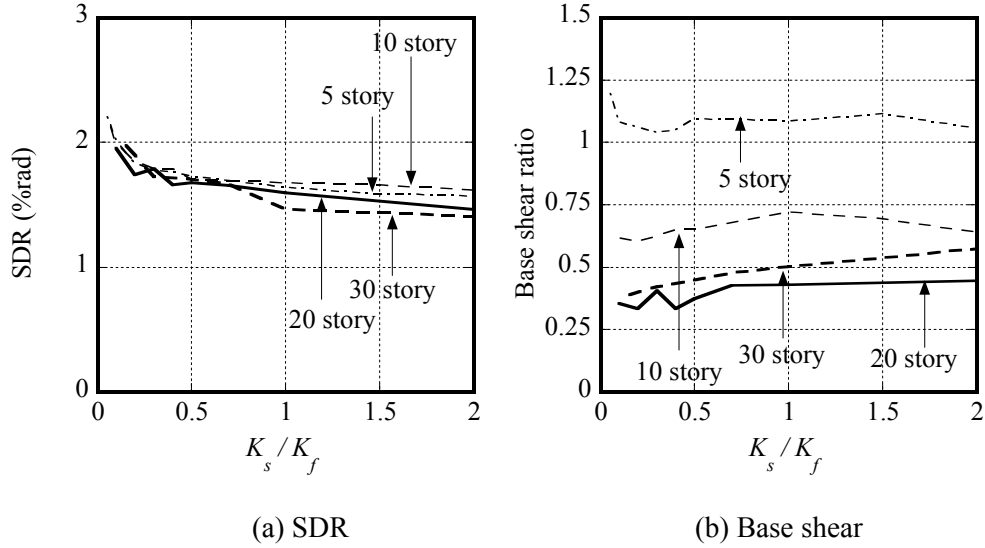


Fig. 5.4 Effect of K_s/K_f on seismic performance of Cnt models ($K_d/K_f=1.0$)

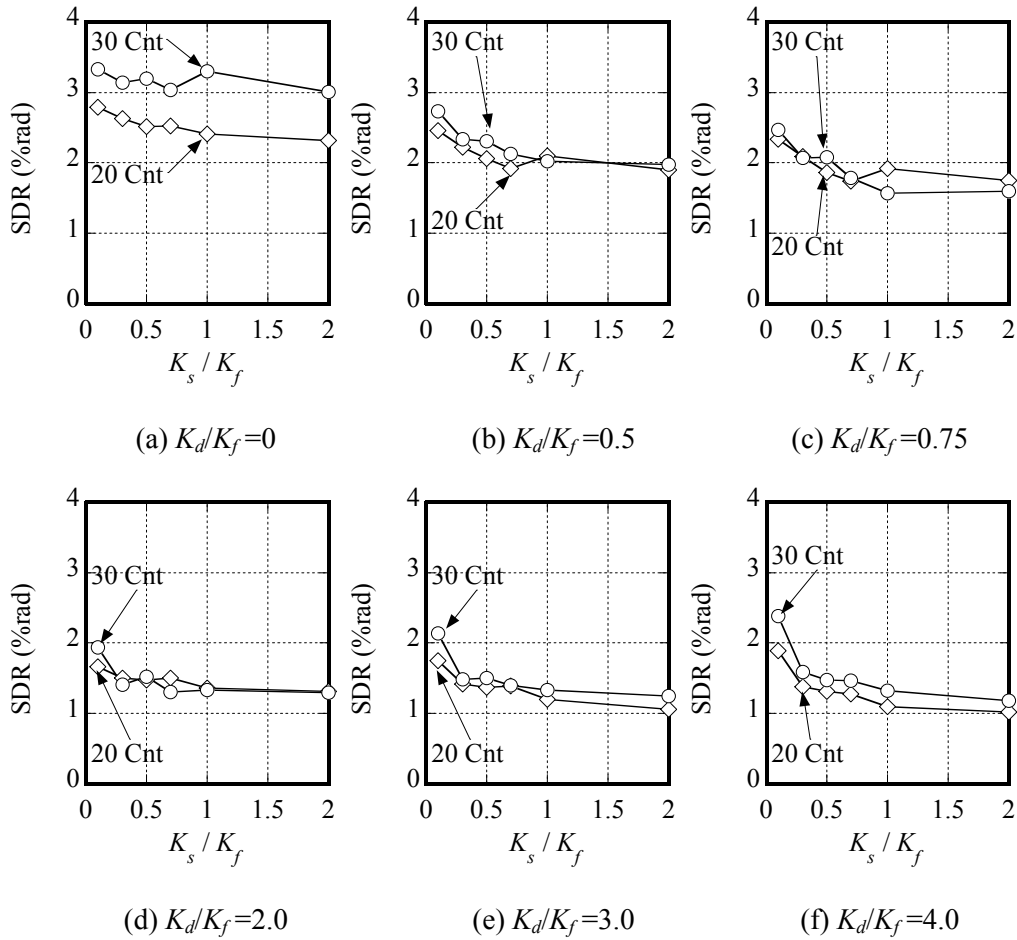


Fig. 5.5.1 Effect of K_s/K_f on SDR of the 20- and 30-story Cnt models

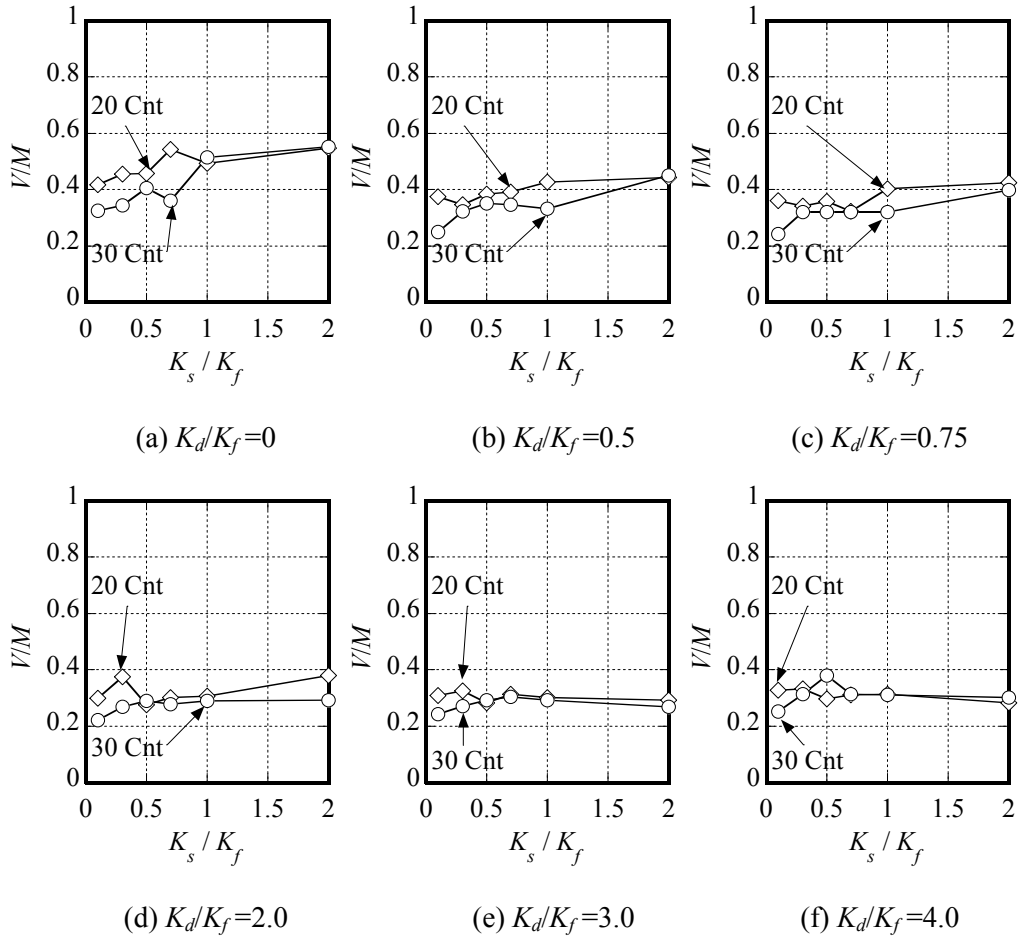


Fig. 5.5.2 Effect of K_s/K_f on base shear ratio of the 20- and 30-story Cnt models

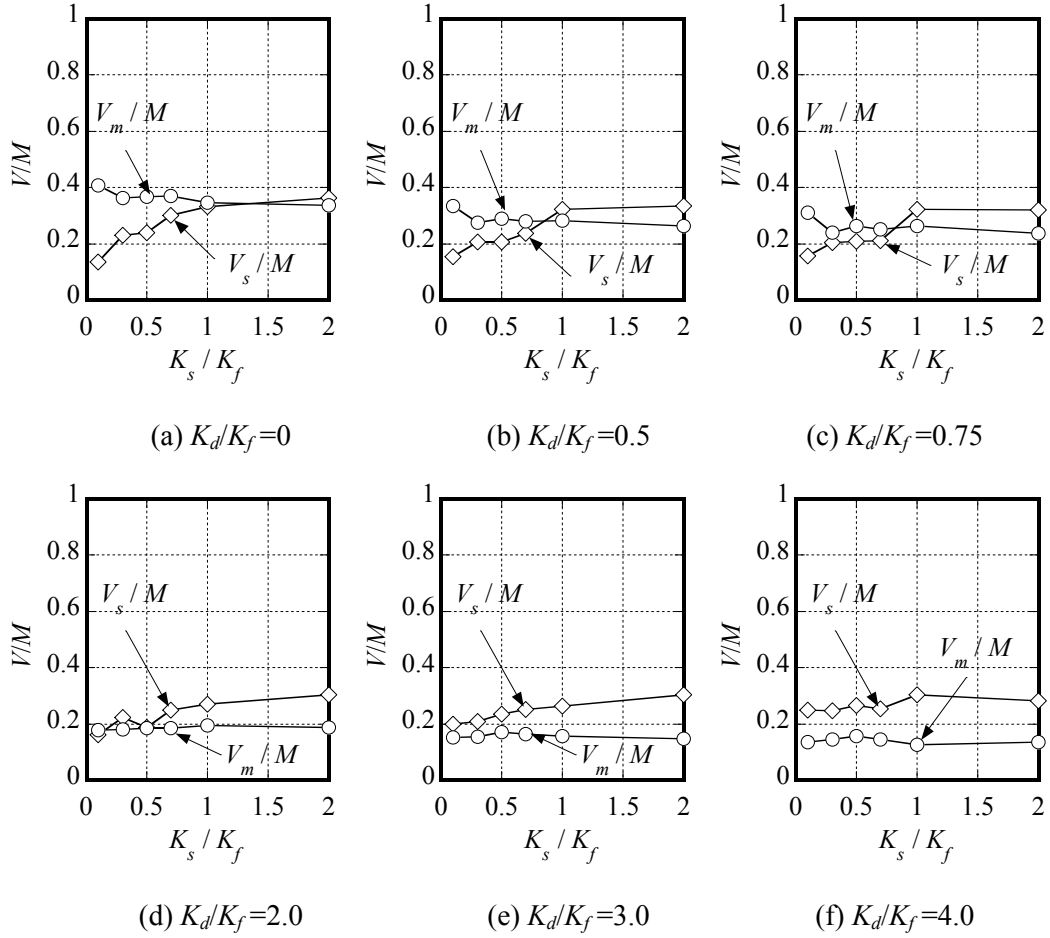
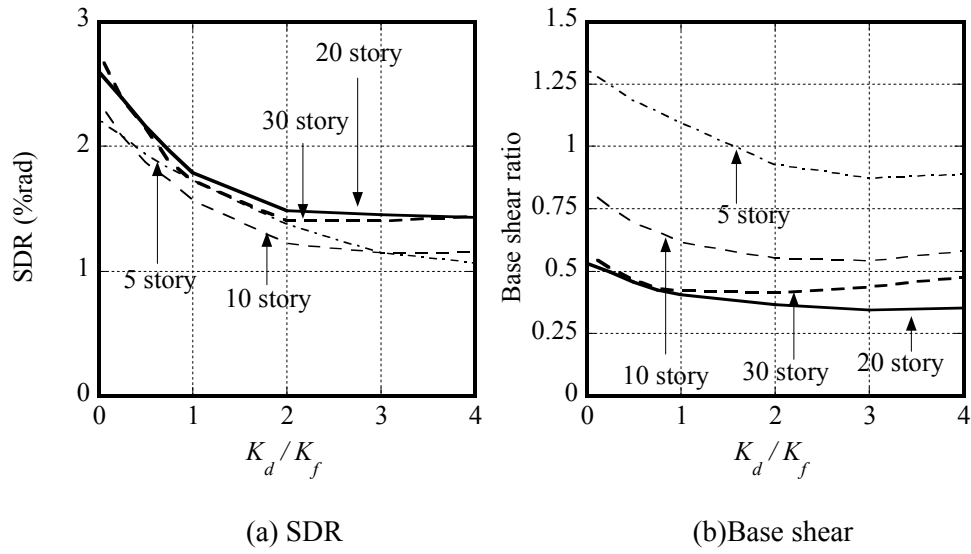
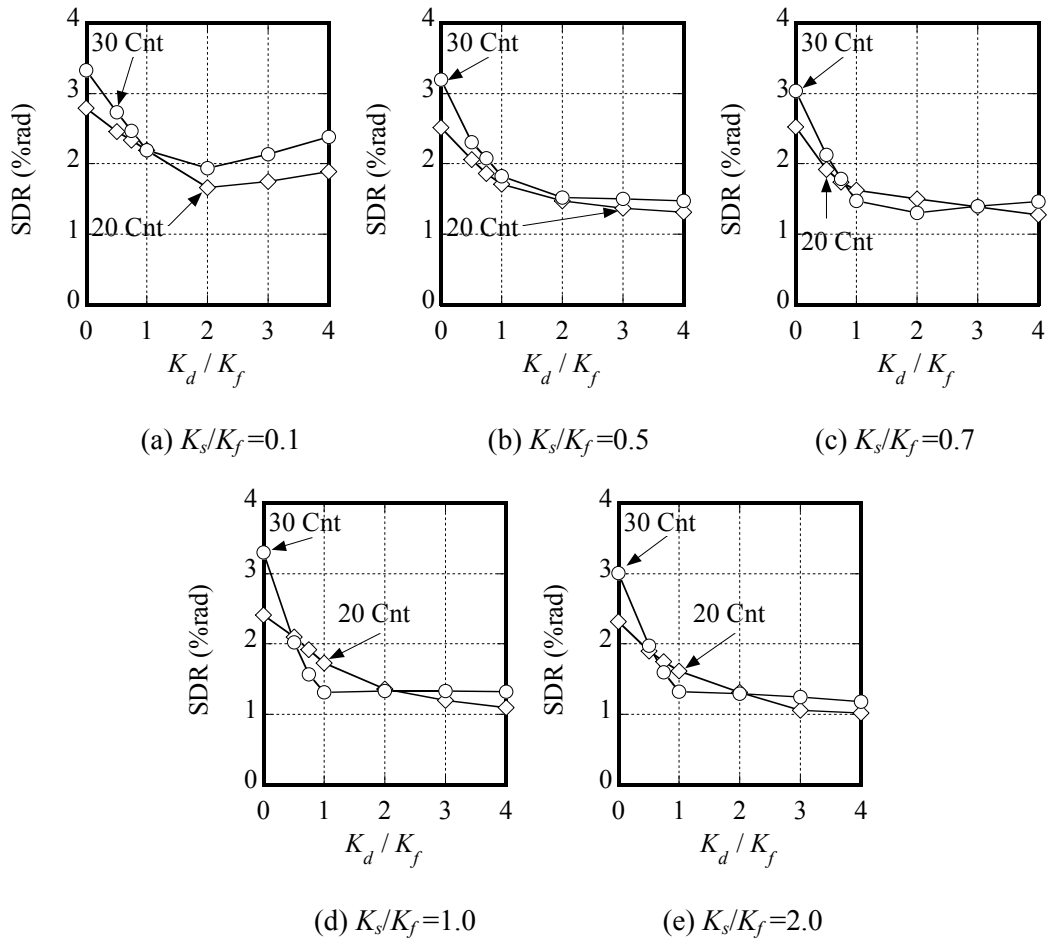


Fig. 5.6 Effect of K_s/K_f on base shear ratio of the spine frame and moment frame in the 20-story Cnt models

5.3.2 Effect of damper-to-moment frame stiffness ratio

Fig 5.7 demonstrates the effect of the damper-to-moment frame stiffness ratio K_d/K_f on the seismic response of the 5-, 10-, 20-, and 30-story Cnt models, with $K_s/K_f=0.5$ in 5- and 10-story models, $K_s/K_f=0.3$ in 20- and 30-story models. Generally, both SDR and base shear of the four models decreases when K_d/K_f increases from 0 to 2.0. Similar phenomenon was observed for the 20- and 30-story models with different K_s/K_f as shown in Fig 5.8.1. Such decreasing is mainly caused by damping effect of BRCs. SDR slightly increased when K_d/K_f was greater than 2.0 and $K_s/K_f=0.1$, indicating that the spine frames were too soft to transfer sufficient deformation on BRCs. Similar with SDR, increasing K_d/K_f also reduced the total base shear despite of the value of K_s/K_f , as shown in Fig 5.8.2. When we check the base shear of spine frames and moment frames separately, as shown in Fig 5.9, base shear of moment frames decrease significantly with K_d/K_f increasing, while base shear of spine frames seems almost irrelevant to K_d/K_f .


 Fig. 5.7 Effect of K_d/K_f on seismic performance of Cnt models ($K_s/K_f = 0.3$)

 Fig. 5.8.1 Effect of K_d/K_f on SDR of the 20- and 30-story Cnt models

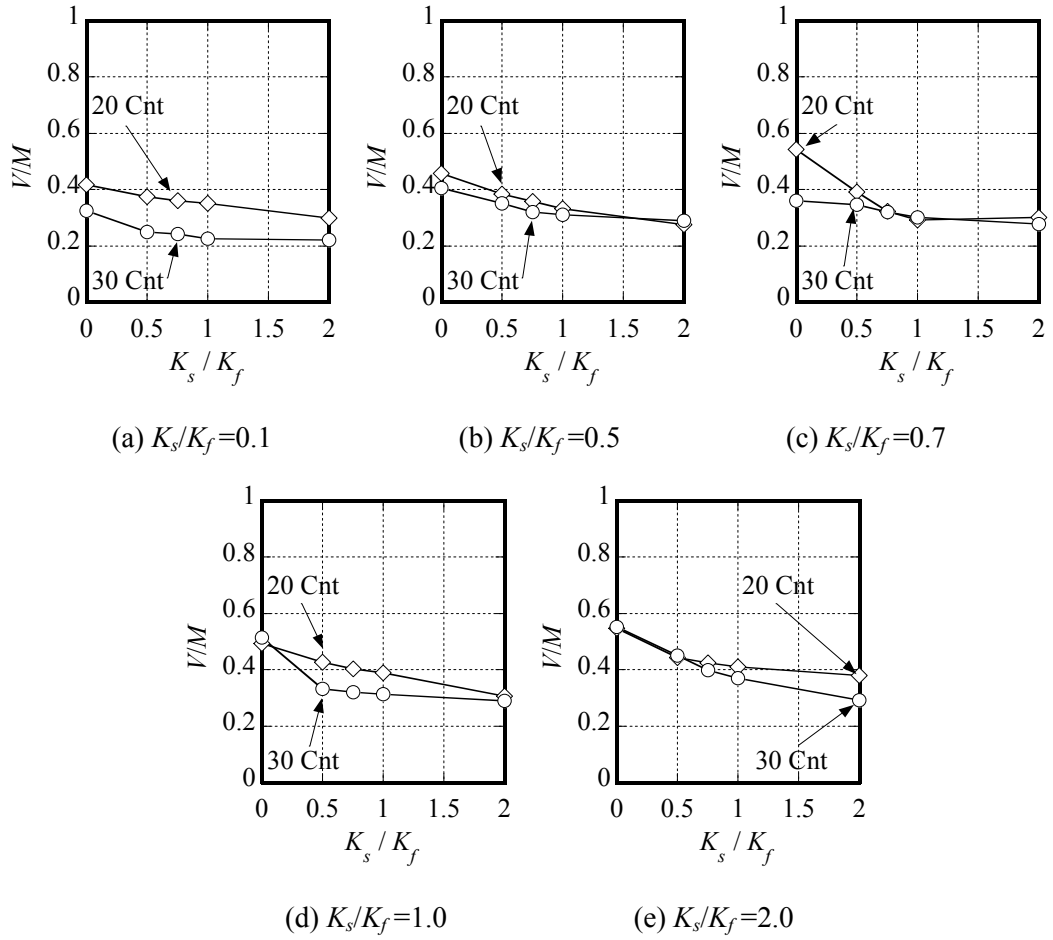


Fig. 5.8.2 Effect of K_d/K_f on base shear ratio of the 20- and 30-story Cnt models

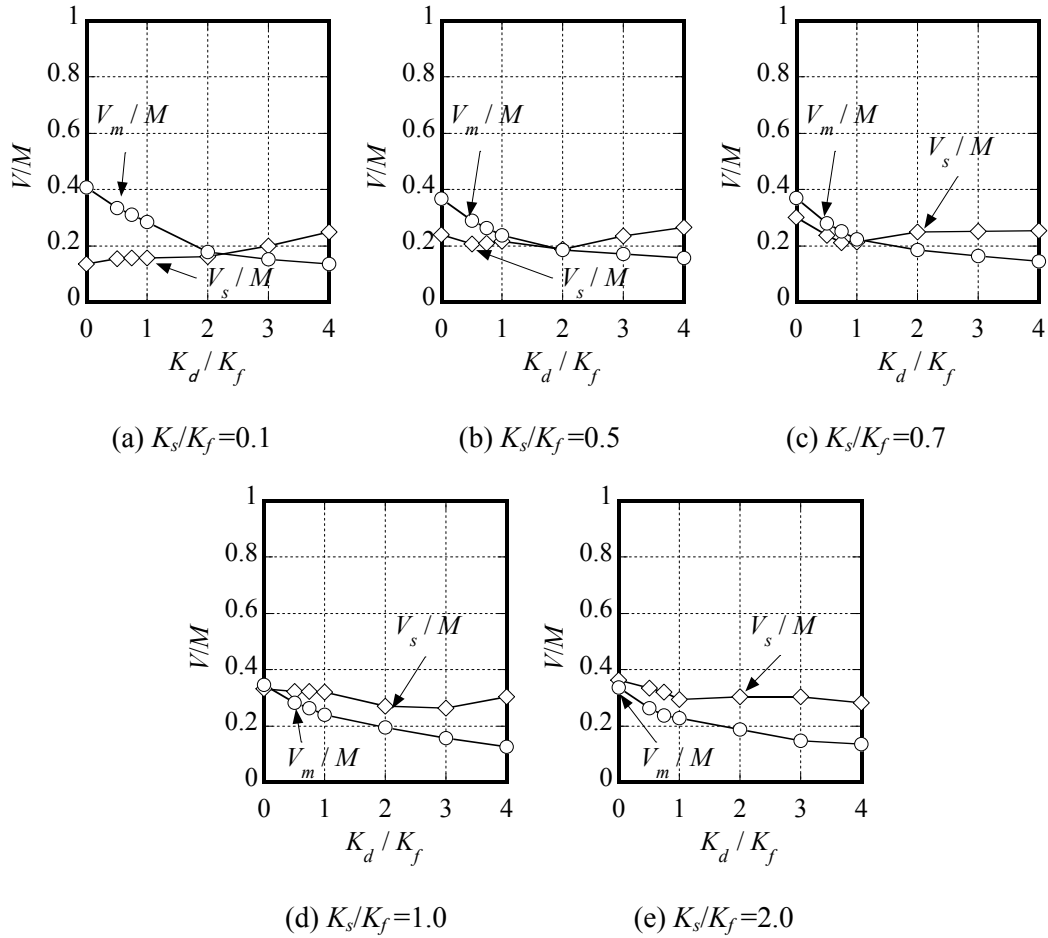


Fig. 5.9 Effect of K_d/K_f on base shear ratio of the spine frame and moment frame in the 20-story Cnt models

5.4 Parametric study of partial spine frame (Prt) models

5.4.1 Concept of Prt model

The continuous spine frames require huge core frames and giant BRCs equipped under the two sides of the core frames, which might be unrealistic in actual practices. To overcome the difficulties, authors attempted two alternative spine frame configurations, the partial spine frame configuration, and the segmented spine frame configuration. Their concepts are illustrated in Fig 5.1 (d). These two alternative configurations were expected to exhibit seismic performance of similar level with the Cnt model, meanwhile to let down the requirement for spine frames and BRCs on stiffness, strength or damping capacity. Similar concepts have been proposed in the past researches for both Sgt spine frames^[5.1-3] and Prt spine frames^[5.4-7]. They found such system could reduce seismic responses and mitigate higher-mode effects. However, most of those studies focused on the spine frame only, but not a dual system. Besides, there is no comparison study between the two systems yet.

In the partial spine frame models, there are two spine frames arranged in series along the height of the structure, the lower one is fixed at the ground level, and the upper one is pin-connected to the center of the lower spine frame with BRCs equipped at two edges. N_{b1} is the number of the story of the first spine frame, and N_{b2} is the sum of story numbers of the first and the second spine frames. Comparison between the Prt model and Cnt model with identical spine frame and BRC amounts has been carried out in this section.

5.4.2 Vibration characteristics of Prt models

Firstly, eigenvalue analysis was carried out for the 20-story Cnt model and Prt models in which the N_{b1} is 5, 10, or 15, with $K_s/K_f=0.3$, $K_d/K_f=1.0$. Table 5.4 lists the results of first three modes, including natural period, percentage of modal effective mass and mode participation factor. Sums of the first three mode effective mass are around 90% for all of the four models. The first three modes natural periods of the Cnt model are the longest among the four models. First mode natural period of the Prt model becomes shorter with the segment story height increasing, indicating the Prt model is getting closer with the SW model. Sums of the modal effective mass and participation factors of the second and third modes in Prt models are slightly larger compared to the Cnt model. Fig 5.10 shows the mode shape, elastic SDR and shear force response of the four models. Generally speaking, difference in maximum elastic responses is negligible. Observable difference exhibited in the mode shape and SDR distribution of the Prt models. Shifting of SDR, i.e. concentrated rotation could be observed at the segment story, particularly in Prt-Nb5 and Prt-Nb10 models.

Table 5.4 Eigenvalue analysis results of the Cnt model and three Prt models

Modes	First mode			Second mode			Third mode		
Models	$T(s)$	$M_{eq}/M(\%)$	β	$T(s)$	$M_{eq}/M(\%)$	β	$T(s)$	$M_{eq}/M(\%)$	β
Cnt	3.02	72	1.45	0.66	17	0.66	0.26	5	0.35
Prt-Nb5	2.80	66	1.44	0.58	17	0.68	0.24	8	0.45
Prt-Nb10	2.67	65	1.46	0.63	19	0.67	0.24	5	0.36
Prt-Nb15	2.64	66	1.46	0.61	16	0.70	0.26	7	0.42

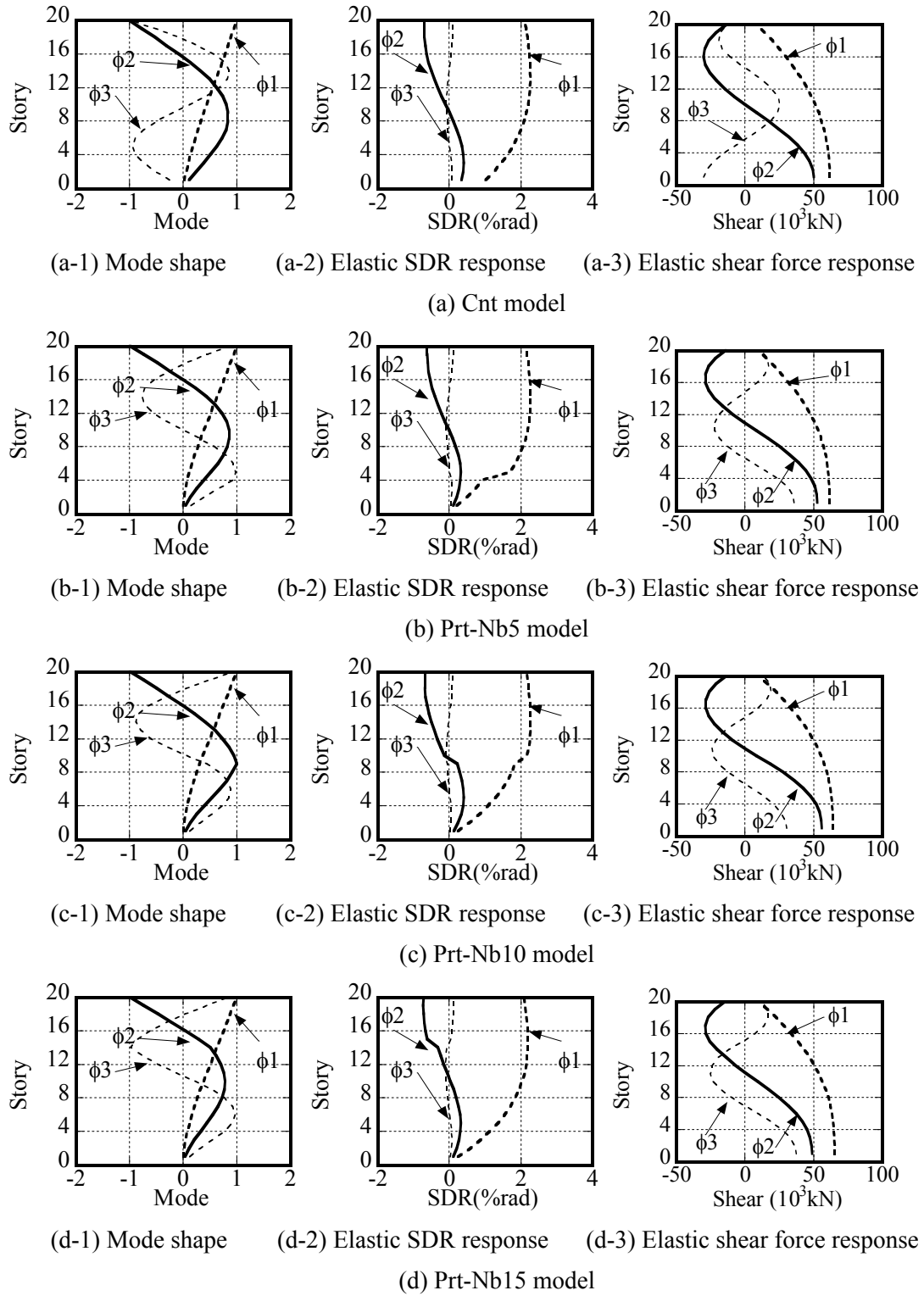


Fig. 5.10 Mode shapes and elastic responses of Prt models

5.4.3 Seismic performance of Prt models

Fig 5.11 (a) shows the SDR distribution of the 20-story Cnt model and Prt models in which the N_{b1} is 5, 10, or 15, with $K_s/K_f=0.3$, $K_d/K_f=1.0$. SDR distribution under the segment story looks similar with the distribution of SW model. When N_{b1} is 5, the SDR shifted by more than 1% to a much larger value at the 5th story, where a concentrated rotation occurred, just like the first story in the Cnt model. When N_{b1} is 10, the shifting amount reduced approximately by half, while the maximum SDR was much larger than the Cnt model. When N_{b1} is 15, shifting in SDR was almost negligible and the overall distribution was quite close to the SW model. The maximum SDR was even larger than the Prt-Nb10 model. It seems that the higher the segment story is, the larger the maximum SDR is.

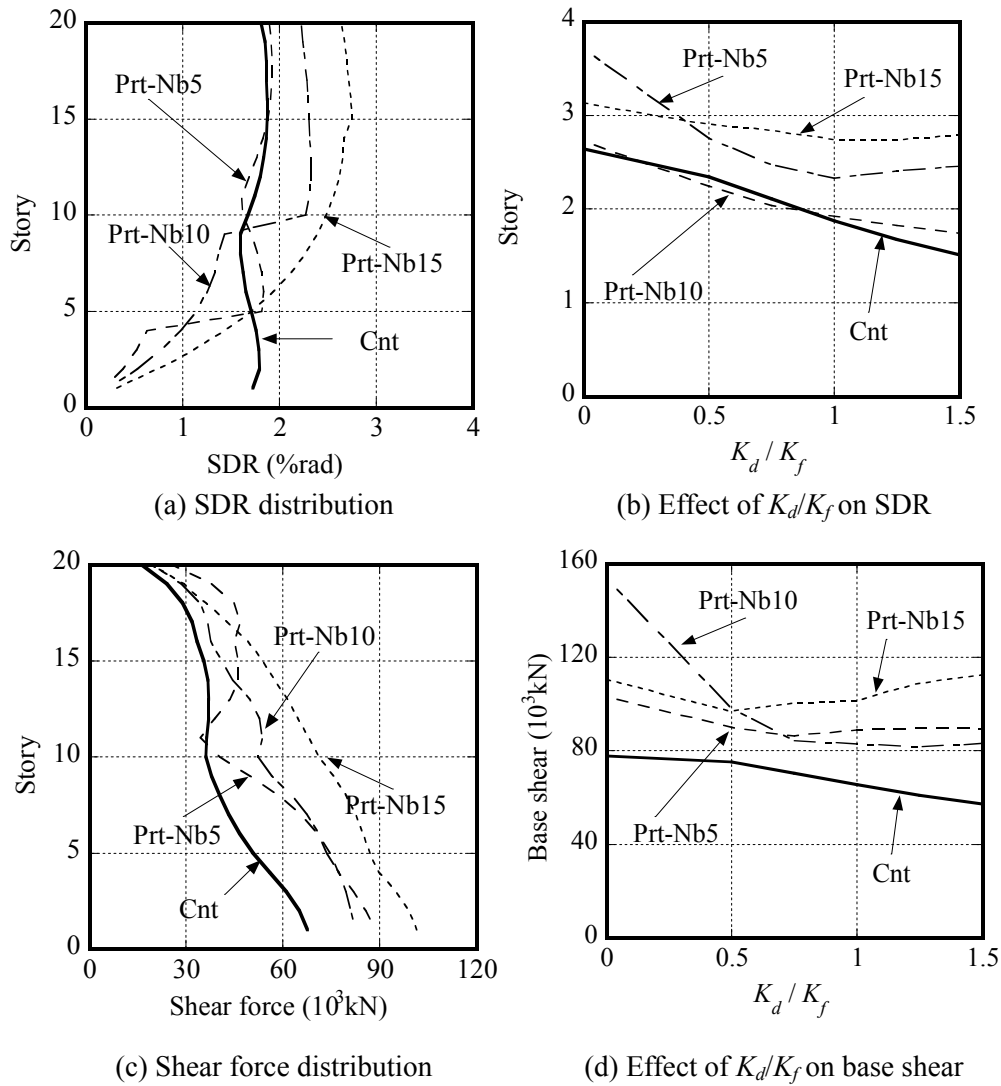


Fig. 5.11 Comparison between 20-story Cnt models and Prt models ($K_s/K_f=0.3$ in (a)~(d), $K_d/K_f=1.0$ in (a) & (c))

To confirm if the seismic performance of Prt model could be enhanced by choosing a different damper amount, various K_d/K_f was tried. Fig 5.11 (b) shows the max SDR results of the Prt-Nb5, Prt-Nb10, Prt-Nb15, and Cnt models with K_d/K_f ranging from 0 to 1.5. The Prt-Nb10 and Prt-Nb15 models exhibit much larger deformation than the Cnt model regardless of how much the damper amount was. Their deformations are even larger than the SW models if without sufficient dampers. The Prt-Nb5 model showed essentially identical SDR results with the Cnt model when K_d/K_f is less than 1.0.

Fig 5.11 (c) and (d) shows the shear force distribution and base shear of the four models with K_d/K_f ranging from 0 to 1.5. Base shear of the Prt-Nb5 and Prt-Nb10 models was smaller than the Cnt model in a very short range of K_d/K_f at around 0.75. On the contrast, when K_d/K_f is smaller than 0.5, base shear of Prt-Nb10 model became significantly large compared to the Cnt model. Similar results were observed on the Prt-Nb15 model when K_d/K_f is larger than 0.5.

The above results indicate that the partial spine frames are not necessarily effective comparing to the continuous spine frames.

5.5 Parametric study of two-segment spine frame (Sgt2) models

5.5.1 Concept of Sgt model

The concept of segmented spine frames is shown in Fig 5.1 (d). In this study, the segmented spine frame models possess two or three spine frames arranged in series along the height of the structure. All of them are pin-connected at the bottom center to the lower spine or to the fundamental structures and with BRCs equipped at both edges.

5.5.2 Vibration characteristics of 20-story Sgt2 models

Firstly, seismic performance of the 2-segment-spine frame (Sgt2) models was investigated based on the 20-story benchmark building. As three typical cases, the Sgt2-Nb5-Kdf1.0-1.0, Sgt2-Nb10-Kdf1.0-1.0, and Sgt2-Nb15-Kdf1.0-1.0 models were compared with the Cnt model in terms of eigenvalue analysis results. K_s/K_f held constant at 0.3.

Table 5.5 Eigenvalue analysis results of the Cnt model and three Sgt2 models

Modes	First mode			Second mode			Third mode		
	T (s)	M_{eq}/M (%)	β	T (s)	M_{eq}/M (%)	β	T (s)	M_{eq}/M (%)	β
Cnt	3.02	72	1.45	0.66	17	0.66	0.26	5	0.35
Sgt2-Nb5	3.09	71	1.44	0.67	18	0.67	0.28	6	0.40
Sgt2-Nb10	3.03	71	1.45	0.72	17	0.64	0.26	5	0.34
Sgt2-Nb15	3.02	72	1.45	0.69	15	0.68	0.29	6	0.38

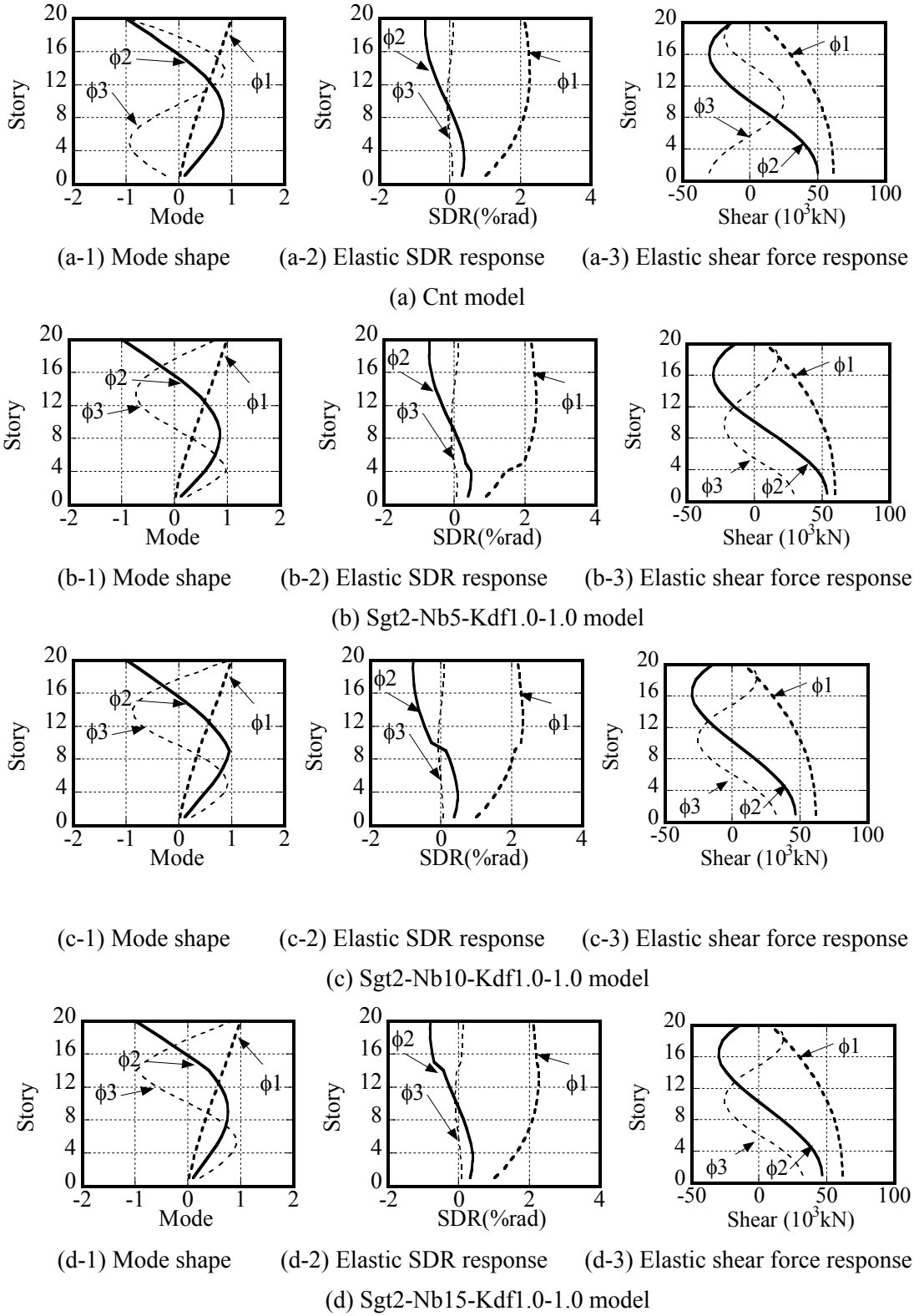


Fig. 5.12 Mode shapes and elastic responses of Sqt2-Nb10 and Nb15 model

Table 5.5 lists the results of first three modes, including natural period, percentage of modal effective mass and mode participation factor. Sums of the first three modes effective mass are around 90% for all of the three Sgt2 models. Generally speaking, difference among the eigenvalue analysis results of the Cnt model and the three Sgt2 models was negligible. Similar with the Prt models, the first mode natural period of the Sgt2 model gets shorter with the segment story height increasing, indicating that the Sgt2 model is getting closer with the Cnt model. The Sgt2-Nb10 model exhibits longest 2nd-mode period, indicating that the 2nd-mode natural period is sensitive to the stiffness of the 10th-story or surrounding stories. The Sgt2-Nb15 model exhibits longest 3rd-mode period, indicating that the 3rd-mode natural period is sensitive to the stiffness of the 15th-story or surrounding stories.

Fig 5.12 shows the mode shape, elastic SDR and shear force response of the four models. Difference in maximum elastic responses is negligible. Observable difference exhibited in the mode shape and SDR distribution of the Sgt2 models. Shifting of SDR, i.e. concentrated rotation could be observed at the segment story, particularly in the 1st-mode of Sgt2-Nb5 model, 1st- and 2nd- modes of Sgt2-Nb10 model, and 2nd-mode of Sgt2-Nb15 model.

5.5.3 Optimal location of segment story of 20-story Sgt2 models

To illustrate effect of the location of the segment story, i.e. location of upper BRCs, eigenvalue analysis and time history analysis of Sgt2 models with various N_{bl} were carried out. Both K_{d1}/K_f and K_{d2}/K_f held constant at 1.0. N_{bl} ranges from 2 to 19 and K_s/K_f varies among 0.1, 0.3, 0.5, 0.7, and 1.0.

Fig 5.13 illustrates the effect of N_{bl} on the maximum SDR and base shear of the whole structure. When K_s/K_f was 0.1, the curves of SDR and base shear were almost flat, indicating that the spine frame is too soft to affect the response of the whole structure. When K_s/K_f was not less than 0.3, the maximum SDRs of Sgt2 models achieved the smallest value when N_{bl} was around 10 ~ 15, but were still similar to that of the Cnt models, as shown in Fig 5.13 (a). From Fig 5.13 (b) we could see that, effect of N_{bl} on base shear was more significant. Base shear of the whole structure reached the smallest value when N_{bl} was around 10 ~ 15, similar with the SDR results. Therefore, in the case of the Sgt2 models with various K_s/K_f , 10th ~ 15th story could be the optimal location for the segment story.

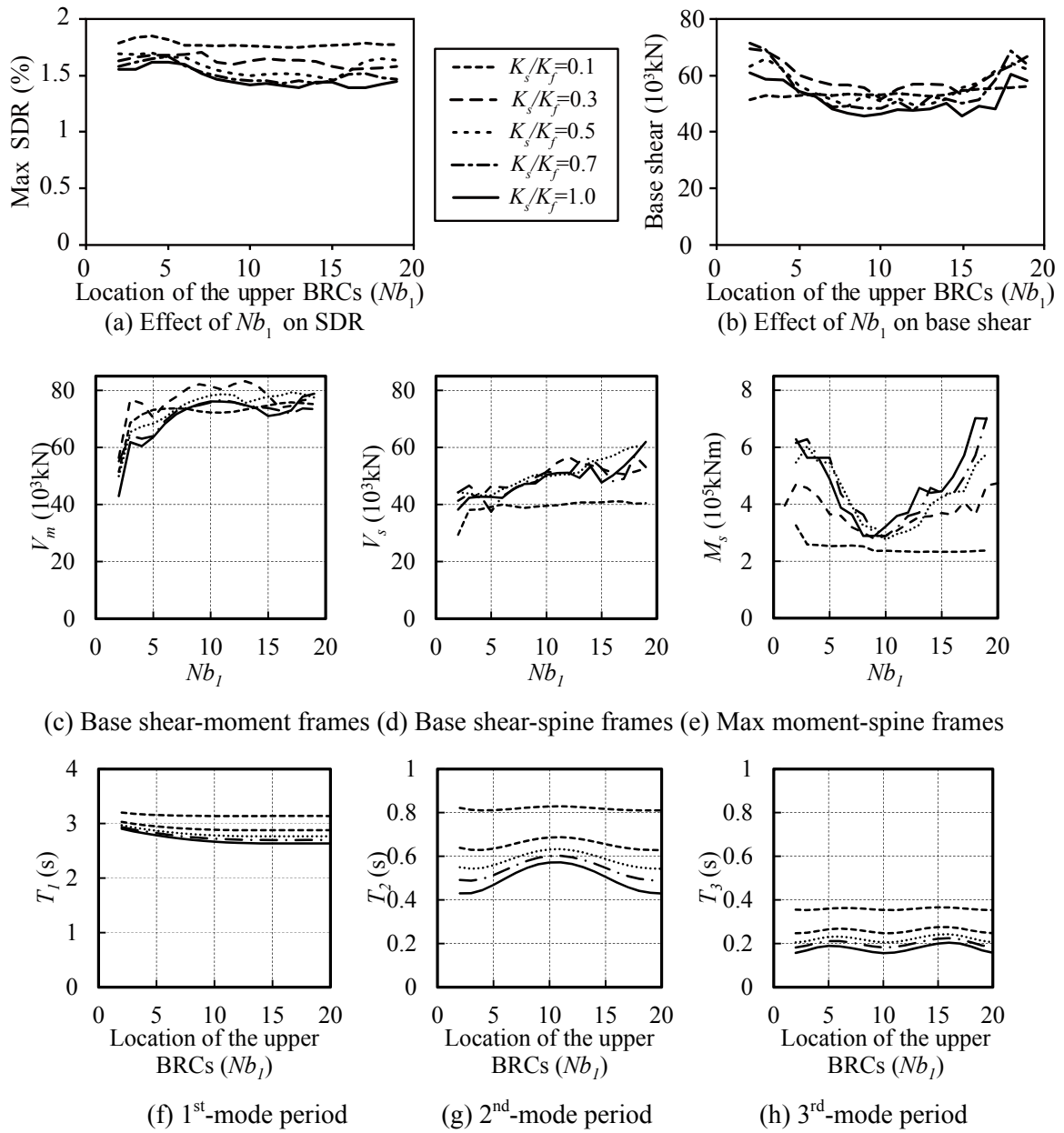


Fig. 5.13 Effect of K_s/K_f and N_{b1} on the seismic performance of the 20-story Sgt2-Kdf1.0-1.0 models

Changing tendency in the base shear of moment frames and spine frames were different from the base shear of the whole structure. No obvious regularity was found for the moment frame, except that the base shear could be largely reduced when the 2nd-story was the segment story. It was mainly because such configuration greatly relieved the constraint at the lower stories of the moment frame, as a consequence the SDR results increased. Base shear of spine frames tended to increase along with the height of the segment story increasing. Maximum “wall base” moment of the spine frames could be significantly reduced by utilizing segmented spine frames,

as in Fig 5.13 (e). Maximum “wall base” moment could decrease by half when the segment story was around 10th story and $K_s/K_f \geq 0.5$. The lowest moment of each Sgt2 model with different K_s/K_f was quite close with each other.

Effect of N_{bl} on the natural period of the first three modes is shown in Fig 5.13 (f-h). The 1st-mode period slightly decreased along with the height of the segment story increasing. The 2nd-mode period reached peak value when the segment story was around 10th story, while the 3rd-mode period reached two peaks when the segment story was around 5th and 15th story. It might be highly related with how the segment configuration changed the modal shapes, as we discussed on Fig 5.12.

5.5.4 Optimal damper amount of 20-story Sgt2 models

In order to search for the optimal damper amount as well as the optimal damper amount ratio between the BRC1 and BRC2, time-history analysis was conducted on two examples among the optimal cases determined from the above discussion, Sgt2-Ksf0.3-Nb10 and Sgt2-Ksf0.3-Nb15 model. Stiffness ratio between BRC1 and the moment frame K_{d1}/K_f varied from 0 to 1.5. Stiffness ratio between BRC2 and BRC1 (defined as R_{kd}) varied among 0.5, 0.75, and 1.0. The concerned results include: maximum SDR, base shear of the whole structure, base shear of moment frames, base shear of spine frames, and “wall base” moment of spine frames.

As for the maximum SDR, the Sgt2-Nb10 model exhibited smaller SDR compared to the Cnt model when K_{d1}/K_f was larger than 0.5, as in Fig 5.14 (a-1). The Sgt2-Nb15 model always gave smaller SDR than the Cnt model, as in Fig 5.14 (a-2). Their smallest results could be achieved when K_{d1}/K_f was around 0.5 – 1.0, which was approximately 10% less than the Cnt model. In both models, the effect of R_{kd} on SDR was negligible. SDR of Sgt2 models was more uniformly distributed along the building height, as in Fig 5.14 (a-3).

As for the base shear of the whole structure, both Sgt2-Nb10 and Sgt2-Nb15 models exhibited smaller base shear compared to the Cnt model. Their smallest results could be achieved when K_{d1}/K_f was around 0.5 – 1.0, which was approximately 30% less than the Cnt model, as in Fig 5.14 (b-1) (b-2). In both models, the effect of R_{kd} on base shear of the whole structure was negligible when K_{d1}/K_f was less than 1.0. When K_{d1}/K_f was larger than 1.0, R_{kd} of 0.5 gave the smallest base shear. Story shear of Sgt2 models was more linearly distributed along the building height compared to the Cnt model, as in Fig 5.14 (b-3).

As for the base shear of moment frames, similar changing tendency with the SDR results could be observed, as in Fig 5.14 (c-1) and (c-2). Their smallest results could be achieved when K_{d1}/K_f was around 0.5 – 1.0, which was approximately 13% less than the Cnt model. Shear force of each story except for the segment story was also slightly reduced compared to the Cnt model, as in Fig 5.14 (c-3).

As for the base shear of spine frames, different from all the above results, both Sgt2-Nb10 and Sgt2-Nb15 models exhibited similar changing tendency along with K_{d1}/K_f increasing. Their smallest results could be achieved when K_{d1}/K_f was around 0.5 – 1.0, which was approximately 20% and 13% less than the Cnt model, as in Fig 5.14 (d-1) (d-2). In both models, the effect of R_{kd} on base shear was negligible when K_{d1}/K_f was less than 1.0. When K_{d1}/K_f was larger than 1.0, R_{kd} of 0.5 gave the smallest base shear. Shear force of each story except for the segment story was significantly reduced compared to the Cnt model, as in Fig 5.14 (d-3).

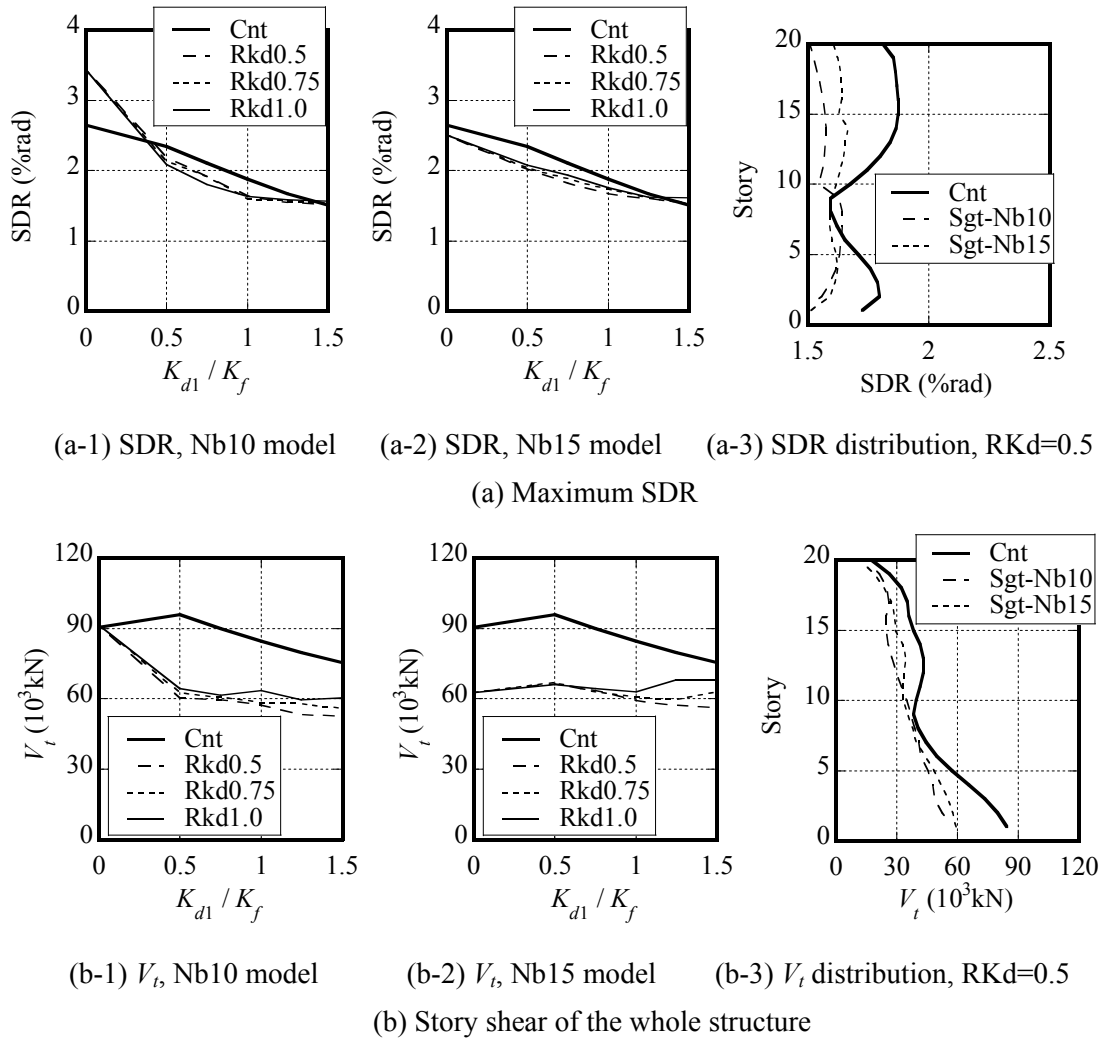
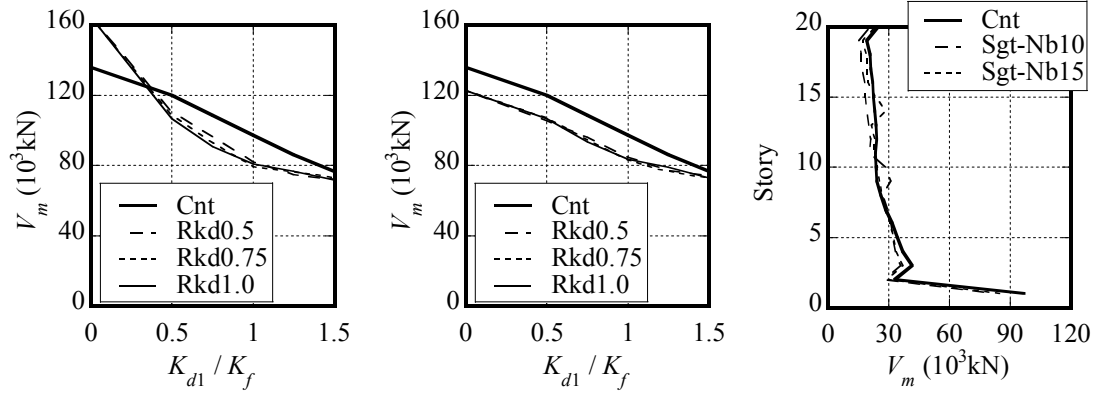


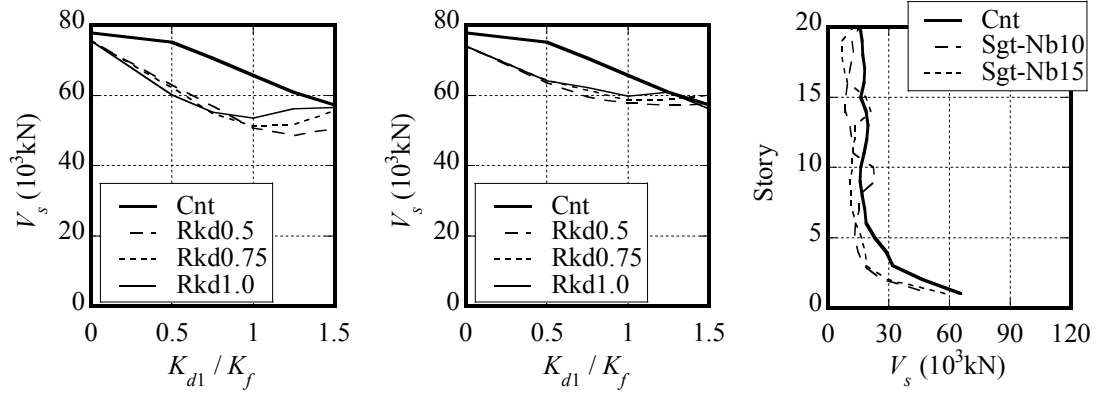
Fig. 5.14 Effect of damper amount and amount ratio between BRC1 and BRC2 on the seismic performance of the Sgt2 models (a, b)


 (c-1) V_m , Nb10 model

 (c-2) V_m , Nb15 model

 (c-3) V_m distribution, RKd=0.5

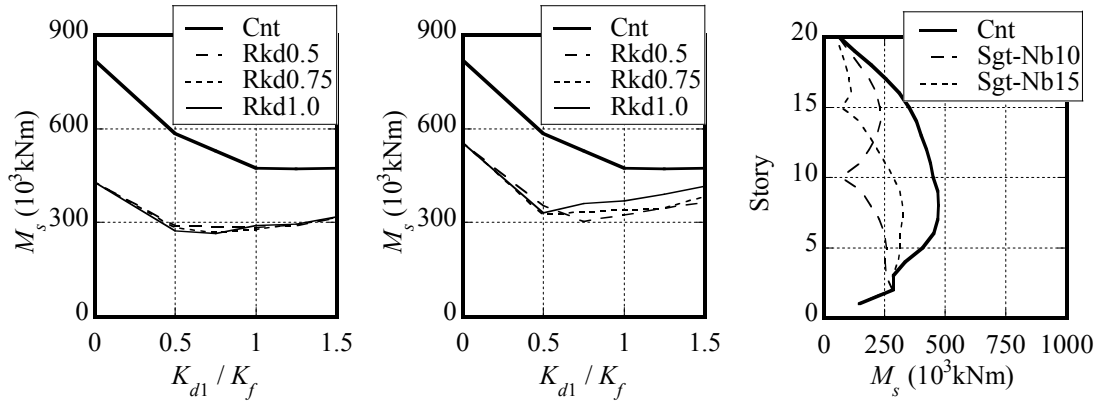
(c) Story shear of moment frames


 (d-1) V_s , Nb10 model

 (d-2) V_s , Nb15 model

 (d-3) V_s distribution, RKd=0.5

(d) Story shear of spine frames


 (e-1) M_s , Nb10 model

 (e-2) M_s , Nb15 model

 (e-3) M_s distribution, RKd=0.5

(e) Moment of spine frames

Fig. 5.14 Effect of damper amount and amount ratio between BRC1 and BRC2 on the seismic performance of the Sgt2 models (c, d, e) (Models used for response distribution are: Sgt2-Ksf0.3-Nb10-Kdf1.0-0.5, Sgt2-Ksf0.3-Nb15-Kdf1.0-0.5, Cnt-Ksf0.3-Kdf1.0)

As for the “wall base” moment of spine frames, both Sgt2-Nb10 and Sgt2-Nb15 models exhibited significantly reduced maximum moment compared to the Cnt model. Their smallest results could be achieved when K_{d1}/K_f was around 0.5 – 1.0, which was approximately 47% and 35% less than the Cnt model, as in Fig 5.14 (e-1, 2). Such difference between Sgt2 and Cnt models decreased with the K_{d1}/K_f increasing. Effect of R_{kd} was negligible when K_{d1}/K_f was less than 0.5. When K_{d1}/K_f was larger than 0.5, R_{kd} of 0.5 gave the smallest base shear. Distribution of “wall base” moment showed the maximum moment reducing of spine frame(Fig 5.14 (e-3)).

Sgt2 and Cnt models possessing same total amount of dampers could also be examined from the results shown by Fig 5.14. In the first two figures showing the effect of K_{d1}/K_f on the maximum response, for instance, the node of $K_{d1}/K_f=0.5$ on the curve of “Rkd1.0” could be compared with the node of $K_{d1}/K_f=1.0$ on the curve of “Cnt”, which were responses of the Sgt2-Kdf0.5-0.5 and Cnt-Kdf1.0 models. They possessed same total amount of dampers. The comparison showed that, although SDR and base shear of moment frames might not be reduced by utilizing the Sgt2 model, base shear of the whole structure and spine frames, as well as maximum moment of spine frames could be significantly reduced compared to the Cnt models.

5.5.5 Vibration characteristics of 30-story Sgt2 models

Seismic performance of the 2-segment-spine frame (Sgt2) models has been investigated based on the 20-story benchmark building. Next, performance of the Sgt2 models was further investigated based on the 30-story benchmark building.

As two typical cases, the 30-story Sgt2-Nb15-Kdf1.0-1.0 and Sgt2-Nb23-Kdf1.0-1.0 models were compared with the Cnt model in terms of eigenvalue analysis results. K_s/K_f held constant at 0.3.

Table 5.6 lists the results of first three modes, including natural period, percentage of modal effective mass and mode participation factor. Sums of the first three mode effective mass are around 90% for all of the three models. Generally speaking, difference among the eigenvalue analysis results of the Cnt model and the Sgt2 models was negligible. Similar with the 20-story models, the first mode natural period of the Sgt2 model gets shorter with the segment story height increasing, indicating that the Sgt2 model is getting closer with the Cnt model. The Sgt2-Nb15 model exhibits longest 2nd-mode period, indicating that the 2nd-mode natural period is sensitive to the stiffness of the 15th-story or surrounding stories. The Sgt2-Nb23 model exhibits longest 3rd-mode period, indicating that the 3rd-mode natural period is sensitive to the stiffness of the 23th-story or surrounding stories.

Fig 5.15 shows the mode shape, elastic SDR and shear force response of the three models. Difference in maximum elastic responses is negligible. Observable difference exhibited in the mode shape and SDR distribution of the Sgt2 models. Shifting of SDR, i.e. concentrated

rotation could be observed at the segment story, particularly in 1st- and 2nd- modes of Sgt2-Nb15 model, and 2nd-mode of Sgt2-Nb23 model.

Table 5.6 Eigenvalue analysis results of the 30-story Cnt model and two Sgt2 models

Modes	First mode			Second mode			Third mode		
Models	T (s)	M_{eq}/M (%)	β	T (s)	M_{eq}/M (%)	β	T (s)	M_{eq}/M (%)	β
Cnt	4.49	70	1.48	0.90	17	0.71	0.34	5	0.37
Sgt2-Nb15	4.52	69	1.49	0.99	18	0.69	0.34	5	0.37
Sgt2-Nb23	4.49	70	1.48	0.93	16	0.74	0.38	6	0.38

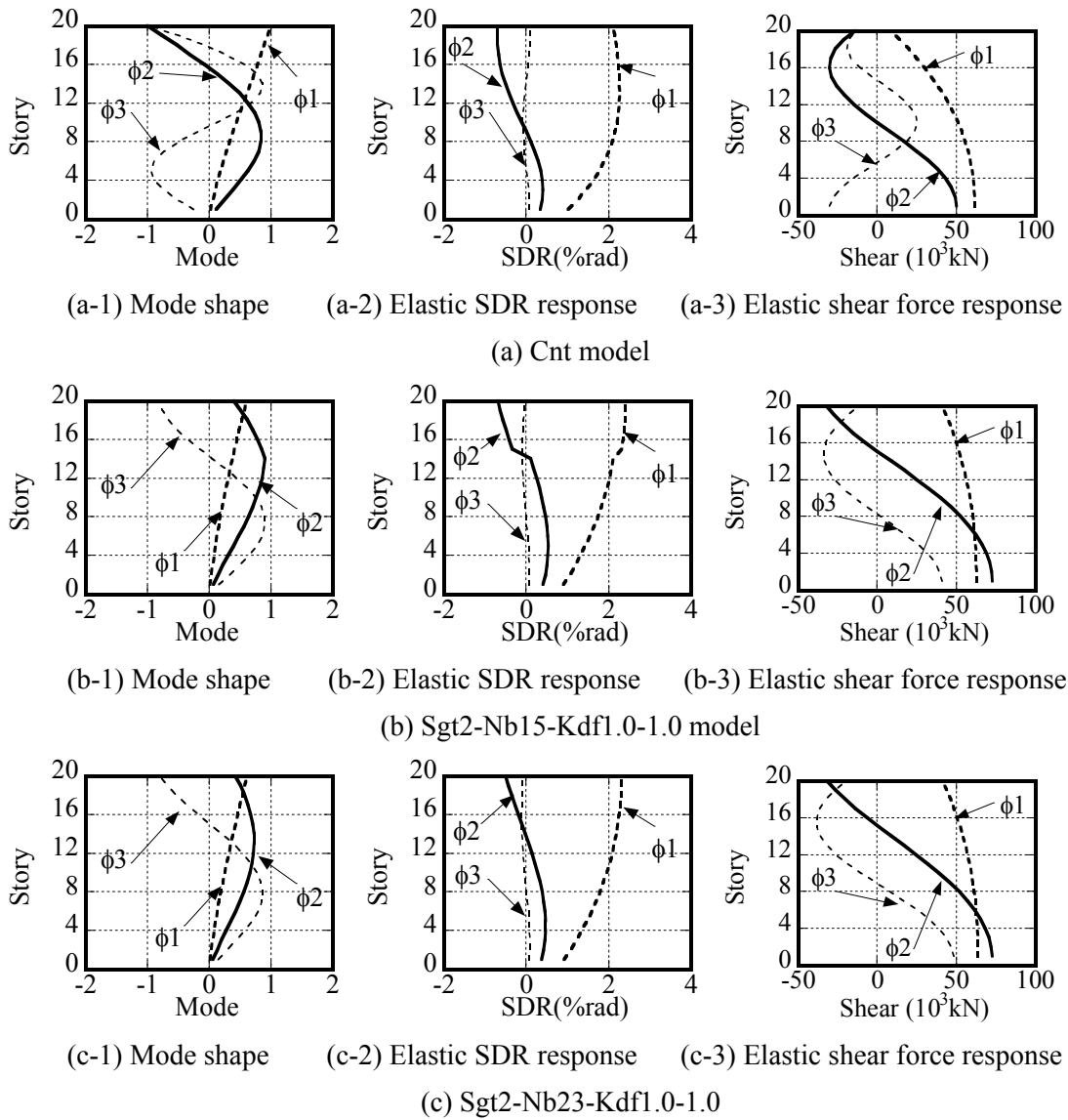


Fig. 5.15 Mode shapes and elastic responses of 30-story Cnt and Sgt2 models

5.5.6 Optimal location of segment story of 30-story Sgt2 models

To illustrate effect of the location of the segment story on seismic performance of 30-story buildings, time history analysis of 30-story Sgt2 models with various N_{b1} were carried out. Both K_{d1}/K_f and K_{d2}/K_f held constant at 1.0. N_{b1} ranges from 2 to 19 and K_s/K_f held constant at 0.3.

Effects of N_{b1} in 30-story models are similar with the 20-story models. As shown in Fig 5.16 (a), influence of N_{b1} on the maximum SDR was obvious. The smallest SDR was achieved when N_{b1} was around 15 - 23. The SDR response was mostly reduced by 15% compared to the Cnt model.

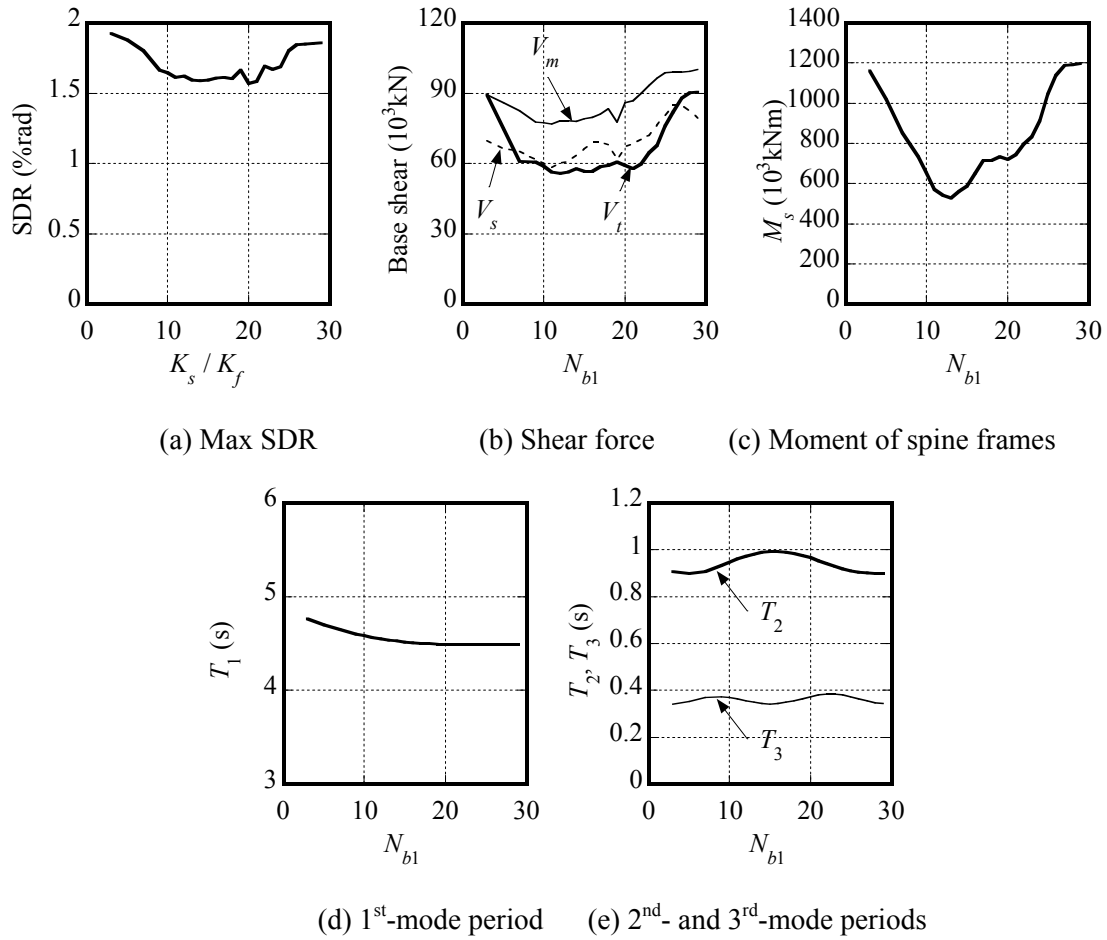
Effect of N_{b1} on the base shear of the 30-story building was also significant, as in Fig 5.16 (b). Similar with the 20-story building, base shear of the whole structure firstly decreased then increased along with N_{b1} increasing. Base shear reached the smallest value when N_{b1} was around 10 - 23.

Changing tendency of the base shear of the spine frames was similar with the 20-story building. It tended to increase along with the height of the segment story increasing. However, base shear of the moment frame achieved smallest value when N_{b1} was around 10, and then increased along with N_{b1} increasing, which was different from the 20-story building. In the 20-story models, no obvious regularity was found for the moment frame.

Maximum “wall base” moment of the spine frames could be significantly reduced by utilizing segmented spine frames, as in Fig 5.16 (c). Maximum “wall base” moment could decrease by more than half when the segment story was around 10th story when $K_s/K_f=0.3$ for the 30-story building.

Effect of N_{b1} on the natural period of the first three modes is shown in Fig 5.16 (d-e). The 1st-mode period slightly decreased along with the height of the segment story increasing. The 2nd-mode period reached peak value when the segment story was around 15th story, while the 3rd-mode period reached two peaks when the segment story was around 10th and 20th story. Similar results were observed from the analysis of 20-story models.

Above all, the optimal value of N_{b1} is 15 - 23, 50%~75% of the total height, in which both the SDR and base shear achieve smallest response. By comparing Fig 5.16 (b-c) and Fig 5.13 (b-e) we could see that, base shear of the whole structure and each component in the 30-story building was approximately 30% higher than the 20-story building, while the maximum moment of the spine frames was almost 100% higher than the 20-story building. This indicates that, for taller buildings, sufficient spine frames could be helpful to control deformation response without significantly increasing the demand on shear strength of the moment frames. However, demand on bending strength of the spine frames might be extremely high when the continuous spine frames are utilized. Segmented spine frames system is promising to solve this problem.

Fig. 5.16 Effect of N_{b1} on seismic performance of 30-story Sgt2 models

5.5.7 Optimal damper amount of 30-story Sgt2 models

In order to search for the optimal damper amount as well as the optimal damper amount ratio between the BRC1 and BRC2 of the 30-story building, time-history analysis was conducted on two examples among the optimal cases determined from the above discussion, Sgt2-Ksf0.3-Nb15 and Sgt2-Ksf0.3-Nb23 models. Same with the 20-story building, stiffness ratio between BRC1 and the moment frame K_{d1}/K_f varied from 0 to 1.5. Stiffness ratio between BRC2 and BRC1 (defined as R_{kd}) varied among 0.5, 0.75, and 1.0. Concerned results include: maximum SDR, base shear of the whole structure, base shear of moment frames, base shear of spine frames, and “wall base” moment of spine frames.

As for the maximum SDR, the Sgt2-Nb15 and Sgt2-Nb23 models exhibited smaller SDR compared to the Cnt model when K_{d1}/K_f was larger than 0.5. Their smallest results could be achieved when K_{d1}/K_f was around 0.5 – 1.0, which was approximately 10% less than the Cnt model, as in Fig 5.17 (a-1) (a-2). In both models, the effect of R_{kd} on SDR was negligible. SDR of Sgt2 models was more uniformly distributed along the building height, except for the

concentrated rotation at the segment story, as in Fig 5.17 (a-3).

As for the base shear of the whole structure, both Sgt2-Nb10 and Sgt2-Nb15 models exhibited much smaller base shear compared to the Cnt model. Their smallest results could be achieved when K_{d1}/K_f was around 0.5 – 1.0, which was approximately 30% less than the Cnt model, as in Fig 5.17 (b-1) (b-2). Effect of R_{kd} was more significant on base shear of the 30-story building compared to the 20-story building. In the Sgt2-Nb15 model, when K_{d1}/K_f was smaller than 1.0, $R_{kd} = 1.0$ gave the smallest base shear; when K_{d1}/K_f was larger than 1.0, $R_{kd} = 0.5$ gave the smallest base shear. In the Sgt2-Nb23 model, $R_{kd} = 0.5$ gave the smallest base shear despite of the value of K_{d1}/K_f . Story shear of Sgt2 models was more linearly distributed along the building height compared to the Cnt model, as in Fig 5.17 (b-3).

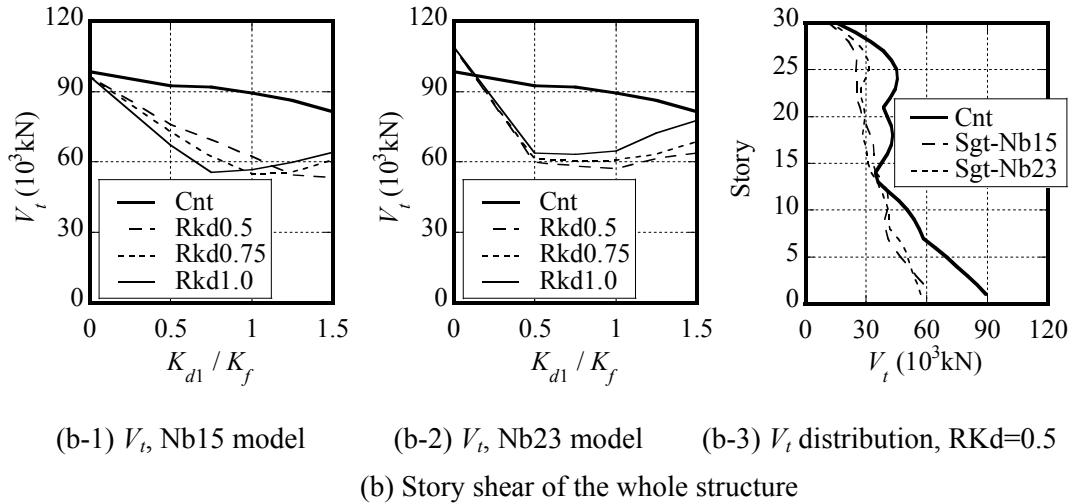
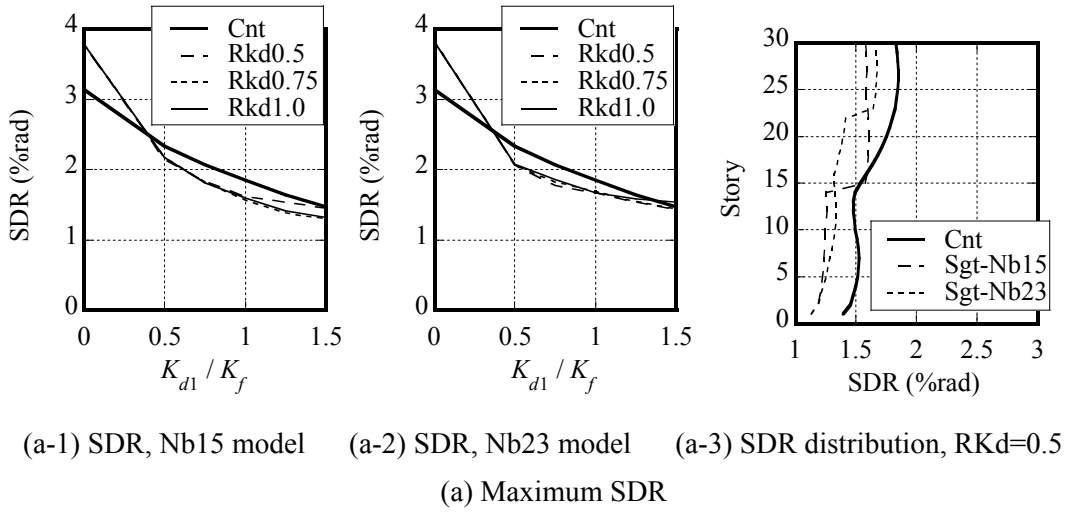
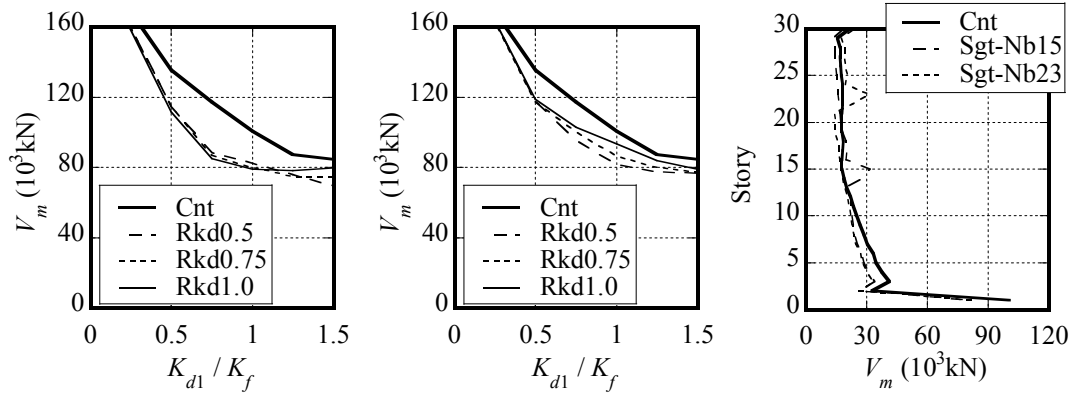
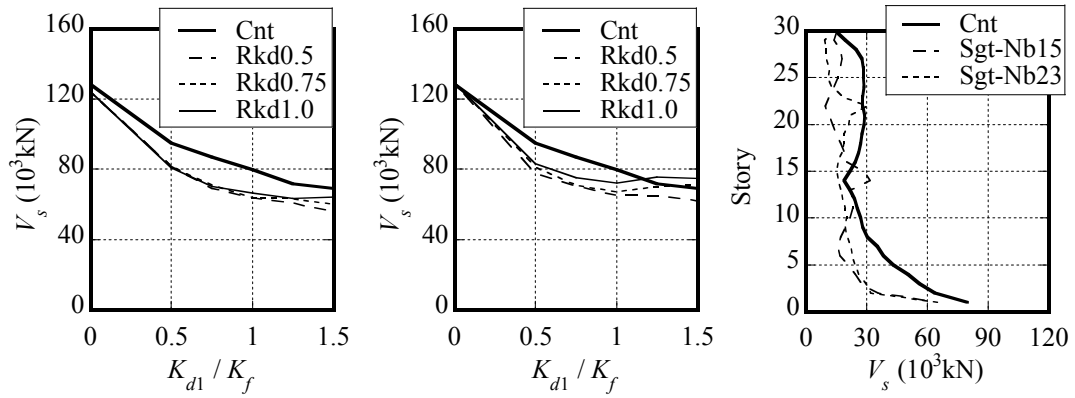


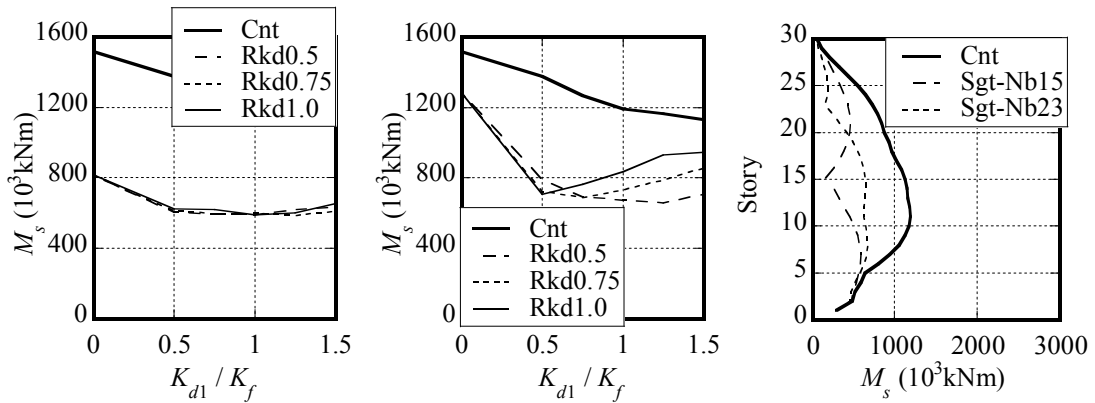
Fig. 5.17 (a, b) Effect of damper amount and amount ratio between BRC1 and BRC2 on seismic performance of 30-story Sgt2 models

(c-1) V_m , Nb15 model(c-2) V_m , Nb23 model(c-3) V_m distribution, RKd=0.5

(c) base shear of moment frames

(d-1) V_s , Nb15 model(d-2) V_s , Nb23 model(d-3) V_s distribution, RKd=0.5

(d) Story shear of spine frames

(e-1) M_s , Nb15 model(e-2) M_s , Nb23 model(e-3) M_s distribution, RKd=0.5

(e) Moment of spine frames

Fig. 5.17 (c, d, e) Effect of damper amount and amount ratio between BRC1 and BRC2 on seismic performance of 30-story Sgt2 models (Model showing distribution are: Sgt2-Ksf0.3-Nb15-Kdf1.0-0.5, Sgt2-Ksf0.3-Nb23-Kdf1.0-0.5, and Cnt-Ksf0.3-Kdf1.0)

As for the base shear of moment frames, the Sgt2 models exhibit smaller base shear compared to the Cnt model and reached the smallest value when K_{d1}/K_f was around 1.0-1.5, which was approximately 20% and 14% less than the Cnt model, as in Fig 5.17 (c-1) and (c-2). Shear force of each story except for the segment story was also slightly reduced compared to the Cnt model, as in Fig 5.17 (c-3).

As for the base shear of spine frames, both Sgt2-Nb10 and Sgt2-Nb15 models exhibited smaller results than the Cnt model. Smallest results were achieved when K_{d1}/K_f was around 1.0-1.5, which was approximately 16% less than the Cnt model, as in Fig 5.17 (d-1) (d-2). In Sgt2-Nb15 model, effect of R_{Kd} on base shear of spine frames was negligible when K_{d1}/K_f was less than 1.0. When K_{d1}/K_f was larger than 1.0, R_{Kd} of 0.5 gave the smallest base shear. In Sgt2-Nb23 model, R_{Kd} of 0.5 always gave the smallest base shear. Shear force of the spine frames at each story except for the segment story was significantly reduced compared to the Cnt model, as in Fig 5.17 (d-3).

As for the “wall base” moment of spine frames, both Sgt2-Nb15 and Sgt2-Nb23 models exhibited significantly reduced maximum moment compared to the Cnt model, as in Fig 5.17 (e-1) (e-2). Smallest moment was reached when K_{d1}/K_f was around 1.0-1.5, which was approximately 50% and 40% less than the Cnt model. Such difference became less significant in the Sgt2-Nb23 model when K_{d1}/K_f was 1.5. Effect of R_{Kd} was negligible in the Sgt2-Nb15 model, while it was significant in the Sgt2-Nb23 model when K_{d1}/K_f was larger than 0.5, in which R_{Kd} of 0.5 gave the smallest moment. Distribution of “wall base” moment was showed in Fig 5.17 (e-3).

Sgt2 and Cnt models possessing same total amount of dampers were also compared based on Fig 5.17. Although SDR and base shear of moment frames might not be reduced by utilizing the Sgt2 model, base shear of the whole structure and spine frames, as well as maximum moment of spine frames could be significantly reduced compared to the Cnt models.

5.6 Parametric study of three-segment spine frame (Sgt3) models

Seismic performance of the 2-segment-spine frame (Sgt2) models has been investigated based on the 20- and 30-story benchmark buildings. In this section, seismic performance of the 3-segment-spine frame (Sgt3) models was investigated based on the 30-story benchmark building.

5.6.1 Vibration characteristics of Sgt3 models

The 30-story Sgt3-Nb10-20-Kdf1.0-1.0-1.0 and Sgt3-Nb16-23-Kdf1.0-1.0-1.0 models were compared with the Sgt2-Nb15-Kdf1.0-1.0 model in terms of eigenvalue analysis results. K_s/K_f held constant at 0.3.

Table 5.7 Eigenvalue analysis results of a Sgt2 model and two Sgt3 models

Modes	First mode			Second mode			Third mode		
Models	T (s)	M_{eq}/M (%)	β	T (s)	M_{eq}/M (%)	β	T (s)	M_{eq}/M (%)	β
Sgt2-Nb15	4.52	69	1.49	0.99	18	0.69	0.34	5	0.37
Sgt3-Nb10-20	4.59	69	1.48	1.00	18	0.72	0.41	6	0.37
Sgt3-Nb16-23	4.51	69	1.49	1.02	17	0.72	0.38	6	0.38

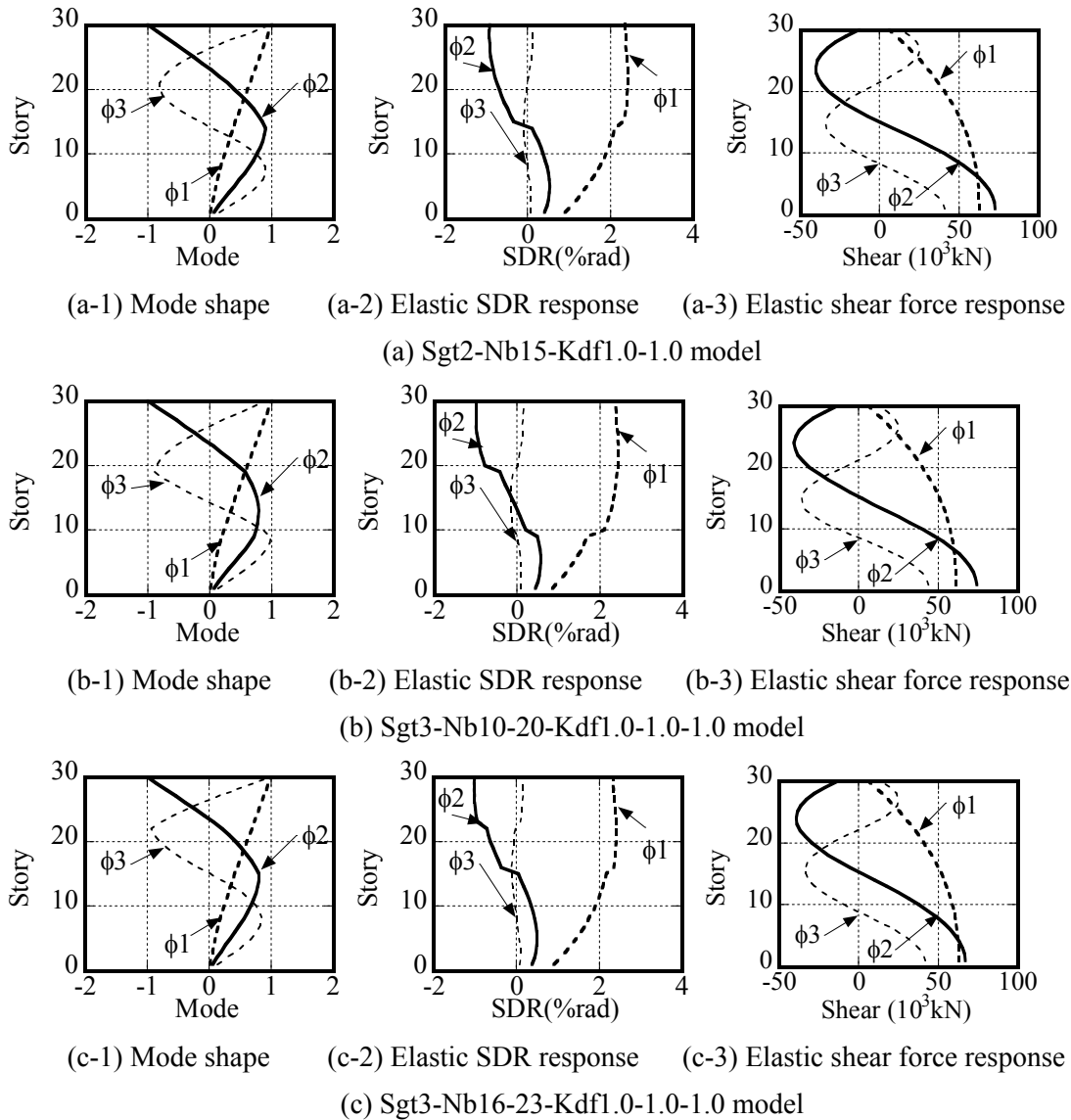


Fig. 5.18 Mode shapes and elastic responses of 30-story Sgt2 and Sgt3 models

Table 5.7 lists the results of first three modes, including natural period, percentage of modal effective mass and mode participation factor. Sums of the first three mode effective mass are around 90% for all of the three models. Generally speaking, difference among the eigenvalue analysis results of the Sgt2 model and the Sgt3 models was negligible due to the sufficient elastic stiffness of BRCs.

By comparing Sgt2-Nb15-Kdf1.0-1.0 and Sgt3-Nb16-23-Kdf1.0-1.0-1.0 we can see that, their first mode periods were quite close, while higher-modes periods of the latter were slightly longer than the former because of the additional segment story.

Fig 5.18 shows the mode shape, elastic SDR and shear force response of the three models. Difference in the maximum elastic responses is negligible. Shifting of SDR, i.e. concentrated rotation at the lower segment story could be observed in the 1st- and 2nd- modes of the Sgt3 models, while the concentrated rotation at the upper segment story could only be observed in the 2nd-mode of the Sgt3 models.

5.6.2 Optimal locations of segment stories

To illustrate effect of the locations of the two segment stories on the seismic performance of the Sgt3 models, eigenvalue analysis and time history analysis of the 30-story Sgt3 models with various N_{b1} and N_{b2} were carried out. Both K_{d1}/K_f and K_{d2}/K_f held constant at 1.0. N_{b1} ranged from 10 to 20; N_{b2} ranged from $N_{b1} + 4$ to 28; K_s/K_f held constant at 0.3.

Effect of N_{b2} was almost negligible on both deformation and force results except for the maximum moment of spine frames, as shown in Fig 5.19. It might be because the yielding drift or elastic stiffness of the BRC3 was too large to generate additional damping effect. Effect of the yielding drift and elastic stiffness of the BRC3 will be demonstrated in the later sections. The changing tendency of seismic performances exhibited in Fig 5.20 was still meaningful since it could be more obvious with a different suit of characteristics for BRC3.

Figures in group (1) showed detailed results of the model with different N_{b1} and N_{b2} , each line represented models with same N_{b1} . Figures in group (2) compared the analysis results of the Sgt2 models and the smallest results among all the Sgt3 models with same N_{b1} .

Changing tendency of each seismic response along with N_{b2} was related with the value of N_{b1} . For example, the deformation result firstly increased and then decreased with N_{b2} increasing when N_{b1} was 10-12; firstly decrease and then increased with N_{b2} increasing when N_{b1} was small when N_{b1} was 14-16; decreased monotonically when N_{b1} was 18-20, as in Fig 5.19 (a-1).

From these figures in group (2) we could see that the Sgt3 spine frame system was possible to further reduce both deformation and force results compared to the Sgt2 configuration. Reduction ratios were 1.3%, 3%, 5.7%, 5.7% in the SDR, base shear of the whole structure, base shear of moment frames and base shear of spine frames, while the reduction ratio in the

maximum moment of spine frame was as large as 15%.

Among the Sgt3 models, those exhibited the smallest results of SDR, V_t , V_m , V_s , M_s were Sgt3-Nb16-20, Sgt3-Nb10-14, Sgt3-Nb12-18, Sgt3-Nb10-20, Sgt3-Nb10-20. Among the Sgt2 models, those exhibited the smallest results of SDR, V_t , V_m , V_s , M_s were Sgt2-Nb20, Sgt2-Nb12, Sgt2-Nb10, Sgt2-Nb12, Sgt2-Nb12. We could preliminarily determine that, in both 2 segments and 3 segments models, N_{b1} around 10 always produced the smallest force results, while the smallest deformation results were often given by higher segment story, i.e. N_{b1} around 20 in Sgt2 models and 16 in Sgt3 models. In the 3 segments models, N_{b2} around 20 always produced both the smallest deformation and force results.

Effect of N_{b2} with different N_{b1} on the natural period of the first three modes is shown in Fig 5.19 (f-1) – (f-3). Regardless of the value of N_{b1} , N_{b2} had less influence on the 1st-mode period, while the 2nd-mode period reached peak value when N_{b2} was around 15 and the 3rd-mode period reached peak when N_{b2} was around 23.

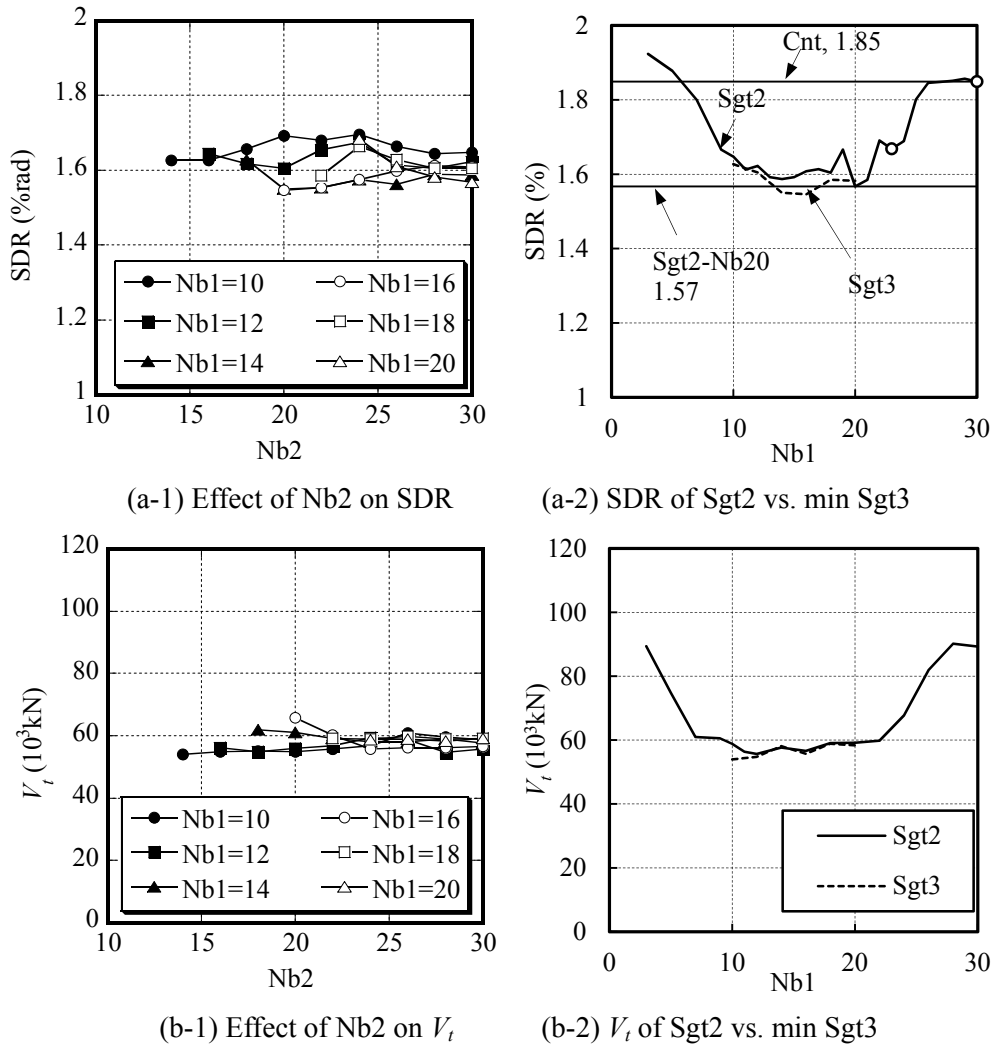


Fig. 5.19 (a, b) Effect of N_{b1} and N_{b2} on SDR and V_t of 30-story Sgt3 models

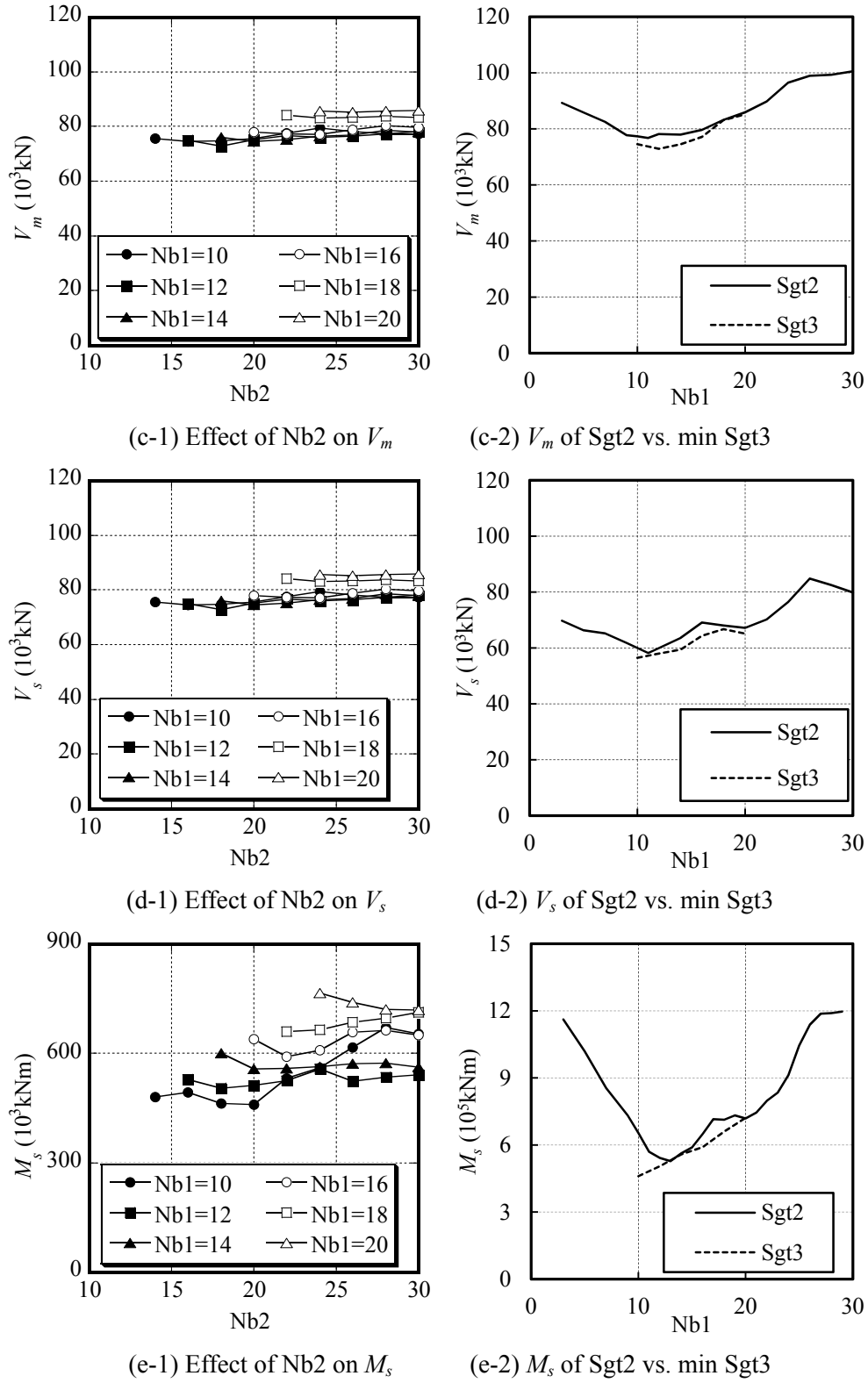
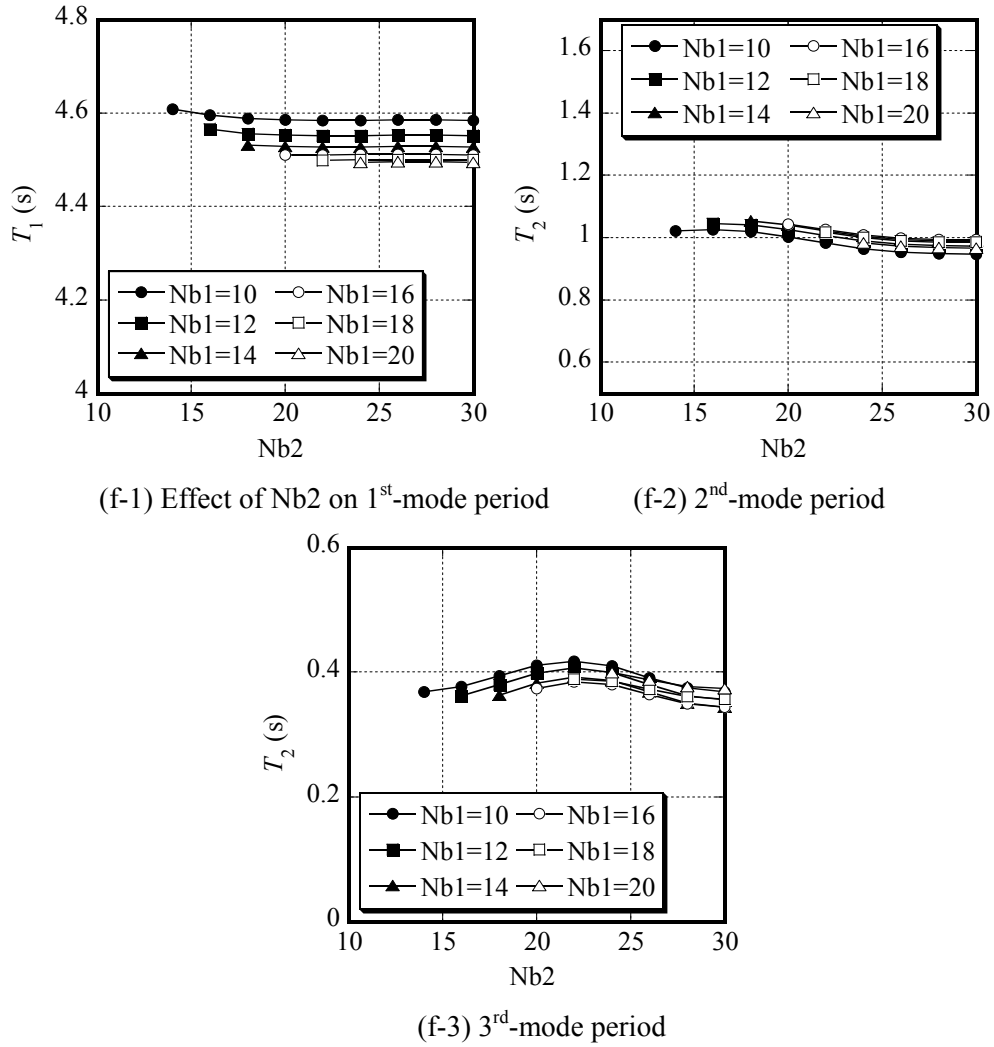


Fig. 5.19 (c, d, e) Effect of N_{b1} and N_{b2} on V_m , V_s , M_s of 30-story Sgt3 models

Fig. 5.19 (f) Effect of N_{b1} and N_{b2} on natural periods of 30-story Sgt3 models

Above all, the effective range of N_{b2} is 15 - 23, 50%~75% of the total height. The optimal value of N_{b2} is around 20, 67% of the total height, in which condition the deformation results could achieve the smallest value when $N_{b1}=16$, and the force results could achieve the smallest value when $N_{b1}=10$.

5.6.3 Optimal damper amount of Sgt3 models

In order to search for the optimal damper amount as well as the optimal damper amount ratio among the BRC1, BRC2, and BRC3 of the Sgt3 model, time-history analysis was conducted on two examples among the optimal cases determined from the above discussion, Sgt3-Ksf0.3-Nb10-20 and Sgt3-Ksf0.3-Nb15-20 models. Their seismic performances were compared with one of the optimal Sgt2 model, the Sgt2-Ksf0.3-Nb15 model with R_{kd} of 0.5. Although it's more nature to compare the Sgt3-Ksf0.3-Nb10-20 model with the

Sgt2-Ksf0.3-Nb10 model, the Sgt2-Ksf0.3-Nb15 was utilized because it exhibited essentially identical maximum seismic response with the Sgt2-Ksf0.3-Nb10 model, and the most concerned comparison was between the smallest response among all the Sgt3 models and the smallest response among all the Sgt2 models. Same with the previous cases, stiffness ratio between BRC1 and the moment frame K_{d1}/K_f varied from 0 to 1.5. Stiffness ratio between BRC2 and BRC1, BRC3 and BRC2 (defined as R_{kd}) varied among 0.5, 0.75, and 1.0. Concerned results include: maximum SDR, base shear of the whole structure, base shear of moment frames, base shear of spine frames, and “wall base” moment of spine frames.

As for the maximum SDR, the Sgt3 models exhibited essentially identical SDR compared to the Sgt2 model, except that the Sgt3-Nb10-20-RKd0.5 model showed slightly larger SDR than the other models, as in Fig 5.20 (a-1) (a-2). In both models, the effect of R_{kd} on SDR was negligible. SDR distribution of the Sgt3-10-20 model consisted of three uniform segments, among which the middle one was the largest. SDR distribution of the Sgt3-Nb15-20 model was identical with that of the Sgt2-Nb15 model, as in Fig 5.20 (a-3).

As for the base shear of the whole structure, both Sgt3-Nb10-20 and Sgt3-Nb15-20 models exhibited much smaller base shear compared to the Sgt2 model in some cases. Their smallest results could be achieved when K_{d1}/K_f was around 0.5 – 1.0, as in Fig 5.20 (b-1) (b-2). Effect of R_{kd} was more significant on base shear of the Sgt3-Nb15-20 model compared to the Sgt3-Nb10-20 model. In the Sgt3-Nb15-20 model, $R_{kd} = 0.5$ generally gave the smallest base shear. Story shear of Sgt3-Nb15-20 model was more linearly distributed along the building height compared to the Sgt2 model and Sgt3-Nb10-20 model, as in Fig 5.20 (b-3).

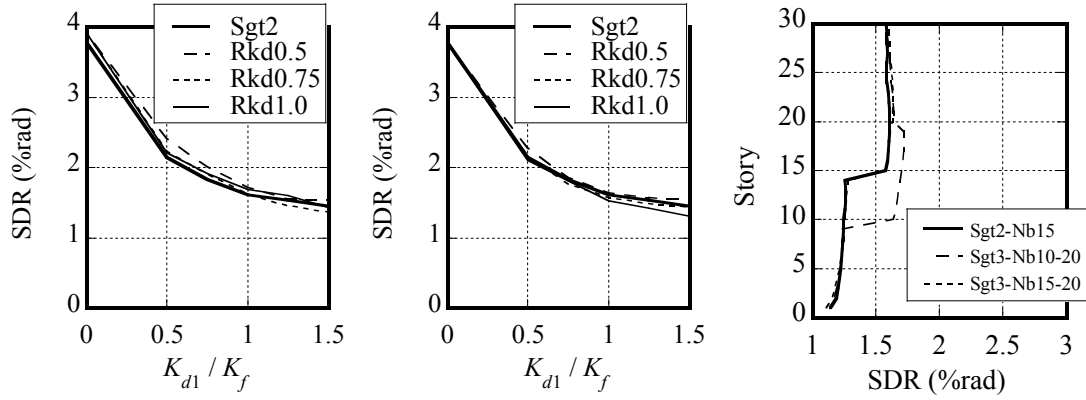
As for the base shear of moment frames, the Sgt3-Nb10-20 model exhibited larger base shear compared to the Sgt2-Nb15 model when K_{d1}/K_f was less than 0.5, while in the other cases the base shears of the two Sgt3 models were essentially identical with the Sgt2 model, as in Fig 5.20 (c-1) and (c-2). Shear force of each story except for the segment story was also essentially identical among the two Sgt3 models and the Sgt2 model. However, shear force at the segment story of the Sgt3-Nb10-20 model were relatively larger than the Sgt3-Nb15-20 and Sgt2 models, as in Fig 5.20 (c-3).

As for the base shear of spine frames, the Sgt3-Nb10-20 model exhibited smaller results than the Sgt2 model, while the Sgt3-Nb15-20 model exhibited essentially identical results. For both models, the smallest results were achieved when K_{d1}/K_f was around 1.0-1.5, as in Fig 5.20 (d-1) (d-2). In Sgt3-Nb10-20 model, effect of R_{kd} on base shear of spine frames was negligible when K_{d1}/K_f was less than 1.0. When K_{d1}/K_f was larger than 1.0, R_{kd} of 0.5 gave the smallest base shear. In Sgt3-Nb15-20 model, R_{kd} of 0.75 always gave the smallest base shear. Shear forces of the spine frames at both the continuous stories and the segment stories of the Sgt3 models were essentially identical with those of the Sgt2 model, as in Fig 5.20 (d-3).

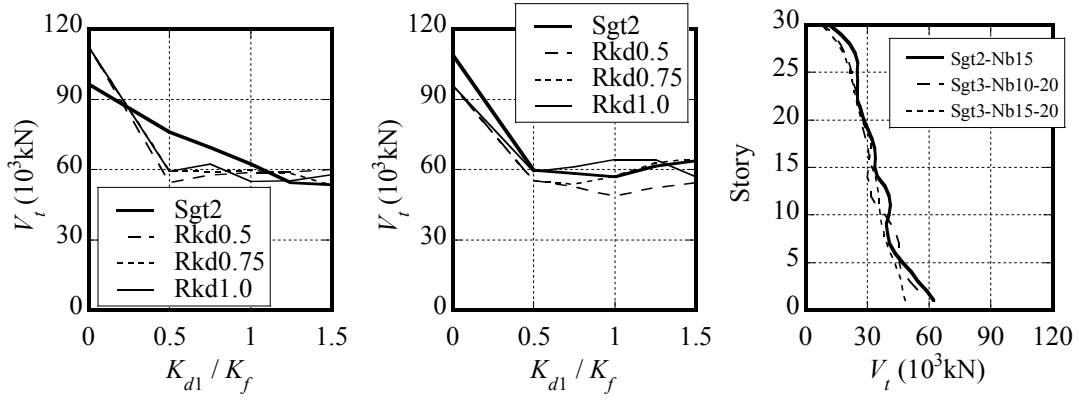
As for the “wall base” moment of spine frames, Sgt3-Nb10-20 model exhibited significantly reduced maximum moment compared to the Sgt2 model, while Sgt3-Nb15-20 model exhibited similar maximum value although the moment of upper stories was greatly reduced, as in Fig 5.20 (e-1) (e-2). In both Sgt3 models, the smallest moment was reached when K_{d1}/K_f was around 0.5. Effect of R_{kd} was not significant in all cases. Anyway R_{kd} of 0.5 always gave the smallest moment in the Sgt3-Nb10-20 model. In the Sgt3-Nb15-20 model, R_{kd} of 1.0 gave the smallest moment when K_{d1}/K_f was less than 0.75; R_{kd} of 0.5 gave the smallest moment when K_{d1}/K_f was over 0.75. Distribution of the “wall base” moment was showed in Fig 5.20 (e-3).

From the above results we could notice that base shear and the maximum moment of the spine frames could be further reduced by utilizing 3 segment spine frames with appropriate segment story, and the deformation response could remain at a similar level with the 2 segment spine frames. Averagely dividing the spine into three segments has been verified as one optimal configuration. When the first segment story was higher than 50% of the total height or the second segment story was higher than 67% of the total height, the Sgt3 configuration might be less effective on reducing the strength demand of the spine frames.

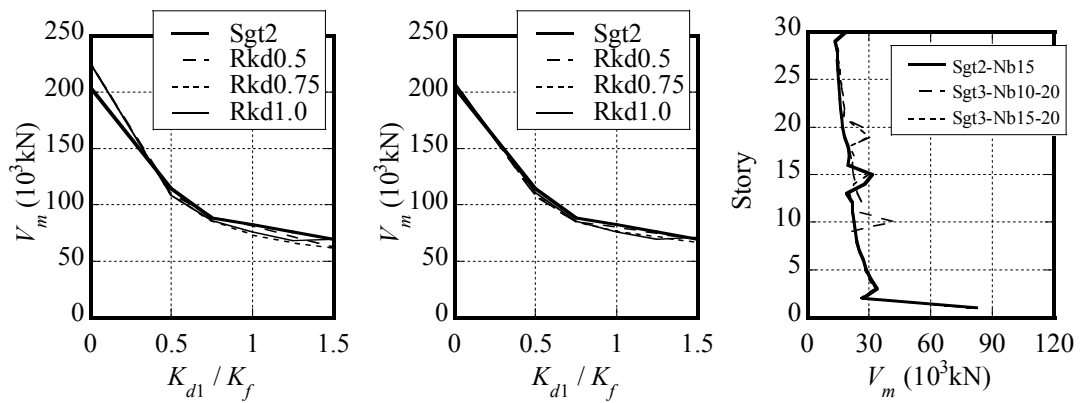
In the discussion on N_{b2} we found the location of the BRC3 had little effect on either deformation or force results except for the maximum moment of spine frames. We surmised that the possible reason lay in the too large yielding drift or elastic stiffness of the BRC3. However, from the above discussion on Fig 5.20 we understood that, reducing the elastic stiffness of the BRC3 couldn't enhance the effectiveness of the Sgt3 configuration on reducing force response much. On the contrary, reducing stiffness of BRC3 might increase the deformation response. Although the effect of yielding drift of the BRC3 is not discussed in the current study, similar results are highly possible to be obtained. It is because large SDR shifting, i.e. concentrated rotation at the segment story directly determines whether the segmented spine frames can work effectively. It is difficult to achieve sufficient concentrated rotation at the upper stories of a tall building without increasing the maximum deformation response, particularly when there are already two segments below. Therefore, two segments might be the maximum number for tall buildings utilizing the proposed spine frames.



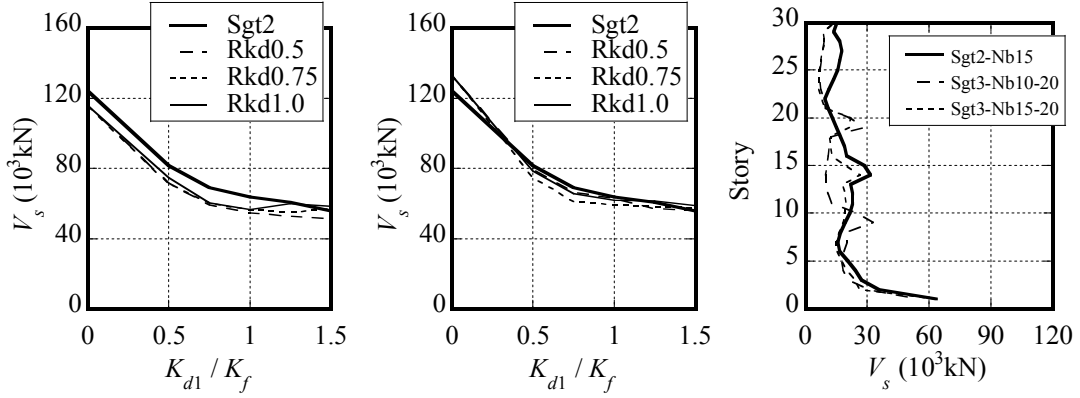
(a-1) SDR, Nb10-20 model (a-2) SDR, Nb15-20 model (a-3) SDR distribution, RKd=0.5
 Fig. 5.20 (a) Effect of damper amount and amount ratio between BRC1, BRC2 and BRC3 on SDR of 30-story Sgt3 models



(b-1) V_t , Nb10-20 model (b-2) V_t , Nb15-20 model (b-3) V_t distribution, RKd=0.5
 (b) Story shear of the whole structure

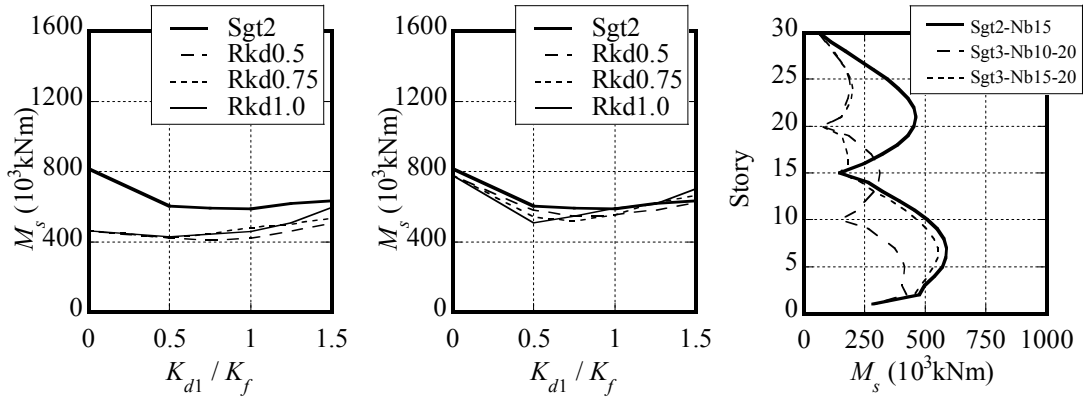


(c-1) V_m , Nb10-20 model (c-2) V_m , Nb15-20 model (c-3) V_m distribution, RKd=0.5
 (c) Story shear of moment frames



(d-1) V_s , Nb10-20 model (d-2) V_s , Nb15-20 model (d-3) V_s distribution, RKd=0.5
(d) Story shear of spine frames

Fig. 5.20 (b, c, d) Effect of damper amount and amount ratio between BRC1, BRC2 and BRC3 on V_t , V_m , V_s of 30-story Sgt3 models



(e-1) M_s , Nb10-20 model (e-2) M_s , Nb15-20 model (e-3) M_s distribution, RKd=0.5
Fig. 5.20 (e) Effect of damper amount and amount ratio between BRC1, BRC2 and BRC3 on M_s of 30-story Sgt3 models

(Models for showing response distribution: Sgt3-Ksf0.3-Nb10-20-Kdf1.0-0.5-0.25, Sgt3-Ksf0.3-Nb15-20-Kdf1.0-0.5-0.25, Sgt2-Ksf0.3-Kdf1.0-0.5)

5.7 Conclusions

In this study, seismic performance of the tall buildings adopting controlled spine frame structures was studied and a two segments spine frames configuration and a three segments spine frames configuration were proposed. Parametric study base on the 20- and 30-story benchmark buildings was conducted to examine the optimal ranges of the key structural parameters-the location of segment story and the damper amount. The following conclusions were drawn from this study:

(1) The stiff spine frame has an effect in achieving a more uniform deformation distribution so as to reduce the maximum SDR even for structures as tall as 30 stories. To ensure the effectiveness of the spine frame and dampers, K_s/K_f should exceed 0.5 for buildings lower than 10 stories and 0.3 for buildings higher than 10 stories.

Decreasing in SDR is significant when the spine frame stiffness increases from a relatively small value, but less effective after the spine frame stiffness exceed some particular value, which is defined as the maximum effective K_s/K_f . When $K_d/K_f \geq 0.5$, the maximum effective K_s/K_f is always approximately 1.0 for 20- and 30-story buildings.

As for the 20- and 30-story buildings, K_s/K_f has little effect on the base shear of moment frames. Base shear of spine frames increases along with K_s/K_f increasing till $K_s/K_f=1.0$. Its increasing range decreases with K_d/K_f increasing.

(2) Increasing the amount of dampers is helpful to reduce both deformation and force responses even for the 20- and 30-story structures. But it is not always effective to reduce the seismic performance. It is recommended to set the damper-to-moment frame stiffness ratio K_d/K_f up to 2.0 for the typical case of $0.3 \leq K_s/K_f \leq 2.0$ for structures lower than 30 stories.

In the 20- and 30-story buildings results, the base shear of moment frames decreased significantly with K_d/K_f increasing, while base shear of spine frames seemed almost irrelevant to K_d/K_f , despite of the value of K_s/K_f .

(3) The partial spine frames exhibited similar seismic performance with the continuous spine frames when $N_{b1} \leq 5$, while they behaved more similarly to the shear wall structures when $N_{b1} \geq 15$. No obvious advantage was observed from the seismic performance of the partial spine frames compared to the continuous configuration. Their deformations could get much larger than the continuous spine frames if without sufficient dampers. Base shear was highly possible to become significantly large as well. Therefore, the partial spine frames are not recommended for tall buildings if the continuous configuration is available.

(4) For buildings taller than 20 stories, as long as $K_s/K_f \geq 0.3$, $N_{b1}/N = 0.5-0.75$, $K_{d1}/K_f = 0.5-1.0$, $K_{d2}/K_{d1} = 0.5-1.0$, the 2 segmented spine frame model could effectively reduce the SDR response by approximately 10%, base shear of moment frames by 13-20%, base shear of spine frames by 13%-20%, as well as the “wall base” moment of spine frames by 35%-50% compared to the continuous single spine frame configuration. Moreover, the SDR of Sgt2 models was more uniformly distributed along the building height, and the story shear of Sgt2 models was more linearly distributed along the building height compared to the Cnt model.

Sgt2 and Cnt models possessing same total amount of dampers have been compared as well. The results showed that, although SDR and base shear of moment frames might not be reduced by utilizing the Sgt2 model, base shear of the whole structure and spine frames, as well as maximum moment of spine frames could be significantly reduced compared to the Cnt models.

The two-segment spine frames configuration is recommended for tall buildings when the amount of BRCs at one story is limited, or when the strength demand on spine frame is too large by utilizing the continuous spine frames.

(5) The maximum moment of the spine frames could be further reduced by utilizing 3 segment spine frames on the expense of increasing the deformation response compared to the two segment spine frames. Averagely dividing the spine into three segments has been verified as an optimal configuration. When N_{b1}/N is larger than 0.5 or N_{b2}/N is larger than 0.67, the Sgt3 configuration might be less effective on reducing the strength demand of the spine frames. It is difficult to achieve sufficient concentrated rotation at the upper stories of a tall building without increasing the maximum deformation response, particularly when there are already two segments below. Therefore, three segments spine frame configuration is not recommended for tall buildings, unless additional damping is equipped.

References

- [5.1] L. Wiebe, C. Christopoulos. Mitigation of higher mode effects in base-rocking systems by using multiple rocking sections. *Journal of Earthquake Engineering*, Vol. 13(SI), p83-108, 2009
- [5.2] L. Wiebe, C. Christopoulos, R. Tremblay, M. Leclerc. Mechanisms to limit higher mode effects in a controlled rocking steel frame. 1: Concept modelling and low-amplitude shake table testing. *Earthquake Engng Struct. Dyn.* Vol.42:1053–1068, 2013
- [5.3] L. Wiebe, C. Christopoulos, R. Tremblay, M. Leclerc. Mechanisms to limit higher mode effects in a controlled rocking steel frame. 2: large amplitude shake table testing. *Earthquake Engng Struct. Dyn.* Vol. 42, p1069–1086, 2013.
- [5.4] T. Paulay, M.J.N. Priestley. Seismic design of reinforced concrete and masonry buildings. John Wiley & Sons, Inc. 1992.
- [5.5] 石原直、小松豊、小豆畑達哉、緑川光正：中間層浮き上がり構造の地震応答に関する模型振動台実験、日本建築学会大会学術講演梗概集、B-2、pp.37-38、2010.
- [5.6] 石原直、緑川光正、小豆畑達哉：中間層で浮き上がりが許容された多層建築物のモード解析，第 60 回理論応用力学講演会，2011.
- [5.7] T. Ishihara, T. Azuhata, M. Midorikawa: Modal analysis of dynamic behavior of buildings allowed to uplift at mid-story. 15th WCEE, Lisboa, 2012.

CHAPTER 6

Evaluation Method and Design Procedure of Controlled Spine Frames Applied in High-rise Buildings

6.1 Introduction 6-1

6.2 Basic concepts of modal pushover analysis

6.2.1 Linearly elastic systems 6-2

6.2.2 Inelastic systems 6-4

6.2.3 Modal combination rules 6-6

6.3 Seismic evaluation methods

6.3.1 Modal pushover analysis (MPA) 6-7

6.3.2 Response spectrum analysis (RSA) 6-7

6.4 Seismic evaluation of Cnt models

6.4.1 Evaluation of Cnt models by MPA methods 6-9

6.4.2 Evaluation of Cnt models by RSA methods 6-30

6.5 Seismic evaluation of Sgt models

6.5.1 Evaluation of Sgt models by MPA methods 6-48

6.5.2 Evaluation of Sgt models by RSA methods 6-60

6.6 Design procedure for high-rise controlled spine frame structures 6-75

6.7 Conclusions 6-79

Chapter 6 – Evaluation Method and Design Procedure for Controlled Spine Frames Applied in High-rise Buildings

6.1 Introduction

Although nonlinear time-history analysis is the most rigorous way for seismic performance evaluation of existing and new structures, nonlinear static pushover analysis is preferred in current structural engineering practice. Modal pushover analysis (MPA) procedure based on structural dynamics theory has been commonly used for seismic evaluation. ^[6.1, 2] In a typical MPA procedure, a suit of monotonically increasing lateral forces with an invariant height-wise distribution is loaded on the structure till a target deformation is reached. Both the force distribution and target deformation are calculated by assuming that the first-mode response is predominant and the mode shape remains unchanged after the yielding mechanism occurs. Those assumptions are mostly restricted for low- and mid-rise structures exhibiting distributed inelastic actions throughout the height of the structure. ^[6.2]

The invariant force distribution cannot consider the redistribution of inertia forces after the yielding mechanism occurs. To overcome such deficiency, some researchers have proposed adaptive force distributions to follow more closely the time-variant distributions of inertia forces. Although these adaptive force distributions may provide better evaluations of seismic performance, they are conceptually and computationally complicated for engineering practice.

Some researchers have also attempted to consider contribution of higher modes for taller buildings. These methods may estimate seismic performance much more accurately. However, “reversal” of a higher-mode pushover curve may occur after the formation of a mechanism. ^[6.3] To solve this problem, Chopra et al. have proposed a modified MPA procedure in which the response contributions of higher modes are computed by assuming the building to be linearly elastic. ^[6.4] This procedure may increase the accuracy and improve the conservatism of MPA results. Such conservatism is acceptably small except for lightly damped system, with damping significantly less than 5%.

A MPA procedure with invariant force distribution considering contribution of higher modes is developed for the proposed continuous spine frame structures applied in tall buildings. The assumptions that the mode shape remains unchanged after the yielding mechanism occurs are essentially satisfied in the first-mode response of the spine frame structures thanks to the spine effect. However, inelastic behavior cannot be ideally uniform throughout the height of the structure even in the first-mode response, not to mention the higher-modes responses. Therefore, the relationship between different floor displacement and base shear obtained from pushover analysis of the original structure leads to different hardening ratio (even reversal deformation) in the force-deformation curve of the corresponding inelastic SDOF system. The effect of such

discrepancy on seismic performance evaluation of the original structure is examined and suitable floor displacement is suggested for determining the inelastic force-deformation curve for each SDOF system.

In previous chapters we have proposed a simplified evaluation method based on equivalent linearization techniques and response spectrum analysis (RSA) for low-rise spine frame structures. This procedure is modified to including higher-modes contribution for tall spine frame structures by referring to MPA results.

6.2. Basic concepts of modal pushover analysis

6.2.1 Linearly elastic systems

6.2.1.1 Equivalent SDOF system of the n th mode MDOF system

When damping is included, the equations of motion for an MDOF system are

$$\mathbf{m}\ddot{\mathbf{u}} + \mathbf{c}\dot{\mathbf{u}} + \mathbf{k}\mathbf{u} = -\mathbf{m}\{1\}\ddot{u}_g \quad (6.1)$$

The displacement vector $\{u\}$ can be expended in terms of modal contributions. Thus, the dynamic response of a system can be expressed as

$$\mathbf{u}(t) = \sum_{r=1}^N \mathbf{\phi}_r q_r(t) \quad (6.2)$$

where $\mathbf{\phi}_r$ is the r -th natural mode of the system without damping, and $q_r(t)$ is the r -th modal coordinate.

Substituting Eq. (6.2) in Eq. (6.1) gives

$$\sum_{r=1}^N \mathbf{m}_r \ddot{q}_r(t) + \sum_{r=1}^N \mathbf{c}_r \dot{q}_r(t) + \sum_{r=1}^N \mathbf{k}_r q_r(t) = -\mathbf{m}\{1\}\ddot{u}_g \quad (6.3)$$

Premultiplying each term in this equation by $\mathbf{\phi}_n^T$ gives

$$\sum_{r=1}^N \mathbf{\phi}_n^T \mathbf{m}_r \ddot{q}_r(t) + \sum_{r=1}^N \mathbf{\phi}_n^T \mathbf{c}_r \dot{q}_r(t) + \sum_{r=1}^N \mathbf{\phi}_n^T \mathbf{k}_r q_r(t) = -\mathbf{\phi}_n^T \mathbf{m}\{1\}\ddot{u}_g \quad (6.4)$$

For systems having classical damping, these modal equations are uncoupled through the damping terms. And because of the orthogonality relations $\mathbf{\phi}_n^T \mathbf{m}_r \mathbf{\phi}_n = 0$, $\mathbf{\phi}_n^T \mathbf{k}_r \mathbf{\phi}_n = 0$, Eq. (6.4) is reduced to

$$\mathbf{\phi}_n^T \mathbf{m}_n \ddot{q}_n(t) + \mathbf{\phi}_n^T \mathbf{c}_n \dot{q}_n(t) + \mathbf{\phi}_n^T \mathbf{k}_n q_n(t) = -\mathbf{\phi}_n^T \mathbf{m}\{1\}\ddot{u}_g \quad (6.5)$$

Which can be rewritten as

$${}_nM {}_n\ddot{q}(t) + {}_nC {}_n\dot{q}(t) + {}_nK {}_nq(t) = -{}_n\boldsymbol{\Phi}^T \mathbf{m}\{1\} \ddot{u}_g \quad (6.6)$$

Where ${}_nM$, ${}_nK$ are called the generalized mass and stiffness for the n -th mode.

$${}_nM = {}_n\boldsymbol{\Phi}^T \mathbf{m} {}_n\boldsymbol{\Phi} \quad (6.7)$$

Dividing Eq. (6.6) by ${}_nM$ gives

$${}_n\ddot{q}(t) + 2{}_nh {}_n\omega {}_n\dot{q}(t) + {}_n\omega^2 {}_nq(t) = -{}_n\beta \ddot{u}_g \quad (6.8)$$

where ${}_nh$ is the damping ratio for the n th mode. ${}_n\beta$ is called a modal participation factor and is obtained from

$${}_n\beta = \frac{{}_n\boldsymbol{\Phi}^T \mathbf{m}\{1\}}{{}_n\boldsymbol{\Phi}^T \mathbf{m} {}_n\boldsymbol{\Phi}} \quad (6.9)$$

Eq (6.8) with ${}_nq(t)$ replaced by ${}_n\beta D(t)$ becomes

$${}_n\ddot{D}(t) + 2{}_nh {}_n\omega {}_n\dot{D}(t) + {}_n\omega^2 {}_nD(t) = -\ddot{u}_g \quad (6.10)$$

Eq. (6.10) governs the response of an SDOF system, the n th-mode SDOF system. Once Eq. (6.10) has been solved for ${}_nD(t)$, ${}_nq(t)$ is readily available, as well as the contribution of the n th mode to nodal displacements:

$${}_n\mathbf{u}(t) = {}_n\beta {}_n\boldsymbol{\Phi} {}_nD(t) \quad (6.11)$$

And the story drift in the i -th story is:

$${}_n\Delta_i(t) = {}_n\beta ({}_n\varphi_i - {}_n\varphi_{i-1}) {}_nD(t) \quad (6.12)$$

Superposing the responses for all n modes gives the response of the system due to total excitation:

$$\mathbf{r}(t) = \sum_{n=1}^N {}_n\mathbf{r}(t) \quad (6.13)$$

6.2.1.2 Equivalent static forces of the earthquake forces

The effective earthquake forces are

$$\mathbf{p}_{\text{eff}}(t) = -\mathbf{m}\{1\} \ddot{u}_g(t) = -\sum_{n=1}^N {}_n\beta \mathbf{m} {}_n\boldsymbol{\Phi} \ddot{u}_g(t) \quad (6.14)$$

The contributions of the n th mode to $\mathbf{p}_{\text{eff}}(t)$ are

$${}_n\mathbf{p}_{\text{eff}}(t) = -{}_n\beta \mathbf{m} {}_n\boldsymbol{\Phi} \ddot{u}_g(t) \quad (6.15)$$

The equations governing the response of the elastic MDOF system to ${}_n\mathbf{p}_{\text{eff}}(t)$ are

$$\mathbf{m}\ddot{\mathbf{u}} + \mathbf{c}\dot{\mathbf{u}} + \mathbf{k}\mathbf{u} = -\beta \mathbf{m}_n \boldsymbol{\phi}_n \ddot{u}_g(t) \quad (6.16)$$

and the response are identical with the n th mode response ${}_nr(t)$, as in Eq. (6.13), which implies that the modes are uncoupled in the elastic MDOF system.

Static analysis of the MDOF system subjected to lateral forces

$$\mathbf{f} = \beta \mathbf{m}_n \boldsymbol{\phi}_n S_a \quad (6.17)$$

will provide the same value of ${}_nr$, the peak value of the n th-mode response ${}_nr(t)$, where S_a is the spectrum ordinate corresponding to the natural period ${}_nT$ and damping ratio ${}_nh$ of the n th mode. Alternatively, this peak modal response can be obtained by linear static analysis of the structure subjected to monotonically increasing lateral forces with an invariant height-wise distribution:

$${}_ns^* = \mathbf{m}_n \boldsymbol{\phi}_n \quad (6.18)$$

Pushing the structure up to the roof displacement, ${}_nu_r$, (r denotes “roof”) the peak value of the roof displacement due to the n th mode, or to any other floor displacement ${}_nu_i$ (i denotes the i th floor), which from Eq. (6.11) is

$${}_nu_i = \beta \mathbf{m}_n \boldsymbol{\phi}_i {}_nD \quad (6.19)$$

where ${}_nD$ is the ordinate of the deformation response spectrum corresponding to the period ${}_nT$ and damping ratio ${}_nh$ of the n th mode.

The peak modal response, ${}_nr$, each determined by one pushover analysis, can be combined according to the modal combination rules, (will be introduced in the next section), to obtain an estimate of the peak value r of the total response. Equivalent to the standard RSA procedure, the MPA procedure offers no advantage for linearly elastic systems, but this interpretation of RSA permits extension of MPA to approximate analysis of inelastic system.

6.2.2 Inelastic systems

6.2.2.1 Equivalent SDOF system of the n th mode MDOF system

The equations governing the response of the inelastic MDOF system to the n th mode effective earthquake force ${}_n\mathbf{p}_{\text{eff}}(t)$ are

$$\mathbf{m}\ddot{\mathbf{u}} + \mathbf{c}\dot{\mathbf{u}} + \mathbf{f}_s(\mathbf{u}) = -\beta \mathbf{m}_n \boldsymbol{\phi}_n \ddot{u}_g(t) \quad (6.20)$$

where $\mathbf{f}_s(\mathbf{u})$ is the inelastic resisting force. It depends on displacement history.

Similarly the response of the n th mode inelastic SDOF system is now governed by

$${}_n\ddot{D}(t) + 2{}_nh{}_n\omega{}_n\dot{D}(t) + {}_nA({}_nD(t)) = -\ddot{u}_g \quad (6.21)$$

The natural vibration modes are no longer uncoupled if the system responds in the inelastic range, therefore, ${}_nA$ should depend on all modal responses ${}_iD(t)$ ($i=1,2,\dots,N$). Previous research has confirmed that the modal coupling is weak and can be neglected.^[6.5] Herein ${}_nA$ only depends

on ${}_nD(t)$. This force-deformation (${}_nA$ — ${}_nD$) relation will be determined by pushover analysis of the MDOF system.

6.2.2.2 Equivalent static forces of the earthquake forces

The peak response ${}_n r$ of the inelastic system to ${}_n \mathbf{p}_{\text{eff}}(t)$ (Eq. (6.20)) is determined by a nonlinear pushover analysis of the MDOF system subjected to lateral forces distributed over the building height according to ${}_n \mathbf{s}^*$ (Eq. (6.18)) with the forces increased to push the structure up to i th floor displacement ${}_n u_i$. This value of the i th floor displacement is also determined from Eq. (6.19), but ${}_n D$ is now the peak deformation of the n th-mode inelastic SDOF system. ${}_n D$ can be estimated directly from the earthquake design spectrum.

Nonlinear static analysis using force distribution leads to the n th-mode pushover curve, a plot of base shear ${}_n V_b$ versus i th floor displacement ${}_n u_i$. From this curve the force-deformation (${}_nA$ — ${}_nD$) curve is obtained for the n th-mode inelastic SDOF system, as in Eq. (6.21). The forces and displacements in the two sets of curves are related as follows:

$${}_n A = \frac{{}_n V_b}{{}_n M_{eq}} \quad {}_n D = \frac{{}_n u_i}{{}_n \beta {}_n \phi_i} \quad (6.22)$$

where ${}_n M_{eq}$ is the effective modal mass.

$${}_n M_{eq} = \frac{({}_n \boldsymbol{\phi}^T \mathbf{m} \{1\})^2}{{}_n \boldsymbol{\phi}^T \mathbf{m} {}_n \boldsymbol{\phi}} \quad (6.23)$$

6.2.2.3 Response evaluation by utilizing equivalent linearization

The force-deformation (${}_nA$ — ${}_nD$) curve obtained from 6.2.2.2 is idealized into a bilinear curve. The n th-mode elastic period ${}_n T_0$, initial stiffness ${}_n K_0$ and hardening stiffness ${}_n K_h$ are computed from the bilinear curve. Knowing the hysteretic curves, by utilizing the equivalent linearization method as introduced in chapter 4, the equivalent damping ratio and equivalent period can be computed from

$${}_n h_{eq} = {}_n h_0 + \frac{2}{\pi {}_n \mu {}_n p} \ln \frac{(1 - {}_n p + {}_n p {}_n \mu)}{({}_n \mu)^{{}_n p}} \quad (6.24)$$

$${}_n T_{eq} = {}_n T_0 \sqrt{\frac{{}_n \mu}{1 + {}_n p ({}_n \mu - 1)}} \quad (6.25)$$

Where, ${}_n p = \frac{{}_n K_h}{{}_n K_0}$ denotes the hardening stiffness ratio of the system, ${}_n \mu = \frac{{}_n D_t}{{}_n D_y}$ denotes the

ductility ratio when the target deformation is assumed as ${}_n D_t$. ${}_n D_0$, ${}_n A_0$ denote the primarily estimated deformation and force corresponding to the initial period ${}_n T_0$ and damping ratio ${}_n h_0$. They are updated by Eq. (6.26) ~ (6.27) according to the equivalent period ${}_n T_{eq}$ and damping ratio ${}_n h_{eq}$, where ${}_n R_d$, ${}_n R_a$ are the deformation and force reduction factors:

$${}_n D = {}_n R_d {}_n D_0, \quad {}_n R_d = \begin{cases} \frac{{}_n T_{eq}}{{}_n T_0} {}_n D_h & T_l \leq {}_n T_0 \leq {}_n T_{eq} \\ \frac{{}_n T_{eq}}{{}_n T_0} {}_n D_h \frac{T_l (2 {}_n T_{eq} - {}_n T_l) - ({}_n T_0)^2}{2 ({}_n T_{eq} - {}_n T_0) {}_n T_0} & {}_n T_0 \leq T_l \leq {}_n T_{eq} \\ \frac{{}_n T_{eq}}{{}_n T_0} {}_n D_h \frac{{}_n T_{eq} + {}_n T_0}{2 {}_n T_0} & {}_n T_0 \leq {}_n T_{eq} \leq T_l \end{cases} \quad (6.26)$$

$${}_n A = {}_n R_a {}_n A_0, \quad {}_n R_a = {}_n R_d \left(\frac{{}_n T_f}{{}_n T_{eq}} \right)^2 \quad (6.27)$$

The ductility ratio updates according to the newly obtained deformation, and Eq. (6.24) ~ (6.26) are repeated to estimate the deformation in the new iteration till its value converges. Detailed procedure has been presented in previous chapters.

The peak modal response, ${}_n r$, each determined by one pushover analysis, can be combined according to the modal combination rules.

6.2.3 Modal combination rules

In general, the modal responses attain their peaks ${}_n r_p$ at different time instants and the combined response attains its peak r_p at yet a different instant. Therefore, approximations must be introduced in combining the peak modal responses determined from the earthquake response spectrum. The absolute sum (ABSSUM) modal combination rule is

$$r_p \leq \sum_{n=1}^N |{}_n r_p| \quad (6.28)$$

This rule assumes that all modal peaks occur at the same time and their algebraic sign is ignored. This upper-bound value is usually too conservative.

The square-root-of-sum-of-squares (SRSS) rule is

$$r_p \approx \left(\sum_{n=1}^N {}_n r_p^2 \right)^{1/2} \quad (6.29)$$

This combination rule provides excellent response estimates for structures with well-separated natural frequencies.

The complete quadratic combination (CQC) rule is

$$r_p \approx \left(\sum_{i=1}^N \sum_{n=1}^N \rho_{in} {}_i r_p {}_n r_p \right)^{1/2} \quad (6.30)$$

This combination rule is applicable to a wider class of structures as it overcomes the limitations of the SRSS rule. ρ_{in} is called as the correlation coefficient for the i th and n th modes. ρ_{in} varies between 0 and 1. $\rho_{in} = 1$ for $i = n$.

The equation for the correlation coefficient due to Der Kiureghian is

$$\rho_{in} = \frac{8\sqrt{h_i h_n} (\alpha_{in} h_i + h_n) \alpha_{in}^{3/2}}{(1 - \alpha_{in}^2)^2 + 4 h_i h_n \alpha_{in} (1 + \alpha_{in}^2) + 4 (h_i^2 + h_n^2) \alpha_{in}^2} \quad (6.31)$$

where $\alpha_{in} = \omega_i / \omega_n$. For structures with well-separated natural frequencies the coefficients ρ_{in} vanish; as a result the CQC rule reduces to the SRSS rule.

6.3 Estimation methods

6.3.1 Modal pushover analysis (MPA)

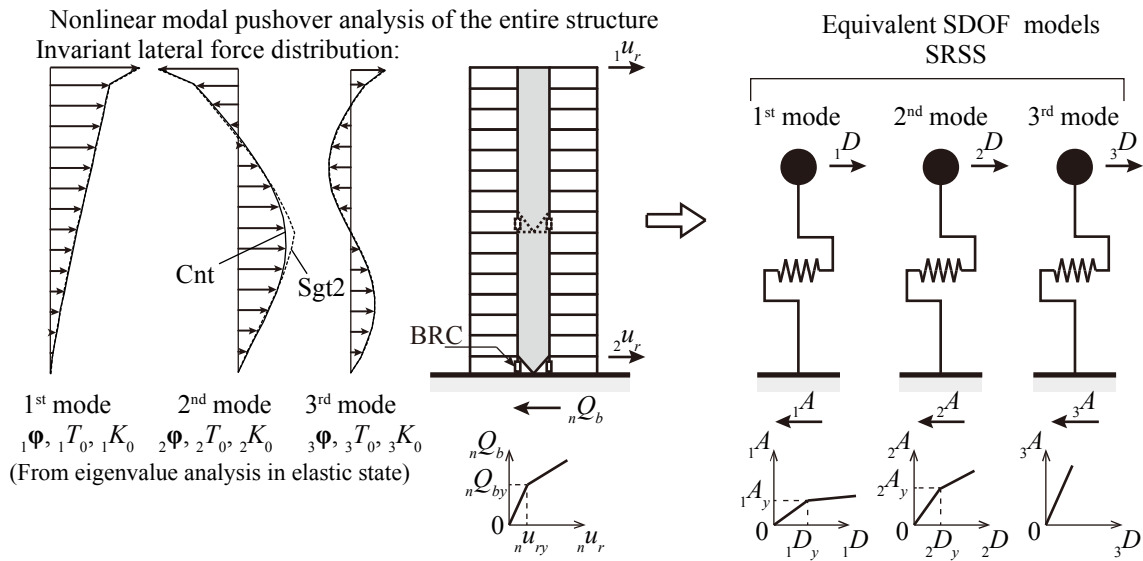


Fig 6.1 Concept of nonlinear modal pushover analysis for spine frame structures

Step 1. Compute the natural frequencies, $n\omega$, and modes, $n\Phi$, for linearly elastic vibration of the building.

Step 2. For the n th mode, develop the base shear-floor displacement, $nV_b - nu_i$, pushover curve by nonlinear static analysis of the building using the lateral force distribution, $n\mathbf{s}^*$ (Eq.(6.18)).

Step 3. Convert the $nV_b - nu_i$ pushover curve to the force-deformation, $nA - nD$, relation for the n th-mode inelastic SDOF system by utilizing Eq. (6.22)

Step 4. Idealize the force-deformation relation for the n th-mode SDOF system as a bilinear curve. Determine the initial stiffness and hardening stiffness of the SDOF system.

Step 5. Evaluate the peak deformation nD by utilizing Eq. (6.24)~(6.27).

Step 6. Inversely convert nD to the peak i th floor displacement nu_i in the inelastic MDOF system.

Step 7. From the pushover database (step 2), extract values of desired response nr at i th floor

displacement equal to ${}_n u_i$.

Step 8. Repeat steps 3 to 7 for as many modes as required for sufficient accuracy.

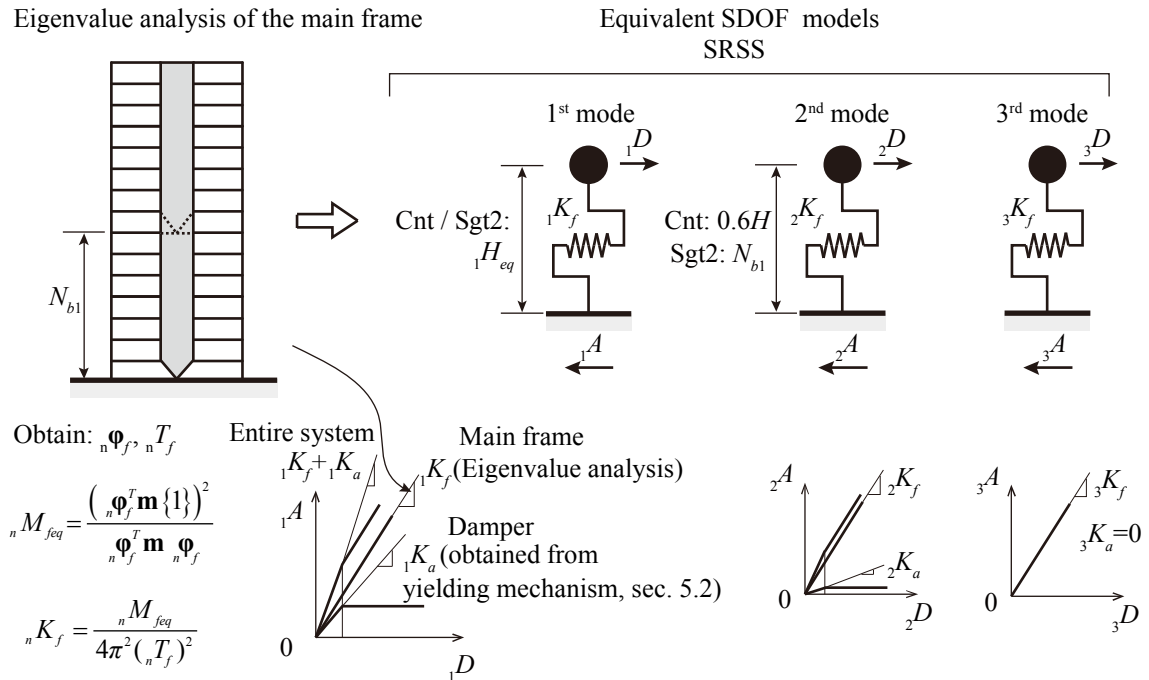
Step 9. Determine the total seismic response by combining the peak modal responses using a modal combination rule.

The MPA procedure can also be used to estimate internal forces in those structural members that remain within their linearly elastic range, but not in those that deform into the inelastic range. In the latter case, the member forces are estimated from the total member deformations.

6.3.2 Response spectrum analysis (RSA)

Authors have proposed a practical design procedure based on the equivalent linearization technique and design response spectrum analysis (RSA) for the spine frame structures applied in low-rise buildings. The previous procedure is generalized to permit inelastic moment frames and spine frames, composed of the main frame, but neglects higher mode effects. It is extended to include higher mode effects for tall buildings in this chapter. To keep the main process clearly, we assume the structural response of the main frame is linearly elastic. Similar to the previous “1st mode only” procedure, the current “multi-modes” procedure is able to be generalized to permit inelastic main frame as well.

Detailed explanation on this procedure is presented in Chapter 4. Following is a brief review after including the estimation of higher-modes response.



Step 1. Compute the natural periods, ${}_nT_f$, and modes, ${}_n\Phi_f$ for linearly elastic vibration of the main frame without BRCs. Obtain the elastic force-deformation ${}_nA - {}_nD$ relation with stiffness ${}_nK_f$ for the SDOF system of each mode by utilizing Eq. (6.22).

Step 2. Evaluate the elastic modal responses ${}_nr_f$ of the main frame with an inherent damping ratio of 0.02. To evaluate forces of structural members, elastic pushover analysis using the lateral force distribution ${}_ns_f^*$ is required.

Step 3. For the n -th mode, compute the additional stiffness ${}_nK_a$ and yielding deformation ${}_nD_y$ contributed by BRCs on the force-deformation relation of the SDOF system. Determine the initial stiffness ${}_nK_{f+a} = {}_nK_f + {}_nK_a$ and hardening stiffness ${}_nK_h$ of the SDOF system.

Step 4. Compute deformation and force reduction factors ${}_nR_d$, ${}_nR_a$ by utilizing Eq. (6.24) ~ (6.27). Eq. (6.26) is replaced with the equation below.

Step 5. Evaluate desired responses of the original structure by multiplying ${}_nR_d$ or ${}_nR_a$.

Step 6. Repeat steps 3 to 5 for as many modes as required for sufficient accuracy.

Step 7. Determine the total seismic response by combining the peak modal responses using a modal combination rule.

$${}_nR_d = \begin{cases} \frac{{}_nT_{eq}}{{}_nT_f} {}_nD_h & T_l \leq {}_nT_{f+a} \leq {}_nT_{eq} \leq {}_nT_f \\ \frac{{}_nT_{eq}}{{}_nT_f} {}_nD_h \frac{T_l(2{}_nT_{eq} - T_l) - {}_nT_{f+a}^2}{2({}_nT_{eq} - {}_nT_{f+a})T_l} & {}_nT_{f+a} \leq T_l \leq {}_nT_{eq} \leq {}_nT_f \\ \frac{{}_nT_{eq}}{{}_nT_f} {}_nD_h \frac{{}_nT_{eq} + {}_nT_{f+a}}{2T_l} & {}_nT_{f+a} \leq {}_nT_{eq} \leq T_l \leq {}_nT_f \\ \frac{{}_nT_{eq}}{{}_nT_f} {}_nD_h \frac{{}_nT_{eq} + {}_nT_{f+a}}{2{}_nT_f} & {}_nT_{f+a} \leq {}_nT_{eq} \leq {}_nT_f \leq T_l \end{cases}$$

Note that static pushover analysis is only required for the main frame in the RSA procedure, and only required when forces of internal structural components are desired. This is different from MPA, because effect of damper amounts is simply estimated by formula calculation but not numerical analysis. The RSA procedure provides a much simpler solution. However, the disadvantage is also obvious. Distributions of responses estimated by this RSA procedure are assumed to be same with those of the elastic main frame, i.e., post-yielding system, which may cause significant error when the structure responses are essentially elastic during earthquake events. To overcome this problem, modification factors are proposed for some responses.

6.4 Seismic evaluation of Cnt models

6.4.1 Evaluation of Cnt models by MPA method

The 20-story Cnt models with $K_{sf}=0.1\sim 2.0$ and $K_{df}=0\sim 4.0$ are estimated by utilizing the

MPA procedure in section 4. Detailed results of each MPA step for the Cnt-Ksf0.3-Kdf1.0 model are demonstrated in the following paragraphs.

Step 1. Compute the natural frequencies, ${}_n\omega$, and modes, ${}_n\phi$, for linearly elastic vibration of the building.

Eigenvalue analysis is carried out for the elastic model and results of the first three modes are summarized in Table 6.1. The inherent modal damping ratio ${}_n\zeta_0$ ($n=1, 2, 3$) is assumed as 0.02, which is widely accepted for steel building structures. Elastic stiffness K_0 as well as the elastic response of base shear V_{b0} and mode coordinate D_0 of the first three modes are also listed in Table 6.1. These results are directly computed according to the natural periods and modes obtained from eigenvalue analysis by assuming the system behaviors elastically. Fig 6.3(a) shows the mode shape, in which the maximum value is standardized as 1.0. Figs 6.3(b) to (e) are the estimated elastic responses of each floor. Herein the peak modal response of lateral force (Fig 6.3 (e)) and floor displacement (Fig 6.3 (b)) are computed by Eq. (6.17) and (6.19). The peak SDR (Fig 6.3 (c)) and story shear force (Fig 6.3 (d)) are computed by Eq (6.32) and Eq (6.33).

$${}_n\Delta_i = {}_n\beta ({}_n\phi_i - {}_n\phi_{i-1}) {}_nD / h_i \quad (6.32)$$

$${}_nV_i = \sum_{j=i}^N {}_n\beta m_j {}_n\phi_j {}_nS_a \quad (6.33)$$

From Fig 6.3 (b) to (e) we can see that the contribution of higher-modes is more significant in the force response than that in the deformation response.

Step 2. For the n th mode, develop the base shear-floor displacement, ${}_nV_b - {}_nu_i$, pushover curve by nonlinear static analysis of the building using the lateral force distribution, ${}_ns^*$ (Eq.(6.18)).

Static pushover analysis is carried out for the 20-story Cnt model. The moment frame and spine frame still behaves elastically but the BRCs deform into the inelastic range. The model is subjected to lateral forces which are always proportional to those obtained from elastic eigenvalue analysis, as in Fig 6.3(e). From the pushover analysis we obtain a series of base shear vs. floor displacement curves. Fig 6.4(a) shows three of them, base shear vs. 1st floor, 14th floor (closest to the equivalent modal height), and the roof. Their initial stiffnesses and hardening stiffnesses are different from each other but the yielding base shears are and should be the same value.

Step 3, 4. Convert the ${}_nV_b - {}_nu_i$ pushover curve to the force-deformation, ${}_nA_s - {}_nD$, relation for the n th-mode inelastic SDOF system by utilizing Eq. (6.22). Idealize the force-deformation relation for the n th-mode SDOF system as a bilinear curve. Determine the initial stiffness and hardening stiffness of the SDOF system.

Table 6.1 Elastic structural characteristics of a Cnt model

Mode	T_0 (s)	M_{eq} (ton)	M_{eq}/M	S_{a0} (gal)	$V_{b0}=S_{a0}M^*$ (10^3 kN)	β	$K_0=(2\pi/T_0)^2$ (s^{-2})	$D_0=\beta S_{a0}(T/2\pi)^2$ (mm)
1	3.15	13411	73%	454.3	60.9	1.45	3.99	1650
2	0.69	3056.6	17%	1654	50.5	0.66	82.9	131.3
3	0.27	922.48	5%	1654	15.3	0.33	538	10.21

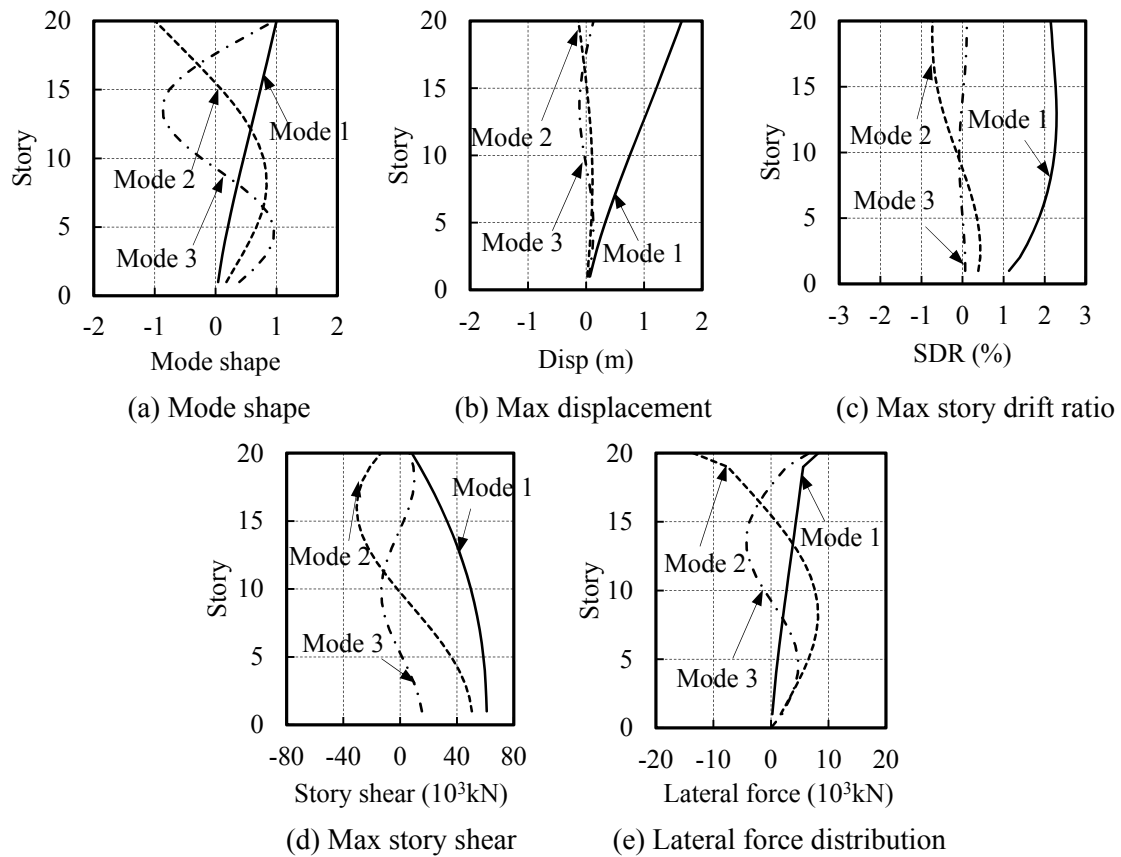
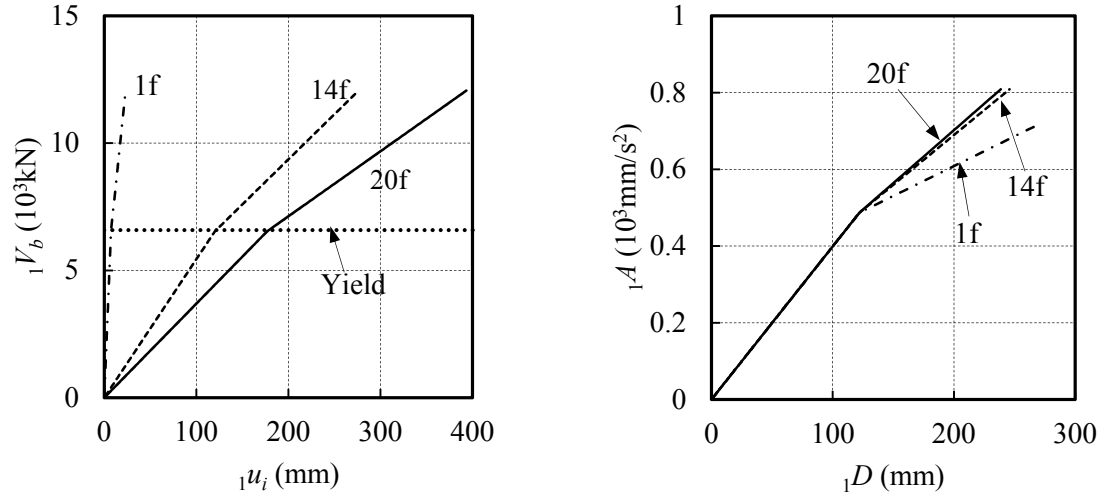


Fig 6.3 Mode shapes and elastic responses of a Cnt model

These curves are converted into force-deformation curves of the first-mode SDOF system by utilizing Eq. (6.22). Computing related ${}_1\varphi_i$ ($i=1, 14, 20$) values are given in Table 6.2. The converted force-deformation curves are shown in Fig 6.4(b). There is no necessary to idealize the force-deformation curves since the base shear-floor displacement curves of the original structure are simple bilinear curves. Three curves exhibit same initial stiffness but rather different hardening stiffness, particularly the curve converted from 1f, also as listed in Table 6.2.



(a) Original structure: base shear - floor disp. (b) SDOF system: force - def.

Fig 6.4 Force-def. relation of 1st-mode SDOF system of a Cnt model obtained in MPA

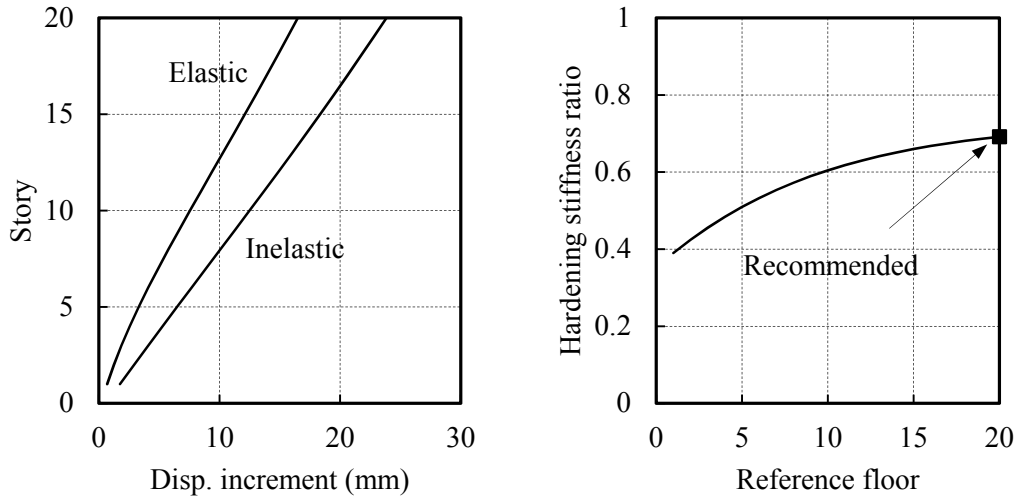
Table 6.2. Modal vector used in converting the 1st-mode SDOF system of a Cnt model

Floor	${}_1\phi_i$	${}_1D_y$ (mm)	${}_1A_y$ (mm/s ²)	${}_1K_0$ (s ⁻²)	${}_1K_h$ (s ⁻²)
1f	0.04	124	491	3.95	1.56
14f	0.68	123	491	3.97	2.60
20f	1.0	123	491	3.97	2.76

The initial stiffnesses are almost same because the floor displacement distribution is same with the elastic mode shape before the formation of yielding mechanism. The initial stiffnesses of the three curves are slightly smaller than that computed from eigenvalue analysis (3.99s). This is because the lateral force increases by an assigned increment in pushover analysis. When yielding phenomenon occurs, the lateral force already exceeds the exact yielding force. The difference is negligible when the force increment is small enough. Herein the base shear increment is 60.9kN, 0.1% of the estimated elastic response. It causes negligible difference, 0.5% to 1%, in the initial stiffnesses of the SDOF system.

Hardening stiffness of the SDOF system increases with the increasing of the height of the floor in which the displacement is used in converting SDOF system, this floor is called as the reference floor, as shown in Fig 6.5 (b). This implies that after formation of the yielding mechanism, inelastic deformation develops more rapidly in the lower stories when the model is subjected to invariant lateral force distribution as the elastic forces. If we check the floor displacement increments of the structure when subjected to the same amount of lateral force increments, we can see that, before the BRCs yield, the deformation shape of the structure is

more similar to a cantilever beam; after the BRCs yield, the deformation shape is almost a straight line, as the rotational constraint at the foundation is largely weakened due to yielding, as in Fig 6.5(a).



(a) Deformation (mode) shape (b) Effect of ref. floor on hardening stiffness ratio

Fig. 6.5 Effect of ref. floor on hardening stiffness ratio of the 1st-mode SDOF system of a Cnt model due to deformation shape changing

Utilizing different reference floors results in different hardening stiffness for the equivalent SDOF system. The lower the floor the smaller the hardening stiffness is. How to determine the most appropriate one will be discussed based on the estimated seismic responses of the structure.

Step 5. Evaluate the peak deformation ${}_nD$ by utilizing Eq. (6.24)~(6.27).

Three difference force-deformation curves of the SDOF system are adopted to evaluate the peak deformation and base shear responses of the structure. Before evaluating the original structure, the equivalent damping ratio, equivalent period, deformation and force response of the SDOF system are computed by iterating Eq. (6.24)~(6.27). Their convergence results are listed in Table 6.3.

Note that ${}_1D$ is proportional to the displacement at different floor, so it is not comparable, while ${}_1A$ is proportional to the base shear of the original structure, thus we can already tell that the 20f converted curve produces the largest estimation value for resisting forces. It also indicates the largest estimation value for floor displacements, since the floor displacement always increases along with the base shear in the original structure. This will be confirmed in the next step.

Table 6.3 Estimation of 1st-mode SDOF system of a Cnt model by MPA method

Floor	${}_1T_{eq}$ (s)	${}_1h_{eq}$	${}_1R_d$	${}_1R_a$	${}_1D$ (mm)	${}_1A$ (mm/s ²)
1f	4.62	0.121	0.89	0.42	1020	1884
14f	3.78	0.063	0.92	0.64	1044	2881
20f	3.69	0.057	0.92	0.67	1052	3052

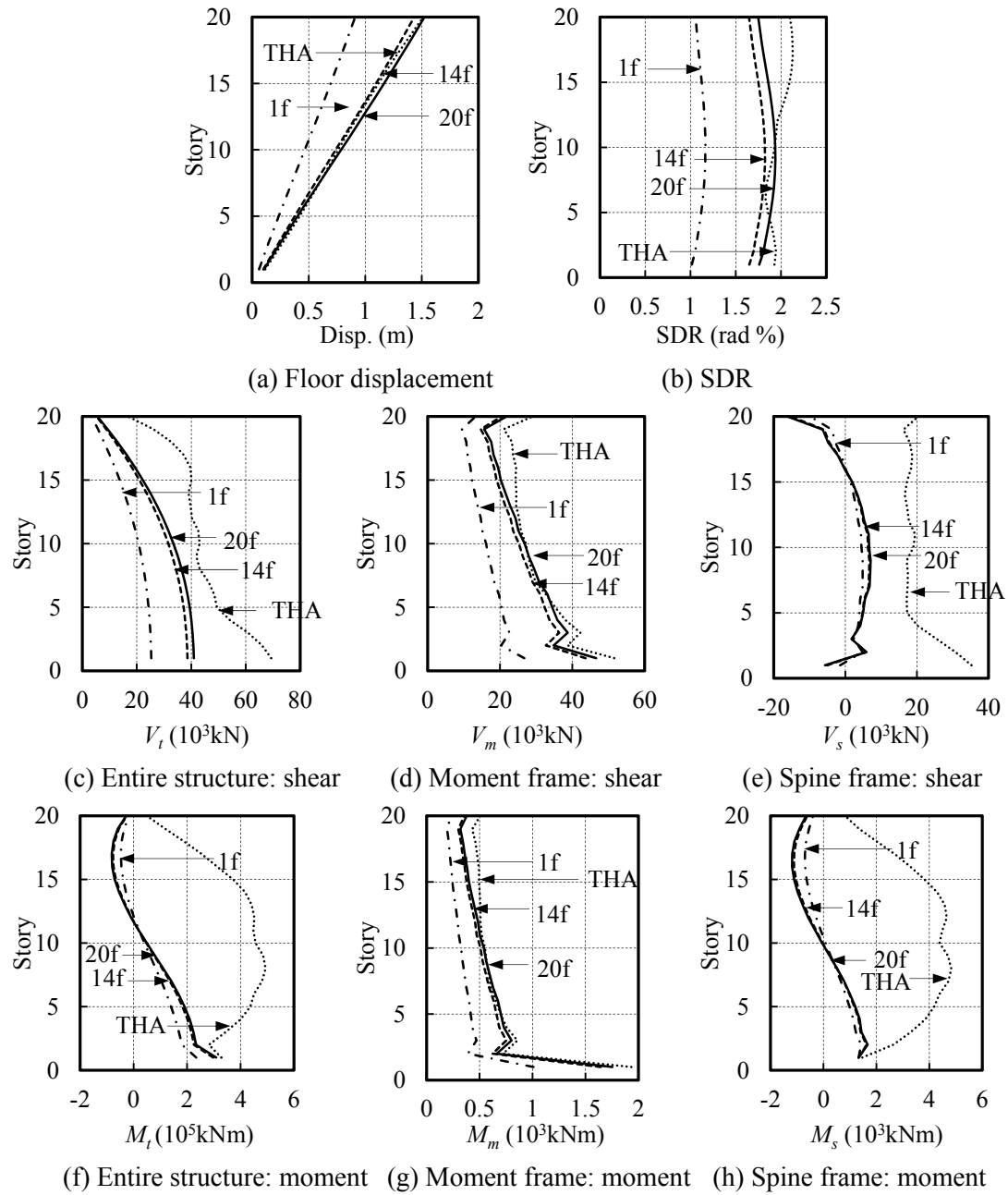
Step 6, 7. Inversely convert ${}_nD$ to the peak i th floor displacement ${}_nu_i$ in the inelastic MDOF system. From the pushover database (step 2), extract values of desired response ${}_nr$ at i th floor displacement equal to ${}_nu_i$.

An alternative way is to locate the analysis step of pushover analysis in which the evaluated ${}_1D$ and ${}_1A$ (Table 6.3) of the SDOF system are achieved. The corresponding responses of the original structure are responses at this analysis step. As listed in Table 6.4, ${}_1D$ and ${}_1A$ are extracted from the pushover database as the closest values to those in Table 6.3, with difference less than 0.1%.

Table 6.4 Estimated 1st-mode responses of the original Cnt structure by MPA method

Floor	Analysis step	${}_1D$ (mm)	${}_1A$ (mm/s ²)	${}_1u_i$ (mm)	${}_1V_b$ (10 ³ kN)
1f	415	1021	1885	61	25.3
14f	634	1043	2880	1026	38.6
20f	672	1052	3053	1524	40.9

Base shear of the original structure ${}_1V_b$ obtained by utilizing 1f pushover curve is only 62% of that obtained from 20f curve, as well as the shear force in other stories, as in Fig. 6.6 (b). SDR response obtained from 1f curve is also much smaller than that obtained from 20f or 14f curves, as shown in Fig. 6.6 (a). Comparing to the time-history analysis results in Fig 6.6, we can see that adopting 1f curves might greatly underestimate both deformation and resisting force, while the 20f estimation seems more reasonable. The preceding results indicate that, the SDOF system with smaller hardening stiffness exhibits larger equivalent period and equivalent damping ratio when subjected to the same earthquake intensity, accordingly the estimated resisting forces for the original structure is also smaller, so as the other responses because their value increase monotonically as the forces are increased in the first mode response. Relation between base shear and roof displacement is preferred in converting the original structure to a SDOF system, since it increases conservatism in the response estimation.

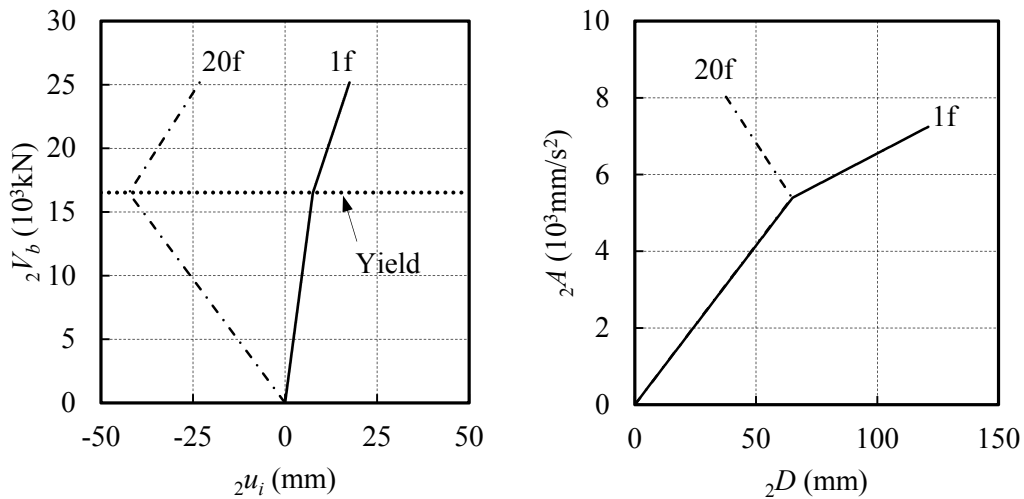
Fig. 6.6 1st-mode responses of a Cnt model estimated with variable reference floors

Note that reversal story shear forces occur in the upper stories as well as the first story of the spine frame. Similarly, structures utilizing shear walls and moment frames generate reversal story shear in the upper stories of the shear walls when subjected to lateral forces. However, reversal story shear occurs at the first story is unique for the spine frame system, and may significantly increase shear strength demand of the moment frame. The spine frame is pin connected to the foundation while the moment frame is rigid connected. Such reversal story shear forms when the lower stories of the moment frame are too stiff to follow the

deformation of spine frames, thus increasing the external lateral forces on the moment frames. To eliminate the additional force demand, we can reduce the lateral stiffness at the lower stories of the moment frame, by increasing the first story height, adopting half-rigid connections, etc.

Step 8. Repeat steps 3 to 7 for as many modes as required for sufficient accuracy.

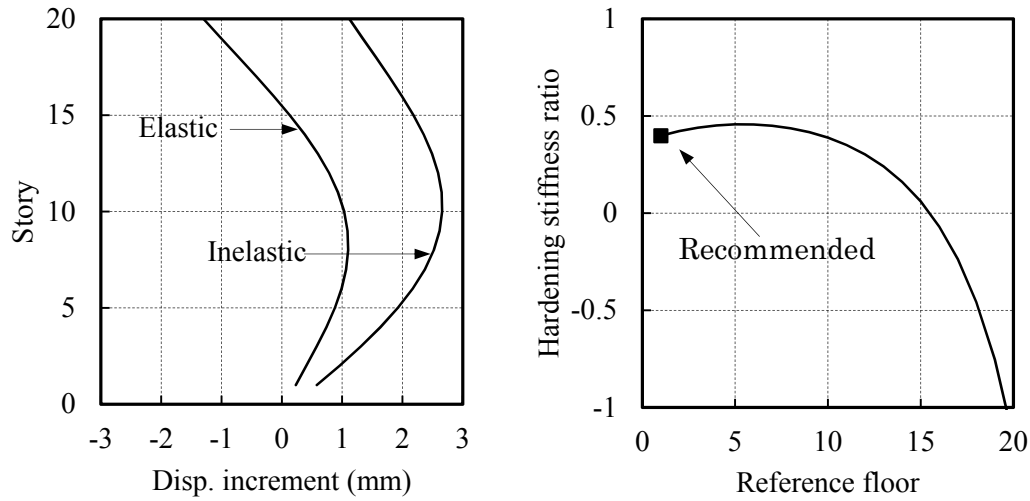
Similarly, the original structure is pushed by lateral forces following the 2nd-mode distribution, as shown in Fig 6.3 (e). Note that, different from the 1st-mode distribution, the higher-modes lateral forces pull some floors but push the others. Fig 6.7 plots the base shear vs. the 1st floor displacement and roof displacement of the original structure, as well as the force vs. deformation relation of the 2nd-mode SDOF system. The 1st floor pushover curve is normal. However, “reversal” occurs in the roof pushover curve, i.e., the roof displacement reverses direction after the BRCs at the first story yield, which indicates that a global rotation of the structure about the foundation might occur and this rotation reverses the direction of the roof movement.



(a) Original structure: base shear - floor disp. (b) SDOF system: force - def.

Fig. 6.7 Reversal stiffness of 2nd-mode SDOF system of a Cnt model obtained in MPA

Changes in the distribution of the floor displacement increments straightforwardly confirmed the formation of global rotation. As shown in Fig 6.8(a), before the BRCs yield, the deformation shape of the structure is same with the 2nd-mode shape; after the BRCs yield, the whole structure rotates clockwise about the foundation, causing the displacement increments of the floors above the 15th floor reverse their direction.



(a) Deformation (mode) shape (b) Effect of ref. floor on hardening stiffness ratio

Fig. 6.8 Effect of ref. floor on hardening stiffness ratio of the 2nd-mode SDOF system of a Cnt model due to deformation shape changing

Previous researchers have also noticed this “reversal” behavior. Recent investigations demonstrate that such “reversal” behavior is caused by specific local story mechanisms, which was found to be very rare in moment-resisting frame structures. However, this “reversal” behavior seems unavoidable in the spine frame structures, since the essential nonlinear members—BRCs are equipped in the first story. Previous researchers pointed three ways to overcome the difficulty. First, this issue is moot if the structure does not deform beyond the elastic range in the modes with “reversal” behavior; this is often the case, but might not for the spine frame system. Second, seismic responses of the structure associated with higher-modes can be estimated by assuming the structure remains elastic; such conservatism is acceptably small except for lightly damped system, with damping significantly less than 5%. Third, any “reversal” of the pushover curve may be eliminated by plotting base shear against the displacement of a different floor above the yielded stories. The current study will compare the estimated responses obtained from method 2 and method 3.

Method 2, i.e. elastic estimation, on the seismic response of the 2nd mode has been computed by eigenvalue analysis. To implement method 3 we need to determine which floor displacement to plot in the pushover curve. Hardening stiffness ratio obtained by using various reference floors is plotted in Fig. 6.8 (b). Floors lower than 16 give positive hardening stiffness and their pushover curves are usable in the MPA procedure. We have understood that the largest hardening stiffness gives the most conservative estimation for base shear, as discussed on the 1st mode response. This rule is same for the 2nd mode. However, this does not ensure the most

conservative estimation for other responses, as they may not always increase monotonically with the base shear. To determine which floor is appropriate, the estimated response of the original structure by utilizing 1st, 13th, 14th, and 15th floor as reference floors were compared. Fig 6.9 plots the base shear vs. floor displacement of the original structure, as well as the force vs. deformation relation of the corresponding 2nd-mode SDOF system. Mode vectors involved in converting and the converted initial and hardening stiffnesses of the SDOF system are listed in Table 5.

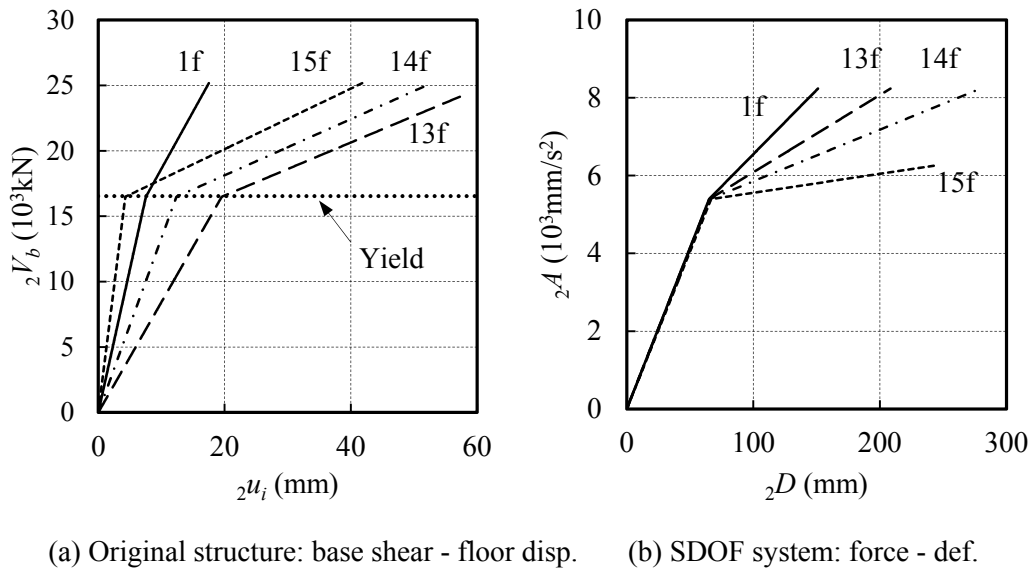


Fig. 6.9 Force-def. relation of 2nd-mode SDOF system of a Cnt model obtained in MPA

Table 6.5. Modal vector used in converting the 2nd-mode SDOF system of a Cnt model

Floor	${}_2\varphi_i$	${}_2D_y$ (mm)	${}_2A_y$ (mm/s ²)	${}_2K_0$ (s ⁻²)	${}_2K_h$ (s ⁻²)
1f	0.18	65.5	5409	82.6	33.0
13f	0.45	66.0	5409	82.0	19.9
14f	0.29	66.5	5409	81.3	13.3
15f	0.10	69.3	5409	78.0	4.87

Table 6.6 Estimation of 2nd-mode SDOF system of a Cnt model by MPA method

Floor	${}_2T_{eq}$ (s)	${}_2h_{eq}$	${}_2R_d$	${}_2R_a$	${}_2D$ (mm)	${}_2A$ (mm/s ²)
1f	0.89	0.098	0.97	0.59	195	9678
13f	0.99	0.133	0.98	0.49	198	8038
14f	1.05	0.155	0.99	0.44	201	7197
15f	1.17	0.189	0.99	0.37	209	6093

Table 6.7 Estimated 2nd-mode responses of the original Cnt structure by MPA method

Floor	Analysis step	${}_2D$ (mm)	${}_2A$ (mm/s ²)	${}_2u_i$ (mm)	${}_2V_b$ (10 ³ kN)
1f	585	195	9676	22.6	29.6
13f	486	198	8039	59.4	24.6
14f	435	201	7195	38.0	22.0
15f	368	209	6087	13.4	18.6

The equivalent damping ratio, equivalent period, deformation and force response of the SDOF system are computed by iterating Eq. (6.24)~(6.27). Their convergence results are listed in Table 6.6. The floor displacement and base shear response of the original structure extracted from the pushover database are listed in Table 6.7.

Base shear of the original structure ${}_2V_b$ obtained by utilizing 1f pushover curve is the largest among all the estimations, as well as the SDR, story shear force of each structural component, and moment of the moment frame, as in Fig. 6.10 (b) (c) (d) (e) (g). The only exceptions are the displacement of the top 2 floors and moment of the spine frame at the base 2 stories, but the difference among those estimations adopting different pushover curves is negligible compared to the total seismic response. Relation between base shear and the 1st-floor displacement is preferred in converting the original structure to a SDOF system, since it increases conservatism in the response estimation. The elastic responses are much larger compared to the inelastic responses, except for the SDR of lower stories, as shown in Fig 6.11. Table 6.6 also tells that force response is reduced by approximately 50% by considering nonlinear behavior. The seismic responses might be largely overestimated if we assume the structure behavior elastically in the higher-modes. We will compare the elastic higher-mode estimation with the inelastic estimation after taking account of the 3rd mode response.

The 3rd-mode responses are estimated by the same procedure with the 2nd mode. The current 20-Cnt model does not deform beyond the elastic range in the 3rd mode. The first story SDR is 0.07% smaller than 0.1%, the SDR when BRCs yield. Fig 6.2 already gives the displacement, SDR, and story shear responses of the 3rd mode of the structure. Estimated deformation responses of the 1st, 2nd, and 3rd mode are combined by utilizing SRSS rules (Eq. (6.29)) since the natural frequencies are well-separated. Force responses except the moment of the BRCs are also combined by SRSS rule since the structural members are assumed as elastic. Peak moment of the BRCs is simply the yielding moment. Fig 6.12 shows the responses estimated by the MPA procedure with the nonlinear time history analysis (THA). The estimated values of responses are computed including 1 mode, 2 modes, or 3 modes.

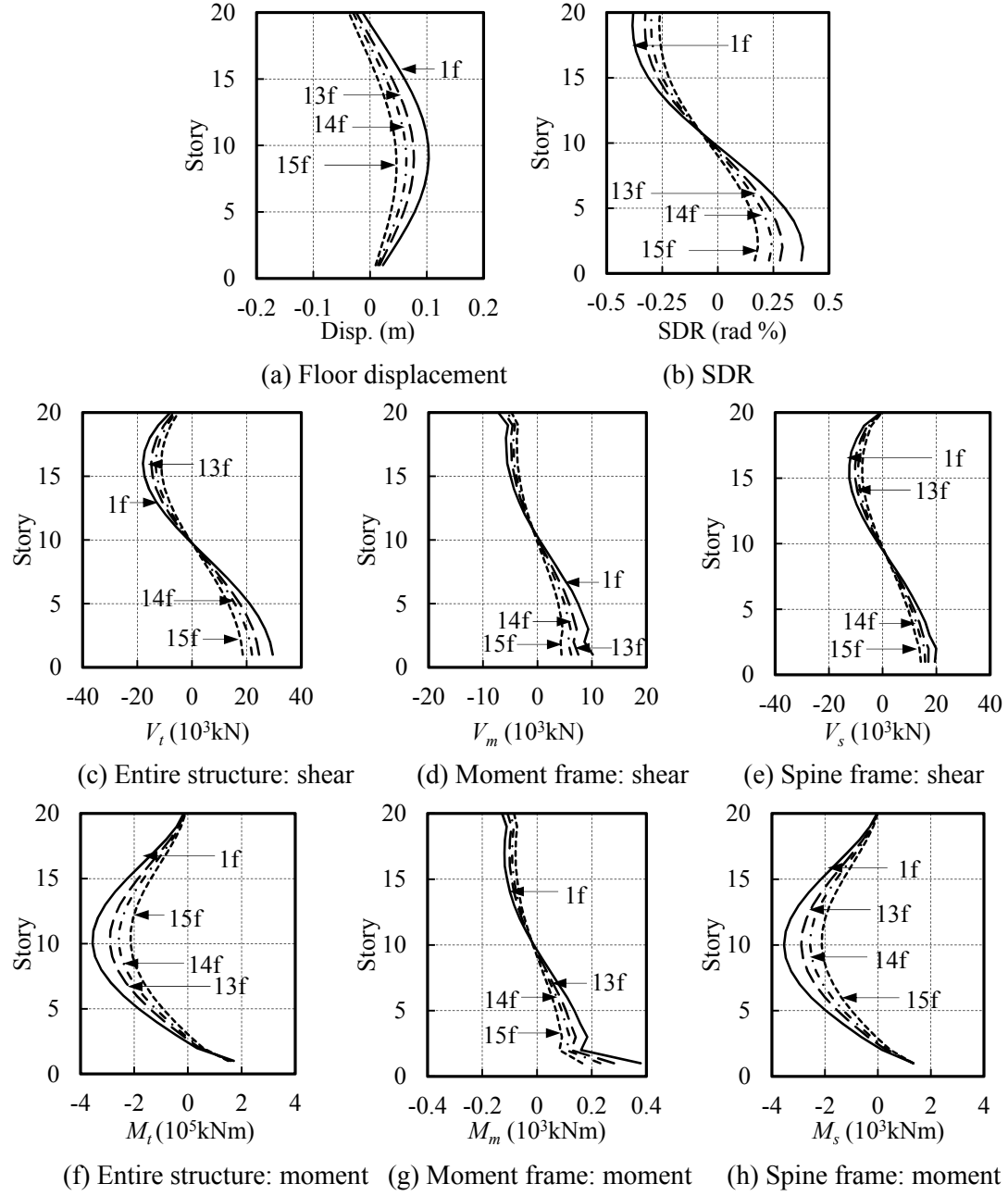


Fig. 6.10 2nd mode responses of a Cnt model estimated by utilizing different ref. floors

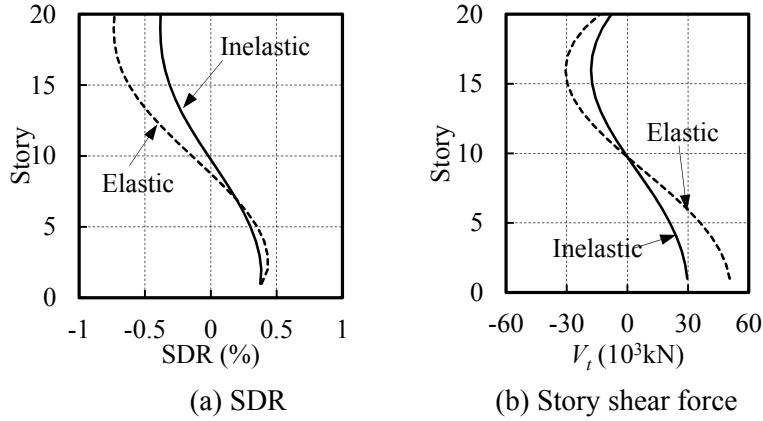


Fig. 6.11 Comparison between inelastic and elastic 2nd-mode response of a Cnt model

The 2nd mode contributes significant response in the story shear and bending moment of the spine frame. Contributions of the 3rd mode are almost negligible in all of the responses. We could preliminarily decide that 3 modes could provide sufficient estimation for the 20-story Cnt spine frame structures.

As shown in Fig 6.12 (a) and (b), the 1st mode response is absolutely primary in terms of floor displacement and SDR. Force response of the moment frame is also dominated by the 1st mode because they are mostly determined by lateral deformation, as in Fig 6.12 (d), (g). However, the resisting force of spine frames relies more on floor rotation. That's why the 2nd mode contributes significant response in the story shear and bending moment of the spine frame.

The peak SDR of the structure in THA is larger at the upper stories, which is different from the nearly constant distribution in the MPA results. Despite the different deformation shape, the maximum roof displacement and SDR are well estimated with 10% and 2% error. As for the moment frame, the estimated results of story shear and moment match very well with the THA results, in which the errors are less than 15% at all the stories. As for the spine frame, base shear and moment of stories lower than 15 are underestimated by over 30%, implying that contribution of the higher modes might be largely underestimated by utilizing SRSS combination rule.

Similar comparison of the MPA procedure assuming elastic higher-mode responses and nonlinear THA results are presented in Fig 6.13. Conservatism of this procedure is too large in the force responses. It may not suitable to use this MPA procedure for tall spine frame structures. Comparison of the MPA procedure utilizing ABSSUM combination rule and nonlinear THA results are presented in Fig 6.14. Higher-mode responses are not assumed to be elastic herein. In

contrast with the SRSS rule, contributions of higher-mode responses are greatly overestimated by utilizing ABSSUM rule.

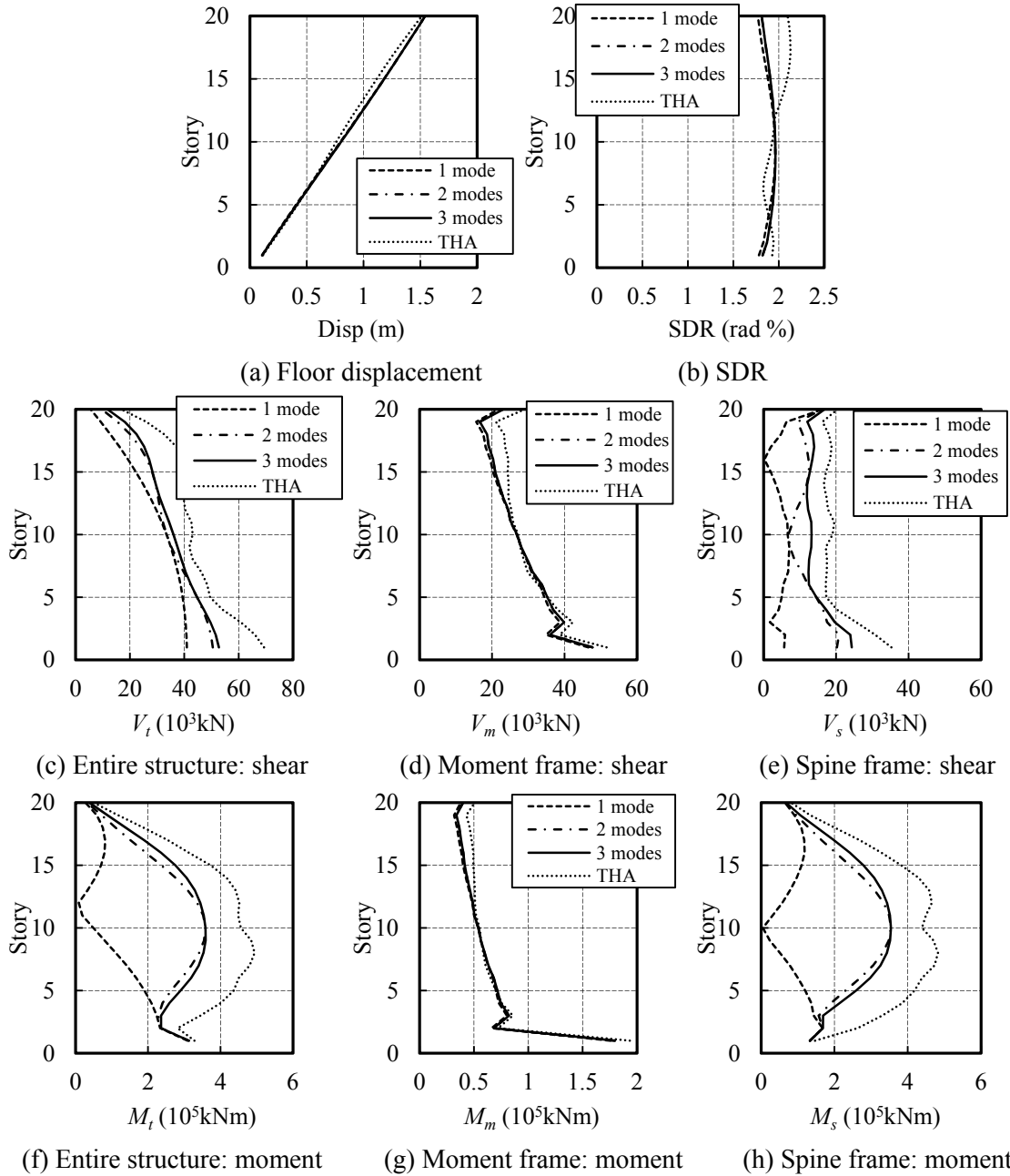


Fig. 6.12 Responses of a Cnt model estimated by MPA with variable number of modes

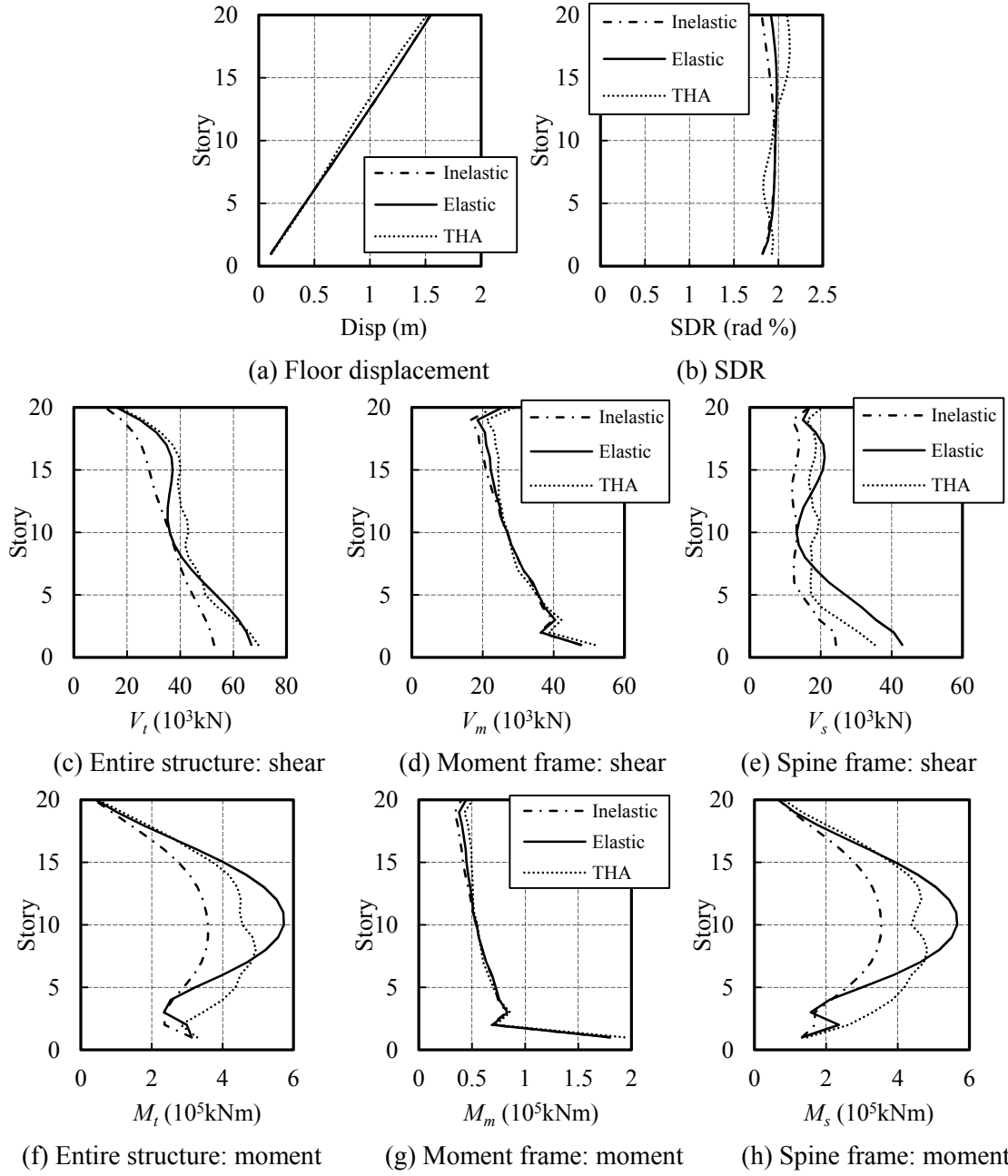


Fig. 6.13 Responses of a Cnt model by MPA assuming elastic higher-modes behavior

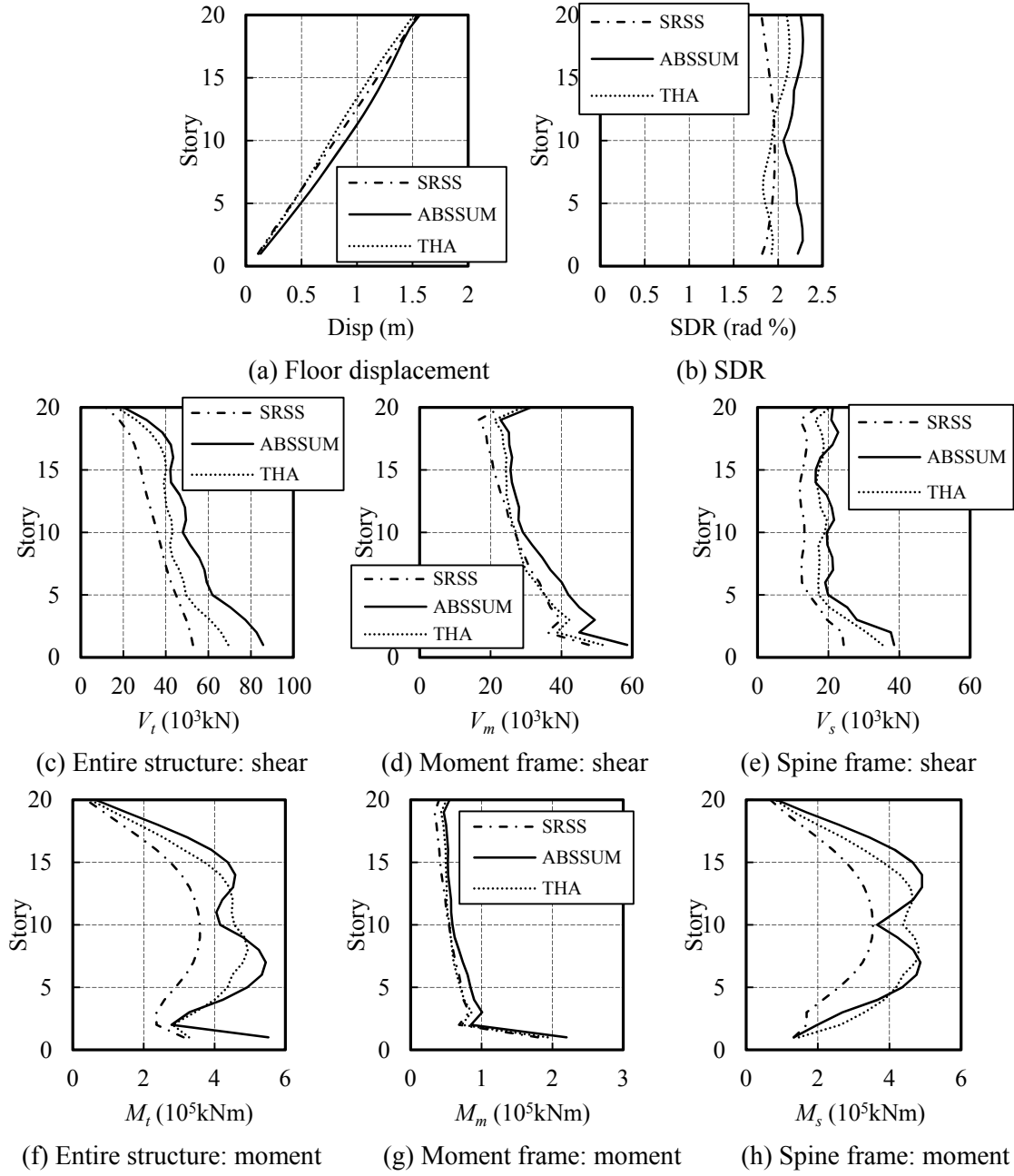


Fig. 6.14 Responses of a Cnt model estimated by MPA with ABSSUM combination rule

Based on the preliminary analysis results, we recommend estimating modal response of the first 3 modes by the nonlinear MPA procedure, and then combining them by SRSS rule as the estimation for the tall spine frame structures.

The 20-story Cnt models with $K_s/K_f=0.1\sim 2.0$ and $K_d/K_f=0\sim 4.0$ are estimated by utilizing the MPA procedure. Fig 6.15 shows some of the estimated responses and the nonlinear THA results. The SDR, roof displacement, base shear of moment frames, as well as overturning moment of moment frames are well estimated with appropriate conservatism.

The ductility ratio of the 2nd mode response is around 2.0 ~ 4.0 when $K_s/K_f = 0.3 \sim 0.7$ and $K_d/K_f=0.5 \sim 2.0$, which are the most practical and effective stiffness range, as in Fig 6.16. Assuming the building to be linearly elastic may significantly overestimate the 2nd mode responses, particularly for the resisting forces.

Base shear and maximum story moment of the spine frame is underestimated by MPA procedure. The main reason might be that the higher modes contribution on forces response is underestimated by utilizing SRSS modal combination rules.

Estimation for deformation and moment frame force responses could be enhanced in the step of converting original structure into the 1st mode SDOF system. Utilizing the curve of base shear and roof displacement leads to the most conservative results, because the impact of local plasticity behavior at the first story gradually weakened along the structure height, which is indicated by the changing ratio of displacement increment before and after yielding.

Fig 6.17 and 6.18 present the detailed results of 20-story Cnt-Ksf0.3-Kdf2.0 model. Relation of base shear and roof displacement is utilized to estimate the 1st mode response in Fig 6.17; while relation of base shear and 8th-floor displacement is utilized to estimate the 1st mode response in Fig 6.18. Changing ratio of displacement increment at the 8th floor is the closest to the average value. Estimated SDR and story displacement in Fig 6.17 are almost identical with the THA results.

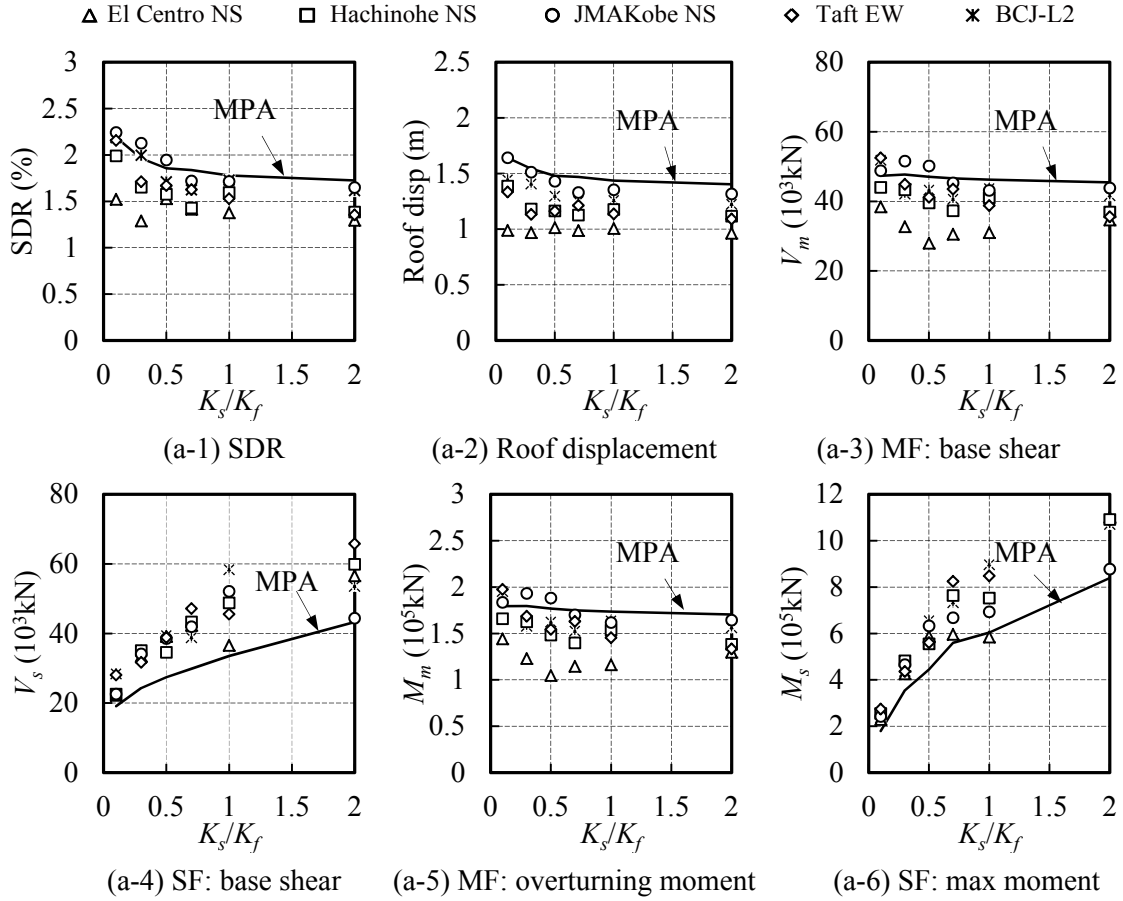


Fig. 6.15 (a) Comparison of MPA and THA results of seismic performances of the 20-story Cnt models with various K_s/K_f ($K_d/K_f=1.0$)

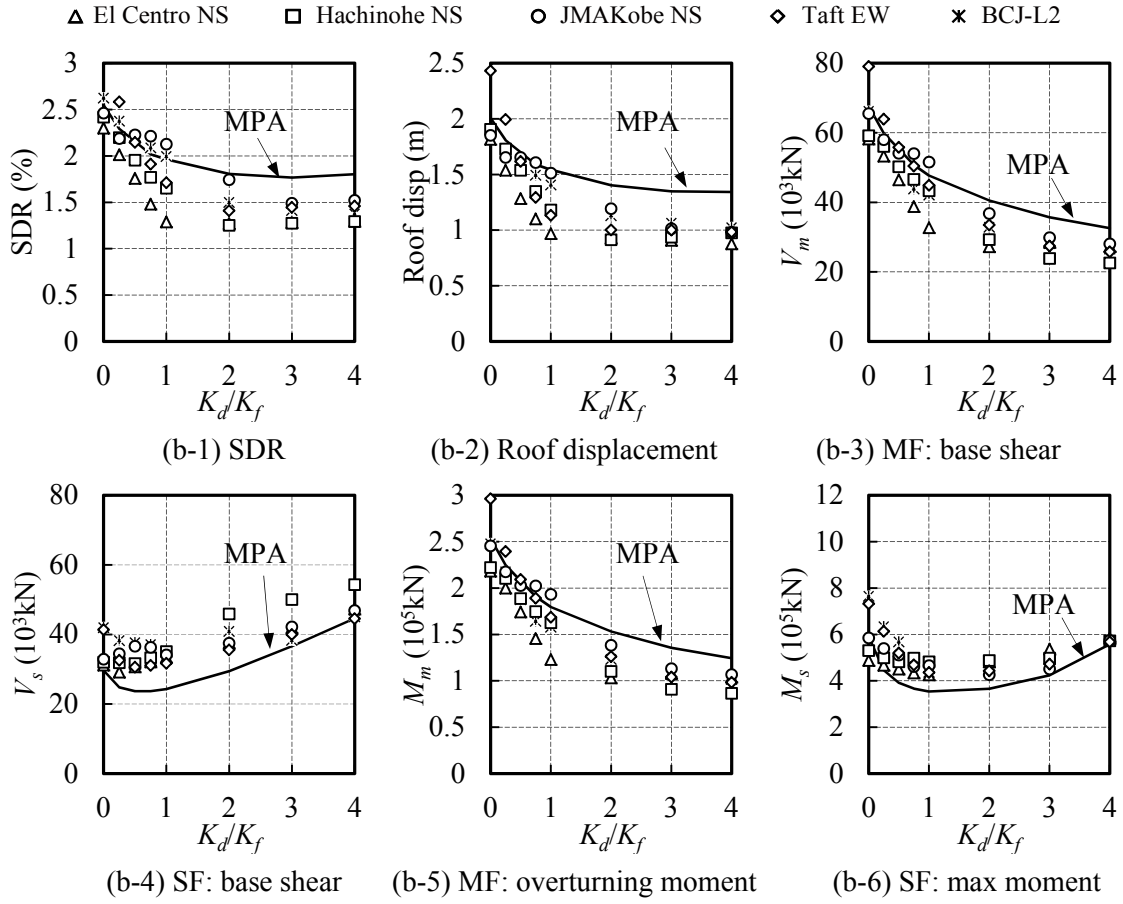


Fig. 6.15 (b) Comparison of MPA and THA results of seismic performances of the 20-story Cnt models with various K_d/K_f ($K_s/K_f=0.3$)

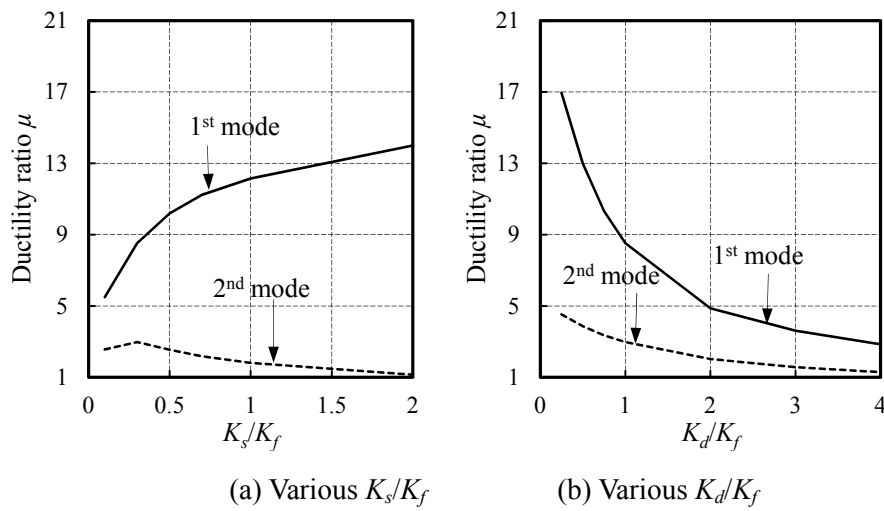


Fig. 6.16 Ductility ratio of the 1st mode and 2nd mode responses of the 20-story Cnt models with various K_s/K_f and K_d/K_f

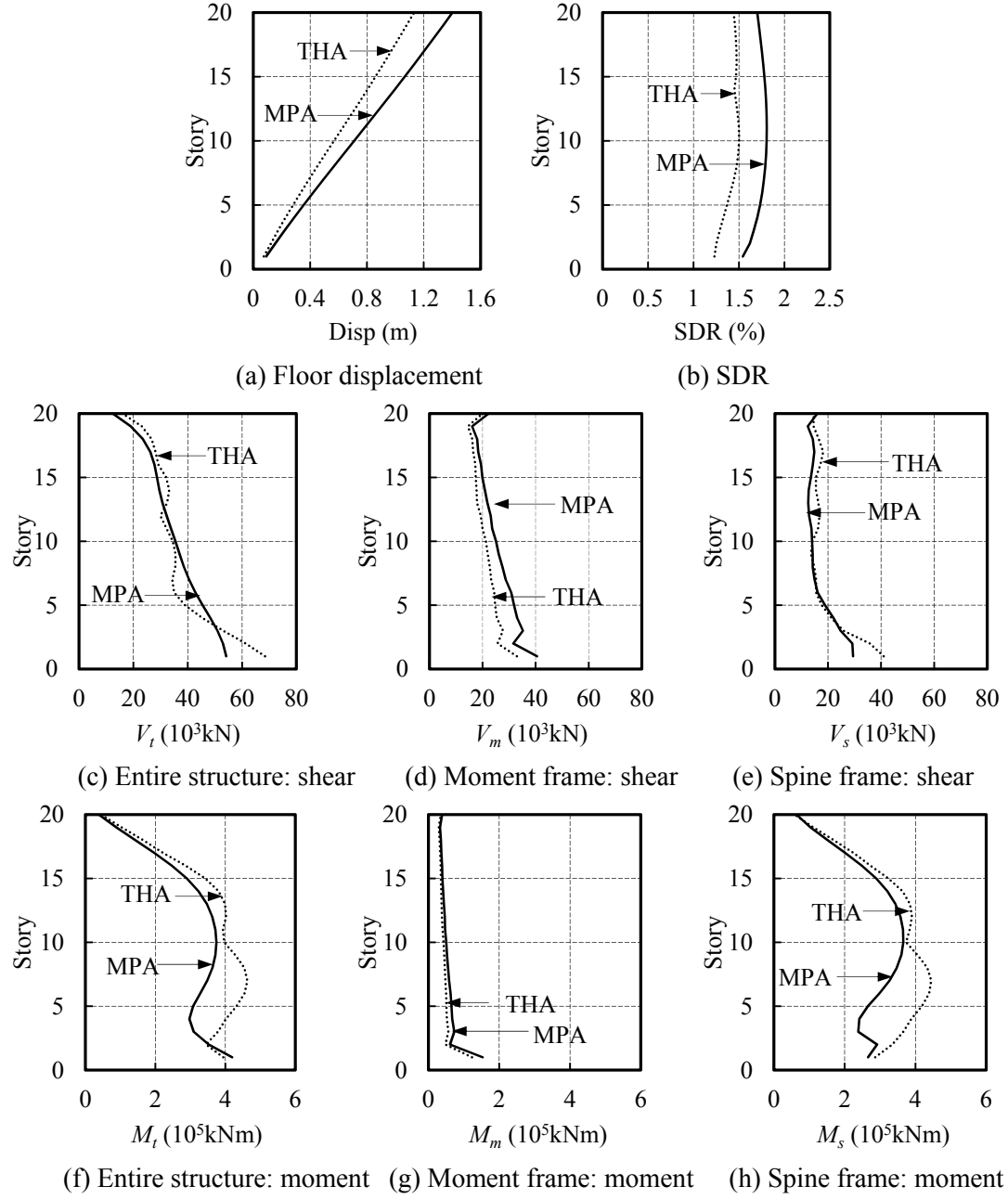


Fig. 6.17 Estimated modal responses of 20-story Cnt-Ksf0.3-Kdf2.0 model

(1st-mode reference floor: 20th floor)

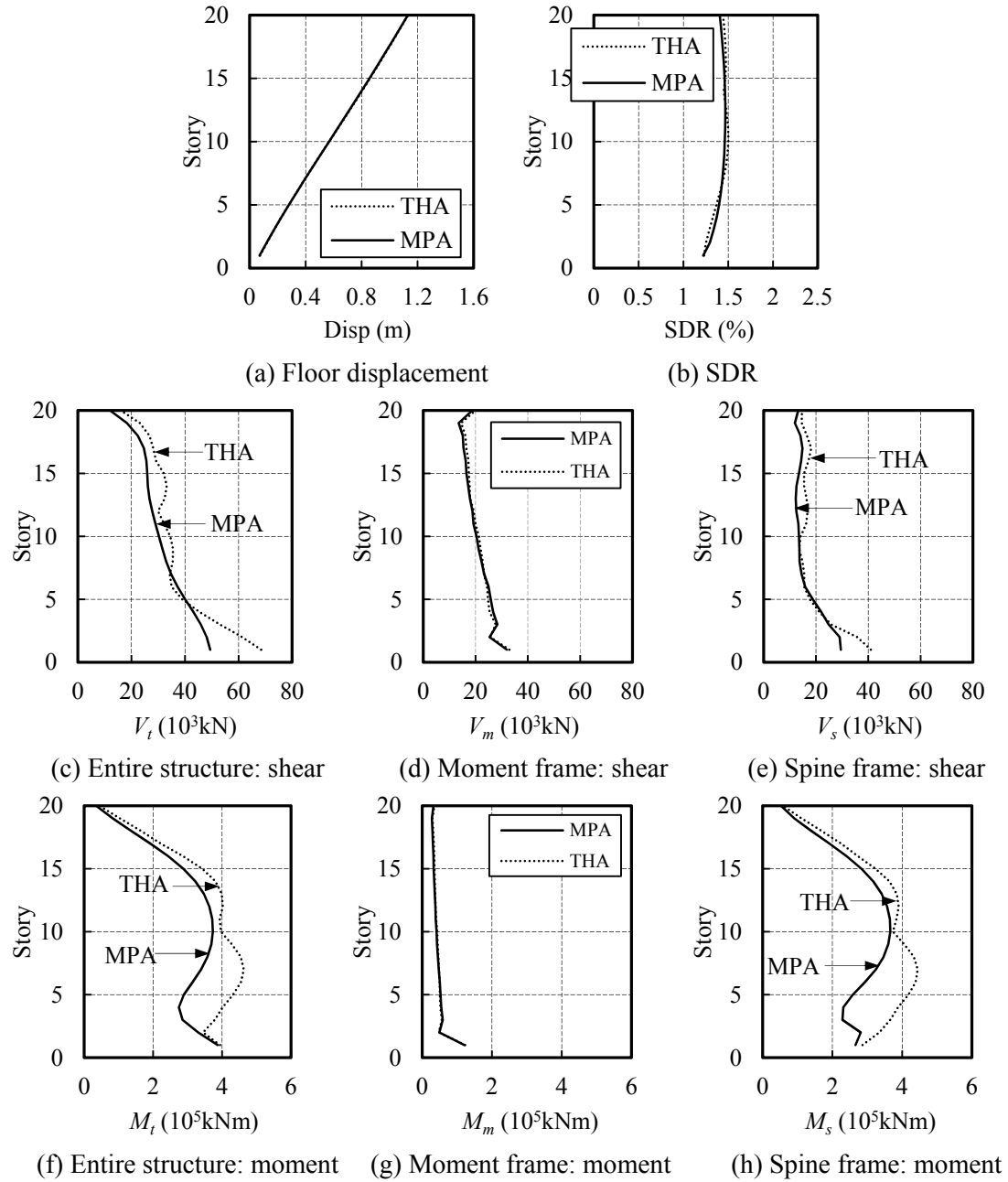


Fig. 6.18 Estimated modal responses of 20-story Cnt-Ksf0.3-Kdf2.0 model

(1st-mode reference floor: 8th floor)

6.4.2 Evaluation of Cnt models by RSA method

The 20-story Cnt models with $K_{sf}=0.1\sim 2.0$ and $K_{df}=0\sim 4.0$ are estimated by utilizing the RSA procedure. Detailed results of each step for the Cnt- $K_{sf}0.3$ - $K_{df}1.0$ model are demonstrated in the following paragraphs.

Step 1&2. Compute the natural periods, ${}_nT_f$, and modes, ${}_n\phi_f$, for linearly elastic vibration of the main frame without BRCs. Obtain the elastic force-deformation ${}_nA - {}_nD$ relation with stiffness K_f for the SDOF system of each mode by utilizing Eq. (6.22). For the n -th mode, evaluate the elastic modal responses ${}_nr_f$ of the main frame with an inherent damping ratio of 0.02. To evaluate forces of structural members, elastic pushover analysis using the lateral force distribution ${}_ns_f^*$ is required.

Eigenvalue analysis is carried out for the elastic main frame without BRCs and results of the first three modes are summarized in Table 6.9. Elastic stiffness K_f as well as the elastic response of base shear V_{bf} and mode coordinate D_f of the first three modes are also listed in Table 6.9. These results are directly computed according to the natural periods and modes obtained from eigenvalue analysis by assuming the system behaviors elastically. Fig 6.19 shows the mode shape and some elastic responses distributions of the main frame by utilizing Eq. (6.17), (6.19), (6.32) and (6.33). The elastic force-deformation ${}_nA - {}_nD$ curves with stiffness ${}_nK_f$ for the SDOF system of each mode are plotted in Fig 6.20.

To obtain the force distribution of moment frames and the spine frame, static pushover analysis is carried out for the main frame. The lateral forces are always proportional to those obtained from elastic eigenvalue analysis, as in Fig 6.19(e). Fig 6.21 shows the shear force and column base moment distribution of the moment frames and the spine frame.

Table 6.9. Structural characteristics of the elastic main frame in a Cnt model

Mode	T_f (s)	M_{eq} (ton)	M_{eq}/M	S_{af} (gal)	$V_{bf}=S_{af}M^*$ (10^3 kN)	β	$K_f=(2\pi/T_f)^2$ (s^{-2})	$D_f=\beta S_{af}(T_f/2\pi)^2$ (mm)
1	3.89	14419	79%	367.6	53.0	1.42	2.61	2000
2	0.77	2495	14%	1654	41.3	0.61	66.1	151.7
3	0.29	687	4%	1654	11.4	0.29	482	9.99

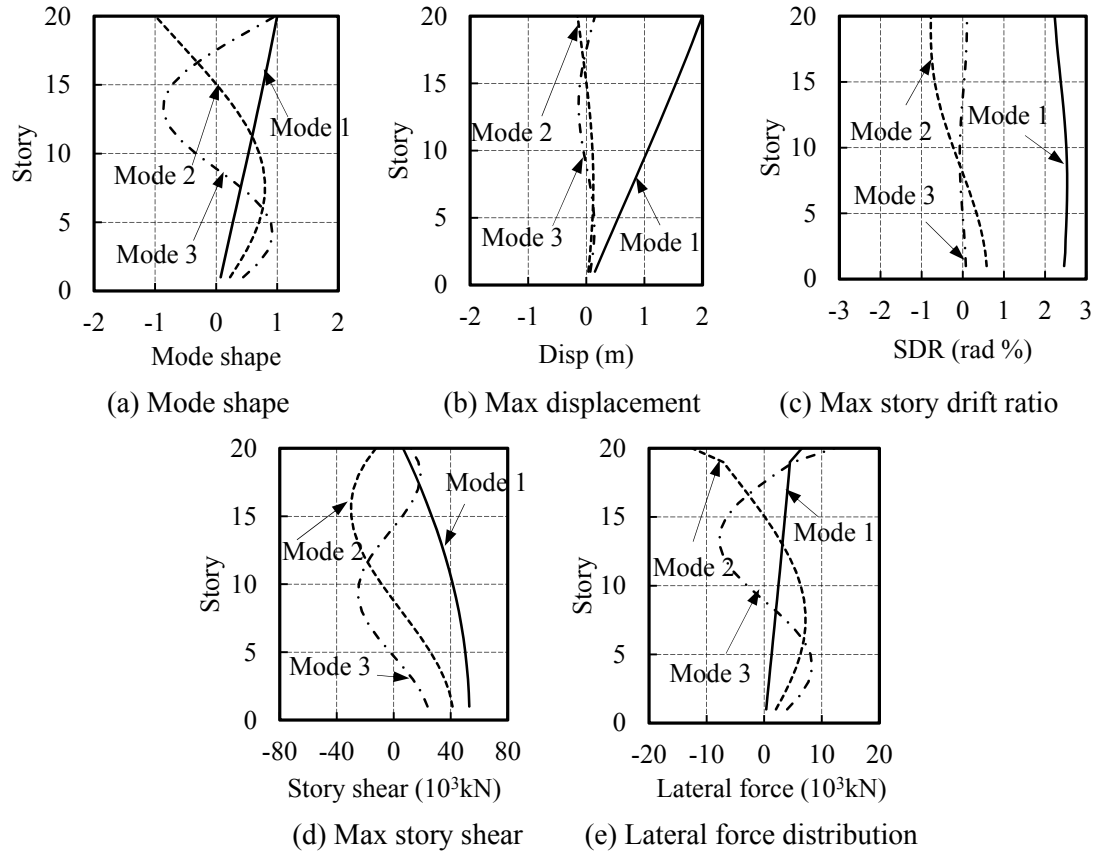


Fig. 6.19 Mode shapes and elastic responses of the main frame in a Cnt model

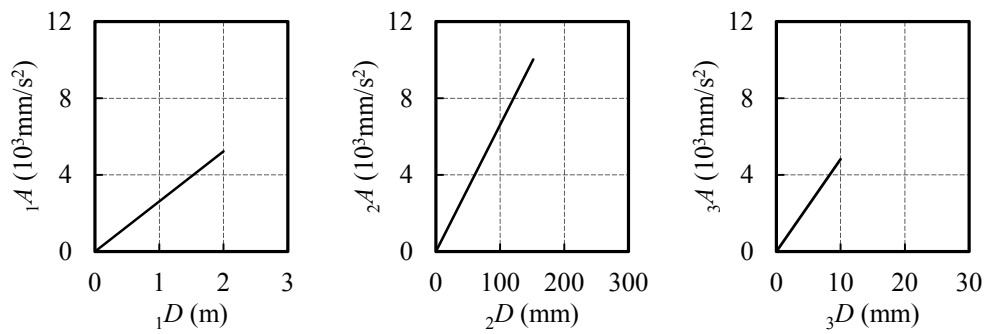


Fig 6.20 Force-def. curves of the 1st- 2nd- , and 3rd-mode SDOF systems of the main frame in a Cnt model

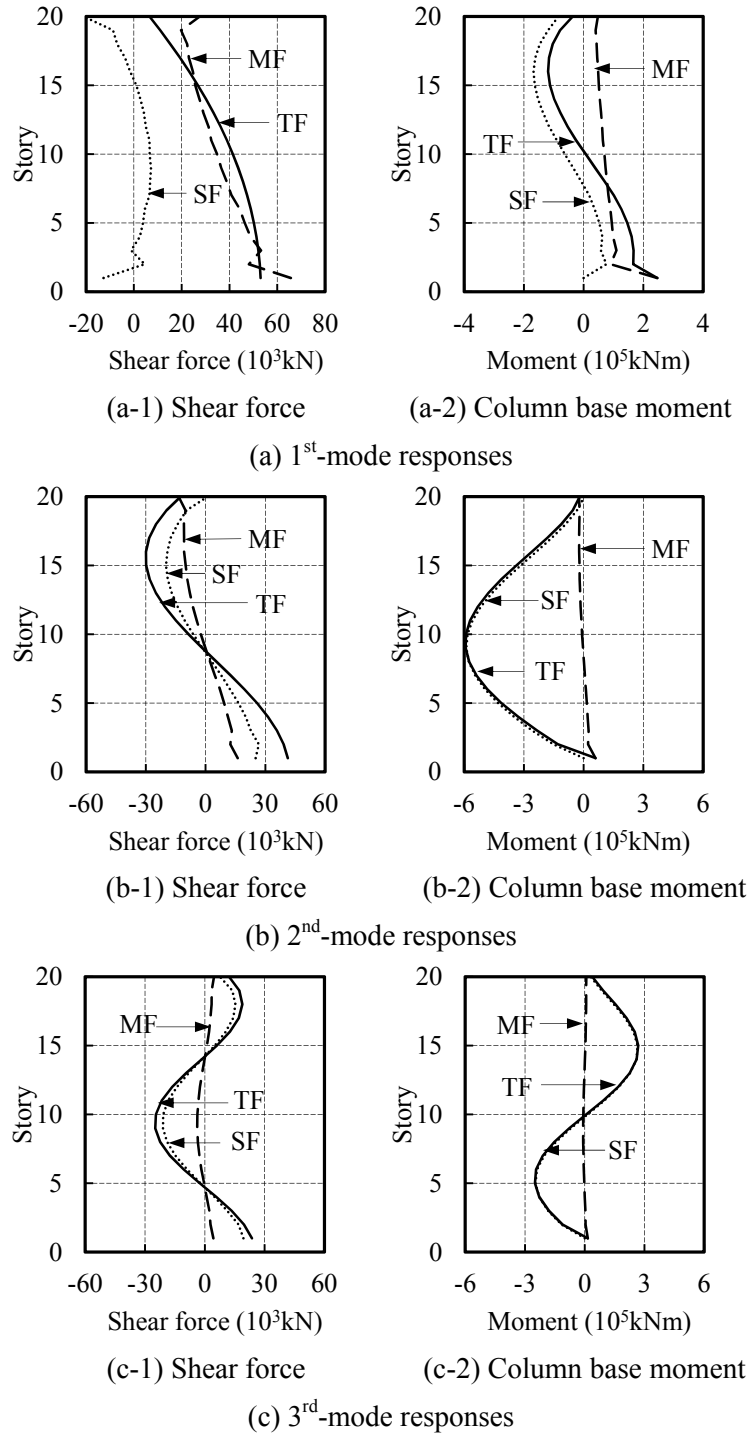


Fig. 6.21 Force distribution of each component of the main frame in a Cnt model

Step 3 ~ 5. For the 1st mode, compute the additional stiffness K_a and yielding deformation D_y contributed by BRCs on the force-deformation relation of the SDOF system. Determine the initial stiffness $K_{f+a} = K_f + K_a$ and hardening stiffness K_f of the SDOF system.

Additional stiffness and yielding deformation of the BRCs are evaluated by utilizing the similar method as that proposed for the low-rise buildings. The spine frame flexural stiffness reduces the effective damper stiffness and must be accounted for. To isolate the spine frame stiffness, eigenvalue analysis is conducted with the dampers substituted with rigid elements (Fig 6.22 (a)), in addition to the main frame with dampers removed (Fig 6.22 (b)). Thus, the stiffness of the spine frame K_c could be isolated from the frame K_f by subtracting the results of the first eigenvalue analysis ($K_c + K_f$) from the second (K_f).

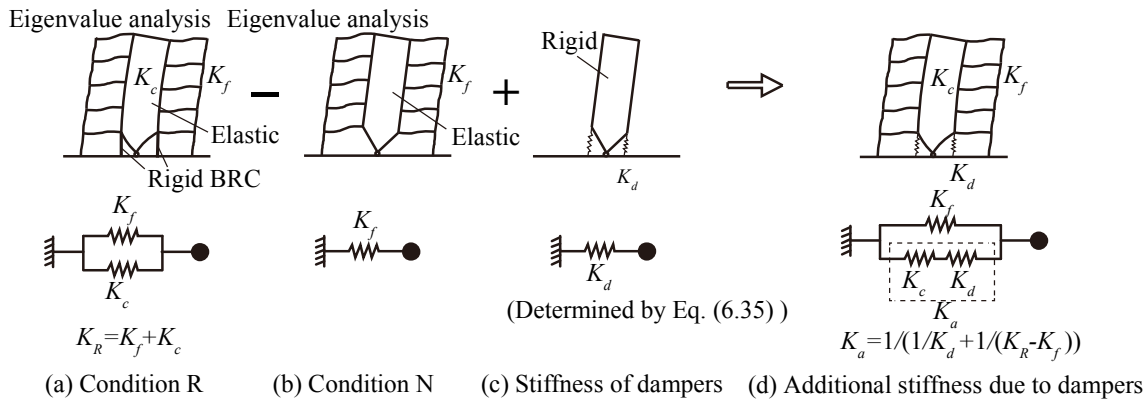


Fig. 6.22 (d) shows the full structural system, with the damper stiffness expressed by Eq. (6.34), including the flexural deformation of the spine frame:

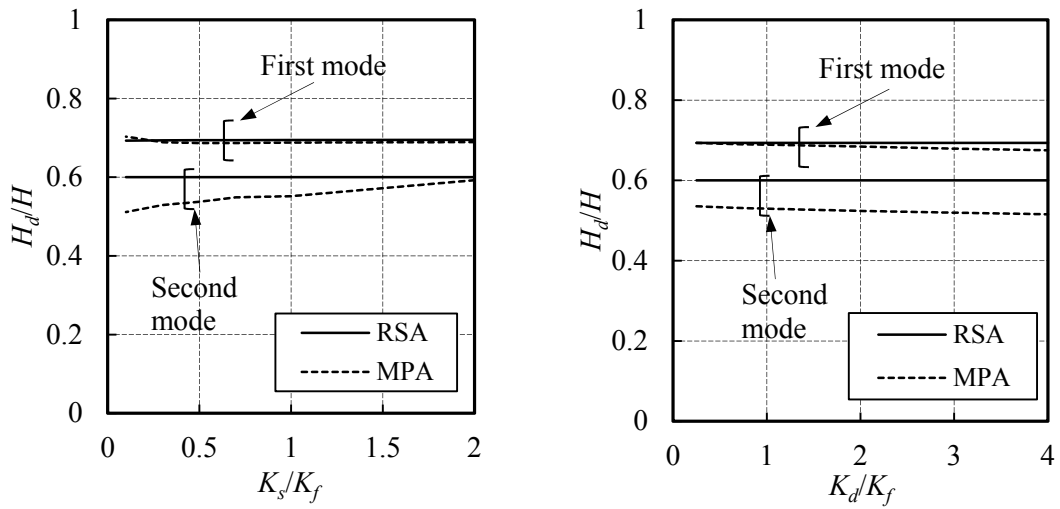
$$K_a = \frac{1}{\frac{1}{K_d} + \frac{1}{K_R - K_f}} \quad (6.34)$$

Estimation of damper stiffness is essential for improving the accuracy of RSA results since the stiffness of main frame and stiffness loss caused by spine frame are obtained directly from eigenvalue analysis, which is regarded to be accurate. Damper stiffness in the first- or second-mode SDOF system of Cnt models is calculated by Eq. (6.35), respectively. Damper stiffness in modes higher than the second mode can be ignored as the generated error on total response is usually less than 0.1% for spine frame structures.

$${}_i K_d = \frac{F_{BRC-y}(b)^2}{2u_{BRC-y}({}_i H_d)^2}, \quad i=1, 2 \quad (6.35)$$

where, for the first mode: ${}_1 H_d = {}_1 H_{eq}$; for the second mode: ${}_2 H_d = 0.6H$

Equivalent damping force location ${}_iH_d$ represents the location of a concentrated horizontal force possessing same value with shear force allocated by the additional damper system and could generate an identical overturning moment as distributed horizontal forces. Elastic modal stiffness obtained by MPA is utilized to calculate H_d for the first- and second-mode SDOF systems in RSA. Fig 6.23 shows that ${}_1H_d$ is almost identical with ${}_1H_{eq}$ and effect of K_s/K_f , K_d/K_f on both of them are negligible. ${}_2H_d$ slightly increases with K_s/K_f and reaches 0.6 when $K_s/K_f=2.0$. Although assuming ${}_2H_d=0.6$ causes larger error when K_d/K_f is small, such difference has little effect on the initial stiffness of the system, because stiffness of main frame is dominant in the second mode vibration. (Fig 6.26)



(a) H_d/H with various K_s/K_f ($K_d/K_f=1.0$)

(b) H_d/H with various K_d/K_f ($K_s/K_f=0.3$)

Fig. 6.23 Verification of H_d for Cnt models by MPA method

Table 6.10 lists some key parameters of BRCs involved in the above calculation. Additional stiffness and the other intermediate stiffnesses are summarized in Table 6.11. The initial stiffness $K_{f+a} = K_f + K_a$ and hardening stiffness K_f of the SDOF system are 3.98 s^{-2} and 2.61 s^{-2} . After determining the yielding deformation D_y , we are able to plot the bilinear force-deformation curve of the SDOF system. D_y is computed by Eq. (6.36) and the solution is 119mm. Fig 6.24 shows the final force-deformation curve of the 1st-mode SDOF system obtained from the RSA procedure as well as the one obtained from the MPA procedure. They are almost identical with each other, which confirm that the hardening stiffness in MPA and the additional stiffness in RSA are both appropriate.

$$D_y = \frac{\theta_{dy}}{\beta \phi_1 / h_1} \cdot \frac{K_a}{K_d} \quad (6.36)$$

Table 6.10. Key parameters of dampers used in 1st-mode SDOF system of a Cnt model

M_{dy} (Nmm)	H_{eq} (mm)	θ_{dy} (%)	K_d (s ⁻²)
1.33×10^{11}	56870	0.1	2.86

Table 6.11. Related stiffnesses (unit: s⁻²) of the 1st-mode SDOF system of a Cnt model

K_f	K_R	K_c	K_a	K_{f+a}
2.61	5.24	2.63	1.37	3.98

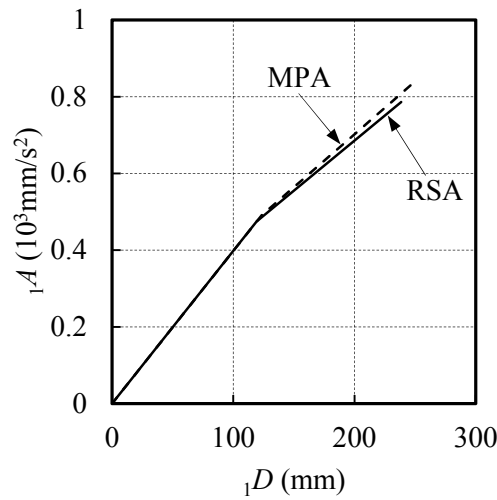


Fig. 6.24 Force-def. curve of the 1st-mode SDOF system of a Cnt model by RSA and MPA

Responses of the SDOF system are computed by iterating Eq. (6.24) ~ (6.27), meanwhile the deformation and force reduction factors R_d , R_a of both the SDOF system and the original structure are determined. Then responses of the original structure are computed by multiplying R_d , or R_a for deformation or force responses. Table 6.12 compares the equivalent period, damping ratio, deformation and force responses of the SDOF system, as well as the maximum SDR and base shear of the original structure obtained by RSA and MPA procedures. Fig 6.25 shows the estimated 1st-mode responses distribution of the original structure. They give very similar results except for the moment of spine frames, which indicates that moment of spine frames might be most sensitive to the difference between the two modal shapes in RSA and MPA procedures.

Table 6.12. Estimated responses of the 1st-mode SDOF system and the entire structure of a Cnt model by RSA method

Procedure	${}_1T_{eq}$ (s)	${}_1h_{eq}$	${}_1D$ (mm)	${}_1A$ (mm/s ²)	${}_1SDR$ (%)	${}_1V_t$ (10 ³ kN)
RSA	3.78	0.062	1047	2897	1.89	41.8
MPA	3.69	0.057	1052	3052	1.96	40.9

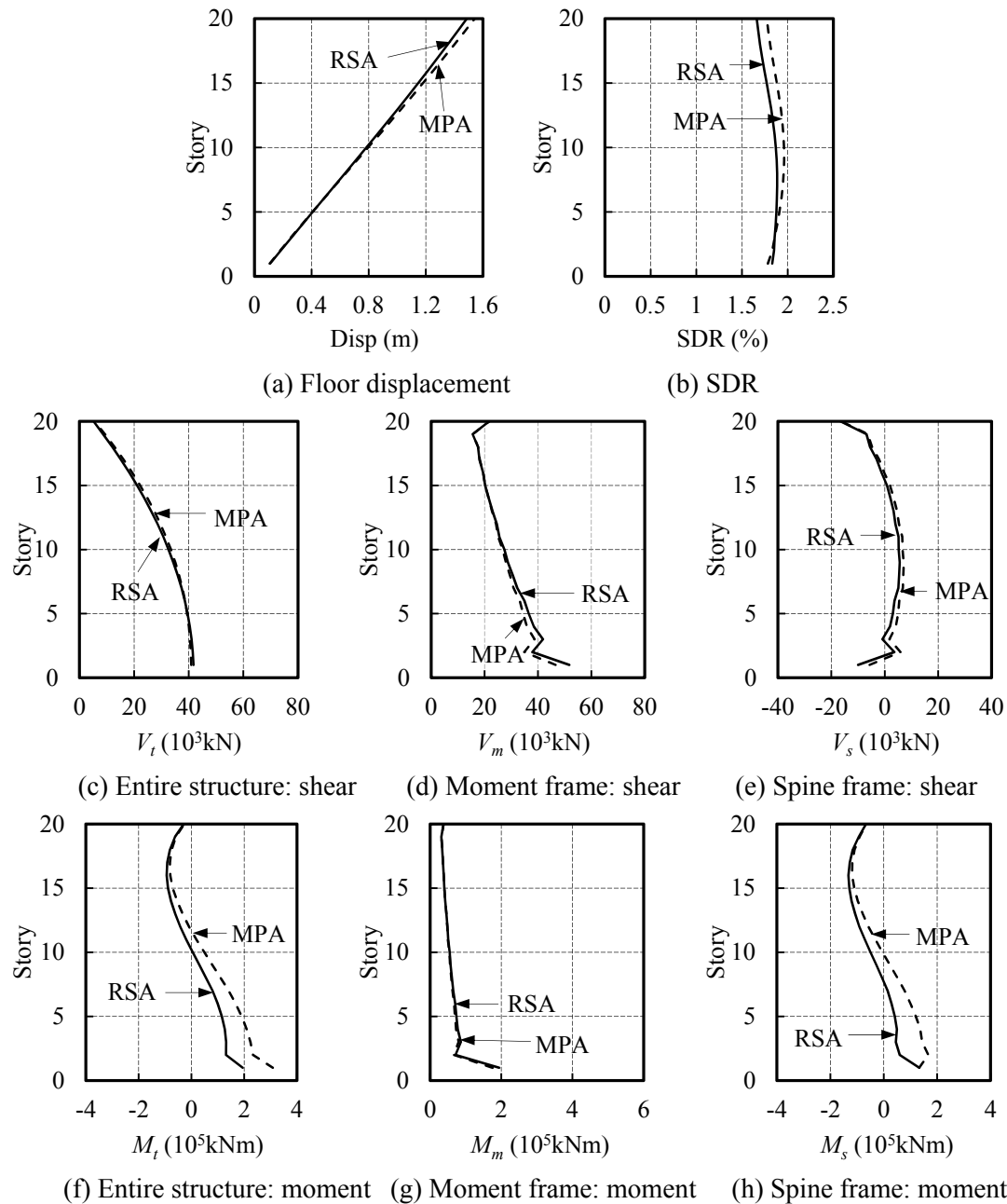


Fig 6.25 Estimated 1st-mode responses of a Cnt model by RSA and MPA methods

Step 6. Repeat steps 3 to 5 for as many modes as required for sufficient accuracy.

Additional stiffness and yielding deformation contributed by BRCs for the 2nd-mode SDOF system are computed by Eq. (6.34) ~ (6.36), same with the 1st-mode SDOF system. Table 6.13 lists some key parameters of BRCs involved in the calculation. Additional stiffness and the other intermediate stiffnesses are summarized in Table 6.14. Hardening stiffness in MPA is much smaller than that in RSA, i.e., stiffness of the main frame without BRCs in RSA, as shown in Fig 6.26. This might be caused by the difference between their lateral force distributions. This distribution in RSA is proportional to mode shape of the main frame, while in MPA is proportional to the mode shape of the whole structure including elastic BRCs.

Table 6.15 compares the equivalent period, damping ratio, deformation and force responses of the SDOF system, as well as the maximum SDR and base shear of the original structure obtained by RSA and MPA procedures. Although there is much difference in hardening stiffness of the SDOF system, the difference in maximum SDR and base shear obtained by RSA and MPA is less than 20% and results of RSA are more conservative. Fig 6.27 compares the estimated response distributions of the original structure. Results obtained by RSA are always more conservative than by MPA.

The 3rd mode responses are estimated by the same procedure with the 2nd mode. Similar to the MPA procedure, this 20-story Cnt building does not deform beyond the elastic range in the 3rd mode. Estimated deformation responses of the 1st, 2nd, and 3rd mode are combined by utilizing SRSS rules (Eq. (6.29)) since the natural frequencies are well-separated. Force responses except the moment of the BRCs are also combined by SRSS rule since the structural members are assumed as elastic. Peak moment of the BRCs is simply the yielding moment. Fig 6.28 shows the responses estimated by the RSA procedure in comparison with results from MPA procedure and nonlinear time history analysis (THA). The estimated values of responses are computed including 3 modes for both RSA and MPA. The RSA procedure provides relatively more conservative results compared to MPA procedure for almost all responses.

Table 6.13. Key parameters of dampers used in 2nd-mode SDOF system of a Cnt model

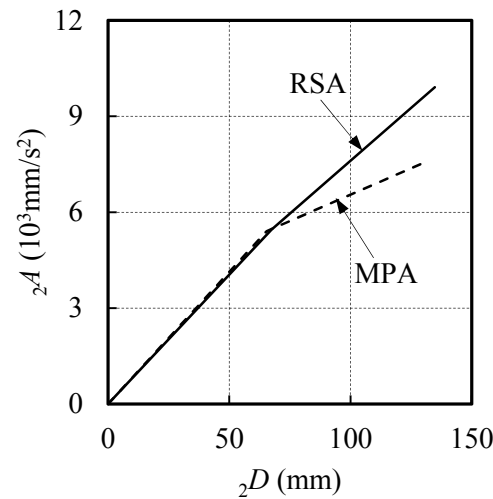
M_{dy} (Nmm)	H_{eq} (mm)	θ_{dy} (%)	K_d (s ⁻²)
1.33×10^{11}	48000	0.1	23.2

Table 6.14. Related stiffnesses (unit: s⁻²) of the 2nd-mode SDOF system of a Cnt model

K_f	K_R	K_c	K_a	K_{f+a}
66.1	108	41.7	14.9	80.9

Table 6.15. Estimated responses of the 2nd-mode SDOF system and the entire structure of a Cnt model by RSA method

Procedure	${}_2T_{eq}$ (s)	${}_2h_{eq}$	${}_2D$ (mm)	${}_2A$ (mm/s ²)	${}_2SDR$ (%)	${}_2V_t$ (10 ³ kN)
RSA	0.75	0.038	197	14032	0.46	35.0
MPA	0.89	0.098	195	9678	0.38	29.6


Fig. 6.26 Force-def. curve of the 2nd-mode SDOF system of a Cnt model obtained by RSA and MPA methods

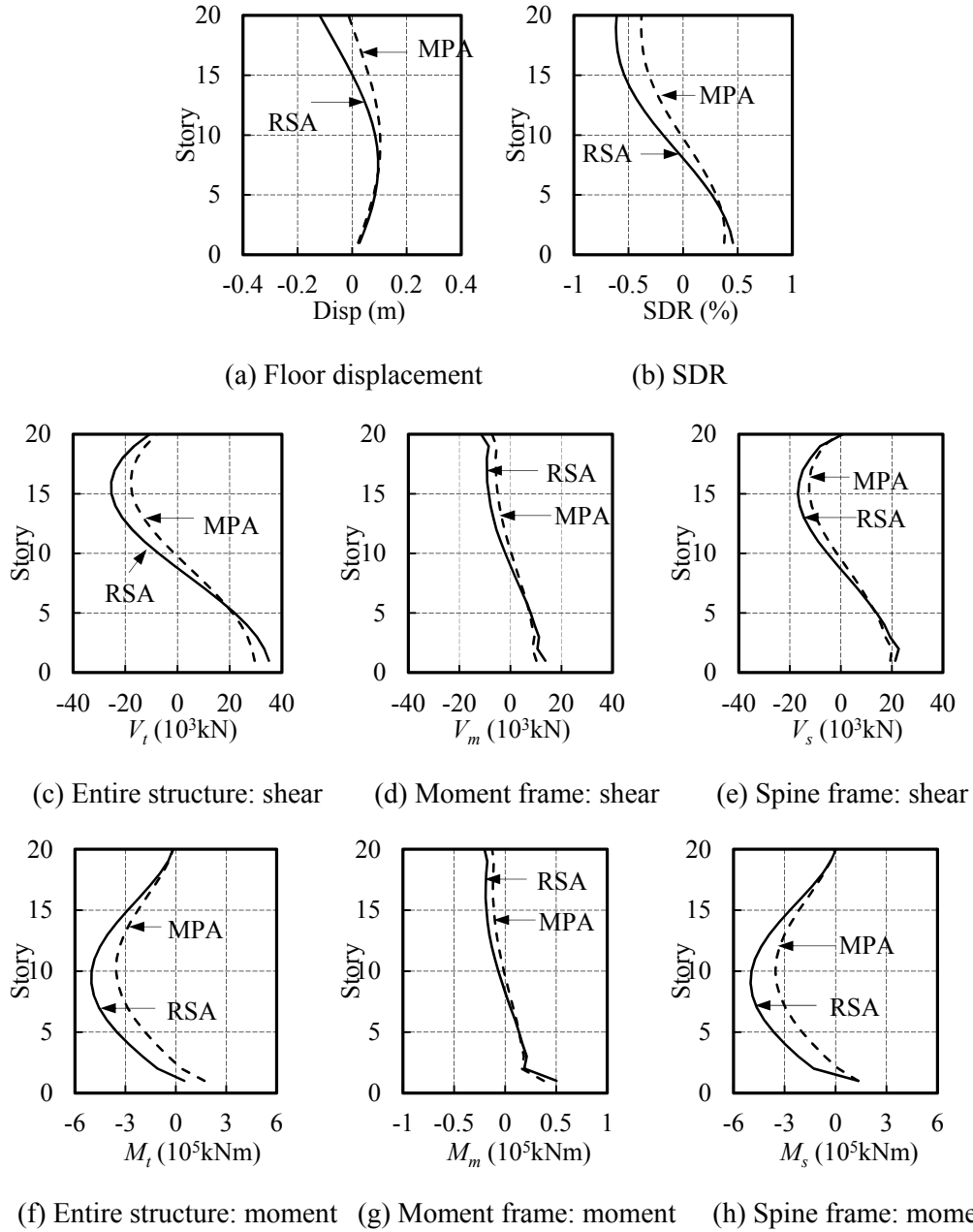


Fig. 6.27 Estimated 2nd-mode responses of a Cnt model by RSA and MPA methods

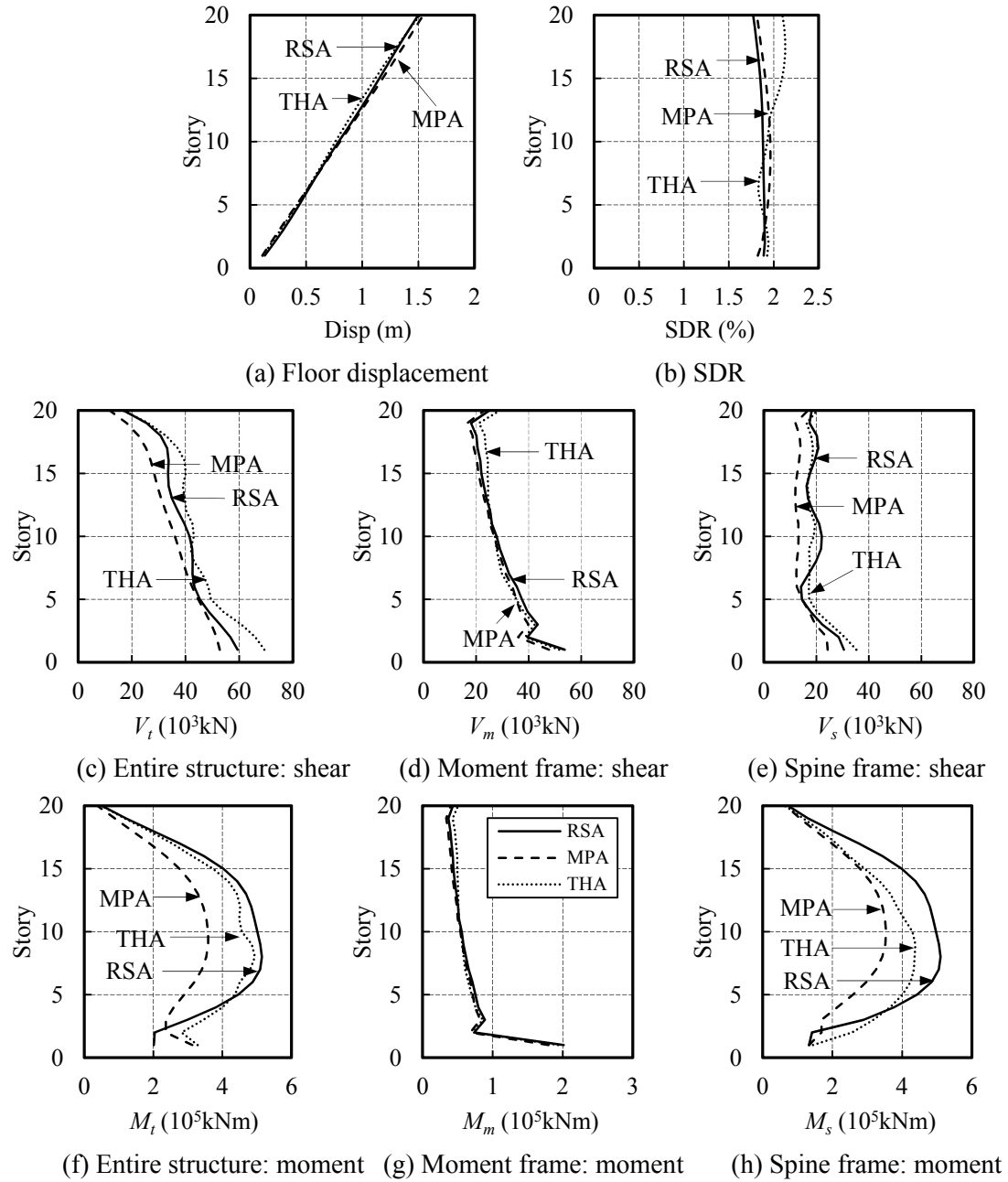


Fig. 6.28 Estimated responses of a Cnt model by RSA, MPA and THA

The 20-story Cnt models with various $K_s/K_f=0.1\sim 2.0$ and $K_d/K_f=0\sim 4.0$ are estimated by utilizing the RSA procedure. The initial stiffness and yielding deformation of both 1st mode and 2nd mode in RSA procedure agree well with those in the MPA procedure. Fig 6.29 and 6.30 show the estimated responses of the 1st-mode and 2nd-mode SDOF system by utilizing RSA and MPA procedure with various K_s/K_f . Fig 6.31 and 6.32 show those results with various K_d/K_f . Results in Fig 6.29 show great agreement between RSA and MPA. However, significant difference occurs in the hardening stiffness ratio and equivalent damping ratio of the 2nd-mode SDOF system, despite of the value of K_s/K_f and K_d/K_f , as in Fig 6.30 (b), 30 (f), 32 (b), 32 (f), which might be caused by the difference in lateral force distributions. As for the 1st mode, difference in the hardening stiffness ratio and equivalent damping ratio of RSA and MPA increases as K_d/K_f increasing, as in Fig 6.32 (b) (f). Reasons for such difference might be same with the previous problem, different lateral force distributions, since difference between 1st-mode modal shapes in RSA and MPA increases along with the stiffness of BRCs.

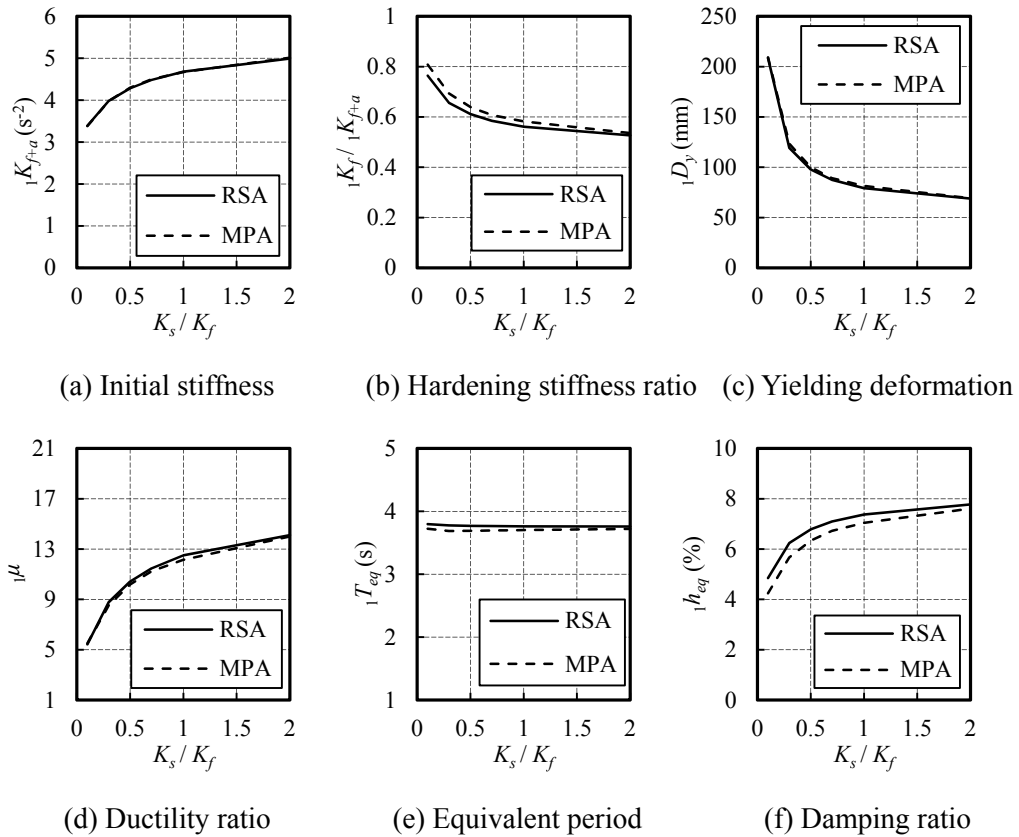


Fig. 6.29 Comparison of RSA and MPA methods on characteristics and responses of the 1st-mode SDOF system of a Cnt model with various K_s/K_f ($K_d/K_f=1.0$)

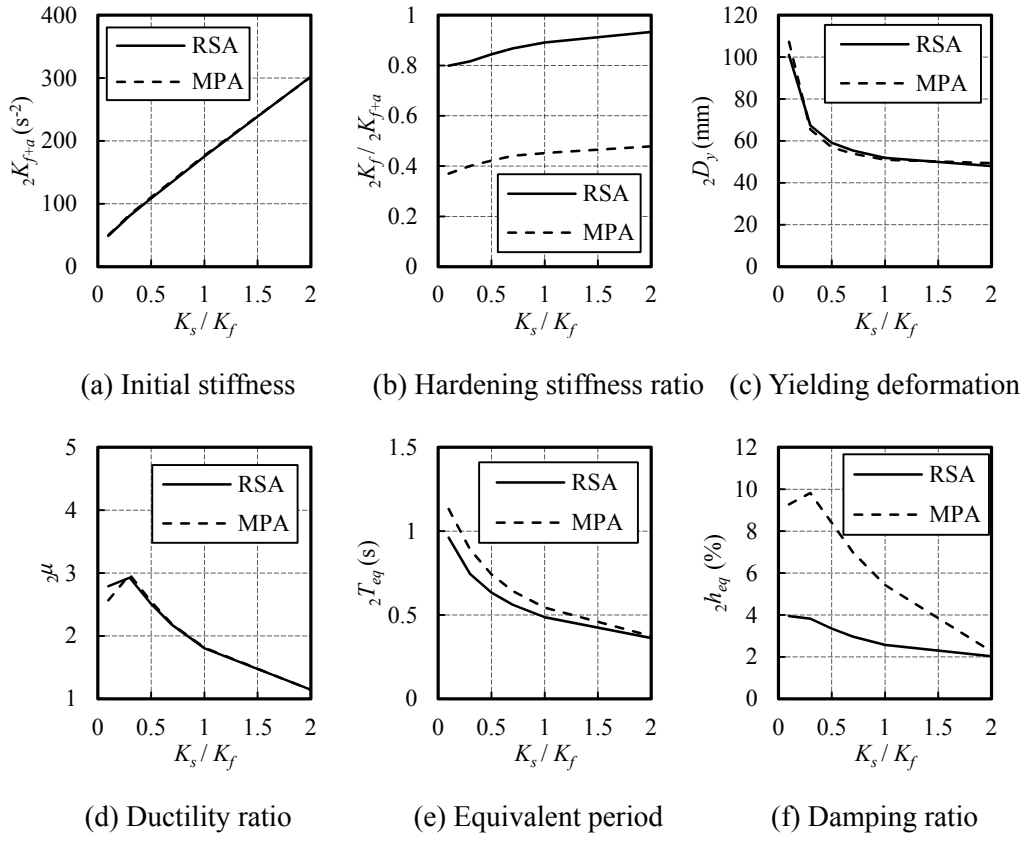


Fig. 6.30 Comparison of RSA and MPA methods on characteristics and responses of the 2nd-mode SDOF system of a Cnt model with various K_s/K_f ($K_d/K_f=1.0$)

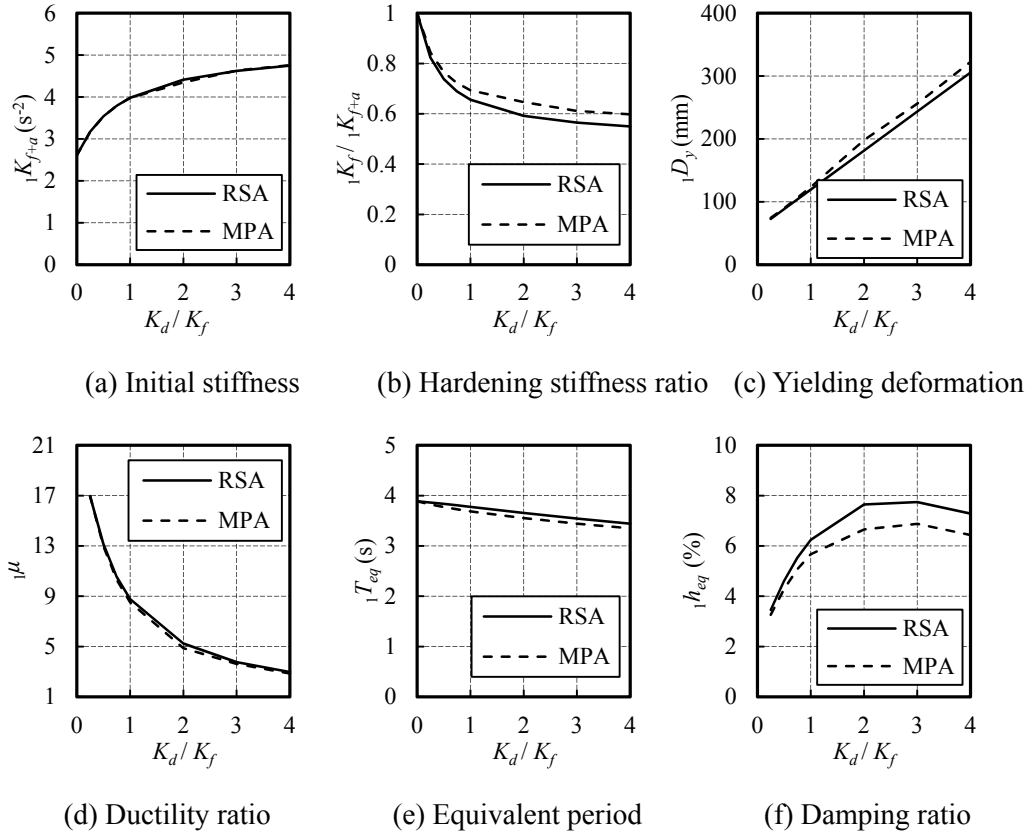


Fig. 6.31 Comparison of RSA and MPA methods on characteristics and responses of the 1st-mode SDOF system of a Cnt model with various K_d/K_f ($K_s/K_f=0.3$)

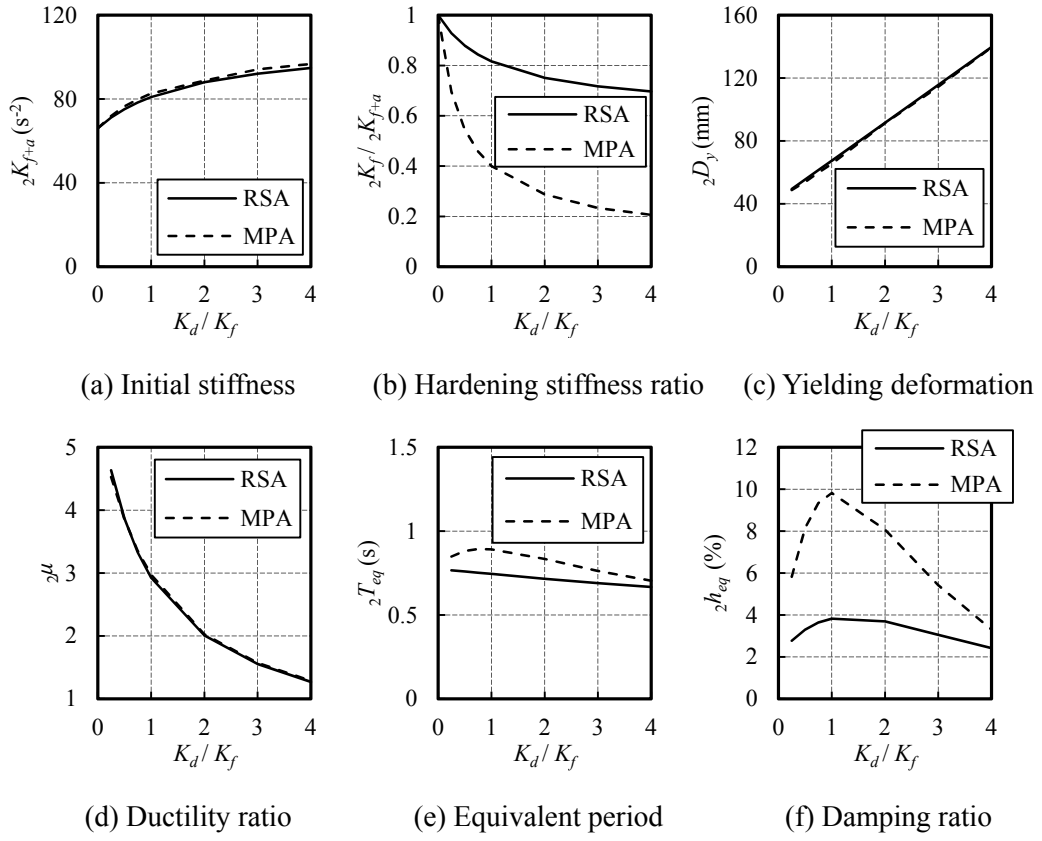


Fig. 6.32 Comparison of RSA and MPA methods on characteristics and responses of the 2nd-mode SDOF system of a Cnt model with various K_d/K_f ($K_s/K_f=0.3$)

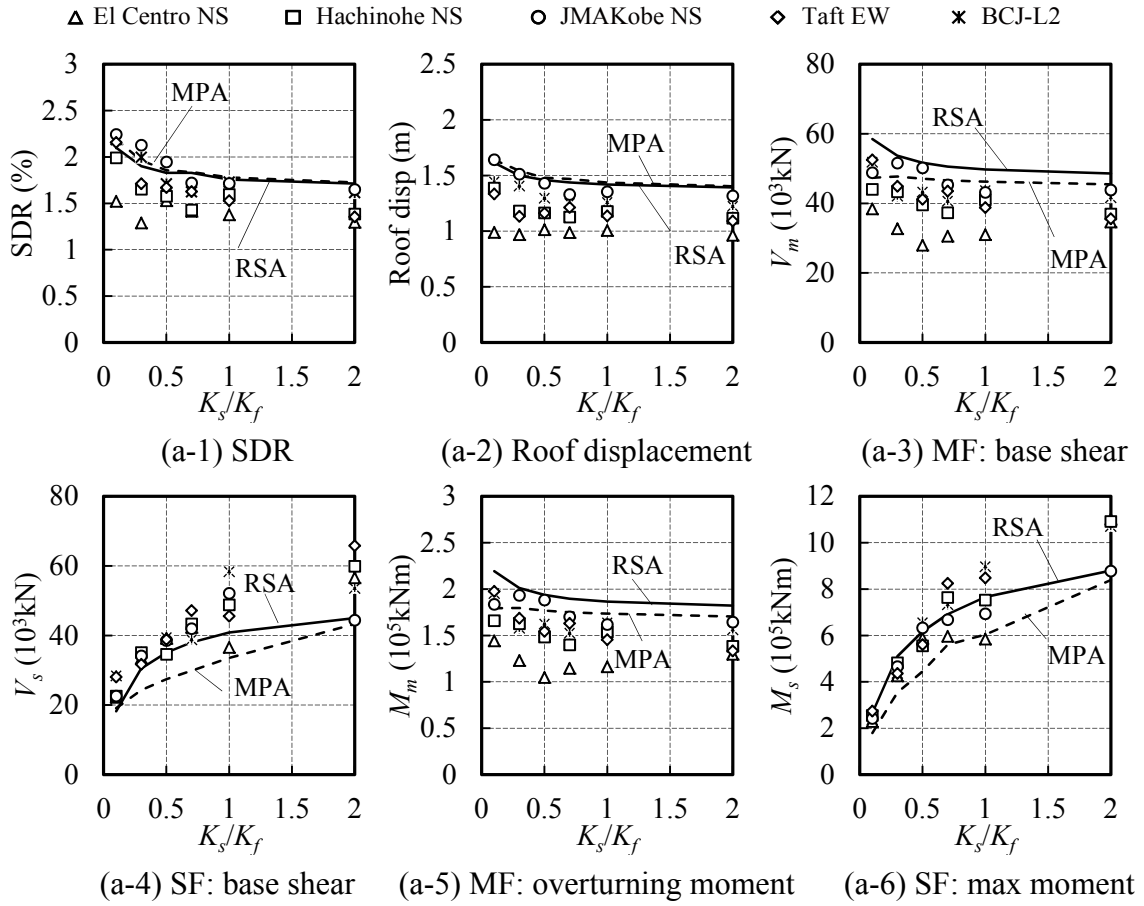


Fig. 6.33 (a) Comparison of RSA, MPA and THA results of seismic performances of the 20-story Cnt models with various K_s/K_f ($K_d/K_f=1.0$)

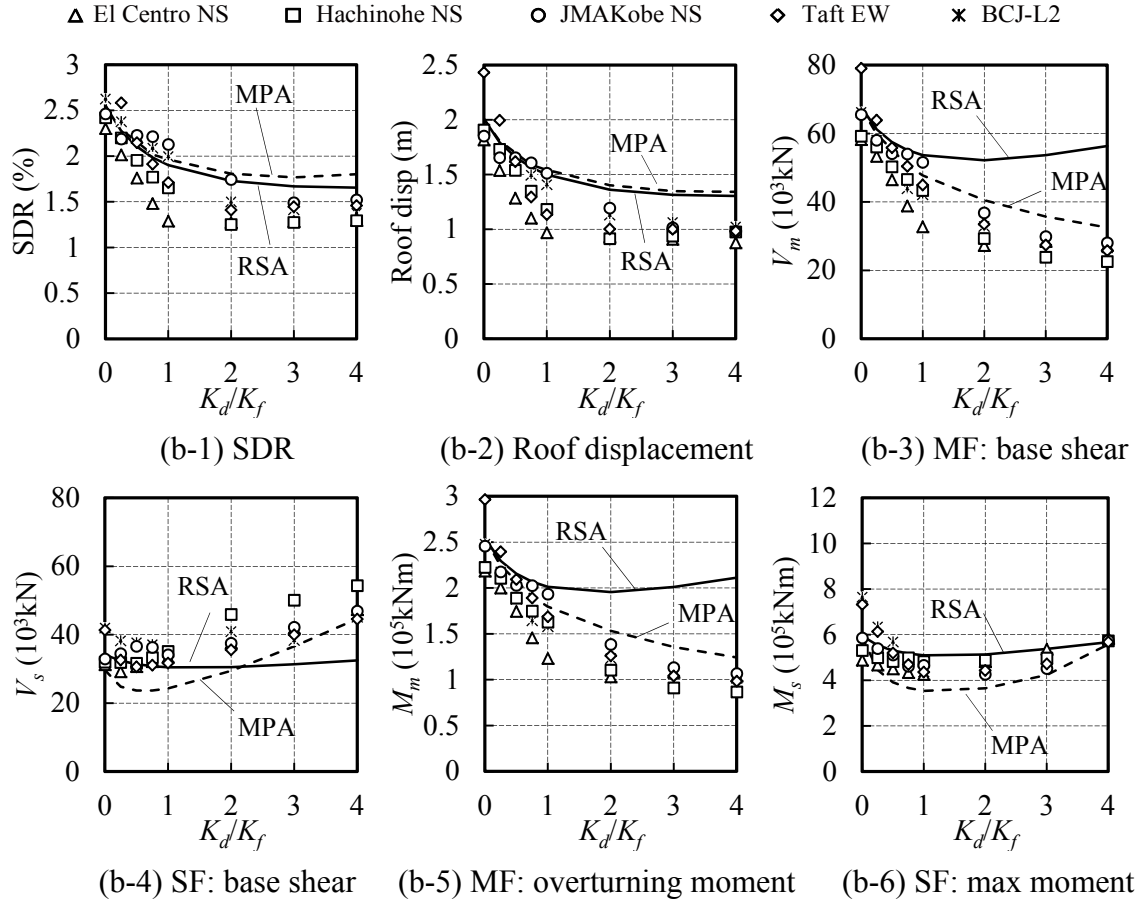


Fig. 6.33 (b) Comparison of RSA, MPA and THA results of seismic performances of the 20-story Cnt models with various K_d/K_f ($K_s/K_f=0.3$)

To judge whether the estimation methods are reasonable, results obtained from RSA and MPA are compared with the nonlinear THA results, as in Fig 6.33. The estimated responses are computed including 3 modes. From Fig 6.33 (a) we can see that, despite the value of K_s/K_f , both RSA and MPA provide well estimation with appropriate conservatism on maximum SDR and roof displacement. RSA gives more conservative estimation on the base shear and overturning moment of the moment frames, however force responses of the spine frame are still smaller than THA, but much closer compared to MPA procedure. From Fig 6.33 (b) we can see that, both RSA and MPA provide good estimation on maximum SDR and roof displacement when $K_d/K_f \leq 2.0$. RSA gives better estimation on base shear and maximum moment of the spine frames compared to MPA, although it still underestimate those values when $K_d/K_f \leq 1.0$. However,

force responses of the moment frames estimated by RSA are ridiculously large compared to THA and MPA, indicating that increasing K_d/K_f has additional effect on reducing resisting force of the moment frames due to changing of the modal shape. Modification factor γ is introduced for force of the moment frames, which is computed by Eq. (6.37)

$$\gamma = 1 - 0.15k_d / k_f \quad (6.37)$$

After multiplying the modification factor γ , force of the moment frames estimated by RSA procedure is much closer to the THA results, as in Fig 34.

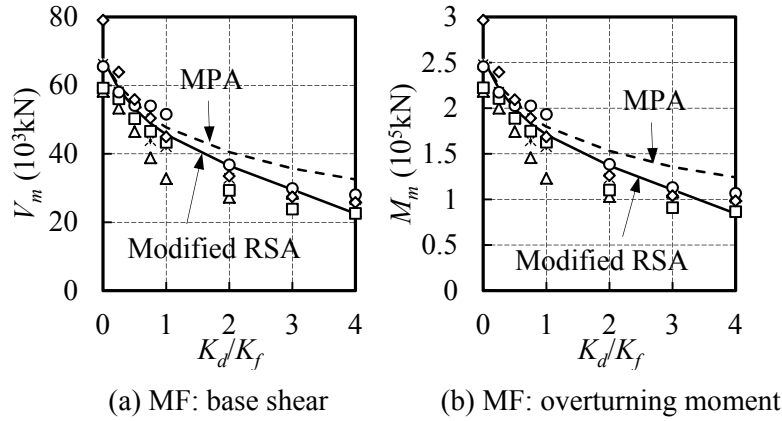


Fig. 6.34 Modified RSA estimation for force of the moment frames in the Cnt models

The RSA method provides better estimation if the structure response distribution is closer to the distribution when dampers yield, because of the assumption of the post-yield response distribution. This is verified by increasing the input ground motion intensity. Fig 6.35 presents the detailed results of 20-story Cnt-Ksf0.3-Kdf2.0 model with two levels of ground motions (BCJ-L2, PGA=525gal, 1050gal). The estimated responses against PGA 1050 gal match better with the time-history analysis results.

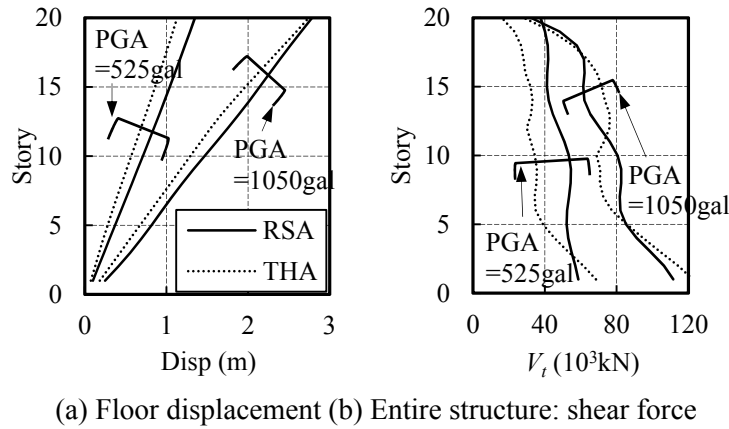


Fig. 6.35 Estimated responses of a Cnt model with variable earthquake intensity

6.5 Seismic evaluation of Sgt models

6.5.1 Evaluation of Sgt models by MPA method

The 20-story Sgt models with $K_s/K_f=0.3$, $K_{d2}/K_{d1}=0.5$, $K_{d1}/K_f=0 \sim 1.5$ are estimated by utilizing the MPA procedure in section 4. Detailed results of the Sgt2-Ksf0.3-Kdf-1.0-0.5 model are demonstrated in the following paragraphs. The Cnt model used for comparison is the 20-story Cnt-Ksf0.3-Kdf1.0 model. Eigenvalue analysis is carried out for the elastic model and results of the first three modes are summarized in Table 6.16. The 2nd-mode natural period is approximately 15% longer than the Cnt model, while the other results are essentially identical. Unlike the Cnt models, the 2nd-mode mode shape of the Sgt model shows a shape rotation from the 9th floor to the 10th floor due to the BRCs in the 10th story, as in Fig 6.36 (a). Such concentrated rotation is also observed in the 1st mode, which is clearly exhibited in Fig 6.36 (c), the SDR distribution.

For the 1st-mode, the base shear-floor displacement, $_nV_b - _nu_i$, pushover curve is obtained by nonlinear pushover analysis using the lateral force following the 1st-mode distribution. Those BRCs equipped at the 10th-story didn't yield during the push, i.e., they are elastic even when the elastic maximum base shear is reached. As a result, there is only one yielding point in the pushover curve, as shown in Fig 6.37. In the converting from base shear-floor displacement curve to force-deformation curve of the equivalent SDOF system, the top floor is chosen as the reference floor, same with the Cnt model. To confirm the validation of using roof displacement, increasing ratios of displacement increment at each floor is plotted in Fig 6.38, in which the top floor displacement presents the highest hardening stiffness ratio, indicating the most conservative estimation.

Table 6.16. Elastic structural characteristics of a Sgt2 model

Mode	T_0 (s)	M_{eq} (ton)	M_{eq}/M	S_{a0} (gal)	$V_{b0}=S_{a0}M^*$ (10^3 kN)	β	$K_0=(2\pi/T_0)^2$ (s ⁻²)	$D_0=\beta S_{a0}(T/2\pi)^2$ (mm)
1	3.16	13279	73%	452.7	60.1	1.45	3.96	1662
2	0.79	3088	17%	1654	51.1	0.63	62.9	165.3
3	0.27	887	5%	1654	14.7	0.33	537	10.17

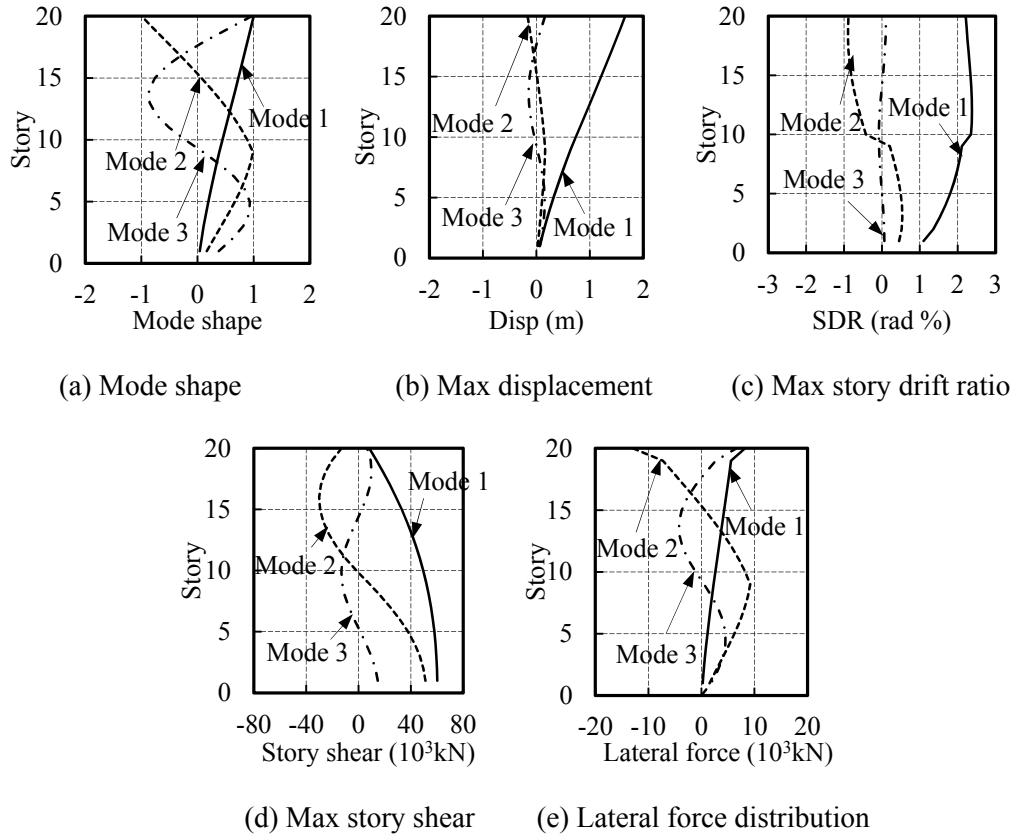


Fig. 6.36 Mode shapes and elastic responses of a Sgt2 model

As shown in Fig 6.37 (b), the force-deformation curve of the 1st-mode SDOF system for the Sgt model is essentially identical with that for the Cnt model, indicating that the estimated peak force and deformation of the SDOF system are essentially identical. Moreover, variables relevant to the converting between the original structure and its 1st-mode SDOF system are all very similar in the Cnt and Sgt models: 1% difference in the estimated base shear assuming elastic response, 1% difference in effective modal mass, 0.4% difference in modal contribution factor.

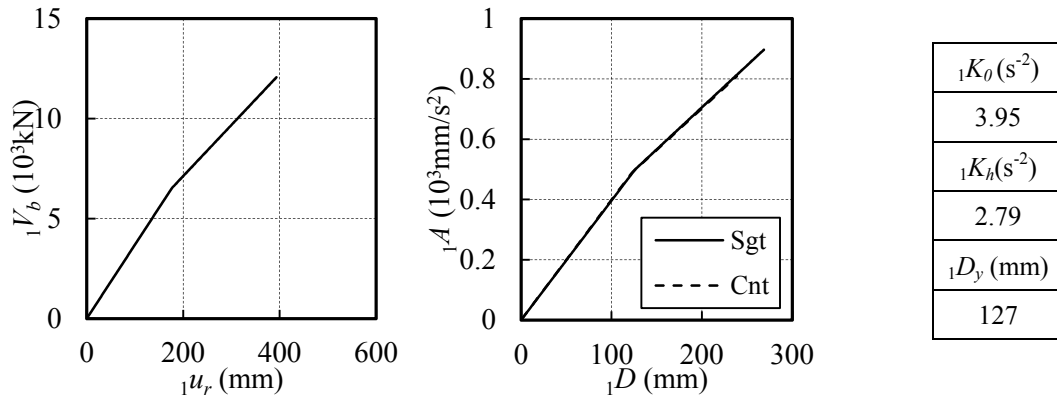


Fig. 6.37 Force-def. relation of 1st-mode SDOF system of a Sgt2 model obtained in MPA

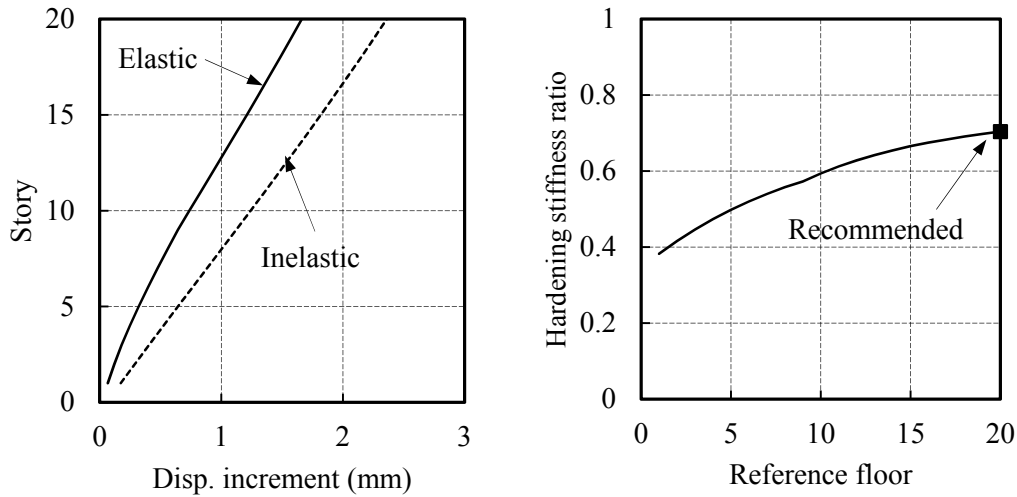


Fig. 6.38 Effect of ref. floor on hardening stiffness ratio of the 1st-mode SDOF system of a Sgt2 model due to deformation shape changing

Unlike the 1st-mode pushover analysis results, both the 1st-story BRCs (refer as BRC1) and the 10th-story BRCs (refer as BRC2) yield in the 2nd-mode pushover analysis before the elastic maximum base shear is reached. As a result, there are two yielding point in the pushover curve, as shown in Fig 6.39 (a). Stiffness degradation is mainly caused due to yielding of BRC1, which reduces the stiffness by over 50%. In the converting from base shear-floor displacement curve to force-deformation curve of the equivalent SDOF system, 1st-floor is chosen as the reference floor, same with the Cnt model. To confirm the validation of using 1st-floor displacement, hardening stiffness ratio is plotted in Fig 6.40, in which the 1st-floor displacement presents the

maximum stiffness, indicating the most conservative estimation. The tri-linear force-deformation curve is simplified into a bilinear curve by taking the second yielding point, BRC1 yielding, as the only yielding point, and secant stiffness computed from the BRC1 yielding point to the origin point is used as the initial stiffness.

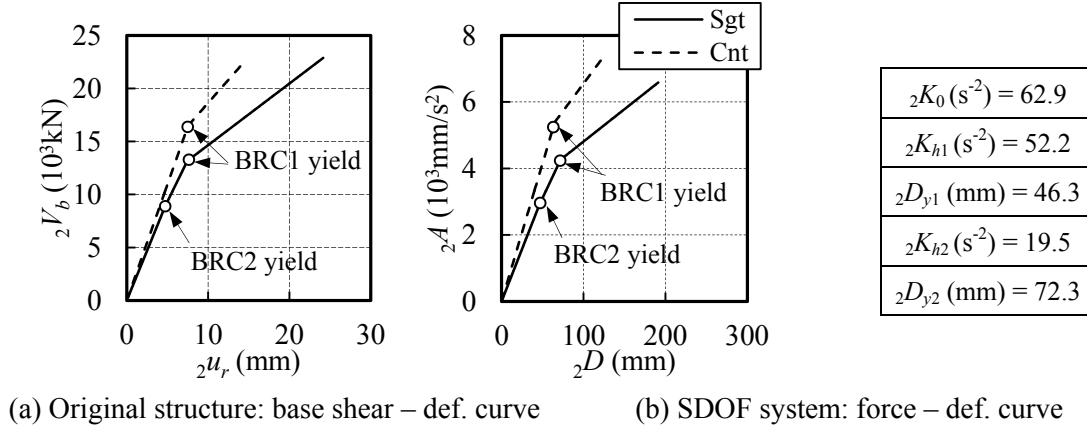


Fig. 6.39 Force-def. relation of 2nd-mode SDOF system of a Sgt2 model by MPA

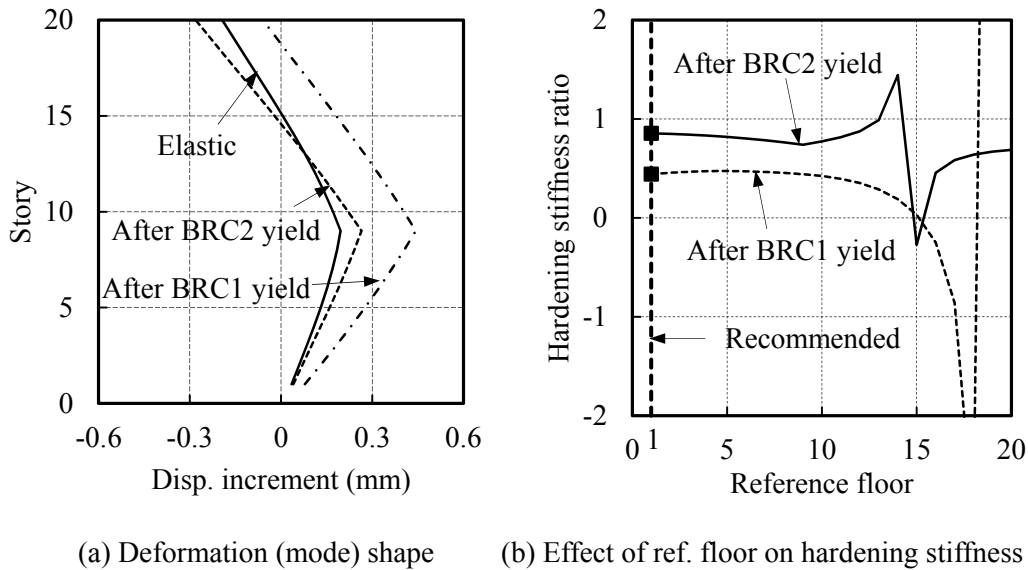


Fig. 6.40 Effect of ref. floor on hardening stiffness ratio of the 2nd-mode SDOF system of a Sgt2 model due to deformation shape changing

3rd-mode responses are estimated by the same procedure with the 2nd mode. The current 20-Sgt model does not deform beyond the elastic range. Deformation and force of the first three modes SDOF systems and the corresponding responses of the original structure are summarized in Table 6.17. Responses of the 1st, 2nd, 3rd modes vibration of the Sgt model are compared with the Cnt model as shown in Fig. 6.41.

Discussion on 1st-mode responses:

As shown in Fig 6.37, the force-deformation curve of the 1st-mode SDOF system for the Sgt model is essentially identical with that for the Cnt model. Moreover, variables relevant to the converting between the original structure and its 1st-mode SDOF system are all very similar in the Cnt and Sgt models. As a result, the estimated base shear and roof displacement of the Sgt model are almost identical with the Cnt model as well.

The only difference may only exist in their distributions. Elastic SDR distribution of Sgt model is obviously different from the Cnt model because of the rotation concentration at the BRC2 story, as in Fig 6.41.1(b). However, during pushover analysis, such difference is eliminated after BRC1 yields but with lateral force still following the elastic distribution, increments of SDR of the lower stories catch up with the upper stories, and thus finally the distribution becomes as same as the Cnt model, as in Fig 6.41.1(a). The MPA method may not be able to capture the deformation reducing effect of the Sgt model, but still, it gives a conservative estimation of deformation response.

As for the story shear and story base moment, their estimated results assuming elastic response are already almost identical and the lateral force distribution doesn't change during pushover. Since the estimated base shears of Sgt and Cnt models are almost same, all the force results are almost same, as shown in Fig 6.41.2-3.

Discussion on 2nd-mode responses:

As shown in Fig 6.39 (b), the initial stiffness and hardening stiffness of the force-deformation curve of the Sgt 2nd-mode SDOF system are both smaller than the stiffnesses of the Cnt model. The estimated maximum Disp. and SDR of the Sgt model is slightly larger than the Cnt model, while the story shear force V_i of the Sgt model is slightly smaller, as in Fig 6.41.1-2. However, story shear of moment frames in the Sgt model is slightly larger than the Cnt model, particularly at around the segment story.

It's worth noting that, column base moment of spine frames is significantly reduced compared to the Cnt model, as in Fig 6.41.2. Besides, the maximum moment of spine frames is reduced by almost 40% due to the BRCs at the 10th story, as in Fig 6.41.3. However, additional moment demand of moment frames is required at the 10th-story due to the discontinuity in spine frames moment capacity. Additional shear force demand of both moment frames and spine frames is required, which also indicates large interaction force due to the concentrated rotation at the 10th-story.

From Fig 6.41.1-3 we can see that the 1st and 3rd mode response of Sgt and Cnt models estimated by MPA method are almost identical. Difference mainly generates in the 2nd-mode response: deformation response, force response of moment frames of Sgt is larger, while force response of spine frame is much smaller compared to the Cnt model.

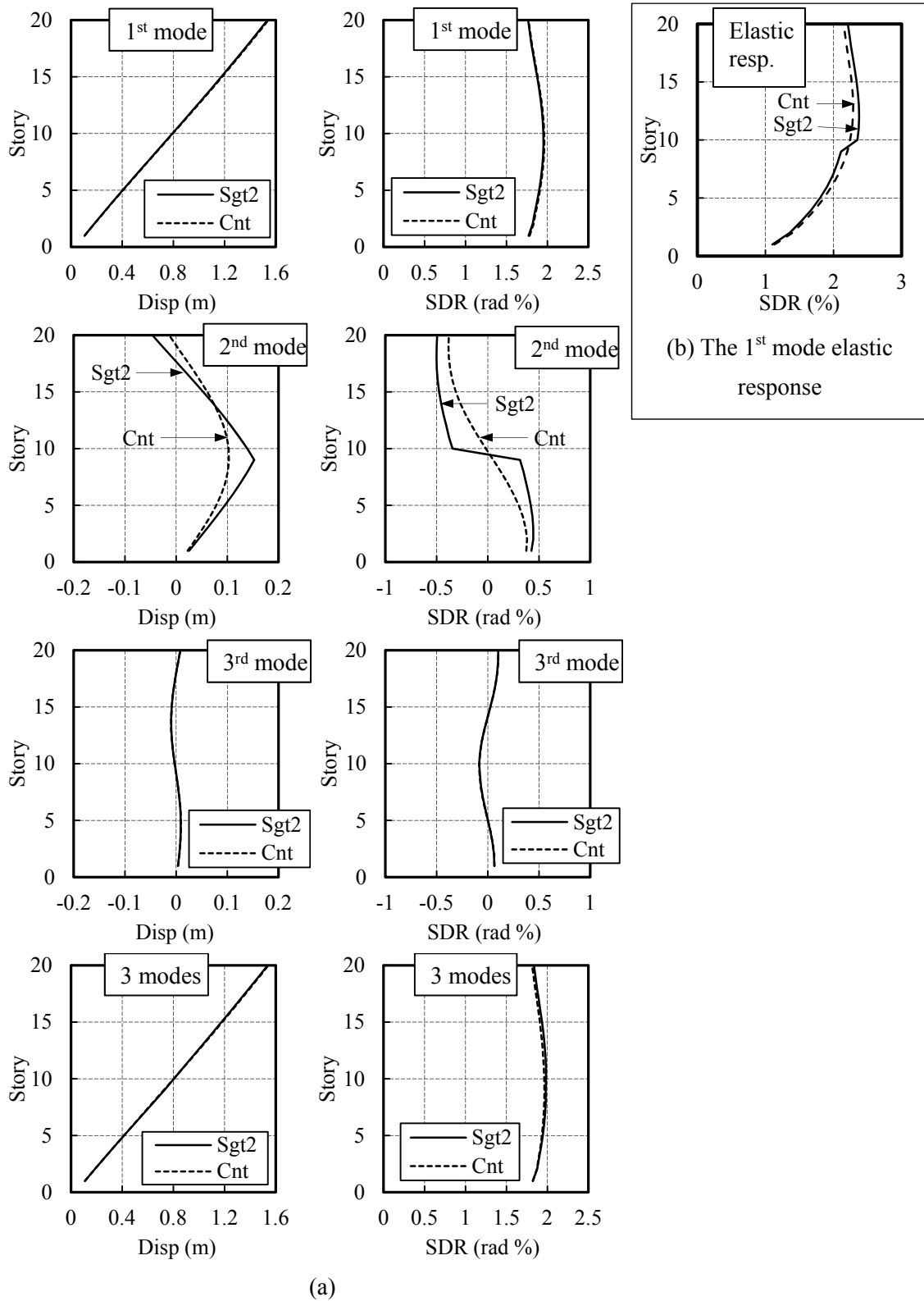


Fig 6.41.1 Disp. & SDR of each mode of the Sgt and Cnt models estimated by MPA

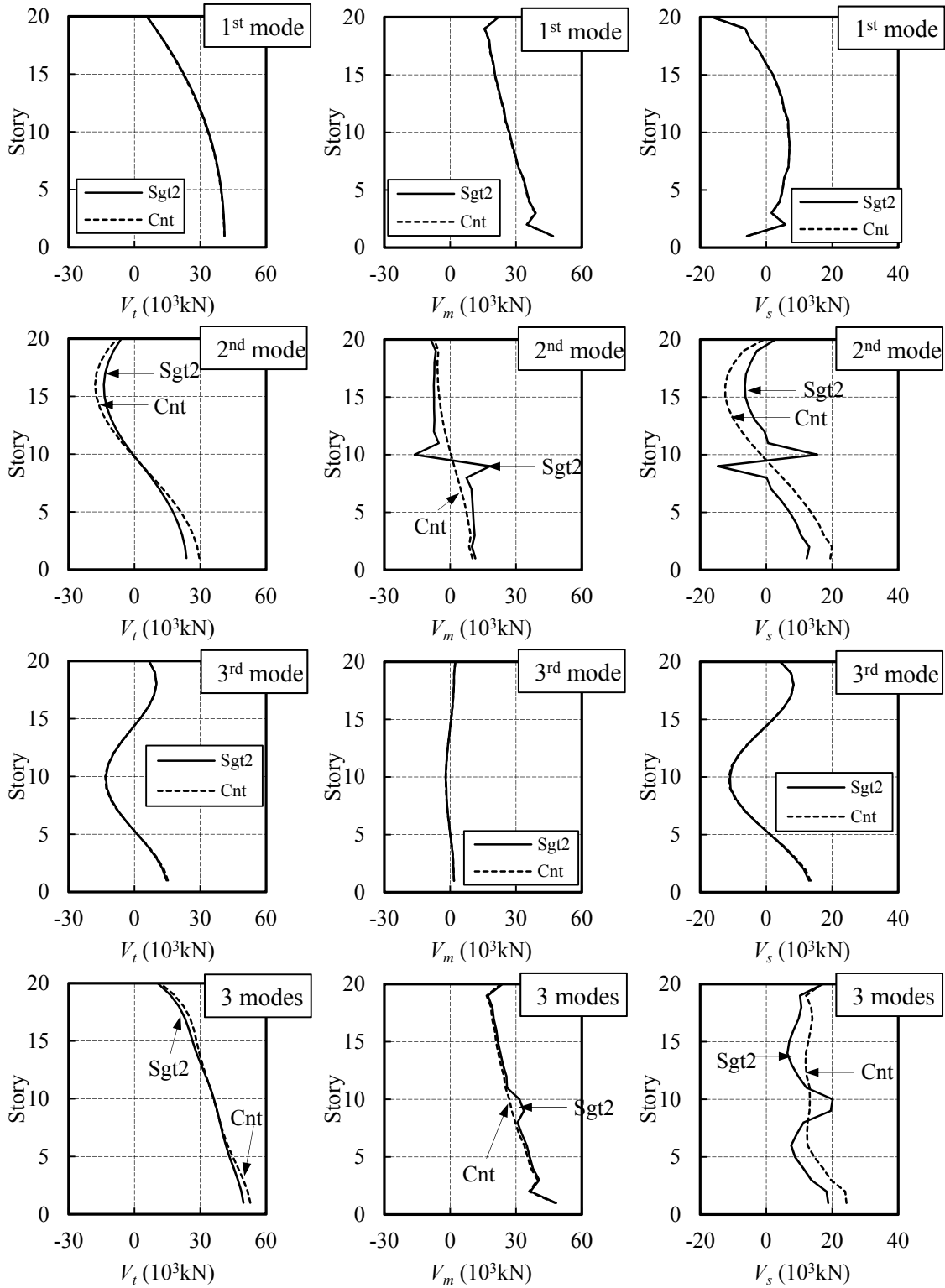


Fig 6.41.2 Shear force of each mode of the Sgt and Cnt models estimated by MPA

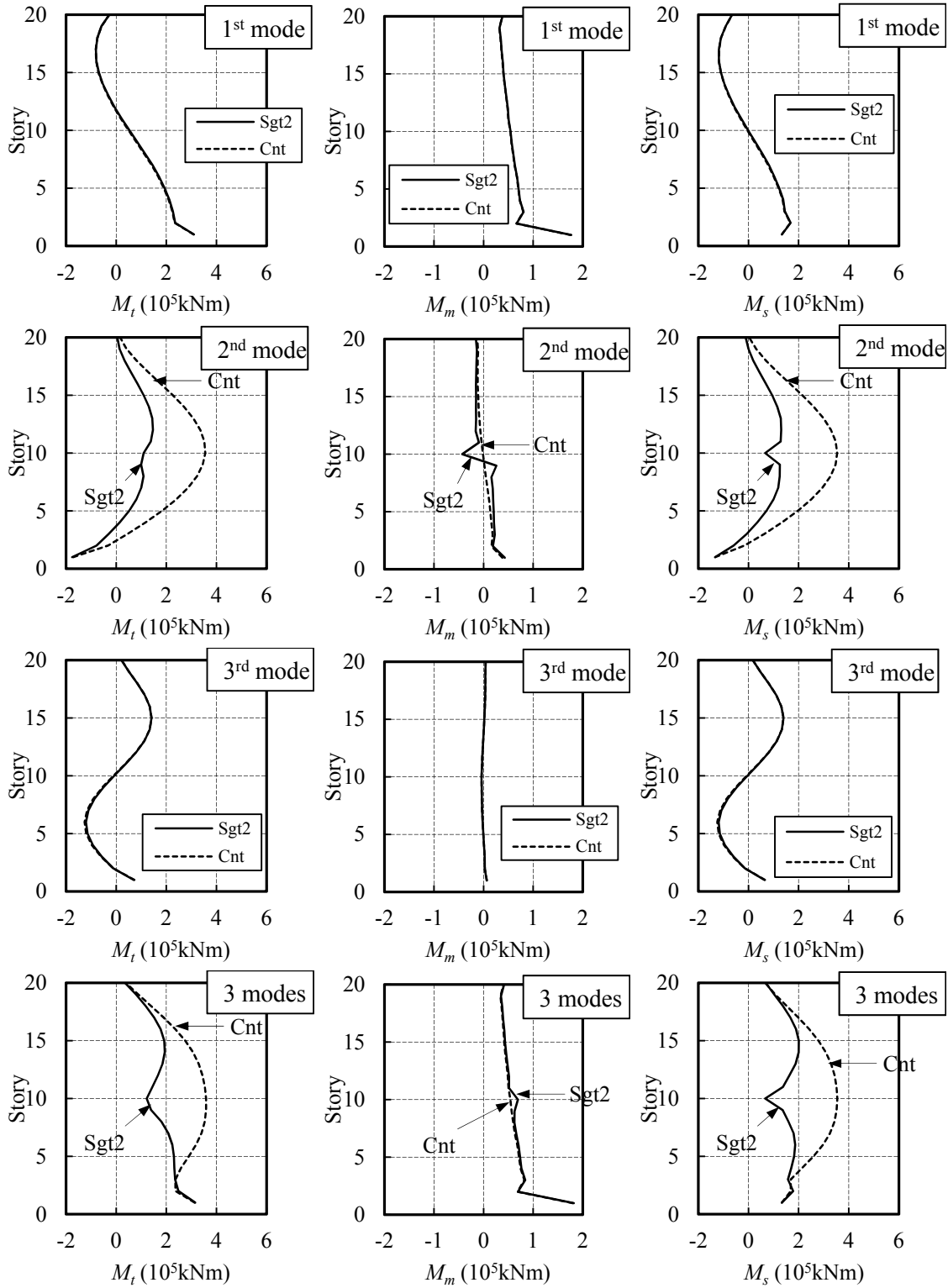


Fig 6.41.3 Story base moment of each mode of the Sgt and Cnt models by MPA

Table 6.17 Estimated responses of the first three modes SDOF systems
and the original structure of a Sgt2 model

Mode	T_{eq} (s)	h_{eq}	R_d	R_a	D (mm)	A (mm/s ²)	SDR (%)	V_b (10 ³ kN)
1	3.67	0.055	0.92	0.68	1056	3091	1.95	41.1
2	1.13	0.122	0.88	0.46	247.2	7672	0.5	23.7
3	0.27	0.02	1.0	1.0	10.17	5462	0.1	14.7

Comparison between MPA and THA for the Sgt model

Fig 6.42 shows the responses estimated by the MPA procedure with the nonlinear time history analysis (THA). The estimated values of responses are computed including 1 mode, 2 modes, or 3 modes. Estimated deformation responses are combined by utilizing SRSS rules since the natural frequencies are well-separated. Force responses except the moment of BRC1 and BRC2 are also combined by SRSS rule since the structural members are assumed as elastic. Peak values of the moment of BRC1 and BRC2 are simply valued at their yielding moment, respectively. The 2nd mode contributes significant response in the story shear and bending moment of the spine frame. Including the first 3 modes is able to provide sufficient estimation for the 20-story Sgt spine frame structures.

The maximum SDR is overestimated by approximately 12%, providing an acceptable conservatism. The overestimation might be because the lateral force distribution invariably follows the elastic distribution, while the coupling effect of different modes after BRC1 and BRC2 yield is not negligible. Stiffness of force-deformation curve of the 1st-mode SDOF system is overestimated could be another reason.

Forces estimated by MPA present a great agreement with the THA results, except for the base shear and maximum moment of spine frames. Similarly to the Cnt model, base shear and maximum moment of the spine frames are underestimated by approximately 30%.

Although the estimated deformations of Sgt and Cnt models are almost identical, because BRC2 doesn't yield in pushover analysis and its elastic stiffness is not much less than the replaced columns in the spine frames, discrepancy in forces is obvious and well captured by the MPA procedure. As shown in Fig 6.44. Difference in forces of moment frames is quite small, while the story shear and moment at each floor of the spine frame is greatly reduced compared to the Cnt model, except for the 10th-story shear force. Utilizing segmented spine frame could significantly reduce the strength or stiffness demand of spine frames. Additional strengthening need to be considered for both moment frames and spine frames at the segment-floor. Estimated results of the other 20-story Sgt models with $K_s/K_f=0.3$, $K_{d1}/K_f=0\sim 2.0$, $K_{d2}/K_{d1}=0.5$ are summarized with the RSA results in Fig. 6.52.

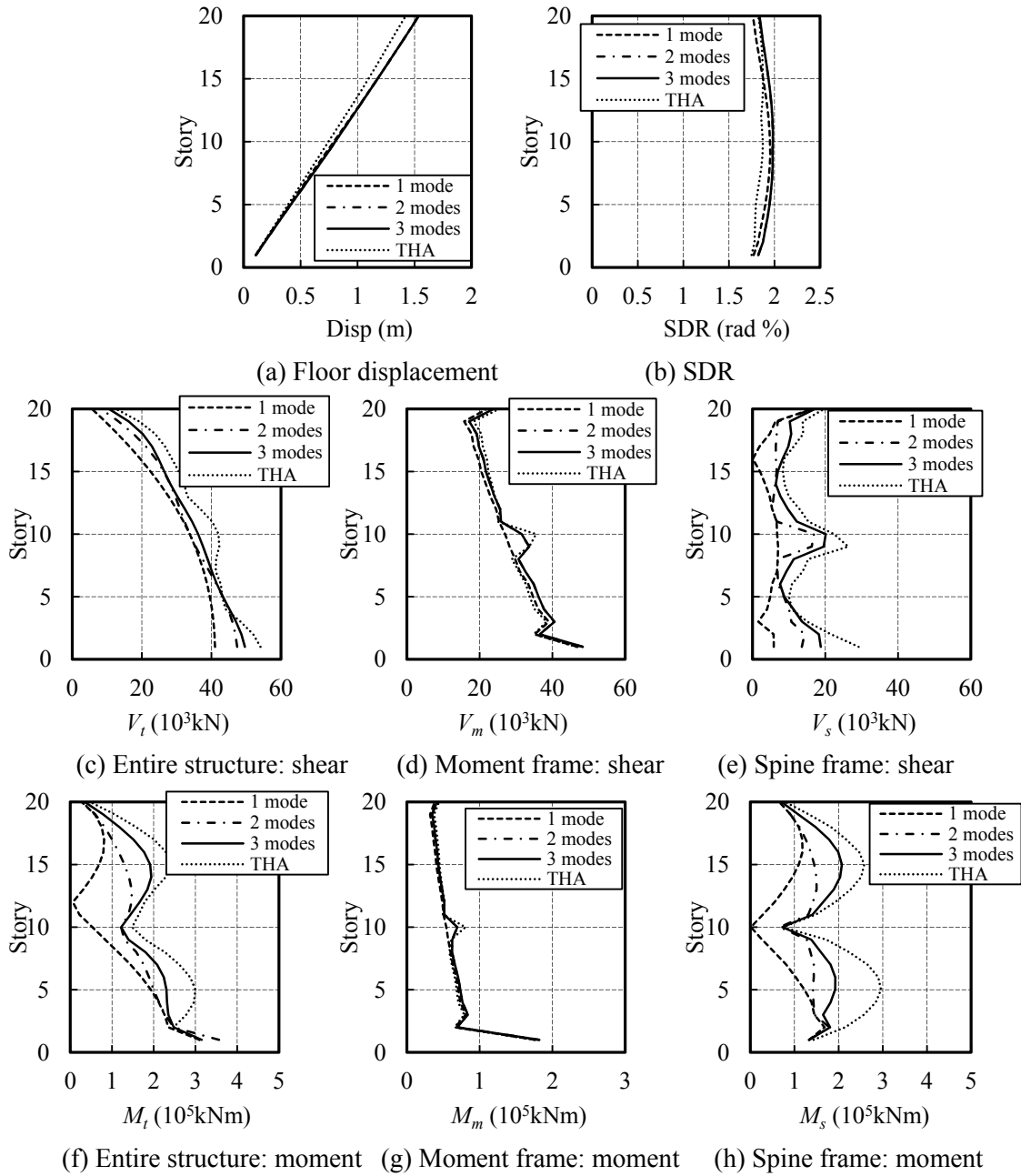


Fig. 6.42 Responses of a Sgt2 model estimated by MPA with variable number of modes

Comparison between Sgt and Cnt models by MPA and THA

Fig 6.43 compares responses of the Sgt2 and Cnt models obtained by THA and by using MPA method including the first 3 modes vibration. From Fig 6.43(a) we can see that the Sgt2 model has smaller SDR and displacement response in the stories except for the segment story. Shear force and column base moment in the moment frames also decrease slightly in the stories other than the segment story, as in Fig 6.43 (b) and (c). In conclusion, the MPA method cannot capture the effect of the segmented spine in reducing response of stories other than the segment story.

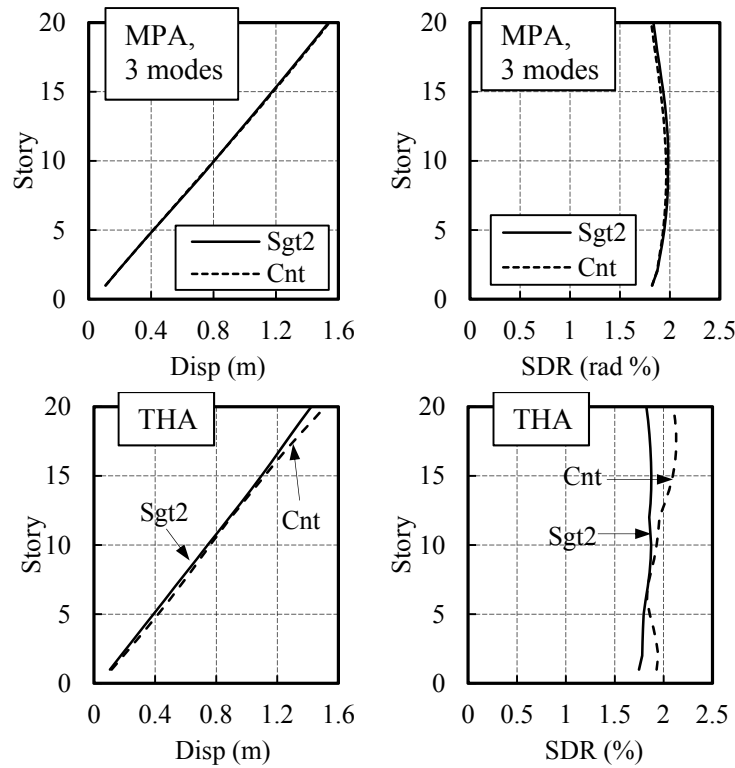


Fig 6.43 (a) Comparison between Disp and SDR results of a Sgt2 and a Cnt model obtained by MPA and THA

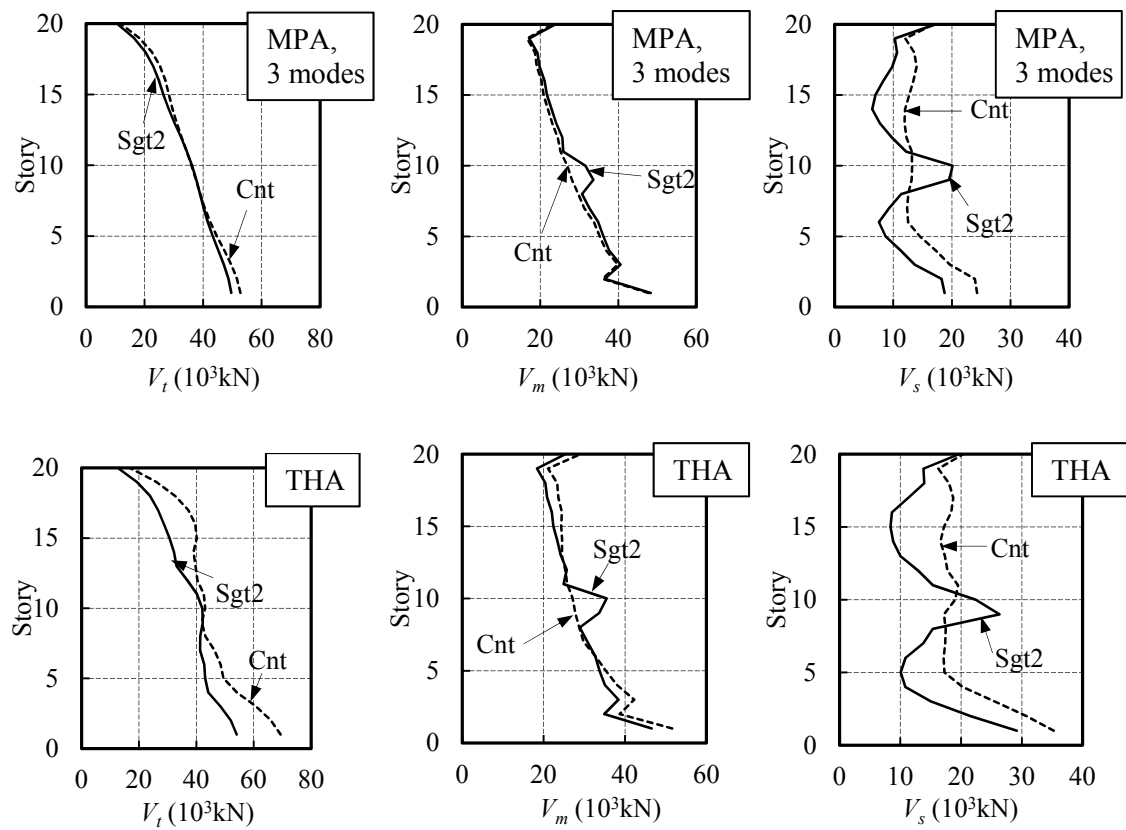


Fig 6.43 (b) Comparison between shear force results of a Sgt2 and a Cnt model obtained by MPA and THA

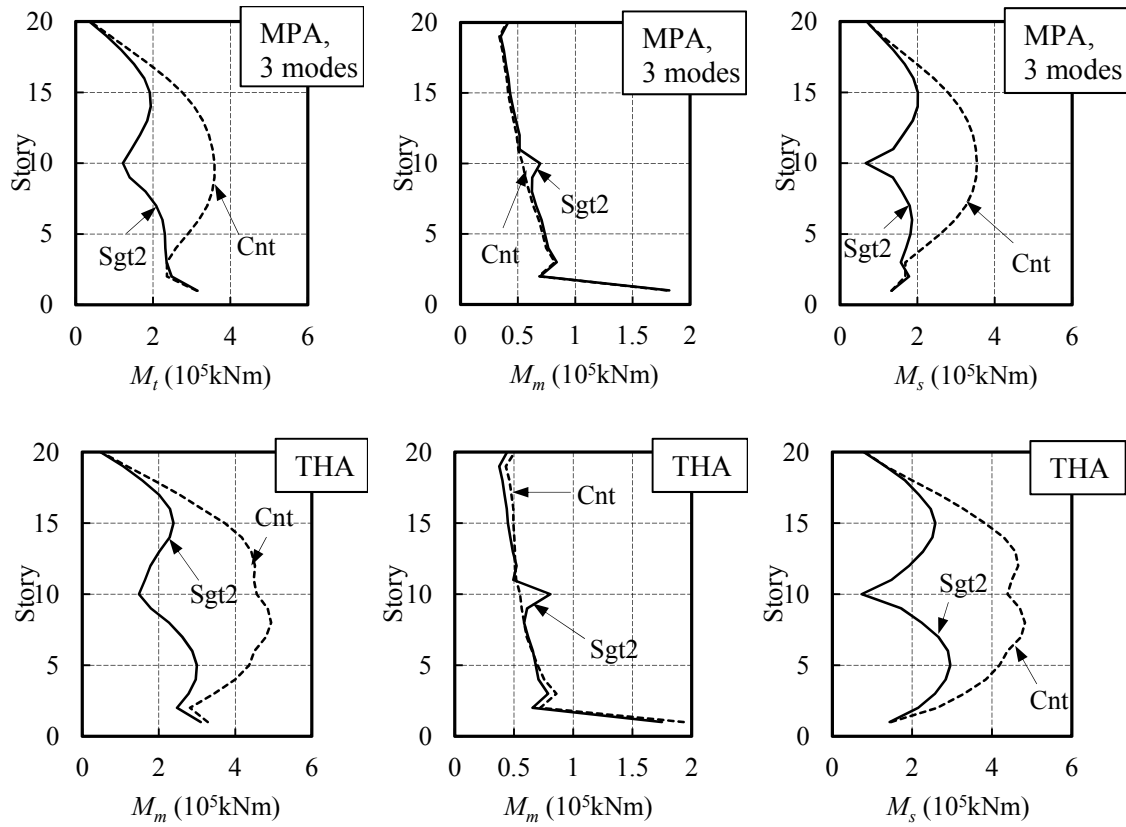


Fig 6.43 (c) Comparison between column base moment results of a Sgt2 and a Cnt model obtained by MPA and THA

6.5.2 Evaluation of Sgt models by RSA method

The RSA procedure including higher modes is utilized to estimate seismic response of the 20-story Sgt models. The first step is to compute elastic vibration characteristics of the main frame without BRCs. Both BRC1s and BRC2s are removed in this step, although pushover analysis in MPA procedure shows that the BRC2s don't yield in the 1st-mode response, its yielding in the 2nd-mode response might affect the 1st mode. Results of eigenvalue analysis for the first three modes are summarized in Table 6.18. Elastic stiffness K_f as well as the elastic response of base shear V_{bf} and mode coordinate D_f of the first three modes are also listed in Table 6.18. These results are directly computed according to the natural periods and modes obtained from eigenvalue analysis by assuming the system behaviors elastically. Fig 6.45 shows the mode shape and some elastic responses distributions of the main frame by utilizing Eq. (6.17), (6.19), (6.32) and (6.33). The elastic force-deformation $nA - nD$ curves with stiffness nK_f for the SDOF system of each mode are plotted in Fig 6.46.

To obtain the force distribution of moment frames and the spine frame, static pushover

analysis is carried out for the main frame. The lateral forces are always proportional to those obtained from elastic eigenvalue analysis, as in Fig 6.45 (e). Fig 6.47 shows the shear force and column base moment distribution of the moment frames and the spine frame.

Table 6.18 Structural characteristics of the elastic main frame in a Sgt2 model

Mode	T_f (s)	M_{eq} (ton)	M_{eq}/M	S_{af} (gal)	$V_{bf}=S_{af}M_{eq}$ (10^3 kN)	β	$K_f=(2\pi/T_f)^2$ (s^{-2})	$D_f=\beta S_{af}(T_f/2\pi)^2$ (mm)
1	3.89	14516	79%	367.2	53.3	1.41	2.61	1992
2	1.11	2157	12%	1654	35.7	0.54	32.3	276.5
3	0.29	760	4%	1654	12.6	0.30	481	10.34

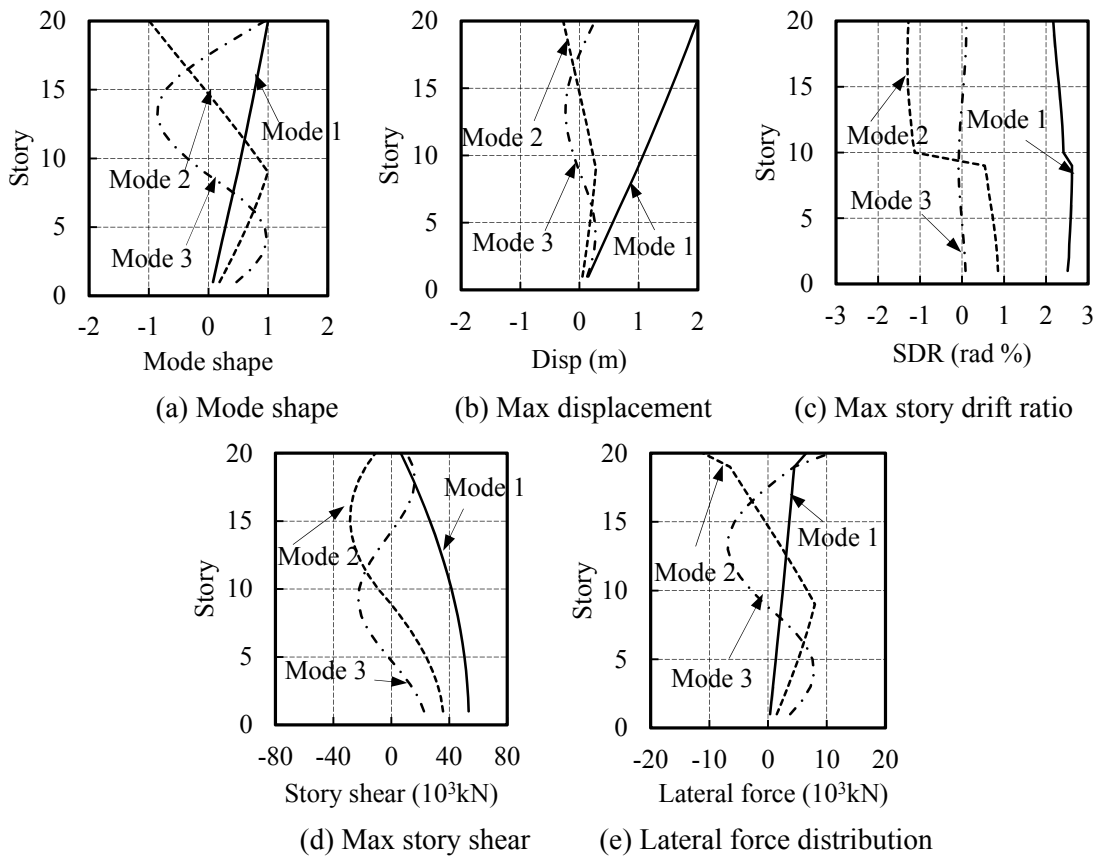
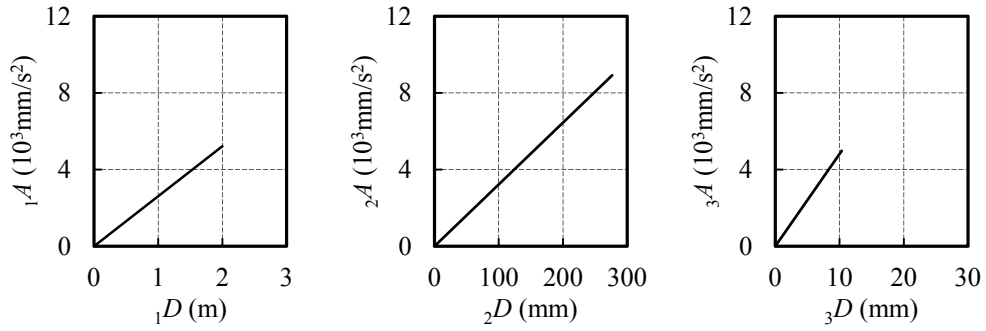


Fig. 6.45 Mode shapes and elastic responses of the main frame in a Sgt2 model



(a) 1st mode, ${}_1K_f=2.61\text{s}^{-2}$ (b) 2nd mode, ${}_2K_f=66.1\text{s}^{-2}$ (c) 3rd mode, ${}_3K_f=482\text{s}^{-2}$

Fig 6.46 Force-def. curves of the 1st-2nd- , and 3rd-mode SDOF systems of the main frame in a Sgt2 model

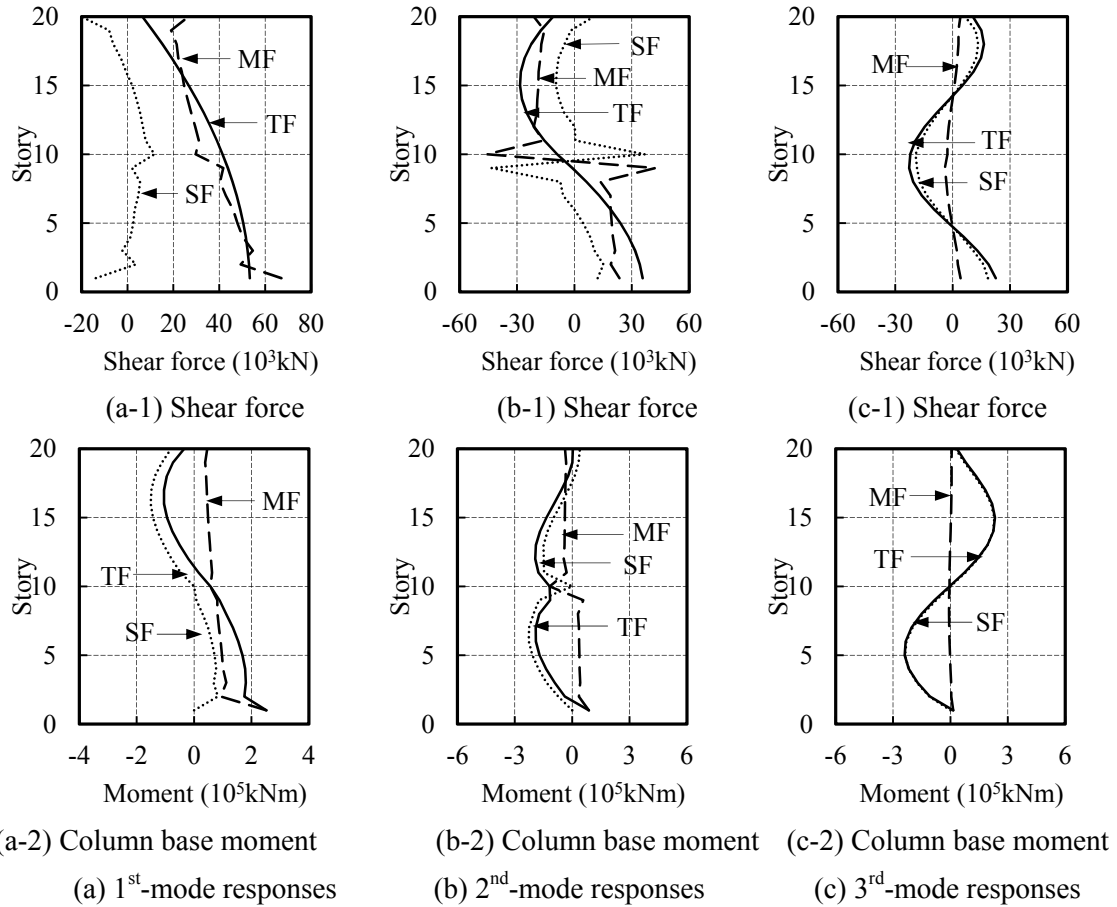


Fig. 6.47 Force distribution of each component of the main frame in a Sgt2 model

Similar to the Cnt model, to isolate the spine frame stiffness, pushover analysis is conducted with the dampers substituted with rigid elements (Fig 6.48(a)), in addition to the main frame with dampers removed (Fig 6.48(b)). Thus, the stiffness of the spine frame K_c could be isolated from the frame K_{mf} by subtracting the results of the first pushover analysis ($K_c + K_{mf}$) from the second (K_{mf}).

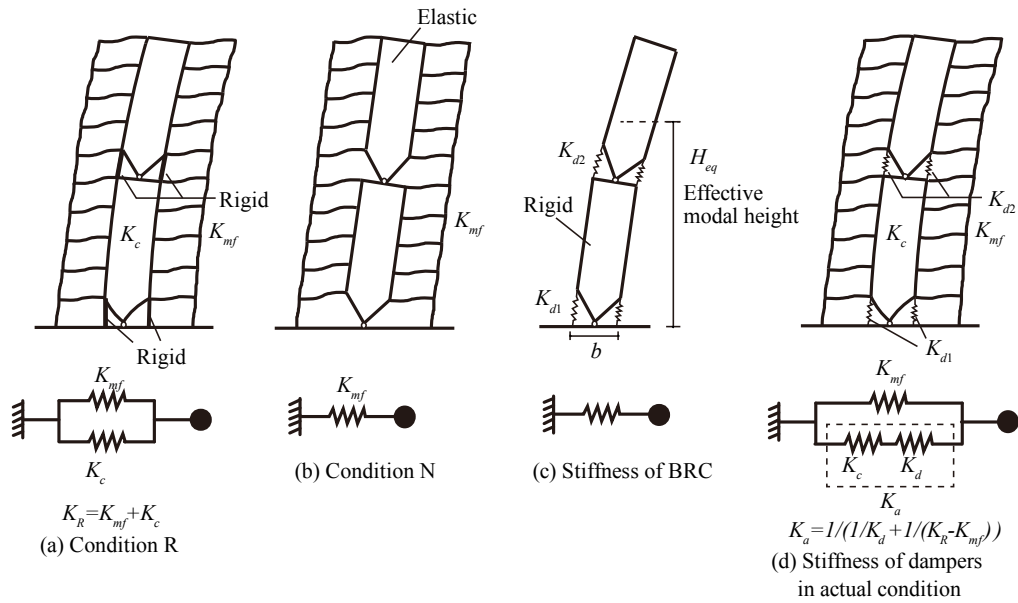


Fig. 6.48 Spring models for each condition of the Sgt2 model

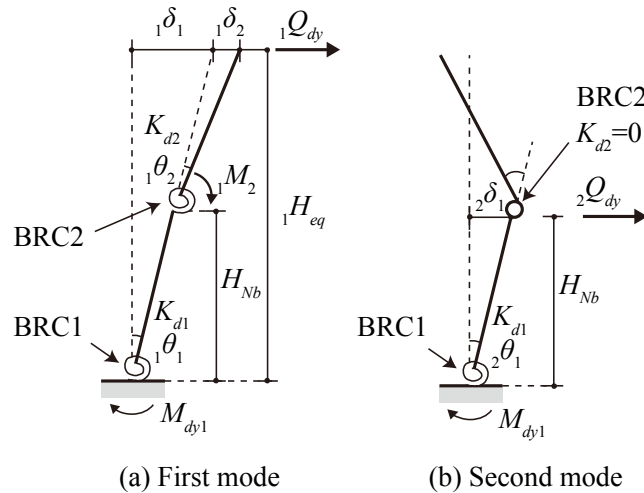


Fig. 6.49 Computation model of damper stiffness for the first and second modes of a Sgt2 model

Computation of damper stiffness K_d is different from the Cnt model. In case of the first mode, BRC2s remain elastic while BRC1 yield, as observed from pushover analysis in MPA procedure. Lateral deformation δ_2 contributed by BRC2 are given by Eq. (6.38)

$$\begin{cases} \theta_2 = M_2 / K_{d2} \\ M_2 = Q_{dy} (H_{eq} - H_{Nb}) \longrightarrow \delta_2 = \frac{Q_{dy} (H_{eq} - H_{Nb})^2}{K_{d2}} \\ \delta_2 = \theta_2 (H_{eq} - H_{Nb}) \end{cases} \quad (6.38)$$

Where, θ_2 , M_2 , K_{d2} are the rotation angle, moment, and stiffness of BRC2s, respectively. H_{eq} is the 1st-mode effective height, H_9 is the height of the 9th floor (top of the 9th story), and F_{dy} is the assumed lateral force at height H_{eq} . lateral deformation contributed by BRC1s are computed by Eq. (6.39)

$$\begin{cases} \theta_1 = M_{dy1} / K_{d1} \\ M_{dy1} = Q_{dy} H_{eq} \longrightarrow \delta_1 = \frac{Q_{dy} H_{eq}^2}{K_{d1}} \\ \delta_1 = \theta_1 \cdot H_{eq} \end{cases} \quad (6.39)$$

Finally the lateral stiffness of the BRCs, K_d , is calculated from Eq. (6.40)

$$K_d = \frac{Q_{dy}}{(\delta_1 + \delta_2) M_{eq}} = \frac{1}{\frac{H_{eq}^2}{K_{d1}} + \frac{(H_{eq} - H_{Nb})^2}{K_{d2}}} \cdot \frac{1}{M_{eq}} \quad (6.40)$$

In case of the second mode, BRC2s yield before BRC1s yield, and its effect on the stiffness degradation of the whole structure is insignificant. Yielding of BRC1s is regarded as the only yielding point in MPA procedure and it provides good estimation compared with the THA results. Here in the RSA procedure, initial stiffness of dampers is also computed based on the same condition, as shown in Fig 6.49 (b), the BRC2s have already yield and cannot resisting additional external force. The equivalent single lateral force is loaded on the top of the 9th story. Stiffness of BRC1s is computed by Eq. (6.37) by substituting H_9 instead of H_{eq} . For both modes, stiffness of the full additional system is computed by Eq (6.38).

Table 6.19 lists some key parameters of BRCs involved in the above calculation. Additional stiffness and the other intermediate stiffnesses are summarized in Table 6.20. Yielding deformation D_y is computed by Eq. (6.39). Fig 6.50.1 shows that H_{eq} and H_{Nb} match well with the height obtained from MPA method. Fig 6.50 shows the final force-deformation curves of the first and second mode SDOF systems in comparison with the curves obtained from the MPA procedure.

As shown in Fig 6.50 (a), initial stiffnesses of the first mode SDOF systems are almost identical between RSA and MPA, which confirms the calculation method for the additional

stiffness K_a in RSA. Hardening stiffness obtained in RSA is slightly smaller compared to MPA. It is mainly because the BRC2s are elastic in MPA while assumed to be yield in RSA.

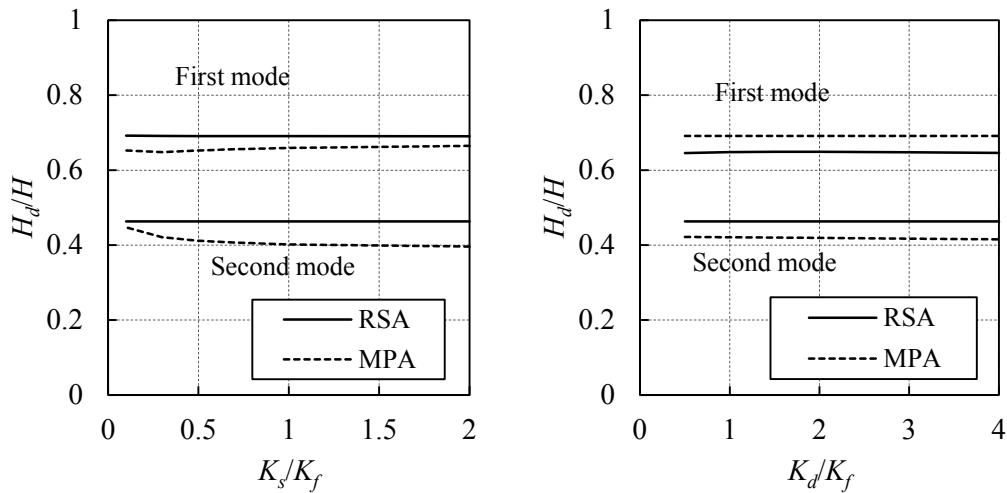
Fig 6.50 (b) compares the second mode force-deformation curves obtained from RSA and MPA. Initial stiffnesses show great agreement, while hardening stiffness in MPA is much smaller than RSA. A similar phenomenon has been observed in the Cnt models. It might be because the external lateral forces in MPA keep following the elastic distribution obtained from eigenvalue analysis of the whole structure, while in RSA the distribution is obtained from eigenvalue analysis of the main frame without BRCs.

Table 6.19 Key parameters of dampers in a Sgt2 model

M_{dy1} (Nmm)	M_{dy2} (Nmm)	H_{eq} (mm)	H_{Nb} (mm)	$\theta_{dy1} = \theta_{dy2}$ (%)
1.33×10^{11}	0.665×10^{11}	56671	38000	0.1

Table 6.20 Related stiffnesses (unit: s^{-2}) of the 1st and 2nd modes of a Sgt2 model

Mode	K_f	K_R	K_c	K_d	K_a	K_{f+a}
1	2.61	5.24	2.63	2.35	1.24	3.85
2	32.3	107.5	75.2	42.8	27.3	59.5



(a) H_d/H with various K_s/K_f ($K_d/K_f=1.0$)

(b) H_d/H with various K_d/K_f ($K_s/K_f=0.3$)

Fig 6.50.1 Verification of H_d for Sgt2 models by MPA method

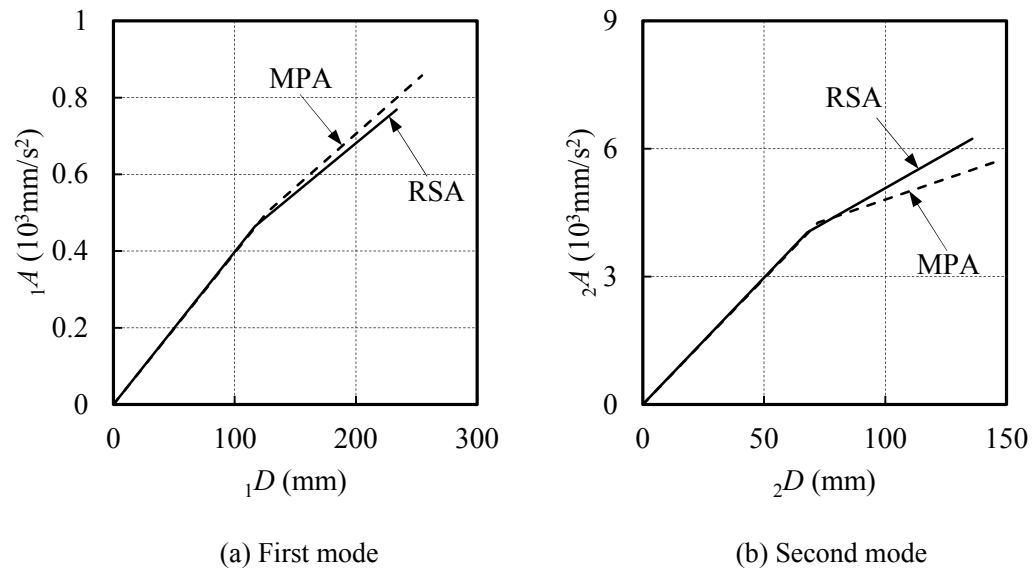


Fig 6.50 Force-def. curve of SDOF systems of a Sgt2 model obtained by RSA and MPA

Table 6.21 Evaluation of the SDOF system and the original structure of a Sgt2 model

Mode	T_{eq} (s)	ζ_0	D (mm)	A (mm/s ²)	SDR (%)	V_t (10 ³ kN)
1	3.80	0.057	1081	2950	2.01	42.8
2	1.00	0.081	254	10055	0.42	27.8
3	0.29	0.02	10.34	4975	0.10	22.5

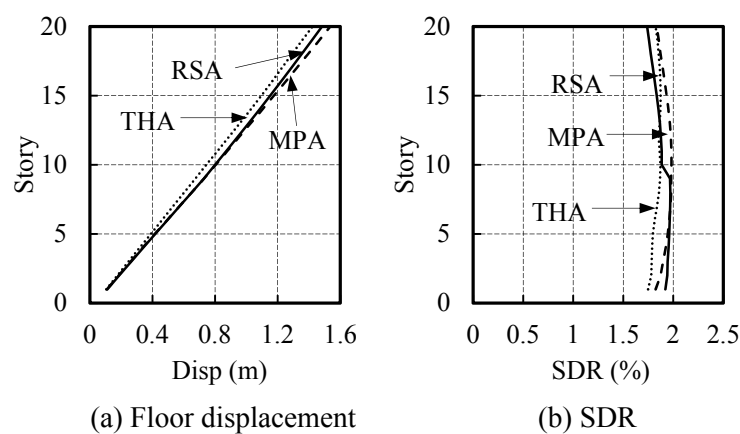


Fig. 6.51 (a,b) Estimated responses of a Sgt2 model by RSA, MPA and THA

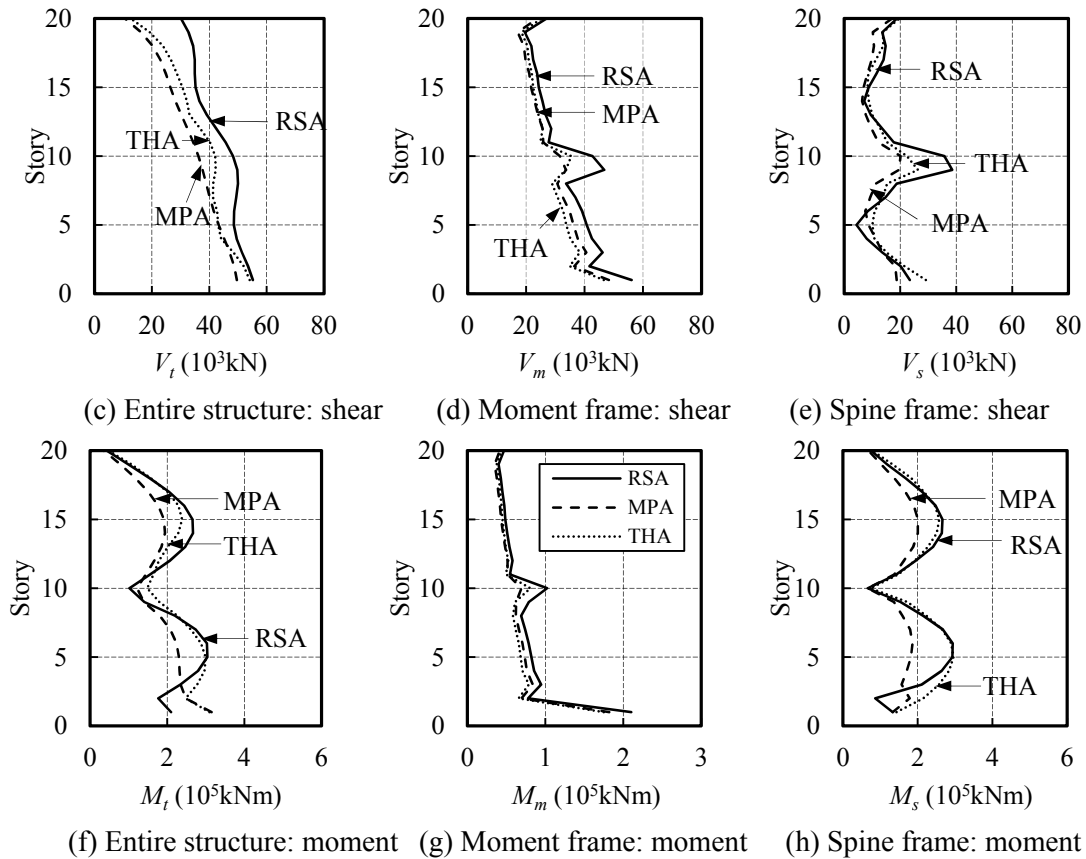


Fig. 6.51 (c-h) Estimated responses of a Sgt2 model by RSA, MPA and THA

Table 6.21 compares the equivalent period, damping ratio, deformation and force responses of the SDOF system, as well as the maximum SDR and base shear of the original structure obtained by RSA and MPA procedures. Although there is much difference in hardening stiffness of the SDOF system, difference in maximum SDR and base shear is less than 5% and 12%. Fig 51 shows the responses estimated by the RSA procedure in comparison with results from MPA procedure and nonlinear time history analysis (THA). The estimated values of responses are computed including 3 modes for both RSA and MPA. The RSA procedure provides relatively more conservative results compared to MPA procedure for almost all responses.

Fig 6.52 compares responses of the Sgt2 and Cnt models obtained by RSA and by using MPA method including the first 3 modes vibration. Similar with the MPA method, the RSA method cannot capture the effect of the spine frame in decreasing deformation and force response in the stories other than the segmented story.

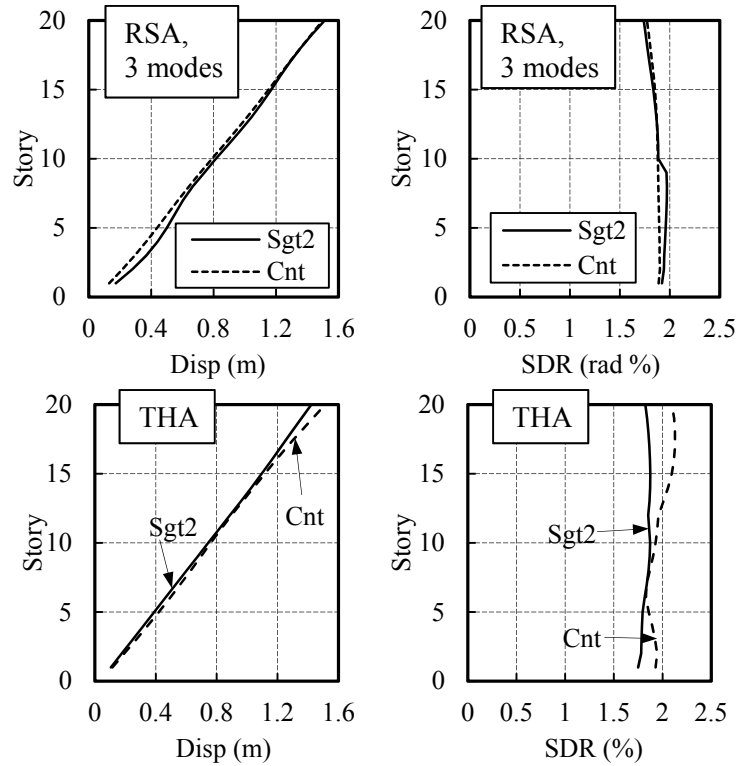


Fig 6.52 (a) Disp and SDR results of a SGT2 and a Cnt model obtained by RSA and THA

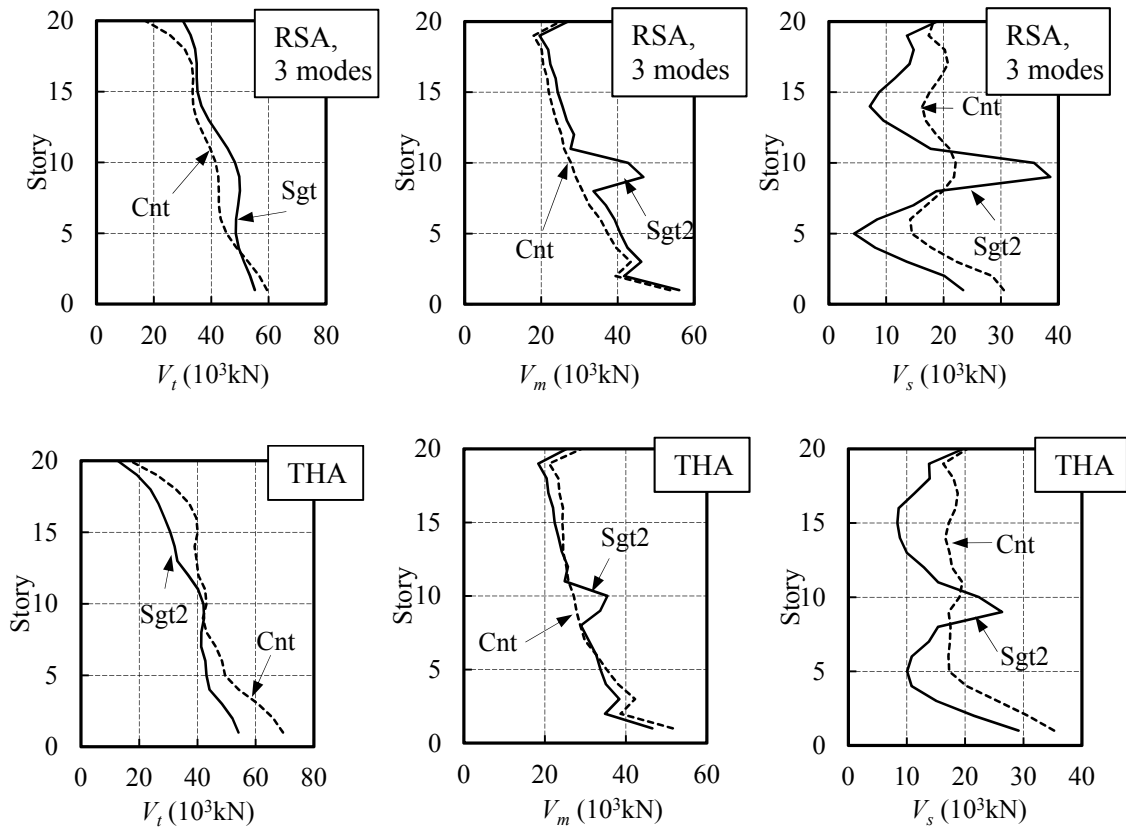


Fig 6.52 (b) Shear force results of a SGT2 and a Cnt model obtained by RSA and THA

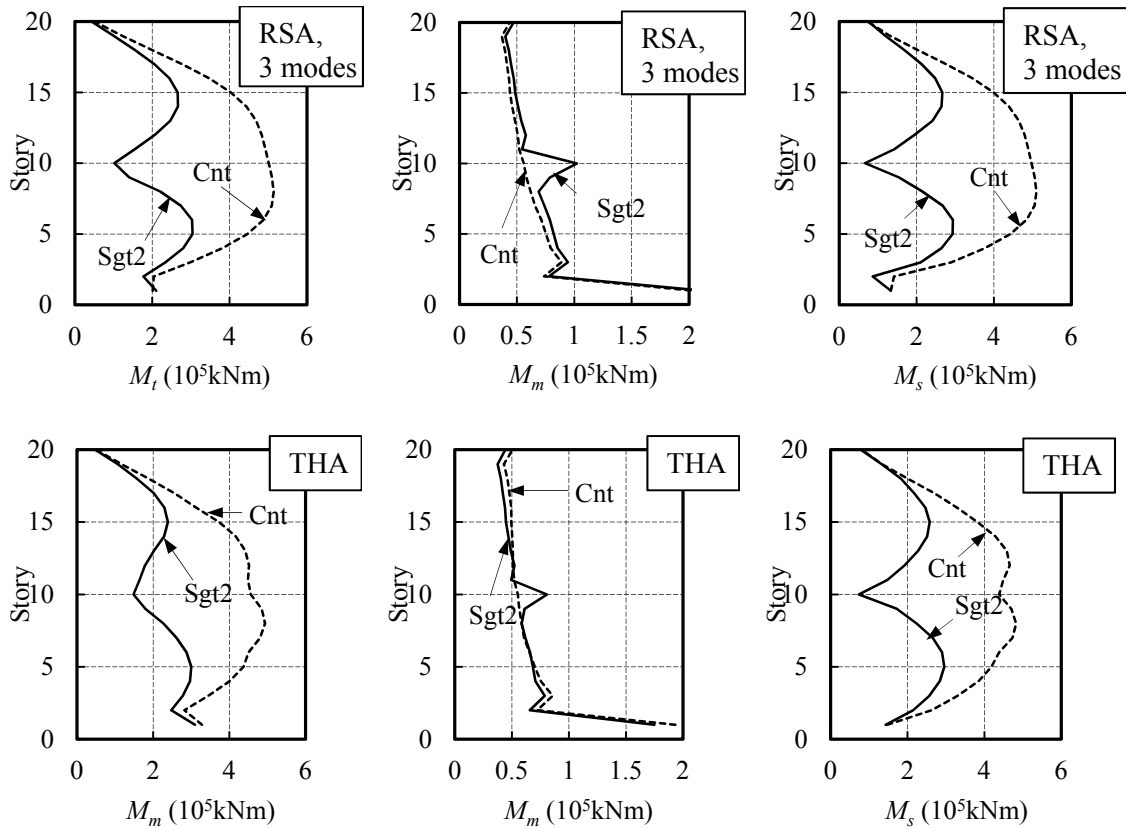


Fig 6.52 (c) Comparison between story base moment results of a Sgt2 and a Cnt model obtained by RSA and THA

The 20-story Sgt models with $K_s/K_f=0.1 \sim 2.0$, $K_{d2}/K_{d1}=0.5$, $K_{d1}/K_f=0 \sim 4.0$ are estimated by utilizing the RSA procedure. Fig 53 and 54 show the estimated responses of the 1st-mode and 2nd-mode SDOF system by utilizing RSA and MPA procedure with various K_s/K_f . Fig 6.55 and 6.56 show those results with various K_d/K_f . Generally speaking, the force-deformation curve of the 1st-mode SDOF system determined by RSA are in good agreement with those determined by MPA when $K_s/K_f=0.1 \sim 2.0$, $K_{d1}/K_f=0 \sim 2.0$, as in Fig 6.52 (a-c), Fig 6.54 (a-c). Additionally, from Fig 6.53 (b) (d) (f) and 6.54 (b) (d) (f) we can see that, the 1st-mode damping ratio is much more sensitive to hardening ratio other than ductility ratio.

Hardening stiffness ratio of the 2nd-mode SDOF system obtained by the two methods presents significant difference. The difference increases along with K_{d1}/K_f increasing, implying that the excessive lateral force determined by eigenvalue analysis of the whole structure including elastic BRCs is the main reason, since the difference between 2nd-mode modal shapes obtained by RSA and MPA increases along with the stiffness of BRCs increasing. Therefore, significant difference is presented by the estimated results, as in Fig 6.54 (d-f), Fig 6.56 (d-f). Additionally, unlike the Cnt models, effect of changing in spine frame stiffness seems negligible on the properties of the 2nd-mode SDOF system when $K_s/K_f \geq 0.5$.

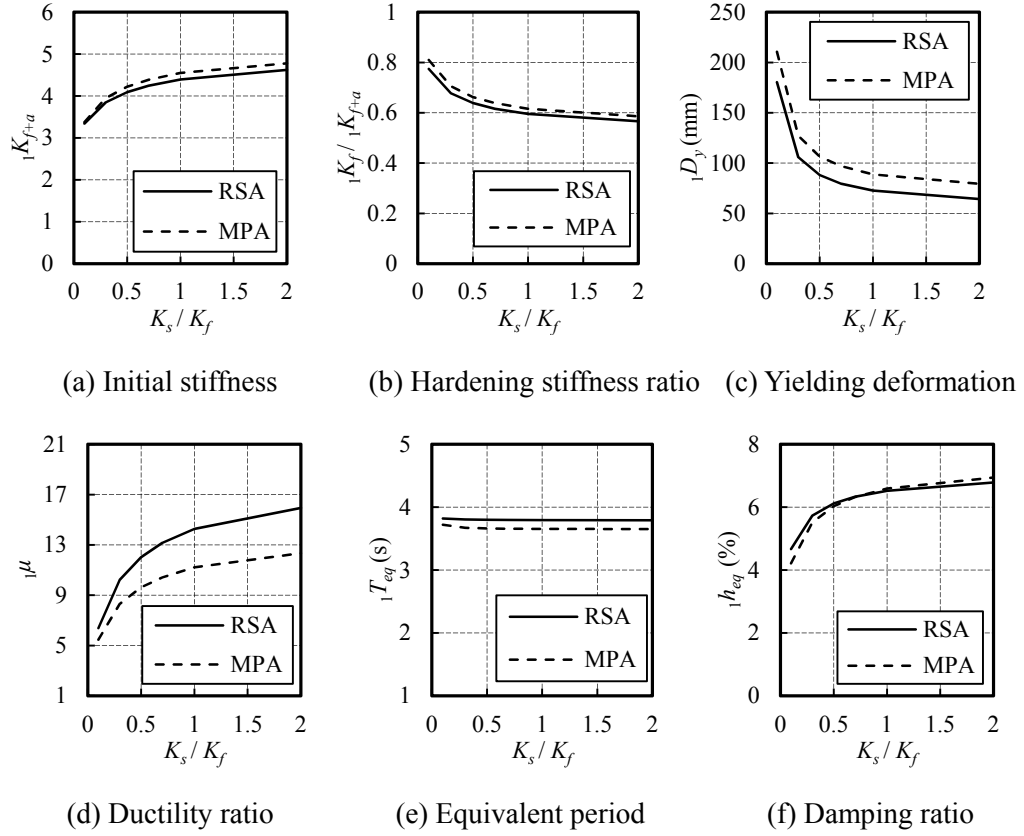


Fig. 6.53 Comparison of RSA and MPA methods on characteristics and responses of the 1st-mode SDOF system of a Sgt2 model with various K_s/K_f ($K_{d1}/K_f=1.0$, $K_{d2}/K_f=0.5$)

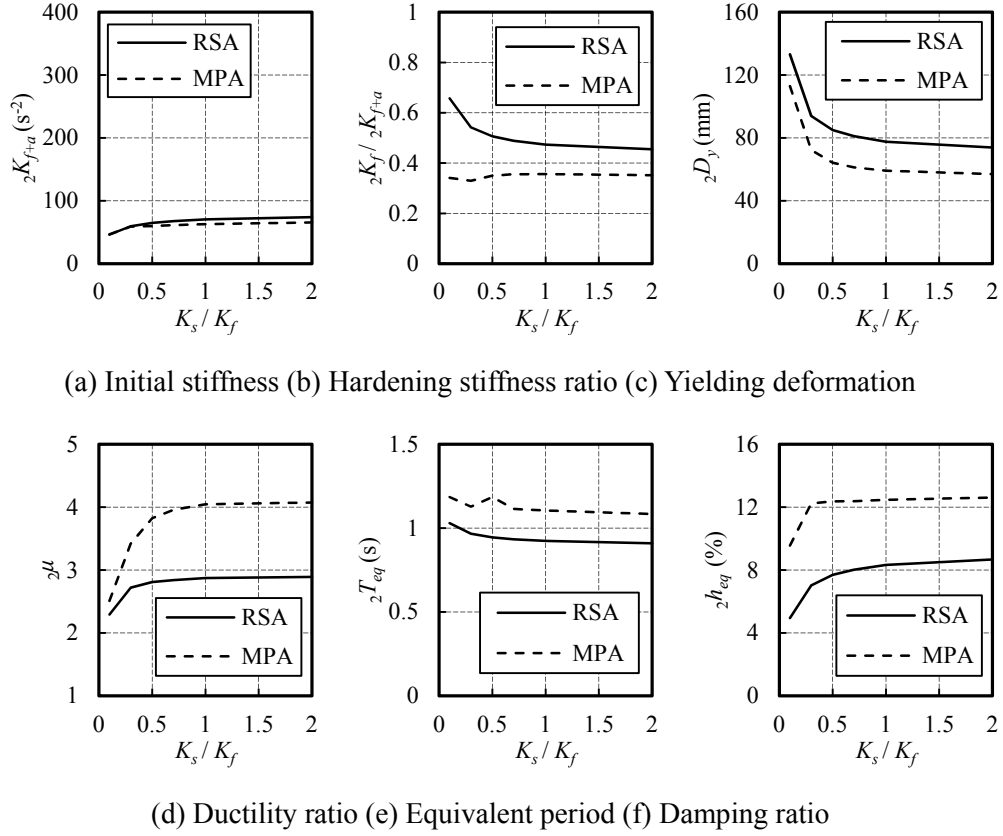


Fig. 6.54 Comparison of RSA and MPA methods on characteristics and responses of the 2nd-mode SDOF system of a Sgt2 model with various K_s/K_f ($K_{d1}/K_f=1.0$, $K_{d2}/K_f=0.5$)

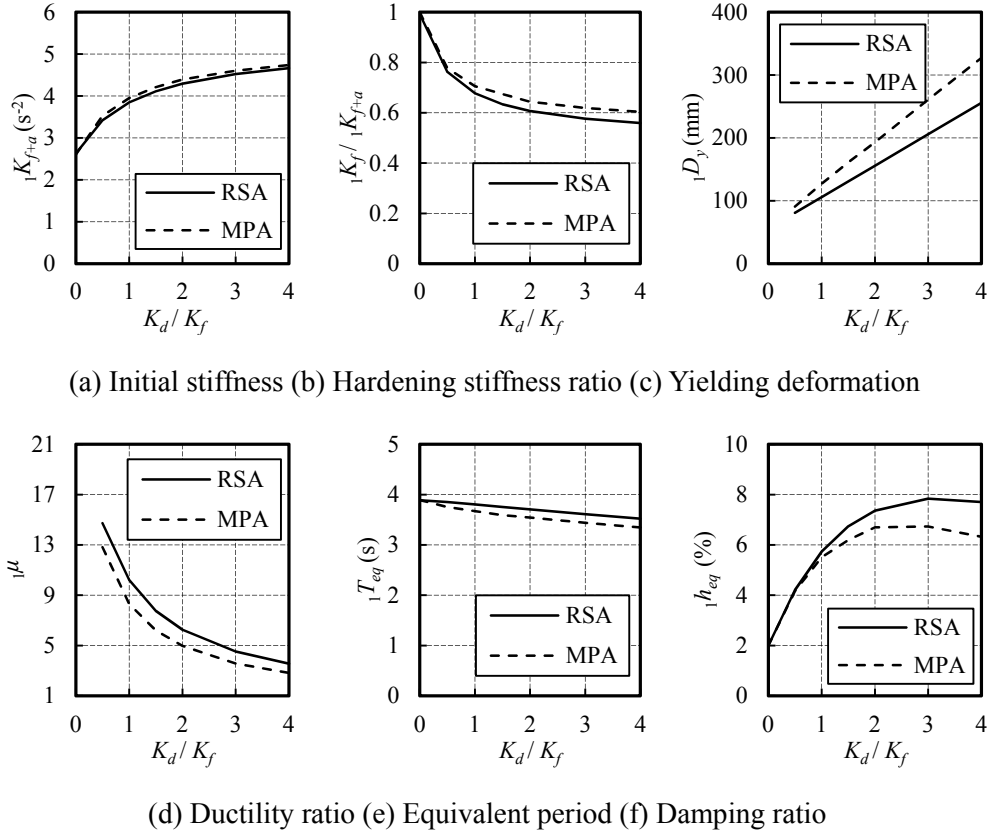


Fig. 6.55 Comparison of RSA and MPA methods on characteristics and responses of the 1st-mode SDOF system of a Sgt2 model with various K_d/K_f ($K_s/K_f=0.3$)

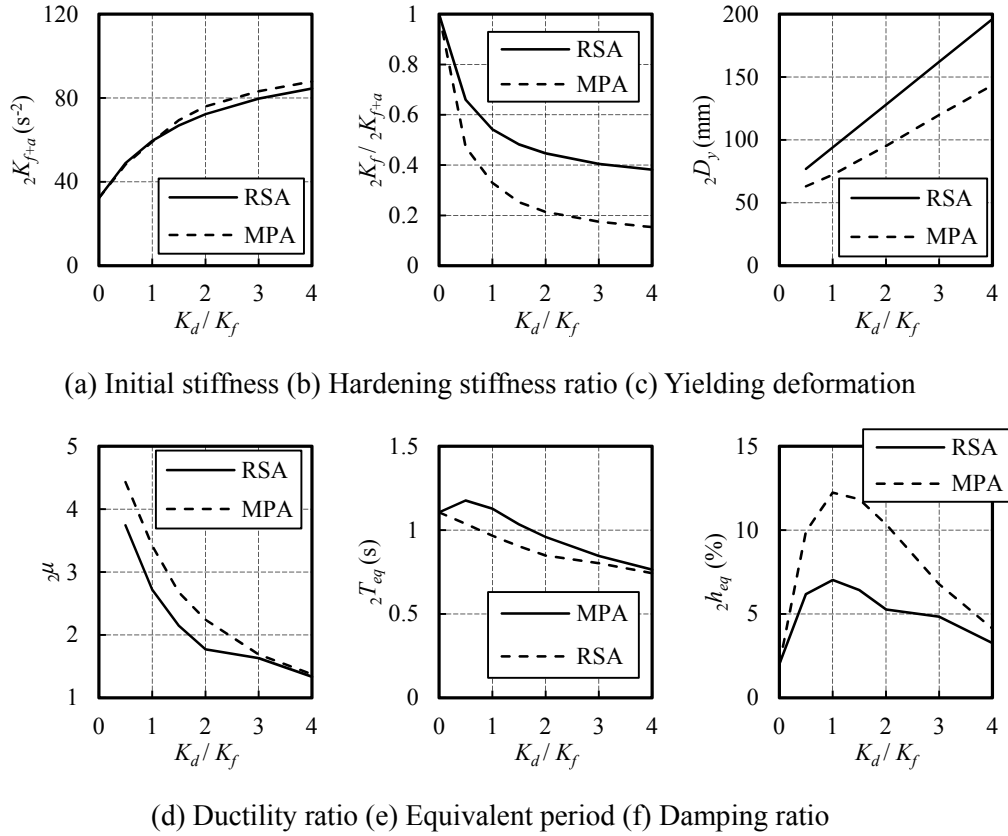


Fig. 6.56 Comparison of RSA and MPA methods on characteristics and responses of the 2nd-mode SDOF system of a Sgt2 model with various K_d/K_f ($K_s/K_f=0.3$)

To judge whether the estimation methods are reasonable, results obtained from RSA and MPA are compared with the nonlinear THA results, as in Fig 6.57. The estimated responses are computed including 3 modes.

From Fig 6.57 (a-1) (a-2) (b-1) (b-2) we can see that, despite the value of K_s/K_f and K_{d1}/K_f , RSA and MPA both overestimate the maximum SDR and roof displacement. Fig 6.57 (a-3) (a-5) (b-3) (b-5) show that, base shear and overturning moment of moment frames in RSA are significantly overestimated compared to THA and MPA. Neither MPA nor RSA procedure could capture the deformation reducing effect of the Sgt models in dynamic analysis. As for force responses, RSA provides much better estimation on base shear and maximum moment of the spine frames compared to MPA, although it still underestimate the base shear of spine frames when $K_{d1}/K_f \geq 0.5$, as in Fig 6.57 (a-4) (a-6) (b-4) (b-6). However, RSA gives over conservative estimation on the base shear and overturning moment of the moment frames. Similar with the Cnt model, it might be because of the assumption that, the structural response distribution is

essentially proportional to the responses of the main frame without BRCs. Error caused by this assumption increases along with K_{d1}/K_f increasing. Modification factor γ is introduced for force of the moment frames, which is computed by Eq. (6.40). After multiplying the modification factor γ , force of the moment frames estimated by RSA procedure is much closer to the THA results, as in Fig 6.57 (b-3) (b-5).

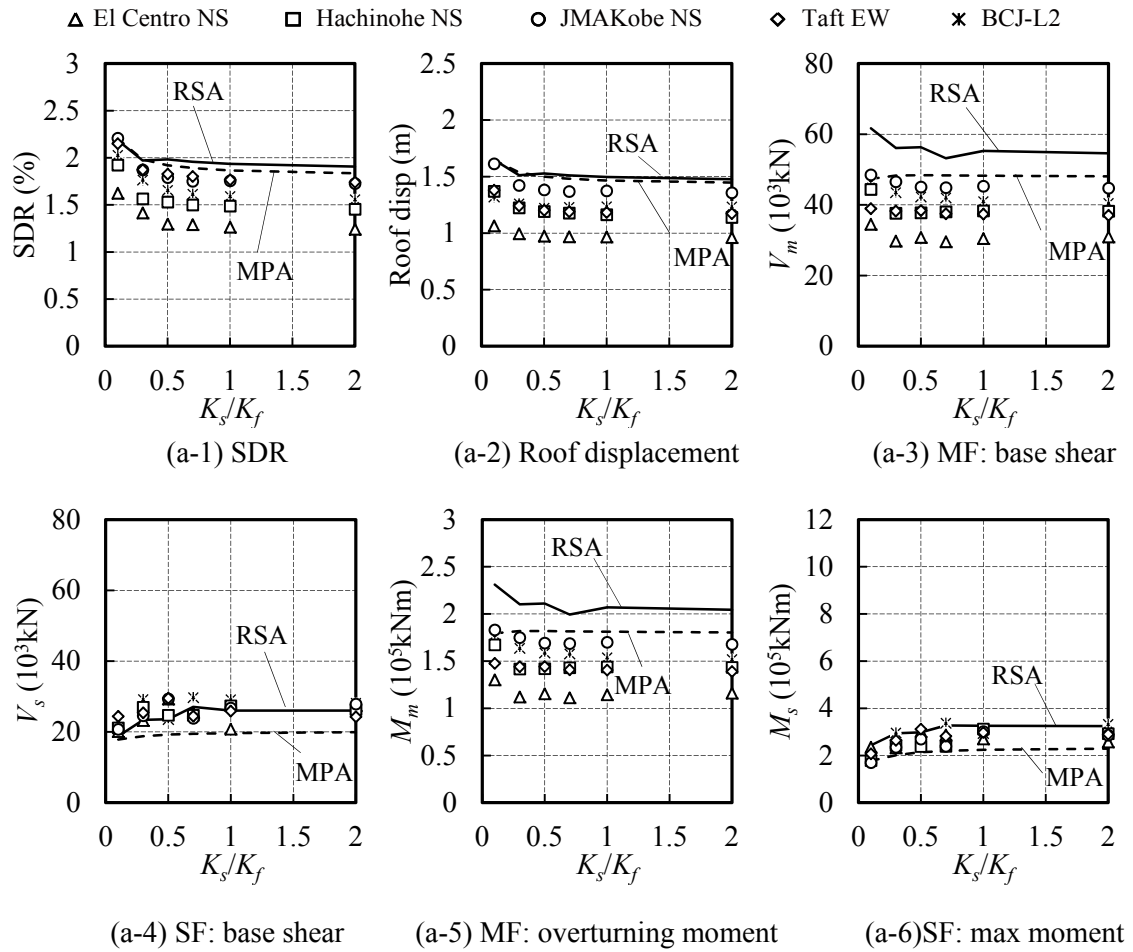


Fig. 6.57 (a) Comparison of RSA, MPA and THA results of the Sgt2 models with various K_s/K_f ($K_d/K_f = 1.0$)

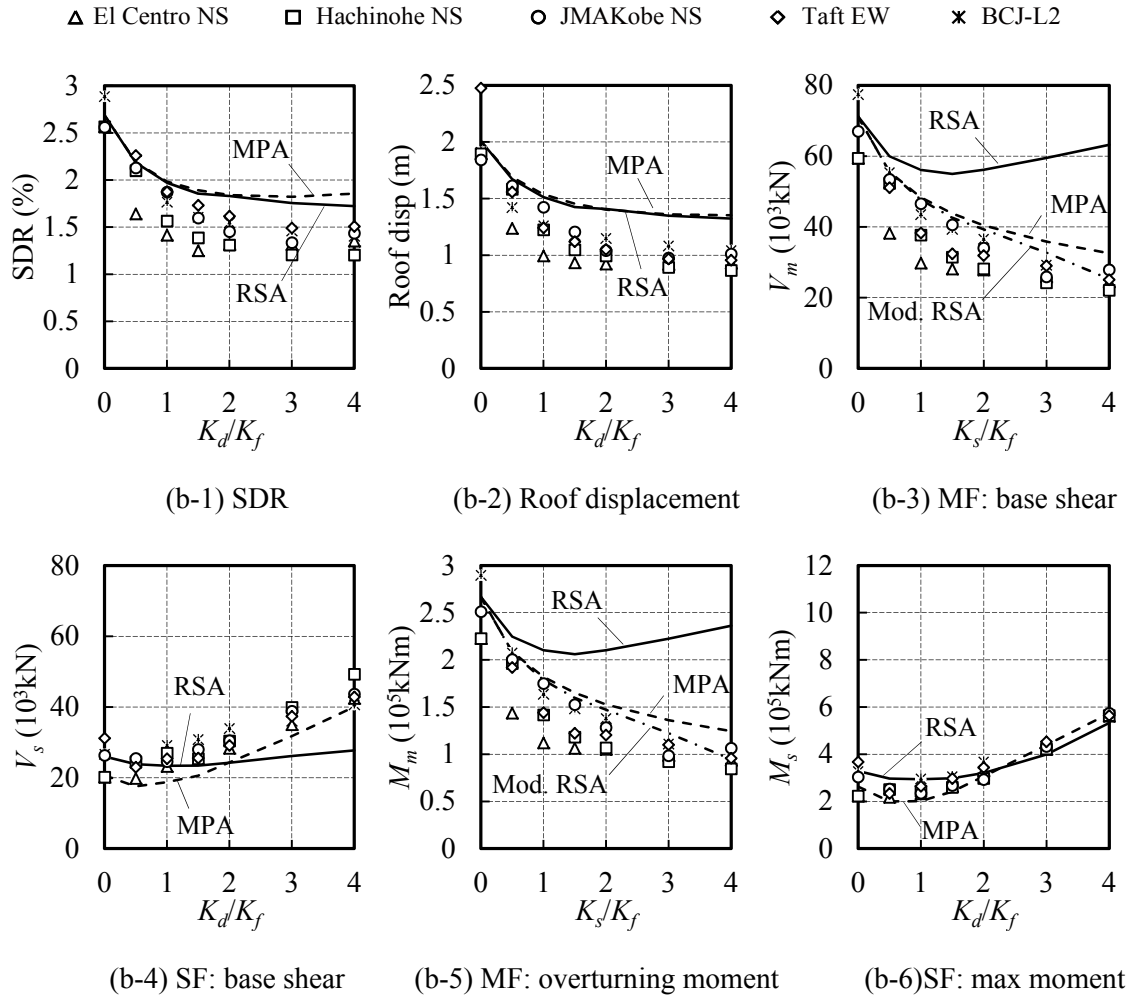


Fig. 6.57 Comparison of RSA, MPA and THA results of the Sgt2 models with various K_d/K_f ($K_s/K_f=0.3$)

6.6 Design procedure for high-rise controlled spine frame structures

Following from the RSA method, a simple design procedure for the high-rise controlled spine frame adopting Cnt or Sgt2 configuration is proposed. Basically, the Cnt configuration is recommended for buildings not higher than 20 stories, while the Sgt2 configuration is more recommended for buildings higher than 20 stories.

Design procedure for Cnt configuration:

- Step 1. Design the moment frame and spine frame for the target drift level without dampers (less than 1.5 times of the target drift with dampers), and ensure the spine-to-moment frame stiffness ratio $K_s/K_f \geq 0.3$.
- Step 2. Evaluate the elastic displacement and force response of the moment frame and spine frame. Compute the required displacement reduction factor of the entire structure and

force reduction factor of the moment frame to achieve the performance targets.

- Step 3. According to the value of K_s/K_f , select the local yielding drift ratio of damper θ_{dy} and damper-to-moment frame stiffness ratio K_d/K_f from the performance curve (Fig 6.58, black curves) that satisfy the target displacement and force response. (or Eq. (6.41-48))
- Step 4. Design the dampers for the selected local yielding drift ratio and stiffness.
- Step 5. Obtain force reduction factor of spine frame according to θ_{dy} , K_s/K_f and K_d/K_f from Fig 6.59. Confirm the required strength of spine frame is satisfied. If not satisfied, then increase the strength of spine frame and repeat the procedure from step 1, or choose segmented spine configuration.
- Step 6. Confirm the final overall response using the equivalent linearization technique. Validate results with time-history analysis as required.

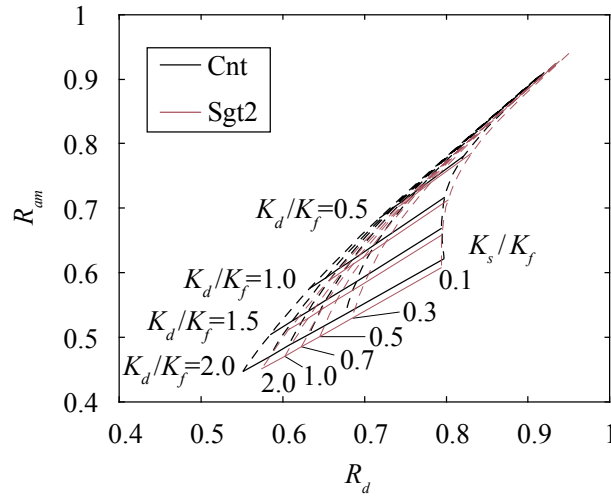


Fig 6.58 Performance curve for 1st-mode dominant response:
SDR, shear force and bending moment of moment frame ($\theta_{dy}=0.1\%$, $R_{Kd}=0.5$)

Design procedure for Sgt2 configuration:

- Step 1. Design the moment frame and spine frame for the target drift level without dampers (less than 1.5 times of the target drift with dampers). Ensure the spine-to-moment frame stiffness ratio $K_s/K_f \geq 0.3$. Decide a segment level from the optimal range: 0.5-0.75 of total height.
- Step 2. Identical with Cnt.
- Step 3. Decide BRC2-to-BRC1 stiffness ratio from the range of 0.5-1.0. According to the value of K_s/K_f , select the local yielding drift ratio of damper θ_{dy} and damper-to-moment frame stiffness ratio K_d/K_f from the performance curve (Fig 6.58, red curves) that satisfy the target displacement and force response. (or using Eq. (6.41-48))
- Step 4. Design the dampers for the selected local yielding drift ratio and stiffness.

Step 5. Obtain force reduction factor of spine frame according to θ_{dy} , K_s/K_f and K_d/K_f from Fig 6.60. Confirm the required strength of spine frame is satisfied. If not satisfied, then increase the strength of spine frame and repeat the procedure from step 1.

Step 6. Confirm the final overall response using the equivalent linearization technique. Validate results with time-history analysis as required.

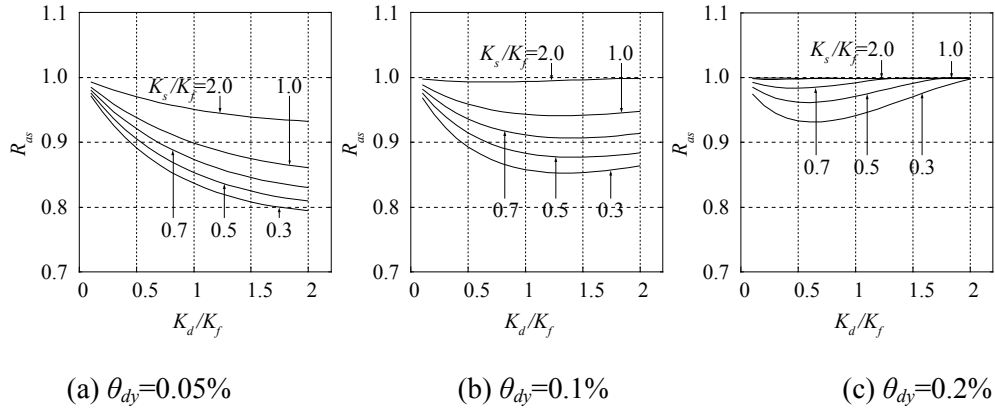


Fig 6.59 Force reduction factor of spine frame in Cnt models ($R_{Kd}=0.5$)

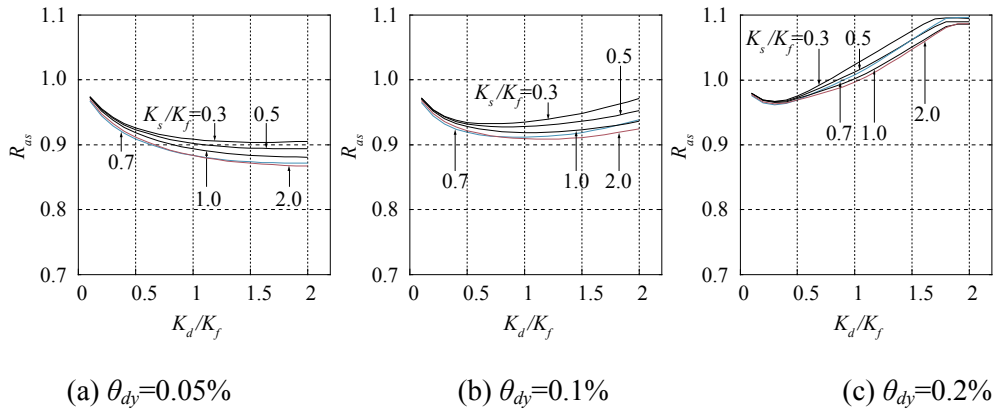


Fig 6.60 Force reduction factor of spine frame in Sgt2 models ($R_{Kd}=0.5$)

In Step 3 of the design procedure, if the value of structural parameters is not included in the provided performance curves, there is an alternative way based on formula calculations:

When the 1st mode vibration period is in the velocity constant range, which is the often case for high-rise spine frame structures, those 1st-mode dominant responses can be evaluated directly by formula calculation without any iteration work. Subscript “1” that notates 1st mode is omitted in the variables in Eq. (6.41-6.48). From Eq. (6.41) and (6.42) we can obtain Eq. (6.43). By introducing an approximation equation (Eq. (6.44)) for the equivalent damping ratio, the ductility ratio μ can be solved as Eq. (6.46). Then the displacement and force reduction factors can be computed from Eq. (6.47) and (6.48).

$$\mu = \frac{D_t}{D_y}, (D_y = \theta_{dy} \left(1 + \frac{K_d}{K_c} \right) \frac{1}{\varphi_{f1} \cdot \beta_f}) \quad (6.41)$$

D_t : target deformation of 1st-mode SDOF system

D_y : yielding deformation of 1st-mode SDOF system

θ_{dy} : local yielding drift ratio of dampers

K_d : damper stiffness

K_c : spine frame stiffness

φ_{f1} : 1st element of 1st natural vibration mode of main frame

β_f : modal participation factor of 1st natural vibration mode of main frame

Damper stiffness K_d is calculated based on deformation mechanism. Spine stiffness K_c is obtained by eigenvalue analysis of the main frame with rigid BRCs and without BRCs. φ_{f1} , β_f are obtained by eigenvalue analysis of the main frame.

$$D_t = D_f D_h \sqrt{\frac{K_f}{K_{eq}}}, \quad D_h = \sqrt{\frac{1 + \alpha h_0}{1 + \alpha h_{eq}}} \quad (6.42)$$

D_f : elastic deformation of main frame in 1st-mode SDOF system

D_h : damping reduction factor ($\alpha=25$ for observed earthquakes, $h_0=0.02$)

h_0 : intrinsic damping ratio

h_{eq} : equivalent damping ratio

K_f : main frame stiffness

K_{eq} : equivalent stiffness of 1st-mode SDOF system

$$\mu \frac{D_y}{D_f} = D_h \sqrt{\frac{K_f}{K_{eq}}} \quad (6.43)$$

$$h_{eq} = a \left(1 - \frac{1}{\mu} \right) \left(\frac{K_a}{K_f} \right)^b, \quad a=0.115, b=0.55 \quad (6.44)$$

K_a : stiffness of additional damper system considering stiffness of spine

$$K_a = \frac{1}{\frac{1}{K_d} + \frac{1}{K_c}} \quad (6.45)$$

$$\mu = \frac{F_1 + F_2}{F_3} \quad (6.46)$$

where, $F_1 = (1 - \kappa)W - \kappa$, $F_2 = \sqrt{[\kappa(1 + W) - W]^2 + 4(1 + W)(W + (1 + \alpha h_0)\zeta^2)}$, $F_3 = \frac{\mu}{\zeta}$

$$\kappa = \frac{K_a}{K_f}, \quad \varsigma = \frac{D_f}{D_y}, \quad W = \alpha a \kappa^b$$

$$R_d = \frac{D_t}{D_f} = \mu \frac{D_y}{D_f} \quad (6.47)$$

$$R_a = R_d \frac{K_{eq}}{K_f} \left(1 - 0.15 \frac{K_d}{K_f} \right) \quad (6.48)$$

6.7 Conclusion

6.7.1 Cnt models evaluated by MPA method

(1) The original member-by-member (MBM) model was converted into several equivalent SDOF systems for the required number of vibration modes. Force-deformation curve of the SDOF system was converted from the relation between base shear and reference floor displacement of the MBM model. As for the first mode vibration, roof was utilized as the reference floor and provided the most conservative estimation. It was mainly because the inelastic deformation developed more rapidly in the lower stories after the formation of yielding mechanism. As for the second mode, responses estimated by assuming the structure remained elastic significantly exceeded the actual nonlinear responses. It was necessary to build the nonlinear force-deformation relation for the second mode vibration, and the first story was utilized as the reference floor to prevent “reversal” occurring in the force-deformation curve and to ensure the conservatism.

(2) The first mode response was absolutely primary in terms of the floor displacement, story drift ratio, as well as shear force and overturning moment of the moment frames. The second mode contributed significant response in the story shear and bending moment of the spine frames.

(3) Responses estimated by utilizing MPA procedure agreed well with the THA results. Accuracy of MPA could be further improved if the floor possessing the average changing ratio of displacement increment was assigned as the reference floor.

6.7.2 Cnt models evaluated by RSA method

(1) Eigenvalue analysis was firstly carried out on the main frame without BRCs to obtain the post-yield stiffness of the SDOF systems. Stiffness of the additional damping system K_a was computed separately for each mode. As for the first mode, the equivalent modal height was adopted to converse the rotational moment of the BRC hinge into base shear. As for the second mode, 60% of the total height was utilized in the conversion.

(2) Force-deformation curve of the first mode SDOF system determined by RSA procedure

was essentially identical with MPA despite the value of K_s/K_f and K_d/K_f . Initial stiffness and yielding deformation of the second mode SDOF system computed by RSA agreed well with MPA, while hardening stiffness of RSA was much larger than MPA, which might be because the lateral force distribution utilized in MPA kept in proportional to the elastic distribution.

(3) RSA and MPA both provided well estimation with appropriate conservatism on maximum SDR, roof displacement, shear force and overturning moment of moment frames when $K_s/K_f = 0.1 \sim 2.0$, $K_d/K_f = 0 \sim 1.0$. Error increased with K_d/K_f increasing, particularly when $K_d/K_f \geq 2.0$. The main source of error in MPA procedure was the reference floor. Choosing a more representative reference floor rather than the most conservative one could greatly improve the accuracy. The main source of error in RSA procedure was the post-yield response distribution. That's why the RSA procedure provided better estimation for structures developing into sufficient plasticity, or structures in which the response distribution didn't change too much after the formation of the yielding mechanism.

(4) Estimation on base shear and maximum moment of spine frames by RSA was closer to THA results compared to MPA. However, force responses of the moment frames estimated by RSA were ridiculously large compared to THA and MPA, which also indicating that increasing damper stiffness could reduce resisting force of moment frames due to changing of the first mode modal shape. A modification factor γ linearly with K_d/K_f was introduced to modify the estimation for moment frames.

6.7.3 Sgt2 models evaluated by MPA method

(1) The Sgt models exhibited slightly longer elastic natural period in the second mode compared to the Cnt model. Concentrated rotation at the BRC2s story was clearly observed in the first and second mode modal shapes.

(2) According to the pushover analysis conducted on the MBM model, the BRC2s remained elastic in the first mode vibration. Therefore there was only one yielding point in the force-deformation curve of the first mode SDOF model. This force-deformation curve was almost identical with that of the Cnt model. As a result, force and deformation of the first mode vibration estimated by MPA for the Sgt2 models were almost identical with the Cnt model. The MPA method was not able to capture the deformation reduction effect of the Sgt model, but still, it gave a conservative estimation.

(3) In the second mode pushover analysis, the BRC2s yielded first and followed by the yielding of BRC1s. Yielding of BRC2s caused less degradation in the system stiffness, while yielding of BRC1s reduced the stiffness by approximately 50%. Force of spine frames was significantly reduced while force of moment frames kept at a similar level compared to the Cnt model. Meanwhile, additional moment demand for moment frames and shear force demand for

both moment frames and spine frames around the BRC2s story level were required.

(4) The MPA procedure estimated the maximum SDR and roof displacement of the Sgt2 models well with proper conservatism. Forces estimated by MPA procedure presented a great agreement with the THA results, except that the base shear and maximum moment of spine frames were underestimated by approximately 30%. Although the deformation estimated for Sgt2 and Cnt models were almost identical, discrepancy in forces was well captured by utilizing the MPA procedure.

6.7.4 Sgt2 models evaluated by RSA method

(1) The original member-by-member model was conversed into several equivalent SDOF systems for the required number of vibration modes. Eigenvalue analysis was firstly carried out on the main frame without any BRCs to obtain the post-yield stiffness of the SDOF systems. Stiffness of the additional damping system K_a was computed separately for each mode. As for the first mode, elastic deformation of both BRC1s and BRC2s were taken into account in the calculation of the dampers stiffness. However, as for the second mode, BRC2s were assumed to yield initially since the BRC2s made little contribution to the stiffness of dampers.

(2) Generally speaking, the force-deformation curve of the 1st-mode SDOF system determined by RSA was in good agreement with those determined by MPA when $K_s/K_f=0.1 \sim 2.0$, $K_{d1}/K_f=0 \sim 2.0$. Initial stiffness of the second mode SDOF system computed by RSA agreed well with those obtained by MPA in despite of K_s/K_f or K_{d1}/K_f . However, hardening stiffness ratio and yielding deformation of the second mode SDOF system computed by RSA were significantly higher than those obtained by MPA procedure. Such difference increased as K_{d1}/K_f increasing, which indicated that the excessive lateral force determined by eigenvalue analysis of the whole structure including elastic BRCs in MPA was the main reason. Additionally, unlike the Cnt model, changing in K_s/K_f of the Sgt model made little difference on the properties of the 2nd-mode SDOF system when $K_s/K_f \geq 0.5$.

(3) The RSA procedure provided relatively more conservative estimation for both deformation and force compared to MPA procedure. Despite the value of K_s/K_f and K_{d1}/K_f , RSA and MPA estimated the maximum SDR and roof displacement well with proper conservatism. As for force responses, RSA provided much better estimation for the spine frames compared to MPA, particularly when $K_{d1}/K_f \leq 1.0$. Nevertheless, similarly with the Cnt models, RSA procedure greatly overestimated the base shear and overturning moment of moment frames in the Sgt models. The modification factor defined for the Cnt models was introduced for the Sgt models as well, and it greatly improved the estimation for forces of moment frames despite the value of K_{d1}/K_f .

6.7.5 Design procedure

Simple design procedure is proposed for high-rise Cnt and Sgt2 spine frames with clear recommendation on optimal structural parameters. Design chart is provided for conveniently determining the value of key structural parameters. 1st-mode dominant responses can also be evaluated by formula calculation without iteration work.

References

- [6.1] Helmut Krawinkler, G. D. P. K. Seneviratna, Pros and cons of a pushover analysis of seismic performance evaluation. *Engineering Structures*, Vol. 20, No. 4-6, pp. 452-464, 1998.
- [6.2] Anil K. Chopra, Rakesh K. Goel. A modal pushover analysis procedure for estimating seismic demands for buildings. *Earthquake Engineering and Structural Dynamics*. Vol. 31, p561-582, 2002.
- [6.3] Anil K. Chopra, Rakesh K. Goel, and Chatpan Chintanapakdee. Evaluation of a modified MPA procedure assuming higher modes as elastic to estimate seismic demands. *Earthquake Spectra*: August, Vol. 20, No. 3, p757-778, 2004.
- [6.4] Rakesh K. Goel, Anil K. Chopra. Role of higher-“mode” pushover analysis in seismic analysis of buildings. *Earthquake Spectra*: November, Vol. 21, No. 4, pp. 1027-1041, 2005.
- [6.5] Anil K. Chopra. *Dynamics of Structures-Theory and applications to earthquake engineering*. 4th edition. Prentice Hall. 2012.

CHAPTER 7

Conclusions

Chapter 7 – Conclusions

This study proposes an innovative controlled spine frame system to prevent damage concentration and ensure continuous usability of buildings after large earthquakes. The proposed structural system consists of stiff spine frames, replaceable energy-dissipating members (i.e., dampers), and envelope moment-resisting frames. The spine frames prevent deformation concentration in specific stories. The envelope moment frames are designed to remain elastic and ensure sufficient self-centering capacity. Input seismic energy is absorbed by dampers, which feature significant energy dissipating capacity, and if required can be easily replaced following a large earthquake.

Superior seismic performance of the proposed system in deformation distribution, energy dissipation, self-centering capacity, robustness against severe earthquakes and irregular stiffness, are validated and compared with the conventional shear damper (SD) and post-tension strands equipped uplifting rocking systems (LU) by dynamic analysis with various ground motion intensities. Structural models are created based on a typical 5-story school building. When subjected to a design level earthquake, the proposed controlled spine frame model exhibited smallest peak deformation, mildest deformation concentration, smallest damage in main frames, and similar small residual deformation as that of the LU model, even when vertical stiffness and strength of the main structure are not well balanced. In incremental dynamic analysis, both regular and irregular spine frame models show stable seismic performance with increased input ground motion intensity. On the contrary, severe damage concentration in the irregular story was observed in the SD model, and the first-story irregular LU model exhibited a high risk in the failure of bottom diagonal members in the rocking frame against larger earthquakes.

Effect of key structural characteristics on seismic performance of the controlled spine frame system with various heights has been investigated by extensive parametric study. A simplified dual multi-degree-of-freedom (DMD) model with a nonlinear dynamic analysis program is developed for the proposed system, which greatly improves the computing efficiency of the parametric analysis. The benchmark model utilized in the numerical analysis represents a typical office building with height ranging from 5 to 30 stories and natural periods ranging from around 0.8s to 5.0s. The stiff spine shows effect in achieving a more uniformed deformation distribution even for structures as tall as 30 stories. To ensure the effectiveness of the spine frame, the minimum requirement of spine-to-frame stiffness ratio is established for buildings with different heights. It is also found that increasing damper amount is not always effective in reducing seismic response of the spine frame structures. The optimal damper-to-frame stiffness ratio is clarified for the typical range of spine-to-frame stiffness.

A concept of segmented spine frames (Sgt) is proposed for an easier application of spine

frames in tall buildings by avoiding immense demand on energy-dissipating amount of dampers or strength of spine frames. In a Sgt structure, there are more than one spine frames arranged in series along the height of the structure. The segmented spines are pin-connected with each other and dampers are equipped at the bottom of each spine frame. Optimal number of segments and optimal location of each segment has been investigated. The 20- or 30-story buildings utilizing the two-segment spine frames (Sgt2) exhibit similar peak story drift and largely reduced strength demand on spines compared to the continuous single spine frame (Cnt) structure, as long as the segment height is 50%-75% of the structural height. Optimal value of the ‘upper damper’-to-‘bottom damper’ stiffness ratio is also established for the Sgt2 structures. Spine frame structures adopting more than two segments does not exhibit advantageous seismic performance compared to the Sgt2 structures for buildings lower than 30 stories. Therefore, two segments configuration is recommended for tall buildings when damper amount at one story is limited.

A simple seismic evaluation and design procedure based on equivalent linearization technique and response spectrum analysis is developed for the proposed spine frame system, based on the further simplified single-degree-of-freedom (SDOF) models. Two sets of processes are developed respectively for structures whose seismic response is first-mode dominant, and structures whose higher-modes effect cannot be ignored. Distinct limitation for applying the design procedure is established in terms of structural vibration characteristics. Boundary of key structural index such as the damper-to-frame stiffness ratio and spine-to-frame stiffness ratio is determined based on a desired accuracy of the evaluated results.

Appendix A

Detailed Information of Prototype Building



Fig A.1 MCES Building

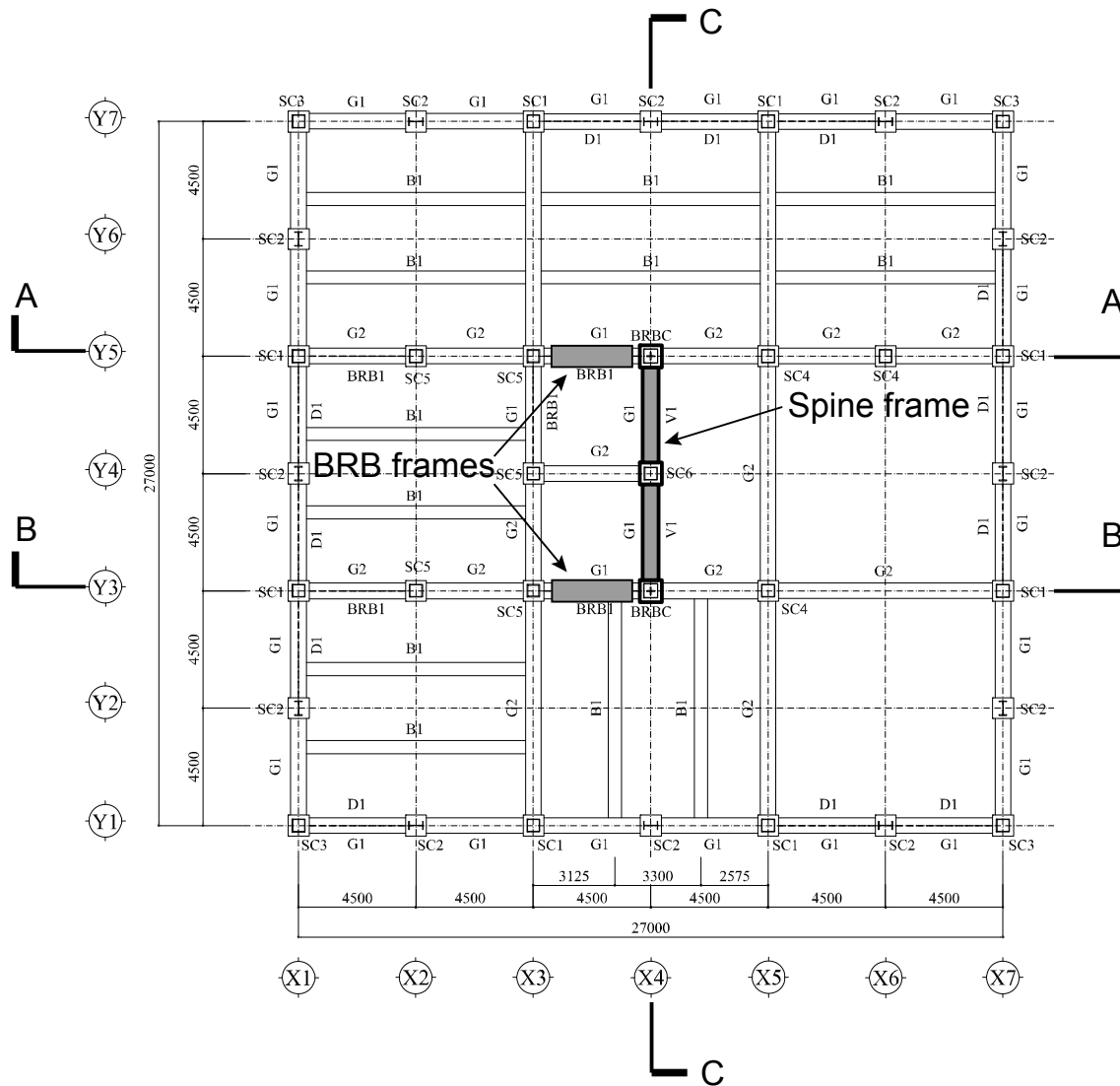
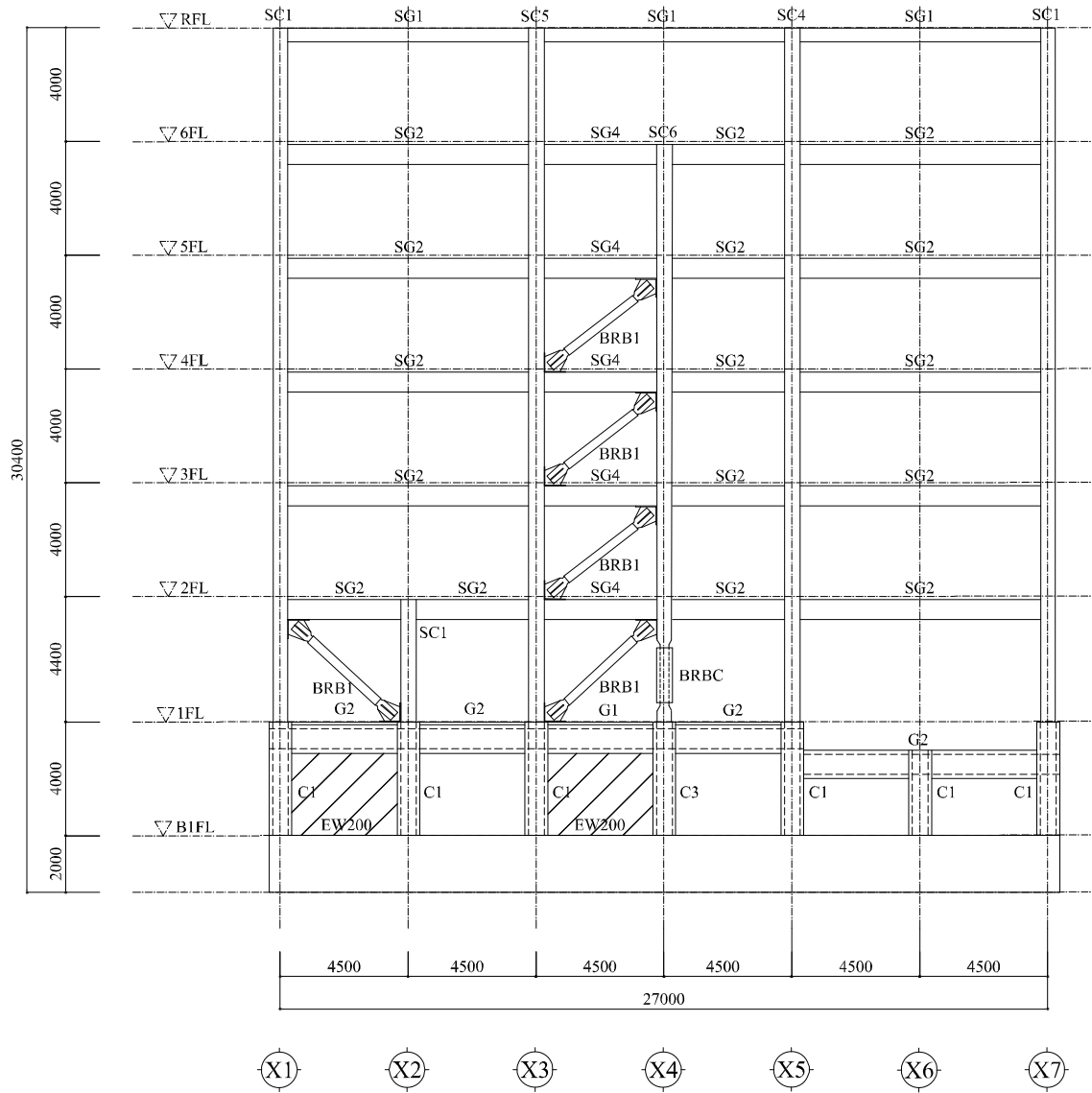
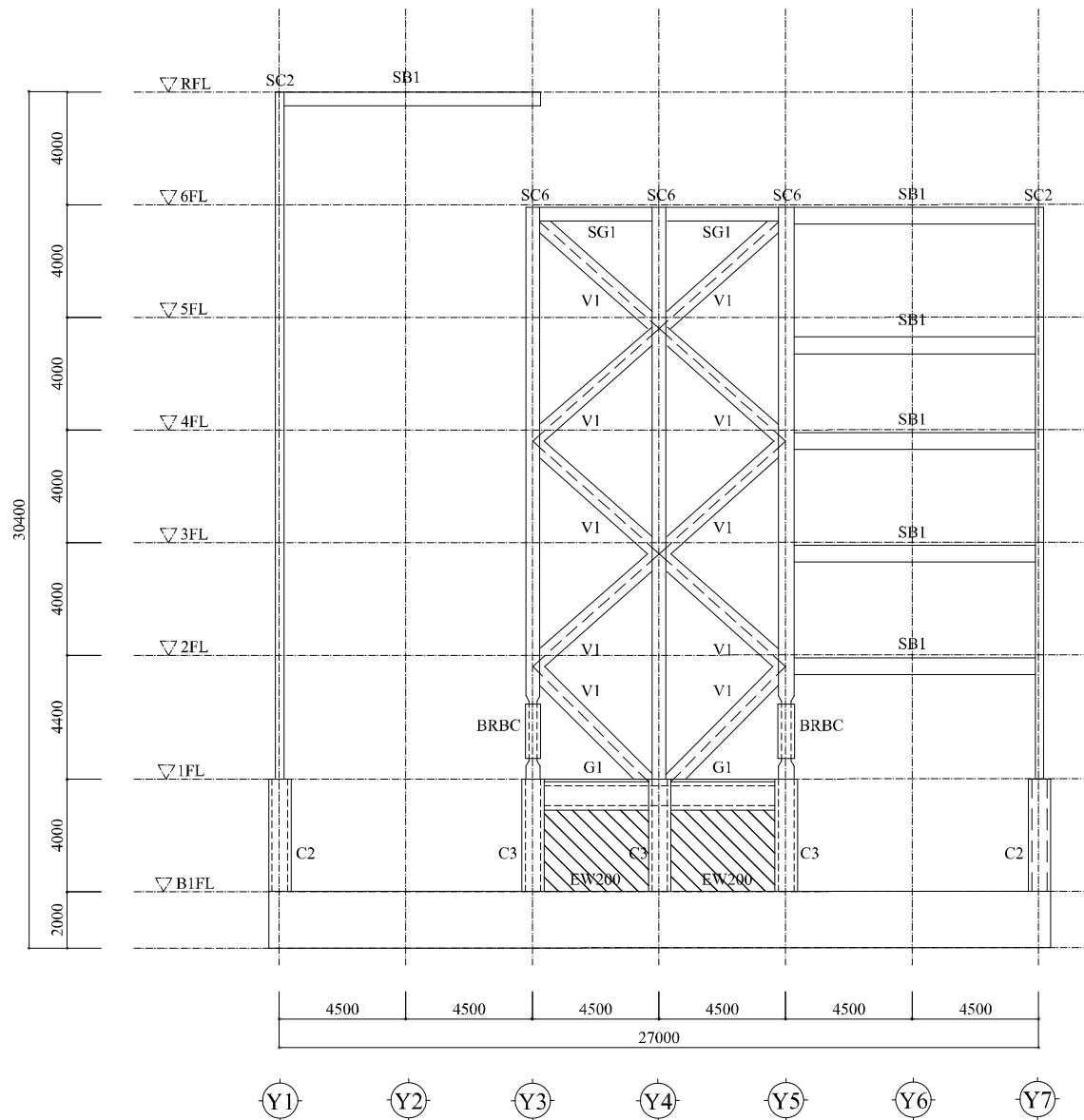


Fig A.2 Structural plan



(a) BRB frame axis (A-A , B-B cross section in Fig A.2)



(b) NL frame axis (C-C cross section in Fig A.2)

Fig A.3 Cross-sectional views

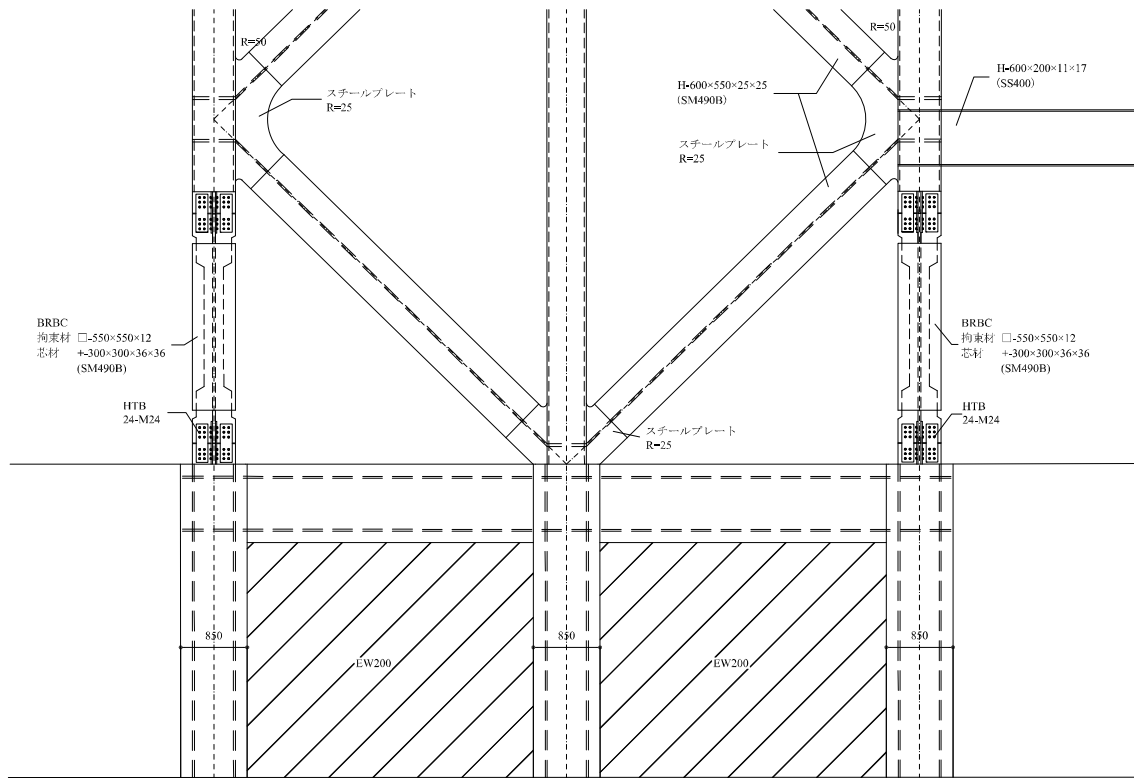


Fig A.4 Details of the spine frame bottom

Table A.1 Column lists

	SC1	SC2	SC3	SC4	SC5	SC6
鋼材種	BCP325T	SM490C	BCP325T	BCP325T	BCP325T	SM490C
RF						
6F	□-500×500×19	H-500×300×16×25	□-500×500×16			
5F	□-500×500×19	H-500×300×16×25	□-500×500×16	□-550×550×22		□-550×550×25
4F	□-500×500×19	H-500×300×16×25	□-500×500×19	□-550×550×22	□-550×550×28	□-550×550×25
3F	□-500×500×22	H-500×300×16×25	□-500×500×22	□-550×550×25	□-550×550×28	□-550×550×25
2F	□-500×500×22	H-500×300×16×25	□-500×500×22	□-550×550×25	□-550×550×28	□-550×550×25
1F	□-500×500×22	H-500×300×16×25	□-500×500×22	□-550×550×25	□-550×550×28	□-550×550×25

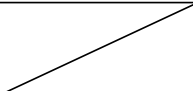
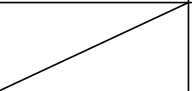
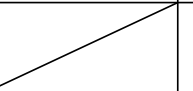
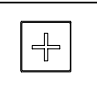
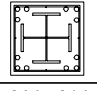
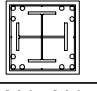
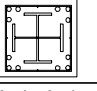

		C1	C2	C3	BRBC
1F	断面図				
	鋼材種				SM490B
	B×D				550×550
	鉄骨				拘束材 □-550×550×12 芯材 + -400×400×36×36
B1F	断面図				
	B×D	800×800	800×800	850×850	
	鉄骨	■-550×300×14×25	■-550×300×14×25	■-550×300×14×25	
	主筋	12-D25	12-D25	12-D25	
	フープ筋	D13@100	D13@100	D13@100	
	補助筋	4-D13	4-D13	4-D13	

Table A.2 Beam lists

	SG1	SG2	SG3	SG4	SB1
鋼材種	SN400B	SN400B	SN400B	SN400B	SS400
RF	H-500×300×12×19	H-700×300×13×24	H-700×300×13×24	H-700×300×13×24	H-600×200×11×17
6F	H-500×300×12×19	H-700×300×13×24	H-700×300×13×24	H-700×300×13×24	H-600×200×11×17
5F	H-500×300×12×19	H-700×300×13×24	H-700×300×13×24	H-700×300×13×24	H-600×200×11×17
4F	H-500×300×12×19	H-700×300×13×24	H-700×300×13×24	H-700×300×13×24	H-600×200×11×17
3F	H-500×300×12×19	H-700×300×13×24	H-700×300×13×24	H-700×300×13×24	H-600×200×11×17
2F	H-500×300×12×19	H-700×300×13×24	H-700×300×13×24	H-700×300×13×24	H-600×200×11×17

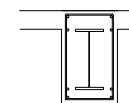
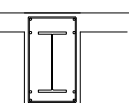
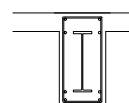
		G1	G2	B1
1F	断面図			
	B×D	600×1000	600×1000	500×1000
	鉄骨	H-700×300×13×24	H-700×300×13×24	H-700×200×14×22
	主筋	8-D25	8-D25	8-D25
	フープ筋	D13@150	D13@150	D13@150

Table A.3 Braces in the spine frame and BRBs in the BRB frames










	V1	BRB1
鋼材種	SM490B	LY225
RF		
6F		
5F		
	H -550×550×19×25	
4F		
	H -550×550×19×25	拘束材 □-300×300×6 芯材 +-200×200×36×36
3F		
	H -550×550×19×25	拘束材 □-300×300×6 芯材 +-250×250×36×36
2F		
	H -600×550×25×25	拘束材 □-400×400×9 芯材 +-300×300×36×36
1F		
	H -600×550×25×25	拘束材 □-400×400×9 芯材 +-250×250×36×36

Table A.4 Material strength^{*1}

Material	Tensile yielding stress (MPa) (characteristic value F)
SN400B, SS400	235
SN490B	325
BCP325	325
BCP235	235

^{*1} Yielding stress of the steel materials in Table A.4 are multiplied by 1.1 in the static and dynamic analysis according to Japan design code, in order to get close to the actual strength of the materials based on the statistical data.

Appendix B

OpenSees Model Scripts of Spine Frame Structure

20-story Cnt / Sgt2 model

```
# unit: mm ton s N
wipe all
model BasicBuilder -ndm 2 -ndf 3

set fileName BRCat10/BRCat10-1.0-0.5-bcj; # recorder folder
file mkdir $fileName
set segFl 9 # INPUT PARAMETER, segment floor, (Cnt model: segFl=19)
set brcFt1 1.0 # INPUT PARAMETER, BRC1, Kd1/Kf
set brcFt2 0.5 # INPUT PARAMETER, BRC2, Ld2/Kf
set period "T10-1.0-0.5.txt" # recorder file for eigenvalue analysis

set outFile BCJL2Level2.txt; # input file
set IDloadTag 100
set GMdirection 1
set dt 0.01; # input time interval
set GMfatt 10.0
set DtAnalysis 0.01; # analysis time interval
set Nsteps 12000
set dph 0.02 # intrinsic damping ratio
set spax 14
set nb1 [expr 11+$segFl]
set nb2 [expr 10+$segFl]

# Material
# BRC material
set matBRC1 8
    uniaxialMaterial Steel01 $matBRC1 [expr $brcFt1*1.3316e11] [expr $brcFt1*1.3316e14]
0.000001
set matBRC2 9
    uniaxialMaterial Steel01 $matBRC2 [expr $brcFt2*1.3316e11] [expr $brcFt2*1.3316e14] 0.000001
# Material of braces in the spine frame
    uniaxialMaterial Elastic 2 205000. 0.
```

```

set floorOffsets {4000. 4000. 4000. 4000. 4000. 4000. 4000. 4000. 4000. 4000. 4000. 4000. 4000. 4000. 4000. 4000. 4000. 4000. 4000. 4000.}
set colOffsets {4500. 4500. 4500. 9000. 9000. 4500. 4500. 4500. 5000. 4500. 4500. 4500. 4500. 4500. 4500. 4500. 4500. 4500. 4500. 4500.}
set colSecNo {3 2 1 2 5 2 1 2 3 4 0 0 0 4 2 4 0 0 0 4 4 0 0 0 4 2 4 0 0 0 4}
set massFloor { 14.12      20.94    21.69    20.94    148.91      20.94    21.69
                20.94    14.12    22.31    28.76    28.76    28.76    31.68    15.52    31.68
                28.76    28.76    28.76    22.31    22.31    28.76    28.76    28.76    31.68
                15.52    31.68    28.76    28.76    28.76    22.31}
set massRoof { 16.69      27.90    28.22    27.90    163.95    27.90    28.22    27.90
               16.69    28.47    45.09    45.09    45.09    46.31    23.13    46.31    45.09
               45.09    45.09    28.47    28.47    45.09    45.09    45.09    46.31    23.13
               46.31    45.09    45.09    45.09    28.47}
set beamSection1 7; set beamSection2 8; set braceSec 6; set BRCSection 101; set RigidSection 202
set beamGeomTrf 1; set colGeomTrf 2; set braceGeomTrf 3; set numIntgrPts 5
set Izcol {3.5018e9 3.5018e9 3.5018e9 3.5018e9 3.5018e9 3.5018e9 3.5018e9 3.5018e9 2.8362e9
2.8362e9 2.8362e9 2.8362e9 2.8362e9 2.8362e9 2.8362e9 2.8362e9 2.4869e9 2.4869e9 2.4869e9
2.4869e9
                2.4475e9 2.4475e9 2.4475e9 2.4475e9 2.4475e9 2.4475e9 2.2422e9 2.2422e9
2.2422e9 2.2422e9 2.2422e9 2.2422e9 2.2422e9 2.2422e9 2.0327e9 2.0327e9 2.0327e9 2.0327e9
2.0327e9 2.0327e9
                3.1745e9      3.1745e9 3.1745e9 3.1745e9 2.8362e9 2.8362e9 2.8362e9
2.8362e9 2.8362e9 2.8362e9 2.8362e9 2.8362e9 2.4869e9 2.4869e9 2.4869e9 2.4869e9 2.4869e9
2.4869e9 2.4869e9 2.4869e9
                5.0488e9 5.0488e9 5.0488e9 5.0488e9 5.0488e9 5.0488e9 5.0488e9 5.0488e9
5.0488e9 5.0488e9 4.7777e9 4.7777e9 4.7777e9 4.7777e9 4.7777e9 4.7777e9 4.7777e9
4.5011e9 4.5011e9
                2.4172e9 2.4172e9 2.4172e9 2.4172e9 2.4172e9 2.4172e9 2.4172e9 2.4172e9
2.4172e9 2.4172e9 2.4172e9 2.4172e9 2.4172e9 2.4172e9 2.4172e9 2.4172e9 2.4172e9
2.4172e9 2.4172e9}
set Acol {64064. 64064. 64064. 64064. 64064. 64064. 64064. 64064. 64064. 50864. 50864. 50864. 50864. 50864.
50864. 50864. 50864. 44156. 44156. 44156. 44156.
                31904. 31904. 31904. 31904. 31904. 31904. 29600. 29600. 29600. 29600. 29600.
29600. 29600. 29600. 27296. 27296. 27296. 27296. 27296. 27296.
                57500. 57500. 57500. 57500. 50864. 50864. 50864. 50864. 50864. 50864. 50864.}

```

```

50864. 44156. 44156. 44156. 44156. 44156. 44156. 44156. 44156.
    79104. 79104. 79104. 79104. 79104. 79104. 79104. 79104. 79104. 79104. 79104. 74400.
74400. 74400. 74400. 74400. 74400. 74400. 74400. 69664. 69664.
    52500. 52500. 52500. 52500. 52500. 52500. 52500. 52500. 52500. 52500. 52500. 52500.
52500. 52500. 52500. 52500. 52500. 52500. 52500. 52500. 52500.}
set Izbm1 {2.4865e9 2.4865e9 2.4865e9 2.4865e9 2.4865e9 2.4865e9 2.3709e9 2.3709e9 2.3709e9
2.2539e9 2.2539e9 2.2539e9 2.0755e9 2.0755e9 2.0755e9 2.0755e9 1.8939e9 1.8939e9 1.8939e9
1.8939e9}
set Abm1 {29376. 29376. 29376. 29376. 29376. 29376. 28240. 28240. 28240. 27104. 27104. 27104.
25400. 25400. 25400. 25400. 23696. 23696. 23696. 23696.}
set Izbm2 [expr 3.8442e9]
set Abm2 31150.
set A5 0.957e7    # INPUT PARAMETER, herein Ksf=0.3
set E5 3.35e4
set I5 0.604e14   # INPUT PARAMETER, herein Ksf=0.3
set G5 1.396e4
set E [expr 2.05e5]
set A [expr 1.0e10]
# calculat properties
set numFloor [expr [llength $floorOffsets]+10]
set numCline [expr [llength $colOffsets]+10]

# set up node and fix the nodes in the first floor
for {set floor 10; set floorLoc 0} {$floor<=$numFloor} {incr floor 1} {
    if {$floor==$numFloor} {
        set mass $massRoof
    } else {
        set mass $massFloor
    }
    for {set colLine 10; set colLoc 0;} {$colLine<=$numCline} {incr colLine 1} {
        node $colLine$floor $colLoc $floorLoc -mass [lindex $mass [expr $colLine-10]] 0.
0.
        if {$floor==10} { fix $colLine$floor 1 1 1 }
        if {$colLine < $numCline} {set colLoc [expr $colLoc+[lindex $colOffsets [expr
$colLine-10]]]}
    }
}

```

```

        if {$floor < $numFloor} {set floorLoc [expr $floorLoc+[lindex $floorOffsets [expr
$floor-10]]]}
    }

# additional nodes for BRCs
node 14101 22500. 0.
node 14201 22500. [expr $segFI*4000.]
fix 14101 1 1 0
puts "Node built!"

# set multi-point constraint
set colLine1 14
for {set colLine 10} {$colLine<=$numCline} {incr colLine 1} {
    set colSec [lindex $colSecNo [expr $colLine-10]]
    if {[expr $colSec!=0&&$colSec!=5]} {
        for {set floor 11} {$floor<=$numFloor} {incr floor 1} {
            equalDOF $colLine1$floor $colLine$floor 1
        }
    }
}

equalDOF $spax$nb2 14201 1 2
puts "equalDOF built!"

# set geometric transformation
geomTransf Linear 1 ;    # Beams
geomTransf Linear 2 ;    # Columns
geomTransf Linear 3 ;    # Braces
puts "Geometric transformation built!"

# set up columns
element ElasticTimoshenkoBeam 141011411 14101 1411 $E5 $G5 $A5 $I5 $A5 $colGeomTrf
element ElasticTimoshenkoBeam 142011421 14201 $spax$nb1 $E5 $G5 $A5 $I5 $A5 $colGeomTrf
element twoNodeLink 141014101 1410 14101 -mat $matBRC1 -dir 3 -doRayleigh
element twoNodeLink 142014201 $spax$nb2 14201 -mat $matBRC2 -dir 3 -doRayleigh
for {set colLine 10} {$colLine<=$numCline} {incr colLine 1} {
    set colSec [lindex $colSecNo [expr $colLine-10]]

```

```

for {set floor1 10; set floor2 11} {$floor2<=$numFloor} {incr floor1 1; incr floor2 1} {
    if {[expr $floor1==10||$floor1==$nb2]&&[expr $colLine==14]} {
        continue
    } elseif {[expr
$colLine==20||$colLine==21||$colLine==22||$colLine==26||$colLine==27||$colLine==28||$colLine==31|
|$colLine==32||$colLine==33||$colLine==37||$colLine==38||$colLine==39]} {
        continue
    } else {
        if {[expr $floor1!=10&&$floor1!=$nb2]&&[expr $colSec==5]} {
            element ElasticTimoshenkoBeam
$colLine$floor1$colLine$floor2 $colLine$floor1 $colLine$floor2 $E5 $G5 $A5 $I5 $A5 $colGeomTrf
        } else {
            #element elasticBeamColumn $colLine$floor1$colLine$floor2
$colLine$floor1 $colLine$floor2 $A $E [lindex $Izcol [expr ($colSec-1)*20+$floor1-10]] $colGeomTrf
            element elasticBeamColumn $colLine$floor1$colLine$floor2
$colLine$floor1 $colLine$floor2 [lindex $Acol [expr ($colSec-1)*20+$floor1-10]] $E [lindex $Izcol
[expr ($colSec-1)*20+$floor1-10]] $colGeomTrf
        }
    }
}

}

puts "Column built!"

# set up beams
for {set colLine1 10; set colLine2 11} {$colLine2<=$numCline} {incr colLine1 1; incr colLine2 1} {
    for {set floor 11} {$floor<=$numFloor} {incr floor 1} {
        if {$colLine1==18||$colLine1==29||$colLine1==13||$colLine1==14} {
            continue
        } elseif
{ $colLine1==19||$colLine1==20||$colLine1==21||$colLine1==22||$colLine1==25||$colLine1==26||$colL
ine1==27||$colLine1==28||$colLine1==30||$colLine1==31||$colLine1==32||$colLine1==33||$colLine1==
36||$colLine1==37||$colLine1==38||$colLine1==39} {
            #element elasticBeamColumn $colLine1$floor$colLine2$floor
$colLine1$floor $colLine2$floor $A $E $Izbm2 $beamGeomTrf
            element elasticBeamColumn $colLine1$floor$colLine2$floor
$colLine1$floor $colLine2$floor $Abm2 $E $Izbm2 $beamGeomTrf

```

```

        } else {
            #element elasticBeamColumn $colLine1$floor$colLine2$floor
            $colLine1$floor $colLine2$floor $A $E [lindex $Izbm1 [expr $floor-1]] $beamGeomTrf
            element elasticBeamColumn $colLine1$floor$colLine2$floor
            $colLine1$floor $colLine2$floor [lindex $Abm1 [expr $floor-1]] $E [lindex $Izbm1 [expr $floor-1]]
            $beamGeomTrf
        }
    }
}

puts "Beam built!"

timeSeries Linear 1 -factor 1
initialize

# # set graphic display-----
# set dAmp 30
# recorder display Pushover2D 10 10 850 450 -wipe
# prp 72500 40100 1;                                # projection reference point (prp); defines
the center of projection (viewer eye)
# vup 0 1 0;                                # view-up vector (vup)
# vpn 0 0 1;                                # view-plane normal (vpn)
# viewWindow -80000 80000 -80000 80000;            # coordiantes of the window relative to
prp
# display 1 2 $dAmp;
# puts "display set!"
set nodeMF2 111; set nodeMF3 112; set nodeMF4 113; set nodeMF5 114; set nodeMF6 115; set
nodeMF7 116; set nodeMF8 117; set nodeMF9 118; set nodeMF10 119; set nodeMF11 120;
set nodeMF12 121; set nodeMF13 122; set nodeMF14 123; set nodeMF15 124; set nodeMF16 125; set
nodeMF17 126; set nodeMF18 127; set nodeMF19 128; set nodeMF20 129; set nodeMF21 130;
set nodeSF 32;
set colF1 2010; set colF2 2011; set colF3 2012; set colF4 2013; set colF5 2014; set colF6 2015; set colF7
2016; set colF8 2017; set colF9 2018; set colF10 2019;
set colF11 2020; set colF12 2021; set colF13 2022; set colF14 2023; set colF15 2024; set colF16 2025;
set colF17 2026; set colF18 2027; set colF19 2028; set colF20 2029;
set beamF1 3011; set beamF2 3012; set beamF3 3013; set beamF4 3014; set beamF5 3015; set beamF6
3016; set beamF7 3017; set beamF8 3018; set beamF9 3019; set beamF10 3020;

```

```

set beamF11 3021; set beamF12 3022; set beamF13 3023; set beamF14 3024; set beamF15 3025; set
beamF16 3026; set beamF17 3027; set beamF18 3028; set beamF19 3029; set beamF20 3030;
set SpBrcF1 4010; set SpBrcF2 4011; set SpBrcF3 4012; set SpBrcF4 4013; set SpBrcF5 4014; set
SpBrcF6 4015; set SpBrcF7 4016; set SpBrcF8 4017; set SpBrcF9 4018; set SpBrcF10 4019;
set SpBrcF11 4020; set SpBrcF12 4021; set SpBrcF13 4022; set SpBrcF14 4023; set SpBrcF15 4024; set
SpBrcF16 4025; set SpBrcF17 4026; set SpBrcF18 4027; set SpBrcF19 4028; set SpBrcF20 4029;
set SpColF1 5010; set SpColF2 5011; set SpColF3 5012; set SpColF4 5013; set SpColF5 5014; set
SpColF6 5015; set SpColF7 5016; set SpColF8 5017; set SpColF9 5018; set SpColF10 5019;
set SpColF11 5020; set SpColF12 5021; set SpColF13 5022; set SpColF14 5023; set SpColF15 5024; set
SpColF16 5025; set SpColF17 5026; set SpColF18 5027; set SpColF19 5028; set SpColF20 5029;
#set spine frame region
region $SpColF1 -ele 141011411
set SpCol 50
for {set Floor1 11; set Floor2 12} {$Floor2<=$numFloor} {incr Floor1 1; incr Floor2 1} {
    if {$Floor1!=[expr 10+$segFl]} {
        region $SpCol$Floor1 -ele $spax$Floor1$spax$Floor2
    } else {
        region $SpCol$Floor1 -ele 142011421
    }
}

#set column region
region $colF1 -ele 10101011 11101111 12101211 13101311 15101511 16101611 17101711 18101811
19101911 23102311 24102411 25102511 29102911 30103011 34103411 35103511 36103611 40104011
region $colF2 -ele 10111012 11111112 12111212 13111312 15111512 16111612 17111712 18111812
19111912 23112312 24112412 25112512 29112912 30113012 34113412 35113512 36113612 40114012
region $colF3 -ele 10121013 11121113 12121213 13121313 15121513 16121613 17121713 18121813
19121913 23122313 24122413 25122513 29122913 30123013 34123413 35123513 36123613 40124013
region $colF4 -ele 10131014 11131114 12131214 13131314 15131514 16131614 17131714 18131814
19131914 23132314 24132414 25132514 29132914 30133014 34133414 35133514 36133614 40134014
region $colF5 -ele 10141015 11141115 12141215 13141315 15141515 16141615 17141715 18141815
19141915 23142315 24142415 25142515 29142915 30143015 34143415 35143515 36143615 40144015
region $colF6 -ele 10151016 11151116 12151216 13151316 15151516 16151616 17151716 18151816
19151916 23152316 24152416 25152516 29152916 30153016 34153416 35153516 36153616 40154016
region $colF7 -ele 10161017 11161117 12161217 13161317 15161517 16161617 17161717 18161817
19161917 23162317 24162417 25162517 29162917 30163017 34163417 35163517 36163617 40164017

```



```
region $colF8 -ele 10171018 11171118 12171218 13171318 15171518 16171618 17171718 18171818
19171918 23172318 24172418 25172518 29172918 30173018 34173418 35173518 36173618 40174018
region $colF9 -ele 10181019 11181119 12181219 13181319 15181519 16181619 17181719 18181819
19181919 23182319 24182419 25182519 29182919 30183019 34183419 35183519 36183619 40184019
region $colF10 -ele 10191020 11191120 12191220 13191320 15191520 16191620 17191720 18191820
19191920 23192320 24192420 25192520 29192920 30193020 34193420 35193520 36193620 40194020
region $colF11 -ele 10201021 11201121 12201221 13201321 15201521 16201621 17201721 18201821
19201921 23202321 24202421 25202521 29202921 30203021 34203421 35203521 36203621 40204021
region $colF12 -ele 10211022 11211122 12211222 13211322 15211522 16211622 17211722 18211822
19211922 23212322 24212422 25212522 29212922 30213022 34213422 35213522 36213622 40214022
region $colF13 -ele 10221023 11221123 12221223 13221323 15221523 16221623 17221723 18221823
19221923 23222323 24222423 25222523 29222923 30223023 34223423 35223523 36223623 40224023
region $colF14 -ele 10231024 11231124 12231224 13231324 15231524 16231624 17231724 18231824
19231924 23232324 24232424 25232524 29232924 30233024 34233424 35233524 36233624 40234024
region $colF15 -ele 10241025 11241125 12241225 13241325 15241525 16241625 17241725 18241825
19241925 23242325 24242425 25242525 29242925 30243025 34243425 35243525 36243625 40244025
region $colF16 -ele 10251026 11251126 12251226 13251326 15251526 16251626 17251726 18251826
19251926 23252326 24252426 25252526 29252926 30253026 34253426 35253526 36253626 40254026
region $colF17 -ele 10261027 11261127 12261227 13261327 15261527 16261627 17261727 18261827
19261927 23262327 24262427 25262527 29262927 30263027 34263427 35263527 36263627 40264027
region $colF18 -ele 10271028 11271128 12271228 13271328 15271528 16271628 17271728 18271828
19271928 23272328 24272428 25272528 29272928 30273028 34273428 35273528 36273628 40274028
region $colF19 -ele 10281029 11281129 12281229 13281329 15281529 16281629 17281729 18281829
19281929 23282329 24282429 25282529 29282929 30283029 34283429 35283529 36283629 40284029
region $colF20 -ele 10291030 11291130 12291230 13291330 15291530 16291630 17291730 18291830
19291930 23292330 24292430 25292530 29292930 30293030 34293430 35293530 36293630 40294030
#set node of main frame region
region $nodeMF2 -node 1011 1111 1211 1311 1511 1611 1711 1811 1911 2311 2411 2511 2911 3011
3411 3511 3611 4011
region $nodeMF3 -node 1012 1112 1212 1312 1512 1612 1712 1812 1912 2312 2412 2512 2912 3012
3412 3512 3612 4012
region $nodeMF4 -node 1013 1113 1213 1313 1513 1613 1713 1813 1913 2313 2413 2513 2913 3013
3413 3513 3613 4013
region $nodeMF5 -node 1014 1114 1214 1314 1514 1614 1714 1814 1914 2314 2414 2514 2914 3014
3414 3514 3614 4014
region $nodeMF6 -node 1015 1115 1215 1315 1515 1615 1715 1815 1915 2315 2415 2515 2915 3015
```

```
3415 3515 3615 4015
region $nodeMF7 -node 1016 1116 1216 1316 1516 1616 1716 1816 1916 2316 2416 2516 2916 3016
3416 3516 3616 4016
region $nodeMF8 -node 1017 1117 1217 1317 1517 1617 1717 1817 1917 2317 2417 2517 2917 3017
3417 3517 3617 4017
region $nodeMF9 -node 1018 1118 1218 1318 1518 1618 1718 1818 1918 2318 2418 2518 2918 3018
3418 3518 3618 4018
region $nodeMF10 -node 1019 1119 1219 1319 1519 1619 1719 1819 1919 2319 2419 2519 2919 3019
3419 3519 3619 4019
region $nodeMF11 -node 1020 1120 1220 1320 1520 1620 1720 1820 1920 2320 2420 2520 2920 3020
3420 3520 3620 4020
region $nodeMF12 -node 1021 1121 1221 1321 1521 1621 1721 1821 1921 2321 2421 2521 2921 3021
3421 3521 3621 4021
region $nodeMF13 -node 1022 1122 1222 1322 1522 1622 1722 1822 1922 2322 2422 2522 2922 3022
3422 3522 3622 4022
region $nodeMF14 -node 1023 1123 1223 1323 1523 1623 1723 1823 1923 2323 2423 2523 2923 3023
3423 3523 3623 4023
region $nodeMF15 -node 1024 1124 1224 1324 1524 1624 1724 1824 1924 2324 2424 2524 2924 3024
3424 3524 3624 4024
region $nodeMF16 -node 1025 1125 1225 1325 1525 1625 1725 1825 1925 2325 2425 2525 2925 3025
3425 3525 3625 4025
region $nodeMF17 -node 1026 1126 1226 1326 1526 1626 1726 1826 1926 2326 2426 2526 2926 3026
3426 3526 3626 4026
region $nodeMF18 -node 1027 1127 1227 1327 1527 1627 1727 1827 1927 2327 2427 2527 2927 3027
3427 3527 3627 4027
region $nodeMF19 -node 1028 1128 1228 1328 1528 1628 1728 1828 1928 2328 2428 2528 2928 3028
3428 3528 3628 4028
region $nodeMF20 -node 1029 1129 1229 1329 1529 1629 1729 1829 1929 2329 2429 2529 2929 3029
3429 3529 3629 4029
region $nodeMF21 -node 1030 1130 1230 1330 1530 1630 1730 1830 1930 2330 2430 2530 2930 3030
3430 3530 3630 4030
#set node of spine frame region
region $nodeSF -node 14101 1411 1412 1413 1414 1415 1416 1417 1418 1419 1420 14201 1421 1422
1423 1424 1425 1426 1427 1428 1429 1430

recorder Drift -file $fileName/Drift.out -time -iNode 1110 1111 1112 1113 1114 1115 1116 1117 1118
```

```

1119 1120 1121 1122 1123 1124 1125 1126 1127 1128 1129 -jNode 1111 1112 1113 1114 1115 1116 1117
1118 1119 1120 1121 1122 1123 1124 1125 1126 1127 1128 1129 1130 -dof 1 -perpDirn 2
recorder Node -file $fileName/FloorDisp_tf_bcj.out -time -node 1011 1012 1013 1014 1015 1016 1017
1018 1019 1020 1021 1022 1023 1024 1025 1026 1027 1028 1029 1030 -dof 1 disp
recorder Node -file $fileName/FloorAcc_tf_bcj.out -time -node 1011 1012 1013 1014 1015 1016 1017
1018 1019 1020 1021 1022 1023 1024 1025 1026 1027 1028 1029 1030 -dof 1 accel
recorder Node -file $fileName/FloorVel_tf_bcj.out -time -node 1011 1012 1013 1014 1015 1016 1017
1018 1019 1020 1021 1022 1023 1024 1025 1026 1027 1028 1029 1030 -dof 1 vel

```

```

recorder Node -file $fileName/RotationMF2.out -time -region $nodeMF2 -dof 3 disp
recorder Node -file $fileName/RotationMF3.out -time -region $nodeMF3 -dof 3 disp
recorder Node -file $fileName/RotationMF4.out -time -region $nodeMF4 -dof 3 disp
recorder Node -file $fileName/RotationMF5.out -time -region $nodeMF5 -dof 3 disp
recorder Node -file $fileName/RotationMF6.out -time -region $nodeMF6 -dof 3 disp
recorder Node -file $fileName/RotationMF7.out -time -region $nodeMF7 -dof 3 disp
recorder Node -file $fileName/RotationMF8.out -time -region $nodeMF8 -dof 3 disp
recorder Node -file $fileName/RotationMF9.out -time -region $nodeMF9 -dof 3 disp
recorder Node -file $fileName/RotationMF10.out -time -region $nodeMF10 -dof 3 disp
recorder Node -file $fileName/RotationMF11.out -time -region $nodeMF11 -dof 3 disp
recorder Node -file $fileName/RotationMF12.out -time -region $nodeMF12 -dof 3 disp
recorder Node -file $fileName/RotationMF13.out -time -region $nodeMF13 -dof 3 disp
recorder Node -file $fileName/RotationMF14.out -time -region $nodeMF14 -dof 3 disp
recorder Node -file $fileName/RotationMF15.out -time -region $nodeMF15 -dof 3 disp
recorder Node -file $fileName/RotationMF16.out -time -region $nodeMF16 -dof 3 disp
recorder Node -file $fileName/RotationMF17.out -time -region $nodeMF17 -dof 3 disp
recorder Node -file $fileName/RotationMF18.out -time -region $nodeMF18 -dof 3 disp
recorder Node -file $fileName/RotationMF19.out -time -region $nodeMF19 -dof 3 disp
recorder Node -file $fileName/RotationMF20.out -time -region $nodeMF20 -dof 3 disp
recorder Node -file $fileName/RotationMF21.out -time -region $nodeMF21 -dof 3 disp

```

```

recorder Node -file $fileName/RotationSF.out -time -region $nodeSF -dof 3 disp
recorder Node -file $fileName/VDispSF.out -time -region $nodeSF -dof 2 disp

```

```

recorder Element -file $fileName/glbForceColF1.out -time -region $colF1 globalForce
recorder Element -file $fileName/glbForceColF2.out -time -region $colF2 globalForce
recorder Element -file $fileName/glbForceColF3.out -time -region $colF3 globalForce

```

```
recorder Element -file $fileName/glbForceColF4.out -time -region $colF4 globalForce
recorder Element -file $fileName/glbForceColF5.out -time -region $colF5 globalForce
recorder Element -file $fileName/glbForceColF6.out -time -region $colF6 globalForce
recorder Element -file $fileName/glbForceColF7.out -time -region $colF7 globalForce
recorder Element -file $fileName/glbForceColF8.out -time -region $colF8 globalForce
recorder Element -file $fileName/glbForceColF9.out -time -region $colF9 globalForce
recorder Element -file $fileName/glbForceColF10.out -time -region $colF10 globalForce
recorder Element -file $fileName/glbForceColF11.out -time -region $colF11 globalForce
recorder Element -file $fileName/glbForceColF12.out -time -region $colF12 globalForce
recorder Element -file $fileName/glbForceColF13.out -time -region $colF13 globalForce
recorder Element -file $fileName/glbForceColF14.out -time -region $colF14 globalForce
recorder Element -file $fileName/glbForceColF15.out -time -region $colF15 globalForce
recorder Element -file $fileName/glbForceColF16.out -time -region $colF16 globalForce
recorder Element -file $fileName/glbForceColF17.out -time -region $colF17 globalForce
recorder Element -file $fileName/glbForceColF18.out -time -region $colF18 globalForce
recorder Element -file $fileName/glbForceColF19.out -time -region $colF19 globalForce
recorder Element -file $fileName/glbForceColF20.out -time -region $colF20 globalForce
```

```
recorder Element -file $fileName/glbForceSpColF1.out -time -region $SpColF1 globalForce
recorder Element -file $fileName/glbForceSpColF2.out -time -region $SpColF2 globalForce
recorder Element -file $fileName/glbForceSpColF3.out -time -region $SpColF3 globalForce
recorder Element -file $fileName/glbForceSpColF4.out -time -region $SpColF4 globalForce
recorder Element -file $fileName/glbForceSpColF5.out -time -region $SpColF5 globalForce
recorder Element -file $fileName/glbForceSpColF6.out -time -region $SpColF6 globalForce
recorder Element -file $fileName/glbForceSpColF7.out -time -region $SpColF7 globalForce
recorder Element -file $fileName/glbForceSpColF8.out -time -region $SpColF8 globalForce
recorder Element -file $fileName/glbForceSpColF9.out -time -region $SpColF9 globalForce
recorder Element -file $fileName/glbForceSpColF10.out -time -region $SpColF10 globalForce
recorder Element -file $fileName/glbForceSpColF11.out -time -region $SpColF11 globalForce
recorder Element -file $fileName/glbForceSpColF12.out -time -region $SpColF12 globalForce
recorder Element -file $fileName/glbForceSpColF13.out -time -region $SpColF13 globalForce
recorder Element -file $fileName/glbForceSpColF14.out -time -region $SpColF14 globalForce

recorder Element -file $fileName/glbForceSpColF15.out -time -region $SpColF15 globalForce

recorder Element -file $fileName/glbForceSpColF16.out -time -region $SpColF16 globalForce
```

```
recorder Element -file $fileName/glbForceSpColF17.out -time -region $SpColF17 globalForce
recorder Element -file $fileName/glbForceSpColF18.out -time -region $SpColF18 globalForce
recorder Element -file $fileName/glbForceSpColF19.out -time -region $SpColF19 globalForce
```

```
recorder Element -file $fileName/glbForceSpColF20.out -time -region $SpColF20 globalForce
```

```
recorder Element -file $fileName/ForceBRC.out -time -ele 141014101 142014201 localForce
recorder Element -file $fileName/DefmBRC.out -time -ele 141014101 142014201
localDisplacement
```

```
# Gravity load definition-----
# pattern Plain 1 1 {
# for {set floor $numFloor} {$floor>=2} {incr floor -1} {
#     for {set colLine 10} {$colLine<=$numCline} {incr colLine 1} {
#         if {$floor==$numFloor} {
#             set gravity [expr -9.8*1000*[lindex $massRoof [expr $colLine-10]]]
#         } else {
#             set gravity [expr -9.8*1000*[lindex $massFloor [expr $colLine-10]]]
#         }
#         load $colLine$floor 0. $gravity 0.
#     }
# }
# }
#
# puts "Gravity load pattern built"
#
## Gravity load analysis
# constraints Transformation
# test EnergyIncr 1e-5 25 2
# integrator LoadControl 0.1
# algorithm Newton
# numberer RCM
# system UmfPack -lvalueFact 100
# analysis Static
# analyze 10
# loadConst -time 0.0
```

```
# puts "Gravity analysis done"

# Eigen analysis-----
set numModes 3
set lambda [eigen -fullGenLapack $numModes]
set omega {}
set f {}
set T {}
set evector {}
set evi {}
set pi 3.141593
set i 0
set evNode {1011 1012 1013 1014 1015 1016 1017 1018 1019 1020 1021 1022 1023 1024 1025 1026
1027 1028 1029 1030}
foreach lam $lambda {
    set i [expr $i+1]
    lappend omega [expr sqrt($lam)]
    lappend f [expr sqrt($lam)/(2*$pi)]
    lappend T [expr (2*$pi)/sqrt($lam)]
    foreach evn $evNode {
        lappend evector [nodeEigenvector $evn $i 1]
    }
}

set Periods [open $period "w"]
foreach t $T {
    puts $Periods " $t"
}
set i 0
foreach ev $evector {
    lappend evi [expr $ev]
    set i [expr $i+1]
    if {$i%20==0} {
        puts $Periods "$evi"
        set evi {}
    }
}
```

```

    }
    close $Periods
    puts "Eigen analysis done!"

# Seismic input-----
constraints Transformation
numberer RCM
system UmfPack -lvalueFact 100
test EnergyIncr 1e-6 100 0
algorithm KrylovNewton
integrator Newmark 0.5 0.25
analysis VariableTransient

set omega1 [lindex $omega 0]
set omega6 [lindex $omega 2]
set alphaM [expr $dph*2*$omega1*$omega6/($omega1+$omega6)]
set betaKinit [expr $dph*2/($omega1+$omega6)]
set betaKcurr 0
set betaKcomm 0
rayleigh $alphaM $betaKcurr $betaKinit $betaKcomm

# Earthquake input
set AccelSeries "Series -dt $dt -filePath $outFile -factor $GMfatt"
pattern UniformExcitation $IDloadTag $GMdirection -accel $AccelSeries
set ok [analyze $Nsteps $DtAnalysis [expr $DtAnalysis/100] [expr $DtAnalysis] 20]
puts "Ground motion done! End Time: [getTime]"

# # Static Push-----
# # mode 1
# # set lateralForce {7831.196275      14265.10795      21512.13723      29476.38492
#           38055.97918      47156.11399      56692.75046      66578.16014
#           76733.7855      87084.17913      97563.94093      108107.4722      118664.474
#           129187.8765      139640.4954      149992.6393      160231.5848
#           170351.2496      180368.3859      265714.918}
# # mode 2
# # set lateralForce {55439.53118      96837.07606      138222.789      177010.6086

```

```

210807.5658      237565.8042      255645.3228      263782.8772
261180.1523      247495.2124      222838.6441      187760.5975
143175.7894      90340.64326      30741.80837      -33965.21783
-102155.2336     -172241.9578     -242946.0451     -437156.9673}
# # mode 3
# # set lateralForce {61994.77905      101859.9512      132959.6505      150689.0338
152221.8451      136903.1139      106213.1469      63627.03613      14116.6321
-36401.31969     -81823.3958     -116514.3439     -136064.1746
-137711.5693     -120653.6963     -86106.69753     -37004.43696
22404.77636      87401.20258      214104.319}
#
# pattern Plain 2 1 {
#     for {set floor 11} {$floor<=$numFloor} {incr floor 1} {
#         set theLateralF [lindex $lateralForce [expr $floor-11]]
#         for {set colLine 10} {$colLine<=$numCline} {incr colLine 1} {
#             load $colLine$floor $theLateralF 0. 0.
#         }
#     }
# }
# constraints Transformation
# test EnergyIncr 1e-5 25 2
# integrator LoadControl 0.001
# #integrator DisplacementControl 1030 1 1
# algorithm Newton
# numberer RCM
# system UmfPack -lvalueFact 100
# analysis Static
# analyze 1000
# puts "Push analysis done"

```


Appendix C

Programming Scripts for Nonlinear Analysis of DMD Model

MAIN.f90 for Cnt models.....	C-1
Subroutine CHLSKY.f90.....	C-13
Subroutine CHOL.f90.....	C-15
Subroutine EVAT.f90 for Cnt models.....	C-17
Subroutine GEIGEN.f90.....	C-20
Subroutine JACOBI.f90.....	C-22
Subroutine MASG.f90.....	C-25
Subroutine MINV.f90.....	C-27
Subroutine MOCH.f90.....	C-28
Subroutine NRES.f90 for Cnt models.....	C-29
Subroutine PROG.f90.....	C-33
Subroutine PRT.f90.....	C-34
Subroutine SKEL.f90.....	C-38
Subroutine STDm.f90.....	C-38
Main.f90 for Sgt2 models.....	C-39
Subroutine NRES.f90 for Sgt2 models.....	C-52

Appendix C —Programming Scripts for Nonlinear Analysis of DMD Model

Main file for comparing responses of DMD and SDOF models of the Cnt spine frame structures in static, eigenvalue, and dynamic analysis

! Intrinsic damping ratio of models = 0.02

! Input wave: BCJ-L2 (Accel. response spectrum is calibrated to following BRI-L2 when damping ratio is 0.05)

! Unit: cm N 0.1ton s

DATA H/400./

INTEGER,PARAMETER:: NP=9 ! analysis case number = number of elements of SFT, BRCFT, ...

! INTEGER,PARAMETER:: N=5,NT=8000,N2=11,N3=16 ! 5-story

! INTEGER,PARAMETER:: N=10,NT=8000,N2=21,N3=31 ! 10-story

INTEGER,PARAMETER:: N=20,NT=8000,N2=41,N3=61 ! 20-story

DIMENSION

EK(N3,N3),EKC(N),EKB(N),EKKC(4,4,N),EKKS(4,4,N),NC(4,N),NS(4,N),NN(N3),EM(N3,N3),EC(N3,N3),EMM(N)

DIMENSION

DDY(NT),ACC(N3,NT),VEL(N3,NT),DIS(N3,NT),SHEAR(N,NT),SSF(N,NT),SMF(N,NT),SDR(N,NT)

DIMENSION

DISMX(N3),VELMX(N3),ACCMX(N3),SHEARMX(N),SSFMX(N),SMFMX(N),SDRMX(N),ReSDR(N),RaSDR(N)

DIMENSION BRCFT(NP),SK1FT(NP),SFT(NP),HBRCFT(NP)

DIMENSION

QFES(N),UFES(N),EV1N(N),ESSN(N),EV1R(N),ESSR(N),EV1B(N),ESSB(N),ESDR(N),TFIN(N),SAI(N),EMEQUIN(N),TFIR(N),SAIR(N),EMEQUIR(N),TFIB(N),SAIB(N),EMEQUIB(N)

DIMENSION EKC0(N),EKB0(N),KCFT(NP),KBFT(NP)

DIMENSION

EP(N),EKR(N,N),SSS(N2,N),SDIS(N),SROT(N2),SDSRT(N3),SSDR(N),SSSF(N),SSMF(N),SSSHEAR(N),SALP(N),CI(N),SSFT(N),SGM(N)

DATA HI/0./,EB/900./,H_BRC0/182.5/

DATA ALPHA2/9.2159/, ALPHA1/788254.2/ ! spine frame parameters

DATA EPS/.00000005/, TOL/.000001/, GFT/1.0/

CHARACTER(LEN=20) :: IFILE='TaftLevel22.txt'

CHARACTER(LEN=10),DIMENSION(NP) :: OFILE=('/R1.txt', 'R2.txt', 'R3.txt', 'R4.txt', 'R5.txt','R6.txt', 'R7.txt', 'R8.txt', 'R9.txt')

```

!
*****
*****

! Kd/Km=0.5, thet_y=0.1%, A_d=5110.3mm2, Ld=3650mm, My/thet_y=1.5e12,BRCFT=2.0,
SK1FT=1.0, HBRCFT=2.0
! Kd/Km=1.0, thet_y=0.1%, A_d=10258.3mm2, Ld=3650mm, My/thet_y=3e12, BRCFT=4.0,
SK1FT=2.0, HBRCFT=2.0
! Kd/Km=2.0,BRCFT=8.0, SK1FT=4.0
! Kd/Km=4.0,BRCFT=16.0, SK1FT=8.0
! /1.,1.,1.,1.,1.,1.,1.,1.,1./ /2.,2.,2.,2.,2.,2.,2.,2./ /4.,4.,4.,4.,4.,4.,4.,4./
! /8.,8.,8.,8.,8.,8.,8.,8./ /16.,16.,16.,16.,16.,16.,16.,16./
!
*****
*****

DATA SFT/2.,4.,8.,12.,16.,20.,40.,60.,80./ ! SFT= 40 when Ks/Km=1.0
DATA BRCFT/16.,16.,16.,16.,16.,16.,16.,16.,16./ ! BRCFT=1.0 when Ad=2564mm2
DATA SK1FT/8.,8.,8.,8.,8.,8.,8.,8./ ! SK1FT=1.0 when My/thet_y=1.5e12

DATA HBRCFT/2.,2.,2.,2.,2.,2.,2.,2./ ! HBRCFT=1.0 when Ld=1825mm
DATA KCFT/1.,1.,1.,1.,1.,1.,1.,1.,1./ ! stiffness factor of columns
DATA KBFT/1.,1.,1.,1.,1.,1.,1.,1.,1./ ! stiffness factor of beams

!! ***whole frame-5 story***
! DATA EKC0/1.4207D+12,1.4207D+12,1.3969D+12,1.3737D+12,1.3737D+12/, &
! & EKB0/9.5829D+11,9.5860D+11,9.5830D+11,9.1946D+11,9.1946D+11/, & !modified
! & EMM/8006.3,8006.3,8006.3,8006.3,11637.2/
! DATA EKS220/2.1855D+12/,A_B0/15.184/,EKmFT/1.0/,SK10/1.5D+12/,A_BRC0/25.646/
! ! *****

!! ***whole frame-10 story***
!
DATA
EKC0/2.1042D+12,2.1042D+12,2.0833D+12,2.0455D+12,2.0045D+12,1.9379D+12,1.9164D+12,1.877
7D+12,1.8562D+12,1.7882D+12/, &
!
&
EKB0/9.1132D+11,9.1078D+11,9.0679D+11,8.6618D+11,8.6462D+11,8.6755D+11,8.3722D+11,8.3172

```

```

D+11,8.3214D+11,8.3519D+11/, & !modified
! & EMM/8084.1,8084.1,8084.1,8084.1,8084.1,8084.1,8084.1,8084.1,11638.3/
! DATA EKS220/6.8522D+12/,A_B0/47.608/,EKmFT/1.0/,SK10/3.21D+12/,A_BRC0/54.728/
! ! *****

! ***whole frame-20 story***
DATA
EKC0/2.1042D+12,2.1042D+12,2.1042D+12,2.1042D+12,2.0833D+12,2.0833D+12,2.0455D+12,2.045
5D+12,2.0045D+12,2.0045D+12,1.9379D+12,1.9379D+12,1.9164D+12,1.9164D+12,1.8777D+12,1.877
7D+12,1.8562D+12,1.8562D+12,1.7882D+12,1.7882D+12/, &
&
EKB0/9.6826D+11,9.6826D+11,9.6826D+11,9.6726D+11,9.5040D+11,9.4644D+11,9.4243D+11,9.3679
D+11,9.1507D+11,9.1906D+11,9.2323D+11,9.2237D+11,8.9491D+11,8.9113D+11,8.8731D+11,8.8444
D+11,8.5316D+11,8.5645D+11,8.5989D+11,8.5989D+11/, & !modified
&
EMM/8084.1,8084.1,8084.1,8084.1,8084.1,8084.1,8084.1,8084.1,8084.1,8084.1,8084.1,8084.1,8
084.1,8084.1,8084.1,8084.1,8084.1,11638.3/
DATA EKS220/2.5738D+13/,A_B0/178.82/,EKmFT/1.0/,SK10/6.63D+12/,A_BRC0/113.808/
! *****

! !Kd=0-----
! DATA SK10/0.003/ A_BRC0/0.00001/! pin bottom
! DATA BRCFT/1.,1.,1.,1.,1.,1.,1.,1.,1./
! DATA SK1FT/1.,1.,1.,1.,1.,1.,1.,1.,1./
! DATA HBRCFT/1.,1.,1.,1.,1.,1.,1.,1.,1./
! !-----

! >>>>>>>input wave
OPEN(100,FILE=IFILE,STATUS='OLD')
READ(100,501) DT,NNN,(DDY(M),M=1,NNN)
! <<<<<<<<input wave

! *****
! MODEL BUILD
! *****
DO 901 II=1,NP

```

```
EKS2=EKS220*SFT(II)
EKS1=EKS2*1D+5

! >>>>>>>MASS MATRIX
! INITIALIZATION
DO 102 J=1,N3
    DO 103 K=1,N3
        EM(J,K)=0.
    103 CONTINUE
102 CONTINUE
! MASS MATRIX
DO 104 L=1,N
    EM(L,L)=EMM(L)
104 CONTINUE
! <<<<<<<MASS MATRIX

! >>>>>>>STIFFNESS MATRIX
! INITIALIZATION
DO 105 J=1,N3
    DO 106 K=1,N3
        EK(J,K)=0.
    106 CONTINUE
105 CONTINUE

DO 118 I=1,N
    EKC(I)=EKC0(I)*KCFT(II)
    EKB(I)=EKB0(I)*KBFT(II)
118 CONTINUE

! PREPARATION
NC(1,1)=0
NC(2,1)=0
NC(3,1)=N+1
NC(4,1)=1
DO 107 I=2,N
    NC(1,I)=I+N-1
```

```
NC(2,I)=I-1
NC(3,I)=I+N
NC(4,I)=I
107 CONTINUE
NS(1,1)=N3    ! STIFFNESS OF EK(N3,N3), THE DOF OF BRC ROTATION
NS(2,1)=0
NS(3,1)=N2
NS(4,1)=1
DO 108 I=2,N
NS(1,I)=I+N2-2
NS(2,I)=I-1
NS(3,I)=I+N2-1
NS(4,I)=I
108 CONTINUE

! COLUMN STIFFNESS
DO 109 I=1,N
EKKC(4,4,I)=EKC(I)*(2./H**2)*EKmFT
EKKC(4,3,I)=EKC(I)*(-1./H)*EKmFT
EKKC(4,2,I)=EKC(I)*(-2./H**2)*EKmFT
EKKC(4,1,I)=EKC(I)*(-1./H)*EKmFT
EKKC(3,4,I)=EKC(I)*(-1./H)*EKmFT
EKKC(3,3,I)=EKC(I)*(2./3.)*EKmFT
EKKC(3,2,I)=EKC(I)*(1./H)*EKmFT
EKKC(3,1,I)=EKC(I)*(1./3.)*EKmFT
EKKC(2,4,I)=EKC(I)*(-2./H**2)*EKmFT
EKKC(2,3,I)=EKC(I)*(1./H)*EKmFT
EKKC(2,2,I)=EKC(I)*(2./H**2)*EKmFT
EKKC(2,1,I)=EKC(I)*(1./H)*EKmFT
EKKC(1,4,I)=EKC(I)*(-1./H)*EKmFT
EKKC(1,3,I)=EKC(I)*(1./3.)*EKmFT
EKKC(1,2,I)=EKC(I)*(1./H)*EKmFT
EKKC(1,1,I)=EKC(I)*(2./3.)*EKmFT
DO 110 J=1,4
DO 111 K=1,4
IF (NC(J,I)*NC(K,I).NE.0) THEN
```

```

      EK(NC(J,I),NC(K,I))=EK(NC(J,I),NC(K,I))+EKKC(J,K,I)
    END IF
111    CONTINUE
110 CONTINUE
109 CONTINUE

! BEAM STIFFNESS
NP1=N+1
DO 115 I=NP1,N2-1
    IMN=I-N
    EK(I,I)=EK(I,I)+EKB(IMN)*EKmFT
115 CONTINUE

! SPINE FRAME STIFFNESS
DO 112 I=1,N
    IF(I.EQ.1) THEN
        EKS=EKS1*EKmFT
        ALPHA=ALPHA1
    ENDIF
    IF(I.GT.1) THEN
        EKS=EKS2*EKmFT
        ALPHA=ALPHA2
    ENDIF
    EKKS(4,4,I)=1./(1+6*ALPHA)*EKS*(2./H**2)
    EKKS(4,3,I)=1./(1+6*ALPHA)*EKS*(-1./H)
    EKKS(4,2,I)=1./(1+6*ALPHA)*EKS*(-2./H**2)
    EKKS(4,1,I)=1./(1+6*ALPHA)*EKS*(-1./H)
    EKKS(3,4,I)=1./(1+6*ALPHA)*EKS*(-1./H)
    EKKS(3,3,I)=1./(1+6*ALPHA)*EKS*(2./3.+ALPHA)
    EKKS(3,2,I)=1./(1+6*ALPHA)*EKS*(1./H)
    EKKS(3,1,I)=1./(1+6*ALPHA)*EKS*(1./3.-ALPHA)
    EKKS(2,4,I)=1./(1+6*ALPHA)*EKS*(-2./H**2)
    EKKS(2,3,I)=1./(1+6*ALPHA)*EKS*(1./H)
    EKKS(2,2,I)=1./(1+6*ALPHA)*EKS*(2./H**2)
    EKKS(2,1,I)=1./(1+6*ALPHA)*EKS*(1./H)
    EKKS(1,4,I)=1./(1+6*ALPHA)*EKS*(-1./H)
```

```

      EKKS(1,3,I)=1./(1+6*ALPHA)*EKS*(1./3.-ALPHA)
      EKKS(1,2,I)=1./(1+6*ALPHA)*EKS*(1./H)
      EKKS(1,1,I)=1./(1+6*ALPHA)*EKS*(2./3.+ALPHA)
      DO 113 J=1,4
        DO 114 K=1,4
          IF (NS(J,I)*NS(K,I).NE.0) THEN
            EK(NS(J,I),NS(K,I))=EK(NS(J,I),NS(K,I))+EKKS(J,K,I)
          END IF
114      CONTINUE
113 CONTINUE
112 CONTINUE
! <<<<<<<<<STIFFNESS MATRIX
EMY=A_BRC0*EKmFT*BRCFT(II)*32500.*EB
A_BRC=A_BRC0*BRCFT(II)*EKmFT
A_B=A_B0*SFT(II)*EKmFT
SK1=SK10*SK1FT(II)*EKmFT
H_BRC=H_BRC0*HBRCFT(II)

CALL
PRT(H,N,N2,N3,EMM,EK,TFN,BETAKN,BETAMN,EMEQN,EHEQN,EKFN,EV1N,ESSN,TFIN,SAI
N,EMEQIN,SSS,EKR) ! no BRC
EKN3=EK(N3,N3)
EK(N3,N3)=EKN3*1.D5
CALL
PRT(H,N,N2,N3,EMM,EK,TFR,BETAKR,BETAMR,EMEQR,EHEQR,EKFR,EV1R,ESSR,TFIR,SAIR,
EMEQIR,SSS,EKR) ! rigid BRC
EK(N3,N3)=EKN3+SK1
CALL
PRT(H,N,N2,N3,EMM,EK,TFB,BETAKB,BETAMB,EMEQB,EHEQB,EKFB,EV1B,ESSB,TFIB,SAIB,
EMEQIB,SSS,EKR) ! elastic BRC
EK(N3,N3)=EKN3

! *****
! SEISMIC EVALUATION
! *****

```



```
CALL
EVAT(GFT,N,N2,N3,H,H_BRC,A_BRC,A_B,SK1,EMY,UF,QF,EHEQN,EMEQN,EKFN,EKFR,TFN,TEQ)

! *****
! DATA PROCESS OF EVALUATED RESULTS
! *****

! DISTRIBUTION OF EVALUATED STORY SHEAR
DO 500 I=1,N
    QFES(I)=ESSN(I)/ESSN(1)*QF
500 CONTINUE

! *****
! STATIC ANALYSIS
! *****

!! SHEAR FORCE - METHOD 1 (obtained from Ai distribution)
! SGM(N)=EMM(N)*9.8*100.0
! DO 310 I=1,N-1
!     SGM(N-I)=SGM(N-I+1)+EMM(N-I)*9.8*100.0
! 310 CONTINUE
!
! DO 311 I=1,N
!     SALP(I)=SGM(I)/SGM(1)
!     CI(I)=1.0+(1.0/SALP(I)**0.5-SALP(I))*2.0*TEQ/(1.0+3.0*TEQ)
!     SSFT(I)=CI(I)*SGM(I)
! 311 CONTINUE

! SHEAR FORCE - METHOD 2 (obtained from seismic evaluation)
DO 311 I=1,N
    SSFT(I)=QFES(I)*1000.
311 CONTINUE

EP(N)=SSFT(N)
DO 312 I=1,N-1
```

```

        EP(I)=SSFT(I)-SSFT(I+1)
312 CONTINUE

CALL MINV(N,EKR,N)
CALL PROG(EKR,EP,SDIS,N,N,1)
CALL PROG(SSS,SDIS,SROT,N2,N,1)
DO 300 I=1,N
        SDSRT(I)=SDIS(I)
300 CONTINUE
DO 301 I=1,N2
        SDSRT(N+I)=-SROT(I)
301 CONTINUE

! *****
! DYNAMIC ANALYSIS
! *****

! >>>>>>>DAMPING MATRIX
        DO 116 I=1,N3
        DO 117 J=1,N3
                EC(I,J)=EK(I,J)*BETAKN
117 CONTINUE
        EC(I,I)=EC(I,I)+EM(I,I)*BETAMN
116 CONTINUE
! <<<<<<<<DAMPING MATRIX

HK=SK1/(1.0/0.0125-1.0)
CALL NRES(GFT,N3,EM,EC,EK,SK1,NNN,DT,DDY,ACC,VEL,DIS,EPS,TOL,H,HK,EMY,HI)

! *****
! DATA PROCESS OF DYNAMIC ANALYSIS RESULTS
! *****

! MAX DISP,VEL,ACC IN EACH STORY
DO 201 J=1,N3

```

```
DISMX(J)=MAXVAL(ABS(DIS(J,:)))
VELMX(J)=MAXVAL(ABS(VEL(J,:)))
ACCMX(J)=MAXVAL(ABS(ACC(J,:)+DDY))
201 CONTINUE
! Max Story Drift Ratio
SDR(1,:)=DIS(1,:)/4.
SDRMX(1)=MAXVAL(ABS(SDR(1,:)))
DO 203 J=2,N
SDR(J,:)=(DIS(J,:)-DIS(J-1,:))/4.
SDRMX(J)=MAXVAL(ABS(SDR(J,:)))
203 CONTINUE

! Residual Story Drift Ratio
DO 215 J=1,N
ReSDR(J)=(MAXVAL(SDR(J,(NT-500):NT))+MINVAL(SDR(J,(NT-500):NT)))/2.0 ! average
RaSDR(J)=MAXVAL(SDR(J,(NT-500):NT))-MINVAL(SDR(J,(NT-500):NT)) ! amplitude
215 CONTINUE

! Note: because the stiffness of the moment frame and spine frame don't change during analysis, we can
calculate their shear force in the main script, otherwise we should calculate them during each integration
step
! SHEAR IN SPINE FRAME
DO 204 I=1,NNN

SSF(1,I)=EKKS(4,4,1)*DIS(1,I)+EKKS(4,3,1)*DIS(N2,I)+EKKS(4,2,1)*0.+EKKS(4,1,1)*DIS(N3,I)
DO 210 K=2,N

SSF(K,I)=EKKS(4,4,K)*DIS(K,I)+EKKS(4,3,K)*DIS(N2+K-1,I)+EKKS(4,2,K)*DIS(K-1,I)+EKKS(4,1
,K)*DIS(N2+K-2,I)
210 CONTINUE
204 CONTINUE

DO 205 J=1,N
SSFMX(J)=MAXVAL(ABS(SSF(J,:)))/1000.
205 CONTINUE
```

! SHEAR IN MOMENT FRAME

DO 206 I=1,NNN

SMF(1,I)=EKKC(4,4,1)*DIS(1,I)+EKKC(4,3,1)*DIS(N+1,I)

DO 211 K=2,N

SMF(K,I)=EKKC(4,4,K)*DIS(K,I)+EKKC(4,3,K)*DIS(N+K,I)+EKKC(4,2,K)*DIS(K-1,I)+EKKC(4,1,
K)*DIS(N+K-1,I)

211 CONTINUE

206 CONTINUE

DO 207 J=1,N

SMFMX(J)=MAXVAL(ABS(SMF(J,:)))/1000.

207 CONTINUE

! TOTAL SHEAR

SHEAR=SSF+SMF

DO 202 J=1,N

SHEARMX(J)=MAXVAL(ABS(SHEAR(J,:)))/1000.

202 CONTINUE

! ! DISTRIBUTION OF EVALUATED STORY SHEAR

! DO 212 I=1,N

! QFES(I)=ESSN(I)/ESSN(1)*QF

! 212 CONTINUE

! ! DISTRIBUTION OF EVALUATED STORY DRIFT

! ESDR(1)=EV1N(1)

! DO 213 I=2,N

! ESDR(I)=EV1N(I)-EV1N(I-1)

! 213 CONTINUE

! ESDRM=MAXVAL(ESDR)

! DO 214 I=1,N

! UFES(I)=ESDR(I)/ESDRM*UF

! 214 CONTINUE

! *****

! DATA PROCESS OF STATIC ANALYSIS RESULTS

! *****

! Max Story Drift Ratio

SSDR(1)=SDIS(1)/4.

DO 302 J=2,N

SSDR(J)=(SDIS(J)-SDIS(J-1))/4.

302 CONTINUE

! SHEAR IN SPINE FRAME

SSSF(1)=(EKKS(4,4,1)*SDSRT(1)+EKKS(4,3,1)*SDSRT(N2)+EKKS(4,2,1)*0.+EKKS(4,1,1)*SDSRT(N3))/1000.

DO 303 K=2,N

SSSF(K)=(EKKS(4,4,K)*SDSRT(K)+EKKS(4,3,K)*SDSRT(N2+K-1)+EKKS(4,2,K)*SDSRT(K-1)+EKKS(4,1,K)*SDSRT(N2+K-2))/1000.

303 CONTINUE

! SHEAR IN MOMENT FRAME

SSMF(1)=(EKKC(4,4,1)*SDSRT(1)+EKKC(4,3,1)*SDSRT(N+1))/1000.

DO 304 K=2,N

SSMF(K)=(EKKC(4,4,K)*SDSRT(K)+EKKC(4,3,K)*SDSRT(N+K)+EKKC(4,2,K)*SDSRT(K-1)+EKKC(4,1,K)*SDSRT(N+K-1))/1000.

304 CONTINUE

! TOTAL SHEAR

SSHEAR=SSSF+SSMF

! *****

! RECORDER

! *****

OPEN(1,FILE=OFILE(II),STATUS='OLD')

WRITE(1,502)

SHEARMX,SSFMX,SMFMX,SDRMX,SSHEAR,SSSF,SSMF,SSDR,QFES,UF,TEQ,TFN,ReSDR,RaSDR

```
! *****
! SHEARMX(N) dy-ana. total shear
! SSFMX(N) dy-ana. shear in spine frame
! SMFMX(N) dy-ana. shear in moment frame
! SDRMX(N) dy-ana. SDR
! SSHEAR(N) st-ana. total shear
! SSSF(N) st-ana. shear in spine frame
! SSMF(N) st-ana. shear in moment frame
! SSDR(N) st-ana. SDR
! QFES(N) eva. total shear
! UF eva. max. SDR
! TEQ eva. 1st-mode period of whole system at max. deformation
! TFN eigenvalue-ana. 1st-mode period of moment frame only without BRCs
! *****
```

901 CONTINUE

STOP

501 FORMAT(T51,F10.2,I10/(F10.5))

502 FORMAT(F18.8)

503 FORMAT(F15.3)

CLOSE(100)

CLOSE(1)

END

Subroutine file - CHLSKY.f90

```
! *****
! SUBROUTINE FOR CHOLESKY DECOMPOSITION OF POSITIVE DEFINITE SYMMETRIC
! MATRIC
! *****
! CODED BY S. SUZUKI
SUBROUTINE CHLSKY(A,B,N,N1,N2,X,DET,MATA,KAI)
DIMENSION A(N1,N2),B(*),X(*)
```

```
IF(MATA.LE.0) THEN
  A(1,1)=SQRT(A(1,1))
  DO 10 J=2,N
    A(1,J)=A(1,J)/A(1,1)
10  CONTINUE
  DO 20 I=2,N
    S=0
    DO 30 K=1,I-1
      S=S+A(K,I)*A(K,I)
30  CONTINUE
    S1=A(I,I)-S
    IF(S1.LE.0) THEN
      KAI=0
      RETURN
    END IF
    A(I,I)=SQRT(S1)
    DO 80 J=I+1,N
      S=0
      DO 90 K=1,I-1
        S=S+A(K,I)*A(K,J)
90  CONTINUE
      A(I,J)=(A(I,J)-S)/A(I,I)
80  CONTINUE
20  CONTINUE
    S=1
    DO 110 I=1,N
      S=S*A(I,I)*A(I,I)
110 CONTINUE
    DET=S
  END IF
  B(1)=B(1)/A(1,1)
  DO 120 I=2,N
    S=0.0
    DO 130 K=1,I-1
      S=S+A(K,I)*B(K)
130 CONTINUE
```

```
      B(I)=(B(I)-S)/A(I,I)
120 CONTINUE
      X(N)=B(N)/A(N,N)
      DO 140 I=1,N-1
          S=0
          DO 150 K=N-I+1,N
              S=S+A(N-I,K)*X(K)
150      CONTINUE
      X(N-I)=(B(N-I)-S)/A(N-I,N-I)
140 CONTINUE
      KAI=1
      RETURN
      END
```

Subroutine file - CHOL.f90

```
! *****
! SUBROUTINE FOR CHOLESKY'S SOLUTION OF LINEAR EQUATIONS
! *****
! CODED BY Y.OHSAKI

SUBROUTINE CHOL(N,A,B,X,ND,IND)

DIMENSION A(ND,ND),B(ND),X(ND)

IF(IND.NE.0) GO TO 160

! FORMATION OF TRIANGULAR MATRIX

A(1,1)=SQRT(A(1,1))
IF(N.EQ.1) GO TO 160
DO 110 J=2,N
    A(1,J)=A(1,J)/A(1,1)
110 CONTINUE
    DO 150 I=2,N
        IM1=I-1
        IP1=I+1
```



```
      S=A(I,I)
      DO 120 K=1,IM1
        S=S-A(K,I)**2
120    CONTINUE
      A(I,I)=SQRT(S)
      IF(I.EQ.N) GO TO 160
      DO 140 J=IP1,N
        S=A(I,J)
        DO 130 K=1,IM1
          S=S-A(K,I)*A(K,J)
130      CONTINUE
        A(I,J)=S/A(I,I)
140    CONTINUE
150  CONTINUE

! SOLUTION OF EQUATIONS
160 B(1)=B(1)/A(1,1)
      IF(N.EQ.1) GO TO 190
      DO 180 I=2,N
        IM1=I-1
        S=B(I)
        DO 170 K=1,IM1
          S=S-A(K,I)*B(K)
170    CONTINUE
        B(I)=S/A(I,I)
180  CONTINUE
190 X(N)=B(N)/A(N,N)
      IF(N.EQ.1) RETURN
      NM1=N-1
      DO 210 I=1,NM1
        NMI=N-I
        S=B(NMI)
        NMIP1=NMI+1
        DO 200 K=NMIP1,N
          S=S-A(NMI,K)*X(K)
200    CONTINUE
```

```
      X(NMI)=S/A(NMI,NMI)
210 CONTINUE
      RETURN
      END
```

Subroutine file – EVAT.f90 (for Cnt spine frame structures)

```
! *****
! SUBROUTINE FOR SEISMIC EVALUATION OF CONTROLLED SPINE FRAME STRUCTURES
! *****

SUBROUTINE
EVAT(GFT,N,N2,N3,H,H_BRC,A_BRC,A_B,SK1,EMY,UF,QF,EHEQ,EMEQ,EKFN,EKFR,TF,TEQ) !
EK SHOULD NOT INCLUDE STIFFNESS OF BRC

EB=900.
PI=3.1415926
U_TOL=0.001
E_B=20500000.
E_BRC=26357100.
EKF=EKFN
! ACCEL SPECTRA RESPONSE
DH0=SQRT((1+25*0.05)/(1+25*0.05))
IF (TF<0.16) THEN
    SA0=3.2+30.*TF
ELSEIF (TF<0.64) THEN
    SA0=8.
ELSE
    SA0=5.12/TF
ENDIF

IF (TF<0.64) THEN
    GS=1.5
ELSEIF (TF<0.864) THEN
    GS=1.5*TF/0.64
ELSE
    GS=2.025
ENDIF
```

SA=SA0*GS*DH0*GFT

! RESPONSE OF MAIN FRAME WITHOUT DAMPER

Q0=SA*EMEQ/10.*1000.

U0=Q0/EKF

! QF=Q0/1000.

! UF=U0/EHEQ*100

! TEQ=TF

! STIFFNESS OF BRC

L_B=SQRT(H**2.+(EB/2.）**2.)

FY_BRC=32500.*A_BRC

EB_H=A_B*E_B*EB/2./L_B**2.

QY=EMY/EHEQ

U_B=QY/EB_H/2.

THET_B=U_B/H

THET_BRC=2.*32500./E_BRC*H_BRC/EB

THET_Y=THET_B+THET_BRC

EKD=QY/(THET_Y*EHEQ)

EKDH=EKD*0.0125

QYD=QY

UYD=QYD/EKD

! STIFFNESS OF BRC AND SF (IN SERIES)

EKD=1/(1/EKD+1/(EKFR-EKFN))

! INITIALLY ASSUMED DISP RESPONSE

U1=0.01*EHEQ

DO 1000

IF (U1<=UYD) THEN

 EMYUD=1.

ELSE

 EMYUD=U1/UYD

ENDIF

! EQUIVALENT PERIOD

```
QQ=EKD/EKF
R=EKF/(EKF+EKD)
EKFD=EKF+EKD
TFD=SQRT(EKF/EKFD)*TF
EK_MYUD=EKD/EMYUD
EK_MYUFD=EK_MYUD+EKF
TEQ=SQRT(EKF/EK_MYUFD)*TF

! EQUIVALENT DAMPING RATIO
HHEQ=0.02+2./PI/EMYUD/R*LOG((1-R+R*EMYUD)/(EMYUD)**R)
DH=SQRT((1+25.*0.05)/(1+25.*HHEQ))
TL=0.864

IF(TF>=TL) THEN
    IF(TEQ>=TL) THEN
        IF(TFD>=TL) THEN
            RD=TEQ/TF*DH
        ELSE
            RD=TEQ/TF*DH*(TL*(2.*TEQ-TL)-TFD**2.)/(2.*(TEQ-TFD)*TL)
        ENDIF
    ELSE
        RD=TEQ/TF*DH*(TEQ+TFD)/(2*TL)
    ENDIF
ELSE
    RD=TEQ/TF*DH*(TEQ+TFD)/(2*TF)
ENDIF

RA=RD*EK_MYUFD/EKF
UF=U0*RD
DFU=ABS(UF-U1)
IF(DFU.LE.U_TOL) THEN
    GOTO 2000
ELSE
    U1=UF
ENDIF
```

```
1000 CONTINUE
2000 QF=Q0*RA/1000.
      UF=UF/EHEQ*100
```

```
RETURN
END
```

Subroutine file – GEIGEN.f90

```
! *****
! SUBROUTINE FOR EIGENPROBLEM SOLUTION
! *****
! INPUT
! N DEGREE OF A,B
! A
! B
! N1 DIMENSION 1 OF MATRIX STORING A,B
! N2 DIMENSION 2 OF MATRIX STORING A,B
! N3 DIMENSION OF F,G,X,Y
! OUTPUT
! Z TARGET EIGEN VALUE
! X TARGET EIGEN VECTOR Z(J)-->X(:,J)
! F
! G
! Y EIGEN VECTOR OF MATRIC G
SUBROUTINE GEIGEN(A,B,N,N1,N2,N3,Z,X)

DIMENSION A(N1,N2),Z(*),B(N1,N2)
DIMENSION F(N3,N3),G(N3,N3),X(N3,N3),Y(N3,N3)
DO 120 I=1,N
      Z(I)=0.
120 CONTINUE
      CALL CHLSKY(B,Z,N,N1,N2,Z,DET,0,KAI)
      DO 10 J=1,N
            DO 20 I=1,J
                  S=0.
                  DO 30 K=1,I-1
```

```

        S=S+B(K,I)*F(J,K)
30      CONTINUE
        F(J,I)=(A(I,J)-S)/B(I,I)
20      CONTINUE
10     CONTINUE
        DO 40 J=1,N
            DO 50 I=J,N
                S=0.
                DO 60 K=1,J-1
                    S=S+B(K,I)*G(J,K)
60                CONTINUE
                DO 65 K=J,I-1
                    S=S+B(K,I)*G(K,J)
65                CONTINUE
                G(I,J)=(F(I,J)-S)/B(I,I)
50            CONTINUE
40        CONTINUE
        DO 70 I=1,N
            DO 80 J=1,I-1
                G(J,I)=G(I,J)
80        CONTINUE
70     CONTINUE
        CALL JACOBI(N,N3,N3,1,G,Z,Y,IROT)
        DO 90 J=1,N
            DO 100 I=N,1,-1
                S=0.
                DO 110 K=I+1,N
                    S=S+B(I,K)*X(K,J)
110                CONTINUE
                X(I,J)=(Y(I,J)-S)/B(I,I)
100            CONTINUE
90        CONTINUE

        DO 220 J=1,N
            SS=0.
            DO 210 I=1,N
```

```
        SS=SS+X(I,J)*X(I,J)
210 CONTINUE
        SS=SQRT(SS)
        DO 230 I=1,N
            X(I,J)=X(I,J)/SS
230 CONTINUE
220 CONTINUE

        RETURN
        END
```

Subroutine file – JACOBI.f90

```
! *****
! SUBROUTINE FOR EIGENPROBLEM SOLUTION BY JACOBI METHOD
! *****

SUBROUTINE JACOBI(N,N1,N2,IVEC,A,D,V,IROT)

DIMENSION A(N1,N2),D(*),V(N1,N2),B(100),Z(100)
IF(IVEC.GT.0) THEN
    DO 70 IP=1,N
        DO 70 IQ=1,N
            IF(IP.EQ.IQ) THEN
                V(IP,IQ)=1.0
            ELSE
                V(IP,IQ)=0.0
            END IF
70    CONTINUE
END IF
DO 80 IP=1,N
    D(IP)=A(IP,IP)
    B(IP)=D(IP)
    Z(IP)=0.0
80 CONTINUE
    IROT=0.0
    DO 90 I=1,50
```

```
SM=0.0
DO 100 IP=1,N-1
    DO 100 IQ=IP+1,N
100 SM=SM+ABS(A(IP,IQ))
IF(SM.EQ.0) THEN
    RETURN
ELSE
    IF(I.LT.4) THEN
        TRESH=0.2*(SM/(N*N))
    ELSE
        TRESH=0.0
    END IF
END IF
DO 160 IP=1,N-1
    DO 160 IQ=IP+1,N
        G=100*ABS(A(IP,IQ))
        IF(I.GT.4) THEN
            IF((ABS(D(IP))+G).EQ.ABS(D(IP))) THEN
                IF((ABS(D(IQ))+G).EQ.ABS(D(IQ))) THEN
                    A(IP,IQ)=0.0
                    GO TO 160
                END IF
            END IF
        END IF
        IF(ABS(A(IP,IQ)).GT.TRESH) THEN
            H=D(IQ)-D(IP)
            IF((ABS(H)+G).EQ.ABS(H)) THEN
                T=A(IP,IQ)/H
            ELSE
                THETA=0.5*H/A(IP,IQ)
                T=1/(ABS(THETA)+SQRT(1+THETA*THETA))
                IF(THETA.LT.0) THEN
                    T=-T
                END IF
            END IF
            C=1/SQRT(1+T*T)
```



```
ELSE
    GO TO 160
END IF
S=T*C
TAU=S/(1+C)
H=T*A(IP,IQ)
Z(IP)=Z(IP)-H
Z(IQ)=Z(IQ)+H
D(IP)=D(IP)-H
D(IQ)=D(IQ)+H
A(IP,IQ)=0.0
DO 270 J=1,IP-1
    G=A(J,IP)
    H=A(J,IQ)
    A(J,IP)=G-S*(H+G*TAU)
    A(J,IQ)=H+S*(G-H*TAU)
270 CONTINUE
DO 280 J=IP+1,IQ-1
    G=A(IP,J)
    H=A(J,IQ)
    A(IP,J)=G-S*(H+G*TAU)
    A(J,IQ)=H+S*(G-H*TAU)
280 CONTINUE
DO 290 J=IQ+1,N
    G=A(IP,J)
    H=A(IQ,J)
    A(IP,J)=G-S*(H+G*TAU)
    A(IQ,J)=H+S*(G-H*TAU)
290 CONTINUE
IF(IVEC.GT.0) THEN
    DO 320 J=1,N
        G=V(J,IP)
        H=V(J,IQ)
        V(J,IP)=G-S*(H+G*TAU)
        V(J,IQ)=H+S*(G-H*TAU)
320 CONTINUE
```

```
        END IF
        IROT=IROT+1
160 CONTINUE
        DO 330 IP=1,N
            B(IP)=B(IP)+Z(IP)
            D(IP)=B(IP)
            Z(IP)=0.0
330 CONTINUE
90 CONTINUE
    RETURN
END
```

Subroutine file – MASG.f90

```
! *****
! SUBROUTINE FOR NON-LINEAR MODEL OF MASGING'S TYPE
! *****

! input
! U: disp at step m
! DU: velocity at step m
! U1: disp at step m-1
! DU1: velocity at step m-1
! SKEL1 SKEL2 SKEL3 SKEL4 SKEL5: define the shape of skeleton curve, used in subroutine SKEL
! SKEL1 SKEL2: abscissa of turning point of the skeleton curve
! SKEL3 SKEL4 SKEL5: stiffness of each segment

! output
! V: restoring force at step m
! ICALL: number of calling this subroutine
! K: number of effective branches
! D: 1 if k=1 (on the skeleton curve); 2 if k>1 (on the hysteretic curve)
! U0: disp of starting point of current branch
! V0: force of starting point of current branch
! ND: dimension of U0, V0 according to main program
SUBROUTINE MASG(U,DU,U1,DU1,SKEL1,SKEL2,SKEL3,V,ICALL,K,D,U0,V0,ND)
```

DIMENSION U0(ND), V0(ND)

! INITIALIZATION

IF(ICALL.NE.1) GO TO 110

K=1

D=1.

U0(1)=0.

V0(1)=0.

! TURNING POINT

110 IF(DU*DU1.GE.0.) GO TO 120

UTN=(DU*U1-DU1*U)/(DU-DU1)

UU=(UTN-U0(K))/D

CALL SKEL(UU,SKEL1,SKEL2,SKEL3,VV)

VTN=D*VV+V0(K)

K=K+1

D=2.

U0(K)=UTN

V0(K)=VTN

GO TO 130

! TERMINAL POINT

120 IF(K.EQ.1) GO TO 150

130 IF(K.EQ.2) UEND=-U0(2)

IF(K.GT.2) UEND=U0(K-1)

IF((UEND-U)*SIGN(1.,DU).GE.0) GO TO 150

IF(K.GT.3) GO TO 140

K=1

D=1.

GO TO 150

140 K=K-2

! RESTORING FORCE

150 UU=(U-U0(K))/D

CALL SKEL(UU,SKEL1,SKEL2,SKEL3,VV)

V=D*VV+V0(K)

RETURN

END

Subroutine file – MINV.f90

! *****

! SUBROUTINE FOR MATRIX INVERSE

! *****

SUBROUTINE MINV(N,A,NMAX)

DIMENSION A(NMAX,NMAX),E(N),X(N),B(NMAX,NMAX)

DO 130 J=1,N

 DO 110 I=1,N

 E(I)=0.

110 CONTINUE

 E(J)=1.

 IND=J-1

 CALL CHOL(N,A,E,X,NMAX,IND)

 DO 120 I=1,N

 B(I,J)=X(I)

120 CONTINUE

130 CONTINUE

 DO 150 J=1,N

 DO 140 I=1,N

 A(I,J)=B(I,J)

140 CONTINUE

150 CONTINUE

 RETURN

END

Subroutine file – MOCH.f90

```
! *****
! SUBROUTINE FOR MODAL CHARACTERISTICS
! *****
! CODED BY Y.OHSAKI
! EM MASS MATRIX
! EK STIFFNESS MATRIX
! W CHARACTERISTIC FRQUENCY
! U MODE MATRIX (EIGENVECTOR*PATICIPATION FACTOR)
SUBROUTINE MOCH(N,EM,EK,W,U,ND,IND,VW1,VW2)
DIMENSION EM(ND,ND), EK(ND,ND),W(ND),U(ND,ND),VW1(ND,ND),VW2(ND,ND)
DO 120 I=1,N
    DO 110 J=1,N
        VW1(I,J)=EK(I,J)
        VW2(I,J)=EM(I,J)
110 CONTINUE
120 CONTINUE
    CALL GEIGEN(VW1,VW2,N,ND,ND,ND,W,U)
    DO 140 J=1,N
        W(J)=SQRT(W(J))
        VW1(1,J)=REAL(J)+0.1
        DO 130 I=1,N
            VW2(I,J)=U(I,J)
130 CONTINUE
140 CONTINUE
        DO 160 K=1,N-1
            DO 150 J=1,N-K
                IF(W(J).LT.W(J+1)) GO TO 150
                TEMP=W(J)
                W(J)=W(J+1)
                W(J+1)=TEMP
                TEMP=VW1(1,J)
                VW1(1,J)=VW1(1,J+1)
                VW1(1,J+1)=TEMP
150 CONTINUE
160 CONTINUE
```

```
      DO 180 J=1,N
        J1=INT(VW1(1,J))
        DO 170 I=1,N
          U(I,J)=VW2(I,J1)
170      CONTINUE
180 CONTINUE
      IF(IND.EQ.0) RETURN
      DO 220 J=1,N
        UTMU=0.0
        UTM1=0.0
        DO 200 K=1,N
          UTM=0.0
          DO 190 L=1,N
            UTM=UTM+U(L,J)*EM(L,K)
190      CONTINUE
          UTMU=UTMU+UTM*U(K,J)
          UTM1=UTM1+UTM
200    CONTINUE
        BETA=UTM1/UTMU
        DO 210 I=1,N
          U(I,J)=BETA*U(I,J)
210    CONTINUE
220 CONTINUE
      RETURN
      END
```

Subroutine file – NRES.f90 (for Cnt spine frame structures)

```
! *****
! SUBROUTINE FOR NONLINEAR RESPONSE OF MULTI-DOF SYSTEM
! *****

! CODED BY X. CHEN
! N3: DOF
! EM: MASS MATRIX
! EC: DAMPING MATRIX
! EK: INITIAL STIFFNESS MATRIX
```

! NN: NUMBER OF DATA IN GROUND MOTION

! DT: TIME INTERVAL OF GROUND MOTION

! DDY: GROUND MOTION DATA

! ACC: ABSOLUTE ACCEL RESPONSE

! VEL: RELATIVE VEL RESPONSE

! DIS: RELATIVE DISP RESPONSE

! QY: yielding overturning moment of BRC

! SK1: initial stiffness of BRC

! EPS TOL: Tolerance for norm of disp and norm of residual force

! H: story height

! HK: parameter related with kinematic hardening

! HI: parameter related with isotropic hardening

SUBROUTINE NRES(GFT,N3,EM,EC,EK,SK1,NN,DT,DDY,ACC,VEL,DIS,EPS,TOL,H,HK,QY,HI)

DIMENSION

EM(N3,N3),EK(N3,N3),EC(N3,N3),DDY(NN),ACC(N3,NN),VEL(N3,NN),DIS(N3,NN),BRCR(NN),BRCQ(NN)

DIMENSION DDELX(N3),DDELR(N3),DELX(N3),RR1(N3),RR2(N3),RR3(N3),EK1(N3,N3)

! >>>>>>>INITIALIZATION

DO 120 I=1,N3

ACC(I,1)=-DDY(1)*GFT

VEL(I,1)=0.

DIS(I,1)=0.

DO 110 J=1,N3

EK1(I,J)=0. ! Stiffness matrix

110 CONTINUE

120 CONTINUE

VK=SK1 ! LOCAL STIFFNESS -- overturning stiffness

BRCR(1)=0.

BRCQ(1)=0.

QB1=0.

UP1=0.

AH1=0.

! <<<<<<<INITIALIZATION

```

! *****

DO 290 M=2,NN    ! For nonlinear analysis, start integration here
! *****

! >>>>>>>Initialization in each step
DO 420 I=1,N3
    DELX(I)=0.
    DIS(I,M)=DIS(I,M-1)
    VEL(I,M)=-VEL(I,M-1)
    ACC(I,M)=-4./DT*VEL(I,M-1)-ACC(I,M-1)
420 CONTINUE
BRCQ(M)=BRCQ(M-1)
KI=0 ! Set iteration counter KI
! <<<<<<<<Initialization in each step

! *****
! Iteration Start
! *****

DO 1234 !STIFFNESS UPDATES DURING ITERATION

! >>>>>>>Formating EFFECTIVE STIFFNESS MATRIX
DO 140 I=1,N3
    DO 320 J=1,N3
        EK1(I,J)=EK(I,J) ! STORE EKR INTO EK1, LATER CHANGE EK1 INTO EFFECTVIE
ETIFFNESS MATRIX
    320 CONTINUE
140 CONTINUE
EK1(N3,N3)=EK(N3,N3)+VK
DO 160 I=1,N3
    DO 150 J=1,N3
        EK1(I,J)=EK1(I,J)+4./DT/DT*EM(I,J)+2./DT*EC(I,J)
    150 CONTINUE
160 CONTINUE
! <<<<<<<<Formating EFFECTIVE STIFFNESS MATRIX

```


! >>>>>>>Formating EFFECTIVE LOAD VECTOR, note: should be put after stiffness updating,
because EK2 is used to get RR1

CALL PROG(EK,DIS(:,M),RR1,N3,N3,1)

CALL PROG(EC,VEL(:,M),RR2,N3,N3,1)

CALL PROG(EM,ACC(:,M),RR3,N3,N3,1)

RNM=0.

RR1(N3)=RR1(N3)+BRCQ(M)

DO 410 I=1,N3

 DDELRI=-DDY(M)*GFT*EM(I,I)-(RR1(I)+RR2(I)+RR3(I)) ! (k+1)-th residual force vector

 RNM=RNM+DDELRI*DDELRI

410 CONTINUE

RNM=SQRT(RNM/N3)

IF((RNM.LE.TOL).AND.(KI.GT.0)) GOTO 4321

! <<<<<<<<Formating EFFECTIVE LOAD VECTOR

! >>>>>>>Solve INCREMENTAL DISP

CALL CHOL(N3,EK1,DDELRI,DDELXI,N3,0)

DNM=0.

DO 710 I=1,N3

 DNM=DNM+DDELXI*DDELXI

710 CONTINUE

DNM=SQRT(DNM/N3)

IF((DNM.LE.TOL).AND.(KI.GT.0)) GOTO 4321

! <<<<<<<<Solve INCREMENTAL DISP

! >>>>>>>Solve RELATIVE ACCEL, VEL, & DISP

DO 190 I=1,N3

 DELXI=DELXI+DDELXI

 DIS(I,M)=DIS(I,M-1)+DELXI

 VEL(I,M)=2./DT*DELXI-VEL(I,M-1)

 ACC(I,M)=4./DT/DT*DELXI-4./DT*VEL(I,M-1)-ACC(I,M-1)

190 CONTINUE

! <<<<<<<<Solve RELATIVE ACCEL, VEL, & DISP

! >>>>>>>STATE DETERMINATION

```
BRCR(M)=DIS(N3,M)
QB=QB1
UP=UP1
AH=AH1
CALL STDM(BRCR(M),UP,QB,SK1,ET,HI,HK,QY,BRCQ(M),AH)
VK=ET
KI=KI+1
1234 CONTINUE ! Go to next iteration

4321 QB1=QB
      UP1=UP
      AH1=AH
!if (M<254) goto 290
!us=U

290 CONTINUE ! Go to next integration step

! OPEN(14,FILE='BRCR.TXT',STATUS='OLD')
! OPEN(15,FILE='BRCQ.TXT',STATUS='OLD')
! WRITE(14,1014) BRCR !ROTATION OF THE BOTTOM OF SPINE FRAME
! WRITE(15,1015) BRCQ !BENDING MOMENT OF THE BOTTOM HINGE
! 1014 FORMAT(F11.8)
! 1015 FORMAT(F15.1)
RETURN
END
```

Subroutine file – PROG.f90

```
! *****
! SUBROUTINE FOR PRODUCT OF GENERAL MATRICES
! *****

SUBROUTINE PROG(A,B,C,NA1,NA2,NB2)

DIMENSION A(NA1,NA2),B(NA2,NB2),C(NA1,NB2)

DO 130 I=1,NA1
```

```

DO 120 J=1,NB2
    S=0.
    DO 110 K=1,NA2
        S=S+A(I,K)*B(K,J)
110    CONTINUE
    C(I,J)=S
120 CONTINUE
130 CONTINUE
    RETURN
END

```

Subroutine file – PRT.f90

```

! *****
! SUBROUTINE FOR OBTAIN PERIOD BY USING STATIC CONDENSATION
! *****

SUBROUTINE
PRT(H,N,N2,N3,EMM,EK,TF,BETAK,BETAM,EMEQ,EHEQ,EKF,EV1,ESS,TFI,SAI,EMEQI,SSS,EK
R)

DIMENSION EMM(N),EMR(N,N),EK(N3,N3),WW(N),UU(N,N),VW11(N,N),VW22(N,N)
DIMENSION EKRR(N,N),EKRS(N,N2),EKSR(N2,N),EKSS(N2,N2),SSS(N2,N),SSR(N,N),EKR(N,N)
DIMENSION EV1(N),EMS(N),ALPHAM(N),AI(N),ESS(N),TFI(N),EMEQI(N),SAI(N)
PI=3.1415926
! >>>>>>>MASS MATRIX
! INITIALIZATION
DO 102 J=1,N
    DO 103 K=1,N
        EMR(J,K)=0.
103 CONTINUE
102 CONTINUE
! MASS MATRIX
DO 104 L=1,N
    EMR(L,L)=EMM(L)
104 CONTINUE
! <<<<<<<<MASS MATRIX

```

```
! Static Condensation
DO 810 I=1,N3
  DO 820 J=1,N3
    IF (I.LE.N) THEN
      IF(J.LE.N) THEN
        EKRR(I,J)=EK(I,J)
      ELSE
        L=J-N
        EKRS(I,L)=EK(I,J)
      ENDIF
    ELSEIF (J.LE.N) THEN
      L=I-N
      EKSR(L,J)=EK(I,J)
    ELSE
      L=I-N
      MM=J-N
      EKSS(L,MM)=EK(I,J)
    ENDIF
  820 CONTINUE
810 CONTINUE
CALL MINV(N2,EKSS,N2)
CALL PROG(EKSS,EKSR,SSS,N2,N2,N)
CALL PROG(EKRS,SSS,SSR,N,N2,N)
DO 910 I=1,N
  DO 920 J=1,N
    EKR(I,J)=EKRR(I,J)-SSR(I,J)
  920 CONTINUE
910 CONTINUE

! >>>>>>>Calculate natural period
IND=1
CALL MOCH(N,EMR,EKR,WW,UU,N,IND,VW11,VW22)
TF=2.*PI/WW(1)
DO 310 I=1,N
  TFI(I)=2.*PI/WW(I)
310 CONTINUE
```

```
! <<<<<<<<<Calculate natural period

! >>>>>>>>Sa according to natural period of each mode
DH0=SQRT((1+25*0.05)/(1+25*0.02))
DO 340 I=1,N
IF (TFI(I)<0.16) THEN
    SA0=3.2+30.*TFI(I)
ELSEIF (TFI(I)<0.64) THEN
    SA0=8.
ELSE
    SA0=5.12/TFI(I)
ENDIF
IF (TFI(I)<0.64) THEN
    GS=1.5
ELSEIF (TFI(I)<0.864) THEN
    GS=1.5*TFI(I)/0.64
ELSE
    GS=2.025
ENDIF
SAI(I)=SA0*GS*DH0*1.0
340 CONTINUE
! <<<<<<<<<Sa according to natural period of each mode

! >>>>>>>>RAYLEIGH DAMPING PARAMETERS
WI=1
WJ=N/2+1
BETAK=2.*0.05/(WW(WI)+WW(WJ))
BETAM=2.*0.05*WW(WI)*WW(WJ)/(WW(WI)+WW(WJ))
! <<<<<<<<<RAYLEIGH DAMPING PARAMETERS

! EQUIVALENT MASS, HEIGHT
DO 320 I=1,N
    EMV=0
    EMV2=0
    DO 330 J=1,N
        EMV=EMV+EMM(J)*UU(J,I)
```

```
      EMV2=EMV2+EMM(J)*UU(J,I)*UU(J,I)
330 CONTINUE
      EMEQI(I)=EMV*EMV/EMV2
320 CONTINUE

EV1=UU(:,1)
EMV=0
EMV2=0
EMH=0
DO 110 I=1,N
      EMV=EMV+EMM(I)*EV1(I)
      EMV2=EMV2+EMM(I)*EV1(I)*EV1(I)
      EMH=EMH+EMM(I)*EV1(I)*I*H
110 CONTINUE
EMEQ=EMV*EMV/EMV2
EHEQ=EMH/EMV
EKF=EMEQ*(2.*PI/TF)**2.

! Ai equiv. static force

DO 210 I=1,N
      EMS(I)=0.
210 CONTINUE
EMS(N)=EMM(N)
DO 220 I=N-1,1,-1
      EMS(I)=EMS(I+1)+EMM(I)
220 CONTINUE

DO 230 I=1,N
      ALPHAM(I)=EMS(I)/EMS(1)
      AI(I)=1.0+(1.0/SQRT(ALPHAM(I))-ALPHAM(I))*2.0*TF/(1.0+3.0*TF)
      ESS(I)=AI(I)*EMS(I)
230 CONTINUE

RETURN
END
```

Subroutine file – SKEL.f90

```
! *****
! SUBROUTINE FOR BILINEAR SKELTON CURVE
! *****
```

```
! U: input displacement/deformation
! (UP1,QP1): first turning point
! (UP2,QP2): second turning point
! SK1, SK2, SK3: stiffness of each segment
```

```
SUBROUTINE SKEL(U,UP1,SK1,SK2,V)
```

```
IF (ABS(U).GT.UP1) GO TO 110
V=SIGN(1.,U)*SK1*ABS(U)
RETURN
110 QP1=SK1*UP1
V=SIGN(1.,U)*(QP1+SK2*(ABS(U)-UP1))
RETURN
END
```

Subroutine file – STDM.f90

```
! *****
! SUBROUTINE FOR THE STATE DETERMINATION OF MATERIAL WITH LINEAR KINEMATIC
& ISOTROPIC HARDENING
! *****
```

```
! U    DISP AT CURRENT ITERATION (INPUT)
! UP   ACCUMULATED PLASTIC DISP  (INPUT & OUTPUT)
! Q    FORCE AT CURRENT ITERATION (OUTPUT)
! QY   YIELD FORCE (INPUT)
! QB   BACK STRESS (INPUT & OUTPUT)
! E    INITIAL STIFFNESS (INPUT)
! HK   KINEMATIC HARDENING STIFFNESS (INPUT)
! HI   PLASTIC STIFFNESS (INPUT)
! AH   A HARDENING VARIABLE RELATED WITH ISOTROPIC HARDENING (INPUT &
OUTPUT)
```

```
! ET    TANGENT STIFFNESS AT CURRENT ITERATION (OUTPUT)
! DBETA ABSOLUTE VALUE OF PLASTIC DISP INCREMENT (Intermediate variables)
! DUP   PLASTIC DISP INCREMENT (Intermediate variables)

SUBROUTINE STDM(U,UP,QB,E,ET,HI,HK,QY,Q,AH)
QTR=E*(U-UP)    ! TRIAL FORCE
YFTR=ABS(QTR-QB)-(QY+HI*AH) ! TRIAL VALUE OF YIELD FUNCTION
IF (YFTR<=0) THEN
    ET=E
    Q=QTR
ELSE
    DBETA=YFTR/(E+HI+HK) ! PLASTIC FLOW
    ET=E*(HK+HI)/(E+HI+HK) ! ELASTO-PLASTIC TANGENT STIFFNESS
    ! DETERMINE PLASTIC DISP INCREMENT AND CORRECT TRIAL STRESS
    DUP=DBETA*SIGN(1.,QTR-QB)
    Q=QTR-E*DUP
    ! UPDATE PLASTIC STRAIN, HARDENING VARIABLE AND BACK STRESS VALUES
    UP=UP+DUP
    AH=AH+DBETA
    QB=QB+HK*DUP
ENDIF

RETURN
END
```

Main file for DMD models of the Sgt2 spine frame structures in static, eigenvalue, and dynamic analysis

```
! DMD & SDOF unit: cm N 0.1ton s
! Intrinsic damping ratio of models = 0.02
! Input wave: BCJ-L2 (Accel. response spectrum is calibrated to following BRI-L2 when damping ratio is
0.05)
DATA H/400./
INTEGER,PARAMETER:: NP=5 ! analysis case number = number of elements of SFT, BRCFT, ...
```



```

INTEGER,PARAMETER:: N=20,NT=15000,N2=41,N3=62 ! 20-story
DIMENSION
EK(N3,N3),EKC(N),EKB(N),EKKC(4,4,N),EKKS(4,4,N),NC(4,N),NS(4,N),NN(N3),EM(N3,N3),EC(N
3,N3),EMM(N)
DIMENSION
DDY(NT),ACC(N3,NT),VEL(N3,NT),DIS(N3,NT),SHEAR(N,NT),SSF(N,NT),SMF(N,NT),SDR(N,NT
)
DIMENSION
DISMX(N3),VELMX(N3),ACCMX(N3),SHEARMX(N),SSFMX(N),SMFMX(N),SDRMX(N),ReSDR(
N),RaSDR(N)
DIMENSION BRCFT(NP),SK1FT(NP),SFT(NP),HBRCFT(NP)
DIMENSION
QFES(N),UFES(N),EV1N(N),ESSN(N),EV1R(N),ESSR(N),EV1B(N),ESSB(N),ESDR(N),TFIN(N),SAI
N(N),EMEQIN(N),TFIR(N),SAIR(N),EMEQIR(N),TFIB(N),SAIB(N),EMEQIB(N),SFALMX(N),SFAL
(N)
DIMENSION EKC0(N),EKB0(N),KCFT(NP),KBFT(NP)
DIMENSION
EP(N),EKR(N,N),SSS(N2,N),SDIS(N),SROT(N2),SDSRT(N3),SSDR(N),SSSF(N),SSMF(N),SSSHEAR(
N),SALP(N),CI(N),SSFT(N),SGM(N)
DATA HI/0./,EB/900./,H_BRC0/182.5/
DATA ALPHA2/9.2159/, ALPHA1/788254.2/ ! spine frame parameters
DATA EPS/.00000005/, TOL/.000001/, GFT/1.0/
CHARACTER(LEN=20) :: IFILE='BCJL2Level2.txt'
CHARACTER(LEN=10),DIMENSION(NP) :: OFILE=('/R1.txt', 'R2.txt', 'R3.txt', 'R4.txt', 'R5.txt'/)
! CHARACTER(LEN=20) :: OFILED='Disp1.txt'

DATA SFT/2.,4.,8.,12.,16./ ! SFT=1 when Ks/Kf=0.025
DATA BRCFT/2.,2.,2.,2.,2./ ! BRCFT=1 when A_BRC=113.8cm2
DATA SK1FT/1.,1.,1.,1.,1./ ! SK1FT=1 when Kd/Kf=0.5

DATA HBRCFT/2.,2.,2.,2.,2./ ! HBRCFT=1.0 when Ld=1825mm
DATA KCFT/1.,1.,1.,1.,1./ ! stiffness factor of columns
DATA KBFT/1.,1.,1.,1.,1./ ! stiffness factor of beams

! ***whole frame-20 story***
DATA

```

```

EKC0/2.1042D+12,2.1042D+12,2.1042D+12,2.1042D+12,2.0833D+12,2.0833D+12,2.0455D+12,2.045
5D+12,2.0045D+12,2.0045D+12,1.9379D+12,1.9379D+12,1.9164D+12,1.9164D+12,1.8777D+12,1.877
7D+12,1.8562D+12,1.8562D+12,1.7882D+12,1.7882D+12/, &
&
EKB0/9.6826D+11,9.6826D+11,9.6826D+11,9.6726D+11,9.5040D+11,9.4644D+11,9.4243D+11,9.3679
D+11,9.1507D+11,9.1906D+11,9.2323D+11,9.2237D+11,8.9491D+11,8.9113D+11,8.8731D+11,8.8444
D+11,8.5316D+11,8.5645D+11,8.5989D+11,8.5989D+11/, & !modified
&
EMM/8084.1,8084.1,8084.1,8084.1,8084.1,8084.1,8084.1,8084.1,8084.1,8084.1,8084.1,8084.1,8
084.1,8084.1,8084.1,8084.1,8084.1,11638.3/
DATA EKS220/2.5738D+13/,A_B0/178.82/,EKmFT/1.0/,SK10/6.657D+12/,A_BRC0/113.808/
! *****

! !special cases-----
! DATA SK10/0.003/ A_BRC0/0.00001/! pin bottom
! DATA BRCFT/1.,1.,1./
! DATA SK1FT/1.,1.,1./
! DATA HBRCFT/1.,1.,1./
! !-----

! >>>>>>>input wave
OPEN(100,FILE=IFILE,STATUS='OLD')
READ(100,501) DT,NNN,(DDY(M),M=1,NNN)
! <<<<<<<input wave

! *****
! MODEL BUILD
! *****
DO 901 II=1,NP
    EKS2=EKS220*SFT(II)
    EKS1=EKS2*1D+5

! >>>>>>>MASS MATRIX
! INITIALIZATION
DO 102 J=1,62
    DO 103 K=1,62

```

```

        EM(J,K)=0.
103 CONTINUE
102 CONTINUE
! MASS MATRIX
DO 104 L=1,N
    EM(L,L)=EMM(L)
104 CONTINUE
! <<<<<<<<MASS MATRIX

! >>>>>>>>STIFFNESS MATRIX
! INITIALIZATION
DO 105 J=1,62
    DO 106 K=1,62
        EK(J,K)=0.
106 CONTINUE
105 CONTINUE

DO 118 I=1,N
    EKC(I)=EKC0(I)*KCFT(II)
    EKB(I)=EKB0(I)*KBFT(II)
118 CONTINUE

! PREPARATION
    NC(1,1)=0
    NC(2,1)=0
    NC(3,1)=N+1
    NC(4,1)=1
DO 107 I=2,N
    NC(1,I)=I+N-1
    NC(2,I)=I-1
    NC(3,I)=I+N
    NC(4,I)=I
107 CONTINUE
    NS(1,1)=61    ! THE DOF OF 1st BRC hinge
    NS(2,1)=0
    NS(3,1)=N2

```

```

      NS(4,1)=1
DO 108 I=2,N
      NS(1,I)=I+N2-2
      NS(2,I)=I-1
      NS(3,I)=I+N2-1
      NS(4,I)=I
108 CONTINUE
      NS(1,11)=62
! COLUMN STIFFNESS
DO 109 I=1,N
      EKKC(4,4,I)=EKC(I)*(2./H**2)*EKmFT
      EKKC(4,3,I)=EKC(I)*(-1./H)*EKmFT
      EKKC(4,2,I)=EKC(I)*(-2./H**2)*EKmFT
      EKKC(4,1,I)=EKC(I)*(-1./H)*EKmFT
      EKKC(3,4,I)=EKC(I)*(-1./H)*EKmFT
      EKKC(3,3,I)=EKC(I)*(2./3.)*EKmFT
      EKKC(3,2,I)=EKC(I)*(1./H)*EKmFT
      EKKC(3,1,I)=EKC(I)*(1./3.)*EKmFT
      EKKC(2,4,I)=EKC(I)*(-2./H**2)*EKmFT
      EKKC(2,3,I)=EKC(I)*(1./H)*EKmFT
      EKKC(2,2,I)=EKC(I)*(2./H**2)*EKmFT
      EKKC(2,1,I)=EKC(I)*(1./H)*EKmFT
      EKKC(1,4,I)=EKC(I)*(-1./H)*EKmFT
      EKKC(1,3,I)=EKC(I)*(1./3.)*EKmFT
      EKKC(1,2,I)=EKC(I)*(1./H)*EKmFT
      EKKC(1,1,I)=EKC(I)*(2./3.)*EKmFT
      DO 110 J=1,4
        DO 111 K=1,4
          IF (NC(J,I)*NC(K,I).NE.0) THEN
            EK(NC(J,I),NC(K,I))=EK(NC(J,I),NC(K,I))+EKKC(J,K,I)
          END IF
        DO 111 K=1,4
      DO 110 J=1,4
111 CONTINUE
110 CONTINUE
109 CONTINUE

! BEAM STIFFNESS

```

```
NP1=N+1
DO 115 I=NP1,N2-1
    IMN=I-N
    EK(I,I)=EK(I,I)+EKB(IMN)*EKmFT
115 CONTINUE

! SPINE FRAME STIFFNESS
DO 112 I=1,N
    IF(I==1 .or. I==11) THEN
        EKS=EKS1*EKmFT
        ALPHA=ALPHA1
    ELSE
        EKS=EKS2*EKmFT
        ALPHA=ALPHA2
    END IF

    EKKS(4,4,I)=1./(1+6*ALPHA)*EKS*(2./H**2)
    EKKS(4,3,I)=1./(1+6*ALPHA)*EKS*(-1./H)
    EKKS(4,2,I)=1./(1+6*ALPHA)*EKS*(-2./H**2)
    EKKS(4,1,I)=1./(1+6*ALPHA)*EKS*(-1./H)
    EKKS(3,4,I)=1./(1+6*ALPHA)*EKS*(-1./H)
    EKKS(3,3,I)=1./(1+6*ALPHA)*EKS*(2./3.+ALPHA)
    EKKS(3,2,I)=1./(1+6*ALPHA)*EKS*(1./H)
    EKKS(3,1,I)=1./(1+6*ALPHA)*EKS*(1./3.-ALPHA)
    EKKS(2,4,I)=1./(1+6*ALPHA)*EKS*(-2./H**2)
    EKKS(2,3,I)=1./(1+6*ALPHA)*EKS*(1./H)
    EKKS(2,2,I)=1./(1+6*ALPHA)*EKS*(2./H**2)
    EKKS(2,1,I)=1./(1+6*ALPHA)*EKS*(1./H)
    EKKS(1,4,I)=1./(1+6*ALPHA)*EKS*(-1./H)
    EKKS(1,3,I)=1./(1+6*ALPHA)*EKS*(1./3.-ALPHA)
    EKKS(1,2,I)=1./(1+6*ALPHA)*EKS*(1./H)
    EKKS(1,1,I)=1./(1+6*ALPHA)*EKS*(2./3.+ALPHA)
DO 113 J=1,4
    DO 114 K=1,4
        IF (NS(J,I)*NS(K,I).NE.0) THEN
            EK(NS(J,I),NS(K,I))=EK(NS(J,I),NS(K,I))+EKKS(J,K,I)
```

```

                END IF
114      CONTINUE
113 CONTINUE
112 CONTINUE
! <<<<<<<<STIFFNESS MATRIX
EMY=A_BRC0*EKmFT*BRCFT(II)*32500.*EB
A_BRC=A_BRC0*BRCFT(II)*EKmFT
A_B=A_B0*SFT(II)*EKmFT
SK1=SK10*SK1FT(II)*EKmFT
H_BRC=H_BRC0*HBRCFT(II)

CALL
PRT(H,N,42,62,EMM,EK,TFN,BETAKN,BETAMN,EMEQN,EHEQN,EKFN,EV1N,ESSN,TFIN,SAIN,
EMEQIN,SSS,EKR) ! no BRC
    EK61=EK(61,61)
    EK50=EK(50,50)
    EK62=EK(62,62)
    EK5062=EK(50,62)
    EK6250=EK(62,50)
    EK(61,61)=EK61*1.D5
    EK(50,50)=EK50+SK1*1.D5
    EK(50,62)=EK5062-SK1*1.D5
    EK(62,50)=EK6250-SK1*1.D5
    EK(62,62)=EK62+SK1*1.D5
CALL
PRT(H,N,42,62,EMM,EK,TFR,BETAKR,BETAMR,EMEQR,EHEQR,EKFR,EV1R,ESSR,TFIR,SAIR,E
MEQIR,SSS,EKR) ! rigid BRC
    EK(61,61)=EK61+SK1
    EK(50,50)=EK50+SK1
    EK(50,62)=EK5062-SK1
    EK(62,50)=EK6250-SK1
    EK(62,62)=EK62+SK1
CALL
PRT(H,N,42,62,EMM,EK,TFB,BETAKB,BETAMB,EMEQB,EHEQB,EKFB,EV1B,ESSB,TFIB,SAIB,E
MEQIB,SSS,EKR) ! elastic BRC
    EK(61,61)=EK61

```

```
EK(50,50)=EK50
EK(50,62)=EK5062
EK(62,50)=EK6250
EK(62,62)=EK62

! *****
! SEISMIC EVALUATION (need revision)
! *****

CALL EVAT(GFT,H,H_BRC,A_BRC,A_B,SK1,EMY,UF,QF,EHEQN,EMEQN,EKFN,EKFR,TFN,TEQ)

! DISTRIBUTION OF EVALUATED STORY SHEAR
DO 500 I=1,N
    QFES(I)=ESSN(I)/ESSN(1)*QF
500 CONTINUE

! *****
! STATIC ANALYSIS (need revision)
! *****

! ! SHEAR FORCE - METHOD 1 (obtained from Ai distribution)
! SGM(N)=EMM(N)*9.8*100.0
! DO 310 I=1,N-1
!     SGM(N-I)=SGM(N-I+1)+EMM(N-I)*9.8*100.0
! 310 CONTINUE
!
! DO 311 I=1,N
!     SALP(I)=SGM(I)/SGM(1)
!     CI(I)=1.0+(1.0/SALP(I)**0.5-SALP(I))*2.0*TEQ/(1.0+3.0*TEQ)
!     SSFT(I)=CI(I)*SGM(I)
! 311 CONTINUE
!
! ! SHEAR FORCE - METHOD 2 (obtained from seismic evaluation)
! DO 311 I=1,N
!     SSFT(I)=QFES(I)*1000.
! 311 CONTINUE
```

```
!  
!   EP(N)=SSFT(N)  
!   DO 312 I=1,N-1  
!       EP(I)=SSFT(I)-SSFT(I+1)  
!   312 CONTINUE  
!  
!   CALL MINV(N,EKR,N)  
!   CALL PROG(EKR,EP,SDIS,N,N,1)  
!   CALL PROG(SSS,SDIS,SROT,N2,N,1)  
!   DO 300 I=1,N  
!       SDSRT(I)=SDIS(I)  
!   300 CONTINUE  
!   DO 301 I=1,N2  
!       SDSRT(N+I)=-SROT(I)  
!   301 CONTINUE  
  
! *****  
! DYNAMIC ANALYSIS  
! *****  
  
! >>>>>>>DAMPING MATRIX  
!   DO 116 I=1,62  
!       DO 117 J=1,62  
!           EC(I,J)=EK(I,J)*BETAKB  
! 117 CONTINUE  
!       EC(I,I)=EC(I,I)+EM(I,I)*BETAMB  
! 116 CONTINUE  
! <<<<<<<<DAMPING MATRIX  
  
HK=SK1/(1.0/0.0125-1.0)  
CALL  
NRES(GFT,62,EM,EC,EK,SK1,NNN,DT,DDY,ACC,VEL,DIS,EPS,TOL,H,HK,EMY,HI,BRCE1M,BRC  
E2M)  
  
! *****  
! DATA PROCESS OF DYNAMIC ANALYSIS RESULTS
```



```
! *****
```

```
! MAX DISP,VEL,ACC IN EACH STORY
```

```
DO 201 J=1,62
```

```
    DISMX(J)=MAXVAL(ABS(DIS(J,:)))
```

```
    VELMX(J)=MAXVAL(ABS(VEL(J,:)))
```

```
    ACCMX(J)=MAXVAL(ABS(ACC(J,:)+DDY))
```

```
201 CONTINUE
```

```
! Max Story Drift Ratio
```

```
SDR(1,:)=DIS(1,:)/4.
```

```
SDRMX(1)=MAXVAL(ABS(SDR(1,:)))
```

```
DO 203 J=2,N
```

```
SDR(J,:)=(DIS(J,:)-DIS(J-1,:))/4.
```

```
SDRMX(J)=MAXVAL(ABS(SDR(J,:)))
```

```
203 CONTINUE
```

```
! Residual Story Drift Ratio
```

```
DO 215 J=1,N
```

```
    ReSDR(J)=(MAXVAL(SDR(J,(NT-500):NT))+MINVAL(SDR(J,(NT-500):NT)))/2.0 ! average
```

```
    RaSDR(J)=MAXVAL(SDR(J,(NT-500):NT))-MINVAL(SDR(J,(NT-500):NT)) ! amplitude
```

```
215 CONTINUE
```

! Note: because the stiffness of the moment frame and spine frame don't change during analysis, we can calculate their shear force in the main script, otherwise we should calculate them during each integration step

```
! SHEAR IN SPINE FRAME
```

```
DO 204 I=1,NNN
```

```
SSF(1,I)=EKKS(4,4,1)*DIS(1,I)+EKKS(4,3,1)*DIS(N2,I)+EKKS(4,2,1)*0.+EKKS(4,1,1)*DIS(61,I)
```

```
SSF(11,I)=EKKS(4,4,11)*DIS(11,I)+EKKS(4,3,11)*DIS(N2+11-1,I)+EKKS(4,2,11)*DIS(11-1,I)+EKKS(4,1,11)*DIS(62,I)
```

```
    DO 210 K=2,10
```

```
SSF(K,I)=EKKS(4,4,K)*DIS(K,I)+EKKS(4,3,K)*DIS(N2+K-1,I)+EKKS(4,2,K)*DIS(K-1,I)+EKKS(4,1,K)*DIS(N2+K-2,I)
```

210 CONTINUE

DO 212 K=12,20

SSF(K,I)=EKKS(4,4,K)*DIS(K,I)+EKKS(4,3,K)*DIS(N2+K-1,I)+EKKS(4,2,K)*DIS(K-1,I)+EKKS(4,1,K)*DIS(N2+K-2,I)

212 CONTINUE

204 CONTINUE

DO 205 J=1,N

SSFMX(J)=MAXVAL(ABS(SSF(J,:)))/1000.

205 CONTINUE

! SHEAR IN MOMENT FRAME

DO 206 I=1,NNN

SMF(1,I)=EKKC(4,4,1)*DIS(1,I)+EKKC(4,3,1)*DIS(N+1,I)

DO 211 K=2,N

SMF(K,I)=EKKC(4,4,K)*DIS(K,I)+EKKC(4,3,K)*DIS(N+K,I)+EKKC(4,2,K)*DIS(K-1,I)+EKKC(4,1,K)*DIS(N+K-1,I)

211 CONTINUE

206 CONTINUE

DO 207 J=1,N

SMFMX(J)=MAXVAL(ABS(SMF(J,:)))/1000.

207 CONTINUE

! TOTAL SHEAR

SHEAR=SSF+SMF

DO 202 J=1,N

SHEARMX(J)=MAXVAL(ABS(SHEAR(J,:)))/1000.

202 CONTINUE

! ! DISTRIBUTION OF EVALUATED STORY SHEAR

! DO 212 I=1,N

! QFES(I)=ESSN(I)/ESSN(1)*QF

! 212 CONTINUE

```

!      ! DISTRIBUTION OF EVALUATED STORY DRIFT
!      ESDR(1)=EV1N(1)
!      DO 213 I=2,N
!          ESDR(I)=EV1N(I)-EV1N(I-1)
!      213 CONTINUE
!      ESDRM=MAXVAL(ESDR)
!      DO 214 I=1,N
!          UFES(I)=ESDR(I)/ESDRM*UF
!      214 CONTINUE

!      ! *****
!      ! DATA PROCESS OF STATIC ANALYSIS RESULTS (need revision)
!      ! *****
!      !
!      ! Max Story Drift Ratio
!      SSDR(1)=SDIS(1)/4.
!      DO 302 J=2,N
!          SSDR(J)=(SDIS(J)-SDIS(J-1))/4.
!      302 CONTINUE
!
!      ! SHEAR IN SPINE FRAME
!
SSSF(1)=(EKKS(4,4,1)*SDSRT(1)+EKKS(4,3,1)*SDSRT(N2)+EKKS(4,2,1)*0.+EKKS(4,1,1)*SDSRT(
N3))/1000.
!      DO 303 K=2,N
!
SSSF(K)=(EKKS(4,4,K)*SDSRT(K)+EKKS(4,3,K)*SDSRT(N2+K-1)+EKKS(4,2,K)*SDSRT(K-1)+EK
KS(4,1,K)*SDSRT(N2+K-2))/1000.
!      303 CONTINUE
!
!      ! SHEAR IN MOMENT FRAME
!      SSMF(1)=(EKKC(4,4,1)*SDSRT(1)+EKKC(4,3,1)*SDSRT(N+1))/1000.
!      DO 304 K=2,N
!
SSMF(K)=(EKKC(4,4,K)*SDSRT(K)+EKKC(4,3,K)*SDSRT(N+K)+EKKC(4,2,K)*SDSRT(K-1)+EKK
C(4,1,K)*SDSRT(N+K-1))/1000.

```

```

!      304 CONTINUE
!
!      ! TOTAL SHEAR
!      SSHEAR=SSSF+SSMF
!
!      DO 305 I=1,N
!          SFAL(I)=ABS(SSSF(I)/SSHEAR(I))
!          SFALMX(I)=ABS(SSFMX(I)/SHEARMX(I))
!      305 CONTINUE

! *****
! RECORDER
! *****
OPEN(1,FILE=OFILE(II),STATUS='OLD')
! OPEN(2,FILE=OFILED,STATUS='OLD')
! WRITE(1,502) EKFN, EKFR, EKFB
! ParaResVer2.0:
WRITE(1,502)
SHEARMX,SSFMX,SMFMX,SDRMX,TFN,TFR,TFB,SSHEAR,SSSF,SSMF,UF,QFES
WRITE(1,503) BRCE1M,BRCE2M
! WRITE(2,502) SDR(1,:)
! *****
! SHEARMX(N) dy-ana. total shear
! SSFMX(N) dy-ana. shear in spine frame
! SMFMX(N) dy-ana. shear in moment frame
! SDRMX(N) dy-ana. SDR
! SSHEAR(N) st-ana. total shear
! SSSF(N) st-ana. shear in spine frame
! SSMF(N) st-ana. shear in moment frame
! SSDR(N) st-ana. SDR
! QFES(N) eva. total shear
! UF eva. max. SDR
! TEQ eva. 1st-mode period of whole system at max. deformation
! TFN eigenvalue-ana. 1st-mode period of moment frame only without BRCs
! *****

```

901 CONTINUE

STOP

501 FORMAT(T51,F10.2,I10/(F10.5))

502 FORMAT(F18.8)

503 FORMAT(F15.1)

CLOSE(100)

CLOSE(1)

END

Subroutine file -- NRES.f90 (for Sgt2 spine frame structures)

! *****

! SUBROUTINE FOR NONLINEAR RESPONSE OF MULTI-DOF SYSTEM

! *****

! CODED BY X. CHEN

! N4: DOF

! EM: MASS MATRIX

! EC: DAMPING MATRIX

! EK: INITIAL STIFFNESS MATRIX

! NN: NUMBER OF DATA IN GROUND MOTION

! DT: TIME INTERVAL OF GROUND MOTION

! DDY: GROUND MOTION DATA

! ACC: ABSOLUTE ACCEL RESPONSE

! VEL: RELATIVE VEL RESPONSE

! DIS: RELATIVE DISP RESPONSE

! QY: yielding overturning moment of BRC

! SK1: initial stiffness of BRC

! EPS TOL: Tolerance for norm of disp and norm of residual force

! H: story height

! HK: parameter related with kinematic hardening

! HI: parameter related with isotropic hardening

SUBROUTINE

```
NRES(GFT,N4,EM,EC,EK,SK1,NN,DT,DDY,ACC,VEL,DIS,EPS,TOL,H,HK,QY,HI,BRCE1M,BRCE2
M)
```

```
DIMENSION
```

```
EM(N4,N4),EK(N4,N4),EC(N4,N4),DDY(NN),ACC(N4,NN),VEL(N4,NN),DIS(N4,NN),BRCE1(NN),
BRCE2(NN),BRCR1(NN),BRCR2(NN),BRCQ1(NN),BRCQ2(NN),BRCE1(NN),BRCE2(NN)
```

```
DIMENSION DDELX(N4),DDELR(N4),DELX(N4),RR1(N4),RR2(N4),RR3(N4),EK1(N4,N4)
```

```
! >>>>>>>INITIALIZATION
```

```
DO 120 I=1,N4
```

```
    ACC(I,1)=-DDY(1)*GFT
```

```
    VEL(I,1)=0.
```

```
    DIS(I,1)=0.
```

```
DO 110 J=1,N4
```

```
    EK1(I,J)=0.    ! Stiffness matrix
```

```
110 CONTINUE
```

```
120 CONTINUE
```

```
VK1=SK1
```

```
VK2=SK1    ! LOCAL STIFFNESS -- overturning stiffness
```

```
BRCR1(1)=0.
```

```
BRCQ1(1)=0.
```

```
BRCR2(1)=0.
```

```
BRCQ2(1)=0.
```

```
BRCE1(1)=0.
```

```
BRCE2(1)=0.
```

```
QB10=0.
```

```
UP10=0.
```

```
AH10=0.
```

```
QB20=0.
```

```
UP20=0.
```

```
AH20=0.
```

```
! <<<<<<<<INITIALIZATION
```

```
! *****
```

```
DO 290 M=2,NN    ! For nonlinear analysis, start integration here
```

```
! *****
```

! >>>>>>>Initialization in each step

DO 420 I=1,N4

DELX(I)=0.

DIS(I,M)=DIS(I,M-1)

VEL(I,M)=-VEL(I,M-1)

ACC(I,M)=-4./DT*VEL(I,M-1)-ACC(I,M-1)

420 CONTINUE

BRCQ1(M)=BRCQ1(M-1)

BRCQ2(M)=BRCQ2(M-1)

KI=0 ! Set iteration counter KI

! <<<<<<<Initialization in each step

! *****

! Iteration Start

! *****

DO 1234 !STIFFNESS UPDATES DURING ITERATION

! >>>>>>>Formating EFFECTIVE STIFFNESS MATRIX

DO 140 I=1,N4

DO 320 J=1,N4

EK1(I,J)=EK(I,J) ! STORE EKR INTO EK1, LATER CHANGE EK1 INTO EFFECTVIE
ETIFFNESS MATRIX

320 CONTINUE

140 CONTINUE

EK1(61,61)=EK(61,61)+VK1

EK1(50,50)=EK(50,50)+VK2

EK1(50,62)=EK(50,62)-VK2

EK1(62,50)=EK(62,50)-VK2

EK1(62,62)=EK(62,62)+VK2

DO 160 I=1,N4

DO 150 J=1,N4

EK1(I,J)=EK1(I,J)+4./DT/DT*EM(I,J)+2./DT*EC(I,J)

150 CONTINUE

160 CONTINUE

! <<<<<<<<Formating EFFECTIVE STIFFNESS MATRIX

! >>>>>>>>Formating EFFECTIVE LOAD VECTOR, note: should be put after stiffness updating,
because EK2 is used to get RR1

CALL PROG(EK,DIS(:,M),RR1,N4,N4,1)

CALL PROG(EC,VEL(:,M),RR2,N4,N4,1)

CALL PROG(EM,ACC(:,M),RR3,N4,N4,1)

RNM=0.

RR1(61)=RR1(61)+BRCQ1(M)

RR1(62)=RR1(62)+BRCQ2(M)

RR1(50)=RR1(50)-BRCQ2(M)

DO 410 I=1,N4

DDELRI=-DDY(M)*GFT*EM(I,I)-(RR1(I)+RR2(I)+RR3(I)) ! (k+1)-th residual force vector

RNM=RNM+DDELRI*DDELRI

410 CONTINUE

RNM=SQRT(RNM/N4)

IF((RNM.LE.TOL).AND.(KI.GT.0)) GOTO 4321

! <<<<<<<<Formating EFFECTIVE LOAD VECTOR

! >>>>>>>>Solve INCREMENTAL DISP

CALL CHOL(N4,EK1,DDELRI,DDELXI,N4,0)

DNM=0.

DO 710 I=1,N4

DNM=DNM+DDELXI(I)*DDELXI(I)

710 CONTINUE

DNM=SQRT(DNM/N4)

IF((DNM.LE.TOL).AND.(KI.GT.0)) GOTO 4321

! <<<<<<<<Solve INCREMENTAL DISP

! >>>>>>>>Solve RELATIVE ACCEL, VEL, & DISP

DO 190 I=1,N4

DELXI(I)=DELXI(I)+DDELXI(I)

DIS(I,M)=DIS(I,M-1)+DELXI(I)

VEL(I,M)=2./DT*DELXI(I)-VEL(I,M-1)

ACC(I,M)=4./DT/DT*DELXI(I)-4./DT*VEL(I,M-1)-ACC(I,M-1)

190 CONTINUE


```
! <<<<<<<<Solve RELATIVE ACCEL, VEL, & DISP

! >>>>>>>>STATE DETERMINATION
BRCR1(M)=DIS(61,M)
QB1=QB10
UP1=UP10
AH1=AH10
CALL STDM(BRCR1(M),UP1,QB1,SK1,ET1,HI,HK,QY,BRCQ1(M),AH1)
VK1=ET1

BRCR2(M)=DIS(62,M)-DIS(50,M)
QB2=QB20
UP2=UP20
AH2=AH20
CALL STDM(BRCR2(M),UP2,QB2,SK1,ET2,HI,HK,QY,BRCQ2(M),AH2)
VK2=ET2

KI=KI+1
1234 CONTINUE ! Go to next iteration

4321 QB10=QB1
      UP10=UP1
      AH10=AH1
      QB20=QB2
      UP20=UP2
      AH20=AH2
!if (M<254) goto 290
!us=U
BRCE1(M)=(BRCQ1(M)+BRCQ1(M-1))/2.0*(BRCR1(M)-BRCR1(M-1))+BRCE1(M-1)
BRCE2(M)=(BRCQ2(M)+BRCQ2(M-1))/2.0*(BRCR2(M)-BRCR2(M-1))+BRCE2(M-1)
290 CONTINUE ! Go to next integration step
BRCE1M=BRCE1(NN)
BRCE2M=BRCE2(NN)
BRCEM=BRCE1(NN)+BRCE2(NN)
! OPEN(14,FILE='BRCR1.TXT',STATUS='OLD')
! OPEN(15,FILE='BRCE1.TXT',STATUS='OLD')
```

```
! OPEN(16,FILE='BRCE2.TXT',STATUS='OLD')
! WRITE(14,1014) BRCE1    !ROTATION OF THE BOTTOM OF SPINE FRAME
! WRITE(15,1015) BRCE1    !BENDING MOMENT OF THE BOTTOM HINGE
! WRITE(16,1015) BRCE2
! 1014 FORMAT(F11.8)
! 1015 FORMAT(F15.1)
RETURN
END
```


本論文に関連して発表した論文

【審査付論文】

第2章：

- 1) 竹内 徹, 陳 星辰, 松井良太：種々のエネルギー吸収部材付き心棒架構の耐震性能, 『日本建築学会構造系論文集』, Vol. 79, No. 706, pp.1941-1949, 2014.12
- 2) T. Takeuchi, X. Chen, R. Matsui: Seismic performance of controlled spine frames with energy-dissipating members, *Journal of Constructional Steel Research*, Vol.115, pp.51-65, 2015.11

第3章, 第4章：

- 3) X. Chen, T. Takeuchi, R. Matsui: Simplified design procedure for controlled spine frames with energy-dissipating members, *Journal of Constructional Steel Research*, Vol.135, pp.242-252, 2017.5

第5章, 第6章：

- 4) X. Chen, T. Takeuchi, R. Matsui: Seismic performance and evaluation of controlled spine frames applied in high-rise buildings, *Journal of Constructional Steel Research*, 2017 (Submitted, under review)

【国際会議】

- 1) X. Chen, T. Takeuchi, R. Matsui: Seismic Performance of various spine frames with energy dissipation members, *8th STESSA Conference on Behavior of Steel Structures in Seismic Areas*, Shanghai, 2015.7
- 2) X. Chen, T. Takeuchi, R. Matsui: Seismic design for controlled spine frames with energy-dissipating members, *2nd Joint Workshop between Tokyo Institute of Technology and Tongji University*, Shanghai, 2015.6
- 3) X. Chen, T. Takeuchi, R. Matsui: Seismic performance of various spine frames with energy dissipation members, *5th Asia Conference on Earthquake Engineering*, Taipei, 2014.10
- 4) X. Chen, T. Takeuchi, R. Matsui: Seismic performance of controlled spine frames with energy-dissipating members, *1st Joint Workshop between Tokyo Institute of Technology and Tongji University*, Tokyo, 2014.7 (Best Presentation Award)

【口頭発表】

- 1) 陳 星辰, 竹内 徹, 松井 良太：種々のエネルギー吸収部材付き心棒架構の耐震性能, 『鋼構造シンポジウム, 鋼構造年次論文報告集』, 日本鋼構造協会, Vol. 22, pp. 222-228, 2014.11
- 2) 岡田康平, 陳 星辰, 竹内徹, 松井良太：種々のエネルギー吸収部材付き心棒架構の耐震性能 その1 設計用入力地震動に対する耐震性能, 『2015 年度 日本建築学会大会(関東), 日本建築学会学術講演梗概集 C-1 分冊 構造 III』, 日本建築学会, pp. 1203-1204, 2015.9

- 3) 陳 星辰, 岡田康平, 竹内徹, 松井良太: 種々のエネルギー吸収部材付き心棒架構の耐震性能 その 2 過大地震入力および低耐力層を持つ架構に対するロバスト性, 『2015 年度 日本建築学会大会(関東), 日本建築学会学術講演梗概集 C-1 分冊 構造 III』, 日本建築学会, pp. 1205-1206, 2015.9
- 4) X. Chen, R. Matsui, T. Takeuchi: Simplified dual multi-degree-of-freedom (DMD) model for controlled spine frame structures, 『2016 年度 日本建築学会大会(九州), 日本建築学会学術講演梗概集 C-1 分冊 構造 III』, 日本建築学会, pp. 637-638, 2016.8
- 5) X. Chen, R. Matsui, T. Takeuchi: Design procedure utilizing single-degree-of-freedom models for controlled spine frames, 『2017 年度 日本建築学会大会(中国) 』, 2017.8

その他の発表論文

【審査付論文】

- 1) X. Ji, H. Kang, X. Chen, J. Qian: Seismic behavior and strength capacity of steel tube-reinforced concrete composite columns. *Earthquake Engineering and Structural Dynamics*, Vol. 43(4), pp.487-505, 2014.

【口頭発表】

- 1) 陳 星辰, 松井 良太, 竹内 徹, 得能将紀: 部材破断を考慮した漸増動的地震応答解析による制振構造の耐震性能: その 2 部材損傷度に着目した耐震性能, 『2013 年度 日本建築学会大会(北海道), 日本建築学会学術講演梗概集 C-1 分冊 構造 III』, 日本建築学会, pp. 1001-1002, 2013.
- 2) 陳 星辰, 堀内 健太郎, 竹内 徹, 松井 良太, 小河 利行, 今村 晃: 鋼管部材の座屈および破断を考慮したトラス鉄塔の崩壊機構: その 2 IDA によるトラス鉄塔の崩壊機構, 『2014 年度 日本建築学会大会(関西), 日本建築学会学術講演梗概集 C-1 分冊 構造 III』, 日本建築学会, pp. 891-892, 2014.